Flavin-Mediated Bioorthogonal Catalysis for Drug Activation

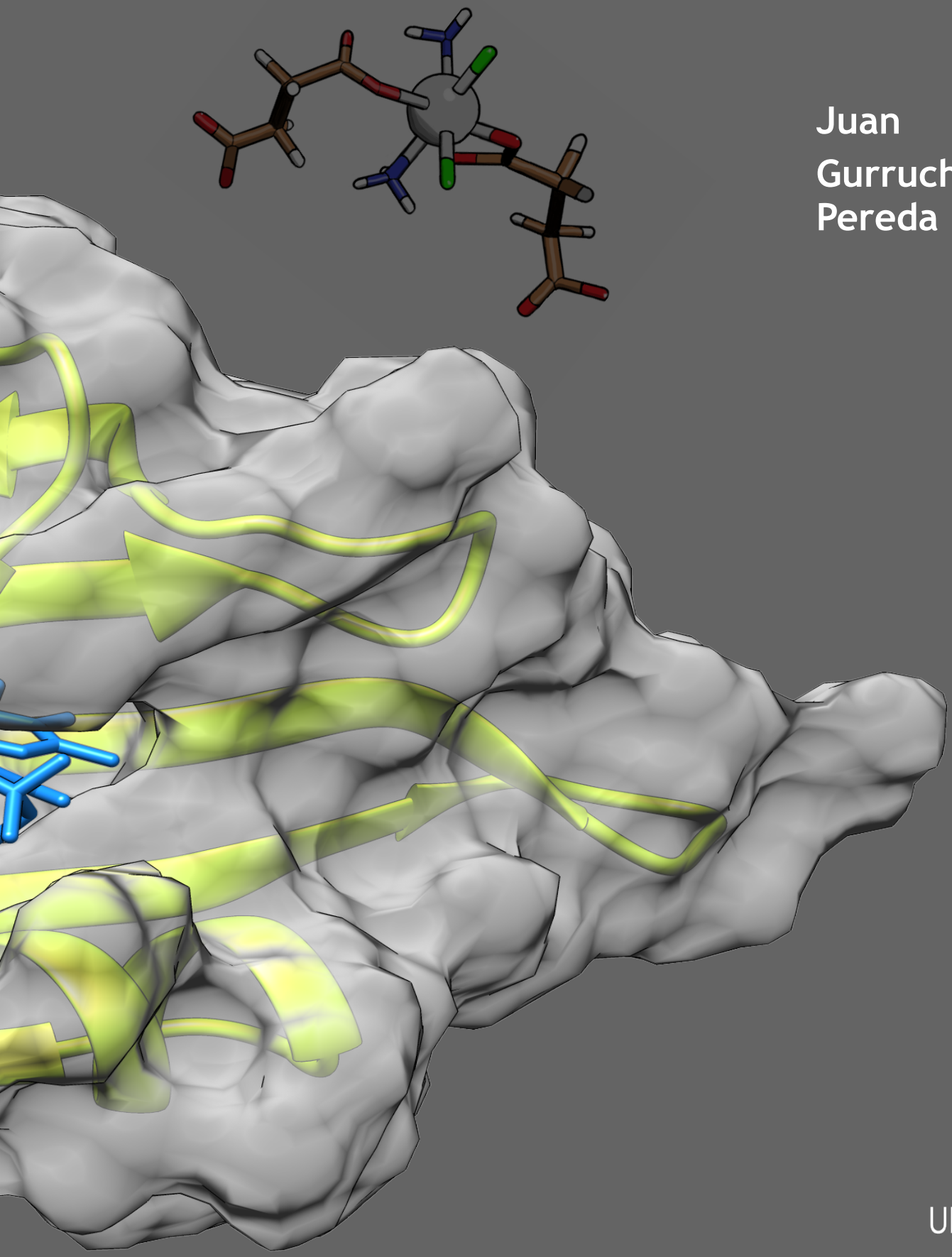

Juan Gurruchaga Pereda

eman ta zabal zazu
UPV EHU

eman ta zabal zazu

Universidad del País Vasco

Euskal Herriko Unibertsitatea

Flavin-Mediated Bioorthogonal Catalysis for Drug Activation

Doctoral Thesis Juan Gurruchaga Pereda

Thesis Supervisors Prof. Luca Salassa

Prof. Aitziber L. Cortajarena

Donostia, 2021

Flavin-Mediated Bioorthogonal Catalysis for Drug Activation

PhD Thesis

JUAN GURRUCHAGA PEREDA

Donostia, 2021

Thesis Supervisors Prof. Luca Salassa
Prof. Aitziber L. Cortajarena

University Tutor Xabier Lopez Pestaña

Table of contents

Summary

Metal catalysis applied to chemotherapy has emerged as an promising option to avoid drawbacks and side effects associated to non-specific drugs. The amplification effect and high selectivity that are intrinsic of many non-natural catalytic reactions provide interesting tools to improve the control over the effects of drugs in biological systems.
The capacity of non-natural reactions to take place in living biological systems without interfering with the normal functions of the host, is designated as bioorthogonal. During the development of the bioorthogonality concept, the combination with metal-based catalysis was explored, giving rise to two main research areas:

The use of metallodrugs as catalysts to induce alterations of relevant biomolecules. Generally, catalytic metallodrugs are able to perform the conversion of several biomolecules and thus, low concentrations of catalyst are sufficient to prompt a harmful response in cells. The toxicity and anticancer action is hence triggered by the degradation of important biomolecules or by the alteration of molecules responsible of cellular homeostasis maintenance.

Metal-based catalysis for prodrug activation. Typically, transition metal catalysts perform the chemical conversion of an inert drug into its cytotoxic counterpart. Within this approach the generation of toxic species occurs in the surroundings of the catalyst, hence favoring the localization of the cellular damage in a specific tissue or organ.

In this thesis, I have investigated a new type of catalytic reactions, in which ***metal complexes are used as substrates instead as catalysts for the bioorthogonal photocatalytic activation of anticancer Pt^{IV} prodrugs***. In this catalytic approach, the photochemical features of flavins are exploited to activate metal prodrugs using light with low-energy wavelengths. I have studied in detail the catalytic mechanism of these reactions, identifying the main catalytic species involved in the reduction of Pt^{IV} complexes. I have also evaluated how subtle changes in the catalyst structure (free flavins and a flavin-containing protein) affect the catalytic performance, rationalizing the differences observed. In addition, I explored the combination of the flavin-catalyzed activation of Pt^{IV} prodrugs with the Pd-triggered deprotection of 5-fluoracil as a new strategy for the bioorthogonal and concurrent application of clinically approved chemotherapeutics.

The first two chapters of this thesis portray the state of the art of my research work, while the following three chapters describe the experimental work that I realized during my Ph.D.

Chapter 1 summarizes the most representative examples on the research of photoactivatable platinum anticancer agents. Within the chapter, I described chronologically, the use of light to improve the control over the toxic features of Pt

complexes, since the finding of Rosenberg from the late 60´s up to date. I concluded the chapter, highlighting some of the most modern and interesting drug delivery and activation strategies.

"Anticancer platinum agents and light" Gurruchaga-Pereda, J.; Martinez, Á.; Terenzi, A.; Salassa, L.; Inorg. Chim. Acta, 2019, 495, 118981.

Chapter 2 reviews the application of bioorthogonal metal-based catalysis for chemotherapeutic purposes. In the chapter, I aimed at highlighting the main difference between existing catalytic strategies. I organized the discussion in three sections: the metal complexes that target relevant biomolecules involved in cellular homeostasis, the activation of inert prodrugs by heterogenous metal catalysts, and the bioorthogonal photocatalytic activation in which Pt^{IV} prodrugs are used as unusual substrates.

Chapter 3 studies in detail the mechanistic details of the flavin-assisted photocatalytic activation of Pt^{IV} substrates. The scope of catalysts and substrates was explored by the use of four flavins, namely, riboflavin (Rf), flavin mononucleotide (FMN), tetra-O-acetyl riboflavin (TARF) and lumiflavin (Lf) and the flavoprotein miniSOG (mini Singlet Oxygen Generator), together with a panel of four Pt^{IV} prodrugs. Reduced flavin species were isolated and identified as responsible for the catalytic conversion of Pt^{IV} prodrugs into Pt^{II} drugs

"Flavin Bioorthogonal Photocatalysis Toward Platinum Substrates" Gurruchaga-Pereda, J.; Martínez-Martínez, V.; Rezabal, E.; Lopez, X.; Garino, C.; Mancin, F.; Cortajarena, A. L.; Salassa, L., ACS Catal. 2020, 10, 187-196.

Chapter 4 explores the application of site-direct mutagenesis for tuning the photocatalytic features of the miniSOG flavoprotein towards Pt^{IV} substrates. The catalytic properties of Q103V, Q50E and Q50W mutants were compared with respect to the wild type (WT), observing that the longest triplet excited-state lifetime of the Q103V mutants resulted in an enhancement of the photocatalytic conversion of two model Pt^{IV} prodrugs.

"Enhancing The Photocatalytic Conversion Of Pt(IV) Substrates By Flavoprotein Engineering" Gurruchaga-Pereda, J.; Martínez-Martínez, V.; Formoso, E.; Azpitarte, O.; Rezabal, E.; Lopez, X.; Cortajarena, L. A.; Salassa, L., J. Phys. Chem. Lett. 2021, 12, 4504–4508.

Chapter 5 investigates the use of two independent bioorthogonal reactions to switch on the toxic effect of two separate anticancer prodrugs by a single heterogeneous biocompatible platform. I combined the Pd-based bioorthogonal depropargylation described by Prof. Unciti-Broceta (University of Edinburgh) with our flavin-assisted photocatalytic reduction of Pt prodrugs. The dual bioorthogonal cleavage of the propargyl

protected 5-fluorouracil prodrug by Pd nanoparticles, and the TARF-prompted reduction of a model Pt^{IV} prodrug. During the thesis, this strategy was tested in the IGROV-1 (human ovarian cancer) cell line observing a notable cell viability reduction. However, the combination of the prodrugs did not enhance the antiproliferative effect of each component alone.

In addition to the previously mentioned work, during my research I collaborated to different research projects and reviews articles. As a result of this cooperative efforts, I published one additional review:.

"Catalysis Concepts In Medicinal Inorganic Chemistry" Alonso-de Castro, S.; Terenzi, A.; Gurruchaga-Pereda, J.; Salassa, L., Chem. Eur. J., 2019, 25, 6651-6660.

1

Anticancer Platinum Agents and Light

Part of the work described in this chapter has been published in *Inorg. Chim. Acta*, 2019, 495, 118981 (authors: Gurruchaga-Pereda, J.; Martínez, Á.; Terenzi, A.; Salassa, L.).

1.1 Introduction

The relationship between Pt anticancer compounds and light dates back to the discovery of cisplatin. After identifying that Pt species were responsible for the abnormal filamentous growth of *Escherichia coli* bacteria exposed to electric fields,[1] Rosenberg and collaborators demonstrated that neutral *cis*-$[PtCl_4(NH_3)_2]$ obtained from UV-irradiated $(NH_4)_2[PtCl_6]$ solutions was highly effective in inhibiting cell division.[2,3] This initial discovery confirmed the potential of Pt complexes as anticancer agents and prompted the identification of cisplatin as lead drug.[4–6]

Later, the field focused on other aspects of the biological chemistry of Pt complexes and the use of light was set aside for several years. However, investigators turned back to explore how photochemistry could affect the cytotoxicity profile of Pt agents once the concept of Pt^{IV} prodrugs was introduced to reduce side effects associated with Pt drugs. Part of these efforts were also motivated by the clinical approval of the first photodynamic therapy agent (photofrin) in 1993.[7]

This chapter aims at summarizing some of the most important achievements in the development of photoactivatable Pt anticancer agents. Three main sections constitute this contribution. In the first two parts, we discuss the effects of light on the biology of Pt^{II} and Pt^{IV} anticancer complexes. In the third part, we highlight innovative delivery and photochemistry strategies developed to trigger the biological activity of Pt^{IV} compounds. It is worth pointing out that the biological activity of irradiated Pt compounds can derive either from an enhancement of the effect of the light provoked by the metal species which increases radical production (metal-enhanced phototoxicity) or from the photoactivation of the metal complex itself (photo-enhanced toxicity). In this review the term phototoxicity will encompass both aspects. For a better understanding of the systems described herein, we start with a brief description of the electronic properties of Pt^{II} and Pt^{IV} complexes. To this aim, we return to Rosenberg's original studies and take cisplatin and *cis*-$[PtCl_4(NH_3)_2]$ as representative models.

1.2 The photochemistry of Pt^{II} and Pt^{IV} complexes

The photochemistry of Pt^{II} and Pt^{IV} complexes of interest in cancer therapy generally involves photodissociation (Pt^{II} and Pt^{IV}) and/or photoreduction (Pt^{IV}) reactions. Such complexes are often non-luminescent and therefore their excited state properties are difficult to characterize via standard spectroscopic techniques. The lack of marked spectroscopic features requires that ultrafast techniques (*e.g.* time-resolved absorption and infrared spectroscopy) are employed for understanding their excited state evolution, as recently reported for a number of Pt^{IV} salts[8,9] and complexes,[10] including azido compounds.[11,12] Nonetheless, several pioneering studies are available in the literature of the 60-90s on the photochemistry of Pt complexes with potential in chemotherapy. Conversely,

Pt^{II} complexes bearing aromatic diamine ligands of the 2,2'-bipyridine type are highly emissive and their photophysics and photochemistry have been extensively investigated for applications in sensing, catalysis and biology.[13]

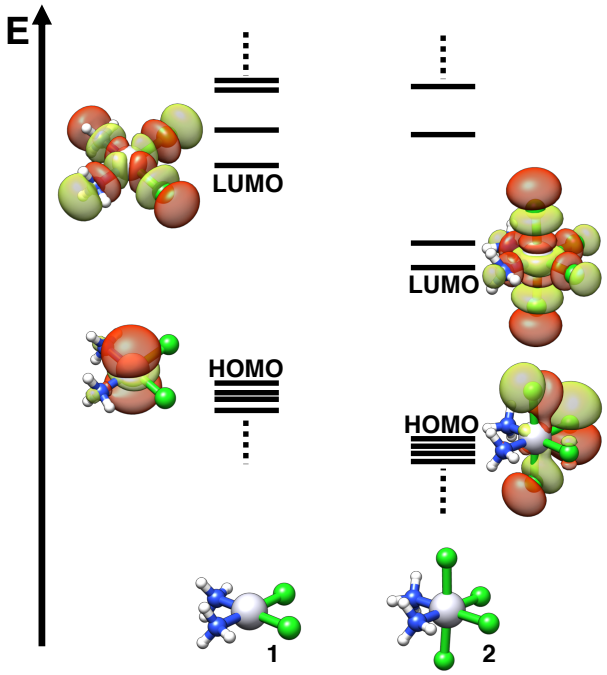

Figure 1. Schematic electronic structure and selected frontiers orbitals of (**1**) *cis*-$[Pt^{II}(NH_3)_2Cl_2]$ and (**2**) *cis*-$[Pt^{IV}(NH_3)_2Cl_4]$ calculated with DFT (density functional theory) at the SDD level.[14] Atom color code: gray = Pt; green = Cl; blue = N; white = H. HOMO = highest occupied molecular orbital; LUMO = lowest unoccupied molecular orbital.

As shown for *cis*-$Pt^{II}(NH_3)_2Cl_2$ (cisplatin, **1**) and *cis*-$[PtCl_4(NH_3)_2]$ (**2**), the electronic structure of Pt^{II} and Pt^{IV} complexes displays LUMOs that have σ-antibonding character (Figure 1). Upon light excitation, these orbitals are populated to afford dissociative excited states that trigger the reactivity of the complexes. Excited states in **1**, **2** and other related systems have ligand-to-metal charge transfer (LMCT) or ligand-field (LF or d-d) nature. LMCT transitions are usually associated with photoreduction and ligand substitution (depending on the ligands), while LF transitions lead to photoisomerization and photoracemization. Another characteristic trait of Pt^{II} and Pt^{IV} complexes such as **1** and **2** is the large HOMO-LUMO energy gap, which results in absorption bands at wavelengths rarely above 400 nm.

In principle, the judicious design of a photoactivatable Pt complex must take into account the stability in the dark and toward biological reductants of the prodrug, but also anticipate its photochemistry. In the case of Pt^{II} and Pt^{IV} complexes, this is not trivial and the photoproducts are often a mixture of substitution, reduction and isomerization species.

1.3 Photoactive Pt^{II} complexes

Direct irradiation of known Pt^{II} anticancer complexes proved to be moderately useful to increase their biologic activity. Brabec and coworkers showed that UV irradiation (up to 5 hours, 365 nm, 4.3 mW·cm^{-2}) of carboplatin increased its DNA binding abilities to levels comparable with cisplatin.[15] Similarly, light irradiation (365 nm, 50 min, 1.77 mW·cm^{-2}) of the inactive transplatin switched on its antiproliferative activity prompting DNA inter-strand and DNA-protein crosslinking.[16] Quiroga, Malina and Bednarski demonstrated that low-energy irradiation at 350 nm (0.12 mW·cm^{-2}) of *trans*-diiodido complexes bearing isopropyl, dimethyl or methylamines produced a 1.5–3-fold enhancement in cytotoxicity when compared with dark conditions. On the contrary, no biological effect was found for the *cis* isomer of the isopropylamine derivative under the same conditions.[17]

The limited biological effects observed under high energy and long irradiation regimes have hampered the use of light with cisplatin-like drugs. For this reason, research focus was set on to the design of Pt^{II} complexes coordinating photoactive ligands, capable of behaving as PDT photosensitizers for the generation of singlet oxygen and other reactive oxygen species (ROS) upon light excitation. It is worth mentioning that those complexes, in which the coordination of the sensitizer to the metal center resulted in better properties than the individual components combined, are the so-called "dual agents", whereas complexes that release active species after irradiation are named "cage compounds".

1.3.1 Light-activatable Pt^{II} complexes as PDT agents and/or cage compounds

Brabec, Kašpárková and coworkers studied the mechanism of action of a cisplatin analogue where one of the ammines was substituted by a 1-methyl-7-azaindole moiety (**3**, Figure 2).

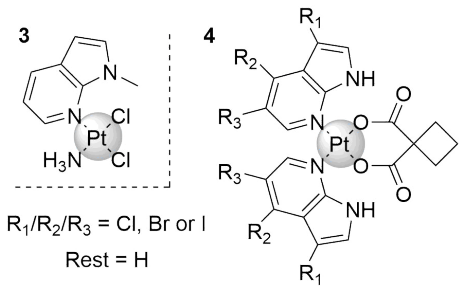

Figure 2. Chemical structure of anticancer azaindole-Pt^{II} complexes.

Compound **3** showed no toxicity in the dark and micromolar IC_{50} values in cisplatin-sensitive ovarian carcinoma (A2780) cells and cisplatin-resistant human prostate adenocarcinoma (LNCaP) cells when irradiated at 365 nm (3.5 mW·cm^{-2}). The complex acted as dual antitumoral agent, with phototoxicity arising from the formation of singlet oxygen and DNA inter-strand crosslinking.[18] Exploiting the same mechanism, complex **4** (Figure 2), a

carboplatin derivative with halo-substituted 7-azaindoles, showed phototoxicity similar to **3** in cisplatin-sensitive and resistant cell lines under irradiation.[19]

Chakravarty and coworkers attached Pt^{II} centers to catecholate or diketonate ligands functionalized with fluorescent anthracene and pyrene moieties (Figure 3). In skin keratinocytes HaCaT and breast cancer MCF-7 cells, catecholate complexes **5** and **6** showed increased toxicity in the dark (IC_{50} ~ 30-50 µM) and similar IC_{50} values (5-20 µM) under light irradiation (400-700 nm, 10 $J \cdot cm^{-2}$) compared with their corresponding ligands alone. Data showed phototoxicity arose from apoptosis induced by generation of ROS, whereas the causes of the higher dark toxicity were not conclusive. In the absence of light, neither hydrolysis of the complex nor coordination to 5'-guanosine monophosphate (GMP) was observed in buffer; however, ligand release was confirmed in the dark in the presence of an excess of glutathione (GSH).[20] Acetylacetonate derivatives **7** and **8** behaved similarly to **5** and **6**; they were stable in solution over 24 hours but released the corresponding ligands when exposed to excess GSH. Due to the presence of pyrene or anthracene, they bound DNA in an intercalative mode and subsequently induced damage upon light irradiation. Complexes **7** and **8** displayed similar phototoxicity values and mechanism of action to those of **5** and **6** in HaCaT cells, inducing apoptosis upon generation of ROS (Figure 3).[21]

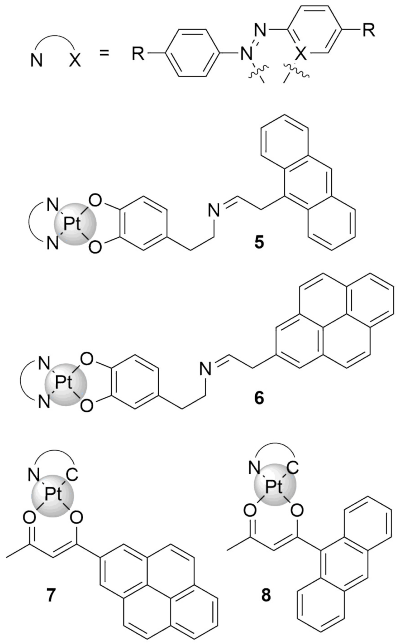

Figure 3. Chemical structure of catecholate- (**5**, **6**) and acetylacetonate-Pt^{II} (**7**, **8**) fluorescent conjugates. **5** and **6**: X=N, R=H; **7** and **8**: X=C, R=OMe.

Chakravarty and coworkers also reported a diammineplatinum complex coordinating curcumin as photoactive moiety (Figure 4). This natural product is a potent anti-inflammatory and anticancer agent, yet prone to hydrolysis and fast metabolization. The Pt^{II} derivative named Platicur (**9**) was designed to protect curcumin from hydrolysis while simultaneously allowing its controlled release and the generation of Pt^{II} species capable of binding DNA upon irradiation with visible light (400–700 nm, 10 $J \cdot cm^{-2}$). Complex **9** was non-toxic in the dark (IC_{50} > 200 µM) and showed 15 µM IC_{50} in HaCaT cells when irradiated,

similarly to curcumin alone, while the value increased to 30 μM in immortalized non-transformed human peripheral lung epithelial (HPL1D) cells.[22] The curcumin derivative **10**, coordinating a diazobenzene ligand instead of ammines, displayed phototoxicity comparable to **9** (11 μM IC_{50} in HaCaT cells, 400-700 nm, 10 $J \cdot cm^{-2}$) but also presented higher toxicity in the dark (56 μM IC_{50}). Toxicity for these derivatives could be ascribed principally to generation of hydroxyl radicals, although singlet oxygen formation was also observed (Figure 4).[21]

Near-infrared (NIR) light (700-1000 nm) penetrates deeper into tissues and causes less damage than visible or UV light. With the aim of developing agents that could be activated in the NIR window, the group of Hart synthesized a NIR light-sensitive (720–740 nm, 3.5 $mW \cdot cm^{-2}$) prodrug by coordinating the dye IR797 to a Pt diammino fragment (**11**). Under NIR light, **11** behaved as a dual-agent, generating singlet oxygen and photoreleasing the Pt-aqua complex *cis*-$[Pt(NH_3)_2(H_2O)_2]^{2+}$. Although the compound showed high dark toxicity in cervix and breast cancer C-33 and MCF-7 cells (8-18 μM), IC_{50} values decreased to nanomolar upon light activation (0.14-0.65 μM), corresponding to phototoxicity indexes of 57 and 27 respectively.[23]

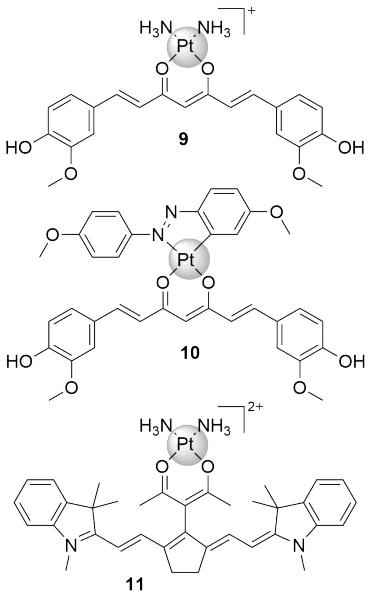

Figure 4. Chemical structure of platicur (**9**), Pt-curcumine acetoacetate (**10**) and NIR active Pt-IR797 conjugate (**11**).

A major limitation of classical PDT systems is the dependency of molecular oxygen to generate reactive oxygen species.[7] This is a fundamental problem in tumors tissues, where oxygen levels are typically much lower than in healthy ones. Adopting an unconventional approach, Palacios and coworkers recently reported a squaramide-based drug precursor (**12**, Figure 5) that displayed phototoxicity only under hypoxic conditions (IC_{50} 69 μM in cisplatin resistant human adenocarcinoma HeLa cells). The squaramide photocleavage mechanism was responsible for the different toxicity. In the absence of oxygen, it generated amino-sulfide fragments that led to the cytotoxic complex **13** (Figure 5). On the contrary,

oxidation of these ligands under normoxia conditions led to the generation of non-toxic complex **14** (Figure 5).[24]

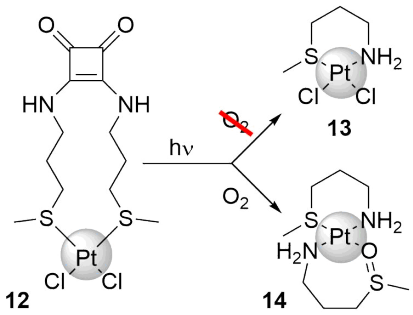

Figure 5. Chemical structure of the squaramide complex **12** and its photoproducts under hypoxic (**13**) or normoxia (**14**) conditions.

1.3.2 Pt^{II} with heterometallic functional units

Besides the use of photoactive ligands, Pt^{II} agents have been coordinated to other metal scaffolds in order to obtain improved photophysical and photochemical properties.

Chakravarty and coworkers have extensively explored this approach, designing heterobimetallic complexes which combine Pt^{II} centers with photoactive ferrocene and DNA-intercalating N,N,N-pincer ligands (Figure 6). The first generation of this family was based on polypyridyl ligands derived from phenantroline (phen) and dipyridophenazine (dppz) (Figure 6). Phen derivatives **15a** and **15b** showed poor or no cytotoxicity either in the dark or under irradiation (365 nm, 6 W), whereas the dppz chlorido **16a** showed to be toxic in the low micromolar range (2-3 μM IC_{50}) in HeLa and MCF-7 and moderately effective (19 μM IC_{50}) in MCF-10A cells when irradiated (365 nm, 6 W). Compound **16a** however also showed modest toxicity in the dark in HeLa cells (18 μM IC_{50}). Substitution of the chloride by ferrocene (**16b**) translated into higher phototoxicity in MCF-10A cells (13 μM IC_{50}) but lower in HeLa and MCF-7 cells (13-16 μM IC_{50}), whereas dark toxicity decreased in all cases (> 25 μM).[25]

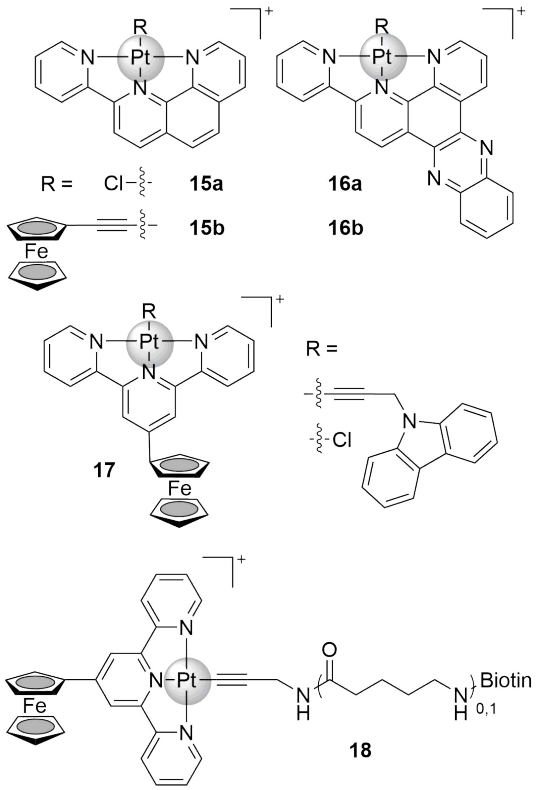

Figure 6. Chemical library of antitumoral ferrocenyl phen (**15**), dppz (**16**) or tpy (**17**, **18**) pincer complexes.

To improve these systems, they prepared complexes with a ferrocene-terpyridine ligand (**17**), selected due to their excellent redox and photophysical properties and the high toxicity of terpyridine-Pt^{II} complexes. They showed good toxicity (10-18 µM IC_{50}) under visible light irradiation (400-700 nm, 2.4 $mW \cdot cm^{-2}$) in HaCaT cells and low toxicity (> 65 µM) in the dark. Although entering the cell nucleus, these compounds showed poor DNA intercalating abilities.[26] In a recent study, a biotin unit was attached onto analogue compounds (**18**) to increase the uptake *via* the biotin-specific streptavidin receptors, known to be overexpressed in cancer cells. Despite the high cell uptake, they retained similar dark/light toxicity profiles (IC_{50} 8-17 µM under irradiation, > 50 µM in the dark) in human breast carcinoma cancer cells (BT474) but IC_{50} values under irradiation increased above 40 µM in human normal breast epithelial HBL-100 cells.[27]

The combination of platinum with heterometallic functional units has also been exploited to produce effects that go beyond PDT (Figure 7). For instance, several optical or radioactive systems were designed to integrate imaging properties and anticancer activity. The combination of a diamminochloridoplatinate unit with BODIPY led to the development of highly photo-cytotoxic and emissive theranostic agents (**19a** and **19b**). By monitoring its emission, **19a** was found to preferentially localize in the mitochondria. Both **19a** and **19b** were essentially non-toxic in the dark and induced apoptotic death under irradiation with visible light (400-700 nm, 10 $J \cdot cm^{-2}$) with IC_{50} values of 100-150 nM in HaCaT and 3-6 µM in MCF-7 cells.[28] DNA binding studies with model 9-ethylguanine showed unconventional monosubstitution of one of the ammines instead of the chloride atoms. Guo, He and

coworkers proved, with a closely related structure (**20**), that a different linkage between Pt and BODIPY units improved the ROS production and intracellular accumulation when compared to BODIPY alone. This was explained in terms of cell membrane damage after short irradiation periods (5 min, 532 nm, 3.5 $mW \cdot cm^{-2}$). IC_{50} values of separated components were all above 40 μM while the Pt-BODIPY conjugate **20** displayed values in the 4–10 μM range for a number of cancer cell lines upon light activation.[29]

The natural emission of an Eu complex upon photodissociation of the Pt center was exploited to build a traceable and controllable cisplatin-delivery molecule (**21**). Complex **21** was non-toxic and non-emissive, but underwent photocleavage upon two-photon excitation (730 nm), simultaneously releasing *cis*-$[Pt(NH_3)_2(H_2O)Cl]^+$ and the emissive Eu unit, allowing to monitor the process. Nonetheless, **21** presented mild dark toxicity in HeLa (22 μM) and A549 (50 μM) cells.[30]

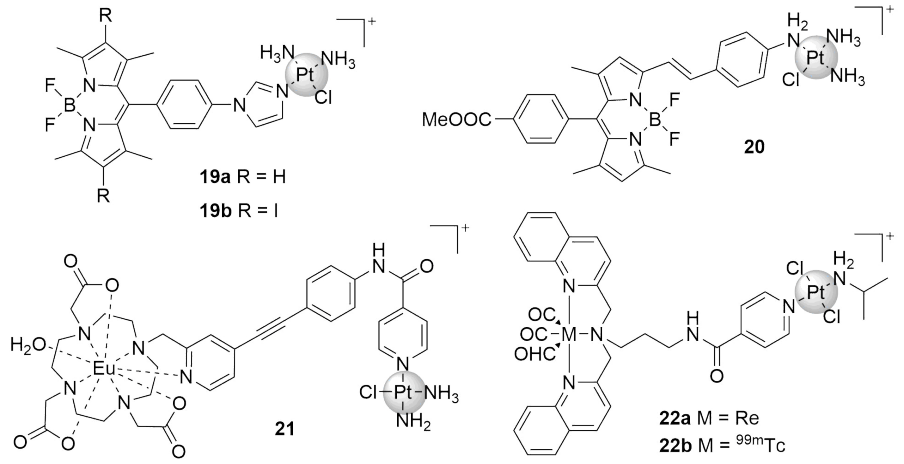

Figure 7. Chemical structure of cisplatin-like BODIPY conjugates (**19** and **20**), Eu-based prodrug for release monitoring (**21**) and theranostic optical and radiolabeled complexes (**22**).

Very recently, a novel template was employed to build theranostic compounds with either optical or radiochemical imaging capability, depending on the metal employed. The conjugate consisted of a Pt^{II} center with *trans* geometry and a pincer unit loaded with an emissive rhenium or radioactive technetium tricarbonyl scaffold. The rhenium compound **22a** displayed lower toxicity in the dark (> 60 μM) than after irradiation (350 nm, 2.58 $J \cdot cm^{-2}$), with IC_{50} values between 10 and 20 μM in HeLa and A2780 cisplatin sensitive and resistant cells. The compound did not produce any DNA adduct and cellular damage was attributed to singlet oxygen production. No CO release study was performed but the formation of singlet oxygen was confirmed and quantified. *In vivo* biodistribution of the radioactive technetium analogue **22b** confirmed the great stability of the complex in the bloodstream, with only minor decomposition 1 hour after injection, and accumulation in liver and kidneys.[31]

1.4 Pt^{IV} anticancer complexes and light activation

The need to tackle clinical problems associated with Pt^{II} drugs prompted, in the last 20 years, an increased interest of the scientific community on Pt^{IV} complexes that display hydrolytic inertness. Generally, Pt^{IV} agents do not undergo fast hydrolysis in biological environments (although this dogma has been recently contradicted[32]) and reduce subsequent unspecific toxicity. This family of octahedral compounds incorporates axial ligands into their chemical structure, which help modulating solubility parameters and biological effect in cells, as well as adding molecular and nano-vectors for targeting specifically cancer cells.[33–35]

Compared to their Pt^{II} counterparts, octahedral Pt^{IV} complexes require additional steps of activation in which they undergo reductive elimination of ligands, either via inner- or outer-sphere electron-transfer mechanisms.[36] The activation process is thought to be principally triggered inside cells by intracellular reducing agents which are able to convert inert Pt^{IV} complexes into Pt^{II} derivatives. These subsequently form reactive aqua species that generate DNA adducts and induce cell death (Figure 8).[37] Much of the research carried out on Pt^{IV} complexes has consisted in improving the pharmacological profiles of Pt drugs, elucidating the details of the $Pt^{IV} \rightarrow Pt^{II}$ activation and its biological effects, obtaining promising toxicity profiles *in vitro*, and overcoming drug resistance caused by previous treatments.

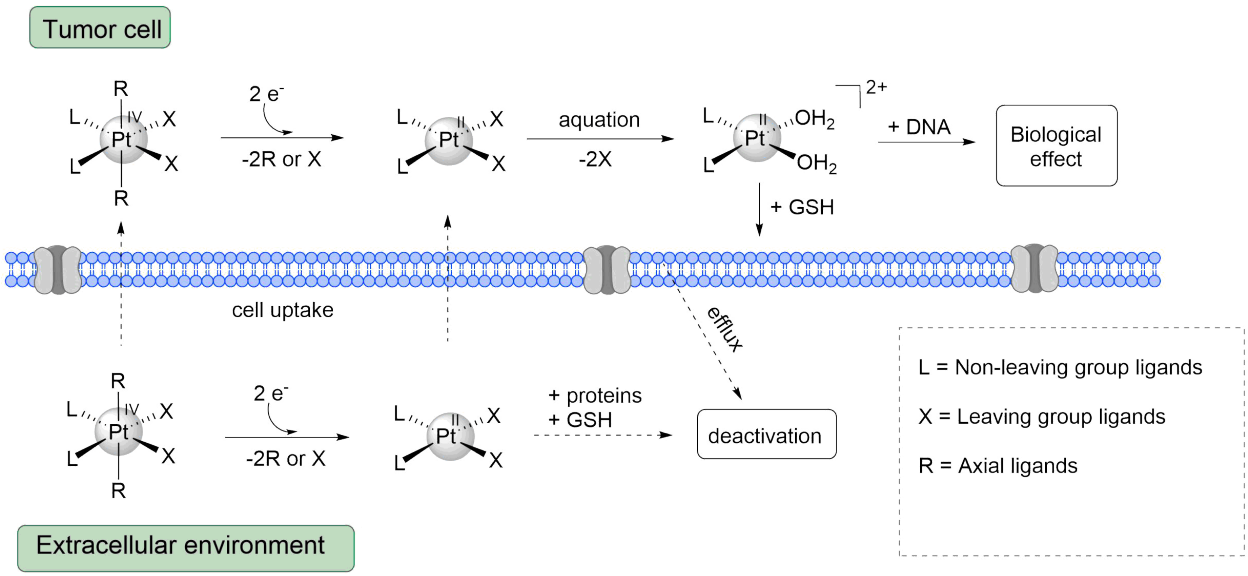

Figure 8. Schematic representation of the activation mechanism of Pt^{IV} prodrugs and their biological action in cells. Scheme adapted from reference.[37]

A number of Pt^{IV} prodrugs entered clinical trials with excellent examples represented by Ormaplatin, Iproplatin and Satraplatin (Figure 9).[38–40] Unfortunately, these three compounds failed to obtain approval by the Food and Drug Administration (FDA) since none of them had anticancer efficacy significantly higher than clinically used Pt^{II} drugs.

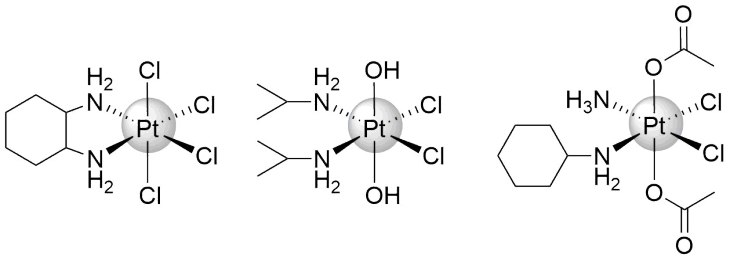

Figure 9. Pt^{IV} prodrugs which entered clinical trials.

Nevertheless, Pt^{IV} complexes remain promising systems to overcome the typical drawbacks of Pt^{II} anticancer drugs and photoactivation has been regarded as an alternative and potentially successful strategy to fine-control the biological effects of Pt^{IV} prodrugs in cancer cells. In the field of photochemotherapy, the initial research focus was to develop stable and non-cytotoxic Pt^{IV} complexes in the dark, capable of reducing cell viability upon light irradiation. More recently, the field interest has aimed at the design of delivery and targeting approaches and at shifting excitation wavelengths towards the therapeutic window, *e.g.* the red and near infrared part of the spectrum. These aspects are discussed here below through selected and representative examples of Pt^{IV} complexes as prodrugs for active Pt^{II} species.

1.4.1 Diiodo-Pt^{IV} complexes

In the 1990's, Bednarski's laboratory was the first to investigate the toxicity of Pt^{IV} complexes upon light activation (Figure 10).[41,42] Complexes **23**–**25** (Figure 10) bearing iodides as leaving ligands and ethylenediamine (en) as non-leaving group were chosen for their favorable LMCT bands at 380-400 nm ($\varepsilon \approx 1 \times 10^3$ M^{-1} cm^{-1}). Furthermore, the *cis* geometry of iodide ligands in **23**–**25** favored photoreduction with respect to photo-substitution reactions. The chelating ethylenediamine instead reduced the occurrence of photoisomerization reactions, potentially leading to *trans* Pt^{II} species which were known to be inactive.

When irradiated at 410 nm, **23** underwent photodecomposition to generate $[PtCl_2(en)]$ which was then able to platinate DNA. Unfortunately, compound **23** was found to decompose and bind to DNA in the dark as well. Consequently, no differences in toxicity toward human cancer cells (human bladder cancer and melanoma cells, TCCSUP and SK-MEL-24 respectively) were found between samples kept in the dark or light irradiated.[42]

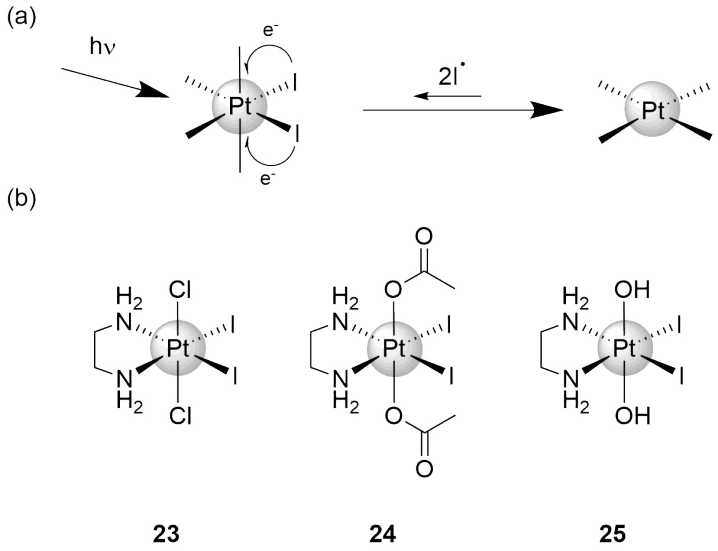

Figure 10. (a) Mechanism proposed for the photoreduction of iodide-based Pt^{IV} compounds. (b) First generation of Pt^{IV} prodrugs based on iodide ligands.

To improve the dark stability of this class of compounds, Bednarski and collaborators changed the axial chlorido ligands of **23** to acetates (**24**) and hydroxides (**25**).[41] When incubated with cell culture medium, derivatives **24** and **25** decomposed after 6.6 and 46.8 h, respectively. The process was much faster (≈ 1 h) under light excitation (> 375 nm). Complex **24** afforded 60% of platinated DNA in buffer after 6 h of irradiation, while almost no platination was observed in the dark. On the other hand, **25** did not lead to DNA adducts even after 6 h of light irradiation, suggesting that the photoproducts were likely Pt^{IV} species. Both **24** and **25** displayed higher cytotoxicity against cancer cells (TCCSUP) when irradiated. The different nature of the photoproducts of the two complexes suggested that this photoinduced cytotoxicity derived from different mechanisms of action. Nevertheless, **24** and **25** could kill cancer cells in the low micromolar range also in the dark. In fact, NMR showed that both compounds were rapidly reduced via inner-sphere mechanism by biothiols such *N*-acetylcysteine and GSH.[43]

Overall, even if diiodo-Pt^{IV} complexes were deemed as photoactivatable drugs, the proof-of-concept studies conducted by Bednarski and his collaborators demonstrated that light could be used for the activation of Pt^{IV}-based prodrugs, paving the way for the design of new and improved derivatives.

1.4.2 Diazido-Pt^{IV} complexes

In the early 2000s, Sadler successfully addressed both the dark stability and the biothiol-mediated reduction issues developing azido-based Pt^{IV} complexes.[44] Azides confer stabilization to Pt^{IV} complexes in the cellular reducing environment due to their strong electron-donating nature. The photochemistry of Pt^{IV} complexes coordinating azido ligands

was known since the end of 1970s when Vogler *et al*. demonstrated that irradiation of *trans*-$[Pt(N_3)_2(CN)_4]^{2-}$ led to azide elimination and photoreduction to Pt^{II} species.[45] The mechanism proposed involved the formation of azide radicals which were then rapidly converted in molecular nitrogen (Figure 11).[45,46] Whereas halide radicals are stable in water and can reconvert Pt^{II} to Pt^{IV} (see Figure 10), azido ligands provide a fast and irreversible photoreduction of the Pt^{IV} complexes.[47]

The first azido-based compounds investigated by Sadler and collaborators were *cis,trans*-$[Pt(en)(N_3)_2(OH)_2]$ and *cis,trans,cis*-$[Pt(N_3)_2(OH)_2(NH_3)_2]$ (**26** and **27**, Figure 11). The two derivatives behaved similarly in solution, being extremely stable in the dark (up to 90 days) also in the presence of biological reductants like GSH (up to weeks).

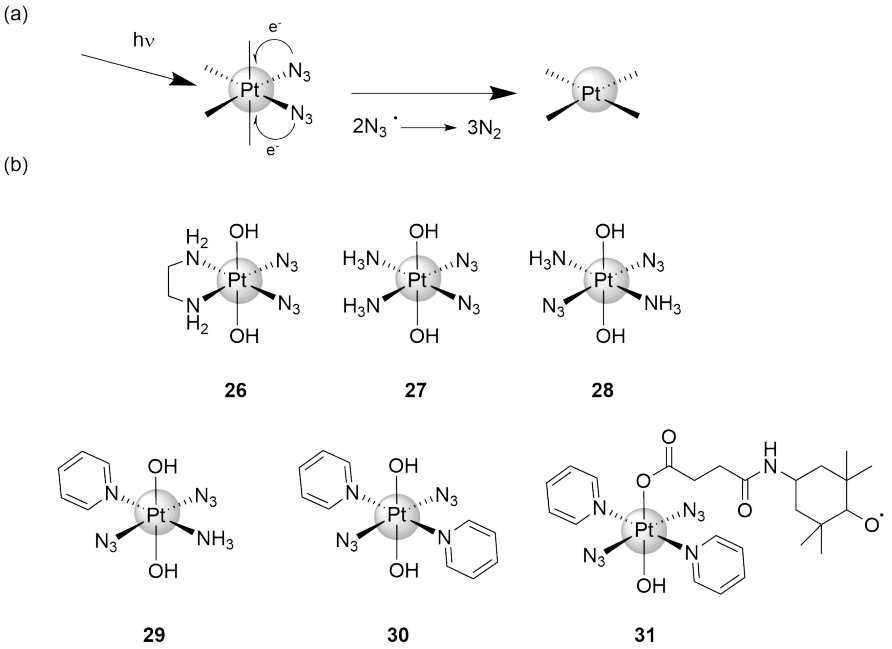

Figure 11. (a) Mechanism proposed for the photoreduction of azido-based Pt^{IV} compounds. (b) Second generation Pt^{IV} prodrugs based on azido ligands.

Complexes **26** and **27** gave rise to species able to bind to DNA nucleobase models 5'-GMP or to d(GpG) only under irradiation.[44,48] They share similar absorption properties with a LMCT band centered at 256 nm ($\varepsilon \approx 1 \times 10^4$ $M^{-1}\cdot cm^{-1}$) with a tail that reaches the visible region. In the presence of 5'-GMP and after irradiation at 458 nm, compound **26** afforded the double adduct $[Pt(en)(5'\text{-GMP-N7})_2]$. The same outcome was observed when **26** was incubated with dGpG and irradiated, leading to the formation of the double adduct with the nucleotide. Under irradiation at 458 nm for 3 h, photoproducts of **26** formed platinated GG crosslinks on plasmid DNA and to stop *in vitro* RNA synthesis by RNA polymerase [48]. Of note, **26** and **27** typically absorb up to 350 nm, yet they showed the capability to undergo photoactivation also in the visible region (> 400 nm). Such photoreactivity was rationalized by DFT modeling which determined the presence of weak electronic transitions in the region between 400–500 nm.[49]

Both **26** and **27** were active against human bladder cancer cells (including the cisplatin-resistant type) only when irradiated at 366 nm, with IC_{50} values reaching 50 μM.[50] Fluorescence microscopy studies demonstrated also that cell morphology changes were not comparable with the ones provoked by cisplatin, implying a different mechanism of action for the light-activated **26** and **27**. The Sadler group later studied the photochemistry and the anticancer activity of *trans,trans,trans*-$[Pt(N_3)_2(OH)_2(NH_3)_2]$ (**28**), the *trans* isomer of **27.**[51,52] Complex **28** was stable in the dark but once irradiated at 365 nm in the presence of 5'-GMP afforded the *trans* bis-G adduct $[Pt(NH_3)_2(5'\text{-GMP-N7})_2]$. This process was significantly more efficient in comparison to the same photoreaction performed on **27**. In the case of **28**, more than 75 % of its photoproducts were bound to 5'-GMP after 1 h. Photoactivation of **28** in solution resulted in the formation of *trans*-$[Pt(NH_3)_2(OH_2)_2]$ and other photoreduction and photoisomerization products. In the presence of DNA, irradiation of **28** led to inter-strand cross-links, as demonstrated for transplatin.[16] In a comparative study, **27**, **28**, cisplatin and transplatin were tested against human keratinocytes (HaCaT cells) and, after irradiation, compound **28** was the most active Pt^{IV} compound so far.[51]

As follow up of the discoveries on **28**, Sadler and collaborators developed two *trans* azido-derivatives (Figure 11) with pyridine (py) ligands, *trans,trans,trans*-$[Pt(N_3)_2(OH)_2(NH_3)(py)]$ (**29**)[50] and *trans,trans,trans*-$[Pt(N_3)_2(OH)_2(py)_2]$ (**30**).[52] Pyridines introduced several advantages compared to NH_3 groups: i) they are bulkier, potentially preventing off-target interaction of the Pt^{IV} complex and of its photoproducts; ii) they can promote π-stacking interactions with DNA favoring the binding of the Pt^{IV} complex to their target and iii) they produce a bathochromic shift in the absorption spectrum. Complexes **29** and **30** proved to be very stable in solutions kept in the dark (more than 20 days), even in the presence of reductants such as GSH and ascorbate.[52,53] After irradiation, which can be performed at 365 and 420 nm, photoproducts of both compounds interacted very efficiently (more than the ones of **28**, for instance) with DNA models (*e.g*. 5'-GMP and ct-DNA).[54] As an example, **30** incubated with DNA and irradiated at 365 nm (4.6 $mW \cdot cm^{-2}$) induced mono- and bifunctional adducts 16-fold more than cisplatin.[55]

Recently, thioredoxin (Trx), an important enzyme overexpressed in several cancer cells,[56] was proposed as potential target of irradiated **30** (and potentially other Pt^{IV} prodrugs). Photoproducts of the complex could indeed bind to histidine, glutamic acid and glutamine residues of Trx upon irradiation with blue light (460 nm).[57] In another recent manuscript, Sadler demonstrated that photoproducts of **30** generated by visible light interacted with two neuropeptides giving rise to oxidized or platinated products, with the nature of the species being dependent on the amino acid composition of the peptide.[58]

The two pyridine derivatives **29** and **30** have been tested against several cancer cell lines and, to date, remain the lead compounds of this kind in terms of phototoxicity. For example, **29**, while being inactive in the dark, killed A2780 human ovarian carcinoma cells and their cisplatin-resistant version in the low micromolar range (at 2 and 16 μM, respectively) only

when irradiated at 366 nm. These cytotoxicity values, 80-fold higher than the ones obtained with cisplatin, were obtained using a low light dose (5 J·cm^{-2} for 30 min).[54] Compound **29** proved to be cytotoxic also using irradiation at 420 nm (5 J·cm^{-2}). Upon light-activation, the complex does not kill cancer cells by the same apoptotic mechanism as cisplatin but rather through a different mechanism of cell death, most likely involving autophagy as indicated by changes in the levels of the autophagic proteins LC3B-II and p62. As a matter of fact, a statistically relevant number of mice bearing OE19 (esophagus) tumors treated with **29** and light (420 nm, 100 J·cm^{-2}) survived after the 35th day, while all the controls (no treated and treated in the dark) died in the same time window.[59] It was recently demonstrated that the acute photocytotoxicity of **30** depended on the generation of azide radicals and Pt^{II} photoproducts.[60] In detail, the Sadler group showed by EPR and NMR that light-associated activity of **30** against cancer cells can be switched off by low concentrations (500 μM) of the amino acid L-tryptophan, which is a well-known mediator of electron transfer in proteins.

Based on the structure activity relationship obtained for complexes **26**–**30**, the same group developed several other azido-based Pt^{IV} prodrugs with diverse ligands (*e.g*. acetate in the axial positions or different N-coordinating ligands in the equatorial positions).[61–63] The outcome in terms of stability, DNA-binding properties and cytotoxicity (against HaCaT and A2780 cells) in the dark and under irradiation were comparable with the one obtained using **29** and **30** and led to the general conclusion that the *trans* derivatives were more active that their *cis* analogues.

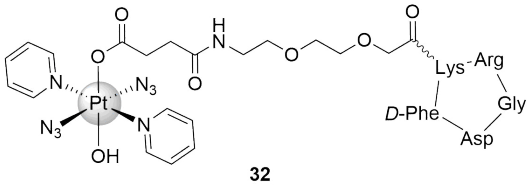

32

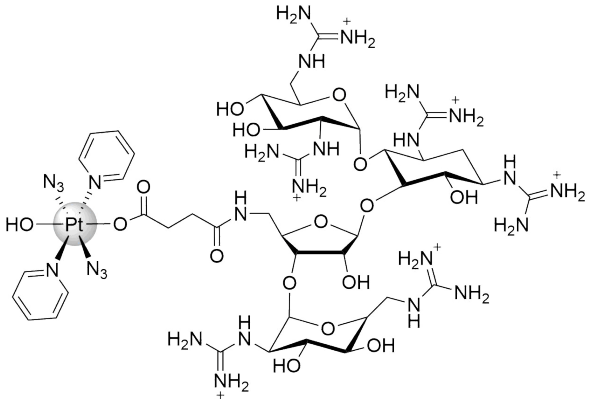

33

Figure 12. Azido-Pt^{IV} prodrugs functionalized with targeting ligands for improved cellular uptake.

Recently, V. Venkatesh *et al*. described the nitroxide spin-labelled photoactivatable Pt^{IV} prodrug *trans,trans,trans*-[Pt(N$_3$)$_2$(OH)(OCOCH$_2$CH$_2$CONH-TEMPO)(py)$_2$] (where TEMPO =

2,2,6,6-tetramethylpiperidine 1-oxyl) (**31**, Figure 11).[64] In order to obtain a compound trackable in vivo by EPR and with simultaneous radical-mediated anticancer activity, compound **31** was designed substituting one of the axial hydroxyl of **30** with a functionalized TEMPO radical. EPR experiments showed that light irradiation of **31** with blue light (465 nm, 50 mW) led to the formation of azidyl and nitroxyl radicals in solution and to a corresponding high cytotoxicity towards A2780 human ovarian carcinoma cells (10-fold higher than cisplatin).[64]

In a collaborative effort, Marchan and Sadler designed new photoactivatable agents with comparable biological activity of derivative **30** but with improved cellular uptake properties. In the case of compound **32** (Figure 12), for instance, the Pt^{IV} prodrug was conjugated to a cyclic peptide containing the RGD sequence (–Arg–Gly–Asp–), which is selectively recognized by transmembrane glycoproteins ($\alpha_V\beta_3$ and $\alpha_V\beta_5$ integrins) overexpressed in different tumor cells.[65] Complex **33** featured instead a guanidinoglycoside (guanidinoneomycin), known to transport cargos into cells in a selective proteoglycan-dependent manner.[66] In both cases, the metal complexes showed a certain degree of selectivity toward human malignant melanoma cells (SK-MEL-28) and retained the ability to bind the DNA model 5'-GMP upon irradiation with blue light, similarly to **30**.[65,66] These agents highlight how photoactivatable Pt^{IV} scaffolds hold great promise for a double control of platinum-associated anticancer activity: one based on the targeting properties conferred by the chosen axial ligands and the other based on the possibility to selectively generate Pt^{II} species by light excitation.

1.4.3 Porphyrin coupled Pt^{IV} complex

The use of porphyrins for PDT applications dates back to the decade of 70´s.[67,68] These organic macrocyclic compounds have been explored as photosensitizers because they show strong absorption in the red region of the spectrum coupled with high production of ROS. Such features make them excellent candidates to trigger cellular damage upon red light. As schematized in Figure 13a, long wavelengths have increased tissue penetration and are hence ideal to activate chemotherapeutic agents that are localized into tissues. Recently, Wang, Zhu and collaborators synthesized a small molecule that combines a red-light photosensitive porphyrin with a Pt^{IV} anticancer complex.[69] The small molecule named Phorbiplatin was composed by pyropheophorbide a (PPA) and a Pt^{IV} prodrug of oxaliplatin (Figure 13b). In the presence of 1 mM of ascorbate and after 10 minutes of light irradiation (λ = 650 nm, 7 mW cm^{-2}), around 80% of 10 μM of phorbiplatin was transformed into oxaliplatin. Authors proposed that upon irradiation, PPA reached initially the singlet excited state and then decayed to the triplet excited state which afforded the reduced form of PPA in the presence of ascorbate. The reduced PPA transferred an electron to the metal center to generate a highly reactive Pt^{III} species that finally resulted into the formation of the toxic Pt^{II} drug oxaliplatin.

Cell studies showed that phorbiplatin was modestly active in the dark, with IC_{50} values above 10 µM. While under irradiation its phototoxicity increased by a factor of 974 and 1786 compared to oxaliplatin, in ovarian cancer resistant (A2780cisR) and human breast cancer (MCF-7) cells lines respectively. Cytotoxicity experiments demonstrated that the toxicity was produced by two independent mechanisms: i) via ROS generation promoted by the photosensitizer and ii) via DNA platination associated to the *in situ* liberation of oxaliplatin. After irradiation of phorbiplatin in A2780 cells, the platinum amount bound to DNA was 4 times higher than in the dark, confirming the presence of DNA-binding Pt^{II} species. Generally, the lack of oxygen in many tumors switches off the capacity of photosensitizers to trigger an effective toxic effect by the generation of ROS. However, in the case of phorbiplatin, cytotoxic Pt^{II} species can be produced overcoming such key limitation of PDT. To demonstrate this idea, the groups of Wang and Zhu treated with phorbiplatin, PPA and oxaliplatin mice bearing a murine mammary adenocarcinoma 4T1. Results demonstrated that light irradiation (660 nm, 100 mW/cm^{-2}) of phorbiplatin produced a significant reduction of the tumor growth (65%) and tumor weight (60%) compared to the control group.[69]

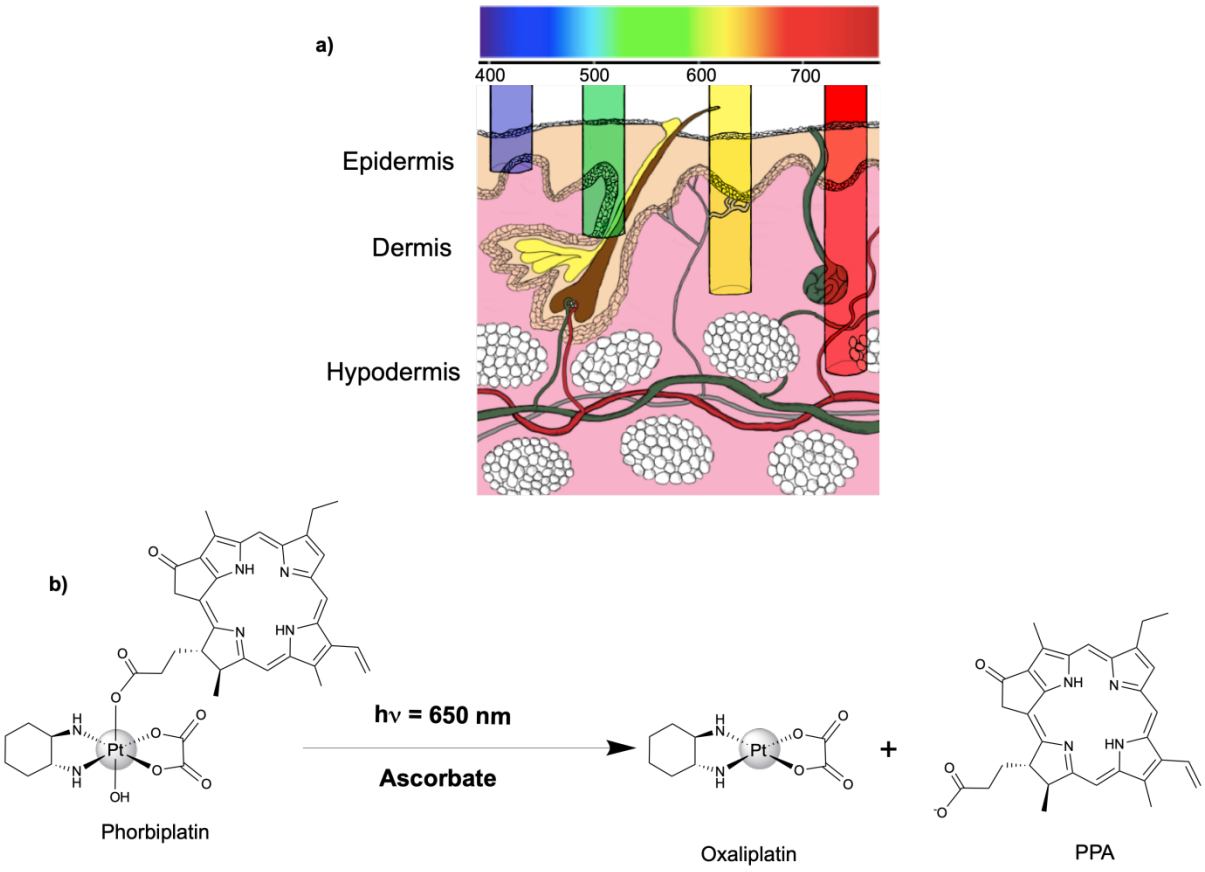

Figure 13. a) Representation of light penetration into the skin and b) Phorbiplatin photoactivation under red light irradiation.[69]

1.5 Nanodelivery of photoactivatable Pt prodrugs

Many efforts have been applied to improve the delivery of Pt anticancer complexes by light activation. In a number of systems, octahedral Pt^{IV} complexes were loaded onto polymeric micelles that upon UVA light (365 nm) released cytotoxic Pt^{II} species.[70–72] For instance, Zheng and collaborators described that copolymeric micelles made of monomethoxy poly(ethylene glycol)-block-poly(ε-caprolactone)-block-poly(L-lysine) loaded with **34** (Figure 14) exhibited greater antineoplastic effects than cisplatin in liver hepatocellular carcinoma (HepG2) and ovarian adenocarcinoma (SKOV3) cells after UVA light irradiation (18 $mW \cdot cm^{-2}$). Upon light excitation, **34** was reduced and Pt^{II} species were released from the polymeric micelles. Uptake studies showed that polymeric encapsulation enhanced the Pt uptake into cells.[70]

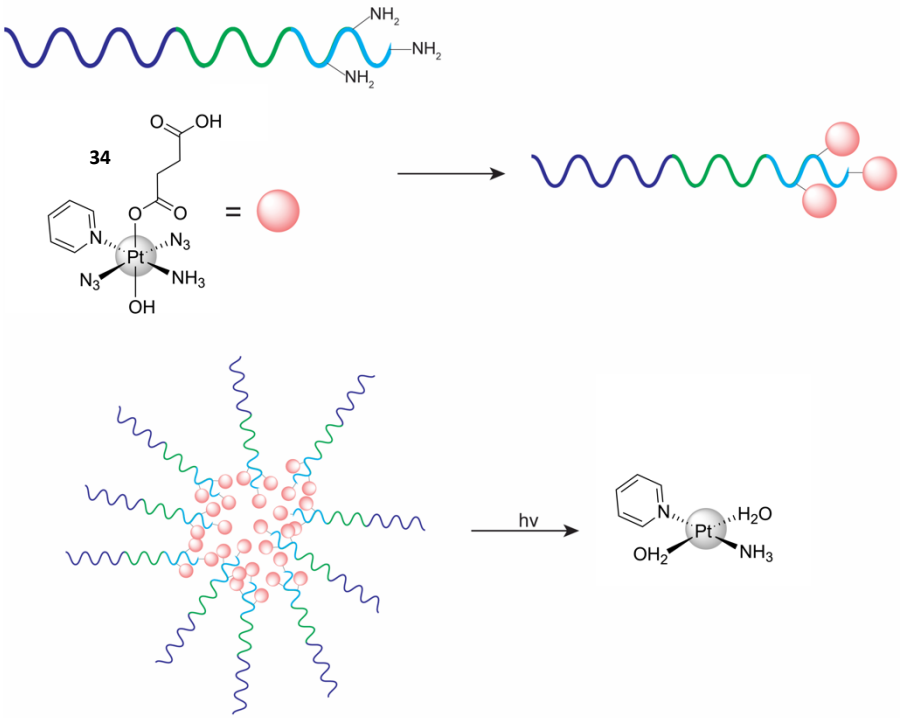

Figure 14. Ilustration of Zheng´s nanopolymeric delivery approach.[70]

Adopting another approach Huang and coworkers, coordinated one or two hydrophilic amino-functionalized lactose to **35** or **36** respectively (Figure 15), forming self-assembled amphiphilic micelles (one lactose derivative) or vesicles (two lactose derivatives). Lactose-based amphiphiles worked as drug carriers and simultaneously were able to target HepG2 cells that overexpress the asialoglycoprotein receptor, a lectin that can be found in the plasma membrane of liver cells.[73] Upon UVA light activation (10 $mW \cdot cm^{-2}$), **35** or **36** were photoreduced producing the breakdown of the lactose carriers and the release of the Pt^{II} species.

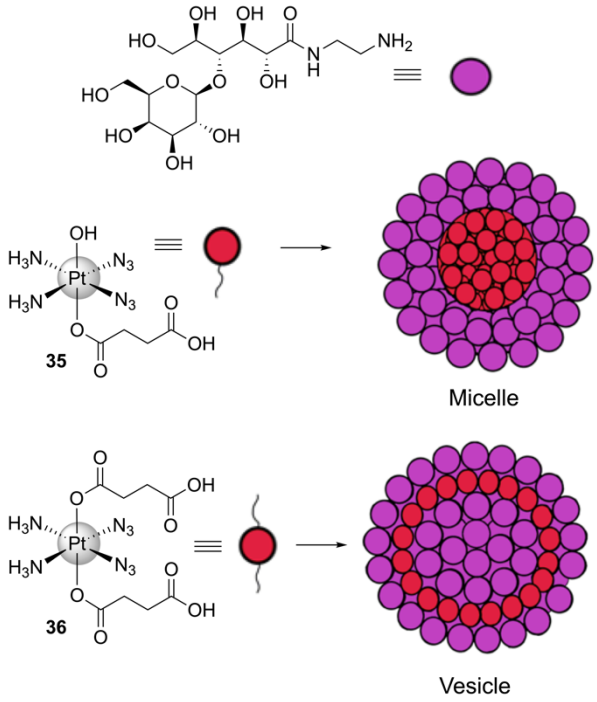

Figure 15. Illustration of Huang´s lactose-based amphiphiles.[71]

In vitro experiments showed that light-irradiated vesicles generated more Pt-DNA adducts than micelles and that Pt accumulation in HepG2 cells was higher than in cell lines that do not overexpress the asialoglycoprotein receptor. Furthermore, vesicles functionalized with the NIR-absorbing dye Cy7.5 could be traced by fluorescence imaging in mice model. *In vivo* testing on a subcutaneous liver cancer model demonstrated that vesicles accumulated into liver cells causing less system toxicity than cisplatin upon light activation.[71]

Sadler´s laboratory exploited the capability of guanosine derivatives to form highly biocompatible hydrogels for the incorporation of compound **37**. The complex was conjugated to a dopamine molecule into a G-quadruplex-based hydrogel by monoborate ester formation (Figure 16). The hydrogel scaffold allowed a slow, sustained and controllable release of cytotoxic Pt^{II} species upon light excitation. The authors showed that under blue light (465 nm 50 $mW \cdot cm^{-2}$), Pt^{II} and Pt^{IV} photoproducts were liberated from the G-quadruplex hydrogel, exhibiting greater toxicity than the parent compound **38** (IC_{50} = 3 µM, and 74 µM, respectively), in cancerous and healthy cells. Notably, the irradiated hydrogel showed 18-fold times greater antiproliferative activity toward cisplatin resistant A2780 human ovarian carcinoma cells (IC_{50} = 3 µM), than for non-cancerous MRC-5 cells (IC_{50} > 50µM).[74]

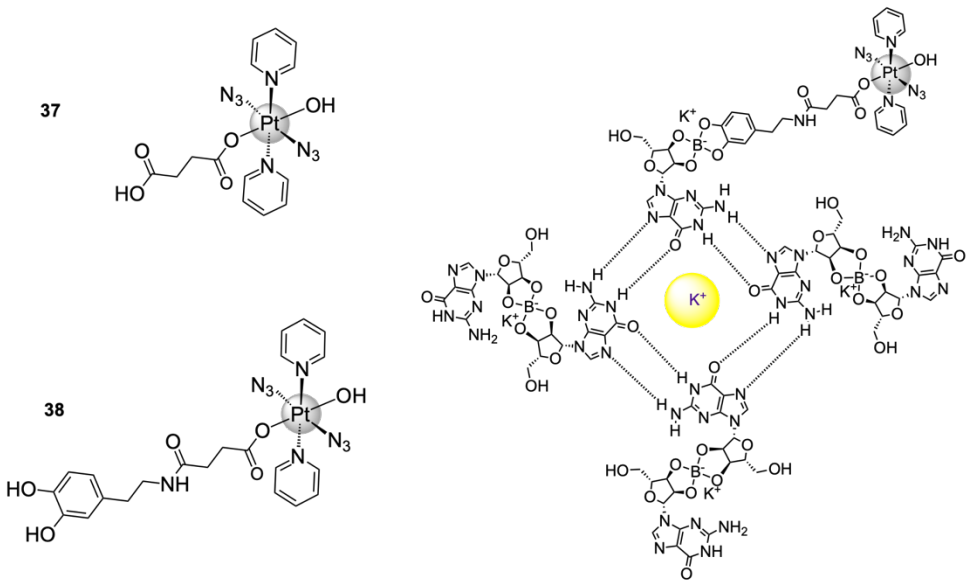

Figure 16. Schematic representation of the Pt^{IV}-guanosine borate hydrogel.[74]

Researchers in the field of photoactivatable anticancer Pt agents have investigated a range of nanoscale materials with photophysical features suitable for triggering photochemical reactions at convenient wavelength range, that is the red and NIR region of the spectrum.

The group of Mareque-Rivas designed micelle-encapsulated CdSe@ZnS core-shell quantum dots (QDs) loaded with complex **39** (Figure 17) and the radioactive technetium tricarbonyl complex *fac*-$[^{99m}Tc(OH_2)_3(CO)_3]^+$ for theranostics. Upon 630-nm light excitation (30 $mW \cdot cm^{-2}$), the nanosconstructs induced the reduction of **39** *via* photoinduced electron transfer, liberating Pt^{II} cytotoxic species. *In vitro* experiments showed that irradiated micelles were active against human prostate cancer PC-3 cells (IC_{50} = 25 µM), while no toxicity was observed for dark controls. Moreover, irradiated **39** alone showed no toxic effect of PC-3 cells (IC_{50} ≈ 500 µM).[75] In a later work, Infante *et al*. showed that the QD-triggered photoreduction of **39** resulted in a different set of photoproducts compared to direct excitation of the metal complex with UVA light.[76]

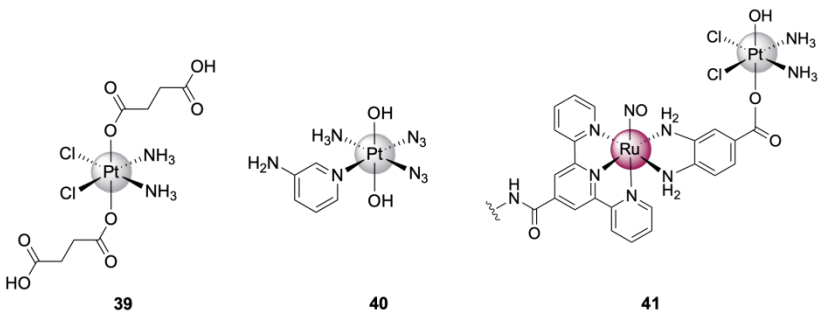

Figure 17: Chemical structure of Pt^{IV} prodrug combined with QDs (**39**), CDs (**40**) and GQDs (**41**).

Carbon Dots (CDs) have been also used as light sensitive carriers for the transport and delivery Pt drugs. Fluorescent CDs functionalized with folic acid and **40** (Figure 17)

selectively targeted cancerous cells overexpressing folate receptors, releasing toxic Pt^{II} species under visible light irradiation (> 400 nm, 200 $mW \cdot cm^{-2}$), and ultimately inducing cell death *via* apoptosis.[77] Similarly, Liu and collaborators loaded the heterobimetallic complex **41** onto folate-functionalized N-doped graphene quantum dots. *In vitro* experiments on HeLa, MCF-7 and normal non-cancer HUVEC cell lines showed that these nanoplatforms preferentially accumulated in HeLa cells. Upon NIR light irradiation (808 nm, 1 $W \cdot cm^{-2}$), **41** showed antiproliferative activity resulting from the synergistic and simultaneous release of NO and Pt^{II} drugs (Figure 17).[78]

Photoactivation of Pt^{IV} complexes with near infrared light was also achieved using upconverting nanoparticles (UCNPs), a class of inert nanomaterials that have emerged for their unique emission properties as well as useful tools for imaging in medicine.[79] These nanoscale materials doped with lanthanide ions have the capability to absorb consecutively two or more photons of low energy and undergo non-linear (anti-Stokes) optical processes[79] that lead to shorter-wavelength (visible and UV) light emission. The luminescence profile of UCNPs are suitable for photochemical activation of metal-based anticancer agents.

For example, our group reported earlier that core-shell $NaYF_4$:Yb,Tm@$NaYF_4$ UCNPs loaded with a Pt^{IV} complex functionalized with an amine PEGylated phospholipid (**42** Figure 18a) could be transformed into biologically active Pt^{IV} and Pt^{II} (30%) complexes under 980-nm irradiation (4.9 $W \cdot cm^{-2}$) for 4 hours (Figure 18a).[80]

Bednarski and collaborators conjugated light sensitive monocarboxylated diiodido derivatives **43** to $NaGdF_4$:Yb,Er UCNPs employing two different strategies (Figure 18b). In one case, UCNPs were functionalized with an aminated silica shell and complexes were covalently attached to the surface *via* amide bonding. In the other case, **43** was attached electrostatically to the surface of the UCNPs by ligand exchange. Results showed that both strategies afforded comparable amount of Pt onto UCNP surfaces. When covalently attached, greater light dependent release of Pt species was observed with respect to electrostatically loaded prodrugs. Besides, covalent UCNP-Pt^{IV} conjugates also showed higher cytotoxicity under dark and upon NIR light irradiation (980 nm, 1.2 $W \cdot cm^{-2}$) in HL60 human leukemia cells, compared to electrostatic loading. XPS measurements demonstrated that in both strategies only around 20% of the Pt on the surface was in the Pt^{IV} oxidation state while 80% was readily transformed to Pt^{II}.[81]

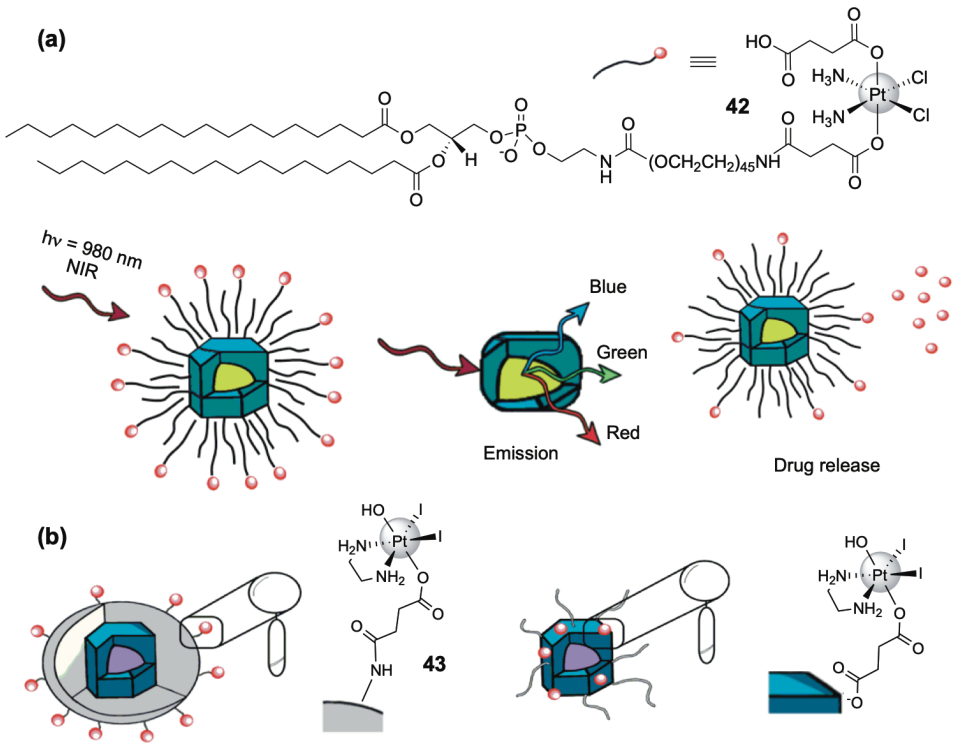

Figure 18. NIR photoactivation of Pt^{IV} prodrug complexes triggered by UCNPs.[80,81]

Dai et *al.*[82] and Min and *al.*[83] reported that Pt^{IV} azido analogues of **29** and **30** anchored to UCNPs nanomaterials displayed activity *in vitro* and in the former case could also induce tumor reduction *in vivo* upon NIR light irradiation. However, despite having received a high number of citations, these two articles lack key characterization and control experiments and fail in providing substantial evidence on the NIR light activation of Pt^{IV} complexes and its link with the biological effects observed. Furthermore, it is important to stress that UCNP-assisted activation of Pt agents has been achieved so far using rather high excitation intensities and 980-nm light sources, a wavelength that causes significant water heating and hence can lead to direct damage of biological components.[84] Nd-sensitized UCNPs and 808-nm excitation is currently being investigated as alternative for PDT application to overcome such limitations.[85]

1.6 Summary

In recent years we have witnessed a remarkable increase of attention on the use of photochemistry as a resource for developing new Pt anticancer agents and drug delivery strategies. In this context, Pt^{IV} azido complexes, developed by Sadler and coworkers, have emerged as the blueprint in the field. Overall, this research area has made significant advances delivering Pt agents with diverse biological activity, cancer cell targeting capability or improved photochemical properties. However, the limited number of *in vivo* studies so

far reported on photoactivatable Pt agents is indicative of how much still remains to be done.

For instance, efforts devoted to red-shifting activation wavelengths of Pt complexes can give major contributions to advance the field further and make this class of compounds a tool worth investigating as alternative or synergy for PDT. Novel photoactivatable platforms based on nanomaterials have partially reached this objective (*e.g*. quantum dots and UCNPs), but their sophistication as drug delivery systems might hamper their approval and application for clinical use. Despite their unique photophysical features, UCNP-mediated prodrug activation presently suffers from low photoconversion efficiency and raises concerns for lanthanide leaching.

At present, metallodrugs in general appear to suffer from a lack of interest by the pharmaceutical sector. This of course extends to photoactivatable Pt anticancer agents, making difficult to predict what this area of research needs to accomplish in order to deliver the next generation of anticancer drugs. Most likely, the mere synthesis and *in vitro* testing of new Pt compounds that are active against cancer cells upon light irradiation is no longer enough. Therefore, convenient strategies for their light-activation and their implementation into biocompatible delivery systems should be integrated in the design of Pt photoactivatable agents from the beginning. Coupling of Pt prodrugs to tumor targeting vectors such as antibodies or serum proteins can for example reduce non-selective accumulation in to tissues and reduce residual systemic side effects of Pt prodrugs. In addition, incorporation of clinically-approved precursors, ligands, sensitizers or additives in the structures of Pt complexes could ease the drug approval process and hence attract the interest of the pharmaceutical industry. Hopefully, the promising results obtained recently by the Ru PDT agent TLD-1433 in human clinical trials will help the field of Pt photoactivatable anticancer agents to gain new momentum.[7]

1.7 References

(1) Rosenberg, B.; Van Camp, L.; Krigas, T. Inhibition of Cell Division in Escherichia Coli by Electrolysis Products from a Platinum Electrode. *Nature* **1965**, *205*, 698–699.

(2) Rosenberg, B.; Van, C. L.; Grimley, E. B.; Thomson, A. J.; Van Camp, L.; Grimley, E. B.; Thomson, A. J. The Inhibition of Growth or Cell Division in Escherichia Coli by Different Ionic Species of Platinum(IV) Complexes. *J. Biol. Chem.* **1967**, *242*, 1347–1352.

(3) Rosenberg, B.; Renshaw, E.; Vancamp, L.; Hartwick, J.; Drobnik, J. Platinum-Induced Filamentous Growth in Escherichia Coli. *J. Bacteriol.* **1967**, *93*, 716–721.

(4) Rosenberg, B.; VanCamp, L.; Trosko, J. E.; Mansour, V. H. Platinum Compounds: A New Class of Potent Antitumour Agents. *Nature* **1969**, *222*, 385–386.

(5) Rosenberg, B.; VanCamp, L. The Successful Regression of Large Solid Sarcoma 180 Tumors by Platinum Compounds. *Cancer Res.* **1970**, *30*, 1799–1802.

(6) Harder, H. C.; Rosenberg, B. Inhibitory Effects of Anti-Tumor Platinum Compounds on DNA, RNA and Protein Syntheses in Mammalian Cells in Vitro. *Int. J. Cancer* **1970**, *6*, 207–216.

(7) Monro, S.; Colón, K. L.; Yin, H.; Roque, J.; Konda, P.; Gujar, S.; Thummel, R. P.; Lilge, L.; Cameron, C. G.; McFarland, S. A. Transition Metal Complexes and Photodynamic Therapy from a Tumor-Centered Approach: Challenges, Opportunities, and Highlights from the Development of TLD1433. *Chem. Rev.* **2019**, *119*, 797–828.

(8) Matveeva, S. G.; Pozdnyakov, I. P.; Grivin, V. P.; Plyusnin, V. F.; Mereshchenko, A. S.; Melnikov, A. A.; Chekalin, S. V.; Glebov, E. M. Primary Photochemical Processes for $PtCl_6^{2-}$ Complex in Acetonitrile Solutions. *J. Photochem. Photobiol. A.* **2016**, *325*, 13–21.

(9) Matveeva, S. G.; Grivin, V. P.; Plyusnin, V. F.; Vasilchenko, D. B.; Glebov, E. M. Mechanism of Chain Photochemical Reaction of $(n\text{-}Bu_4N)_2[PtCl_6]$ in Chloroform. *J. Photochem. Photobiol. A.* **2018**, *359*, 80–86.

(10) Glebov, E. M.; Pozdnyakov, I. P.; Vasilchenko, D. B.; Zadesenets, A. V.; Melnikov, A. A.; Magin, I. M.; Grivin, V. P.; Chekalin, S. V.; Plyusnin, V. F. Photochemistry of cis,trans-$[Pt(En)(I)_2(OH)_2]$ Complex in Aqueous Solutions. *J. Photochem. Photobiol. A.* **2018**, *354*, 78–85.

(11) Shushakov, A. A.; Pozdnyakov, I. P.; Grivin, V. P.; Plyusnin, V. F.; Vasilchenko, D. B.; Zadesenets, A. V.; Melnikov, A. A.; Chekalin, S. V.; Glebov, E. M. Primary Photochemical Processes for Pt(IV) Diazido Complexes Prospective in Photodynamic Therapy of Tumors. *Dalton Trans.* **2017**, *46*, 9440–9450.

(12) Vernooij, R. R.; Joshi, T.; Horbury, M. D.; Graham, B.; Izgorodina, E. I.; Stavros, V. G.; Sadler, P. J.; Spiccia, L.; Wood, B. R. Spectroscopic Studies on Photoinduced Reactions of the Anticancer Prodrug, trans,trans,trans-$[Pt(N_3)_2(OH)_2(Py)_2]$. *Chem. Eur.*

J. **2018**, *24*, 5790–5803.

(13) Li, K.; Tong, G. S. M.; Wan, Q.; Cheng, G.; Tong, W.-Y.; Ang, W.-H.; Kwong, W.-L.; Che, C.-M.; Ming Tong, G. S.; Wan, Q.; et al. Highly Phosphorescent Platinum(II) Emitters: Photophysics, Materials and Biological Applications. *Chem. Sci.* **2016**, *7*, 1653–1673.

(14) T. H. Dunning Jr. and P.J.Hay. Gaussian Basis Sets for Molecular Calculations, in *Modern Theoretical Chemistry, Volume 3: Methods of Electronic Structure Theory*; Plenum, **1977**; pp 1–28.

(15) Mlcouskova, J.; Stepankova, J.; Brabec, V. Antitumor Carboplatin Is More Toxic in Tumor Cells When Photoactivated : Enhanced DNA Binding. *J. Biol. Inorg. Chem.* **2012**, *17*, 891–898.

(16) Heringova, P.; Woods, J.; Mackay, F. S.; Kasparkova, J.; Sadler, P. J.; Brabec, V. Transplatin Is Cytotoxic When Photoactivated: Enhanced Formation of DNA Cross-Links. *J. Med. Chem.* **2006**, *49*, 7792–7798.

(17) Navas, F.; Perfahl, S.; Garino, C.; Salassa, L.; Novakova, O.; Navarro-Ranninger, C.; Bednarski, P. J.; Malina, J.; Quiroga, A. G. A. G. Increasing DNA Reactivity and in Vitro Antitumor Activity of trans Diiodido Pt(II) Complexes with UVA Light. *J. Inorg. Biochem.* **2015**, *153*, 211–218.

(18) Prachařová, J.; Intini, F. P.; Natile, G.; Kasparkova, J.; Brabec, V. Potentiation of Cytotoxic Action of cis-[$PtCl_2(NH_3)$(1M7AI)] by UVA Irradiation. Mechanistic Insights. *Inorg. Chim. Acta.* **2018**, *472*, 199–206.

(19) Štarha, P.; Trávníček, Z.; Dvořák, Z.; Radošová-Muchová, T.; Prachařová, J.; Vančo, J.; Kašpárková, J. Potentiating Effect of UVA Irradiation on Anticancer Activity of Carboplatin Derivatives Involving 7-Azaindoles. *PLoS One.* **2015**, *10*, e0123595.

(20) Mitra, K.; Patil, S.; Kondaiah, P.; Chakravarty, A. R. 2-(Phenylazo)Pyridineplatinum(II) Catecholates Showing Photocytotoxicity, Nuclear Uptake, and Glutathione-Triggered Ligand Release. *Inorg. Chem.* **2015**, *54*, 253–264.

(21) Raza, M. K.; Mitra, K.; Shettar, A.; Basu, U.; Kondaiah, P.; Chakravarty, A. R. Photoactive Platinum(II) β-Diketonates as Dual Action Anticancer Agents. *Dalton Trans.* **2016**, *45*, 13234–13243.

(22) Mitra, K.; Gautam, S.; Kondaiah, P.; Chakravarty, A. R. The cis-Diammineplatinum(II) Complex of Curcumin: A Dual Action DNA Crosslinking and Photochemotherapeutic Agent. *Angew. Chem., Int. Ed.* **2015**, *54*, 13989–13993.

(23) Mitra, K.; Lyons, C. E.; Hartman, M. C. T. T. A Platinum(II) Complex of Heptamethine Cyanine for Photoenhanced Cytotoxicity and Cellular Imaging in Near-IR Light. *Angew. Chem., Int. Ed.* **2018**, *57*, 10263–10267.

(24) Morales, K.; Samper, K. G.; Peña, Q.; Hernando, J.; Lorenzo, J.; Rodríguez-Diéguez, A.; Capdevila, M. M.; Figueredo, M.; Palacios, Ò.; Bayón, P.; et al. Squaramide-Based Pt(II) Complexes as Potential Oxygen-Regulated Light-Triggered Photocages. *Inorg. Chem.* **2018**, *57*, 15517–15525.

(25) Maity, B.; Gadadhar, S.; Goswami, T. K.; Karande, A. A.; Chakravarty, A. R. Photo-Induced Anticancer Activity of Polypyridyl Platinum(II) Complexes. *Eur. J. Med. Chem.* **2012**, *57*, 250–258.

(26) Mitra, K.; Basu, U.; Khan, I.; Maity, B.; Kondaiah, P.; Chakravarty, A. R. Remarkable Anticancer Activity of Ferrocenyl-Terpyridine Platinum(II) Complexes in Visible Light with Low Dark Toxicity. *Dalton Trans.* **2014**, *43*, 751–763.

(27) Mitra, K.; Shettar, A.; Kondaiah, P.; Chakravarty, A. R. Biotinylated Platinum(II) Ferrocenylterpyridine Complexes for Targeted Photoinduced Cytotoxicity. *Inorg. Chem.* **2016**, *55*, 5612–5622.

(28) Raza, M. K.; Gautam, S.; Garai, A.; Mitra, K.; Kondaiah, P.; Chakravarty, A. R. Monofunctional BODIPY-Appended Imidazoplatin for Cellular Imaging and Mitochondria-Targeted Photocytotoxicity. *Inorg. Chem.* **2017**, *56*, 11019–11029.

(29) Xue, X.; Zhu, C.; Chen, H.; Bai, Y.; Shi, X.; Jiao, Y.; Chen, Z.; Miao, Y.; He, W.; Guo, Z. A New Approach to Sensitize Antitumor Monofunctional Platinum(II) Complexes via Short Time Photo-Irradiation. *Inorg. Chem.* **2017**, *56*, 3754–3762.

(30) Li, H.; Lan, R.; Chan, C.-F. F.; Jiang, L.; Dai, L.; Kwong, D. W. J. J.; Lam, M. H.-W. W.; Wong, K.-L. L. Real-Time in Situ Monitoring via Europium Emission of the Photo-Release of Antitumor Cisplatin from a Eu-Pt Complex. *Chem. Commun.* **2015**, *51*, 14022–14025.

(31) Quental, L. L.; Raposinho, P.; Mendes, F.; Santos, I.; Navarro-Ranninger, C.; Alvarez-Valdes, A.; Huang, H.; Chao, H.; Rubbiani, R.; Gasser, G.; et al. Combining Imaging and Anticancer Properties with New Heterobimetallic Pt(II)/M(I) (M = Re, 99mTc) Complexes. *Dalton Trans.* **2017**, *46* (42), 14523–14536.

(32) Kastner, A.; Poetsch, I.; Mayr, J.; Burda, J. V.; Roller, A.; Heffeter, P.; Keppler, B. K.; Kowol, C. R. Doubt on a Dogma: Aquation of Equatorial Ligands of Pt(IV) Complexes under Physiological Conditions. *Angew. Chem., Int. Ed.* **2019**, *58*, 7464-7469.

(33) Johnstone, T. C.; Suntharalingam, K.; Lippard, S. J. The Next Generation of Platinum Drugs: Targeted Pt(II) Agents, Nanoparticle Delivery, and Pt(IV) Prodrugs. *Chem. Rev.* **2016**, *116*, 3436–3486.

(34) Gibson, D. Platinum(IV) Anticancer Prodrugs-Hypotheses and Facts. *Dalton Trans.* **2016**, *45*, 12983–12991.

(35) Hall, M. D.; Hambley, T. W. Platinum(IV) Antitumour Compounds: Their Bioinorganic Chemistry. *Coord. Chem. Rev.* **2002**, *232*, 49–67.

(36) Sinisi, M. M.; Intini, F. P.; Natile, G. Dependence of the Reduction Products of Platinum(IV) Prodrugs upon the Configuration of the Substrate, Bulk of the Carrier Ligands, and Nature of the Reducing Agent. *Inorg. Chem.* **2012**, *51*, 9694–9704.

(37) Varbanov, H. P.; Jakupec, M. A.; Roller, A.; Jensen, F.; Galanski, M.; Keppler, B. K. Theoretical Investigations and Density Functional Theory Based Quantitative Structure-Activity Relationships Model for Novel Cytotoxic Platinum(IV) Complexes.

J. Med. Chem. **2013**, *56*, 330–344.

(38) Gibbons, G. R.; Wyrick, S.; Chaney, S. G. Rapid Reduction of Tetrachloro(D,L-trans)1,2-Diaminocyclohexaneplatinum(IV) (Tetraplatin) in RPMI 1640 Tissue Culture Medium. *Cancer Res.* **1989**, *49*, 1402–1407.

(39) Brown, D.; Swindell, R.; Timms, M. S.; Wagstaff, J.; Crowther, D.; Palmer, P.; Lind, M. J.; McGregor, J.; Anderson, H. Comparative Toxicity of Cisplatin, Carboplatin (CBDCA) and Iproplatin (CHIP) in Combination with Cyclophosphamide in Patients with Advanced Epithelial Ovarian Cancer. *Eur. J. Cancer Clin. Oncol.* **1988**, *24*, 1471–1479.

(40) Sternberg, C. N.; Whelan, P.; Hetherington, J.; Paluchowska, B.; Slee, P. H. T. J.; Vekemans, K.; Van Erps, P.; Theodore, C.; Koriakine, O.; Oliver, T.; et al. Phase III Trial of Satraplatin, an Oral Platinum plus Prednisone vs. Prednisone Alone in Patients with Hormone-Refractory Prostate Cancer. *Oncology* **2005**, *68*, 2–9.

(41) Kratochwil, N. A.; Zabel, M.; Range, K.-J. J.; Bednarski, P. J. Synthesis and X-Ray Crystal Structure of trans,cis-[Pt(OAc)$_2$I$_2$(En)]: A Novel Type of Cisplatin Analog That Can Be Photolyzed by Visible Light to DNA-Binding and Cytotoxic Species in Vitro. *J. Med. Chem.* **1996**, *39*, 2499–2507.

(42) Kratochwil, N. A.; Bednarski, P. J.; Mrozek, H.; Vogler, A.; Nagle, J. K. Photolysis of an Iodoplatinum(IV) Diamine Complex to Cytotoxic Species by Visible Light. *Anticancer. Drug Des.* **1996**, *11*, 155–171.

(43) Parkinson, J. A.; Sadler, P. J.; Kratochwil, N. A.; Bednarski, P. J.; Guo, Z.; del Socorro Murdoch, P. Electron-Transfer-Driven Trans-Ligand Labilization: A Novel Activation Mechanism for Pt(IV) Anticancer Complexes. *J. Am. Chem. Soc.* **1998**, *120*, 8253–8254.

(44) Müller, P.; Schröder, B.; Parkinson, J. A.; Kratochwil, N. A.; Coxall, R. A.; Parkin, A.; Parsons, S.; Sadler, P. J. Nucleotide Cross-Linking Induced by Photoreactions of Platinum(IV)–Azide Complexes. *Angew. Chem., Int. Ed.* **2003**, *42*, 335–339.

(45) Vogler, A.; Kern, A.; Hüttermann, J. Photochemical Reductive trans-Elimination from trans-Diazidotetracyanoplatinate(IV). *Angew. Chem., Int. Ed. Engl.* **1978**, *17*, 524–525.

(46) Weber, W.; Van Eldik, R. Charge-Transfer Photochemistry under High Pressure: Reductive Elimination from Trans-Diazidotetracyanoplatinate(IV). *Inorg. Chim. Acta.* **1986**, *111*, 129–131.

(47) Vogler, A.; Kern, A.; Fußeder, B.; Hüttermann, J. Photochemical Reductive Trans-Elimination from trans-Diacidotetracyanoplatinate(IV) Complexes. *Zeitschrift für Naturforsch. B.* **1978**, *33*, 1352–1356.

(48) Kašpárková, J.; Mackay, F. S.; Brabec, V.; Sadler, P. J.; Kasparkova, J.; Mackay, F. S.; Brabec, V.; Sadler, P. J. Formation of Platinated GG Cross-Links on DNA by Photoactivation of a Platinum(IV) Azide Complex. *J. Biol. Inorg. Chem.* **2003**, *8*, 741–745.

(49) Salassa, L.; Phillips, H. I. A. A.; Sadler, P. J. Decomposition Pathways for the Photoactivated Anticancer Complex cis,trans,cis-$[Pt(N_3)_2(OH)_2(NH_3)_2]$: Insights from DFT Calculations. *Phys. Chem. Chem. Phys.* **2009**, *11*, 10311–10316.

(50) Bednarski, P. J.; Grünert, R.; Zielzki, M.; Wellner, A.; Mackay, F. S.; Sadler, P. J. Light-Activated Destruction of Cancer Cell Nuclei by Platinum Diazide Complexes. *Chem. Biol.* **2006**, *13*, 61–67.

(51) Mackay, F. S.; Woods, J. A.; Moseley, H.; Ferguson, J.; Dawson, A.; Parsons, S.; Sadler, P. J. A Photoactivated trans-Diammine Platinum Complex as Cytotoxic as Cisplatin. *Chem. Eur. J.* **2006**, *12*, 3155–3161.

(52) Farrer, N. J.; Woods, J. A.; Salassa, L.; Zhao, Y.; Robinson, K. S.; Clarkson, G.; MacKay, F. S.; Sadler, P. J. A Potent trans-Diimine Platinum Anticancer Complex Photoactivated by Visible Light. *Angew. Chem., Int. Ed.* **2010**, *49*, 8905–8908.

(53) Westendorf, A. F.; Bodtke, A.; Bednarski, P. J. Studies on the Photoactivation of Two Cytotoxic trans,trans,trans-Diazidodiaminodihydroxo-Pt(IV) Complexes. *Dalton Trans.* **2011**, *40*, 5342–5351.

(54) Mackay, F. S.; Woods, J. A.; Heringová, P.; Kašpárková, J.; Pizarro, A. M.; Moggach, S. A.; Parsons, S.; Brabec, V.; Sadler, P. J. A Potent Cytotoxic Photoactivated Platinum Complex. *Proc. Natl. Acad. Sci.* **2007**, *104*, 20743–20748.

(55) Novakova, O.; Zerzankova, L.; Pracharova, J.; Kasparkova, J.; Stepankova, J.; Brabec, V.; Farrer, N. J.; Sadler, P. J.; Zerzankova, L.; Stepankova, J.; et al. Interactions of DNA with a New Platinum(IV) Azide Dipyridine Complex Activated by UVA and Visible Light: Relationship to Toxicity in Tumor Cells. *Chem. Res. Toxicol.* **2012**, *25*, 1099–1111.

(56) Zhang, J.; Li, X.; Han, X.; Liu, R.; Fang, J. Targeting the Thioredoxin System for Cancer Therapy. *Trends Pharmacol. Sci.* **2017**, *38*, 794–808.

(57) Du, J.; Wei, Y.; Zhao, Y.; Xu, F.; Wang, Y.; Zheng, W.; Luo, Q.; Wang, M.; Wang, F. A Photoactive Platinum(IV) Anticancer Complex Inhibits Thioredoxin-Thioredoxin Reductase System Activity by Induced Oxidization of the Protein. *Inorg. Chem.* **2018**, *57*, 5575–5584.

(58) Wootton, C. A.; Sanchez-Cano, C.; Lopez-Clavijo, A. F.; Shaili, E.; Barrow, M. P.; Sadler, P. J.; O'Connor, P. B. Sequence-Dependent Attack on Peptides by Photoactivated Platinum Anticancer Complexes. *Chem. Sci.* **2018**, *9*, 2733–2739.

(59) Westendorf, A. F.; Woods, J. A.; Korpis, K.; Farrer, N. J.; Salassa, L.; Robinson, K.; Appleyard, V.; Murray, K.; Grünert, R.; Thompson, A. M.; et al. trans,trans,trans-$[Pt^{IV}(N_3)_2(OH)_2(Py)(NH_3)]$: A Light-Activated Antitumor Platinum Complex That Kills Human Cancer Cells by an Apoptosis-Independent Mechanism. *Mol. Cancer Ther.* **2012**, *11*, 1894–1904.

(60) Butler, J. S.; Woods, J. A.; Farrer, N. J.; Newton, M. E.; Sadler, P. J. Tryptophan Switch for a Photoactivated Platinum Anticancer Complex. *J. Am. Chem. Soc.* **2012**, *134*, 16508–16511.

(61) Mackay, F. S.; Farrer, N. J.; Salassa, L.; Tai, H.-C.; Deeth, R. J.; Moggach, S. A.; Wood, P. A.; Parsons, S.; Sadler, P. J. Synthesis, Characterisation and Photochemistry of Pt(IV) Pyridyl Azido Acetato Complexes. *Dalton Trans.* **2009**, 13, 2315–2325.

(62) Mackay, F. S.; Moggach, S. A.; Collins, A.; Parsons, S.; Sadler, P. J. Photoactive trans Ammine/Amine Diazido Platinum(IV) Complexes. *Inorg. Chim. Acta* **2009**, *362*, 811–819.

(63) Farrer, N. J.; Woods, J. A.; Munk, V. P.; Mackay, F. S.; Sadler, P. J. Photocytotoxic trans-Diam(m)Ine Platinum(IV) Diazido Complexes More Potent than Their cis Isomers. *Chem. Res. Toxicol.* **2010**, *23*, 413–421.

(64) Venkatesh, V.; Wedge, C. J.; Romero-Canelón, I.; Habtemariam, A.; Sadler, P. J.; Romero-Canelon, I.; Habtemariam, A.; Sadler, P. J.; Wedge, C. J.; Romero-Canelon, I.; et al. Spin-Labelled Photo-Cytotoxic Diazido Platinum(IV) Anticancer Complex. *Dalton Trans.* **2016**, *45*, 13034–13037.

(65) Gandioso, A.; Shaili, E.; Massaguer, A.; Artigas, G.; González-Cantó, A.; Woods, J. A.; Sadler, P. J.; Marchán, V. An Integrin-Targeted Photoactivatable Pt(IV) Complex as a Selective Anticancer pro-Drug: Synthesis and Photoactivation Studies. *Chem. Commun.* **2015**, *51*, 9169–9172.

(66) Shaili, E.; Fernández-Giménez, M.; Rodríguez-Astor, S.; Gandioso, A.; Sandín, L.; García-Vélez, C.; Massaguer, A.; Clarkson, G. J.; Woods, J. A.; Sadler, P. J.; et al. A Photoactivatable Platinum(IV) Anticancer Complex Conjugated to the RNA Ligand Guanidinoneomycin. *Chem. Eur. J.* **2015**, *21*, 18474–18486.

(67) Dougherty, T. J.; Grindey, G. B.; Fiel, R.; Weishaupt, K. R.; Boyle, D. G. Photoradiation Therapy. II. Cure of Animal Tumors with Hematoporphyrin and Light. *J. Natl. Cancer Inst.* **1975**, *55*, 115–121.

(68) Granelli, S. G.; McDonagh, A. F.; Wilson, C. B.; Nielsen, S. L. Photochemotherapy of Glioma Cells by Visible Light and Hematoporphyrin. *Cancer Res.* **1975**, *35*, 2567–2570.

(69) Wang, Z.; Wang, N.; Cheng, S. C.; Xu, K.; Deng, Z.; Chen, S.; Xu, Z.; Xie, K.; Tse, M. K.; Shi, P.; et al. Phorbiplatin, a Highly Potent Pt(IV) Antitumor Prodrug That Can Be Controllably Activated by Red Light. *Chem* **2019**, *5*, 3151–3165.

(70) Song, H.; Kang, X.; Sun, J.; Jing, X.; Wang, Z.; Yan, L.; Qi, R.; Zheng, M. Nanoparticle Delivery of Sterically Hindered Platinum(IV) Prodrugs Shows 100 Times Higher Potency than That of Cisplatin upon Light Activation. *Chem. Commun.* **2016**, *52*, 2281–2283.

(71) He, S.; Li, C.; Zhang, Q.; Ding, J.; Liang, X.-J.; Chen, X. X.; Xiao, H.; Chen, X. X.; Zhou, D.; Huang, Y. Tailoring Platinum(IV) Amphiphiles for Self-Targeting All-in-One Assemblies as Precise Multimodal Theranostic Nanomedicine. *ACS Nano* **2018**, *12*, 7272–7281.

(72) Guo, D.; Xu, S.; Huang, Y.; Jiang, H.; Yasen, W.; Wang, N.; Su, Y.; Qian, J.; Li, J.; Zhang, C.; et al. Platinum(IV) Complex-Based Two-in-One Polyprodrug for a Combinatorial Chemo-Photodynamic Therapy. *Biomaterials* **2018**, *177*, 67–77.

(73) D'Souza, A. A.; Devarajan, P. V. Asialoglycoprotein Receptor Mediated Hepatocyte Targeting—Strategies and Applications. *J. Control. Release* **2015**, *203*, 126–139.

(74) Venkatesh, V.; Mishra, N. K.; Romero-Canelón, I.; Vernooij, R. R.; Shi, H.; Coverdale, J. P. C. C.; Habtemariam, A.; Verma, S.; Sadler, P. J.; Romero-Canelon, I.; et al. Supramolecular Photoactivatable Anticancer Hydrogels. *J. Am. Chem. Soc.* **2017**, *139*, 5656–5659.

(75) Maldonado, C. R.; Gómez-Blanco, N.; Jauregui-Osoro, M.; Brunton, V. G.; Yate, L.; Mareque-Rivas, J. C. QD-Filled Micelles Which Combine SPECT and Optical Imaging with Light-Induced Activation of a Platinum(IV) Prodrug for Anticancer Applications. *Chem. Commun.* **2013**, *49*, 3985–3987.

(76) Infante, I.; Azpiroz, J. M.; Blanco, N. G.; Ruggiero, E.; Ugalde, J. M.; Mareque-Rivas, J. C.; Salassa, L. Quantum Dot Photoactivation of Pt(IV) Anticancer Agents: Evidence of an Electron Transfer Mechanism Driven by Electronic Coupling. *J. Phys. Chem. C* **2014**, *118*, 8712–8721.

(77) Yang, X. D.; Xiang, H. J.; An, L.; Yang, S. P.; Liu, J. G. Targeted Delivery of Photoactive Diazido Pt(IV) Complexes Conjugated with Fluorescent Carbon Dots. *New J. Chem.* **2015**, *39*, 800–804.

(78) Shi, S.-W.; Li, Y.-H.; Zhang, Q. Q.-L.; Yang, S.-P. S.; Liu, J.-G. Targeted and NIR Light-Controlled Delivery of Nitric Oxide Combined with a Platinum(IV) Prodrug for Enhanced Anticancer Therapy. *J. Mater. Chem. B* **2019**, *7*, 1867–1874.

(79) Haase, M.; Schäfer, H. Upconverting Nanoparticles. *Angew. Chem., Int. Ed.* **2011**, *50*, 5808–5829.

(80) Ruggiero, E.; Hernández-Gil, J.; Mareque-Rivas, J. C.; Salassa, L. Near Infrared Activation of an Anticancer Pt(IV) Complex by Tm-Doped Upconversion Nanoparticles. *Chem. Commun.* **2015**, *51*, 2091–2094.

(81) Perfahl, S.; Natile, M. M.; Mohamad, H. S.; Helm, C. A.; Schulzke, C.; Natile, G.; Bednarski, P. J. Photoactivation of Diiodido-Pt(IV) Complexes Coupled to Upconverting Nanoparticles. *Mol. Pharm.* **2016**, *13*, 2346–2362.

(82) Dai, Y.; Xiao, H.; Liu, J.; Yuan, Q.; Ma, P.; Yang, D.; Li, C.; Cheng, Z.; Hou, Z.; Yang, P.; et al. In Vivo Multimodality Imaging and Cancer Therapy by Near-Infrared Light-Triggered Trans-Platinum Prodrug-Conjugated Upconverison Nanoparticles. *J. Am. Chem. Soc.* **2013**, *135*, 18920–18929.

(83) Min, Y.; Li, J.; Liu, F.; Yeow, E. K. L.; Xing, B. Near-Infrared Light-Mediated Photoactivation of a Platinum Antitumor Prodrug and Simultaneous Cellular Apoptosis Imaging by Upconversion-Luminescent Nanoparticles. *Angew. Chem., Int. Ed.* **2014**, *53*, 1012–1016.

(84) Wu, S.; Blinco, J. P.; Barner-Kowollik, C. Near-IR Photoinduced Reactions Assisted by Upconverting Nanoparticles. *Chem. Eur. J.* **2017**, *23*, 8325–8332.

(85) Wang, D.; Xue, B.; Kong, X.; Tu, L.; Liu, X.; Zhang, Y.; Chang, Y.; Luo, Y.; Zhao, H.;

Zhang, H. 808 Nm Driven Nd3+-Sensitized Upconversion Nanostructures for Photodynamic Therapy and Simultaneous Fluorescence Imaging. *Nanoscale* **2015**, *7*, 190–197.

2

Bioorthogonal Chemotherapeutic Activation

2.1 Introduction

Cancer is one of the most frequent severe disease nowadays and is associated with ageing of the population, environmental pollutants and life style.[1] The term cancer refers to a group of diseases that have as common feature the abnormal, undifferentiated and unstopped growth and cell division. These abnormal cells are invasive, they hamper the normal functioning of healthy cells and are able to avoid the programmed cell death.[2] These malignant cancerous cells can invade other nearby tissues, replicating the cancer in another place of the body. There are many kinds of cancers, such as, carcinoma, melanoma, leukemia, etc. and each one has its own specific features.[2] The first evidence of human cancer was reported around three thousand years B.C. in the ancient Egypt but the word cancer was coined in the ancient Greece by the medical doctor Hippocrates. [3,4]

Being one of the most extended fatal diseases of our time, cancer has been intensively investigated and many kinds of treatments have been developed. The applicability of each therapeutic approach depends on the type and the stage of the cancer. Most of the patients that suffer cancer, receive one or a combination of the following treatments:[5]

- ***Surgery***: a physical procedure to remove the cancerous tissue.
- ***Radiation therapy***: a therapy in which high doses of radiation, usually X-rays, are used to kill the cancerous cells.
- ***Chemotherapy***: a treatment consisting in the use of cytotoxic drugs to kill the cancerous cells. After high doses of chemotherapy patients may have stem cells transplant to restore bone marrow cells killed by the chemotherapy.
- ***Immunotherapy***: an approach in which the immune system of the patient is stimulated to fight against the cancer. Cytokines or antibodies that stimulate the intrinsic immune system and vaccines and checkpoint inhibitors that prepare the immune response against antigens are the most representative examples of this treatment.
- ***Hormone therapy***: administration of hormones to slow down or suppress the growth of specific tumors.
- ***Gene therapy***: a vector, normally a virus is used to deliver a specific genetic information into cancer cells changing their native features. This delivered information can be useful to improve the action of other treatments such as immunotherapy. Even though this treatment is attractive and promising, it is at an early stage of development and must be optimized for future applications.

Surgery, radiotherapy and chemotherapy have been the most used anticancer treatments worldwide to date. As the understanding of cancer biology grows, other treatments such as immunotherapy are gaining momentum, although nowadays are

less extended than chemotherapy. In this context, until these new-born treatments are more developed, much effort have been expended to improve classic treatments and above all chemotherapy. Many organic and inorganic compounds have been designed and synthesized in the last decades as anticancer agents, but only few of them have reached approval by the Food and Drug Administration (FDA) or the European Medicines Agency (EMA).

The majority of approved antineoplastic compounds trigger their cytotoxic activity interrupting cell division. Since cancerous cells divide faster than healthy cells, drugs preferentially affect tumor cells.[6] However, this occurs often with very low selectivity for cancerous tissues, hence causing severe systemic side effects such as nephro and neurotoxicity.[7]

Against this drawback, physicochemical modifications of pharmacologically active drugs arose as possible strategies to avoid undesired side effects. Prodrugs are inert or less toxic masked derivatives of parent drugs which under certain conditions become active.[8] The rationale behind the use of prodrugs is to overcome issues associated with the absorption, distribution, metabolism, excretion, and unwanted toxic effects of the parent drugs.[9] There are two main designs of prodrugs. On one hand, carrier-linked prodrugs in which the active molecule is linked to a carrier that later is cleaved releasing the drug. On the other hand, structurally modified drugs which are chemically transformed into the active compound by biological components.[8] Overall, prodrugs constrain undesired toxic effects and at the same time can enhance the effectiveness of the treatment by the selective exhibition of pharmacological effect at the needed location.

To achieve maximum selectivity in the activation process, biorthogonal chemistry emerged as a very attractive tool. Bertozzi and coworkers defined as bioorthogonal chemistry, those reactions that take place in biological media without interfering with native biological processes. The term was conceived to describe the selective labelling of azide containing glycoproteins with phosphine probes via Staudinger ligation in cellular environments (Figure 1).[10] Despite the term biorthogonal chemistry was coined to describe this protein labelling reaction, it now extends to non-natural reactions inside cells with a high degree of selectivity such as, protein, lipid and glycan modifications, azide alkyne reactions, prodrug uncaging and activation reactions, among others.[11]

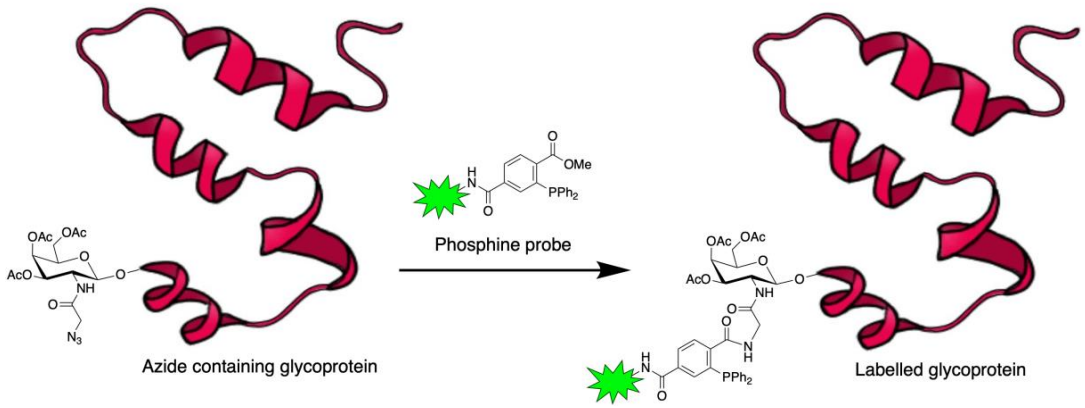

Figure 1. Schematic representation of glycoprotein labelling described by Bertozzi et al.[10]

Since chemists and biologists began to share knowledge to obtain a deeper understanding of life, enzymes became the focus of attention. Enzymes, are proteins able to perform a myriad of selective and efficient catalytic reactions inside biological organisms. A third of all the known enzymes, require metal ions for their function.[12] This fact inspired chemists to synthesize metal catalysts that mimic natural enzymes, able to react with many copies of targeted substrates in cells. Catalytic reactions suitable for chemotherapeutic purposes can provide new tools for the development of antineoplasic drug activation strategies. In fact, biorthogonal catalytic reactions can amplify a biological response and induced a therapeutic effect inside organisms with unmatched selectivity.[13] All biorthogonal reactions have in common that are biocompatible, selective and take place in aqueous media. Therefore, biorthogonal catalysts must be not toxic at the concentration needed to perform the desired catalytic reaction and work selectively in a very demanding aqueous media, full of other potential substrates (such as, sugars, amino acids, lipids and all kinds of biomolecules) that can give secondary reactions.[14] One of the most challenging objectives in the field of biorthogonal catalysis is still the controlled delivery and reactivity of catalysts due the complexity of multicellular organisms.

This chapter discusses relevant examples of the different biorthogonal catalysis approaches employed for application in cancer chemotherapy, distinguishing three main strategies based on the nature of the catalyst:

- Bioorthogonal catalysis mediated by metal complexes
- Nanobots mediated catalytic activation
- Bioorthogonal photocatalysis using metal complexes as substrates

2.2 Bioorthogonal catalysis mediated by metal complexes

Catalysis can be defined as a chemical reaction that in the presence of a mediator called catalyst increases its rate without a net change in the amount of the catalyst.[15] Metal catalyst have been widely used as mediators to transform organic molecules into added value molecules.[16] However, in the last decade, some groups dedicated to the field of inorganic medicinal chemistry have used metal catalysts for chemotherapeutic purposes, exploiting their unique physicochemical properties. Nowadays, metal catalysts allow to perform a diversity of transformations in biological media that are impossible to achieve by classical methodologies.[17] In this section, metal catalysis occurring in biological environments are divided in two groups depending on their application in medicinal chemistry. Catalytic metallodrugs that trigger a toxic effect and metal catalysts that transform caged substrates for imaging or therapeutic applications.

2.2.1 Catalytic metallodrugs

Herein, it is reported a summary of the most representative examples of catalytic metallodrugs that alter the regular function of cells, disturb the redox system, or degrade essential biomolecules of cells.

The redox system is essential in regulating of cellular homeostasis. There is a delicate balance between oxidant and antioxidant species and the alteration of this equilibrium can result in fatal consequences.[18] In photodynamic therapy (PDT) a photosensitizer is irradiated catalyzing the generation of reactive oxygen species (ROS), altering the redox balance and inducing oxidative damage. This therapy has been approved for the treatment of concrete cancers, being Photofrin the only photosensitizer approved worldwide for PDT treatment.[19] Recently, Ru^{II} polypyridyl complexes have been revisited as photosensitizing agents for PDT due their unique photochemical properties. For example, TLD-1433 compound (**1**, Figure 2) synthesized by the group of McFarland showed promising chemotherapeutic effects and completed phase Ib trials for the treatment of bladder cancer.[20]

The group of Sadler exploited the sensitivity of cells to redox balance alterations for chemotherapeutic purposes. They reported phenylazopyridinate Ru^{II} catalysts (**2**a and **2**b, Figure 2) that oxidize the tripeptide glutathione (GSH) into glutathione disulfide (GSSG) inside cells. GSH is the most important low molecular weight antioxidant available inside cells.[21] Catalysts **2**a and **2**b achieved Turn Over Frequency (TOF) and Turn Over Number (TON) values around 0.33 h^{-1} and 40. The TOF is the maximum number of moles of substrate transformed per unit of time, while the TON is the total number of moles of substrate that are transformed at the end of the reaction. These

compounds showed great antiproliferative effects in A549 human lung and A2780 human ovarian cancer lines with IC_{50} values of 2-6 µM. Besides the toxicity produced by the unbalance of GSH/GSSG levels, these ruthenium catalyst generated ROS.[22]

The same group demonstrated that it is possible to alter the redox balance of oxidized and reduced nicotine adenine dinucleotide (NAD^+/NADH) inside cells by Noyori type Ru^{II} sulfonamido ethyleneamine complexes such as **3** (Figure 2) in the presence of non-toxic quantities of formate. Nicotine adenine dinucleotide is an essential cofactors involved in several redox reactions inside cells.[23] In their work, Sadler and coworkers showed that NAD^+ was reduced to NADH by **3**, obtaining TOF values in the range of 0.2-7 h^{-1}. The complex displayed an IC_{50} value of 13.6 µM in A2780 cells. In addition, authors reported that apart from the reduction of NAD^+, other biomolecules, such as ketones or imines could be reduced by **3**, therefore indicating that this catalytic metallodrug was not completely selective.[24]

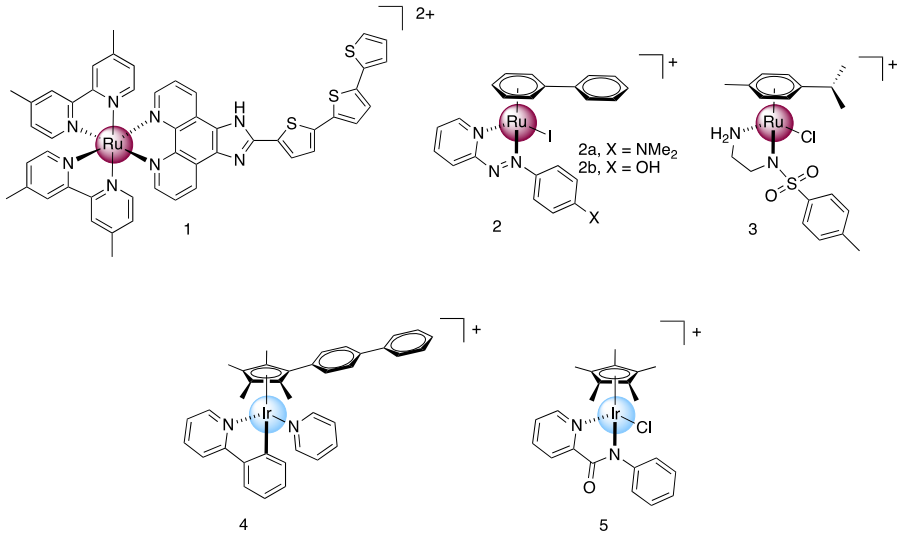

Figure 2. Chemical structure of Ru^{II} and Ir^{III} catalyst employed to generate oxidative stress.

In 2014, the same group synthesized a Ir^{III} catalyst (**4**, Figure 2) able to generate H_2O_2 using NADH as hydride source. Such reactivity was instrumental to affect the redox balance of the cell, ultimately inducing a potent cytotoxic effect (IC_{50} value of 120 nM).[25] Shortly after, Do and collaborators designed the Ir^{III} catalysts **5** (Figure 2) to reduce aldehydes to alcohols for activating an aldehyde-caged fluorophore. Complex **5** catalyzed the hydride transfer from NADH to the protected dye, switching on its fluorescence in biological media. Several aldehydes are formed in metabolic processes and are strongly implicated in a variety of metabolic diseases, neurodegenerative disorders, and cancers.[26] The discoveries of the Do group suggest that it is possible to perform the catalytic detoxification of disease-causing agents by metal catalysts.[26,27]

Another typology of catalytic metallodrugs known since the 1990s is represented by those metal catalysts that are able to decompose or cleave targeted biomolecules such

as proteins, peptides and nucleic acids that are essential for the proper functioning of cells.[28,29] However, the lack of selectivity of many of these metal catalysts towards specific substrates has been one of their main limitations. One of the promising options to improve selectivity, is to incorporate a substrate selective binding motif, restricting the promiscuity of the catalyst.

One of the first examples of metal catalysts that cleave biomolecules was reported in the 90´s by the group of Perrin. They discovered that Cu 1,10-phenanthroline and Fe ethylenediaminetetraacetate complexes acted as artificial nucleases, that induce DNA/RNA cleavage.[28] Later, the group of Sigman synthesized the catalyst **6** (Figure 3) with the sulfonamide inhibitor coordinated to the phenanthroline moiety. This conjugate could bind to the catalytic site of the carbonic anhydrase enzyme and in the presence of ascorbate and O_2 cleaved the enzyme within discrete fragments.[30] Meanwhile, the group of Schultz synthesized Cu and Fe EDTA biotin conjugates (**7**, Figure 3) that bound streptavidin and performed and oxidative cleavage of the polypeptide backbone in the presence of mercaptoethanol and O_2.[31] Su *et al.* synthesized the Co^{III} cyclen catalyst (**8**, Figure 3) that catalytically cleaved the peptide deformylase enzyme via hydrolysis. This compound was studied for the hydrolysis of ß-amyloids and other disease associated proteins.[32]

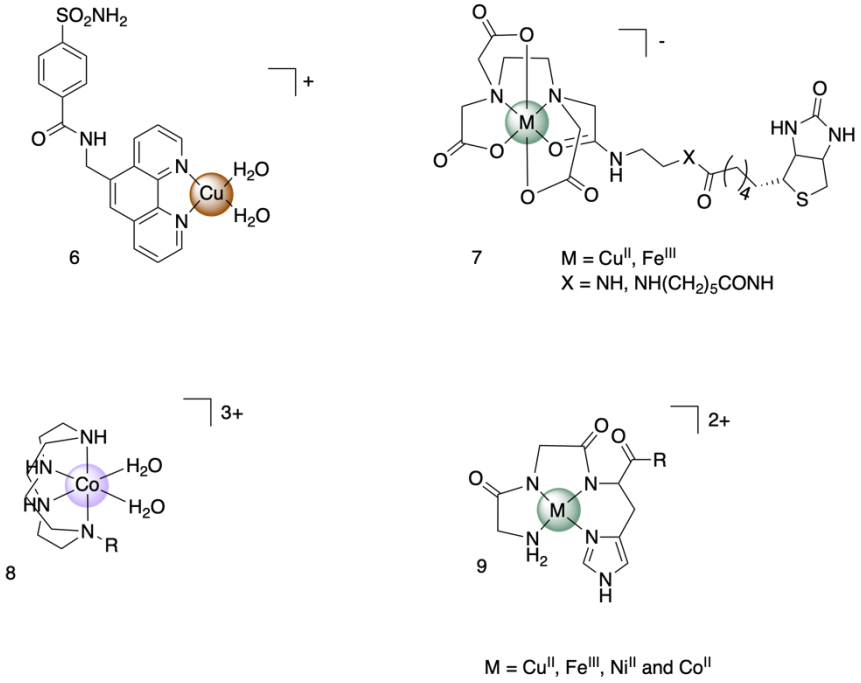

Figure 3. Chemical structure of catalytic metallodrugs that cleave biomolecules.[30-38]

ATCUN (amino terminal Cu^{II} and Ni^{II} binding) peptide motif occurs in certain natural proteins and has been demonstrated to bind $Cu^{2+}$and Ni^{2+} with high affinity. Cowan and collaborators used this ATCUN motifs to coordinate (Cu^{II}, Ni^{II}, Fe^{III} and Co^{II}) different metal ions (**9**, Figure 3) and perform a targeted oxidative or hydrolytic cleavage of different biomolecules. This group reported the cleavage of the

angiotensin converting enzyme[33], the RNA of Hepatitis C [34,35] and VIH [36,37], and fucose.[38]

2.2.2 Metal catalysts that transform caged substrates

Most of the examples of biorthogonal catalytic transformations concern caged substrates and their cleavage and cross coupling reactions. Meggers and Streu described in 2006 for the first time the catalytic cleavage of an allylcarbamate (alloc) protected rhodamine dye inside HeLa cells by a Ru^{II} half sandwich catalyst (**10**, Figure 4). In the presence of thiophenol, **10** uncaged the dye switching on its fluorescence achieving TON values of 4.[39]

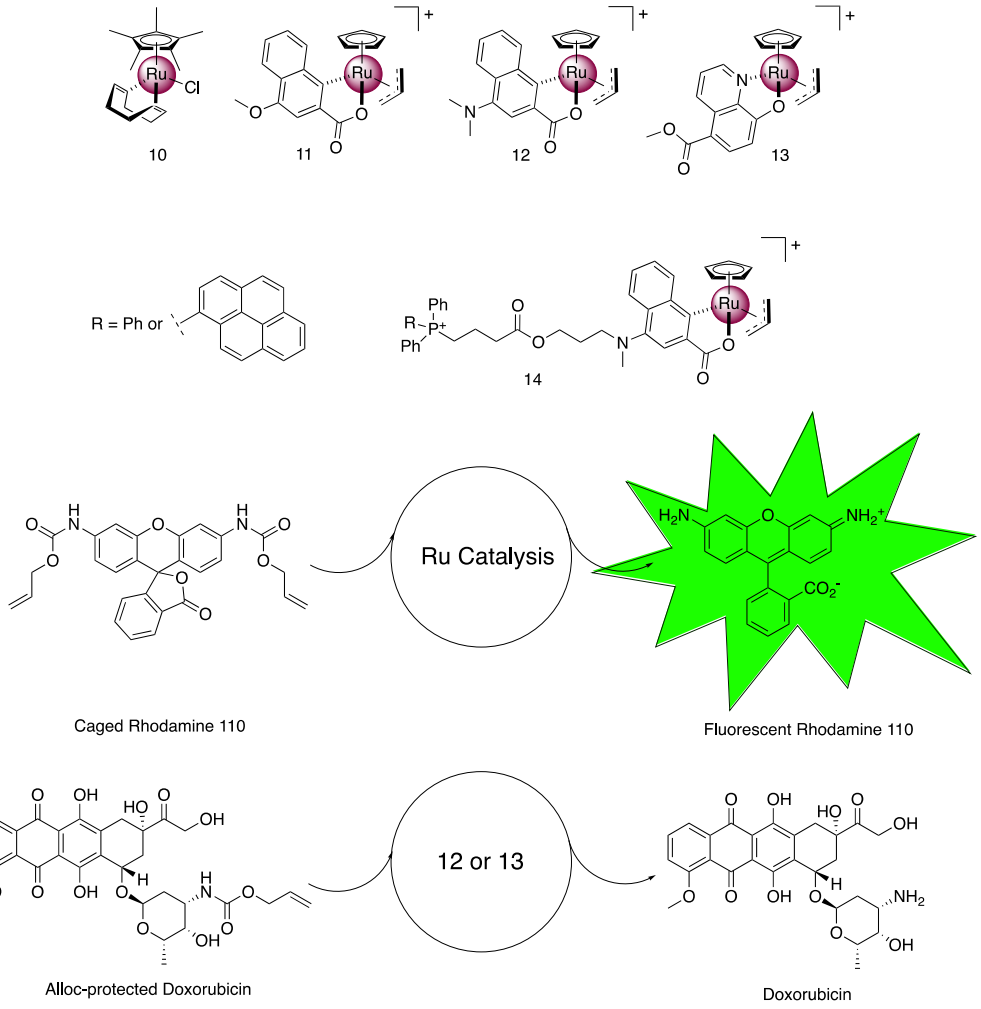

Figure 4. Chemical structures of ruthenium catalysts used inside cells and catalytic activation of protected Rhodamine 110 dye and doxorubicin prodrug. [39-40]

Afterwards, Meggers and collaborators improved the design of their Ru catalysts, synthesizing a set of Ru^{IV} quinoline complexes able to perform the same catalytic cleavage reaction at higher reaction rates in the presence of weaker nucleophiles, such as the endogenous glutathione.[40,41] The quinoline ligand provided higher stability and reactivity to the catalyst, increasing the turn over numbers to 150 and 270 in the case

of **11** and **12** respectively (Figure 4). [40] In addition, they reported that the replacement of quinoline-2-carboxylate by 8-hydroxyquinolinate to generate catalyst **13** (Figure 4), and enhanced the TON over 300 with a reaction rate of 580 M^{-1} s^{-1}.[41] Using **12** and **13,** the Meggers group achieved the catalytic activation of N-(allyloxycarbonyl) protected doxorubicin (alloc-protected doxorubicin, Figure **3**) inside HeLa cells demonstrating the potential of their approach in chemotherapy.[40,41] Doxorubicin is an anthracycline drug that intercalates into DNA and disrupts topoisomerase-II mediated DNA repair and/or generates ROS to produce cellular damage.[42] Catalytic amounts of **13** (2.5 % loading) incubated with alloc-protected doxorubicin showed similar IC_{50} compared to the administration of the parental drug.[40]

In 2014, the group of Mascareñas demonstrated the catalytic activation of alloc-protected DNA binders such as 4´,6-diamidine-2´-phenylindole (DAPI) or ethidium bromide (EtBr) inside cells by catalyst **10**.[43] Later, the same group designed a triphenylphosphonium (TPP) ruthenium conjugate (**14**, Figure 4) that uncaged profluorophores in the mitochondria of mammalian cell. The use of the TPP targeting groups, which are known to accumulate preferentially in mitochondria, allowed to direct the catalyst into this specific organelle. [44]

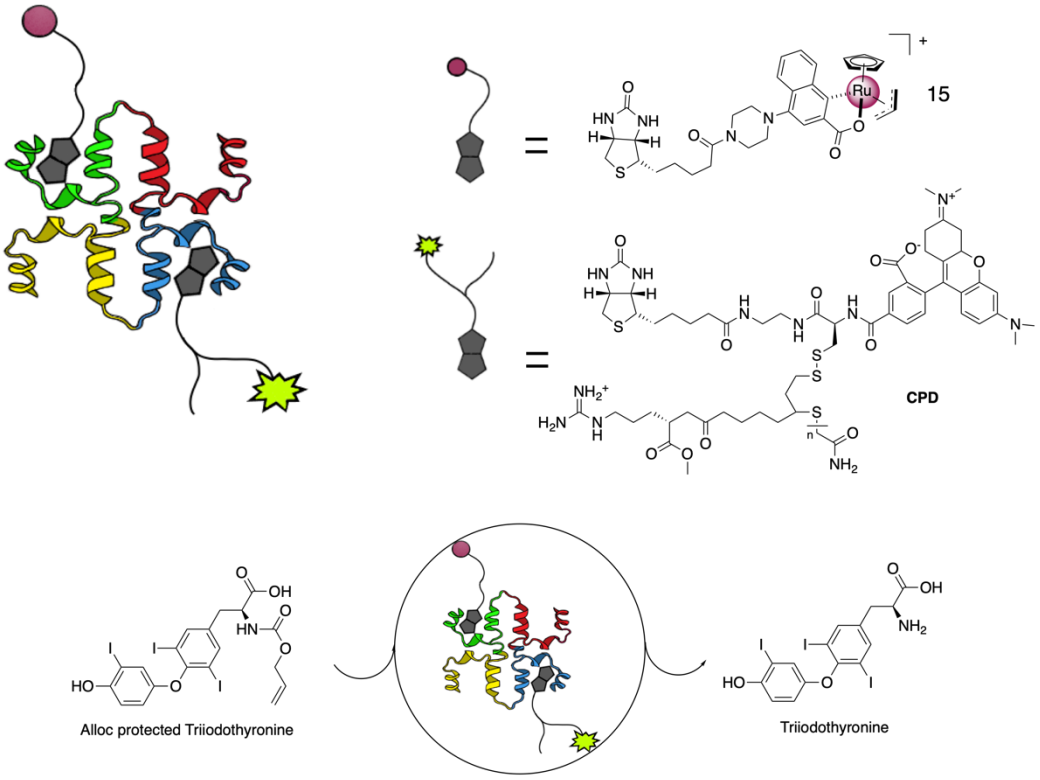

Figure 5. Schematic representation of Streptadivin hybrid catalyst, chemical structures of biotinylated CPD and ruthenium catalyst and catalytic deprotection of triiodothyronine hormone.[45]

In this context, it is also worth mentioning examples of artificial metalloenzyme (ArM) designs, that combine Ru catalysts and protein scaffolds. In 2018, Ward and

collaborators generated a ruthenium streptavidin hybrid catalyst that uncaged the alloc-protected thyroid hormone triiodothyronine in HEK-293T cells, which displayed the thyroid hormone-responsive gene switch (Figure 5). Such hormone is involved in thermogenesis, carbohydrate metabolism, and lipid homeostasis in all tissues. The homotetrameric nature of the streptavidin allowed the integration of the biotinylated Ru catalyst **15** (Figure 5) and a cell-penetrating moiety poly(disulfide) (CPD) attached to the fluorescent tetramethylrhodamine (TAMRA) probe. The protein served as protecting scaffold while the Ru catalyst uncaged the protected hormone. Besides, the poly(disulfide) moiety enhanced the cell uptake and the attached fluorophore enabled the localization of the ArM.[45]

A year later, Tanaka and collaborators developed an artificial glycoalbumin that contained the Ru complex **16** (Figure 6) buried into the protein pocket and performed the catalytic activation of a prodrug of the anticancer agent umbelliprenin via ring-closing metathesis. The protein scaffold protected the catalytic activity of **16** even in the presence of 20 mM of glutathione. This ArM was functionalized with an N-glycan targeting moiety which, accumulated in SW620 colon adenocarcinoma, A549 and HeLa cell lines, probably due the overexpression of galactin-8 receptor.[46]. They tested their artificial metalloenzyme prodrug system *in vitro* in SW620, A549 and HeLa cell lines observing a similar cytotoxicity to the parental drug when the ArM and the prodrug were incubated together.[47]

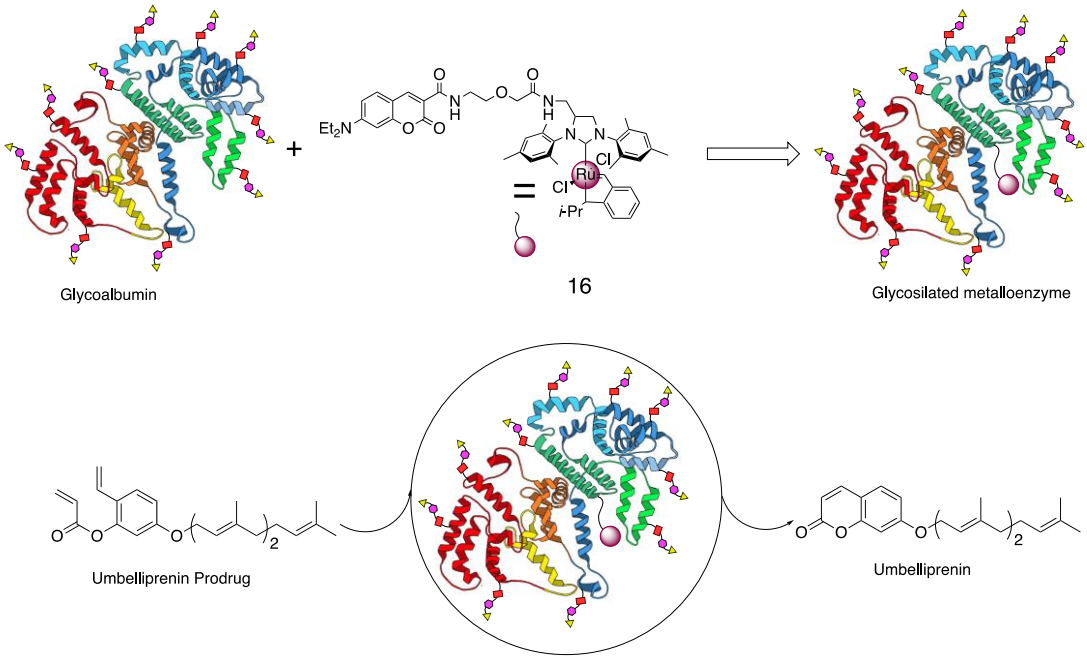

Figure 6. Schematic representation of Tanaka´s ArM, chemical structure of the Ru catalyst **16** and catalytic activation of a umbelliprenin prodrug.[47]

There is a variety of palladium (Pd) mediated biorthogonal reactions, such as biomolecule modifications or deprotection of prodrugs inside cells. In 2014, Chen and

collaborators reported the deprotection of alloc or propargyloxycarbonyl (proc) caged lysine amino acids by Pd^0 **17** and Pd^{II} **18** catalysts *in vitro* (Figure 7). The activity of certain enzymes, in which lysines play an essential role at the catalytic site, can be controlled by this strategy. Gram negative pathogenic bacteria, often deliver OspF phosphothreonine lyase in host cells to modulate the signaling pathways and promote pathogen infection.[48] It irreversibly dephosphorylates mitogen-activated kinases such as phosphorylated ErK (p-Erk); a protein involved in inflammatory response.[49] By the protection of OspF lysines with proc, its dephosphorylating activity on p-Erk was switched off. However, after incubation with catalyst **17** or **18** the dephosphorylation was restored.[50] A couple of years later, they demonstrated that Pd mediated biorthogonal chemistry, offers the possibility to activate other enzymes in which tyrosines are the essential amino acids to carry out their enzymatic activity.[51]

Recently, the group of Bradley, demonstrated that N-heterocyclic carbene based palladium catalyst such as **19** (Figure 7) were able to perform the intracellular deprotection of fluorescent probes and of the proc-protected 5-Fluorouracil (5FU, Figure 7). Remarkably, the deprotection of proc-5FU showed comparable toxic effect to 5FU directly administered.[52]

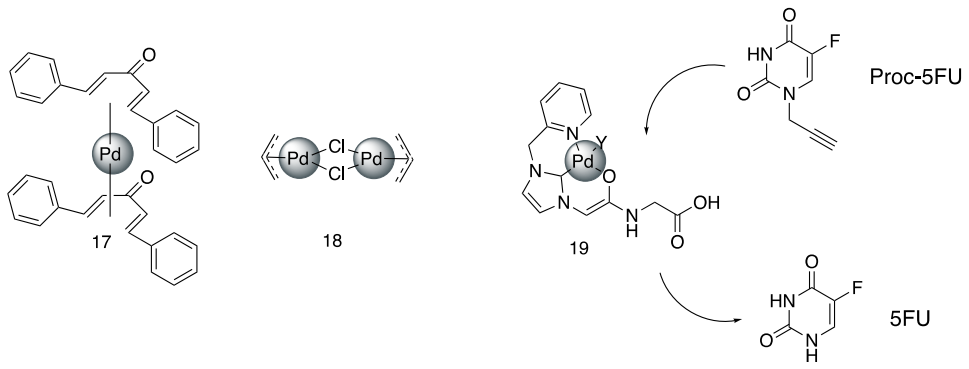

Figure 7. Chemical structure of palladium catalysts employed by Chen, Lin and Bradley.[50-52]

2.3 Nanobots mediated catalytic activation

Despite direct administration of transition metal catalysts has been extensively explored for therapeutic goals, it is still challenging due to limitations associated to solubility, stability and biocompatibility.[53] Given those limitations, the incorporation of transition metal catalysts into artificial nano-scale scaffolds has appeared as a promising strategy to overcome these drawbacks. These structures, called catalytic nanobots, are artificial nanodevices designed to perform biorthogonal catalytic reactions in living systems.[53] In this section the nanobots have been classified in three types, based on their features.

The first class of nanobot, was designed and created by Rotello and coworkers in 2015.[54] The Ru **10** and the Pd **20** catalysts were integrated into the functionalization of small Au nanoparticles (NPs) (around 2 nm) to activate a caged fluorescent probe and an anticancer prodrug (Figure 8). The coating of the NPs was composed by a thiolated hydrophobic alkane chain layer in which the catalysts were encapsulated. The ligand chain also contained a tetraethylene glycol layer to provide a hydrophobic spacer, and a terminal unit formed by a dimethylbenzylammonium group capable to bind to cucurbit uril (CB[7]) that functioned as gatekeeper. Bound CB[7], inhibited the access of the caged substrate to the location of the catalyst by steric hindrance. However, when the competitive guest molecule for CB[7] 1-adamantylamine (ADA) was added, deprotection of the caged substrates took place as represented in Figure 8. So, nanobots that were loaded with catalyst **10** or **20** activated the alloc-protected Rhodamine 110 dye in Hela cells. While catalyst **20**, activated the propargyl-protected 5FU prodrug (Figure 8), that produced a substantial reduction on cell viability. [54]

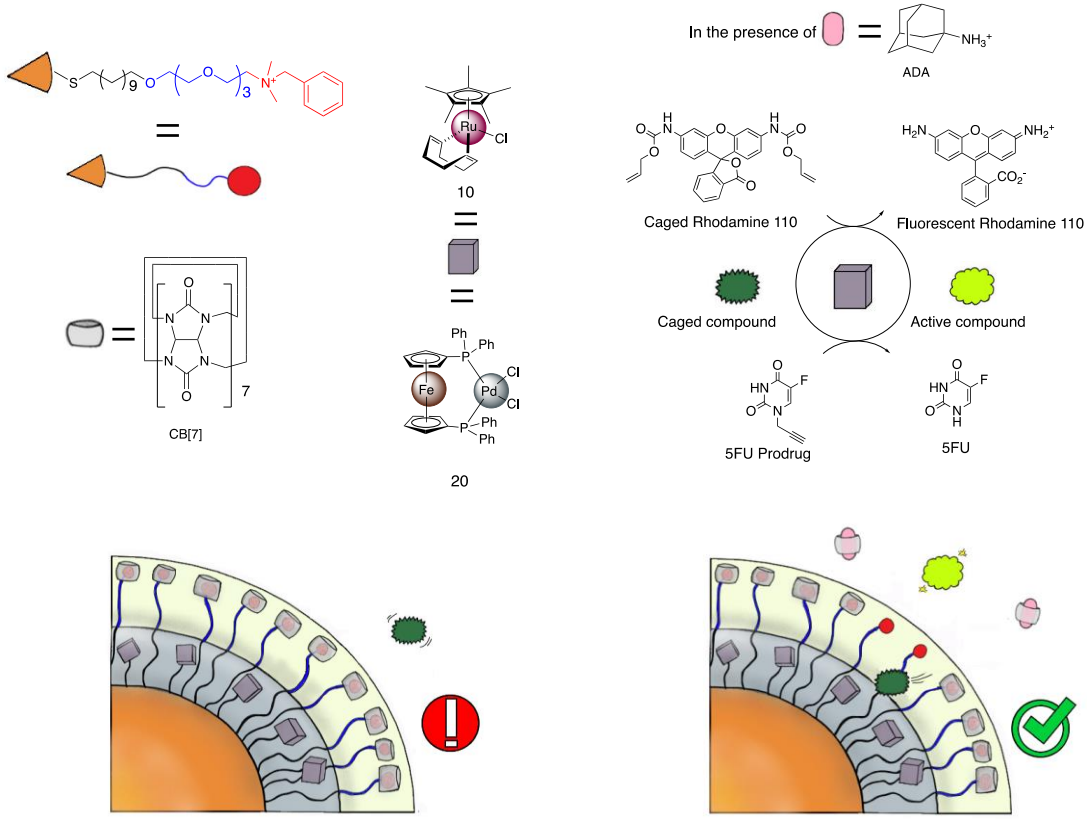

Figure 8. Schematic representation of Rotello and coworker´s Au nanobot. In the absence of ADA, the protected substrate did not suffer any transformation (left), while when ADA was added, CB[7] was released and the transformation of the substrate took place.[54]

Three years later, the same group showed that the modification of the headgroup of the Au NPs coating, could modulate the localization of the NPs and therefore, the catalytic activity of the nanobot. The Ru catalyst **10** was integrated into the coating of the Au nanoplatform to uncage the alloc-protected doxorubicin prodrug **21** intra or

extra cellularly (Figure 9), depending on the headgroup used in the functionalization of the NPs. Authors synthesized two types of Au NPs with different coatings. On one hand, NPs functionalized with the cationic ligand (Pos in Figure 9) were internalized by the cells and therefore the activation of prodrug **21** happened intracellularly. On the other hand, NPs functionalized with the zwitterion ligand (ZW in Figure 9) showed lower levels of uptake and hence the transformation of **21** occurred in the extracellular environment.[55] Despite Rotello and workmates reported a very thorough study about the mechanism of the nanobot, it is important to highlight that their work lacked information regarding the catalytic features such as the turnover number or the turnover frequency of the catalysts.

The second type of nanobot was described Weissleder´s group in 2017.[56] They encapsulated separately a caged substrate and a catalyst into polymeric NPs made of biocompatible poly(lactic-co-glycolic acid)-b-polyethyleneglycol (PLGA-PEG). PLGA-PEG NPs were employed as vehicles to transport simultaneously the prodrug **21** and the Pd catalyst **22** through the cellular environment. After NPs released the loading, the catalyst **22** were capable of activating **21** producing a cytotoxic effect. Among several tested Pd catalysts, **22** showed the highest efficiency on the deprotection of caged substrates under physiologically relevant conditions and in the HT1080 fibrosarcoma cancer cell line. In addition, the activation of **21** was tested in mice bearing two distinct tumor models (ES2 ovarian cancer and H1080 epithelial cancer) showing a great inhibition of the tumoral growth.[56]

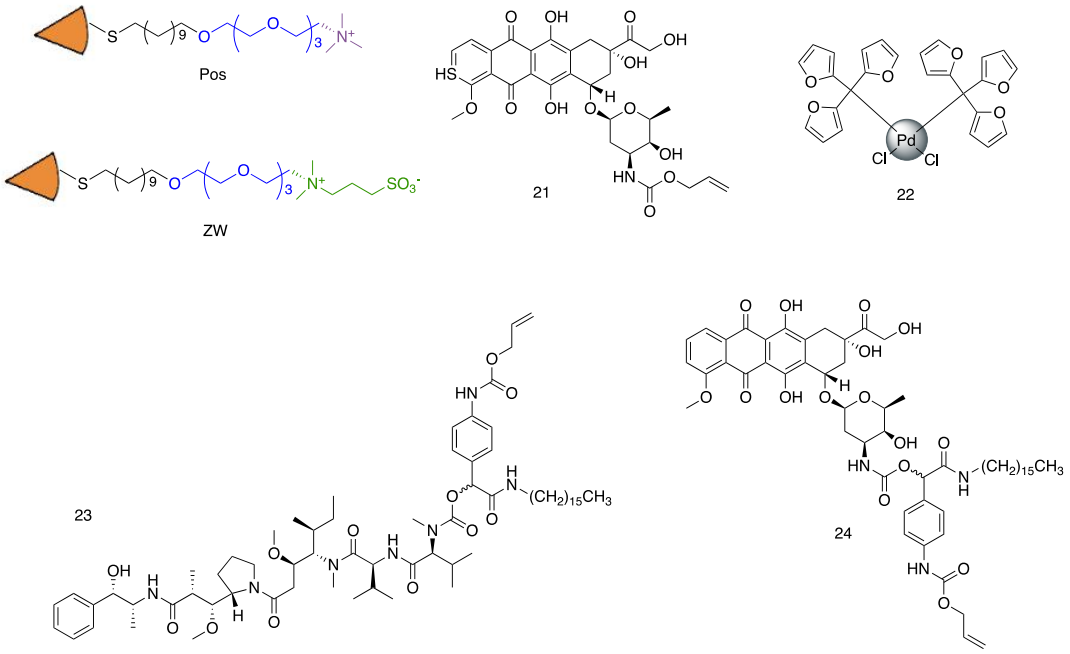

Figure 9. Chemical structures of coating headgroups and alloc protected doxorubicin prodrug (**21**) employed by Rotello[55] and the Pd precatalyst (**22**), MMAE (**23**) and doxorubicin (**21** and **24**) prodrugs used by Weissleder.[56,57]

One year later, the same group encapsulated catalyst **22** with two specifically designed prodrugs and performed their activation in biological media. They conjugated an allyl protected self-immolative linker functionalized with an aliphatic anchor to monomethyl auristatin E (MMAE) (**23**) or doxorubicin (**24**) to generate the prodrugs. MMAE is a highly potent antimitotic agent that inhibits the polymerization of tubulin in dividing cells.[58] They tested this strategy in vitro in ES2 (ovarian), 4T1 (breast), MC38 (colon) and HT1080 (epithelial) cancer cell lines, observing that the prodrugs were less toxic than the parental drug. Nevertheless, when prodrugs were incubated with **22** similar toxicity to the parental drug was measured. In vivo experiments employing the encapsulated MMAE prodrug in combination with the Pd catalyst in MC38 and HT1080 cancer models showed that the treatment was not curative but blocked tumor growth.[57] These studies did not report any catalytic parameter about the efficiency of the catalytic deprotection of the substrates either and they focused mostly on the therapeutic effect of the substrate-catalyst pair. However, based on the results presented by the authors, the catalyst was able to transform stoichiometric quantities of substrate. Therefore, the turnover number assignable to the catalyst should be around 1.

The third class of nanobot was reported by Bradley and Unciti-Broceta.[59] They explored the use of heterogeneous polymeric scaffolds loaded with metallic NPs to perform what they called bioorthogonal organometallic (BOOM) reactions. In their first work, embedded Pd NPs (around 5 nm) into amino functionalized polystyrene micrometric resins, catalyzed allylcarbamate cleavage reactions inside HeLa cells. They showed that the alloc-caged amsacrine anticancer prodrug and the alloc-caged rhodamine 110 dye (Figure 10) were deprotected *in vitro* by the Pd NP containing resins.[59] Turnover number up to 30 was reported for the deprotection of the caged dye in the presence of mM concentration of glutathione.

Further studies employing these resins showed that the propargyl-caged 5-FU prodrug (Figure 10) was efficiently deprotected in HCT116 and BxPC-3 cancer cell lines inducing a reduction on the cell viability comparable to the parental drug. They also demonstrated that these resins were able to switch on the fluorescence of a caged dye (Figure 10) in the yolk sac of zebrafish embryos without producing any toxic effect.[60] The versatility of the resins was later proved in a series of works in which they demonstrated the deprotection of prodrug derivatives of gemcitabine,[61] floxuridine,[62] vorinostat,[63] doxorubicin[64], and irinotecan[65] (Figure 10) in diverse cancer cell lines.

The group of Bradley enhanced the tumor specificity of Pd NPs containing resins with the cyclic peptide RGD cancer targeting functionality (antagonist of $\alpha_v\beta_3$ receptor which is overexpressed in some cancer cells).[66,67] This RGD functionalized fluorescent Pd resin generated the PP-121 compound (phosphatidylinositol-3-OH kinase inhibitor), from a non-toxic precursors (Figure 10) by a Suzuki-Miyaura cross-coupling reaction

and at the same time deprotected propargyl-protected 5FU prodrug. Uptake results, showed that the RGD functionalized resins were selectively internalized by U87-MG cells, which overexpress $\alpha_v\beta_3$ receptors, while almost no resins could be found inside MCF-7 cells which do not overexpress this receptors.[68]

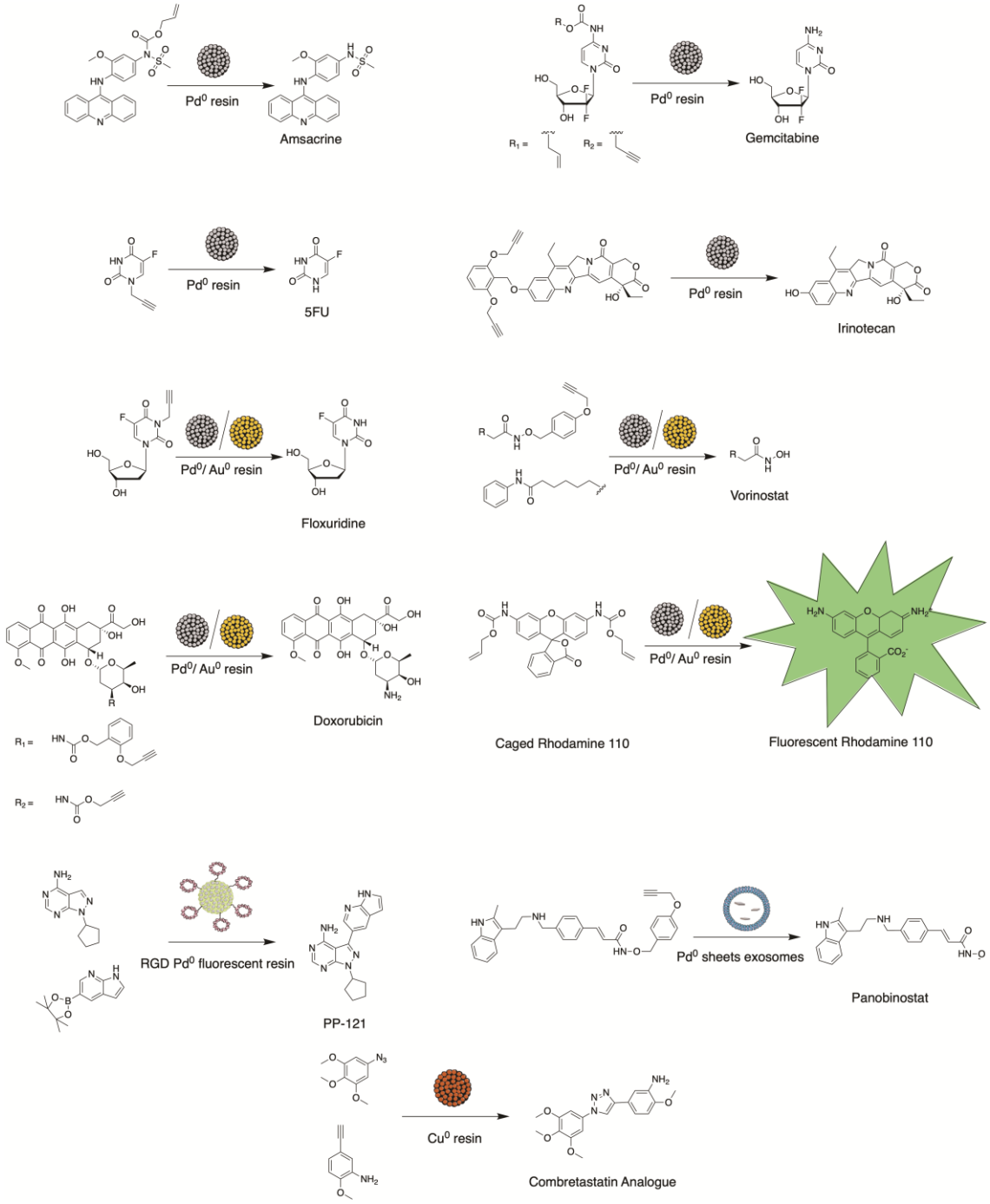

Figure 10. Metallic NPs mediated deprotection Amsacrine,[59] 5FU,[60] Gemcitabine,[61] Floxuridine,[62,71] Vorinostat,[63,71] Doxorubicin,[64,71] Irinotecan[65] and panobinostat[69] prodrugs and Rhodamine 110 probe and generation of PP-121[68] and Combrestatin[72] anticancer drugs.

One of the most recent examples of Pd NPs mediated prodrug activation was reported in 2019 by Unciti-Broceta and collaborators.[69] They developed cancer-derived exosomes loaded with nano Pd sheets that show a preference to target their parental cancer cell line, hence allowing activation of a protected prodrug in a localized manner. Exosomes are extracellular vesicles that modulate cell-to-cell communication and it has been demonstrated that released exosomes from cancerous cells are involved in cancer progression.[70] The researchers showed that these bioartificial devices can be employed as vehicles to target A549 cell line to perform the catalytic deprotection of a panobinostat prodrug in a selective manner (Figure 10).[69]

In 2017, the same group showed that Au NPs (around 30 nm) incorporated into polymeric resins, deprotected anticancer prodrugs of floxuridine, vorinostat and doxorubicin (Figure 10) in lung cancer A549 cells, producing a notable antiproliferative effect. The biocompatible Au resins, were able to switch on fluorescence of rhodamine probe in zebrafish brain without producing any damage.[71]

As final example of this class of nanobots, the group of Bradley employed Cu NPs loaded into amino functionalized polymeric beads to perform an azide-alkyne cycloaddition from two non-toxic precursors (Figure 10) to create an analogue of the combretastatin anticancer compound in HeLa and SKOV-3 cell lines.[72] Combretastatin is known to inhibit tubulin polymerization,[73] however they reported that this analogue, exhibited quite remarkable cytotoxic effect (IC_{50} 1.3μM) but not a great antitubulin effect (IC_{50} >20 μM) in K562 leukemia cell line. [72,74]

These three typologies of nanobots have been successfully employed for biorthogonal activation of different prodrugs in cell environment showing the potential of these strategies, however in many of the cases there is a lack of mechanistic details. It must be pointed out, that in many of the experiments, the concentration of the catalyst is higher than the concentration of the substrate. This fact indicates that very low turnover numbers and turnover frequencies were obtained when nanobots were used to activate prodrugs. Ultimately, these results suggest that the reactions promoted by nanobots are ultimately not catalytic, rather stoichiometric. Therefore, in order to take advantage of the potential of biorthogonal nanobots, fundamental studies are required to describe the mechanisms behind and enable the design and fabrication of truly and efficient catalytic systems.

2.4 Bioorthogonal photocatalysis using metal complexes as substrates

As described in the previous chapter, extensive research has been carried out in the field of Pt^{IV} prodrug photoactivation. During the last 3 years, it has been discovered

that certain biomolecules such as vitamins or proteins as well as selected metal complexes can be employed to favor the bioorthogonal photoactivation of Pt anticancer compounds.[75–78] These new approaches provide new tools for controlling the therapeutic effect of Pt based drugs with light.

In 2017, in the first work of the Salassa group in this field, the prodrug cis,cis,trans-$[Pt(NH_3)_2(Cl)_2(O_2CCH_2CH_2CO_2H)_2]$ (**25**), was photocatalytically transformed into cisplatin by riboflavin (Rf) upon 460-nm light excitation in the biological environment (Figure 11, a).[75] The unique photoredox features of Rf[79] enabled to use sub-stoichiometric concentrations of this biomolecule to simultaneously photosensitize and photocatalyze the reduction of **25** under extremely low doses of blue light (0.75 J cm^{-2}), using 2-morpholinoethanesulfonic acid (MES) as sacrificial electron donor. Under the experimental conditions, Rf was able to achieve a TOF value of 0.22 s^{-1} and a TON value of 38.

Rf is vitamin B2, a natural antioxidant present in variety of foods and it is the precursor of Flavin Adenine Dinucleotide (FAD) and Flavin Mononucleotide (FMN) (Figure 11, b). In nature, these flavin cofactors are bound to proteins and enzymes that participate in a wide range of one or two electron transfer processes in animals and plants.[80–82] This prompted the group to also explore FMN and FAD containing flavoproteins as biorthogonal photocatalysts for the transformation of Pt^{IV} prodrugs. FAD, FMN and mini singlet oxygen generator protein (miniSOG), NADH oxidase (NOX) (Figure 11,c), Glucose Oxidase (GOX) and Glutathione Reductase (GR) were explored as photocatalysts for the activation of Pt^{IV} (**25**, **26** and **27**) and Ru^{II} (**28** and **29**) anticancer prodrugs in the presence of mM concentration of MES or NADH (Figure 11, b).

In a solution that contained mM concentration of NADH, free FAD photocatalyzed the transformation of **25**, **27** and **28** with the highest TOF values ranging 5–9 min^{-1} and with a TTN value of 20; which expressed the total transformation of the substrate. The photocatalytic study of the flavoproteins was performed with **25** and **27** due their relevance as derivatives of approved antineoplastic Pt drugs. The chemical environment surrounding the flavin cofactor is different in each flavoprotein. The electrostatic surface in the proximity of the binding pocket are neutral in NOX and GR, whereas in miniSOG and GOX are positive and negative, respectively. Additionally, NOX, GOX and GR contained FAD as flavin cofactor while miniSOG contains FMN.

Photocatalytic reactions employing miniSOG and NOX were as efficient as naked FAD, while GR and GOX showed lower efficiency. Remarkably, in the presence of NADH, NOX was able to transform **25** and **27** in the dark with a TOF value of 4.3 and 8.3 respectively. Oppositely, miniSOG showed great light dependency and the prodrugs remained stable in the dark. The complexity of the protein structures and the distinct chemical environment surrounding the flavin cofactors, make difficult to understand completely the catalytic process.[77] Nevertheless, this work brought the first

experimental evidences of the use of free flavins and flavin containing flavoproteins for the transformation of Ru^{II} and Pt^{IV} substrates. The research opened a huge spectrum of opportunities to design light controllable enzymes to activate prodrugs of approved anticancer agents.

To test the applicability of the strategy for the treatment of cancer, the group first evaluated the effect of the catalytic activation of **25** by Rf in PC-3 prostate cancer cell line. Cell viability results showed the catalyst-substrate pair Rf/**25**, was not toxic in the dark, while upon blue light irradiation, induced comparable antiproliferative effect to cisplatin. The toxicity produced by the combination of Rf/**25** and light was mainly produced by Pt^{II} species. Nevertheless it is described that in the presence of O_2, irradiation of flavins promotes the generation of harmful reactive oxygen species (ROS).[81,83] This fact suggests that this approach can potentially trigger cellular damage by two simultaneous mechanisms: oxidative stress due photogeneration of ROS in aerobic tissues and DNA damaging by the formation of Pt^{II} species. The group evaluated the effect of the O_2 on the catalytic reaction and instead of getting worse, the absence of O_2, improves the catalytic conversion of the Pt prodrug.[77] This discovery suggests that the photocatalytic activation of Pt^{IV} complexes by Rf can be employed to activate Pt prodrugs in a more effective way inside hypoxic tissues.

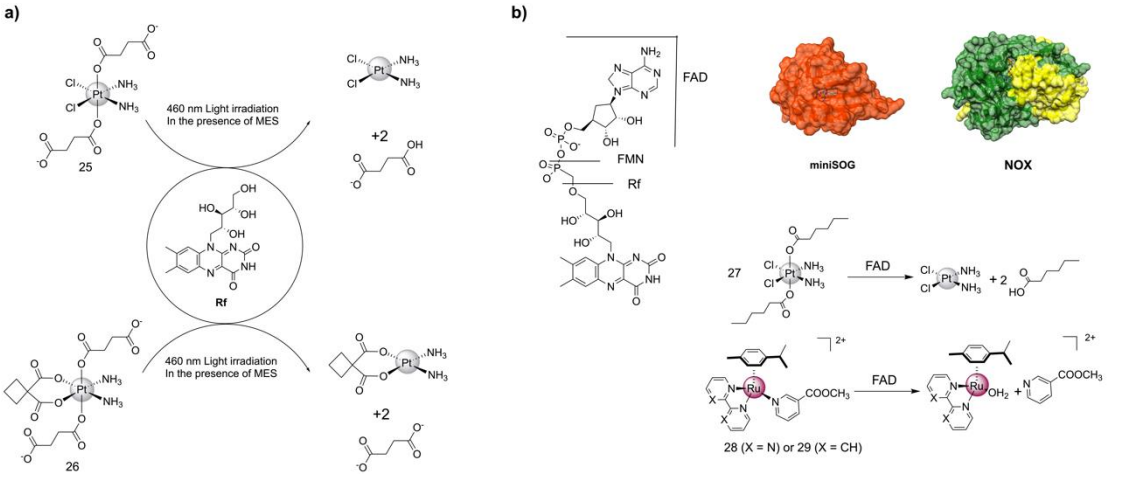

Figure 11. a) Photocatalytic activation of Cisplatin (**25**) and Carboplatin (**26**) prodrugs; and b) Structures of: FAD, FMN, Rf; mini Singlet oxygen Generator, miniSOG; NADH Oxidase, NOX catalysts and Pt^{IV} (**27**) and Ru^{II} (**28** and **29**) substrates.

In a follow-up work, the photocatalytic activation of **25** and **26** (Figure 11, a) by Rf was tested in Capan-1 pancreatic cancer cell line. Capan-1 cell line was selected because it shows high tolerance against cellular damage produced by ROS.[84–86] Uptake experiments demonstrated that the activation of Pt^{IV} prodrugs took place intracellularly, at least partially. The irradiation of **25** or **26** in the presence of Rf showed similar antiproliferative effect than the parental approved cisplatin and carboplatin drugs. Binding of *cis*-Pt^{II} drugs to DNA, produces alterations on the DNA structure, what resulted in a cellular death.[87] Circular dichroism showed that

irradiation of Rf/**25** generated Pt species that mainly form intra-strand crosslink adducts with a double stranded DNA model (ODN ds26).

Some cancerous cell lines can develop resistance against Pt based drugs, inhibiting the chemotherapeutic effect of the drugs. It is reported that the upregulation of major vault protein (MVP) is involved in cisplatin resistance.[88] Photocatalytic activation of **25** lowered the expression of MVP, suggesting that this strategy can result in new mechanisms of action that are capable overcome the MVP mediated cisplatin resistance.[76]

Few years after our group reported the first photocatalytic activation of Pt^{IV} anticancer complexes, Bradley and coworkers described an approach in which a ruthenium photosensitizer activated an oxaliplatin Pt^{IV} prodrug. Complex **30** (Figure 12) was activated by the mitochondria targeting ruthenium polypyridyl photosensitizer (**31**, Figure 12) under low power blue light irradiation (0.58 mW cm^{-2}). Upon light irradiation, **31** showed a TON value around 45 in aqueous solution. However, 1 hour of light exposure was required to convert around 45 µM of **30**, implying extremely low TOF value. Cell work with SKOV-3 ovarian cancer cells established that the generated toxicity was a combination of the effects prompted by oxaliplatin and the ROS generated by **31**.[78] Authors did not evaluate how the absence of molecular O_2 and therefore the lack of ROS, affected on the biological output of the photoactivation strategy.

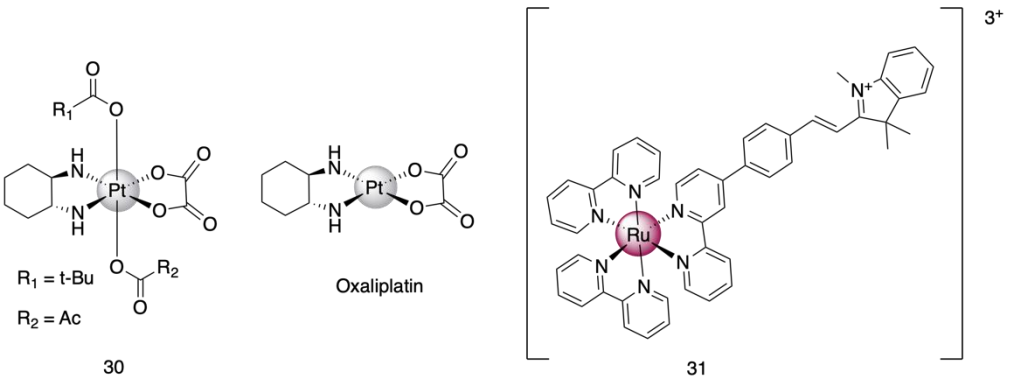

Figure 12. Chemical structures of Bradley´s ruthenium catalyst, oxaliplatin prodrug and drug.[78]

2.5 Summary and future perspectives

Bioorthogonal prodrug activation have emerged as one of the most promising tools to control the effect of antineoplastic drugs. As shown in this chapter, several strategies are currently being developed and tested to control the activation of prodrugs within cellular environments. Despite many of them showed great efficacy in vitro, the main limitation is still to discriminate between normal and cancerous tissues in complex

living organism. However, it is necessary to extend the pool of these biorthogonal reactions and a more detailed understanding of the mechanisms for a proper design and evaluation of their applicability to concrete diseases. Although the strategies reported here were designed for cancer related illnesses, it does not mean that they are not applicable to improve the delivery or treatments of drugs for other diseases. Therefore, it is pivotal that the community keeps increasing the efforts in this new-born medicinal chemistry field.

2.6 References

(1) Cancer Research UK. Causes of cancer and reducing your risk. https://www.cancerresearchuk.org/about-cancer/causes-of-cancer.

(2) National Cancer Institute. What is Cancer? https://www.cancer.gov/about-cancer/understanding/what-is-cancer.

(3) Faguet, G. B. A Brief History of Cancer: Age-Old Milestones Underlying Our Current Knowledge Database. *Int. J. Cancer* **2015**, *136*, 2022–2036.

(4) The American Cancer Society. Early History of Cancer. https://www.cancer.org/cancer/cancer-basics/history-of-cancer/what-is-cancer.

(5) National Cancer Institute. Types of Cancer Treatment https://www.cancer.gov/about-cancer/treatment/types.

(6) Freres, P.; Jerusalem, G.; Moonen, M. Categories of Anticancer Treatments. In *Anti-Cancer Treatments and Cardiotoxicity*; Elsevier, **2017**, pp 7–11.

(7) Cancer Research UK. Side effects of cancer drugs https://www.cancerresearchuk.org/about-cancer/cancer-in-general/treatment/cancer-drugs/side-effects.

(8) Zawilska, J. B.; Wojcieszak, J.; Olejniczak, A. B. Prodrugs: A Challenge for the Drug Development. *Pharmacol. Rep.* **2013**, *65*, 1–14.

(9) Huttunen, K. M.; Raunio, H.; Rautio, J. Prodrugs-from Serendipity to Rational Design. *Pharmacol. Rev.* **2011**, *63*, 750–771.

(10) Hang, H. C.; Yu, C.; Kato, D. L.; Bertozzi, C. R. A Metabolic Labeling Approach toward Proteomic Analysis of Mucin-Type O-Linked Glycosylation. *Proc. Natl. Acad. Sci.* **2003**, *100*, 14846–14851.

(11) Sletten, E. M.; Bertozzi, C. R. Bioorthogonal Chemistry: Fishing for Selectivity in a Sea of Functionality. *Angew. Chem., Int. Ed.* **2009**, *48*, 6974–6998.

(12) Punekar, N. S. *ENZYMES: Catalysis, Kinetics and Mechanisms*; Springer Singapore, **2018**, pp 33–34.

(13) Alonso-de Castro, S.; Terenzi, A.; Gurruchaga-Pereda, J.; Salassa, L. Catalysis Concepts in Medicinal Inorganic Chemistry. *Chem. Eur. J.* **2019**, *25*, 6651–6660.

(14) Thiel, Z.; Nguyen, J.; Rivera-Fuentes, P. Genetically Encoded Activators of Small Molecules for Imaging and Drug Delivery. *Angew. Chem., Int. Ed.* **2020**, *59*, 7669–7677.

(15) Muller, P. Glossary of Terms Used in Physical Organic Chemistry. *Pure & Appl. Chem.* **1994**, *66*, 1077–1184.

(16) Gurruchaga-Pereda, J.; Martínez-Martínez, V.; Rezabal, E.; Lopez, X.; Garino, C.;

Mancin, F.; Cortajarena, A. L.; Salassa, L. Flavin Bioorthogonal Photocatalysis Toward Platinum Substrates. *ACS Catal.* **2020**, *10*, 187–196.

(17) Martínez-Calvo, M.; Mascareñas, J. L. Organometallic Catalysis in Biological Media and Living Settings. *Coord. Chem. Rev.* **2018**, *359*, 57–79.

(18) Trachootham, D.; Lu, W.; Ogasawara, M. A.; Valle, N. R. Del; Huang, P. Redox Regulation of Cell Survival. *Antioxid. Redox Signal.* **2008**, *10*, 1343–1374.

(19) McFarland, S. A.; Mandel, A.; Dumoulin-White, R.; Gasser, G. Metal-Based Photosensitizers for Photodynamic Therapy: The Future of Multimodal Oncology? *Curr. Opin. Chem. Biol.* **2020**, *56*, 23–27.

(20) Monro, S.; Colón, K. L.; Yin, H.; Roque, J.; Konda, P.; Gujar, S.; Thummel, R. P.; Lilge, L.; Cameron, C. G.; McFarland, S. A. Transition Metal Complexes and Photodynamic Therapy from a Tumor-Centered Approach: Challenges, Opportunities, and Highlights from the Development of TLD1433. *Chem. Rev.* **2019**, *119*, 797–828.

(21) Forman, H. J.; Zhang, H.; Rinna, A. Glutathione: Overview of Its Protective Roles, Measurement, and Biosynthesis. *Mol. Aspects Med.* **2009**, *30*, 1–12.

(22) Dougan, S. J.; Habtemariam, A.; McHale, S. E.; Parsons, S.; Sadler, P. J. Catalytic Organometallic Anticancer Complexes. *Proc. Natl. Acad. Sci.* **2008**, *105*, 11628–11633.

(23) Sorci, L.; Kurnasov, O.; Rodionov, D. A.; Osterman, A. L. Genomics and Enzymology of NAD Biosynthesis. *Comprehensive Natural Products II*; Elsevier, **2010**, pp 213–257.

(24) Soldevila-Barreda, J. J.; Romero-Canelón, I.; Habtemariam, A.; Sadler, P. J. Transfer Hydrogenation Catalysis in Cells as a New Approach to Anticancer Drug Design. *Nat. Commun.* **2015**, *6*, 6582.

(25) Liu, Z.; Romero-Canelón, I.; Qamar, B.; Hearn, J. M.; Habtemariam, A.; Barry, N. P. E. E.; Pizarro, A. M.; Clarkson, G. J.; Sadler, P. J. The Potent Oxidant Anticancer Activity of Organoiridium Catalysts. *Angew. Chem., Int. Ed.* **2014**, *53*, 3941–3946.

(26) Ngo, A. H.; Ibañez, M.; Do, L. H. Catalytic Hydrogenation of Cytotoxic Aldehydes Using Nicotinamide Adenine Dinucleotide (NADH) in Cell Growth Media. *ACS Catal.* **2016**, *6*, 2637–2641.

(27) Bose, S.; Ngo, A. H.; Do, L. H. Intracellular Transfer Hydrogenation Mediated by Unprotected Organoiridium Catalysts. *J. Am. Chem. Soc.* **2017**, *139*, 8792–8795.

(28) Sigman, D. S.; Mazumder, A.; Perrin, D. M. Chemical Nucleases. *Chem. Rev.* **1993**, *93*, 2295–2316.

(29) Stadtman, E. R. Metal Ion-Catalyzed Oxidation of Proteins: Biochemical Mechanism and Biological Consequences. *Free Radical Biol. Med.* **1990**, *9*, 315–

325.

(30) Gallagher, J.; Zelenko, O.; Walts, A. D.; Sigman, D. S. Protease Activity of 1,10-Phenanthroline-Copper(I). Targeted Scission of the Catalytic Site of Carbonic Anhydrase. *Biochemistry.* **1998**, *37*, 2096–2104.

(31) Cuenoud, B.; Tarasow, T. M.; Schepartz, A. A New Strategy for Directed Protein Cleavage. *Tetrahedron Lett.* **1992**, *33*, 895–898.

(32) Lee, T. Y.; Suh, J. Target-Selective Peptide-Cleaving Catalysts as a New Paradigm in Drug Design. *Chem. Soc. Rev.* **2009**, *38*, 1949–1957.

(33) Joyner, J. C.; Hocharoen, L.; Cowan, J. A. Targeted Catalytic Inactivation of Angiotensin Converting Enzyme by Lisinopril-Coupled Transition-Metal Chelates. *J. Am. Chem. Soc.* **2012**, *134*, 3396–3410.

(34) Bradford, S. S.; Ross, M. J.; Fidai, I.; Cowan, J. A. Insight into the Recognition, Binding, and Reactivity of Catalytic Metallodrugs Targeting Stem Loop IIb of Hepatitis C IRES RNA. *ChemMedChem.* **2014**, *9*, 1275–1285.

(35) Bradford, S.; Cowan, J. A. Catalytic Metallodrugs Targeting HVC IRES RNA. *Chem. Commun.* **2012**, *48*, 3118–3120.

(36) Jin, Y.; Cowan, J. A. Cellular Activity of Rev Response Element RNA Targeting Metallopeptides. *J. Biol. Inorg. Chem.* **2007**, *12*, 637–644.

(37) Joyner, J. C.; Keuper, K. D.; Cowan, J. A. Kinetics and Mechanisms of Oxidative Cleavage of HIV RRE RNA by Rev-Coupled Transition Metal–Chelates. *Chem. Sci.* **2013**, *4*, 1707–1718.

(38) Yu, Z.; Cowan, J. A. Design of Artificial Glycosidases: Metallopeptides That Remove H Antigen from Human Erythrocytes. *Angew. Chem., Int. Ed.* **2017**, *56*, 2763–2766.

(39) Streu, C.; Meggers, E. Ruthenium-Induced Allylcarbamate Cleavage in Living Cells. *Angew. Chem., Int. Ed.* **2006**, *45*, 5645–5648.

(40) Völker, T.; Meggers, E. Chemical Activation in Blood Serum and Human Cell Culture: Improved Ruthenium Complex for Catalytic Uncaging of Alloc-Protected Amines. *ChemBioChem.* **2017**, *18*, 1083–1086.

(41) Völker, T.; Dempwolff, F.; Graumann, P. L.; Meggers, E. Progress towards Bioorthogonal Catalysis with Organometallic Compounds. *Angew. Chem., Int. Ed.* **2014**, *53*, 10536–10540.

(42) Thorn, C. F.; Oshiro, C.; Marsh, S.; Hernandez-Boussard, T.; McLeod, H.; Klein, T. E.; Altman, R. B. Doxorubicin Pathways: Pharmacodynamics and Adverse Effects. *Pharmacogenet. Genomics.* **2011**, *21*, 440–446.

(43) Sánchez, M. I.; Penas, C.; Vázquez, M. E.; Mascareñas, J. L. Metal-Catalyzed Uncaging of DNA-Binding Agents in Living Cells. *Chem. Sci.* **2014**, *5*, 1901–1907.

(44) Tomás-Gamasa, M. M.; Martínez-Calvo, M.; Couceiro, J. R.; Mascarenãs, J. L.; Mascareñas, J. L. Transition Metal Catalysis in the Mitochondria of Living Cells. *Nat. Commun.* **2016**, *7*, 12538.

(45) Okamoto, Y.; Kojima, R.; Schwizer, F.; Bartolami, E.; Heinisch, T.; Matile, S.; Fussenegger, M.; Ward, T. R. A Cell-Penetrating Artificial Metalloenzyme Regulates a Gene Switch in a Designer Mammalian Cell. *Nat. Commun.* **2018**, *9*, 1943.

(46) Ogura, A.; Urano, S.; Tahara, T.; Nozaki, S.; Sibgatullina, R.; Vong, K.; Suzuki, T.; Dohmae, N.; Kurbangalieva, A.; Watanabe, Y.; et al. A Viable Strategy for Screening the Effects of Glycan Heterogeneity on Target Organ Adhesion and Biodistribution in Live Mice. *Chem. Commun.* **2018**, *54*, 8693–8696.

(47) Eda, S.; Nasibullin, I.; Vong, K.; Kudo, N.; Yoshida, M.; Kurbangalieva, A.; Tanaka, K. Biocompatibility and Therapeutic Potential of Glycosylated Albumin Artificial Metalloenzymes. *Nat. Catal.* **2019**, *2*, 780–792.

(48) Li, H.; Xu, H.; Zhou, Y.; Zhang, J.; Long, C.; Li, S.; Chen, S.; Zhou, J.-M.; Shao, F. The Phosphothreonine Lyase Activity of a Bacterial Type III Effector Family. *Science.* **2007**, *315*, 1000–1003.

(49) Arbibe, L.; Kim, D. W.; Batsche, E.; Pedron, T.; Mateescu, B.; Muchardt, C.; Parsot, C.; Sansonetti, P. J. An Injected Bacterial Effector Targets Chromatin Access for Transcription Factor NF-KB to Alter Transcription of Host Genes Involved in Immune Responses. *Nat. Immunol.* **2007**, *8*, 47–56.

(50) Li, J.; Yu, J.; Zhao, J.; Wang, J.; Zheng, S.; Lin, S.; Chen, L.; Yang, M.; Jia, S.; Zhang, X.; et al. Palladium-Triggered Deprotection Chemistry for Protein Activation in Living Cells. *Nat. Chem.* **2014**, *6*, 352–361.

(51) Wang, J.; Zheng, S.; Liu, Y.; Zhang, Z.; Lin, Z.; Li, J.; Zhang, G.; Wang, X.; Li, J.; Chen, P. R. Palladium-Triggered Chemical Rescue of Intracellular Proteins via Genetically Encoded Allene-Caged Tyrosine. *J. Am. Chem. Soc.* **2016**, *138*, 15118–15121.

(52) Cherukaraveedu, D.; Cowling, P. T.; Birch, G. P.; Bradley, M.; Lilienkampf, A. Solid-Phase Synthesis of Biocompatible N-Heterocyclic Carbene-Pd Catalysts Using a Sub-Monomer Approach. *Org. Biomol. Chem.* **2019**, *17*, 5533–5537.

(53) Zhang, X.; Huang, R.; Gopalakrishnan, S.; Cao-Milán, R.; Rotello, V. M. Bioorthogonal Nanozymes: Progress towards Therapeutic Applications. *Trends Chem.* **2019**, *1*, 90–98.

(54) Tonga, G. Y.; Jeong, Y.; Duncan, B.; Mizuhara, T.; Mout, R.; Das, R.; Kim, S. T.; Yeh, Y. C.; Yan, B.; Hou, S.; et al. Supramolecular Regulation of Bioorthogonal Catalysis in Cells Using Nanoparticle-Embedded Transition Metal Catalysts. *Nat. Chem.* **2015**, *7*, 597–603.

(55) Das, R.; Landis, R. F.; Tonga, G. Y.; Cao-Milán, R.; Luther, D. C.; Rotello, V. M. Control of Intra- versus Extracellular Bioorthogonal Catalysis Using Surface-

Engineered Nanozymes. *ACS Nano.* **2019**, *13*, 229–235.

(56) Miller, M. A.; Askevold, B.; Mikula, H.; Kohler, R. H.; Pirovich, D.; Weissleder, R. Nano-Palladium Is a Cellular Catalyst for in Vivo Chemistry. *Nat. Commun.* **2017**, *8*, 15906.

(57) Miller, M. A.; Mikula, H.; Luthria, G.; Li, R.; Kronister, S.; Prytyskach, M.; Kohler, R. H.; Mitchison, T.; Weissleder, R. Modular Nanoparticulate Prodrug Design Enables Efficient Treatment of Solid Tumors Using Bioorthogonal Activation. *ACS Nano.* **2018**, *12*, 12814–12826.

(58) Francisco, J. A.; Cerveny, C. G.; Meyer, D. L.; Mixan, B. J.; Klussman, K.; Chace, D. F.; Rejniak, S. X.; Gordon, K. A.; DeBlanc, R.; Toki, B. E.; et al. CAC10-VcMMAE, an Anti-CD30-Monomethyl Auristatin E Conjugate with Potent and Selective Antitumor Activity. *Blood.* **2003**, *102*, 1458–1465.

(59) Yusop, R. M.; Unciti-Broceta, A.; Johansson, E. M. V.; Sánchez-Martín, R. M.; Bradley, M. Palladium-Mediated Intracellular Chemistry. *Nat. Chem.* **2011**, *3*, 239–243.

(60) Weiss, J. T.; Dawson, J. C.; Macleod, K. G.; Rybski, W.; Fraser, C.; Torres-Sánchez, C.; Patton, E. E.; Bradley, M.; Carragher, N. O.; Unciti-Broceta, A. Extracellular Palladium-Catalysed Dealkylation of 5-Fluoro-1-Propargyl-Uracil as a Bioorthogonally Activated Prodrug Approach. *Nat. Commun.* **2014**, *5*, 3277.

(61) Weiss, J. T.; Dawson, J. C.; Fraser, C.; Rybski, W.; Torres-Sánchez, C.; Bradley, M.; Patton, E. E.; Carragher, N. O.; Unciti-Broceta, A. Development and Bioorthogonal Activation of Palladium-Labile Prodrugs of Gemcitabine. *J. Med. Chem.* **2014**, *57*, 5395–5404.

(62) Weiss, J. T.; Carragher, N. O.; Unciti-Broceta, A. Palladium-Mediated Dealkylation of N-Propargyl-Floxuridine as a Bioorthogonal Oxygen-Independent Prodrug Strategy. *Sci. Rep.* **2015**, *5*, 9329.

(63) Rubio-Ruiz, B.; Weiss, J. T.; Unciti-Broceta, A. Efficient Palladium-Triggered Release of Vorinostat from a Bioorthogonal Precursor. *J. Med. Chem.* **2016**, *59*, 9974–9980.

(64) Bray, T. L.; Salji, M.; Brombin, A.; Pérez-López, A. M.; Rubio-Ruiz, B.; Galbraith, L. C. A.; Patton, E. E.; Leung, H. Y.; Unciti-Broceta, A. Bright Insights into Palladium-Triggered Local Chemotherapy. *Chem. Sci.* **2018**, *9*, 7354–7361.

(65) Adam, C.; Pérez-López, A. M.; Hamilton, L.; Rubio-Ruiz, B.; Bray, T. L.; Sieger, D.; Brennan, P. M.; Unciti-Broceta, A. Bioorthogonal Uncaging of the Active Metabolite of Irinotecan by Palladium-Functionalized Microdevices. *Chem. Eur. J.* **2018**, *24*, 16783–16790.

(66) Zitzmann, S.; Ehemann, V.; Schwab, M. Arginine-Glycine-Aspartic Acid (RGD)-Peptide Binds to Both Tumor and Tumor-Endothelial Cells in Vivo. *Cancer Res.* **2002**, *62*, 5139–5143.

(67) Danhier, F.; Breton, A. Le; Préat, V. RGD-Based Strategies to Target Alpha(v) Beta(3) Integrin in Cancer Therapy and Diagnosis. *Mol. Pharm.* **2012**, *9*, 2961–2973.

(68) Clavadetscher, J.; Indrigo, E.; Chankeshwara, S. V.; Lilienkampf, A.; Bradley, M. In-Cell Dual Drug Synthesis by Cancer-Targeting Palladium Catalysts. *Angew. Chem., Int. Ed.* **2017**, *56*, 6864–6868.

(69) Sancho-Albero, M.; Rubio-Ruiz, B.; Pérez-López, A. M.; Sebastián, V.; Martín-Duque, P.; Arruebo, M.; Santamaría, J.; Unciti-Broceta, A. Cancer-Derived Exosomes Loaded with Ultrathin Palladium Nanosheets for Targeted Bioorthogonal Catalysis. *Nat. Catal.* **2019**, *2*, 864–872.

(70) Osaki, M.; Okada, F. Exosomes and Their Role in Cancer Progression. *Yonago Acta Med.* **2019**, *62*, 182–190.

(71) Pérez-López, A. M.; Rubio-Ruiz, B.; Sebastián, V.; Hamilton, L.; Adam, C.; Bray, T. L.; Irusta, S.; Brennan, P. M.; Lloyd-Jones, G. C.; Sieger, D.; et al. Gold-Triggered Uncaging Chemistry in Living Systems. *Angew. Chem., Int. Ed.* **2017**, *56*, 12548–12552.

(72) Clavadetscher, J.; Hoffmann, S.; Lilienkampf, A.; Mackay, L.; Yusop, R. M.; Rider, S. A.; Mullins, J. J.; Bradley, M. Copper Catalysis in Living Systems and In Situ Drug Synthesis. *Angew. Chem., Int. Ed.* **2016**, *55*, 15662–15666.

(73) Tron, G. C.; Pirali, T.; Sorba, G.; Pagliai, F.; Busacca, S.; Genazzani, A. A. Medicinal Chemistry of Combretastatin A4: Present and Future Directions. *J. Med. Chem.* **2006**, *49*, 3033–3044.

(74) Odlo, K.; Fournier-Dit-Chabert, J.; Ducki, S.; Gani, O. A. B. S. M.; Sylte, I.; Hansen, T. V. 1,2,3-Triazole Analogs of Combretastatin A-4 as Potential Microtubule-Binding Agents. *Bioorg. Med. Chem.* **2010**, *18*, 6874–6885.

(75) Alonso-de Castro, S.; Ruggiero, E.; Ruiz-de-Angulo, A.; Rezabal, E.; Mareque-Rivas, J. C.; Lopez, X.; López-Gallego, F.; Salassa, L. Riboflavin as a Bioorthogonal Photocatalyst for the Activation of a Pt(IV) Prodrug. *Chem. Sci.* **2017**, *8*, 4619–4625.

(76) Alonso-de Castro, S.; Terenzi, A.; Hager, S.; Englinger, B.; Faraone, A.; Martínez, J. C.; Galanski, M.; Keppler, B. K.; Berger, W.; Salassa, L. Biological Activity of Pt(IV) Prodrugs Triggered by Riboflavin-Mediated Bioorthogonal Photocatalysis. *Sci. Rep.* **2018**, *8*, 17198.

(77) Alonso-de Castro, S.; Cortajarena, A. L.; López-Gallego, F.; Salassa, L.; Lopez-Gallego, F.; Salassa, L.; López-Gallego, F.; Salassa, L. Bioorthogonal Catalytic Activation of Platinum and Ruthenium Anticancer Complexes by FAD and Flavoproteins. *Angew. Chem., Int. Ed.* **2018**, *57*, 3143–3147.

(78) Norman, D. J.; Gambardella, A.; Mount, A. R.; Murray, A. F.; Bradley, M. A Dual Killing Strategy: Photocatalytic Generation of Singlet Oxygen with Concomitant Pt(IV) Prodrug Activation. *Angew. Chem., Int. Ed.* **2019**, *58*, 14189–14192.

(79) Brondani, P. B.; Fraaije, M. W.; de Gonzalo, G. Recent Developments in Flavin-Based Catalysis. In *Green Biocatalysis*; John Wiley & Sons, **2016**, pp 149–164.

(80) Saedisomeolia, A.; Ashoori, M. *Riboflavin in Human Health: A Review of Current Evidences*; Elsevier, **2018**, pp 57–81.

(81) Heelis, P. F. The Photophysical and Photochemical Properties of Flavins (Isoalloxazines). *Chem. Soc. Rev.* **1982**, *11*, 15–39.

(82) Bates, C. J. Riboflavin. In *Encyclopedia of Human Nutrition*; Elsevier, **2013**, pp 158–165.

(83) Oster, G.; Bellin, J. S.; Holmström, B. Photochemistry of Riboflavin. *Experientia,* **1962**, *18*, 249–253.

(84) Bown, S. G. Photodynamic Therapy for Cancer of the Pancreas. *Acta Endoscopica,* **2003**, *33*, 531–538.

(85) Celli, J. P.; Solban, N.; Liang, A.; Pereira, S. P.; Hasan, T. Verteporfin-Based Photodynamic Therapy Overcomes Gemcitabine Insensitivity in a Panel of Pancreatic Cancer Cell Lines. *Lasers Surg. Med.* **2011**, *43*, 565–574.

(86) Ouyang, G.; Liu, Z.; Huang, S.; Li, Q.; Xiong, L.; Miao, X.; Wen, Y. Gemcitabine plus Cisplatin versus Gemcitabine Alone in the Treatment of Pancreatic Cancer: A Meta-Analysis. *World J. Surg. Oncol.* **2016**, *14*, 59.

(87) Dasari, S.; Bernard Tchounwou, P. Cisplatin in Cancer Therapy: Molecular Mechanisms of Action. *Eur. J. Pharmacol.* **2014**, *740*, 364–378.

(88) Steiner, E.; Holzmann, K.; Elbling, L.; Micksche, M.; Berger, W. Cellular Functions of Vaults and Their Involvement in Multidrug Resistance. *Curr. Drug Targets.* **2006**, *7*, 923–934.

3

Flavin Bioorthogonal Photocatalysis Toward Platinum Substrates

The work presented in this chapter has been published in *ACS Catal.* 2020, 10, 187-196 (authors: Gurruchaga-Pereda, J.; Martínez-Martínez, V.; Rezabal, E.; Lopez, X.; Garino, C.; Mancin, F.; Cortajarena, A. L.; Salassa, L.).

3.1 Introduction

In catalysis, coordination and organometallic complexes typically act as catalysts to kinetically favor the conversion of organic substrates into added-value products. Recently, we subverted such a paradigm to conceive new approaches for the activation of metal-based anticancer prodrugs (Figure 1).[1–4] We demonstrated that flavins (FLs) can perform under light-irradiation as catalysts to prompt the transformation of transition metal substrates into their biologically active counterparts. In the presence of electron donors, flavin cofactors and certain flavoproteins are able to photoconvert Pt^{IV} precursors into cisplatin or carboplatin within biological environments, switching on the antiproliferative activity of the Pt^{II} drugs *in vitro*. This unconventional approach expands the substrate scope and versatility of bioorthogonal catalytic reactions currently available in drug development,[1,5,6] potentially creating new uses for a myriad of inorganic biological agents that have been developed over the last decades as chemotherapeutics and antibacterial agents. The term bioorthogonal here refers to the capacity of these catalysts to attain multiple substrate turnovers and high selectivity towards the Pt^{IV}-to-Pt^{II} conversion in a complex biological environment.

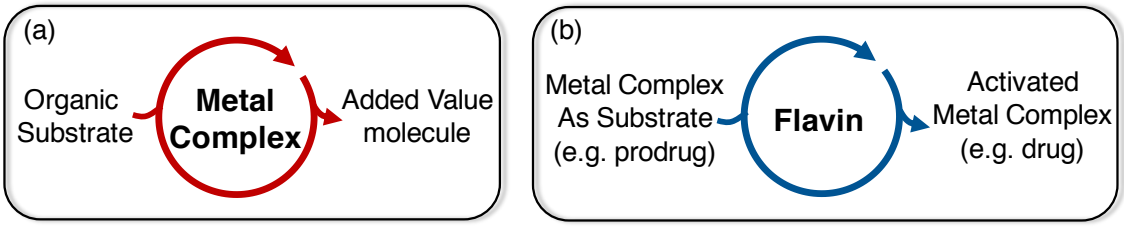

Figure 1. (a) Metal-based catalysis and (b) catalysis towards metal substrates.

Our proof-of-concept studies on flavins, Megger's enantioselective synthesis of $[Ru(bpy)_3]^{2+}$ via organocatalysis[7] and the recent aromatic amination of cyclometallated Ru^{II} and Rh^{III} octahedral complexes reported by Leonori[8] are, to the best of our knowledge, unique examples of catalytic reactions that use metal complexes as substrates. This uncharted territory may offer intriguing opportunities to expand synthetic inorganic chemistry and foster new catalysis-based applications for coordination and organometallic compounds.

In view of such a perspective, this study aims at expanding the boundaries of catalysis towards metal substrates by providing a detailed understanding of the mechanism through which flavins (photo)catalyze the activation of Pt^{IV} complexes. Herein, we gather novel insights into the catalytic mechanism and rationalize how changes in the structure of flavin catalysts and Pt^{IV} substrates significantly affect reaction outcomes.

This work also reports fundamental information on the redox chemistry of flavins towards transition metals. For instance, flavoenzymes such as mercuric reductase regulates Hg resistance in several organisms by promoting the conversion of highly toxic Hg^{II} species to

less dangerous Hg^0.[9] Hence, findings described in this manuscript may have potential implications in the biochemistry and in the cell homeostasis of metals.

3.2 Results and Discussion

3.2.1 Catalysis studies

We employed five flavins and four Pt^{IV} prodrug complexes to investigate the catalyst and substrate scope for the reduction of anticancer metal complexes (Figure 2). We selected riboflavin (**Rf**), riboflavin-5'-phosphate (**FMN**), 2',3',4',5'-tetraacetylriboflavin (**TARF**) and lumiflavin (**Lf**) to assess the role of the ribityl side chain in the catalytic transformation of metal substrates. As shown in Figure S1 and in previous studies,[10] the photostability of flavin derivatives strongly depends on this fragment (**TARF** ~ **Lf** > **Rf** ~ **FMN**). The flavoprotein **miniSOG** (mini Singlet Oxygen Generator)[11] was included in our panel of catalysts to gauge the impact of an amino acid scaffold around the flavin catalytic core on the catalysis. **MiniSOG** is a small FMN-containing fluorescent protein developed as CLEM (correlative light and electron microscopy) tag[11] and investigated as photosensitizing agent,[12,13] including for photodynamic therapy.[14,15]

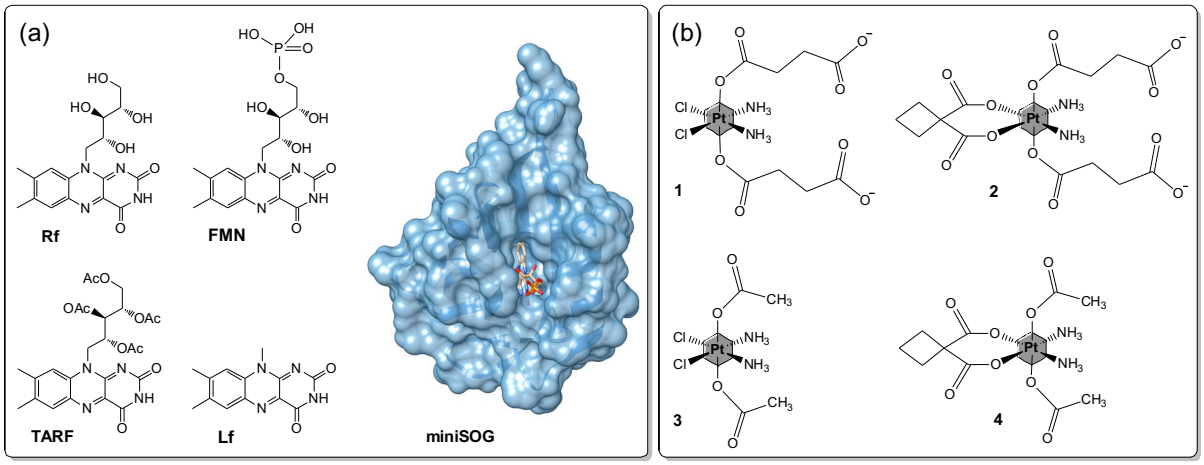

Figure 2. Structures of (a) catalysts and (b) substrates employed in this work. Catalysts: riboflavin (**Rf**), riboflavin-5'-phosphate (**FMN**), 2',3',4',5'-tetraacetylriboflavin (**TARF**), lumiflavin (**Lf**), mini Singlet Oxygen Generator (**miniSOG**). Substrates: *cis,cis,trans*-$[Pt(NH_3)_2(Cl_2)(O_2CCH_2CH_2CO_2)_2]^{2-}$ (**1**), *cis,cis,trans*-$[Pt(NH_3)_2(O_4C_6H_6)(O_2CCH_2CH_2CO_2)_2]^{2-}$ (**2**), *cis,cis,trans*-$[Pt(NH_3)_2(Cl_2)(O_2CCH_3)_2]$ (**3**), *cis,cis,trans*-$[Pt(NH_3)_2(O_4C_6H_6)(O_2CCH_3)_2]$ (**4**).

We opted for *cis,cis,trans*-$[Pt(NH_3)_2(Cl_2)(O_2CCH_2CH_2CO_2)_2]^{2-}$ (**1**), *cis,cis,trans*-$[Pt(NH_3)_2(O_4C_6H_6)(O_2CCH_2CH_2CO_2)_2]^{2-}$ (**2**), *cis,cis,trans*-$[Pt(NH_3)_2(Cl_2)(O_2CCH_3)_2]$ (**3**), *cis,cis,trans*-$[Pt(NH_3)_2(O_4C_6H_6)(O_2CCH_3)_2]$ (**4**) as Pt^{IV} substrates because they are structurally similar and yet present features that could influence the catalytic process. We envisaged

that differences in the equatorial (chlorido *versus* cyclobutane dicarboxylato) and axial (succinato *versus* acetato) ligands of the complexes could affect the catalysis. Moreover, these complexes are of relevance in medicinal inorganic chemistry since they are either prodrugs of cisplatin (**1** and **3**) or carboplatin (**2** and **4**), two anticancer drugs clinically-approved worldwide.[16,17]

Unless otherwise stated, all photocatalysis experiments were performed in phosphate buffer (PB, 18 mM pH 7) using 25 µM catalyst (5% loading), 500 µM substrate (**1**–**4**) and 1 mM NADH (nicotinamide adenine dinucleotide) as electron donor. The choice of NADH was motivated by its participation in numerous biochemical redox reactions carried out by flavoproteins.[18] Nevertheless, biological electron donors such as ascorbate can also be employed, whereas glutathione (GSH) is not efficacious in these reactions (Figure S2 and S3). Samples were irradiated with a 460-nm LED light source (6 $mW \cdot cm^{-2}$) in the presence of O_2. We evaluated reaction progression by ^1H NMR, monitoring the appearance and disappearance of diagnostic peaks corresponding to the coordinated and free succinato or acetato ligands of **1**–**4**. The release of such ligands corresponds to the formation of biologically active Pt^{II} species.[2]

The stability of complexes **1**–**4** (500 µM) was initially tested in PB (18 mM) with NADH (1 mM) over 48 h in the dark. We observed no decomposition of the Pt^{IV} substrates in the absence of FLs (Figure S4). When flavins (25 µM) were added to the PB buffered solution, conversion of **1**–**4** slowly occurred reaching 40 to 100 % after 16 h, except in the case of samples containing **miniSOG** that showed barely any change after 48 h (Figure S5–S9). Experiments performed using **Rf** and **1** (Figure S10) revealed that the dark conversion of the substrate was faster at higher concentrations of **Rf** (50–150 µM) and NADH (2.5 and 5 mM).

Dark reactivity of the different catalysts towards the substrates did not follow any specific trend. Complexes **2** and **4** partially afforded (5–40%) free cyclobutane dicarboxylato (CBDA) ligand as reaction product in the presence of **FMN**, **TARF** and **Lf**. In addition, the photostability of metal substrates **1**–**4** was tested in the presence of 1 mM NADH (18 mM PB, pH 7) under 460 nm light irradiation. Complexes **1** and **3** underwent approximately 20% conversion over 3 h, while carboplatin derivatives did not show any light-induced reactivity (Figure S11). Under light irradiation, solutions containing **1**–**4** and catalytic amounts of **Rf** did not present any significant substrate conversion in the absence of NADH (Figure S12), confirming the need for an electron donor for the catalysis to occur.

Table 1 and Figure 3 summarize catalysis results obtained for the different flavin catalysts and metal substrates under the conditions described above (see also, Figure S13–17).

Table 1. Catalytic parameters for for the flavin-catalyzed photoactivation of **1**–**4** in the presence of NADH.

Complex	TOF (min^{-1})	TON	Conv. [%]
Rf			
1	17.3 ± 0.6	20	100
2	8.1 ± 0.4	20	100
3	20.3 ± 2.0	20	100
4	10.0 ± 0.3	20	100
FMN			
1	19.3 ± 1.7	20	100
2	13.4 ± 0.9	17.9 ± 0.2	89.9 ± 0.9
3	23.2 ± 1.7	20	100
4	15.5 ± 1.4	20	100
TARF			
1	24.1 ± 5.1	20	100
2	13.7 ± 0.2	18.5 ± 0.2	92.4 ± 1.0
3	26.0 ± 1.1	20	100
4	22.7 ± 5.6	20	100
Lf			
1	9.2 ± 0.1	20	100
2	2.6 ± 1.6	20	100
3	13.3 ± 0.5	20	100
4	7.9 ± 1.0	20	100
miniSOG			
1	3.7 ± 0.2	20	100
2	1.3 ± 0.3	14.7 ± 0.7	73.4 ± 3.8
3	5.6 ± 0.3	18.7 ± 1 .1	93.7 ± 5.5
4	2.6 ± 0.4	17.5 ± 0.6	87.7 ± 3.1

* TOF: Turnover Frequency; number of cycles per unit of time (TOFs, min^{-1}), TON: Turnover Numbers, total number of cycles, and Conv. [%]: Final Conversion Percentages of **1**–**4.**

Photocatalytic reactions reached full conversion of **1**–**4** and turnover numbers (TONs) of 20 upon few minutes of light irradiation, the only exception being **2** with **FMN** and **TARF** and **2**–**4** with **miniSOG**. TOF values for free **FMN** were 4-6 times higher compared to FMN-embedded in **miniSOG**, and in the case of **2** even up to 10-fold higher. Notably, TONs reached significantly higher values when lower catalyst loading (0.2%, 1 μM) and longer irradiation periods were employed. In the case of **Rf**, we observed TONs of 500 for **1** and **3** and of 423 and 468 for **2** and **4** respectively, upon approximately 2 h of light irradiation (Figure S18).

In general, cisplatin prodrugs **1** and **3** were more efficiently converted compared to their carboplatin analogues **2** and **4**, affording superior turnover frequency values (TOF, min^{-1}).

The preference for cisplatin prodrugs was confirmed in substrate competitive experiments in which the conversion of couples of substrates was simultaneously tested (Figure S19 and S20).

Complex **3** showed the highest TOF for all flavin catalysts. The catalytic activity of **Lf** resulted in significantly lower TOFs compared to other flavins, reasonably suggesting that the ribityl chain plays an important role in the catalytic process (*vide infra*). Overall, **miniSOG** resulted the least efficient catalyst, with TOF values ranging 1.3–5.6 min^{-1}, and showed similar reactivity as **Lf** towards substrate **2**. On average, the protein scaffold of **miniSOG** lowered reaction rates 6.4 times compared to free **FMN** which can be explained by the reduced substrate accessibility to the **FMN** when embedded in the protein.

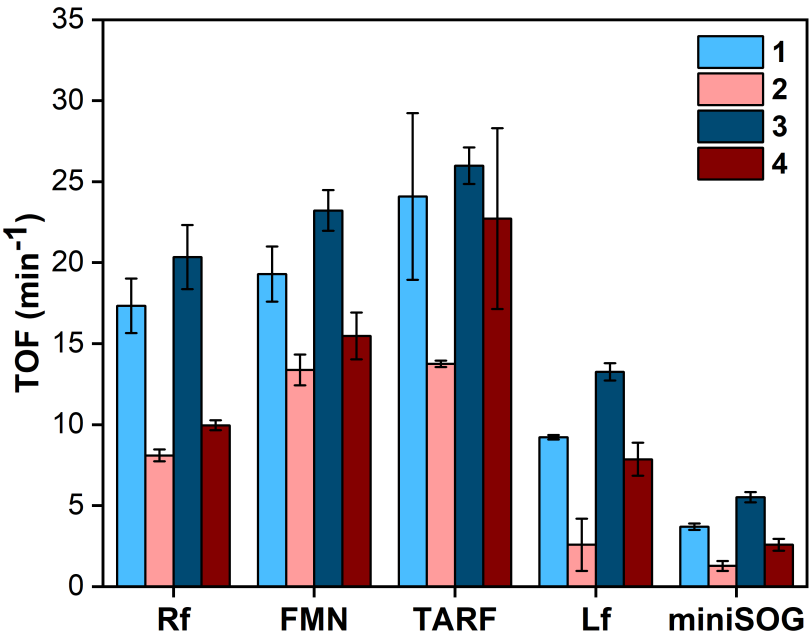

Figure 3. Turnover frequency values (TOF, min^{-1}) for the flavin-catalyzed photoactivation of **1**–**4**.

3.2.1 Catalysis in cell culture medium

The application of catalysis towards metal substrates in the context of medicinal inorganic chemistry relies on the capability of flavins to convert the Pt^{IV} prodrugs in the biological environment, i.e. generate selectively Pt^{II} species in cells and/or their surroundings.[2,3] Therefore, we studied how the flavin catalysts performed the activation of Pt^{IV} substrates in cell culture medium including fetal bovine serum (FBS). Such milieu contains a variety of chemicals and biological molecules that can interfere with the catalysis.

Substrates **1**–**4** were stable in medium containing 1 mM NADH for over 24 h in the dark (Figure S21). Upon addition of **Rf** (25 µM) the substrates were instead slowly transformed into their reaction products without the need for light excitation. Reactions were slow, and less than 40% conversion was observed in the first 8 h (Figure S22). The behavior of the other flavin catalysts was studied using **1** and **4**, because of their structural differences. In

the dark, **FMN** and **Lf** performed similarly to **Rf**, promoting only partial substrate conversion at 8 h and full conversion at 24 h (Figure S23 and S24). **TARF** instead achieved full transformation of **1** and **4** within 1 h in the dark (Figure S25). Conversely, **miniSOG** did not show the capacity to carry out the activation of the substrates (24 h) in the absence of light (Figure S26), which is a potential advantage for controlling the effects associated with the activation of Pt^{IV} prodrugs in cells.

Under light irradiation, all FLs were dramatically efficient in converting **1** and **4**. For all catalysts, the Pt^{IV} prodrugs were fully activated within 1 min, except in the case of **miniSOG** which required more than 6–10 min (Figure S27 and S28). The quantification of reaction efficiencies was problematic in cell culture medium due to the crowded spectrum and signal overlapping. However, ^{1}H spectra evidenced that catalytic reactions were slightly faster than in buffer solutions, suggesting that catalysts were not noticeably inactivated in a more stringent biological environment and that they still recognized Pt^{IV} substrates despite the presence of numerous other chemical and biological reactants. Therefore, these results highlighted the bioorthogonal selectivity of flavin-mediated catalysis towards Pt substrates and indicated that other electron donors present in the medium likely contributed to the catalysis as well.

3.2.1 Catalytic mechanism

A plausible assumption for the mechanism of the Pt^{IV}-to-Pt^{II} photocatalytic conversion of **1**–**4** implicates the formation of the triplet excited state ($^{3}FL^{*}$) of the flavin photocatalyst through intersystem crossing after exciting its singlet state. $^{3}FL^{*}$ is a strong oxidant capable of extracting 2 electrons from donors, such as NADH, to afford H_2FL or HFL^{-} depending on the pH of the solution.[18] Such reduced flavin forms are the active catalytic species that prompt the effective and bioorthogonal transformation of **1**–**4** (Scheme 1). In the absence of light, the formation of H_2FL/HFL^{-} still takes place but is significantly less efficient. Indeed, comparative experiments under O_2-free conditions showed that the consumption of NADH by **FMN** is much slower in the dark than under irradiation (Figure S29–S31). Furthermore, reduced flavins are readily oxidized by O_2 under aerobic conditions to ultimately give H_2O_2.[19] Thus, the conversion of Pt^{IV} substrates is much slower in the absence of light, being H_2FL/HFL^{-} present at lower concentrations.

To validate this mechanistic hypothesis, we studied in detail the reactivity of H_2FL/HFL^{-} towards **1** under oxygen-free conditions. N_2-purged solution of **FMN** and NADH (1:1, 15 μM in PB, pH 7.4) were irradiated at 460 nm for few seconds to obtain **HFMN**$^{-}$ as confirmed by the appearance of its characteristic absorption spectrum and the concomitant disappearance of **FMN** bands at 400–500 nm (Figure 4a).[20] At pH above 7.0, HFL^{-} is the most abundant species for the catalysts tested in this work.[18] Nevertheless, experiments at different pH, run using **1** and **3** and **FMN** indicated that both H_2FL and HFL^{-} could perform the catalysis with similar efficiency (Figure S14 and S32).

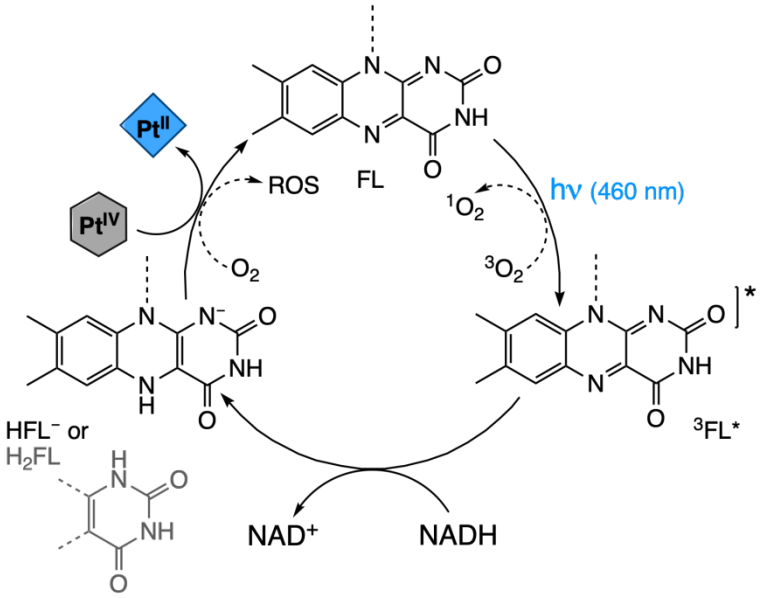

Scheme 1. Proposed mechanism for the catalytic conversion of substrates **1**–**4** by flavin catalysts.

Of note, work by Hollmann[21,22] demonstrated that light irradiation of flavin catalysts could boost reaction rates for the aerobic oxidation of reduced nicotinamide cofactors. Correspondingly, our results showed that use of NADH and visible light was effective in generating doubly reduced free flavins in oxygen free atmosphere. Compared to other established procedures,[23] this approach is advantageous since it avoids the use of high concentrations of strong reductants (e.g. sodium dithionite or borohydride) or the need of long photoreduction reactions with oxalate and UV light.

We obtained proof that **HFMN**$^-$ is the catalytic active species by monitoring the evolution of its UV-Vis spectrum upon addition of **1** (54 µM, final concentration) under anaerobic conditions. As shown in Figure 4a, **HFMN**$^-$ was promptly re-oxidized and the absorption features of **FMN** restored once the Pt^{IV} substrate was added. Under similar conditions (i.e. no O_2, 3.3 mM **FMN** and NADH, PB, pH 7.4), ^{1}H NMR resonances of **FMN** disappeared in the presence of NADH upon light irradiation (Figure 4b), consistently with the conversion to **HFMN**$^-$, and reemerged only after successive additions of **1** (4 mM, final concentration). The presence of the singlet signal correspondent to free succinate confirmed the conversion of the Pt^{IV} substrate. Once an excess of substrate was added (Figure 4b), signals relative to unreacted **1** became clearly visible again. As previously reported by Gschwind and coworkers,[24,25] line broadening due to proton exchange prevented direct detection of ^{1}H NMR signals relative to reduced flavin species in aqueous solutions. Equivalent results were obtained by UV-Vis for **TARF** and **Lf** using **1** as substrate (Figure S33 and S34).

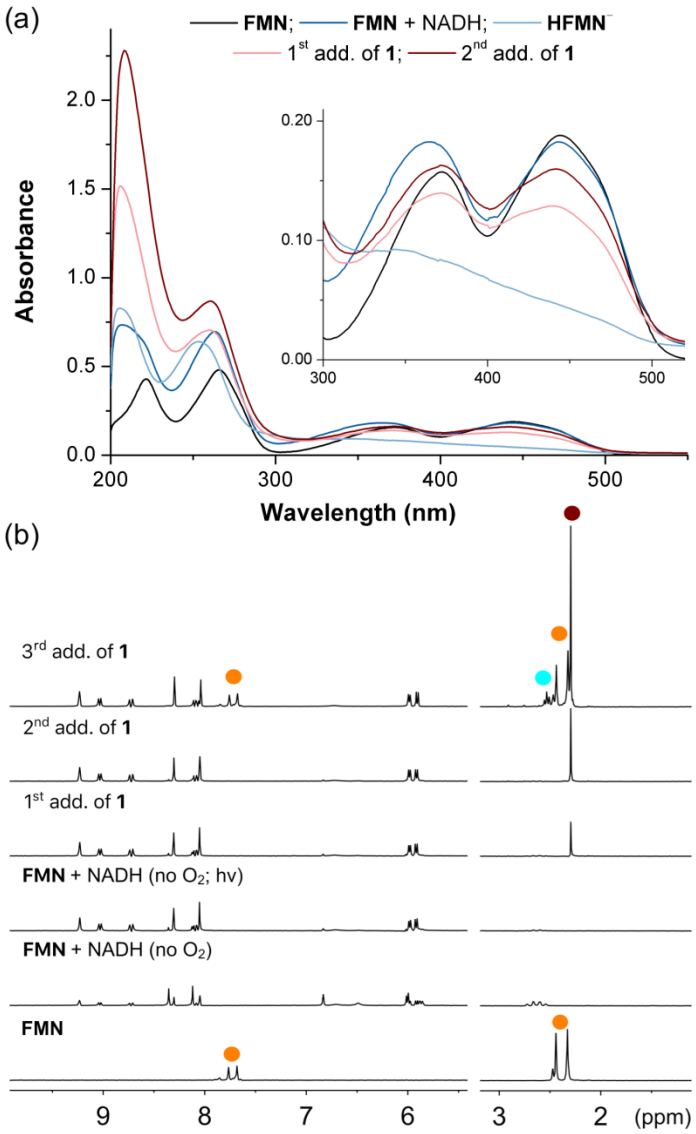

Figure 4. (a) UV-Vis and (b) NMR characterization of the key catalytic species **HFMN**$^{-}$ and its reactivity towards **1**. **HFMN**$^{-}$ (a: 15 µM; b: 3.3 mM) generated using 1 mol equiv. of NADH upon 460 nm light irradiation (6 mW·cm^{-2}, a: 40 s; b: 360 s) in the absence of O_2 (18 mM PB, pH 7.4). Final concentrations of **1** were 54 µM and 4 mM for UV-Vis and NMR experiments, respectively. ^{1}H NMR signal labelling: ● **FMN**; ● free $^{-}O_2CCH_2CH_2CO_2^{-}$; ● **1** (Pt–OCO$CH_2CH_2CO_2^{-}$).

Time-resolved optical spectroscopy proved that generation of HFL^{-} occurred via initial reductive quenching of the ^{3}FL* excited state by NADH. In first instance, fluorescence emission lifetime measurements performed on **FMN** (λ_{exc} = 445 nm, λ_{em} = 540 nm, Figure S35) indicated that its singlet excited state decay (τ_{Fluo} = 4.7 ns) was not altered by the presence of NADH (1:20) or NADH and **1** (1:20:20), therefore ruling out the involvement of such state in the catalytic process. However, the case for the **^{3}FMN*** excited state was different, as demonstrated by flash photolysis experiments (Figure 5, Figure S36). Previous work[26] showed that the evolution of the triplet state of **Rf** in the presence of quenchers can be monitored by the decay of its characteristic triplet-triplet absorption band. For this reason, we measured the transient absorption spectrum of **FMN** (λ_{exc} = 445 nm) in a de-

aerated solution and determined the triplet lifetime in the presence of NADH and **1**. Consistently with the literature, ^{3}**FMN*** displayed an intense and negative contribution in the 420–480 nm range, corresponding to the ground state bleaching associated with the $S_0 \rightarrow S_1$ transition. The positive band at around 600–720 nm was attributed to the absorption of the T_1 state. The assignation of the triplet-state absorption was also confirmed by its quenching in the presence of O_2. The **FMN** triplet lifetime in a de-aerated solution (τ_0^T) was 14 µs (Figure 5) long enough for an efficient quenching by O_2, which indeed reduced τ^T to 4 µs in air-saturated samples (Figure S36). In the presence of an NADH excess (1:20), we observed that τ_0^T decreased as well, from 14 µs to 2.3 µs, confirming the reductive quenching of ^{3}**FMN*** by this electron donor. Nevertheless, no further significant changes were observed on τ_0^T once **1** (1:20:20) was added to the solution containing both **FMN** and NADH. This result indicated that the Pt^{IV} conversion process does not involve ^{3}**FMN***, but rather the ground-state **HFMN**$^-$ species in agreement with UV-Vis and NMR data (Figure 4). Similar findings were obtained tracking the triplet excited state decay in air saturated solutions (Figure S36).

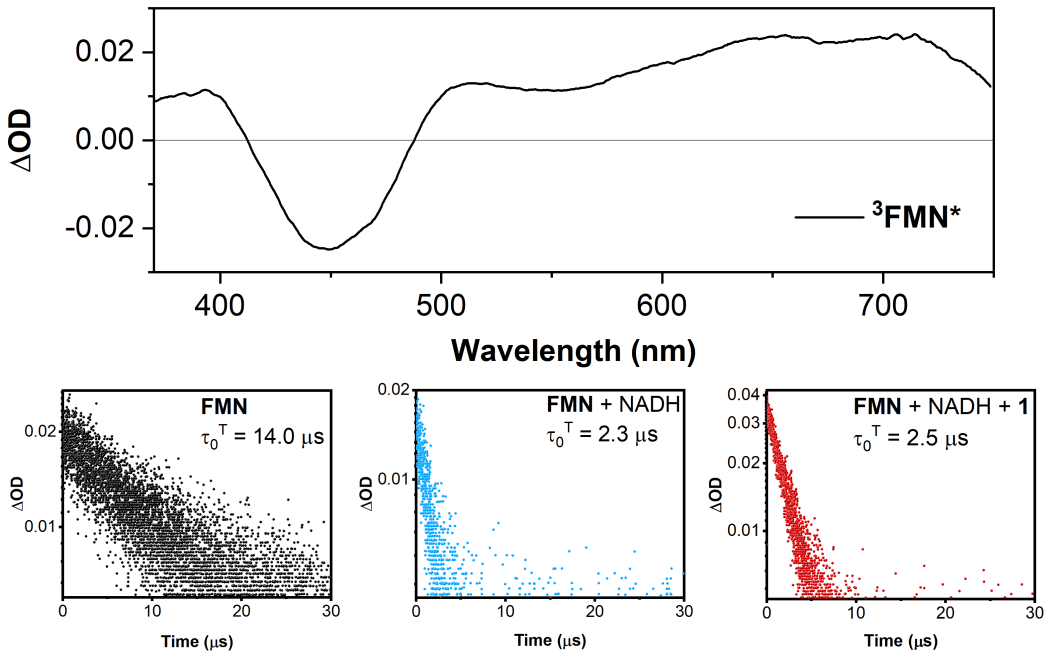

Figure 5. Transient absorption spectrum (λ_{exc} 445 nm) of ^{3}**FMN*** and decays (τ_0^T) of the triplet-triplet absorption at 700 nm for N_2-deareated solutions of **FMN** (20 µM), **FMN** (20 µM) + NADH (400 µM), and **FMN** (20 µM) + NADH (400 µM) + **1** (400 µM).

Considering that reduction potentials for **1**–**4** are more negative (Figure S37) than FLs, an outer sphere reduction of the substrates would be a neat uphill reaction. For this reason, formation of substrate-H_2FL/HFL$^-$ intermediates, and possibly a ligand-bridged inner sphere mechanism, might promote the flavin-mediated reduction of Pt^{IV} complexes.[27] These adducts could trigger the conversion of **1**–**4** in to their Pt^{II} counterparts at a less negative potential.[12] Furthermore, specific catalyst-substrate interactions could also explain the bioorthogonal selectivity of these reactions.

Density functional theory (DFT) calculations indicated that such a scenario is reasonable. Indeed, we optimized a number of substrate-H_2**Rf**/H**Rf**$^-$ adducts stabilized by hydrogen bonding interactions between the ligands of the Pt complexes and the isoalloxazine and ribityl moieties of FLs (Figure 6, Figure S38 and S39). Consistently with the occurrence of reduction and ligand elimination reactions, optimized geometries displayed electronic structures in which the HOMO (highest occupied molecular orbital) is centered on H_2**Rf**/H**Rf**$^-$, while the LUMO (lowest unoccupied molecular orbital) and LUMO+1 are σ-antibonding orbitals localized on **1**–**4** (Figure S40–42). All optimized structures showed interactions of the Pt-bound ligands with the ribityl chain, confirming that lack of this fragment was consistent with a decrease in catalytic activity as observed for **Lf** towards all substrates (Table 1 and Figure 3). Furthermore, DFT highlighted that H-bonding between **TARF** and the substrates were still possible, despite the acetylated ribityl chain of this catalyst. In particular, we could optimize adduct geometries in which the NH_3 ligand of **1**–**4** formed H-bonds with the C=O(2'C) of the ribityl and/or the N(5) of the isoalloxazine unit of **TARF** (Figure S43).

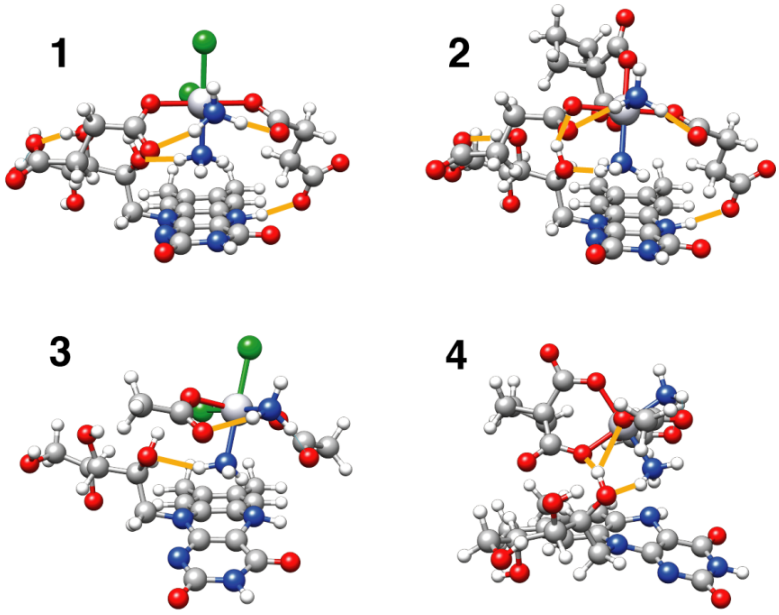

Figure 6. DFT-optimized (pbe0/def2-SVP) structures of adducts between **1**–**4** and **RfH**$^-$ (H-bond contacts highlighted with orange lines)

The overall lower conversion efficiency for the carboplatin derivatives **2** and **4** compared to their cisplatin counterparts **1** and **3** could instead be ascribed to the intrinsic thermodynamic stability of the Pt complexes. In fact, the corresponding axial and equatorial ligand exchange energy, calculated with different DFT functionals (Figure S44), indicated that **1** and **3** are less stable than **2** and **4**, respectively. The same holds true for succinato versus acetato ligands, having **3** lower stability than **1** and **4** than **2**. These trends are also in good agreement with reduction potentials of the complexes (Figure S37).

In order to further rationalize the lower stability of cisplatin derivatives with respect to carboplatin ones, we also analyzed the DFT atomic charge of the Pt atom in **1**–**4** and their corresponding Pt^{II} drugs. Irrespective of the functional or the atomic charge evaluation method used, the Pt atom showed a significant lower positive charge in cisplatin than in carboplatin, as well as in their corresponding Pt^{IV} prodrugs (Figure S37). Therefore, the electrostatic interaction between the Pt center and its equatorial ligands is weaker in the case of cisplatin derivatives compared to carboplatin complexes, and consequently **1** and **3** are more easily converted than **2** and **4**. On the other hand, since succinato ligands bear a doubly negative charge at neutral pH (pK_{a1} = 4.2 and pK_{a2} = 5.6), whereas acetato ligands (pK_a = 5.5) are only singly negatively charged, the Pt-acetato bond is weaker than the Pt-succinato one, and therefore easier to activate. These stability trends for **1**–**4** can be traced back to the stabilization of the Pt-ligand bonds, and provide an overall good explanation for the different prodrug conversion efficiencies found in this work.

MiniSOG has an FMN embedded in the protein structure and showed a more intricated photochemistry. Upon light irradiation and in the absence of electron donors and O_2, **miniSOG** generated the $FMN^{\bullet-}$ radical (semiquinone) that displayed a broad absorption peak at ca. 600 nm (Figure S46). This process was previously ascribed to the oxidation of certain amino acids and is known to compete with the capacity of **miniSOG** to generate $^1O_2$ with high yields.[28–30] Upon exposing irradiated solutions of **miniSOG** to the oxygen-containing ambient atmosphere, the spectral features of $FMN^{\bullet-}$ disappeared and the absorbance at 450 nm was almost completely recovered (Figure S46). Conversely, **1** poorly reacted with the radical when incubated with **miniSOG**. This effect was observed by UV-Vis and ^1H NMR experiments (Figure S47 and S48), in which stochiometric quantities of light-irradiated **miniSOG** in the absence of O_2 could transform **1** much slower than under the standard aerobic catalysis conditions.

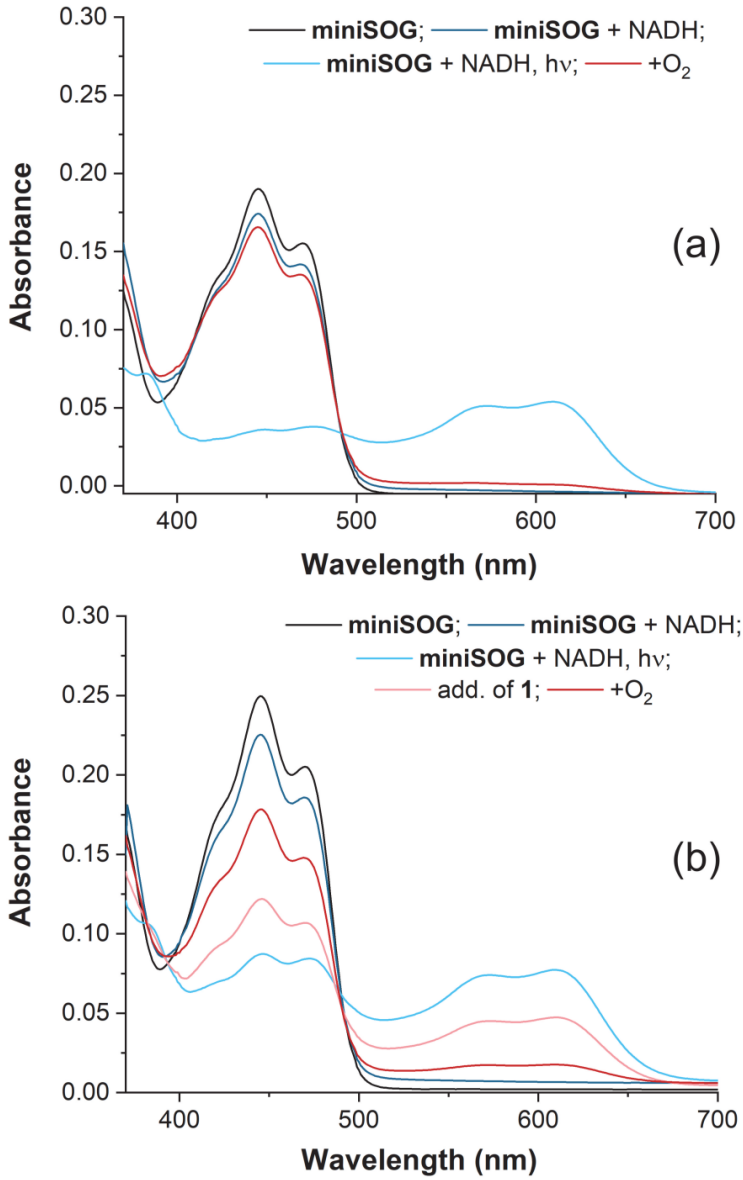

Figure 7. UV-Vis monitoring of light-irradiated **miniSOG** under anaerobic conditions upon addition of electron acceptors: (a) O_2 and (b) **1** (120 µM). Solutions of **miniSOG** (15 µM, 18 mM PB, pH 7.4) were irradiated (6 mW·cm^{-2}, 180 s) in the presence of 1 mol equiv. of NADH and in the absence of O_2.

In the presence of NADH, electron transfer from the protein scaffold was not shut down and the $FMN^{\bullet-}$ radical could still be detected (Figure 7a and b). Nevertheless, UV-Vis spectra revealed that doubly-reduced FMN was also obtained, as indicated by the marked absorbance decrease at 400–500 nm. Exposure of such solution to either O_2 or **1** (120 µM) caused the regeneration of FMN indicating that $HFMN^-$ was likely the major active catalytic species towards the Pt substrates for **miniSOG** as well. So, quenching of FMN excited state by photooxidation of amino acid residues competed with the formation of the active catalysts, in a similar fashion to what has been observed for $^1O_2$ sensitization. Compared to other FLs tested herein, the lower conversions and TOF values of **miniSOG** should also be ascribed to the reduced substrate accessibility of its FMN.

As shown here for **miniSOG** and for other FL catalysts in Figure S49, O_2 functioned as electron sink to deactivate doubly and singly-reduced FLs. This behavior is not surprising considering the biochemistry of flavins and flavoproteins. However, it suggests that the role of O_2 in the catalytic conversion of **1**–**4** ought to be evaluated for a thorough comprehension of the catalytic mechanism. In addition, FLs such as the one tested in this work are well known singlet-oxygen ($^1O_2$) photosensitizers.[13,31]

Monitoring the photoactivation kinetics of **1**–**4** in aerated solutions, we observed an induction period for all FL catalysts (Figure S50) at short light irradiation times. This finding is consistent with the presence of competitive catalytic cycles that involve the transformation of O_2 in $^1O_2$ and reactive oxygen species (ROS). Under anaerobic conditions, conversion of substrates readily occurs. Conversely, as shown for **1** and **FMN** (Figure S51), the reaction does not reach completion and kinetics is significantly slower when air is bubbled into the solution.

FL catalysts can interact with O_2 in the ^{3}FL* excited state to give $^1O_2$ or once reduced to HFL^- to generate ROS such as $O_2^{\bullet-}$ and H_2O_2 (Scheme 1). We confirmed the occurrence of both pathways by means of indirect optical methods previously validated for **FMN** and **miniSOG**.[12,29] That is, we employed uric acid and hydroethidine as molecular probes for the formation of $^1O_2$ and ROS, respectively. We observed that **FMN** and **miniSOG** solutions irradiated in the presence of an excess of NADH and **1** showed indeed production of both (Figure S52–S54). As described previously,[12,29] free **FMN** is a better $^1O_2$ photosensitizer than FMN embedded in the **miniSOG** scaffold, in agreement with the self-quenching of its triplet excited state by the protein matrix in the latter case. However, **miniSOG** generation of ROS was almost comparable to **FMN**, reasonably because $O_2^{\bullet-}$ is readily formed by photoinitiated electron-transfer reactions involving the protein (e.g. from $FMN^{\bullet-}$). Control experiments run in the absence of NADH and **1** did not show a significant decrease in the generation of $^1O_2$ and ROS, suggesting that O_2 was immediately converted by flavins in such photoproducts, before the catalysis towards Pt substrates took place.

3.3 Conclusions

This work expands the scope of flavin-mediated photocatalysis towards platinum substrates, providing new fundamental mechanistic details. The reduced H_2FL/HFL^- species has been identified by optical spectroscopy and NMR under anaerobic conditions as the active catalyst. H-bond interactions between H_2FL/HFL^- and the Pt^{IV} substrates may be crucial in promoting the conversion to Pt^{II} drugs, possibly via a ligand-bridged inner sphere reduction mechanism. The ribityl chain could stabilize these putative intermediates and increase the catalytic efficiency of the reactions. For this reason, **Lf** showed the lowest TOFs among the free FLs tested. Self-quenching of the **miniSOG** excited states by protein amino acids reduced the efficiency of this catalyst, as similarly observed for its $^1O_2$ photosensitization

capacity. Structural modifications of the ribityl group in free FLs and site mutagenesis in **miniSOG** are worth investigating in the future to boost their catalytic activity and widen the repertoire of this new chemistry towards different metals.

3.4 Experimental details

Materials. Riboflavin (**Rf**), riboflavin 5´-monophosphate sodium salt hydrate (**FMN**), potassium phosphate monobasic, potassium phosphate dibasic, β-nicotinamide adenine dinucleotide, reduced disodium salt hydrate, sodium dithionite, RPMI-1640 medium were purchased from Sigma-Aldrich, potassium tetrachloroplatinate(II) from Precious Metals Online. All chemicals were used as received without additional purification. The fetal bovine serum (10%) added to the RPMI-1640 medium was purchased from Invitrogen.

Preparation of substrates and catalysts. Complexes *cis,cis,trans*-$[Pt(NH_3)_2(Cl_2)(O_2CCH_2CH_2CO_2)_2]^{2-}$ (**1**), *cis,cis,trans*-$[Pt(NH_3)_2(O_4C_6H_6)(O_2CCH_2CH_2CO_2)_2]^{2-}$ (**2**), *cis,cis,trans*-$[Pt(NH_3)_2(Cl_2)(O_2CCH_3)_2]$ (**3**), *cis,cis,trans*-$[Pt(NH_3)_2(O_4C_6H_6)(O_2CCH_3)_2]$ (**4**) were synthesized and characterized as previously reported.[32–34] Tetra-O-acetyl riboflavin (**TARF**) and lumiflavin (**Lf**) were prepared following the procedure reported by I. Jhulki *et al*.[35] **MiniSOG** was prepared and purified as previously reported by us.[3]

Methods

Nuclear magnetic Resonance (NMR). ^{1}H NMR spectra of the various samples were recorded on a Fourier TM Bruker 300 NMR and on an AVANCE III Bruker 500 NMR spectrometer using standard pulse programs. Chemical shifts were reported in parts-per-million (δ, ppm) and referenced to the residual solvent peak.

Catalysis experiments. Unless otherwise specified, all reactions were carried out in air at 298 K and pH 7.0 using 25 μM catalyst, 500 μM substrate (1–4) and 1 mM NADH. Light irradiation experiments were performed employing an LED light source (λ_{max} = 460 nm, 6 $mW{\cdot}cm^{-2}$).[4] Turnover frequency (TOF), turnover number (TON) and % conversion for the catalytic reactions were determined by quantifying the amount of converted 1–4 via ^{1}H NMR. Integration of the free succinato and acetato ligand signals (singlets at 2.25–2.35 ppm and at approx. 1.80 ppm respectively) were used for monitoring the reaction progress. TOF values were obtained at substrate conversions of 25–35%.

UV-Vis absorption spectroscopy (UV-Vis). All spectra were acquired in optical quartz cuvettes in aqueous solutions or buffers using a JASCO V-730 spectrophotometer.

Fluorescence emission and lifetimes. The emission spectrum of FMN (20 μM) was recorded on a spectrofluorimeter Edinburgh Instruments (FL920 model) with a 450 W xenon flash lamp as the excitation source. Fluorescence radiative decay curves were recorded with a

time-correlated single-photon counting technique (Edinburgh Instruments, model FL920) at λ_{em} = 540 nm after excitation at λ_{exc} = 445 nm by means of a fianium supercontinuous wavelength tunable-laser with 150 ps FWHM pulses using a microchannel plate detector (Hamamatsu C4878) with picosecond time resolution. Fluorescence lifetimes were obtained after deconvolution of the instrumental response signal from the recorded decay curves by means of an iterative method. The goodness of the exponential fit was controlled by statistical parameters (χ^2 and analysis of the residuals). Measurements were performed on air-saturated solutions of (a) **FMN** (20 μM), (b) **FMN** (20 μM) and NADH (400 μM), and (c) **FMN** (20 μM), NADH (400 μM) and **1** (400 μM).

Transient absorption and triplet lifetimes. Nanosecond transient absorption measurements were recorded on a LP980 laser flash photolysis spectrometer (Edinburgh Instruments, Livingston, UK). Samples were excited by a nanosecond pulsed laser (Nd:YAG laser/OPO, LOTIS TII 2134) at the absorption maxima (445 nm) operating at 1 Hz and with a pulse width of 7 ns at a 10 mJ excitation power. Samples with an optical absorbance of 0.3 at the excitation wavelength were either deaerated with nitrogen for ca. 10 min or aerated for ca. 10 min with air. Transient spectra were recorded on ICCD detector (DH320T TE cooled, Andor Technology). The decay of triplet-triplet absorption in the presence and absence of oxygen (nitrogen and air saturated solutions) were collected at 700 nm on single detector (PMT R928P) and oscilloscope. Triplet lifetimes in absence and presence of oxygen (τ_0^T and τ^T) were obtained from the slope of the recorded decay curves by means of an iterative method by LP900 software. The goodness of the exponential fit was controlled by statistical parameters (χ^2). Solutions of (a) **FMN** (20 μM), (b) **FMN** (20 μM) and NADH (400 μM), and (c) **FMN** (20 μM), NADH (400 μM) and **1** (400 μM) were employed for in this set of experiments.

Singlet oxygen and ROS production. Quantification of $^1O_2$ and ROS was achieved using methods previously established for **FMN** and **miniSOG**.[12,29] Indirect measurement of $^1O_2$ was performed using uric acid (UA) as probe[36] and monitoring the changes of its absorbance at 292 nm over light irradiation time. We exposed to 460-nm light (6 $mW \cdot cm^{-2}$) optically-matched solutions containing UA (50 μM) and (a) **FMN**/**miniSOG** (5 μM), (b) **FMN**/**miniSOG** (5 μM) and NADH (30 μM), and (c) **FMN**/**miniSOG** (5 μM), NADH (30 μM) and **1** (15 μM).

Photooxidation of hydroethidine (HE) was instead used to evaluate the production of other ROS (particularly $O_2^{\bullet -}$) since the transformation of this probe does not occur upon interaction with $^1O_2$.[29,37] Also in this case, HE (50 μM) solutions containing (a) **FMN**/**miniSOG** (5 μM), (b) **FMN**/**miniSOG** (5 μM) and NADH (30 μM), and (c) **FMN**/**miniSOG** (5 μM), NADH (30 μM) and **1** (15 μM) were irradiated at 460 nm and their fluorescence intensity collected at different time points (λ_{ex} = 525 nm, λ_{em} = 550–800 nm) as described previously.[29]

Electrochemistry. Cyclic voltammetry experiments were performed using a Metrohm Autolab 302 N potentiostat. The electrochemical cell was a single-compartment cell equipped with a standard three-electrode set-up: a glassy carbon working electrode (Ø = 1 mm), a Pt-wire counter electrode and and a saturated calomel electrode (SCE) as reference.

All measurements were carried out in deoxygenated condition under argon atmosphere, employing a 0.05 M phosphate buffer (pH 7.4) containing 0.15 M NaCl. Solutions for metal complexes were $5.0 \cdot 10^{-4}$ M. **FMN** and **Rf** were measured at $2.7. \cdot 10^{-4}$ and $2.0 \cdot 10^{-4}$ M respectively, while **TARF** and **Lf** voltammogram were obtained using saturated solutions due to poor solubility. The working electrode was polished with alumina, rinsed with distilled water and dried before each potential sweep to ensure reproducible surface for all experiments.

Computational methods. All calculations were performed with Gaussian 16, Revision B01.[38] Geometry optimizations of substrate-riboflavin adducts were run at the DFT level using the pbe0/def2-SVP combination.[39,40] Solvent was introduced by means of the polarized continuum model (PCM) with water as implicit solvent, and dispersion interactions were taken into account using Grimme's dispersion correction with Becke and Johnson's damping.[41] The frequencies were then used to evaluate the zero-point vibrational energy (ZPVE) and the thermal (T = 298 K) vibrational corrections to the enthalpies and Gibbs free energies within the harmonic oscillator approximation. To calculate the entropy, the different contributions to the partition function were evaluated using the standard statistical mechanics expressions in the canonical ensemble and the harmonic oscillator and rigid rotor approximation. Energy calculations for the relative stability of substrates **1**–**4** were performed using the def2-TVP basis set[40] and three different functionals, namely pbe0, wb97xd[42] and m062x.[43] We calculated atomic charges using the same combination of functionals and basis set together with the nbo[44] and chelpg[45] methods.

3.5 References

(1) Alonso-de Castro, S.; Terenzi, A.; Gurruchaga-Pereda, J.; Salassa, L. Catalysis Concepts in Medicinal Inorganic Chemistry. *Chem. Eur. J.* **2019**, *25*, 6651–6660.

(2) Alonso-de Castro, S.; Terenzi, A.; Hager, S.; Englinger, B.; Faraone, A.; Martínez, J. C.; Galanski, M.; Keppler, B. K.; Berger, W.; Salassa, L. Biological Activity of Pt^{IV} Prodrugs Triggered by Riboflavin-Mediated Bioorthogonal Photocatalysis. *Sci. Rep.* **2018**, *8*, 17198.

(3) Alonso-de Castro, S.; Cortajarena, A. L.; López-Gallego, F.; Salassa, L. Bioorthogonal Catalytic Activation of Platinum and Ruthenium Anticancer Complexes by FAD and Flavoproteins. *Angew. Chem., Int. Ed.* **2018**, *57*, 3143–3147.

(4) Alonso-de Castro, S.; Ruggiero, E.; Ruiz-de-Angulo, A.; Rezabal, E.; Mareque-Rivas, J. C.; Lopez, X.; López-Gallego, F.; Salassa, L. Riboflavin as a Bioorthogonal Photocatalyst for the Activation of a Pt(IV) Prodrug. *Chem. Sci.* **2017**, *8*, 4619–4625.

(5) Ngo, A. H.; Bose, S.; Do, L. H. Intracellular Chemistry: Integrating Molecular Inorganic Catalysts with Living Systems. *Chem. Eur. J.* **2018**, *24*, 10584–10594.

(6) Martínez-Calvo, M.; Mascareñas, J. L. Organometallic Catalysis in Biological Media and Living Settings. *Coord. Chem. Rev.* **2018**, *359*, 57–79.

(7) Gong, L.; Lin, Z.; Harms, K.; Meggers, E. Isomerization-Induced Asymmetric Coordination Chemistry : From Auxiliary Control to Asymmetric Catalysis. *Angew. Chem., Int. Ed.* **2010**, *49*, 7955–7957.

(8) Ruffoni, A.; Juliá, F.; Svejstrup, T. D.; McMillan, A. J.; Douglas, J. J.; Leonori, D. Practical and Regioselective Amination of Arenes Using Alkyl Amines. *Nat. Chem.* **2019**, *11*, 426–433.

(9) Barkay, T.; Miller, S. M.; Summers, A. O. Bacterial Mercury Resistance from Atoms to Ecosystems. *FEMS Microbiol. Rev.* **2003**, *27*, 355–384.

(10) Edwards, A. M.; Bueno, C.; Saldaño, A.; Silva, E.; Kassab, K.; Polo, L.; Jori, G. Photochemical and Pharmacokinetic Properties of Selected Flavins. *J. Photochem. Photobiol. B Biol.* **1999**, *48*, 36–41.

(11) Shu, X.; Lev-Ram, V.; Deerinck, T. J.; Qi, Y.; Ramko, E. B.; Davidson, M. W.; Jin, Y.; Ellisman, M. H.; Tsien, R. Y. A Genetically Encoded Tag for Correlated Light and Electron Microscopy of Intact Cells, Tissues, and Organisms. *PLoS Biol.* **2011**, *9*, e1001041.

(12) Agut, M.; Ruiz-González, R.; Cortajarena, A. L.; Flors, C.; Mejias, S. H.; Nonell, S. Singlet Oxygen Generation by the Genetically Encoded Tag MiniSOG. *J. Am. Chem. Soc.* **2013**, *135*, 9564–9567.

(13) Rodríguez-Pulido, A.; Cortajarena, A. L.; Torra, J.; Ruiz-González, R.; Nonell, S.; Flors, C. Assessing the Potential of Photosensitizing Flavoproteins as Tags for Correlative Microscopy. *Chem. Commun.* **2016**, *52*, 8405–8408.

(14) Proshkina, G. M.; Shramova, E. I.; Shilova, O. N.; Ryabova, A. V.; Deyev, S. M. Phototoxicity of Flavoprotein MiniSOG Induced by Bioluminescence Resonance Energy Transfer in Genetically Encoded System NanoLuc-MiniSOG Is Comparable with Its LED-Excited Phototoxicity. *J. Photochem. Photobiol. B Biol.* **2018**, *188*, 107–115.

(15) Souslova, E. A.; Mironova, K. E.; Deyev, S. M. Applications of Genetically Encoded Photosensitizer MiniSOG: From Correlative Light Electron Microscopy to Immunophotosensitizing. *J. Biophotonics* **2017**, *10*, 338–352.

(16) Varbanov, H. P.; Jakupec, M. A.; Roller, A.; Jensen, F.; Galanski, M.; Keppler, B. K. Theoretical Investigations and Density Functional Theory Based Quantitative Structure–Activity Relationships Model for Novel Cytotoxic Platinum(IV) Complexes. *J. Med. Chem.* **2013**, *56*, 330–344.

(17) Englinger, B.; Pirker, C.; Heffeter, P.; Terenzi, A.; Kowol, C. R.; Keppler, B. K.; Berger, W. Metal Drugs and the Anticancer Immune Response. *Chem. Rev.* **2019**, *119*, 1519–1624.

(18) Weber, S.; Walker, J. M. *Flavins and Flavoproteins.; Springer,* ***2014***

(19) Chaiyen, P.; Fraaije, M. W.; Mattevi, A. The Enigmatic Reaction of Flavins with Oxygen. *Trends Biochem. Sci.* **2012**, *37*, 373–380.

(20) Ghisla, S.; Massey, V.; Lhoste, J.-M.; Mayhew, S. G. Fluorescence and Optical Characteristics of Reduced Flavines and Flavoproteins. *Biochemistry.* **1974**, *13*, 589–597.

(21) Gargiulo, S.; Arends, I. W. C. E.; Hollmann, F. A Photoenzymatic System for Alcohol Oxidation. *ChemCatChem.* **2011**, *3*, 338–342.

(22) Rauch, M.; Schmidt, S.; Arends, I. W. C. E.; Oppelt, K.; Kara, S.; Hollmann, F. Photobiocatalytic Alcohol Oxidation Using LED Light Sources. *Green Chem.* **2017**, *19*, 376–379.

(23) Kao, Y.-T.; Saxena, C.; He, T.-F.; Guo, L.; Wang, L.; Sancar, A.; Zhong, D. Ultrafast Dynamics of Flavins in Five Redox States. *J. Am. Chem. Soc.* **2008**, *130*, 13132–13139.

(24) Feldmeier, C.; Bartling, H.; Magerl, K.; Gschwind, R. M. LED-Illuminated NMR Studies of Flavin-Catalyzed Photooxidations Reveal Solvent Control of the Electron-Transfer Mechanism. *Angew. Chem., Int. Ed.* **2015**, *54*, 1347–1351.

(25) Bartling, H. Dissertation: NMR Spectroscopic Investigations on Photocatalytic Reactions and Photochromic Materials., Ph.D. Thesis Universität Regensburg, **2016**.

(26) Cardoso, D. R.; Franco, D. W.; Olsen, K.; Andersen, M. L.; Skibsted, L. H. Reactivity of Bovine Whey Proteins, Peptides, and Amino Acids toward Triplet Riboflavin as Studied by Laser Flash Photolysis. *J. Agric. Food Chem.* **2004**, *52*, 6602–6606.

(27) Dabbish, E.; Ponte, F.; Russo, N.; Sicilia, E. Antitumor Platinium(IV) Prodrugs: A Systematic Computational Exploration of Their Reduction Mechanism by l -Ascorbic Acid. *Inorg. Chem.* **2019**, *58*, 3851–3860.

(28) Torra, J.; Lafaye, C.; Signor, L.; Aumonier, S.; Flors, C.; Shu, X.; Nonell, S.; Gotthard, G.; Royant, A. Tailing MiniSOG: Structural Bases of the Complex Photophysics of a Flavin-Binding Singlet Oxygen Photosensitizing Protein. *Sci. Rep.* **2019**, *9*, 2428.

(29) Westberg, M.; Holmegaard, L.; Pimenta, F. M.; Etzerodt, M.; Ogilby, P. R. Rational Design of an Efficient, Genetically Encodable, Protein-Encased Singlet Oxygen Photosensitizer. *J. Am. Chem. Soc.* **2015**, *137*, 1632–1642.

(30) Pimenta, F. M.; Jensen, R. L.; Breitenbach, T.; Etzerodt, M.; Ogilby, P. R. Oxygen-Dependent Photochemistry and Photophysics of "MiniSOG," a Protein-Encased Flavin. *Photochem. Photobiol.* **2013**, *89*, 1116–1126.

(31) Silva, A. V.; López-Sánchez, A.; Junqueira, H. C.; Rivas, L.; Baptista, M. S.; Orellana, G. Riboflavin Derivatives for Enhanced Photodynamic Activity against Leishmania Parasites. *Tetrahedron.* **2015**, *71*, 457–462.

(32) Varbanov, H. P.; Valiahdi, S. M.; Kowol, C. R.; Jakupec, M. A.; Galanski, M.; Keppler, B. K. Novel Tetracarboxylatoplatinum(IV) Complexes as Carboplatin Prodrugs. *Dalton. Trans.* **2012**, *41*, 14404–14415.

(33) Gramatica, P.; Papa, E.; Luini, M.; Monti, E.; Gariboldi, M. B.; Ravera, M.; Gabano, E.; Gaviglio, L.; Osella, D. Antiproliferative Pt(IV) Complexes: Synthesis, Biological Activity, and Quantitative Structure–Activity Relationship Modeling. *J. Biol. Inorg. Chem.* **2010**, *15*, 1157–1169.

(34) Tetko, I. V; Varbanov, H. P.; Galanski, M.; Talmaciu, M.; Platts, J. A.; Ravera, M.; Gabano, E. Prediction of LogP for Pt(II) and Pt(IV) Complexes: Comparison of Statistical and Quantum-Chemistry Based Approaches. *J. Inorg. Biochem.* **2016**, *156*, 1–13.

(35) Jhulki, I.; Chanani, P. K.; Abdelwahed, S. H.; Begley, T. P. A Remarkable Oxidative Cascade That Replaces the Riboflavin C8 Methyl with an Amino Group during Roseoflavin Biosynthesis. *J. Am. Chem. Soc.* **2016**, *138*, 8324–8327.

(36) Rabello, B. R.; Gerola, A. P.; Pellosi, D. S.; Tessaro, A. L.; Aparício, J. L.; Caetano, W.; Hioka, N. Singlet Oxygen Dosimetry Using Uric Acid as a Chemical Probe: Systematic Evaluation. *J. Photochem. Photobiol. A.* **2012**, *238*, 53–62.

(37) Gomes, A.; Fernandes, E.; Lima, J. L. F. C. Fluorescence Probes Used for Detection of Reactive Oxygen Species. *J. Biochem. Biophys. Methods* **2005**, *65*, 45–80.

(38) Frisch, M. J.; Trucks, G. W.; Schlegel, H. B.; Scuseria, G. E.; Robb, M. A.; Cheeseman, J. R.; Scalmani, G.; Barone, V.; Petersson, G. A.; Nakatsuji, H.; Li, X.; Caricato, M.;

Marenich, A. V; Bloino, J.; Janesko, B. G.; Gomperts, R.; Mennucci, B.; Hratchian, H. P.; Ortiz, J. V; Izmaylov, A. F.; Sonnenberg, J. L.; Williams-Young, D.; Ding, F.; Lipparini, F.; Egidi, F.; Goings, J.; Peng, B.; Petrone, A.; Henderson, T.; Ranasinghe, D.; Zakrzewski, V. G.; Gao, J.; Rega, N.; Zheng, G.; Liang, W.; Hada, M.; Ehara, M.; Toyota, K.; Fukuda, R.; Hasegawa, J.; Ishida, M.; Nakajima, T.; Honda, Y.; Kitao, O.; Nakai, H.; Vreven, T.; Throssell, K.; Montgomery Jr., J. A.; Peralta, J. E.; Ogliaro, F.; Bearpark, M. J.; Heyd, J. J.; Brothers, E. N.; Kudin, K. N.; Staroverov, V. N.; Keith, T. A.; Kobayashi, R.; Normand, J.; Raghavachari, K.; Rendell, A. P.; Burant, J. C.; Iyengar, S. S.; Tomasi, J.; Cossi, M.; Millam, J. M.; Klene, M.; Adamo, C.; Cammi, R.; Ochterski, J. W.; Martin, R. L.; Morokuma, K.; Farkas, O.; Foresman, J. B.; Fox, D. J. Gaussian 16, Revision B.01. **2016**.

(39) Adamo, C.; Barone, V. Toward Reliable Density Functional Methods without Adjustable Parameters: The PBE0 Model. *J. Chem. Phys.* **1999**, *110*, 6158–6170.

(40) Weigend, F.; Ahlrichs, R. Balanced Basis Sets of Split Valence, Triple Zeta Valence and Quadruple Zeta Valence Quality for H to Rn: Design and Assessment of Accuracy. *Phys. Chem. Chem. Phys.* **2005**, *7*, 3297–3305.

(41) Grimme, S.; Ehrlich, S.; Goerigk, L. Effect of the Damping Function in Dispersion Corrected Density Functional Theory. *J. Comput. Chem.* **2011**, *32*, 1456–1465.

(42) Chai, J.-D.; Head-Gordon, M. Long-Range Corrected Hybrid Density Functionals with Damped Atom–Atom Dispersion Corrections. *Phys. Chem. Chem. Phys.* **2008**, *10*, 6615–6620.

(43) Zhao, Y.; Truhlar, D. G. The M06 Suite of Density Functionals for Main Group Thermochemistry, Thermochemical Kinetics, Noncovalent Interactions, Excited States, and Transition Elements: Two New Functionals and Systematic Testing of Four M06-Class Functionals and 12 Other Function. *Theor. Chem. Acc.* **2008**, *120*, 215–241.

(44) Reed, A. E.; Curtiss, L. A.; Weinhold, F. Intermolecular Interactions from a Natural Bond Orbital, Donor-Acceptor Viewpoint. *Chem. Rev.* **1988**, *88*, 899–926.

(45) Chirlian, L. E.; Francl, M. M. Atomic Charges Derived from Electrostatic Potentials: A Detailed Study. *J. Comput. Chem.* **1987**, *8*, 894–905.

4

Enhancing The Photocatalytic Conversion Of Pt^{IV} Substrates By Flavoprotein Engineering

The work described in this chapter has been published in *J. Phys. Chem. Lett.* 2021, 12, 4504–4508 (authors: Gurruchaga-Pereda J.; Martínez-Martínez V.; Formoso E.; Azpitarte O.; Rezabal E.; Lopez X.; Cortajarena L. A.; Salassa L.).

4.1 Introduction

Flavoproteins and flavoenzymes are capable of photocatalyzing the reduction of metal complexes in the presence of electron donors.[1] Recently, we demonstrated that flavoproteins such as the NOX (NADH oxidase) enzyme and miniSOG (mini Singlet Oxygen Generator) converted Pt^{IV} anticancer agents into their biological active Pt^{II} counterparts (e.g. cisplatin) with remarkable turnover numbers (TONs) and frequencies (TOFs), including in biological environments.[2–4] Key steps in the catalytic mechanism of these reactions are the light-induced formation of the flavin triplet-excited state (^{3}FL*) and its subsequent reductive quenching by electron donors, which affords the flavin hydroquinone form (e.g. HFL^-) capable of reducing Pt^{IV} substrates (Figure 1a).

Besides providing one of the rare examples of catalytic reactions that use metal complexes as substrates,[5,6] this unconventional chemistry has interest in the design of new strategies for the (photo)activation of metal-based prodrugs and their application in photochemotherapy.[4,7]

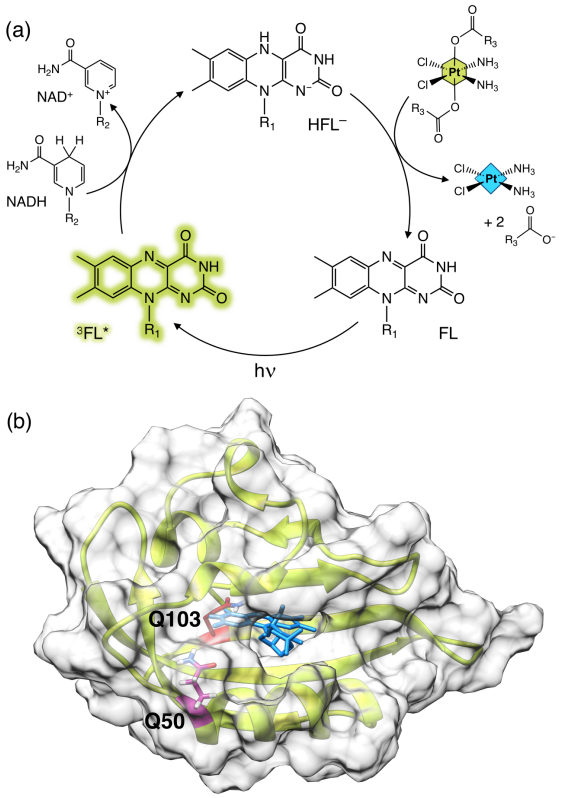

Figure 1. (a) General photocatalytic mechanism for the Pt^{IV} prodrug activation by flavins; R_1 = e.g. ribityl, ribityl phosphate, R_2 = adenosine diphosphate ribose and R_3 = CH_2CH_2COOH (**1**) or CH_3 (**2**). (b) molecular model of miniSOG structure based on the structure of iLOV protein (PBD ID: 6GPU). The backbone of miniSOG is shown as a yellow ribbon, FMN as blue sticks, and the amino acids in the mutation positions in violet (Q50) and red (Q103).

Considering the spectacular results obtained by protein engineering in catalysis,[8,9] we wondered how modification of flavoprotein structures could affect their capacity to catalytically transform Pt^{IV} substrates and whether or not site-directed mutagenesis could enhance their activation efficiency upon light irradiation. For this reason, we selected the FMN-containing miniSOG flavoprotein and investigated the catalytic performance of its Q103V, Q50E and Q50W mutants with respect to the wild type (WT). miniSOG is a suitable model for this task since mutants of this protein and their photophysics have been thoroughly studied for use in correlative light and electron microscopy (CLEM) and for $^1O_2$ sensitization purposes.[10–15]

The photophysics of the Q103V mutant and its Q103L (SOPP, singlet oxygen photosensitizing protein) analogue were previously investigated by several groups.[12,14,15] The glutamine residue in the 103 position has been suggested to form a hydrogen bond with FMN (Figure 1b), likely enhancing quenching of ^{3}FMN* and formation of $O_2^{\bullet-}$.[15] Substitution of the Q residue for an amino acid with a hydrophobic side chain such as valine or leucine proved to increase significantly the ^{3}FMN* lifetime and the overall capacity of miniSOG to sensitize $^1O_2$.[12,14,15] Q50E and Q50W are instead novel mutants that we generated based on the proximity of the Q50 position to the FMN-containing pocket (Figure 1b), with the aim of evaluating the effects of a negatively charged (glutamic acid, E, pK_a 4.5) and a bulky aromatic amino acid (tryptophan, W) on the catalysis. Furthermore, W is known to be optically active and an excited-state quencher for flavins.[16,17]

4.2 Results and Discussion

In order to test the capacity of the different mutants to catalyze the conversion of Pt^{IV} complexes, we employed the cisplatin prodrugs *cis,cis,trans*-$[Pt(NH_3)_2(Cl)_2(O_2CCH_2CH_2CO_2H)_2]$ (**1**) and *cis,cis,trans*-$[Pt(NH_3)_2(Cl)_2(O_2CCH_3)_2]$ (**2**), together with NADH as electron donor (Figure 1a).

To the best of our knowledge this is the first attempt to engineer a protein for enhancing a catalytic process involving the transformation of metal-containing compounds. These studies may have key implications in biology as well as in the development of new technologies for medicine.

4.2.1 Photophysical and photochemical studies

Firstly, we characterized the photophysical and photochemical properties of the four miniSOG catalysts employing different optical methods and experimental conditions (Figure S1–S8). The four proteins displayed absorption and emission profiles typical of the FMN chromophore, with fluorescence lifetimes falling in the 4–5 ns range (Figure S1). The Q50W mutant had the shortest fluorescence lifetime (4 ns) indicating that the W residue favors

deactivation of the ^{1}FMN excited state, which confirmed the expected coupling between W and FMN from the design hypothesis. Transient absorption spectra for the miniSOG mutants and the WT showed the characteristic features of ^{3}FMN, that is a negative band for ground-state bleaching at 420−480 nm and a positive band at 550−750 nm, corresponding to the absorption of the T1 state (Figure 2).[2,16] We determined the ^{3}FMN lifetime in aerated solutions by monitoring the mono-exponential decay of the triplet−triplet absorption at 720 nm (Figure 2 and Figure S2). Compared to miniSOG WT (35 µs), Q103V and Q50W mutants showed triplet lifetimes (τ^T) that were significantly longer and shorter respectively (102 *vs* 1.8 µs). The dramatic τ^T reduction observed for Q50W can be attributed to electron transfer processes involving the tryptophan and ^{3}FMN moieties, including the formation of radical pairs.[16,17] Conversely, Q50E resembled the WT displaying a ^{3}FMN decay of 31 µs. The lifetime values obtained in this work for WT and Q103V are consistent with data previously reported.[11]

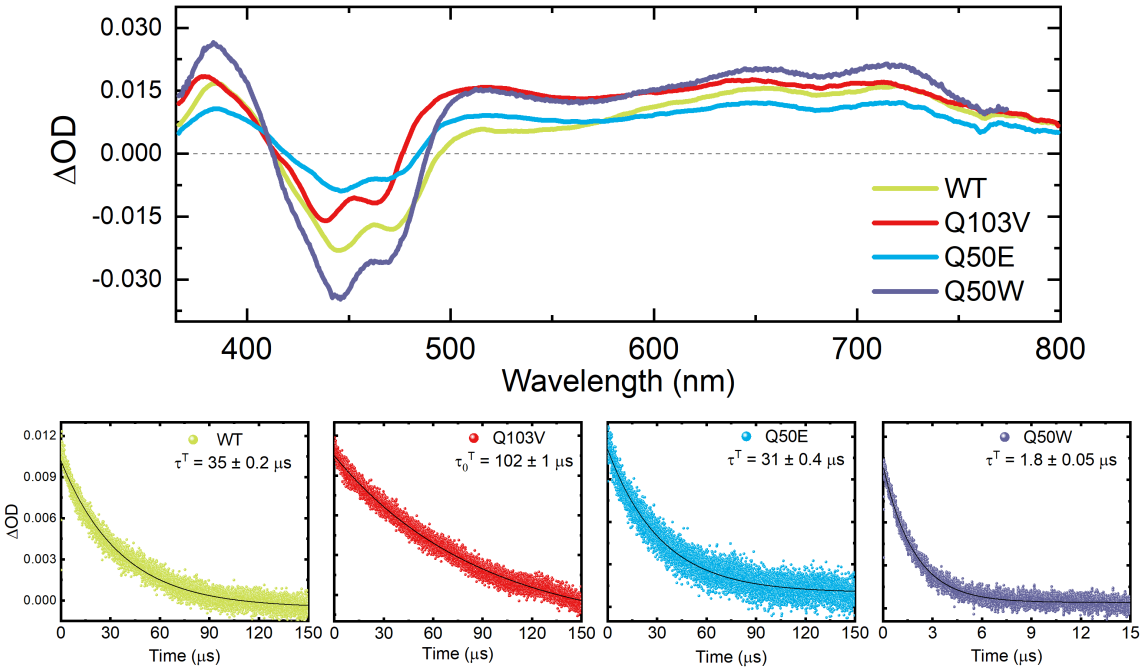

Figure 2. Transient absorption spectra (λ_{exc} = 445 nm) and decays (τ^T) of the triplet−triplet absorption at 720 nm for miniSOG WT and its Q103V, Q50E and Q50W mutants. All measurements were performed in PB solutions (20 mM, pH 7, air-saturated) of the miniSOG proteins.

Photostability is pivotal in the performance of a photocatalyst, hence we investigated the behavior of the four miniSOGs under light irradiation (460 nm, 6 mW·cm^{-2}) and different experimental conditions. In oxygenated solutions, all samples showed a decrease in the absorbance band at 450 nm, characteristic of FMN degradation (Figure S3 and S4).[11,14,15,18] The WT and mutants displayed rather similar photodecomposition rates at short irradiation times (< 10 min), that is in the timeframe of the catalysis experiments (*vide infra*). When exposed to blue light for longer time periods, a band at 600 nm was observed in the spectra of the WT and Q50W, corresponding to the formation of an FMN radical (semiquinone).[18]

This species is observed particularly in oxygen-free conditions where the ^{3}FMN* can be efficiently deactivated by electron transfer processes involving the miniSOG amino acidic scaffold.[15] Furthermore, after prolonged irradiations (ca. > 20 min), Q103V underwent photodecomposition in a more pronounced manner compared to the other miniSOG forms. Such result is consistent with the increased capacity of this mutant to produce $^1O_2$ and other ROS (especially $O_2^{\bullet-}$), as determined by indirect methods employed previously for miniSOG (Figure S5 and S6).[11,13] Importantly, Bregnhøj *et al.* recently showed that detection of $^1O_2$ using uric acid as probe suffers from limitations.[19]

The formation of the FMN radical was more pronounced for all miniSOG variants in the absence of O_2 (Figure S7), which acts as quencher of the one-electron reduced FMN (either in its semiquinone or anionic form)[18] to give $O_2^{\bullet-}$ via a second electron transfer. Importantly, the FMN radical rapidly disappeared when sample were re-exposed to oxygen-containing ambient atmosphere. Concomitantly, the FMN-associated band at 400–500 nm recovered almost completely, although this could be in part ascribed to the formation of lumichrome.[15] Among the miniSOG proteins, Q103V and Q50W showed the lowest formation of FMN radical. In the case of the former, previous work demonstrated that mutation of the Q103 position led to reducing the rate of electron transfer from the protein to FMN.[11,14] For the latter instead, the generation of FMN$^{\bullet-}$/Trp$^{\bullet+}$ radical pairs and back electron transfer processes may explain the low intensity of the 600-nm band, as well as the shorter ^{3}FMN* lifetime observed by transient absorption.[17] Nevertheless, deactivation of the ^{1}FMN excited state by Trp may also contribute to these distinct spectral features for Q50W, as observed by fluorescence lifetime experiments. Notably, circular dichroism spectra of light-irradiated miniSOG variants showed that formation of the FMN radical did not cause major changes in the protein structure (Figure S8).

4.2.2 Catalytic studies

Next, we evaluated how the photophysical and photochemical properties of the different miniSOG proteins impacted the catalytic transformation of complexes **1** and **2**. Catalysis experiments were run using PB solutions containing 25 µM miniSOG (5% loading), 500 µM Pt^{IV} substrate and 1 mM NADH. Previous work showed that such concentration of electron donor did not caused any significant decomposition of the Pt^{IV} substrates.[2] The progression of the reactions in the dark and under light irradiation was monitored by ^{1}H NMR by following the release of the axial ligands coordinated to the Pt^{IV} center (Supporting Information), which in these flavin-catalyzed reactions mostly corresponds to the formation of cisplatin.[4]

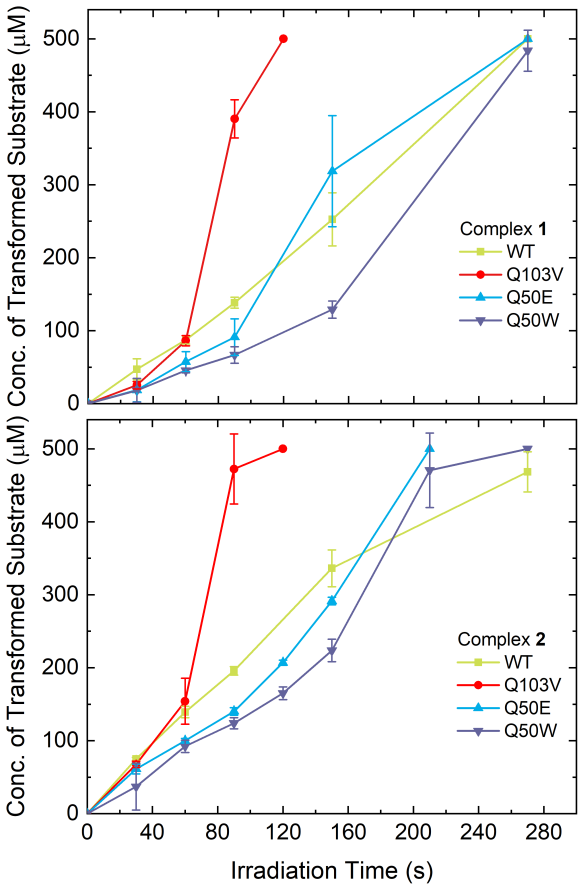

Figure 3. Kinetics profiles for the photocatalytic conversion of **1** and **2** by miniSOG variants. Reactions were monitored by NMR and performed in PB solutions (18 mM PB, pH 7.0, 10% D_2O) containing 25 μM miniSOG catalysts, 500 μM **1** or **2** and 1 mM NADH.

Initial control experiments confirmed that the substrate conversion was rather ineffective in the dark (Figure S9 and S10). We detected no activity in the first hours and only 20% of **1** and 60–80% of **2** were transformed by miniSOG WT and mutants after 48 h in the absence of light. On the contrary, under light irradiation, the reactions were considerably faster for both **1** and **2** (Figure 3, Figure S11 and S12). As summarized in Table 1, all photocatalysts practically achieved full conversion of the substrates within 5 min (1.8 $J \cdot cm^{-2}$), corresponding to turnover numbers (TON) of 20. In addition, experiments with reduced photocatalyst loadings (0.1%) afforded TON_{max} values comprised between 610 and 738 within 30 min of light irradiation (Figure S13).

Anyhow, as expected from the photophysical studies, Q103V displayed the highest catalytic activity among all proteins. Already after 90 s of light irradiation, this mutant converted approximately more than 80% of Pt^{IV} substrate. For instance, in the case of **1**, this corresponded to 2.8- and 5.8-fold increase in the turnover frequency (TOF) compared to WT and Q50W, respectively. Results also showed that Q50E behaved rather similarly to WT in terms of catalytic efficiency (Table 1).

The long ^{3}FMN* lifetime of Q103V is crucial for its enhanced catalytic activity since it favors NADH-promoted reductive quenching,[2] which ultimately results in higher concentrations of the flavin hydroquinone HFL^-, that is the active catalyst that converts Pt^{IV} prodrugs in cisplatin. Indeed, we observed that short light irradiation intervals (30–90 sec) caused a more rapid decrease of the 450-nm FMN band in the case of Q103V than Q50W, implying that the former mutant more effectively generated the flavin hydroquinone (Figure S14). It is also worth highlighting that the presence of Pt^{IV} substrate and NADH did not induce significant changes in the capacity of the proteins to undergo electron transfer reactions and form the radical species (Figure S15 and Figure S16). The only exception appeared to be Q103V which displayed a higher absorbance intensity at 600 when **1** was present (with or without NADH, Figure S16 and S17), likely due to a (radical) side reaction involving the complex and the FMN contained in the protein scaffold. All together such findings suggest that the protein quenching channel of ^{3}FMN* is still active under the catalysis conditions and competes with the substrate conversion.

Table 1. Turnover Frequencies (TOFs, min^{-1}), Turnover Numbers (TONs), and Conversion Percentages (Conv.) for the miniSOG-catalyzed Photoactivation of **1** and **2** in the presence of NADH.

Complex	TOF (min^{-1})	TON	Conv. (%)	TON_{max}
WT				
1	3.7±0.2	20	100	610
2	5.2±0.2	19	94	-
Q103V				
1	10.4±0.7*	20	100	673
2	12.6±1.3*	20	100	-
Q50E				
1	2.4±0.7	20	100	738
2	3.7±0.1	20	100	-
Q50W				
1	1.8±0.3	20	100	734
2	3.3±0.2	20	100	-

* determined at 79-94% substrate conversion (90 s of light irradiation)

We gained further insights by performing dynamic molecular simulations of the WT, Q103V and Q50W bearing the FMN in its oxidized form. All miniSOG variants showed rather similar structure and FMN-protein interaction pattern, with the isoalloxazine ring and ribityl chain of the FMN buried in the protein binding pocket, leaving the phosphate group accessible through an entrance channel. Overall, during the simulation, the residue in the 50 position (Q or W) alternated between two conformations (Figure S18 and S19), being oriented either towards the interior of the channel (“closed”) or outwards (“open”). None of these two conformations appeared able to hinder the passage through the channel in the case of Q103V or WT, hence suggesting that the higher catalytic activity of such mutant compared

to WT could be ascribed exclusively to the ^{3}FMN* excited state properties and the lack of quenching from the residue in position 103.

Conversely, few differences were observed in the case of Q50W. Although the entrance channel of this mutant remained open during most of the simulation (contrary to Q103V and WT), its "closed" conformation was more hindered, due to the bulky nature of the W residue. More importantly, we observed that the non-polar nature of the W side chain reduced the diffusion of charged particles such as Na^+ ions through the channel to the FMN phosphate group, even in the open channel conformation (Figure S20). The finding indicates that this residue establishes attractive interactions enabling the access to the phosphate group in FMN. Similar behavior should be expected for other charged or polar molecules, i.e. Pt^{IV} substrates or NADH, inferring that the lowest catalytic activity of Q50W might not only be linked to its excited state features but also to a less efficient entrance channel.

4.3 Conclusions

Our proof-of-concept study demonstrates for the first time that site directed mutagenesis can be employed to alter and enhance the catalytic activity of flavoproteins in artificial reactions involving metal complexes as substrates. Such a result was principally achieved by tuning the miniSOG photophysics properties via protein engineering. Moreover, we envision that far greater improvements could be accomplished introducing structural modifications in flavoproteins that are capable of influencing substrate binding and product release steps of catalytic reactions. Currently, we seek to reach such goals by tailoring flavoenzymes that have higher structural and functional complexity than miniSOG.

4.4 Experimental details

Materials and Methods

Riboflavin 5´-monophosphate sodium salt hydrate (FMN), potassium phosphate monobasic, potassium phosphate dibasic, β-nicotinamide adenine dinucleotide, reduced disodium salt hydrate were purchased from Sigma-Aldrich, potassium tetrachloroplatinate(II) from Precious Metals Online. All chemicals were used as received without additional purification.

Preparation of Pt^{IV} complexes. Complexes *cis,cis,trans*-$[Pt(NH_3)_2(Cl_2)(O_2CCH_2CH_2CO_2H)_2]$ (**1**) and *cis,cis,trans*-$[Pt(NH_3)_2(Cl_2)(O_2CCH_3)_2]$ (**2**) were synthesized and characterized as previously reported.[20]

Site-directed mutagenesis, protein expression and purification. QuikChange site directed mutagenesis was employed to introduce Q50W and Q50E mutations into pPRO-EX-HTA plasmid encoding miniSOG. The reactions were transformed into *Escherichia coli* DH10b

competent cells, the plasmid DNA of the selected colonies extracted using a miniprep kit (Omega Bio-Tek) and the identity of the mutants confirmed by sequencing (Table S1). The previously reported Q103V mutant was cloned into pBAD-Myc-His plasmid. Bacteria carrying the plasmids were stored at −80 °C in 20% glycerol (v/v). The WT, Q50W and Q50E proteins were expressed in *E. coli* (C41) and purified following our previous work,[1] while the Q103V mutant was expressed as described by Flors and collaborators using DH10β cells.[14]

Table S1. Part of the sequences of miniSOG visualized by pDRAW.

Name	Mutation Position	Native residue	Substituted residue	Primer(5'-3') (Rev)
Q50E	50	Q	E	CTGAACAGTTGCTTCATCGGTTTCCGG
Q50W	50	Q	W	CTGAACAGTTGCCCAATCGGTTTCCGG
WT sequence				
M E K S F V I T D P R L P D N P I I F A S D G F L E L T E Y S R E E I L G R N G R F L Q G P E T D Q A T V Q K I R D A I R D Q R E I T V Q L I N Y T K S G K K F W N L L H L Q P M R D Q K G E L Q Y F I G V Q L D G				
Q50E sequence				
M E K S F V I T D P R L P D N P I I F A S D G F L E L T E Y S R E E I L G R N G R F L Q G P E T D **E** A T V Q K I R D A I R D Q R E I T V Q L I N Y T K S G K K F W N L L H L Q P M R D Q K G E L Q Y F I G V Q L D G				
Q50W sequence				
M E K S F V I T D P R L P D N P I I F A S D G F L E L T E Y S R E E I L G R N G R F L Q G P E T D **W** A T V Q K I R D A I R D Q R E I T V Q L I N Y T K S G K K F W N L L H L Q P M R D Q K G E L Q Y F I G V Q L D G				

UV-Vis absorption spectroscopy (UV-Vis). All spectra were acquired in optical quartz cuvettes in PB solutions (20 mM, pH 7) using a JASCO V-730 spectrophotometer.

Fluorescence emission and lifetimes. The emission spectrum of **FMN** (20 µM) was recorded on a spectrofluorimeter Edinburgh Instruments (FLS1000 model) with a 450 W xenon flash lamp as the excitation source. Fluorescence decay curves (τ^S) were recorded with a time-correlated single-photon counting technique at λ_{em} = 520 nm after excitation at λ_{exc} = 485 nm by means of a EPL-485 laser with 100 ps FWHM pulses using a microchannel plate detector with picosecond time resolution. Fluorescence lifetimes were obtained after deconvolution of the instrumental response signal from the recorded decay curves by means of an iterative method. The goodness of the exponential fit was controlled by statistical parameters (χ^2 and analysis of the residuals). Measurements were performed on PB solutions (20 mM, pH 7, air-saturated) of miniSOG WT and its Q103V, Q50E and Q50W mutants. Emission and lifetime measurements were performed using 3 and 15 µM solutions of the miniSOG proteins, respectively.

Transient absorption and triplet lifetimes. Nanosecond transient absorption measurements were recorded on a LP980 laser flash photolysis spectrometer (Edinburgh Instruments,

Livingston, UK). Samples were excited by a nanosecond pulsed laser (Nd:YAG laser/OPO, LOTIS TII 2134) at the absorption maxima (445 nm) operating at 1 Hz and with a pulse width of 7 ns at a 6.5 mW excitation power (10 mW in the case of Q50W). Air-saturated samples were prepared with an optical absorbance of 0.3 at the excitation wavelength. Transient spectra were recorded on gated ICCD detector (DH320T air cooled, Andor Technology). The decay of triplet-triplet absorption in the presence of oxygen (air saturated solutions) were collected at 720 nm on PMT detector (R928P, Hamamatsu) and oscilloscope. Triplet lifetimes in the presence of oxygen (τ^T) were obtained from the slope of the recorded decay curves by means of an iterative method by LP900 software. The goodness of the exponential fit was controlled by statistical parameters (χ^2). PB solutions (20 mM, pH 7, air-saturated) containing 20 μM of the miniSOG proteins (31 μM in the case of Q50W) were employed for this set of experiments.

Singlet oxygen and ROS production. Quantification of $^1O_2$ and ROS was achieved using methods previously established for FMN and miniSOG.[11,13] Indirect measurement of $^1O_2$ was performed using uric acid (UA) as probe[21] and monitoring the changes of its absorbance at 292 nm over light irradiation time. We exposed to 460-nm light (6 mW·cm^{-2}) optically-matched solutions containing UA (30 μM) miniSOG proteins (3 μM).

Photooxidation of hydroethidine (HE) was instead used to evaluate the production of other ROS (particularly $O_2^{\bullet-}$) since the transformation of this probe does not occur upon interaction with $^1O_2$.[11,22] In this case, HE (30 μM) solutions containing miniSOG catalysts (3 μM) were irradiated at 460 nm and their fluorescence intensity collected at different time points (λ_{ex} = 525 nm, λ_{em} = 550–800 nm) as previously described.[11]

Circular dichroism. CD spectra were recorded at room temperature on a Jasco J-1500 spectrophotometer, using 0.1 cm path length cuvettes and the following parameters: sensitivity 200 mdeg; data pitch 0.1 nm; scanning speed 50 nm/min; response 8 sec; band width 1 nm. Measurements were performed using 3 μM solution of the miniSOG variants, acquiring data in the 190–260 nm region.

Nuclear magnetic Resonance (NMR). ^{1}H NMR spectra of the various samples were recorded on a Fourier TM Bruker 300 NMR spectrometer using standard pulse programs. Chemical shifts were reported in parts-per-million (δ, ppm) and referenced to the residual solvent peak.

Catalysis experiments. All reactions were carried out in air at 298 K and pH 7.0 using 25 μM catalyst, 500 μM substrate (**1** and **2**) and 1 mM NADH. Light irradiations were performed employing an LED light source (λ_{max} = 460 nm, 6 mW·cm^{-2}). Turnover frequency (TOF), turnover number (TON) and % conversion for the catalytic reactions were determined by quantifying the amount of converted **1** and **2** via ^{1}H NMR. Integration of the free succinato and acetato ligand signals (singlets at 2.25–2.35 ppm and at approx. 1.80 ppm respectively) were used for monitoring the reaction progress. TOF values were obtained at substrate

conversions of 25–35% (90 s of light irradiation), except in the case of the Q103V for which the substrate conversion was 80–94%. TON_{max} values were determined employing 1 μM of miniSOG proteins, 1 mM of **1** and 1 mM of NADH.

Computational methods. All-atom Molecular Dynamics (MD) simulations were carried out for miniSOG WT, Q50W and Q103V, bearing the FMN in its oxidized form. The starting structure for MD simulation of miniSOG complexed with FMN in solution was obtained from the Protein Data Bank (PDB: 6GPU).[15] This X-ray structure was prepared for all-atom MD simulations adding hydrogen atoms and choosing an orientation for residues resolved with two possible orientations. The parameters used for the protein corresponded to the all-atom force field AMBER99SB-ILDN with extension to the TIP3P water model.[23] The AMBER parameter database was used for FMN.[24] Q50W and Q103W mutations were performed using VMD software.[25] The aqueous solvation environment was created by solvating the system with a rhombic dodecahedrical box,[26] where the distance from the protein to the last layer of the water box is 12 Å. Afterwards, Na^+ and Cl^- ions were added at random positions, in order to neutralize the systems and to mimic the physiologic extracellular concentration of 0.15 M.

Periodic Boundary conditions were used along with the isothermal-isochoric ensemble (NVT) during equilibration steps and isothermal-isobaric ensemble (NPT) at 1 atm and 300 K via Parrinello-Rahman barostat[27] and Nosé-Hoover thermostat[28] during the production phase. Newton's equations of motion were integrated numerically using the leapfrog Verlet algorithm[29] within a 2 fs time step. The covalent bond lengths involving hydrogen were constrained with the LINCS algorithm.[30]

Water molecules were initially relaxed for 10000 steps of steepest descent[31] energy minimization keeping all solute atoms and ion positions restrained to their initial coordinates using a harmonic potential constant of 5,000 kJ/mol^{-1} nm^{-1}. The restraints on the ions were then relaxed and the solvent (water and ions) was relaxed for another 10000 steps of steepest descent minimization, keeping the solute atoms restrained. From this starting point, the equilibration step of 4 ns began. During the first 2 ns of the equilibration procedure, restrained molecular dynamics was performed at 300 K using NVT ensemble via Bussi thermostat. The harmonic restraints on the solute atoms were slowly released during the course of this simulation. The last 2 ns of the equilibration step were performed using NPT ensemble at 1 atm and 300 K. Finally, the production phase molecular dynamics began and covered 100 ns. All the simulations were performed with GROMACS molecular dynamics package, version 2018.[32]

Radial Distribution Functions (RDF)[33] of Na^+ cations around the FMN phosphoryl oxygens were calculated using GROMACS RDF tool. The Solvent Accessible Area (SAS) and the electrostatic potential surface of the systems were calculated using the PDB2PQR and Adaptive Poisson-Boltzmann Solver (APBS) software.[33,34]

4.5 References

(1) Alonso-de Castro, S.; Cortajarena, A. L.; López-Gallego, F.; Salassa, L.; Lopez-Gallego, F.; Salassa, L.; López-Gallego, F.; Salassa, L. Bioorthogonal Catalytic Activation of Platinum and Ruthenium Anticancer Complexes by FAD and Flavoproteins. *Angew. Chem., Int. Ed.* **2018**, *57*, 3143–3147.

(2) Gurruchaga-Pereda, J.; Martínez-Martínez, V.; Rezabal, E.; Lopez, X.; Garino, C.; Mancin, F.; Cortajarena, A. L.; Salassa, L. Flavin Bioorthogonal Photocatalysis Toward Platinum Substrates. *ACS Catal.* **2020**, *10*, 187–196.

(3) Alonso-de Castro, S.; Ruggiero, E.; Ruiz-de-Angulo, A.; Rezabal, E.; Mareque-Rivas, J. C.; Lopez, X.; López-Gallego, F.; Salassa, L. Riboflavin as a Bioorthogonal Photocatalyst for the Activation of a Pt(IV) Prodrug. *Chem. Sci.* **2017**, *8*, 4619–4625.

(4) Alonso-de Castro, S.; Terenzi, A.; Hager, S.; Englinger, B.; Faraone, A.; Martinez, J. C.; Galanski, M.; Keppler, B. K.; Berger, W.; Salassa, L. Biological Activity of Pt(IV) Prodrugs Triggered by Riboflavin-Mediated Bioorthogonal Photocatalysis. *Sci. Rep.* **2018**, *8*, 1–10.

(5) Ruffoni, A.; Juliá, F.; Svejstrup, T. D.; McMillan, A. J.; Douglas, J. J.; Leonori, D. Practical and Regioselective Amination of Arenes Using Alkyl Amines. *Nat. Chem.* **2019**, *11*, 426–433.

(6) Gong, L.; Lin, Z.; Harms, K.; Meggers, E. Isomerization-Induced Asymmetric Coordination Chemistry: From Auxiliary Control to Asymmetric Catalysis. *Angew. Chem., Int. Ed.* **2010**, *49*, 7955–7957.

(7) Mazzei, L. F.; Martínez, Á.; Trevisan, L.; Rosa-Gastaldo, D.; Cortajarena, A. L.; Mancin, F.; Salassa, L. Toward Supramolecular Nanozymes for the Photocatalytic Activation of Pt(IV) Anticancer Prodrugs. *Chem. Commun.* **2020**, *56*, 10461–10464.

(8) Chen, K.; Arnold, F. H. Engineering New Catalytic Activities in Enzymes. *Nat. Catal.* **2020**, *3*, 203–213.

(9) Arnold, F. H. Innovation by Evolution: Bringing New Chemistry to Life (Nobel Lecture). *Angew. Chem., Int. Ed.* **2019**, *58*, 14420–14426.

(10) Shu, X.; Lev-Ram, V.; Deerinck, T. J.; Qi, Y.; Ramko, E. B.; Davidson, M. W.; Jin, Y.; Ellisman, M. H.; Tsien, R. Y. A Genetically Encoded Tag for Correlated Light and Electron Microscopy of Intact Cells, Tissues, and Organisms. *PLoS Biol.* **2011**, *9*, e1001041.

(11) Westberg, M.; Holmegaard, L.; Pimenta, F. M.; Etzerodt, M.; Ogilby, P. R. Rational Design of an Efficient, Genetically Encodable, Protein-Encased Singlet Oxygen Photosensitizer. *J. Am. Chem. Soc.* **2015**, *137*, 1632–1642.

(12) Westberg, M.; Bregnhøj, M.; Etzerodt, M.; Ogilby, P. R. Temperature Sensitive Singlet Oxygen Photosensitization by LOV-Derived Fluorescent Flavoproteins. *J. Phys. Chem. B* **2017**, *121*, 2561–2574.

(13) Ruiz-González, R.; Cortajarena, A. L.; Mejias, S. H.; Agut, M.; Nonell, S.; Flors, C. Singlet Oxygen Generation by the Genetically Encoded Tag Minisog. *J. Am. Chem. Soc.* **2013**, *135*, 9564–9567.

(14) Rodríguez-Pulido, A.; Cortajarena, A. L. L.; Torra, J.; Ruiz-González, R.; Nonell, S.; Flors, C. Assessing the Potential of Photosensitizing Flavoproteins as Tags for Correlative Microscopy. *Chem. Commun.* **2016**, *52*, 8405–8408.

(15) Torra, J.; Lafaye, C.; Signor, L.; Aumonier, S.; Flors, C.; Shu, X.; Nonell, S.; Gotthard, G.; Royant, A. Tailing MiniSOG: Structural Bases of the Complex Photophysics of a Flavin-Binding Singlet Oxygen Photosensitizing Protein. *Sci. Rep.* **2019**, *9*, 1–10.

(16) Cardoso, D. R.; Franco, D. W.; Olsen, K.; Andersen, M. L.; Skibsted, L. H. Reactivity of Bovine Whey Proteins, Peptides, and Amino Acids toward Triplet Riboflavin as Studied by Laser Flash Photolysis. *J. Agric. Food Chem.* **2004**, *52*, 6602–6606.

(17) Bialas, C.; Barnard, D. T.; Auman, D. B.; McBride, R. A.; Jarocha, L. E.; Hore, P. J.; Dutton, P. L.; Stanley, R. J.; Moser, C. C. Ultrafast Flavin/Tryptophan Radical Pair Kinetics in a Magnetically Sensitive Artificial Protein. *Phys. Chem. Chem. Phys.* **2019**, *21*, 13453–13461.

(18) Pimenta, F. M.; Jensen, R. L.; Breitenbach, T.; Etzerodt, M.; Ogilby, P. R. Oxygen-Dependent Photochemistry and Photophysics of "MiniSOG," a Protein-Encased Flavin. *Photochem. Photobiol.* **2013**, *89*, 1116–1126.

(19) Bregnhøj, M.; Dichmann, L.; McLoughlin, C. K.; Westberg, M.; Ogilby, P. R. Uric Acid: A Less-than-Perfect Probe for Singlet Oxygen. *Photochem. Photobiol.* **2019**, *95*, 202–210.

(20) Gramatica, P.; Papa, E.; Luini, M.; Monti, E.; Gariboldi, M. B. B.; Ravera, M.; Gabano, E.; Gaviglio, L.; Osella, D. Antiproliferative Pt(IV) Complexes: Synthesis, Biological Activity, and Quantitative Structure-Activity Relationship Modeling. *J. Biol. Inorg. Chem.* **2010**, *15*, 1157–1169.

(21) Rabello, B. R.; Gerola, A. P.; Pellosi, D. S.; Tessaro, A. L.; Aparício, J. L.; Caetano, W.; Hioka, N. Singlet Oxygen Dosimetry Using Uric Acid as a Chemical Probe: Systematic Evaluation. *J. Photochem. Photobiol. A.* **2012**, *238*, 53–62.

(22) Gomes, A.; Fernandes, E.; Lima, J. L. F. C. Fluorescence Probes Used for Detection of Reactive Oxygen Species. *J. Biochem. Biophys. Methods* **2005**, *65*, 45–80.

(23) Jorgensen, W. L.; Chandrasekhar, J.; Madura, J. D.; Impey, R. W.; Klein, M. L. Comparison of Simple Potential Functions for Simulating Liquid Water. *J. Chem. Phys.* **1983**, *79*, 926–935.

(24) Schneider, C.; Sühnel, J. A Molecular Dynamics Simulation of the Flavin Mononucleotide–RNA Aptamer Complex. *Biopolymers* **1999**, *50*, 287–302.

(25) Humphrey, W.; Dalke, A.; Schulten, K. VMD: Visual Molecular Dynamics. *J. Mol. Graph.* **1996**, *14*, 33–38.

(26) Bekker, H.; Van Den Berg, J. P.; Wassenaar, T. A. A Method to Obtain a Near-Minimal-Volume Molecular Simulation of a Macromolecule, Using Periodic Boundary Conditions and Rotational Constraints. *J. Comput. Chem.* **2004**, *25* (8), 1037–1046.

(27) Parrinello, M.; Rahman, A. Polymorphic Transitions in Single Crystals: A New Molecular Dynamics Method. *J. Appl. Phys.* **1981**, *52*, 7182–7190.

(28) Nosé, S. A Molecular Dynamics Method for Simulations in the Canonical Ensemble. *Mol. Phys.* **1984**, *52*, 255–268.

(29) Hockney, R. W.; Goel, S. P.; Eastwood, J. W. Quiet High-Resolution Computer Models of a Plasma. *J. Comput. Phys.* **1974**, *14*, 148–158.

(30) Hess, B.; Bekker, H.; Berendsen, H. J. C.; Fraaije, J. G. E. M. LINCS: A Linear Constraint Solver for Molecular Simulations. *J. Comput. Chem.* **1997**, *18*, 1463–1472.

(31) Abraham, M. J.; van der Spoel, D.; Lindahl, E.; Hess, B. and the G. development team. GROMACS User Manual Version **2018**.

(32) Abraham, M. J.; Murtola, T.; Schulz, R.; Páll, S.; Smith, J. C.; Hess, B.; Lindahl, E. GROMACS: High Performance Molecular Simulations through Multi-Level Parallelism from Laptops to Supercomputers. *SoftwareX* **2015**, *1–2*, 19–25.

(33) Verlet, L. Computer "Experiments" on Classical Fluids. II. Equilibrium Correlation Functions. *Phys. Rev.* **1968**, *165*, 201–214.

(34) Jurrus, E.; Engel, D.; Star, K.; Monson, K.; Brandi, J.; Felberg, L. E.; Brookes, D. H.; Wilson, L.; Chen, J.; Liles, K.; et al. Improvements to the APBS Biomolecular Solvation Software Suite. *Protein Sci.* **2018**, *27*, 112–128.

5

Dual Bioorthogonal Activation of Prodrugs by Flavin and Palladium Chemistry

5.1 Introduction

Prodrug activation approaches enable switching on the cytotoxic effect of a drug by chemical transformation of an inert precursor in a specific tissue area. Generally, prodrugs are synthesized by a reversible chemical modification of an active compound to tune features, such as stability, permeability, targeting capability, etc. A key feature that share all prodrug strategies is that they aim at achieving the highest specificity to avoid undesired systemic side effects and to improve the pharmacokinetics of the drug.[1–4]

In recent years, bioorthogonal catalysis has been utilized to improve the selectivity of anticancer prodrug activation approaches. As previously discussed (Chapter 2), new catalysis concepts have been developed and have delivered a plethora of opportunities to carry out selective non-natural chemical reactions into complex biological systems, without interfering with natural biological processes.[5] Overall, bioorthogonal catalysis has shown the potential to improve the control over the activation of anticancer compounds, hence potentially reducing side effects.[6]

Over the first and second chapter of this thesis, we reported several examples of bioorthogonal catalytic activation strategies of inert compounds. Among these, we can however distinguish three main general strategies:

a) Metallodrugs with catalytic activity towards relevant biomolecules. The disruption of normal cellular homeostasis by targeting relevant biomolecules through the activity of catalytic metallodrugs has been extensively explored as a possible strategy that could minimize side effects of anticancer treatments. The group of Sadler showed that the activity of Ru^{II} [7,8] and Ir^{III} [9] complexes, produced alterations in the redox balance of GSH/GSSG or NADH/NAD^+ inside cells, finally causing cell death. The same group recently reported a variety chiral Os^{II} arene sulfonamide complexes, that perform a highly enantioselective reduction of pyruvate into D-lactate. In the presence of non-toxic formate or N-formylmethionine acting as sacrificial hydride source, chiral Os^{II} complexes displayed a great antiproliferative activity in A2780 human ovarian cancer cells, although it is not completely understood how they induce the cellular damage.[10]

b) Bioorthogonal transition metal catalysts for prodrug activation. Transition metal complexes that perform selective catalytic cleavages or deprotections of organic prodrugs have emerged as a powerful solution for bioorthogonal catalysis since 2014, when Meggers demonstrated that Ru^{II} catalyst deprotected a doxorubicin prodrug in cells.[11] Bradley and Unciti-Broceta exploited similar chemistry loading transition metal nanocatalysts into polymeric beads to perform a selective activation of a variety of organic prodrugs.[12–14] Despite these transition metal nanocatalysts have shown suitable features for medicinal chemistry, such as biocompatibility and bioactivity. The activation mechanism of these Pd-based materials, is not fully understood and a high ratio catalyst/substrate is required to achieve the activation of the masked prodrug (Chapter 2, page 15-18).

c) Bioorthogonal photocatalytic activation for metal based prodrugs. The flavin and flavoprotein assisted photoactivation of Pt anticancer prodrugs proposed a new approach in bioorthogonal catalysis. This strategy introduced concept of metal complexes in catalytic reactions acting as a substrate, instead of catalyst. This new paradigm expanded the applicability of catalytic bioorthogonal reactions to a new range of substrates.[6] Riboflavin (Vitamin B2) derivatives and some flavoproteins, efficiently converted inert Pt^{IV} prodrugs, into their highly toxic Pt^{II} counterparts upon blue light irradiation.[15] In the presence relevant of coenzymes, such as reduced nicotine adenine dinucleotide (NADH), some flavoproteins performed up to 700 conversion cycles.[16]

In this context, and to the best of our knowledge, the literature does not report so far any example of two distinct bioorthogonal catalytic reactions performed simultaneously for chemotherapeutic purposes by the same device. The application of such strategy would enable to control the activation of multiple prodrug molecules in a localized manner, producing a high concentration of the cytotoxic species in the catalyst surroundings over time. Besides, dual activation has the potential to modulate the biological effect of each single drug accordingly to the kinetics of the bioorthogonal catalytic reactions.

To this aim, we report herein our studies aimed at developing a catalysis scheme to switch on the antiproliferative effect of two anticancer drugs, namely cisplatin and 5-fluorouracil (**5FU**). We combined the Pd-mediated bioorthogonal deprotection chemistry developed by the group of Unciti-Broceta with our flavin-catalyzed photocatalytic conversion of Pt^{IV} complexes (Figure 1) to afford a dual catalytic device (**TARF@PdNPs**).

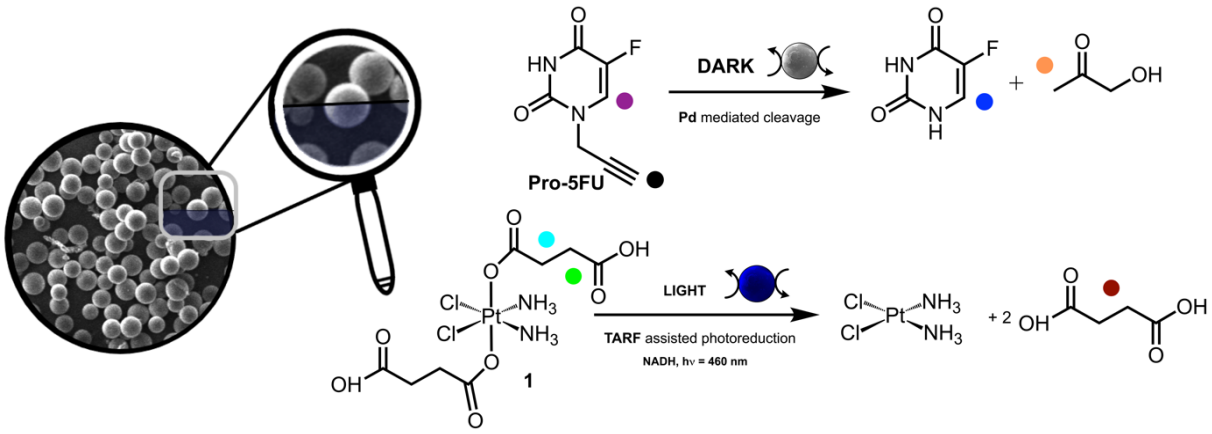

Figure 1. Schematic illustration of the dual activation performed by **TARF@PdNPs** resins.

5FU works as an antimetabolite due to its similarity to the pyrimidine metabolite. Inside cells, it is converted to 5-fluorodeoxyuridine, fluorodeoxyuridine triphosphate or fluorouridine triphosphate monophosphate as products that can covalently bind to the thymidylate synthase enzyme and be incorporated into RNA or DNA, disrupting their normal functions.[17,18] The group of Unciti-Broceta demonstrated in 2014, that propargyl protected **Pro-5FU** exhibited can be activated with high efficiency by **PdNPs** resins and negligible toxicity in high concentrations in several cell lines.[12,19]

Tetraacetylated riboflavin (**TARF**) has shown the capability to selectively convert Pt^{IV} prodrugs, such as **1**, into biologically active Pt^{II} species in a complex environment containing a handful of biomolecules.[20] Recently, our group has shown that flavin-assisted bioorthogonal photocatalytic reactions could efficiently trigger the activation of Pt^{IV} prodrugs *in vitro,* resulting in a dramatic reductions of cell viability in different cancer cell lines.[15,21]

Cisplatin and 5FU, are worldwide used as chemotherapeutic agents for various cancers and their combination is used in some cases for anal, head, neck and eosophageal cancers.[22] In the 80´s, the combination of both drugs was tested *in vitro* in the A2780 ovarian cancer (cell line) for the first time, showing that the pretreatment of cells with cisplatin, enhanced their sensitivity to 5FU and induced 7 times more cell reduction than either drugs alone.[17] The combination of both drugs was evaluated by intraperitoneal administration in phase II trials for ovarian cancer. However results were not conclusive due to the limited number of patients and further investigation are needed.[23,24] These results motivated us to explore the dual catalytic activation of the Pt and **5FU** prodrugs shown in Figure 1 and the effects of such strategy in IGROV-1 ovarian cancer cells.

5.2 Results and Discussion

5.2.1 Preparation of Prodrugs and Catalysts

5.2.1.1 Prodrugs

The Pt^{IV} prodrug *cis,cis,trans*-$[Pt(NH_3)_2(Cl_2)(O_2CCH_2CH_2CO_2H)_2]$ (**1**) employed in this study, was synthesized following the procedure reported by Osella and coworkers[25] with minor variations based on the synthesis described by the group of Keppler.[26] Full description of the synthetic details and characterization of **1** are reported in the experimental section. In brief, **1** was obtained by reacting succinic anhydride with the corresponding dihydroxo Pt^{IV} precursor in DMF.

The potential of Pt^{IV} prodrugs for anticancer treatment has been widely investigated and numerous candidates have been developed in the last decades.[27] In particular, analogues of **1** have been designed to functionalize a variety of scaffolds for drug delivery strategies.[28–33] In this work, we selected **1** for multiple reasons. Firstly, the succinate ligands and their pendant carboxylate functional groups make this platinum compound highly soluble in aqueous solutions.[34] Secondly, **1** has a low reduction potential that confers resistance to biological reductants, slowing its kinetic conversion to Pt^{II} derivatives and limiting its cytotoxicity in a broad number of cell lines.[15,25,35] Finally, our research group accumulated significant knowledge in previous studies using this complex as preferred model substrate for the flavin-assisted photocatalytic conversion of Pt^{IV} prodrugs.[21,36]

The 5-fluoro-1-propargyl-uracil prodrug (**Pro-5FU**) was synthesized following the procedure described by the group of Unciti-Broceta in one step by mixing the chemotherapeutic agent fluorouracil (5FU), propargyl bromide and DBU as co-reactant in dry DMF.[12] Full account of the synthesis and characterization of **Pro-5FU** is reported in the experimental section below. Among the different **5FU** prodrugs reported in the literature,[37] we selected **Pro-5FU** due to the straightforward synthesis and because the group of our collaborator Dr. Unciti-Broceta successfully demonstrated that such prodrug has negligible toxicity in several cell lines such as colorectal (HCT116), pancreatic (BxPC-3), breast (MCF-7 and R-SKBR3a) and ovarian (PE04) cancer cells lines. Furthermore, the same group previously reported that co-administration of Pd-based nanocatalysts cleaved the propargyl moiety switching on the toxicity of **5FU**.[12,19] Of note, **Pro-5FU** has been also evaluated as possible antiviral agent against HIV but showed no activity up to 100 μM.[38]

5.2.1.2 Synthesis of Catalysts

Based on previous findings, two bioorthogonal catalysts were selected and prepared in order to achieve the activation of the two anticancer substrates: tetra-O-acetyl riboflavin (**TARF**) for the photoredox conversion of **1** and μm-sized PEG-polystyrene spheres encapsulating Pd nanoparticles (**Pd NPs**) for the cleavage of the propargyl protecting group of **Pro-5FU**.

TARF was synthesized as Jhulki and collaborators reported with minor changes[39] by dissolving riboflavin in a mixture of acetic anhydride and acetic acid (1:1) to which perchloric acid was added. Flash chromatography afforded pure **TARF** in high yields (see experimental section).
TARF has been widely investigated as photocatalyst for the transformation of variety of organic substrates.[40–46] Nevertheless, few studies have explored the use of this flavin for anticancer purposes and all of them are focused on its photosensitization features and capacity to produce ROS.[47,48] For instance, Juarez et *al.* showed that **TARF** was a better photosensitizer than riboflavin (Rf) or riboflavin monophosphate (FMN) in squamous carcinoma (SCC-13) and melanoma cells (WM115). **TARF** high capacity to produce cellular damage could be ascribed, on one hand, to lower levels of photodecomposition and, on the other hand, to the increased uptake driven by the hydrophobic acetyl groups.

Pd NPs were synthesized by Dr. Pérez-López of the Unciti-Broceta group, following the procedure described by Bradley and Unciti-Broceta.[49,50] Shortly, after loading Pd^{II} acetate into the PEG-polystyrene beads, they were added to a methanol solution that contained hydrazine (10%) as reducing agent to induce atom nucleation. In a previous work, Unciti-Broceta and co-workers confirmed the presence nanoparticulated Pd trapped into the PEG-polystyrene devices by electron microscopy, ICPOES (inductively coupled plasma-optical emission spectrometry) and X-ray diffractometry.[12] NPs embedded into the beads were

regularly distributed over the resins with a size of around 5 nm and the palladium content into the beads was 2.83%. In addition, X-ray diffraction experiments showed the characteristic pattern of crystalline Pd^0.

During my research stay at the Cancer Research UK Edinburgh Centre of the MRC Institute of Genetics & Molecular Medicine (University of Edinburgh), we developed a novel synthetic procedure for the preparation of **PdNPs** resins loaded with **TARF** (**TARF@PdNPs**). Briefly, after the *in situ* formation of **PdNPs** by hydrazine and the subsequent purification steps, **TARF** was added to a dimethyl formamide (DMF)/dichloromethane (DCM) solution that contained the glutamic acid derivative (Fmoc-Glu-OH), oxyma and N,N´-diisopropylcarbodiimide (DIC), to trap the NPs and the flavin by cross-linking of the amino groups present on the surface of the beads.[12] The synthetic procedure is described in more detail in the Experimental Section (5.3).

As shown in Figure 2, Scanning electron microscopy (SEM) images confirmed the uniformity of the prepared **TARF@PdNPs** and Energy dispersive X-ray (EDX) analysis display, the characteristic peak of Pd (Figure S1).

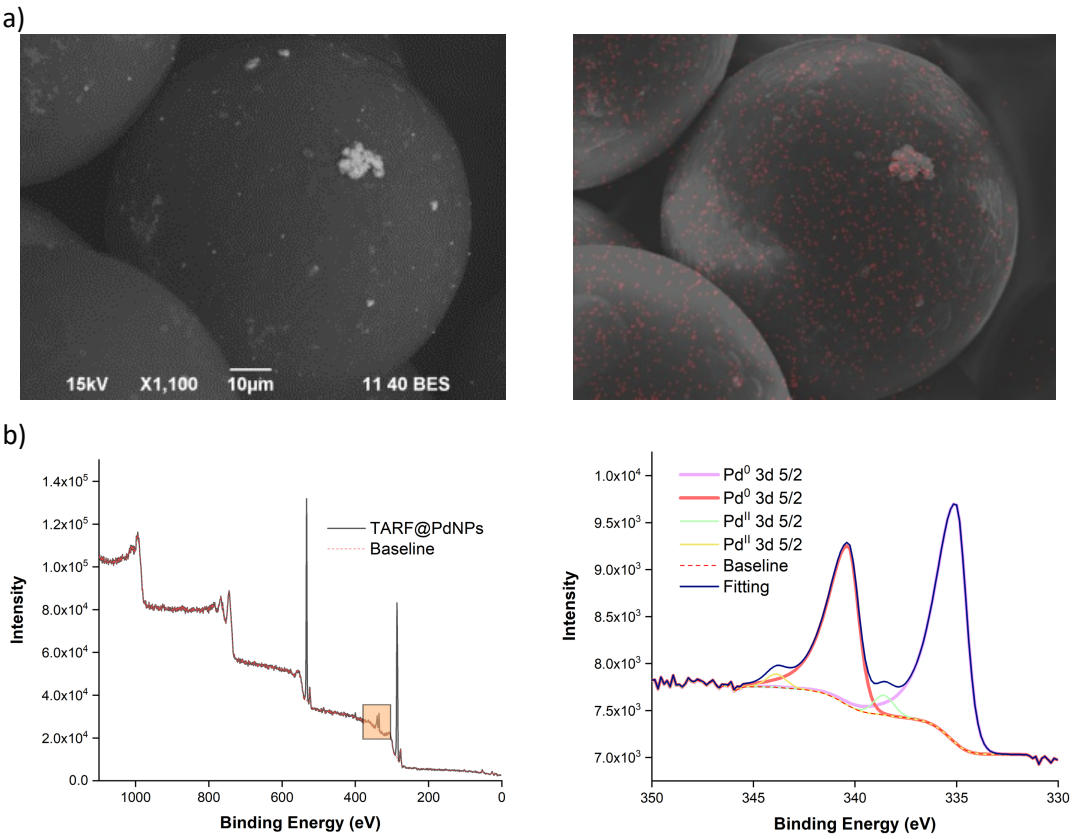

Figure 2. a) SEM image of **TARF@Pd NPs** resin and co-localization analysis with EDX data, b) XPS spectra of **TARF@PdNPs**; survey spectrum and high resolution spectrum of the Pd 3d region (% of Pd^{II}, less than 5% after deconvolution).

Co-localization analysis determined that the Pd content was homogenously distributed through the beads, although a pronounced size polydispersity of Pd particles was apparent

(Figure S1). X-ray photoelectron spectroscopy (XPS) measurements showed the distinctive doublet with a spitting of 5.3 eV in the Pd 3d region. The $3d_{5/3}$ is reported at 335.4 eV for Pd^0,[51,52] which confirmed metallic Pd was the most abundant oxidation state for the catalyst (Figure 2b). Nevertheless, peak analysis indicated that the % of Pd^{II} was < 5%. In addition, based on ICP-MS results summarized in Table S1, the Pd % into the beads was determined to be 3.38 % (w/w).

The loading of **TARF** onto **Pd NPs** was assessed using optical methods. Fluorescence microscopy images collected with the Cytation5 cell imaging reader showed the intense green emission of **TARF** at 525 nm upon excitation at 460 nm (Figure 3).

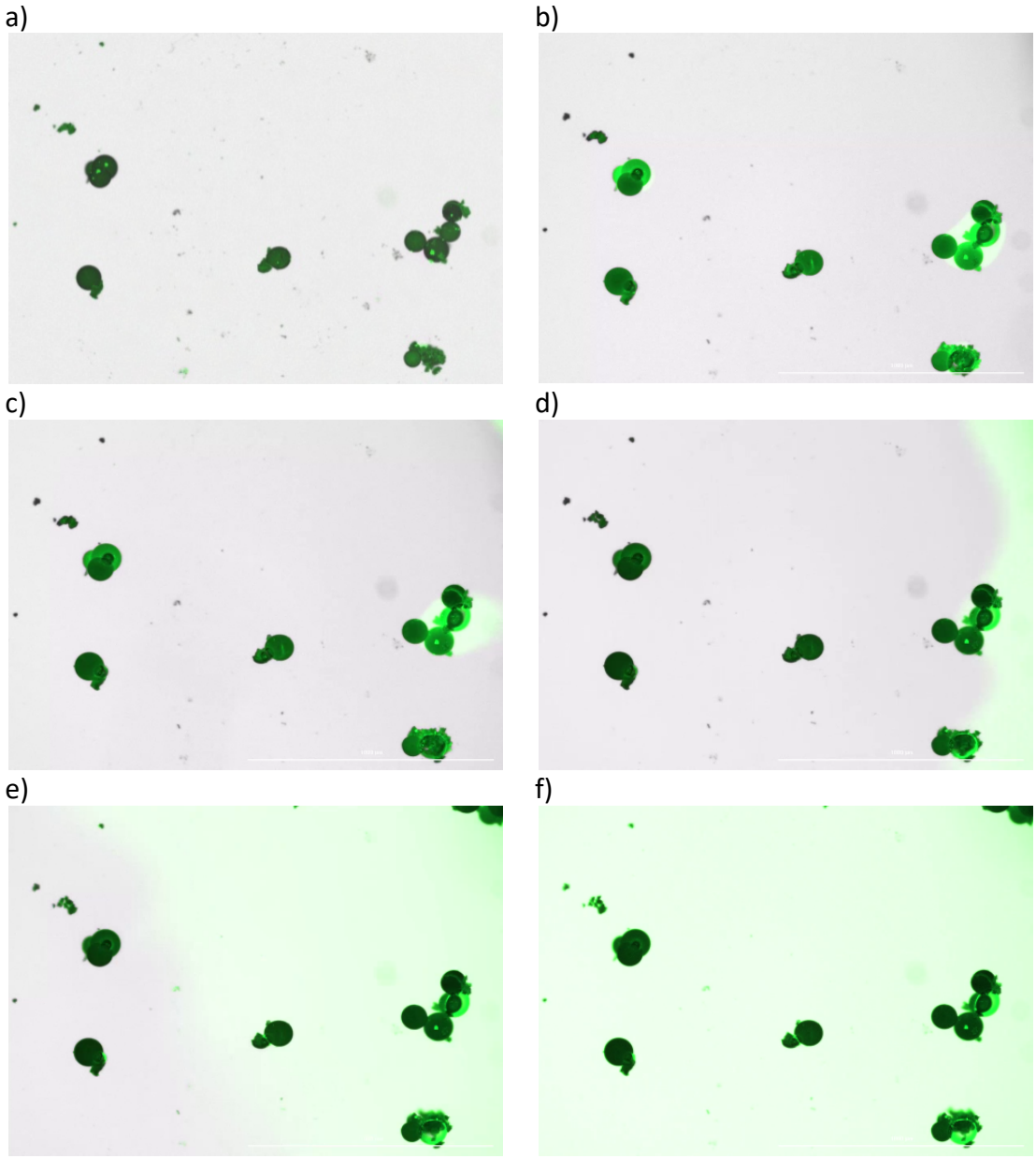

Figure 3. Fluorescence microscopy images of **TARF@PdNPs** resins a) before and b-f) after the addition of 100 µL of PBS (t =0–10 min).

As shown in Figure 3a, fluorescence was localized onto the resins in the absence of solvent, whereas **TARF** progressively diffused from the beads to the media once the solvent (PBS) was added (Figure 3b-f). This translated into an increase of the fluorescence background as the TARF release advanced, which is evident in Figure 3e and 3f. In addition, confocal microscopy images determined that the dye was mostly localized on the outer layers of the resin surface (Figure S2).

We monitored and quantified the **TARF** released from 1.2 mg/mL **TARF@PdNPs** in PBS by determining the fluorophore concentration in the supernatant via UV-Vis (Figure 3) spectroscopy. In order to estimate the total concentration of **TARF** loaded onto **PdNPs**, we firstly recorded a series of UV-Vis over time using a 1:1 DCM/DMF solution, since this mixture of solvents is capable of washing out the flavin rapidly and almost completely. Using the calibration curves reported in Figure S3 and the extinction coefficient of **TARF** at 445 nm,[53] we estimated that 1.7 µM **TARF** was released in DCM/DMF after 15 min and 1.9 µM after 60 min. In PBS, the first step of the process is significantly slower and overall only 52 % of the loaded **TARF** was found in the supernatant within the time frame of the experiment.

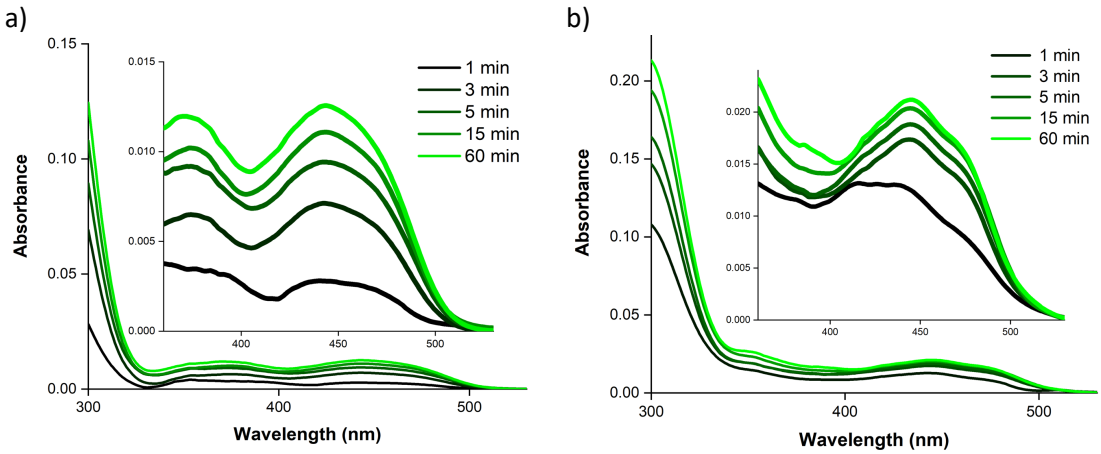

Figure 4. UV-Vis spectra of 1.2 mg/mL **TARF@PdNPs** resins in: a) PBS and b) DCM/DMF (1:1) stirring at room temperature over 1 hour.

5.2.3 Prodrug Activation studies

We next tested the capacity of **TARF@PdNPs** to catalytically activate **1** and **Pro-5FU**. Initially, catalytic reactions were performed using one substrate at the time in order to compare the activity of the dual catalysts with its single components. At a second stage, both substrates were simultaneously added to the reaction solution and their conversion evaluated. The light source employed for the photocatalysis experiments on **1** was an LED plate with a maximum-wavelength emission at 460 nm and an optical density of 6 $mW \cdot cm^2$.[21]

5.2.3.1 Single prodrug activation

To investigate the activation of prodrugs **1** and **Pro-5FU**, we employed 500 µM substrate, 1 mM NADH as electron donor and 1.2 mg **TARF@PdNPs** in PBS (pH 7.4, stirring at 1200 rpm, at 37 °C). We monitored the conversion of the prodrugs by ^{1}H NMR, following the disappearance/appearance of diagnostic peaks that corresponded to the starting compounds and reaction products (Figure 1).

The conversion of **1** was followed by the transformation of 2 triplets (coordinated succinate ligands, ●●), into a singlet (free succinate ligand, ●). Previous work from the group demonstrated that the flavin-catalyzed release of succinates from **1** majorly afforded cisplatin as Pt-containing photoproduct.[15] In the case of **Pro-5FU**, we tracked the reaction following the signals of the **5FU** core and of the propargyl ligand. The disappearance of the doublet at 7.86 ppm and its appearance at 7.58 ppm (prodrug ● and drug ●) corresponded to the H located in the fluorouracil ring (position 3), with fluorine giving it the appearance of a doublet that shifted when the deprotection took place. At the same time, we monitored the disappearance of the triplet at 2.82 ppm that corresponded to the terminal H of the propargyl group (●) and the appearance of a singlet at 1.18 ppm corresponded to the **CH$_3$**OCH$_2$OH of hydroxyacetone product (●), which confirmed the release of the protective groups to the solution.

In a control experiment, negligible transformation of the Pt^{IV} prodrug was detected after 24 h in the dark when **1** was incubated with **PdNPs** resins alone or/and NADH (1 mM) (Figure S4). Such findings confirmed that **PdNPs** are not capable to perform efficiently the reduction of the Pt^{IV} prodrug into Pt^{II} species under our experimental conditions. In the case of **TARF@PdNPs**, **1** underwent after 24 h, less than 20% conversion in the dark or under blue light irradiation in the absence of electron donor (Figure S5 a and b). When NADH was added to the PBS solution, the conversion of **1** slightly increased in the dark (35% in 24 h), while 10 minutes of blue light irradiation only were sufficient to transform 70% of **1** (Figure S5 c and d). Considering that 1 µM **TARF** was released from the resins according to UV-Vis quantification in the first 15 minutes, we can estimate a total turnover number (TTN) of around 350 for the conversion of **1**. Although we assumed that trapped **TARF** onto the resins could be less efficient than free flavin, we found a consistent TTN value with the previously reported in Chapter 3 for **FMN** and **1**.[20]

Once we demonstrated the applicability of **TARF@PdNPs** to convert **1** into cisplatin, we investigated the capacity of this catalyst to perform the cleavage reaction of the propargyl group in **Pro-5**, as well as the occurrence of any possible undesired reactions prompted by the electron donor. When **Pro-5FU** was incubated together with **TARF@PdNPs** for 24 h, we observed that a modest conversion of the prodrug occurred. We monitored the reaction using 1.2 or 2.4 mg/mL of **TARF@PdNPs**, observing that higher catalyst loadings led to a higher substrate conversion rate i.e. 10% and 20% respectively (Figure S6). Data analysis

showed that after 24h, the TTN was approximately 0.13 and the TOF 0.0054 h^{-1} in the case of the higher catalyst concentration. The deprotection of **Pro-5FU** was negligible in the presence of 25 μm of **FMN**, both in the dark or under light irradiation (Figure S6). For this control experiment, we selected **FMN** due to its higher solubility in aqueous media and because **TARF** and **FMN** showed similar catalytic activity towards **1**.

Next, the deprotection of **Pro-5FU** in the presence of **NADH** and **FMN** was tested in the dark and upon light irradiation. Under both conditions, **FMN**, did not deprotect **Pro-5FU**, confirming that this prodrug was not able to act as substrate in the photocatalytic reaction. In addition, the incubation of **Pro-5FU** in the presence of **NADH** (1 mM) for 7 days, showed that no interaction between the two took place (Figure S7). As control experiment, we investigated the transformation of **Pro-5FU** when **NADH** and **TARF@PdNPs** were present at 25°C. The presence of **NADH** did not interfere in a direct way in the formation of the active counterpart achieving a conversion of 80% after 14 days. If we compare de conversion to analogue experiments of this work, the lower substrate conversion rate can be attributed to the lower temperature (25 °C versus 37 °C). Based on the Pd % determined by ICP-MS, we can estimate that the Pd^0 concentration was around 382 μM. Therefore, the **TARF@PdNPs** achieved a TTN value of around 1 for the conversion of **Pro-FU** after 14 days.

5.2.3.2 Dual prodrug activation

First, we explored simultaneous bioorthogonal activation of the two prodrugs. **TARF@PdNPs** was incubated with both **Pro-5FU** and **1** and the conversion of the substrates was followed over 7 days (168 h). As shown in Figure 5, when **NADH** was present and in the beginning of the experiment, signals of both prodrugs were clearly distinguishable. However, after 15 minutes upon irradiation, the efficient release of the succinate ligands from **1** occurred, reaching almost complete conversion of the Pt^{IV} prodrug (90%, 450 μM, TTN 450). Signals relative to **Pro-FU** did not change after this irradiation period, which indicated a selective activation of the Pt prodrug. During the rest of the experiment, we observed a gradual conversion of **Pro-FU**, being necessary 7 days to achieve approximate conversion of around 75% (375 μM). The 7^{th} day, when the experiment was halted, **PdNPs** achieved a TON value of around 1 for the conversion of the **Pro-FU**.

It is worth noting that for an unknown species a signal (●) appeared close to the doublet of **5FU** at 7.5 ppm during the conversion of **Pro-FU.** We hypothesize that the formation of such species is linked to the photogeneration of cisplatin. As recently proved independently by Oliveira *et al*. and Huang, Pt^{II} species, and cisplatin in particular, are able to perform the depropargylation of protected drugs, although with very low efficiency.[54,55] In this case, we speculate that the presence of cisplatin altered the progression of the **Pro-FU** deprotection reaction,[12] resulting into more fluorouracil derivative products. In addition, 20 year ago

Glushonok *et al.* reported that the hydration of hydroxyacetone can lead to several products,[56] complicating the reaction outcome.

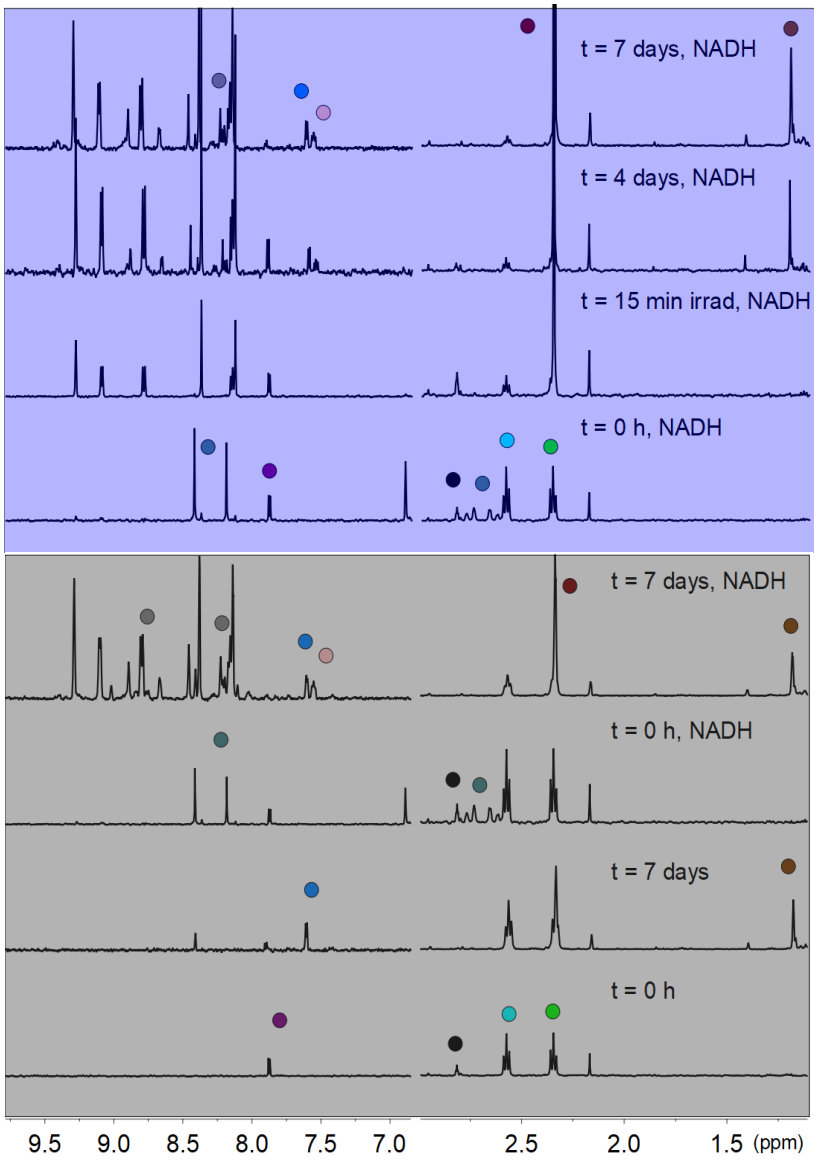

Figure 5. Activation prodrugs, i.a. (500 µM of each, PBS, pH 7.4, 10% D_2O) in the presence of 1 mM **NADH**, 1.2 mg/mL **TARF@Pd NPs** resins monitored by ^{1}H NMR. Samples in the grey box were kept in the dark, while samples in the blue box, were irradiated for 15 minutes (λ = 460 nm). ^{1}H NMR signal labeling: ● NAD^+, ● **NADH**, ● **Pro-5FU**, ● **Pro-5FU**–CH_2CCH, ● **5FU**, ● hydroxyacetone, ● Pt–$OCO\mathbf{CH_2}CH_2CO_2^-$, ● Pt–$OCOCH_2\mathbf{CH_2}CO_2^-$, ● free $^-O_2C\mathbf{CH_2CH_2}CO_2^-$ ● 5FU side reaction product.

When we compared the conversion of the two prodrugs on the 7th day under diverse experimental conditions, we found some remarkable differences. As shown in Figure 7, the conversion of **1** was ineffective and less than 20% of free succinate was determined in the absence of **NADH** and in the dark. Experiments in the presence of **NADH** (dark), **1** reached 60% of conversion, while the transformation of **1** upon blue light irradiation achieved essentially the full conversion in few minutes (*vide supra*). Under the three different

experimental conditions, the conversion of **Pro-FU** reached similar values (75%). Therefore, the activation of the two prodrugs took place at different rates, the activation of **1** was instantaneous upon irradiation, while the activation of **Pro-FU** was slower and prolonged over time. The progression of individual reaction is shown in Figure S8.

5.2.4 In vitro application

The human ovarian adenocarcinoma cell line IGROV-1 was chosen to perform activation studies in the presence of cancer cells, motivated by previous results in clinical trials demonstrating synergistic effects of cisplatin and 5FU in ovarian cancer.[23,24]

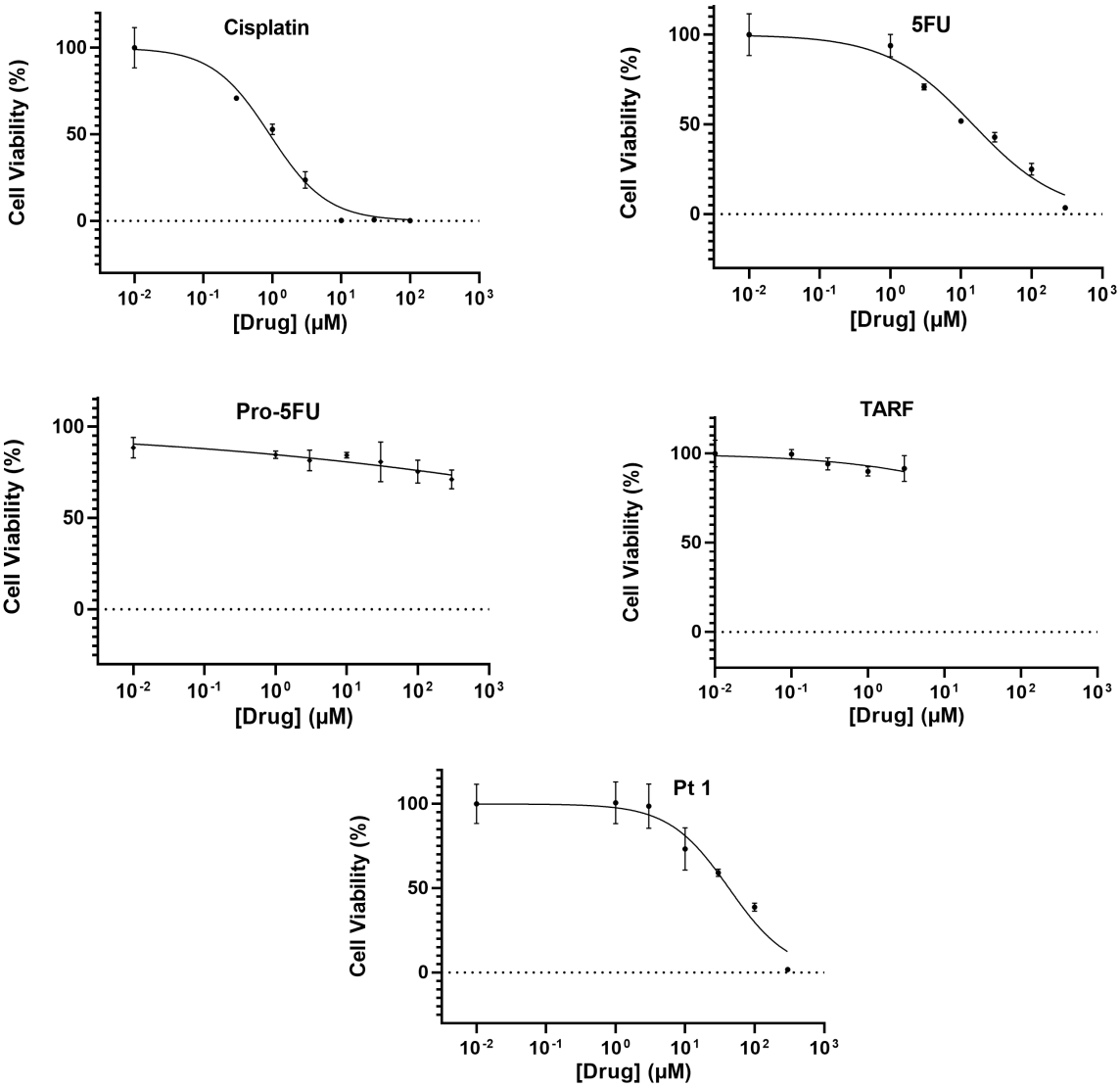

Figure 7. Cell viability results of IGROV-1 cell line after 5 days of treatment using different concentration of anticancer agents: cisplatin (from 0.3 μM to 100 μM), **1** (from 1 μM to 300 μM), **Pro-5FU** (from 1 μM to 300 μM), **5FU** (from 1 μM to 300 μM) and **TARF** (from 0.1 μM to 3 μM).

Firstly, we tested individually the antiproliferative activity of the drugs and their prodrug precursors to gauge suitable concentrations of each one for dual activation experiments.

After seeding, cells were grown for 48 hours and later, the treatment with the agents was applied for five days before determining the relative viability by the resazurin assay (Figure 7).

On the basis of the toxicity profiles obtained in these screening experiments, we opted then to follow our biological studies using fixed concentrations of cisplatin (1 µM), **1** (1 µM), **5FU** (3 µM), **Pro-5FU** (100 µM) and **TARF** (1 µM). These values are such that prodrugs do not induce significant cell death whereas cisplatin and **5FU** reduce cell viability 50% and 30% respectively. The light irradiation time used in the photoactivation was selected based on our previous studies demonstrating that 30 second at 6 $mW \cdot cm^{-2}$ were enough to fully convert 1 µM **1** into cisplatin, and that **TARF** had negligible effects (due to singlet oxygen sensitization).[20] Under these experimental conditions, prodrugs did not show any remarkable toxic effect. When we combined drugs and prodrugs with or without the **TARF** catalyst, no differences were observed compared to the administration of them alone (Figure 8). Importantly, the absence of any cytotoxic effect in cells treated with **1** and **TARF** under light irradiation is consistent with our early findings which showed that an electron donor is mandatory to convert the Pt substrate.

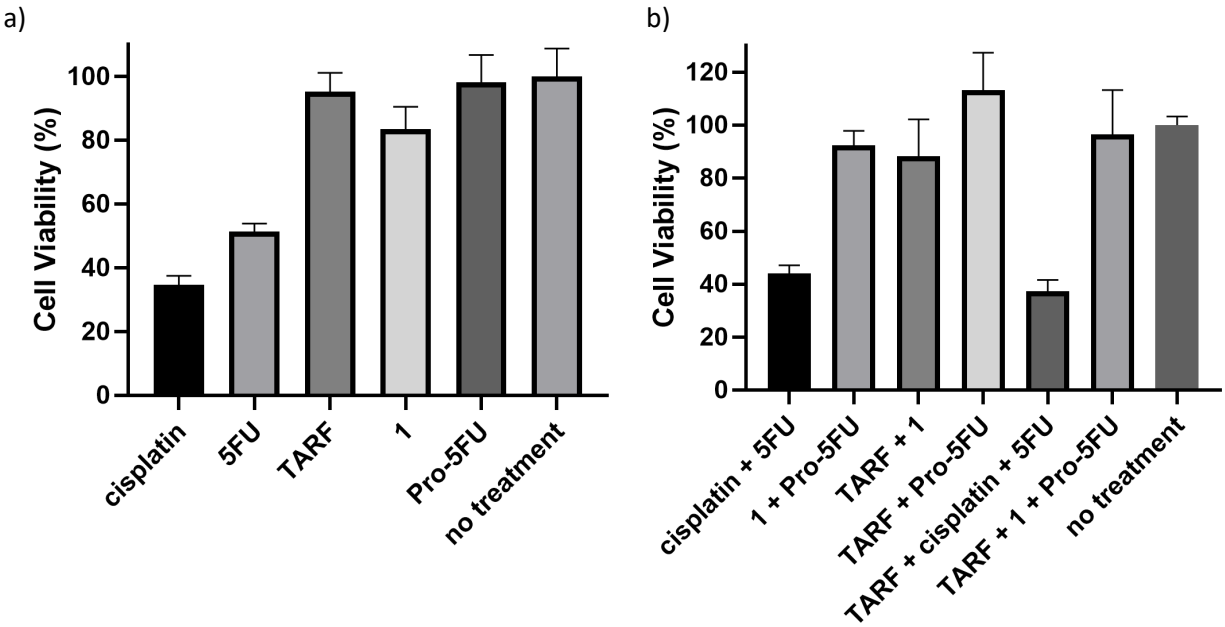

Figure 8. Cell viability results of drugs and prodrugs at the selected concentrations after 30 seconds of blue light irradiation: a) reactants alone and b) in combination. Employed concentrations (alone or in combination): Cisplatin (1 µM), **5FU** (3 µM), **TARF** (1 µM), **1** (1 µM), and **Pro-5FU** (100 µM).

As shown in Figure 9, significant differences were found between experiments in the dark and under light irradiation when we added **NADH** to the reaction mixture. For example, shining light on cells exposed to **TARF** and NADH led to the generation of reactive oxygen species (ROS) and reduction of cell viability. Furthermore, when **1** was also added to the mixture the toxicity significantly increased (Figure S9).

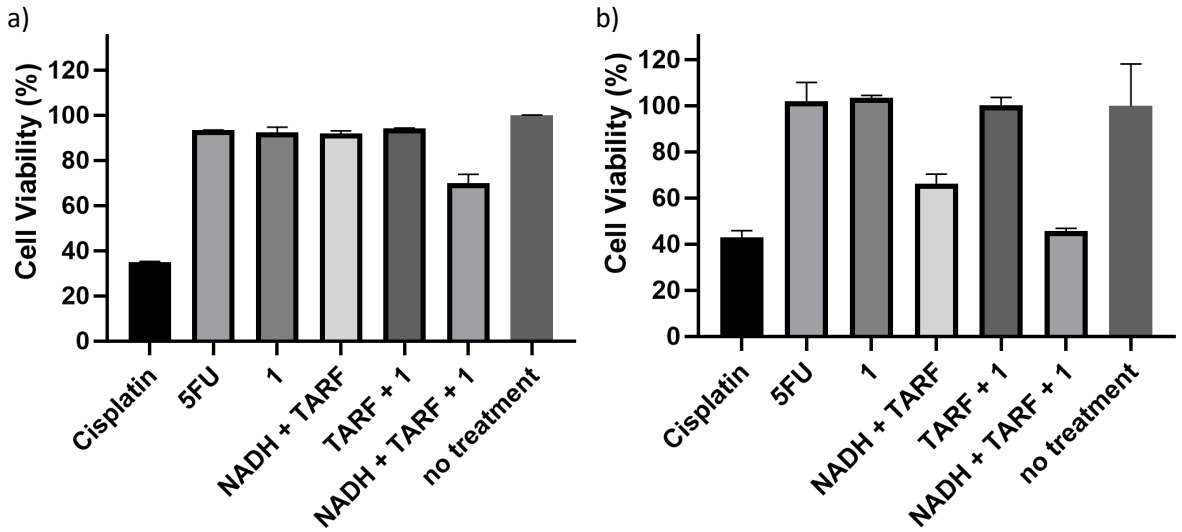

Figure 9. Cell viability results of drugs and prodrugs at the selected concentrations in the presence of **NADH** (50μM): a) in the dark and b) after 30 second of blue light irradiation. Employed concentrations: Cisplatin (1 μM), **5FU** (3 μM), **TARF** (1 μM) and **1** (1 μM).

After these screening and control experiments, we tested the capacity of **TARF@PdNPs** resins to prompt the deprotection and activation of the prodrugs **pro-5FU** and **1** (Figure 10). Experiments were performed in 6 well plates employing 1 mL of cell culture medium in the presence of 1.2 mg/mL of **TARF@PdNPs**, 1 μM of **1**, 50 μM of **NADH** or/and 100 μM of **Pro-5FU**. When the prodrugs were added independently, our resins converted the substrates as observed in solution by NMR, causing a drastic reduction in the cellular proliferation.

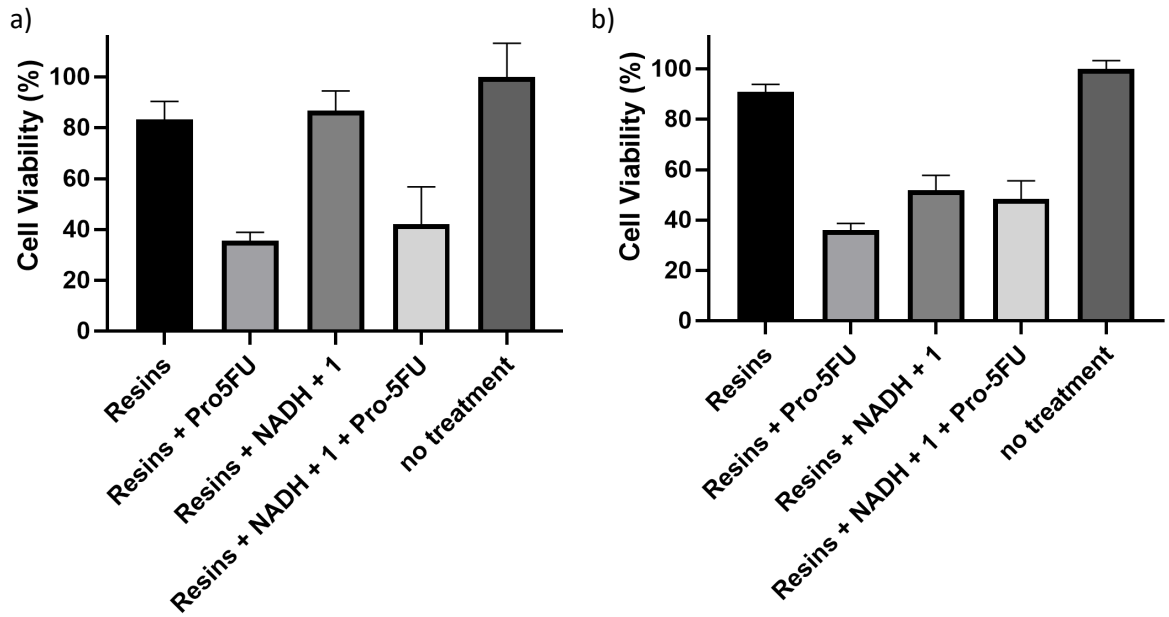

Figure 10. Cell viability results for anticancer agents in the presence of 1.2 mg/mL of **TARF@PdNPs**, 1 μM of **1**, 50 μM of **NADH** or/and 100 μM of **Pro-5FU**, a) in the dark and b) after 30 seconds of blue light.

In the case of **1**, light was required to damage the cells, while in the dark cell viability was much higher. When both prodrugs were present, consistently cell viability was reduced but

results were comparable to the effect produced by **Pro-5FU** alone and no notable differences were observed between dark and light experiments.

5.3 Conclusions

This work reported the synthesis and characterization of the first heterogeneous catalyst for the bioorthogonal dual activation of two anticancer drugs, namely **5FU** and cisplatin. We merged Pd and flavin catalysis to prompt the selective cleavage of a protecting propargyl group and the reduction of a Pt^{IV} complex to the Pt^{II} drug cisplatin. Studies in solution demonstrate that **TARF@PdNPs** catalyst performed the activation reactions with unaltered efficiency compared to single components alone. When present simultaneously in solution, both substrates could be converted accordingly with each reaction kinetics, being the conversion of **pro-5FU** much slower (days) than the photocatalytic activation of the Pt^{IV} prodrug (minutes). In principle such difference could be exploited to tune the effects of the two anticancer drugs on cancer cells overtime.

In vitro experiments confirmed that the **TARF@PdNPs** was capable of catalyzing the transformation of the two prodrugs. In the presence of **1** only, few minutes of light irradiation were sufficient to generate toxic concentration of cisplatin which induced a remarkable reduction in cell viability compared to dark controls or in the absence of catalyst. Similarly, when **pro-5FU** was administered alone the effect of its catalytic activation were also clear and we observed extensive cell death. Despite a preliminary screening aimed at selecting optimal concentrations of substrates and drugs, our experiments with both prodrugs did not demonstrate that a synergistic effect between **5FU** and cisplatin was occurring in IGROV cells. Importantly, we did find a significant reduction in cell viability, however the toxicity of **5FU** at the released concentration was too high to appreciate any effect due to cisplatin.

We believe that different drug administration protocols that use different activation and incubation intervals could help observing synergistic effects between the two drugs and hence improve their therapeutic potential. This work will be carried out in the future by other researchers in the group.

5.4 Experimental details

General Methods

UV-Vis absorption spectroscopy (UV-Vis). All spectra were acquired in optical quartz cuvettes in aqueous solutions or buffers using a JASCO V-730 spectrophotometer.

Nuclear magnetic Resonance (NMR). ^{1}H NMR spectra of the various samples were recorded on a Fourier TM Bruker 300 NMR and on an AVANCE III Bruker 500 NMR spectrometer using standard pulse programs. Chemical shifts were reported in parts-per-million (δ, ppm) and referenced to the residual solvent peak.

Fluorescence spectroscopy in 96-well plates. Relative fluorescence intensity measurements were recorded on a Synergy H1 microplate reader (Biotek) using 96-well plates. Samples were excited at 544 nm and the emission was recorded at 590 nm.

Cytation5 Cell Imaging Reader (Biotek Instruments) Images were obtained on a clear bottom black 96 well microplate. The simple was observed with a Plan Fuorite 4X phase objective with a numerical aperture of 0.13 and coupled to an apotome grid WD with a working distance of 17 mm. GFP filter was used for fluorescent imaging of **TARF**, while the brightfield cannel was also recorded to detect any change of microbead position during the experiment, preventing artifacts introduction in subsequent image analysis.

Scanning Electron Microscope (SEM). Measurements were performed on JEOL JSM-6490LV at 5kV or 15KV, running in a point by point scanning mode. Images were measured using Secondary Electron (SE) and Backscattered Electron (BE) detectors

Fluorescence Confocal microscope. Confocal images were taken on a Zeiss LSM 880 Airyscan confocal microscope with an Ar laser with an excitation wavelength of 488nm. A pinhole 1 AU was used to optimize z-sectioning.

X-ray Photoelectron Spectroscopy (XPS). Experiments were performed in a SPECS Sage HR 100 Spectrometer with a non-monochromatic X-ray source (Magnesium Kα line of 1253.6 eV energy and 252 W), placed perpendicular to the analyzer axis and calibrated using the $3d_{5/2}$ line of Ag with a full width at half maximum (FWHM) of 1.1 eV. Peaks were deconvoluted using standard symmetric and asymmetric Gaussian-Lorentzian functions after a Shirley background correction. Spectra were charge-corrected fixing the C sp3 from adventitious carbon at 284.8 eV.

Inductively coupled plasma mass spectrometry (ICP-MS). Pd quantification was performed in a Thermo Fisher iCAP spectrometer. 7.2 mg of **TARF@Pd NPs** were digested in 600 µL HNO_3 and 200 µL H_2SO_4 overnight before the measurement, determining the Pd % of 3.38 (w/w).

Synthetic procedures.

Prodrugs

***cis,cis,trans*-[Pt(NH$_3$)$_2$(Cl$_2$)(O$_2$CCH$_2$CH$_2$CO$_2$H)$_2$]** (**1**).[25,26] The synthesis of **1** was performed reacting *cis,cis,trans*-[Pt(NH$_3$)$_2$(Cl$_2$)(OH)$_2$] with 2 equivalents of succinic anhydride in DMF and stirring overnight at 70°C. The solution was concentrated under reduced pressure and

the crude was dissolved in a small volume of acetone followed by the addition of diethyl ether to force the precipitation of the desired product. Separation was achieved by centrifugation and solid was further purified by repeating the process several times, eventually obtaining a fine white powder (Yield ~ 60%). ^{1}H NMR (300 MHz, 90% H_2O and 10% D_2O, 300MHz) δ 2.53 (t, 4H) 2.3 (t, 4H) Figure S10.

5-fluoro-1-propargyl-uracil (**Pro-5FU**).[12] 1 equivalent of **5FU** was reacted with 1.5 equivalent of DBU as nitrogen activator and the reaction was cooled to 4°C. Later, 1.3 equivalents of propargyl bromide were added dropwise under N_2 atmosphere. This mixture was maintained under stirring overnight at room temperature. The solvent was removed under vacuum and the product was purified by flash chromatography, employing silica as stationary phase and 3% MeOH in DCM as solvent. The obtained product was a white powder (Yield ~ 30%). ^{1}H NMR (300 MHz, 90% H_2O and 10% D_2O, 300MHz) δ 7.85 (d, 1H) 4.5 (s, 2H) 2.78 (t, 1H) Figure S11.

Catalysts

Tetra-O-acetyl riboflavin (TARF).[39] Riboflavin was dissolves in a mixture of an excess of acetic anhydride and acetic acid (1:1). Then, 1 ml of concentrated perchloric acid was added dropwise to the mixture and the reaction was stirred for 30 minutes at 40 °C. The solution was cooled down into an ice bath and diluted to the half with water. The solution was extracted with chloroform and the organic phase, washed three times with water, saturated sodium bicarbonate and water. Afterwards, the product was purified by flash chromatography column using silica as stationary phase and a progressive DCM/methanol mixture (starting from 99:1 to 9:1) as solvent to remove traces of acetic acid (Yield ~80%). ^{1}H NMR(300 MHz, $CDCl_3$): δ 8.47 (s, 1H) 8.05 (s, 1H) 7.58 (s, 1H) 5.67 (m, 1H) 5.45 (m, 2H) 5.02 (bm, 2H) 4.3 (dd, 2H) 2.59(s, 3H) 2.47(s, 3H) 2.3 (s, 3H) 2.23(s, 3H) 2.1 (s, 3H) (Figure S12).

Pd NPs. Pd^{II} acetate and TentaGel ®HL NH_2 beads of 75 μm (0.4-0.6 NH_2 mmol/g) were added in toluene and the mixture was heated at 80°C for 10 minutes followed by 2 hours of stirring at room temperature. The solution turned black after few minutes. Afterward, the free Pd acetate was washed with DCM and methanol. Then **Pd NPs** were dispersed in methanol that contained hydrazine (10%) and the mixture was stirred for 25 minutes. After washed again with DCM and methanol and the formed black resins were added to a mixture of oxyma, DIC and Fmoc-Glu (OH)-OH in DCM/DMF (2:1, DCM/DMF) and stirred for 2 hours. To conclude, they were washed with DCM, MeOH and H_2O and dried under vacuum at 40 °C for 3 days.

TARF@Pd NPs. The **TARF@Pd NPs** resins were synthesized following the same procedure described for Pd NPs. After the nucleation step and its corresponding washing, an excess of TARF was added together with oxyma, DIC and Fmoc-Glu (OH)-OH in DCM/DMF (2:1,

DCM/DMF). Finally, they were collected and washed with DCM, methanol and water, observing that the excess of TARF was eluted with DCM and methanol.

Cell Viability experiments

96-well plates were used to test antiproliferative effect of the reactants, seeding 1000 cells/well in a volume of 100 µL. We tested our double activation approach in IGROV-1 cell line (Human Ovarian carcinoma). All the experiments were carried out at 37 ºC with 5% of CO_2 in RPMI1640 supplemented with 2 mM of L-glutamine and 10% of FBS. We performed all our experiment seeding 10.000cells/ml at the well plates and were incubated for 48 hours and the treatment was applied for additional 5 days. Then, the supernatant of the wells was substituted for a 0.2mg/ml resazurin RPMI media solution and the cellular viability was determined, measuring the relative fluorescence intensity at 590nm after 6 hours.

5.5 References

(1) Rautio, J.; Meanwell, N. A.; Di, L.; Hageman, M. J. The Expanding Role of Prodrugs in Contemporary Drug Design and Development. *Nat. Rev. Drug Discov.* **2018**, *17*, 559–587.

(2) Ji, X.; Pan, Z.; Yu, B.; De La Cruz, L. K.; Zheng, Y.; Ke, B.; Wang, B. Click and Release: Bioorthogonal Approaches to "On-Demand" Activation of Prodrugs. *Chem. Soc. Rev.* **2019**, *48*, 1077–1094.

(3) Najjar, A.; Najjar, A.; Karaman, R. Newly Developed Prodrugs and Prodrugs in Development; an Insight of the Recent Years. *Molecules.* **2020**, *25*, 884.

(4) Zawilska, J. B.; Wojcieszak, J.; Olejniczak, A. B. Prodrugs: A Challenge for the Drug Development. *Pharmacol. Reports* **2013**, *65*, 1–14.

(5) Sletten, E. M.; Bertozzi, C. R. Bioorthogonal Chemistry: Fishing for Selectivity in a Sea of Functionality. *Angew. Chem., Int. Ed.* **2009**, *48*, 6974–6998.

(6) Alonso-de Castro, S.; Terenzi, A.; Gurruchaga-Pereda, J.; Salassa, L.; Alonso-de Castro, S.; Terenzi, A.; Gurruchaga-Pereda, J.; Salassa, L. Catalysis Concepts in Medicinal Inorganic Chemistry. *Chem. Eur. J.* **2019**, *25*, 6651–6660.

(7) Dougan, S. J.; Habtemariam, A.; McHale, S. E.; Parsons, S.; Sadler, P. J. Catalytic Organometallic Anticancer Complexes. *Proc. Natl. Acad. Sci.* **2008**, *105*, 11628–11633.

(8) Soldevila-Barreda, J. J.; Romero-Canelón, I.; Habtemariam, A.; Sadler, P. J. Transfer Hydrogenation Catalysis in Cells as a New Approach to Anticancer Drug Design. *Nat. Commun.* **2015**, *6*, 6582.

(9) Liu, Z.; Romero-Canelón, I.; Qamar, B.; Hearn, J. M.; Habtemariam, A.; Barry, N. P. E.; Pizarro, A. M.; Clarkson, G. J.; Sadler, P. J. The Potent Oxidant Anticancer Activity of Organoiridium Catalysts. *Angew. Chem., Int. Ed.* **2014**, *53*, 3941–3946.

(10) Coverdale, J. P. C.; Romero-Canelón, I.; Sanchez-Cano, C.; Clarkson, G. J.; Habtemariam, A.; Wills, M.; Sadler, P. J. Asymmetric Transfer Hydrogenation by Synthetic Catalysts in Cancer Cells. *Nat. Chem.* **2018**, *10*, 347–354.

(11) Völker, T.; Dempwolff, F.; Graumann, P. L.; Meggers, E. Progress towards Bioorthogonal Catalysis with Organometallic Compounds. *Angew. Chem., Int. Ed.* **2014**, *53*, 10536–10540.

(12) Weiss, J. T.; Dawson, J. C.; Macleod, K. G.; Rybski, W.; Fraser, C.; Torres-Sánchez, C.; Patton, E. E.; Bradley, M.; Carragher, N. O.; Unciti-Broceta, A. Extracellular Palladium-Catalysed Dealkylation of 5-Fluoro-1-Propargyl-Uracil as a Bioorthogonally Activated Prodrug Approach. *Nat. Commun.* **2014**, *5*, 3277.

(13) Pérez-López, A. M.; Rubio-Ruiz, B.; Sebastián, V.; Hamilton, L.; Adam, C.; Bray, T. L.; Irusta, S.; Brennan, P. M.; Lloyd-Jones, G. C.; Sieger, D.; Santamanría, J.; Unciti-Broceta, A. Gold-Triggered Uncaging Chemistry in Living Systems. *Angew. Chem., Int.*

Ed. **2017**, *56*, 12548–12552.

(14) Bray, T. L.; Salji, M.; Brombin, A.; Pérez-López, A. M.; Rubio-Ruiz, B.; Galbraith, L. C. A.; Patton, E. E.; Leung, H. Y.; Unciti-Broceta, A. Bright Insights into Palladium-Triggered Local Chemotherapy. *Chem. Sci.* **2018**, *9*, 7354–7361.

(15) Alonso-de Castro, S.; Terenzi, A.; Hager, S.; Englinger, B.; Faraone, A.; Martínez, J. C.; Galanski, M.; Keppler, B. K.; Berger, W.; Salassa, L. Biological Activity of Pt(IV) Prodrugs Triggered by Riboflavin-Mediated Bioorthogonal Photocatalysis. *Sci. Rep.* **2018**, *8*, 17198.

(16) Gurruchaga-Pereda, J.; Martínez-Martínez, V.; Formoso, E.; Azpitarte, O.; Rezabal, E.; Lopez, X.; Cortajarena, A. L.; Salassa, L. Enhancing the Photocatalytic Conversion of Pt(IV) Substrates by Flavoprotein Engineering. *J. Phys. Chem. Lett.* **2021**, *12*, 4504–4508.

(17) Scanlon, K. J.; Newman, E. M.; Lu, Y.; Priest, D. G. Biochemical Basis for Cisplatin and 5-Fluorouracil Synergism in Human Ovarian Carcinoma Cells. *Proc. Natl. Acad. Sci.* **1986**, *83*, 8923–8925.

(18) Longley, D. B.; Harkin, D. P.; Johnston, P. G. 5-Fluorouracil: Mechanisms of Action and Clinical Strategies. *Nat. Rev. Cancer.* **2003**, *3*, 330–338.

(19) Weiss, J. T.; Fraser, C.; Rubio-Ruiz, B.; Myers, S. H.; Crispin, R.; Dawson, J. C.; Brunton, V. G.; Patton, E. E.; Carragher, N. O.; Unciti-Broceta, A. N-Alkynyl Derivatives of 5-Fluorouracil: Susceptibility to Palladium-Mediated Dealkylation and Toxigenicity in Cancer Cell Culture. *Front. Chem.* **2014**, *2*, 59.

(20) Gurruchaga-Pereda, J.; Martínez-Martínez, V.; Rezabal, E.; Lopez, X.; Garino, C.; Mancin, F.; Cortajarena, A. L.; Salassa, L. Flavin Bioorthogonal Photocatalysis Toward Platinum Substrates. *ACS Catal.* **2020**, *10*, 187–196.

(21) Alonso-de Castro, S.; Ruggiero, E.; Ruiz-de-Angulo, A.; Rezabal, E.; Mareque-Rivas, J. C.; Lopez, X.; López-Gallego, F.; Salassa, L. Riboflavin as a Bioorthogonal Photocatalyst for the Activation of a Pt(IV) Prodrug. *Chem. Sci.* **2017**, *8*, 4619–4625.

(22) National Cancer Institute. Cisplatin and fluorouracil (FU) https://www.cancerresearchuk.org/about-cancer/cancer-in-general/treatment/cancer-drugs/drugs/cisplatin-fluorouracil-5fu.

(23) Braly, P. S.; Berek, J. S.; Blessing, J. A.; Homesley, H. D.; Averette, H. Intraperitoneal Administration of Cisplatin and 5-Fluorouracil in Residual Ovarian Cancer: A Phase II Gynecologic Oncology Group Trial. *Gynecol. Oncol.* **1995**, *56*, 164–168.

(24) Morgan, R. J.; Braly, P.; Leong, L.; Shibata, S.; Margolin, K.; Somlo, G.; McNamara, M.; Longmate, J.; Schinke, S.; Raschko, J.; et al. Phase II Trial of Combination Intraperitoneal Cisplatin and 5- Fluorouracil in Previously Treated Patients with Advanced Ovarian Cancer: Long-Term Follow-Up. *Gynecol. Oncol.* **2000**, *77*, 433–438.

(25) Gramatica, P.; Papa, E.; Luini, M.; Monti, E.; Gariboldi, M. B.; Ravera, M.; Gabano, E.; Gaviglio, L.; Osella, D. Antiproliferative Pt(IV) Complexes: Synthesis, Biological

Activity, and Quantitative Structure-Activity Relationship Modeling. *J. Biol. Inorg. Chem.* **2010**, *15*, 1157–1169.

(26) Reithofer, M.; Galanski, M.; Roller, A.; Keppler, B. K. An Entry to Novel Platinum Complexes: Carboxylation of Dihydroxoplatinum(IV) Complexes with Succinic Anhydride and Subsequent Derivatization. *Eur. J. Inorg. Chem.* **2006**, *2006*, 2612–2617.

(27) Johnstone, T. C.; Suntharalingam, K.; Lippard, S. J. The Next Generation of Platinum Drugs: Targeted Pt(II) Agents, Nanoparticle Delivery, and Pt(IV) Prodrugs. *Chem. Rev.* **2016**, *116*, 3436–3486.

(28) He, S.; Li, C.; Zhang, Q.; Ding, J.; Liang, X.-J.; Chen, X. X.; Xiao, H.; Chen, X. X.; Zhou, D.; Huang, Y. Tailoring Platinum(IV) Amphiphiles for Self-Targeting All-in-One Assemblies as Precise Multimodal Theranostic Nanomedicine. *ACS Nano* **2018**, *12*, 7272–7281.

(29) Maldonado, C. R.; Gómez-Blanco, N.; Jauregui-Osoro, M.; Brunton, V. G.; Yate, L.; Mareque-Rivas, J. C. QD-Filled Micelles Which Combine SPECT and Optical Imaging with Light-Induced Activation of a Platinum(IV) Prodrug for Anticancer Applications. *Chem. Commun.* **2013**, *49*, 3985–3987.

(30) Ruggiero, E.; Hernández-Gil, J.; Mareque-Rivas, J. C.; Salassa, L. Near Infrared Activation of an Anticancer Pt(IV) complex by Tm-Doped Upconversion Nanoparticles. *Chem. Commun.* **2015**, *51*, 2091–2094.

(31) Dhar, S.; Kolishetti, N.; Lippard, S. J.; Farokhzad, O. C. Targeted Delivery of a Cisplatin Prodrug for Safer and More Effective Prostate Cancer Therapy in Vivo. *Proc. Natl. Acad. Sci.* **2011**, *108*, 1850–1855.

(32) Della Rocca, J.; Liu, D.; Lin, W. Nanoscale Metal-Organic Frameworks for Biomedical Imaging and Drug Delivery. *Acc. Chem. Res.* **2011**, *44*, 957–968.

(33) Santi, M.; Mapanao, A. K.; Cassano, D.; Vlamidis, Y.; Cappello, V.; Voliani, V. Endogenously-Activated Ultrasmall-in-Nano Therapeutics: Assessment on 3D Head and Neck Squamous Cell Carcinomas. *Cancers.* **2020**, *12*, 1063.

(34) Maag, H. Prodrugs of Carboxylic Acids. In *Prodrugs*; Springer, **2007**, pp 703–729.

(35) Varbanov, H. P.; Jakupec, M. A.; Roller, A.; Jensen, F.; Galanski, M.; Keppler, B. K. Theoretical Investigations and Density Functional Theory Based Quantitative Structure-Activity Relationships Model for Novel Cytotoxic Platinum(IV) Complexes. *J. Med. Chem.* **2013**, *56*, 330–344.

(36) Alonso-de Castro, S.; Cortajarena, A. L.; López-Gallego, F.; Salassa, L.; Lopez-Gallego, F.; Salassa, L.; López-Gallego, F.; Salassa, L. Bioorthogonal Catalytic Activation of Platinum and Ruthenium Anticancer Complexes by FAD and Flavoproteins. *Angew. Chem., Int. Ed.* **2018**, *57*, 3143–3147.

(37) Malet-Martino, M.; Jolimaitre, P.; Martino, R. The Prodrugs of 5-Fluorouracil. *Curr. Med. Chem. Anticancer Agents.* **2002**, *2*, 267–310.

(38) Lazrek, H. B.; Taourirte, M.; Oulih, T.; Barascut, J. L.; Imbach, J. L.; Pannecouque, C.; Witrouw, M.; De Clercq, E. Synthesis and Anti-HIV Activity of New Modified 1,2,3-Triazole Acyclonucleosides. *Nucleosides, Nucleotides and Nucleic Acids.* **2001**, *20*, 1949–1960.

(39) Jhulki, I.; Chanani, P. K.; Abdelwahed, S. H.; Begley, T. P. A Remarkable Oxidative Cascade That Replaces the Riboflavin C8 Methyl with an Amino Group during Roseoflavin Biosynthesis. *J. Am. Chem. Soc.* **2016**, *138*, 8324–8327.

(40) Mühldorf, B.; Wolf, R. C-H Photooxygenation of Alkyl Benzenes Catalyzed by Riboflavin Tetraacetate and a Non-Heme Iron Catalyst. *Angew. Chem., Int. Ed.* **2016**, *55*, 427–430.

(41) Guo, H.; Xia, H.; Ma, X.; Chen, K.; Dang, C.; Zhao, J.; Dick, B. Efficient Photooxidation of Sulfides with Amidated Alloxazines as Heavy-Atom-Free Photosensitizers. *ACS Omega* **2020**, *5*, 10586–10595.

(42) Feldmeier, C.; Bartling, H.; Magerl, K.; Gschwind, R. M. LED-Illuminated NMR Studies of Flavin-Catalyzed Photooxidations Reveal Solvent Control of the Electron-Transfer Mechanism. *Angew. Chem., Int. Ed.* **2015**, *54*, 1347–1351.

(43) Svoboda, J.; Schmaderer, H.; König, B. Thiourea-Enhanced Flavin Photooxidation of Benzyl Alcohol. *Chem. Eur. J.* **2008**, *14*, 1854–1865.

(44) Dang, C.; Zhu, L.; Guo, H.; Xia, H.; Zhao, J.; Dick, B. Flavin Dibromide as an Efficient Sensitizer for Photooxidation of Sulfides. *ACS Sustain. Chem. Eng.* **2018**, *6*, 15254–15263.

(45) Hering, T.; Mühldorf, B.; Wolf, R.; König, B. Halogenase-Inspired Oxidative Chlorination Using Flavin Photocatalysis. *Angew. Chem., Int. Ed.* **2016**, *55*, 5342–5345.

(46) Düsel, S. J. S.; König, B. Visible-Light-Mediated Nitration of Protected Anilines. *J. Org. Chem.* **2018**, *83*, 2802–2807.

(47) Juarez, A. V.; Sosa, L. D. V.; De Paul, A. L.; Costa, A. P.; Farina, M.; Leal, R. B.; Torres, A. I.; Pons, P. Riboflavin Acetate Induces Apoptosis in Squamous Carcinoma Cells after Photodynamic Therapy. *J. Photochem. Photobiol. B.* **2015**, *153*, 445–454.

(48) Wolnicka-Glubisz, A.; Pawlak, A.; Insinska-Rak, M.; Zadlo, A. Analysis of Photoreactivity and Phototoxicity of Riboflavin's Analogue 3MeTARF. *J. Photochem. Photobiol. B.* **2020**, *205*, 111820.

(49) Yusop, R. M.; Unciti-Broceta, A.; Johansson, E. M. V.; Sánchez-Martín, R. M.; Bradley, M. Palladium-Mediated Intracellular Chemistry. *Nat. Chem.* **2011**, *3*, 239–243.

(50) Unciti-Broceta, A.; Johansson, E. M. V; Yusop, R. M.; Sánchez-Martín, R. M.; Bradley, M. Synthesis of Polystyrene Microspheres and Functionalization with Pd(0) Nanoparticles to Perform Bioorthogonal Organometallic Chemistry in Living Cells. *Nat. Protoc.* **2012**, *7*, 1207–1218.

(51) J. F. Moulder, W. F. Stickle, P. E. Sobol, and K. D. B. *Handbook of X-Ray Photoelectron Spectroscopy*; Physical Electronics, **1995**.

(52) Biesinger, M. X-ray Photoelectron Spectroscopy (XPS) Reference Pages http://www.xpsfitting.com/search/label/Palladium.

(53) Larson, R. A.; Stackhouse, P. L.; Crowley, T. O. Riboflavin Tetraacetate: A Potentially Useful Photosensitizing Agent for the Treatment of Contaminated Waters. *Environ. Sci. Technol.* **1992**, *26*, 1792–1798.

(54) Oliveira, B. L.; Stenton, B. J.; Unnikrishnan, V. B.; De Almeida, C. R.; Conde, J.; Negrão, M.; Schneider, F. S. S.; Cordeiro, C.; Ferreira, M. G.; Caramori, G. F.; et al. Platinum-Triggered Bond-Cleavage of Pentynoyl Amide and N-Propargyl Handles for Drug-Activation. *J. Am. Chem. Soc.* **2020**, *142*, 10869–10880.

(55) Sun, T.; Lv, T.; Wu, J.; Zhu, M.; Fei, Y.; Zhu, J.; Zhang, Y.; Huang, Z. General Strategy for Integrated Bioorthogonal Prodrugs: Pt(II)-Triggered Depropargylation Enables Controllable Drug Activation in Vivo. *J. Med. Chem.* **2020**, *63*, 13899–13912.

(56) Glushonok, G. K.; Glushonok, T. G.; Maslovskaya, L. A.; Shadyro, O. I. A 1H and 13C NMR and UV Study of the State of Hydroxyacetone in Aqueous Solutions. *Russ. J. Gen. Chem.* **2003**, *73*, 1027–1031.

Conclusions

Bioorthogonal catalytic approaches have attracted much attention in the last decade as viable solutions for solving drawbacks of currently used therapies. Among the three main biorthogonal catalytic strategies discussed in this Ph.D thesis, my work specifically intended to develop and expand the unconventional bioorthogonal photocatalytic reactions that use metal complexes as substrates rather than catalysts. The discovery of riboflavin as photocatalyst for triggering the conversion of Pt^{IV} complexes motivated the exploration of this unique non-natural reactions in more detail. Free and protein-encapsulated flavins displayed the capability to perform the selective and highly efficient conversion of inert Pt^{IV} prodrugs into highly toxic Pt^{II} species upon low doses of blue light, even in a biological media containing numerous biomolecules.

During the Ph.D, I have expanded the scope of flavin mediated photocatalysis towards platinum substrates. Four platinum substrates and five flavin catalysts were investigated, extending the photocatalytic reaction catalogue. Computational methods, in agreement with experimental data, suggested that the ribityl chain influenced the catalytic efficiency favoring the interaction between the reduced flavin form (active catalyst species) and the metal substrate. In the case of the miniSOG (mini Singlet Oxygen Generator) flavoprotein, the lowest catalytic efficiency could be related to the triplet excited state quenching by the protein scaffold that surrounds the FMN chromophore. Catalytic active species involved in the photoreduction of Pt^{IV} complexes were identified and fundamental mechanistic details were revealed by optical and NMR spectroscopy in oxygen free conditions.

Within this Ph.D project, the miniSOG flavoprotein and three variants (Q103V, Q50E and Q50W) were examined under different conditions and their capacity to convert two cisplatin prodrugs was evaluated in the presence of sacrificial electron donors such as NADH. The mutation in the position 103 with a hydrophobic amino acid such as valine (V) prolonged the triplet excited state lifetime of FMN from 35 μs (WT) to 102 μs. This resulted in the highest catalytic activity of the Q103V mutant towards Pt^{IV} complexes with respect of the others miniSOG derivatives. It is worth noting that the mutation in the position 50 with a bulky tryptophan (W) caused a reduction of the triplet excited state lifetime from 35 μs (WT) to 1.8 μs, overall affording a less efficient photocatalyst. The use of site direct mutagenesis for enhancing enzymatic catalytic processes is well established, however, the use of it for tuning the catalytic activation of Pt^{IV} prodrugs (i.e. metal substrates) has never been explored before.

The final part of this work explored the possible application of a dual bioorthogonal catalytic activation strategy developed during my stay in the group of Dr. Unciti-Broceta at the University of Edinburgh. The bioorthogonal activation of two prodrugs by a single biocompatible device was investigated by nuclear magnetic resonance (NMR) demonstrating a significant difference on the transformation rate of the prodrugs. The

efficient transformation of the Pt^{IV} precursor of cisplatin was instantaneous upon blue light irradiation, while the conversion the fluorouracil prodrug required longer time and a much higher catalyst/substrate ratio. The dual activation dramatically reduced the cell viability of ovarian carcinoma IGROV-1 cells *in vitro*. Nevertheless, results did not show a synergistic effect between cisplatin and fluorouracil, likely because of the non-optimal concentrations of the two anticancer agents. Further studies are needed to elucidate the appropriateness of the combination of these independent biorthogonal activation reactions for anticancer purposes.

In general, this thesis contributes to the understanding of the mechanism of flavin-mediated photocatalysis towards Pt^{IV} substrates. It is a step forward in the long-term development of catalytic reactions that use metal complexes and metal-containing species as unconventional substrates. Importantly, many aspects involved in the flavin catalyzed conversion of Pt prodrugs should still be clarified, in order to achieve the optimal efficacy of prodrug activation in biological systems.

In that regard, I conceive that the following facets are indispensable to progress in the biorthogonal photocatalytic activation of anticancer metal prodrugs for therapeutic aims:

- Determining the actual influence and impact of side reactions generated upon flavins stimulation with blue light. The formation of reactive oxygen species due to the excitation of the chromophore needs to be quantified in order to get a deeper understanding of the photocatalytic process to finally optimize it. In addition, as determined by computational and experimental methods, the dissociation of the ligands in the carboplatin derivatives is not limited to axial position. This is not the case for the cisplatin analogues; however it can cause a loss of efficiency and therefore structural changes of the prodrugs could be helpful to improve a more selective dissociation and hence a more effective activation.
- Studying the chemical alterations of amino acids in flavoproteins produced upon blue light irradiation by different techniques (i.e. NMR, electron paramagnetic resonance EPR) can provide relevant information to guide site directed mutagenesis and boost photocatalytic efficiency (i.e. avoid radical formation, back electron transfer processes).
- Employing dual catalytic prodrug activation strategies that employ drugs with actual multitargeting ability with the aim of avoiding/reducing cell resistance mechanisms. The induction of cellular damage by distinct mechanisms can enhance the toxic effect of antineoplastic agents and catalytic systems can provide a spatio-temporal control over the activation of the prodrugs.
- Changing the chromophore structure (e.g. porphyrins), and as consequence its photochemical features, may allow shifting the absorption properties of the photocatalyst to longer wavelengths which are more suitable for therapeutic purposes, since red light penetrates deeper into tissues and is less harmful to biological systems.

Appendix Chapter 3

Flavin Bioorthogonal Photocatalysis Towards Platinum Substrates

Supporting Information

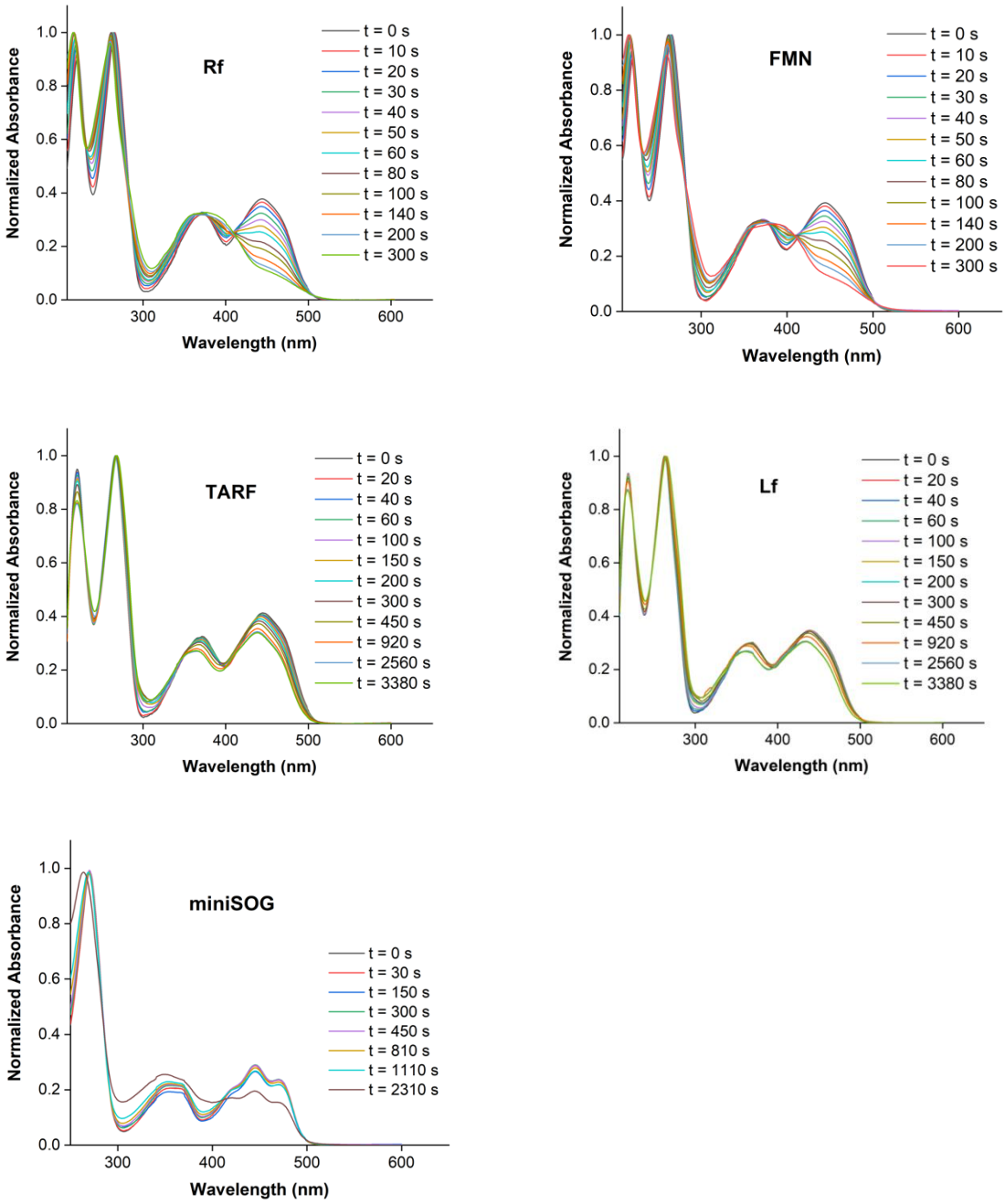

Figure S1. Photostability of flavin catalysts (13 µM) in PB (20 mM, pH 7) under blue light irradiation (460 nm, 6 mW·cm^{-2}).

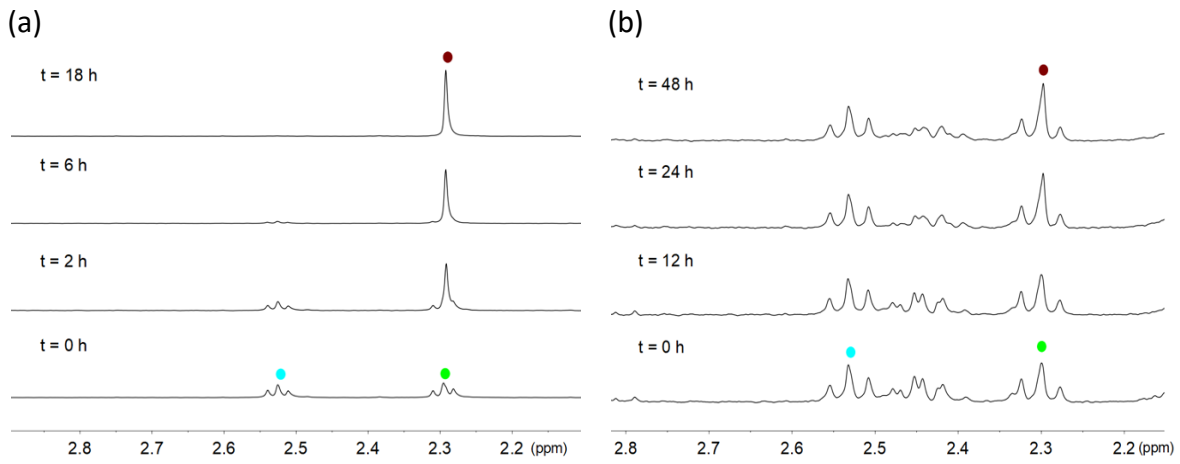

Figure S2. Dark stability of complex **1** (500 µM) in 18 mM PB (pH 7.0, 10% D_2O) in the presence of 1 mM of ascorbate (a) and glutathione (b).
^{1}H NMR signal labelling: ● NADH, ● Pt–OCO**CH$_2$**CH$_2$CO$_2^-$, ● Pt–OCOCH$_2$**CH$_2$**CO$_2^-$, ● free $^-$O$_2$C**CH$_2$CH$_2$**CO$_2^-$.

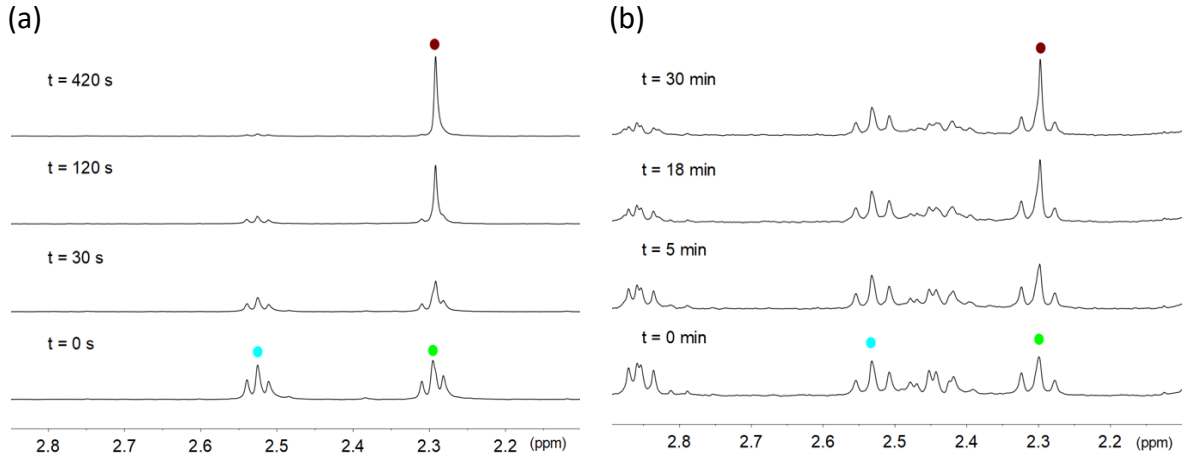

Figure S3. Photocatalytic activation of complex **1** (500 µM) in 18 mM PB (pH 7.0, 10% D_2O) in the presence of 1 mM ascorbate (a) or glutathione (b) and 1 µM **Rf** under 460-nm light irradiation (6 mW·cm^{-2}). ^{1}H NMR signal labelling: ● NADH, ● Pt–OCO**CH$_2$**CH$_2$CO$_2^-$, ● Pt–OCOCH$_2$**CH$_2$**CO$_2^-$, ● free $^-$O$_2$C**CH$_2$CH$_2$**CO$_2^-$.

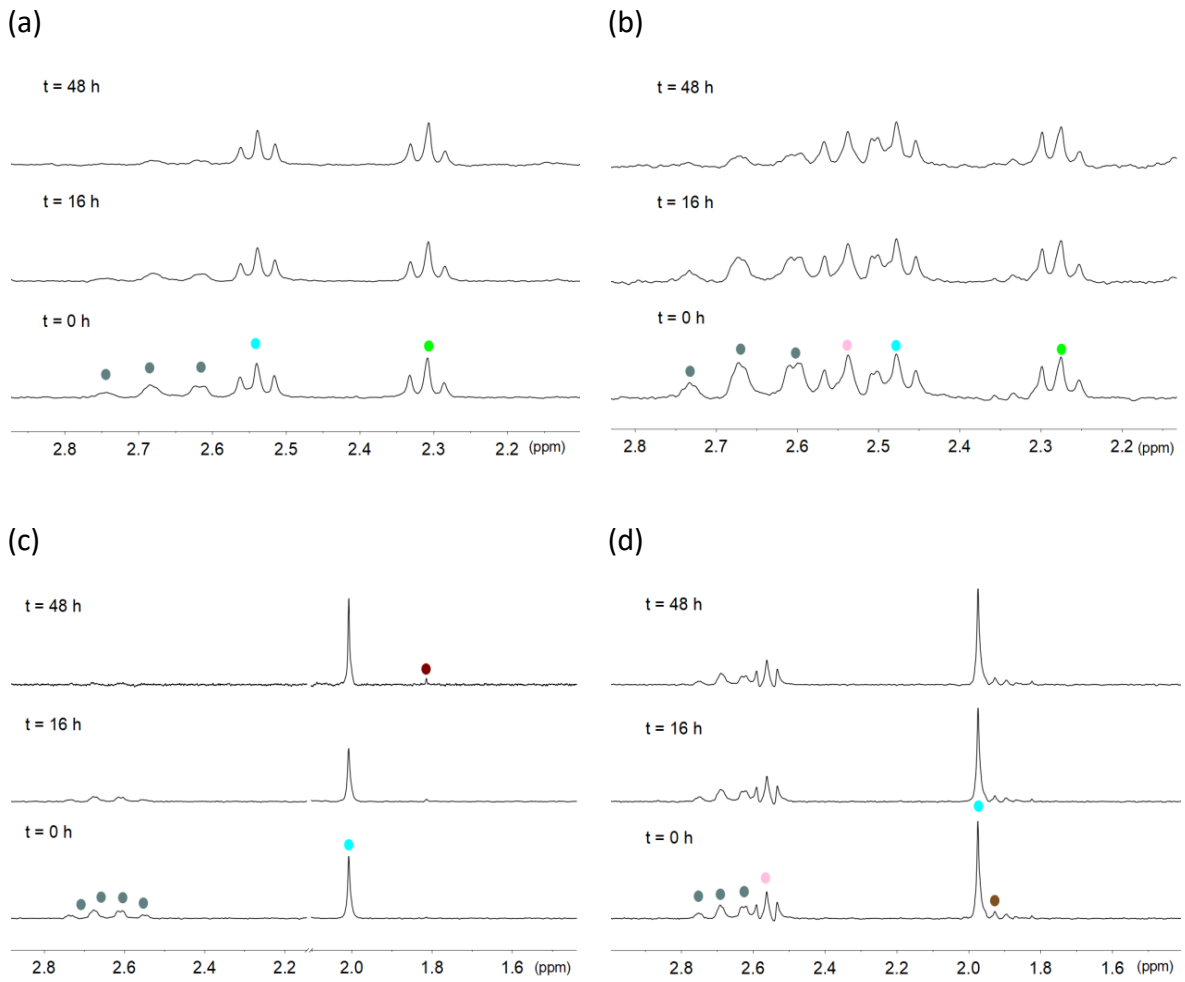

Figure S4. Dark stability of complexes **1–4** (500 µM) in 18 mM PB (pH 7.0, 10% D_2O) in the presence of 1 mM of NADH for 48 h.
^{1}H NMR signal labelling: ● NADH, (a) **1**, ● Pt–OCO**CH$_2$**$CH_2CO_2^-$, ● Pt–OCOCH_2**CH$_2$**CO_2^-; (b) **2**, ● Pt–OCO**CH$_2$**$CH_2CO_2^-$, ● Pt–OCOCH_2**CH$_2$**CO_2^-, ● Pt–[(OCO)$_2$C(**CH$_2$**)$_2$**$_2$**CH_2]; (c) **3**, ● Pt–OCO**CH$_3$**, ● free $^-$OCO**CH$_3$** and (d) **4**, ● Pt–OCO**CH$_3$**, ● Pt–[(OCO)$_2$C(**CH$_2$**)$_2$**$_2$**CH_2], ● Pt–[(OCO)$_2$C$(CH_2)_2$**CH$_2$**].

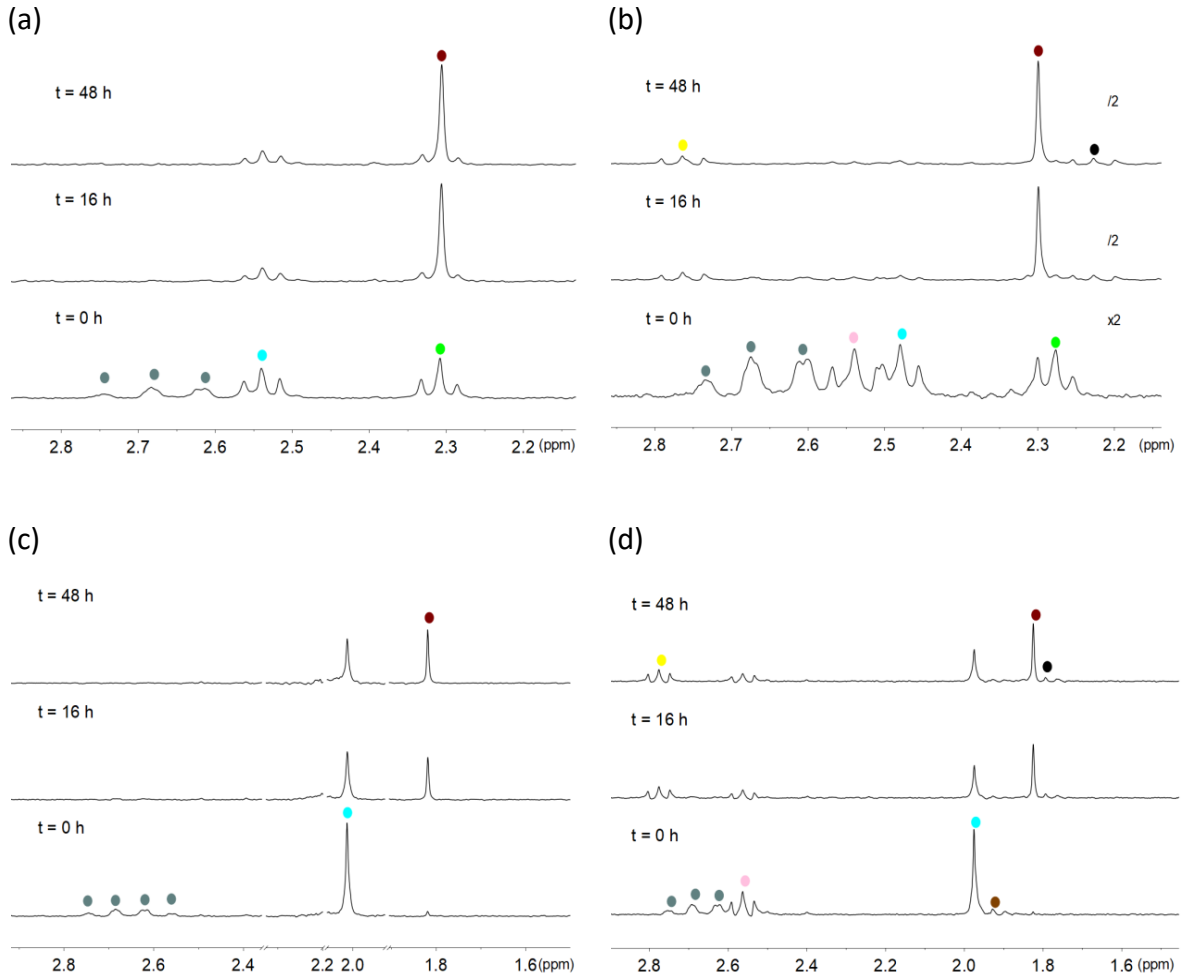

Figure S5. Dark stability of complexes **1**–**4** (500 µM) in 18 mM PB (pH 7.0, 10% D_2O) in the presence of 1 mM NADH and 25 µM **Rf** for 48 h.
^{1}H NMR signal labelling: ● NADH, (a) **1**, ● Pt–OCO**CH$_2$**CH$_2$CO$_2^-$, ● Pt–OCOCH$_2$**CH$_2$**CO$_2^-$, ● free $^-$O$_2$C**CH$_2$CH$_2$**CO$_2^-$; (b) **2**, ● Pt–OCO**CH$_2$**CH$_2$CO$_2^-$, ● Pt–OCOCH$_2$**CH$_2$**CO$_2^-$, ● Pt–[(OCO)$_2$C(**CH$_2$**)$_2$**$_2$**CH$_2$], ● free $^-$O$_2$C**CH$_2$CH$_2$**CO$_2^-$, ● Pt^{II}–[(OCO)$_2$C(**CH$_2$**)$_2$**$_2$**CH$_2$], ● free [($^-$OCO)$_2$C**(CH$_2$)$_2$**$_2$CH$_2$]; (c) **3**, ● Pt–OCO**CH$_3$**, ● free $^-$OCO**CH$_3$** and (d) **4**, ● Pt–OCO**CH$_3$**, ● Pt–[(OCO)$_2$C(**CH$_2$**)$_2$**$_2$**CH$_2$], ● Pt–[(OCO)$_2$C(CH$_2$)$_2$**CH$_2$**], ● Pt^{II}–[(OCO)$_2$C(**CH$_2$**)$_2$**$_2$**CH$_2$], ● Pt^{II}–[(OCO)$_2$C(CH$_2$)$_2$**CH$_2$**], ● free $^-$OCO**CH$_3$**.

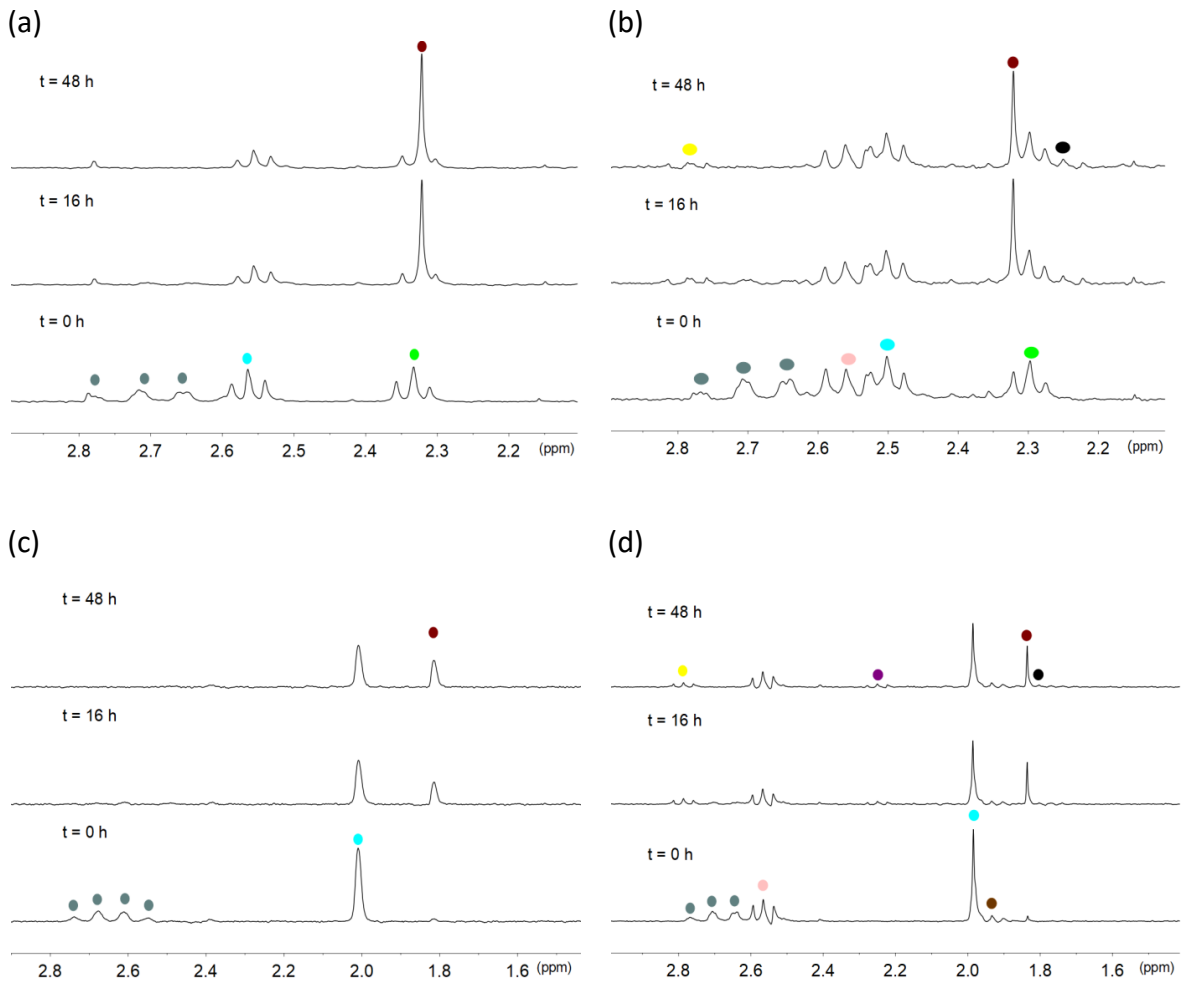

Figure S6. Dark stability of complexes **1**–**4** (500 µM) in 18 mM PB (pH 7.0, 10% D_2O) in the presence of 1 mM NADH and 25 µM **FMN** for 48 h.
^{1}H NMR signal labelling: ● NADH, (a) **1**, ● Pt–OCO**CH$_2$**CH$_2$CO$_2^-$, ● Pt–OCOCH$_2$**CH$_2$**CO$_2^-$, ● free $^-$O$_2$C**CH$_2$CH$_2$**CO$_2^-$; (b) **2**, ● Pt–OCO**CH$_2$**CH$_2$CO$_2^-$, ● Pt–OCOCH$_2$**CH$_2$**CO$_2^-$, ● Pt–[(OCO)$_2$C(**CH$_2$**)$_2$**$_2$**CH$_2$], ● free $^-$O$_2$C**CH$_2$CH$_2$**CO$_2^-$, ● Pt^{II}–[(OCO)$_2$C(**CH$_2$**)$_2$**$_2$**CH$_2$], ● free [($^-$OCO)$_2$C(**CH$_2$**)$_2$**$_2$**CH$_2$]; (c) **3**, ● Pt–OCO**CH$_3$**, ● free $^-$OCO**CH$_3$** and (d) **4**, ● Pt–OCO**CH$_3$**, ● Pt–[(OCO)$_2$C(**CH$_2$**)$_2$**$_2$**CH$_2$], ● Pt–[(OCO)$_2$C(CH$_2$)$_2$**CH$_2$**], ● Pt^{II}–[(OCO)$_2$C(**CH$_2$**)$_2$**$_2$**CH$_2$], ● Pt^{II}–[(OCO)$_2$C(CH$_2$)$_2$**CH$_2$**], ● free $^-$OCO**CH$_3$**, ● free [($^-$OCO)$_2$C(**CH$_2$**)$_2$**$_2$**CH$_2$].

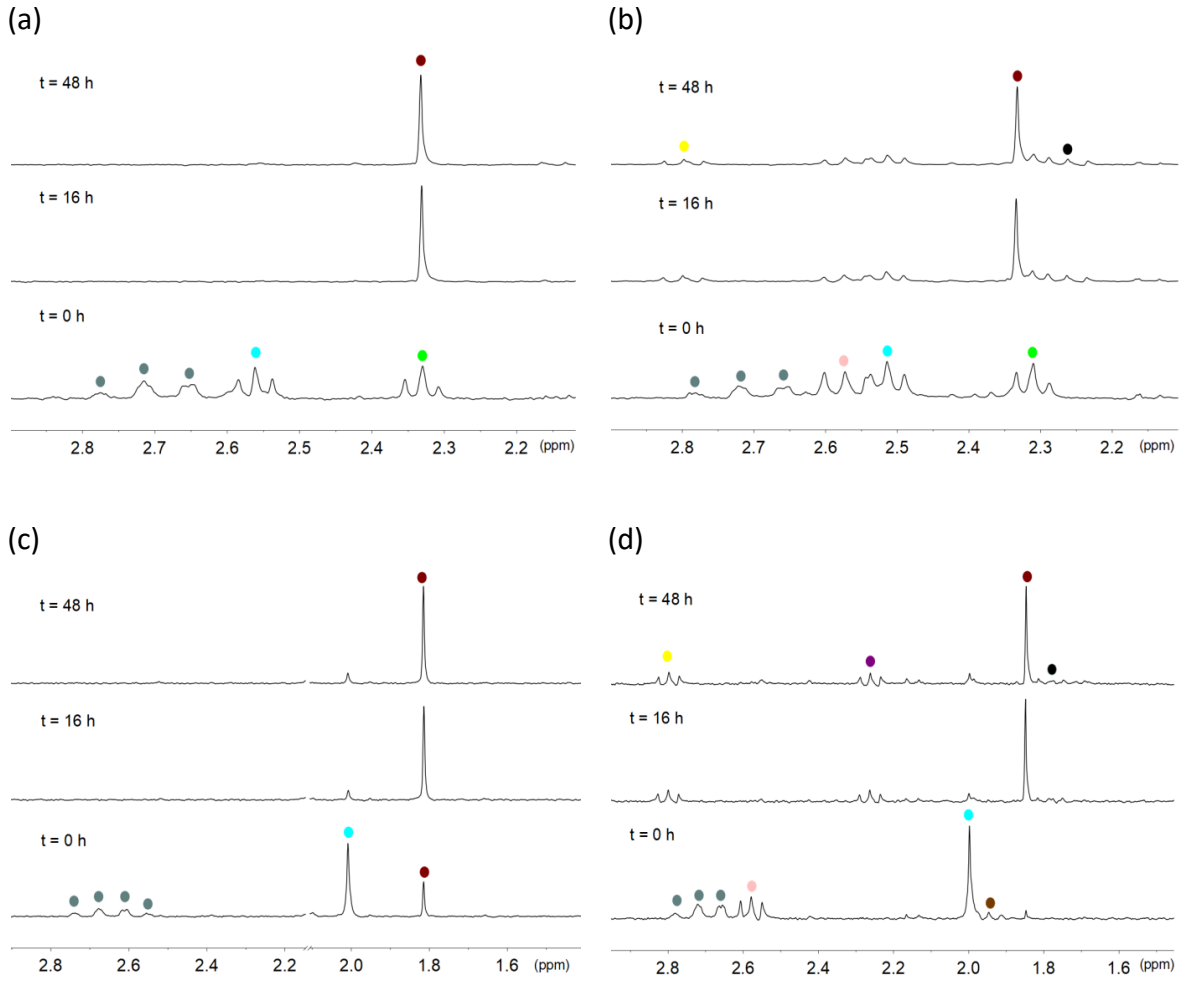

Figure S7. Dark stability of complexes **1**–**4** (500 µM) in 18 mM PB (pH 7.0, 10% D_2O) in the presence of 1 mM NADH and 25 µM **TARF** for 48 h.
^{1}H NMR signal labelling: ● NADH, (a) **1**, ● Pt–OCO**CH$_2$**CH$_2$CO$_2^-$, ● Pt–OCOCH$_2$**CH$_2$**CO$_2^-$, ● free $^-$O$_2$C**CH$_2$CH$_2$**CO$_2^-$; (b) **2**, ● Pt–OCO**CH$_2$**CH$_2$CO$_2^-$, ● Pt–OCOCH$_2$**CH$_2$**CO$_2^-$, ● Pt–[(OCO)$_2$C(**CH$_2$**)$_2$**$_2$**CH$_2$], ● free $^-$O$_2$C**CH$_2$CH$_2$**CO$_2^-$, ● Pt^{II}–[(OCO)$_2$C(**CH$_2$**)$_2$**$_2$**CH$_2$], ● free [($^-$OCO)$_2$C(**CH$_2$**)$_2$**$_2$**CH$_2$]; (c) **3**, ● Pt–OCO**CH$_3$**, ● free $^-$OCO**CH$_3$** and (d) **4**, ● Pt–OCO**CH$_3$**, ● Pt–[(OCO)$_2$C(**CH$_2$**)$_2$**$_2$**CH$_2$], ● Pt–[(OCO)$_2$C(CH$_2$)$_2$**CH$_2$**], ● Pt^{II}–[(OCO)$_2$C(**CH$_2$**)$_2$**$_2$**CH$_2$], ● Pt^{II}–[(OCO)$_2$C(CH$_2$)$_2$**CH$_2$**], ● free $^-$OCO**CH$_3$**, ● free [($^-$OCO)$_2$C**(CH$_2$)$_2$**$_2$**CH$_2$].

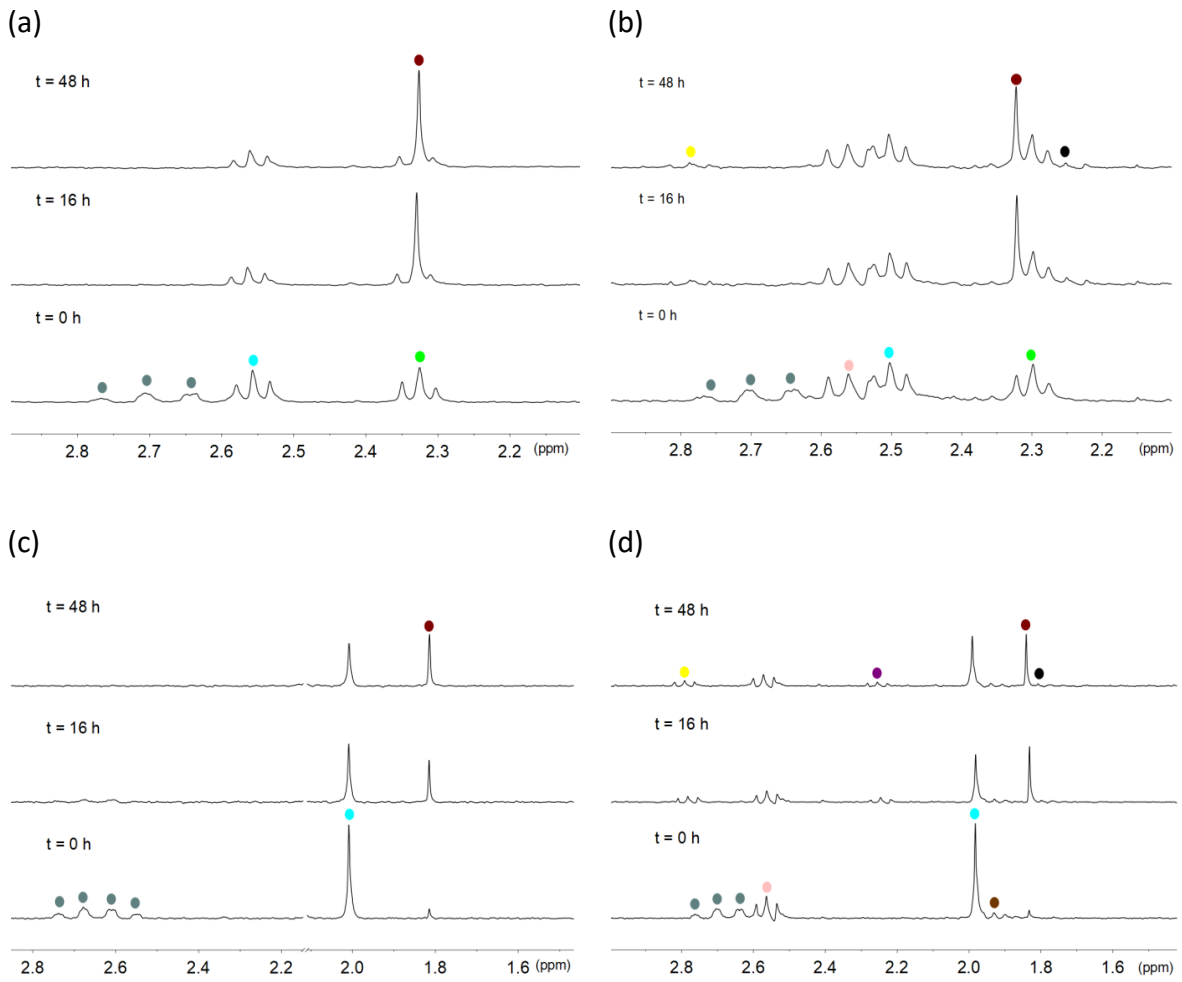

Figure S8. Dark stability of complexes **1**–**4** (500 µM) in 18 mM PB (pH 7.0, 10% D_2O) in the presence of 1 mM NADH and 25 µM **Lf** for 48 h.
^{1}H NMR signal labelling: ● NADH, (a) **1**, ● Pt–OCO**CH$_2$**CH$_2$CO$_2^-$, ● Pt–OCOCH$_2$**CH$_2$**CO$_2^-$, ● free $^-$O$_2$C**CH$_2$CH$_2$**CO$_2^-$; (b) **2**, ● Pt–OCO**CH$_2$**CH$_2$CO$_2^-$, ● Pt–OCOCH$_2$**CH$_2$**CO$_2^-$, ● Pt–[(OCO)$_2$C(**CH$_2$**)$_2$**$_2$**CH$_2$], ● free $^-$O$_2$C**CH$_2$CH$_2$**CO$_2^-$, ● Pt^{II}–[(OCO)$_2$C(**CH$_2$**)$_2$**$_2$**CH$_2$], ● free [($^-$OCO)$_2$C(**CH$_2$**)$_2$**$_2$**CH$_2$]; (c) **3**, ● Pt–OCO**CH$_3$**, ● free $^-$OCO**CH$_3$** and (d) **4**, ● Pt–OCO**CH$_3$**, ● Pt–[(OCO)$_2$C(**CH$_2$**)$_2$**$_2$**CH$_2$], ● Pt–[(OCO)$_2$C(CH$_2$)$_2$**CH$_2$**], ● Pt^{II}–[(OCO)$_2$C(**CH$_2$**)$_2$**$_2$**CH$_2$], ● Pt^{II}–[(OCO)$_2$C(CH$_2$)$_2$**CH$_2$**], ● free $^-$OCO**CH$_3$**, ● free [($^-$OCO)$_2$C(**CH$_2$**)$_2$**$_2$**CH$_2$].

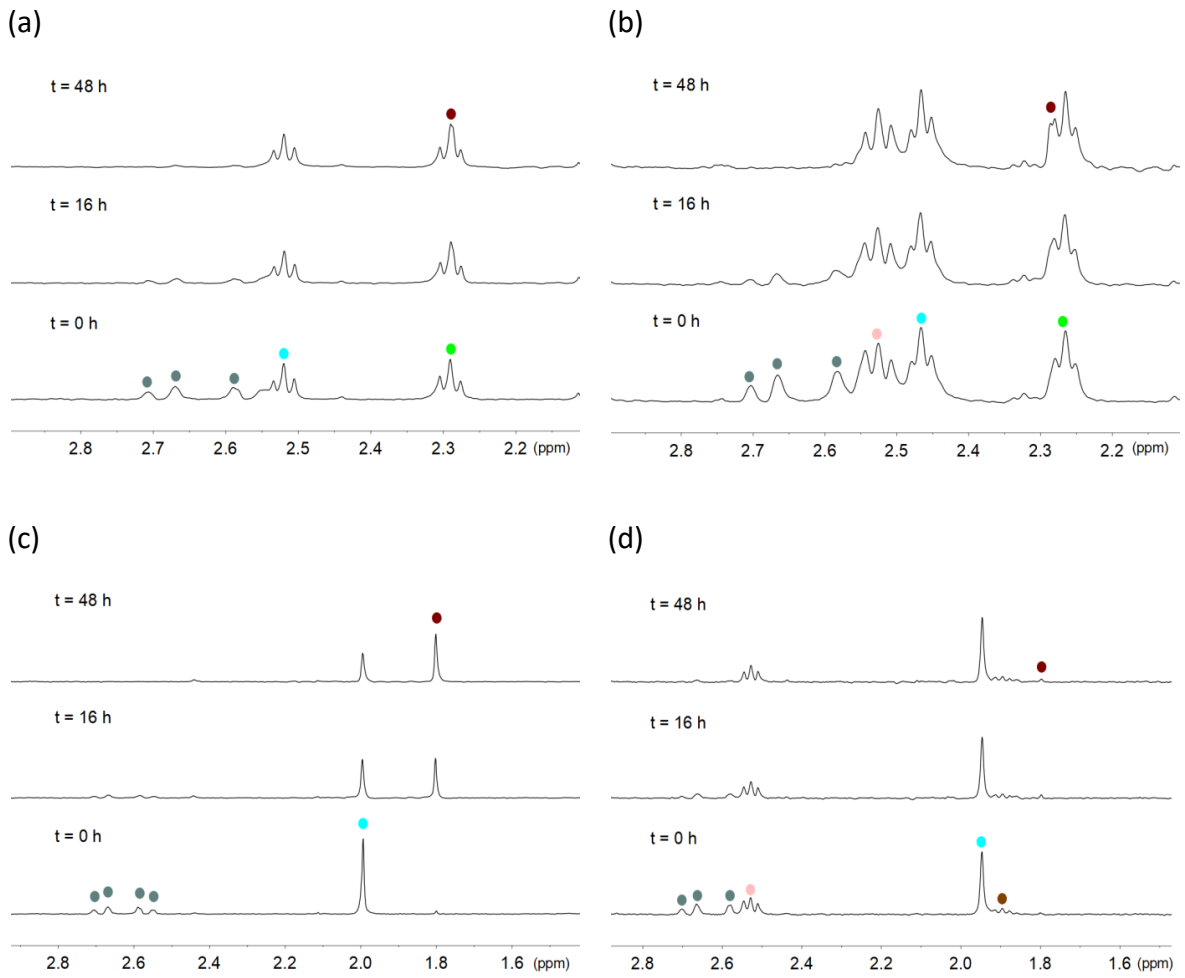

Figure S9. Dark stability of complexes **1**–**4** (500 µM) in 18 mM PB (pH 7.0, 10% D_2O) in the presence of 1 mM NADH and 25 µM **miniSOG** for 48 h.
^{1}H NMR signal labelling: ● NADH, (a) **1**, ● Pt–OCO**CH$_2$**CH$_2$CO$_2^-$, ● Pt–OCOCH$_2$**CH$_2$**CO$_2^-$, ● free $^-$O$_2$C**CH$_2$CH$_2$**CO$_2^-$; (b) **2**, ● Pt–OCO**CH$_2$**CH$_2$CO$_2^-$, ● Pt–OCOCH$_2$**CH$_2$**CO$_2^-$, ● Pt–[(OCO)$_2$C(**CH$_2$**)$_2$**$_2$**CH$_2$], ● free $^-$O$_2$C**CH$_2$CH$_2$**CO$_2^-$; (c) **3**, ● Pt–OCO**CH$_3$**, ● free $^-$OCO**CH$_3$** and (d) **4**, ● Pt–OCO**CH$_3$**, ● Pt–[(OCO)$_2$C(**CH$_2$**)$_2$**$_2$**CH$_2$], ● Pt–[(OCO)$_2$C(CH$_2$)$_2$**CH$_2$**], ● free $^-$OCO**CH$_3$**.

(a)

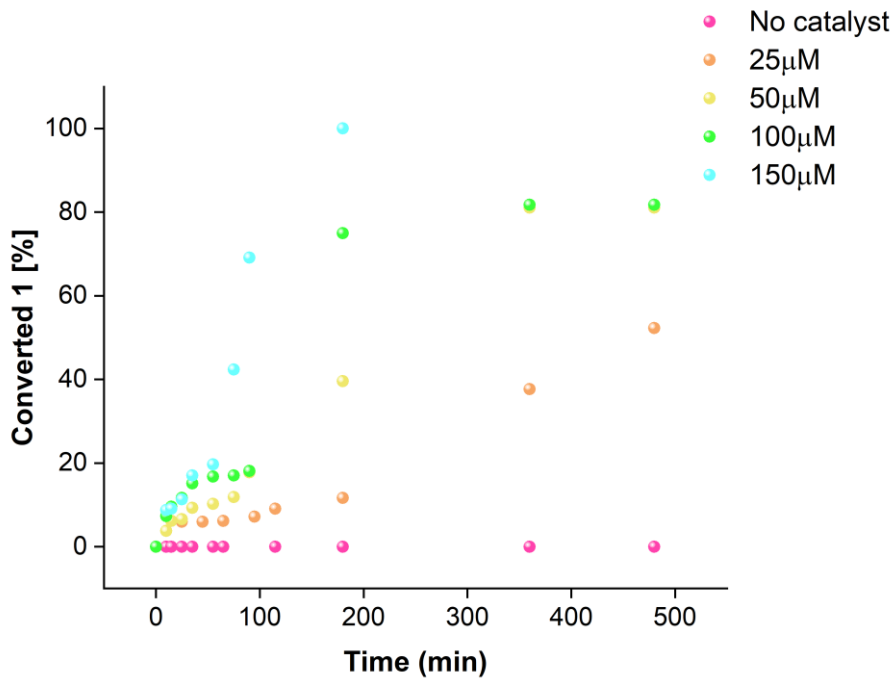

(b)

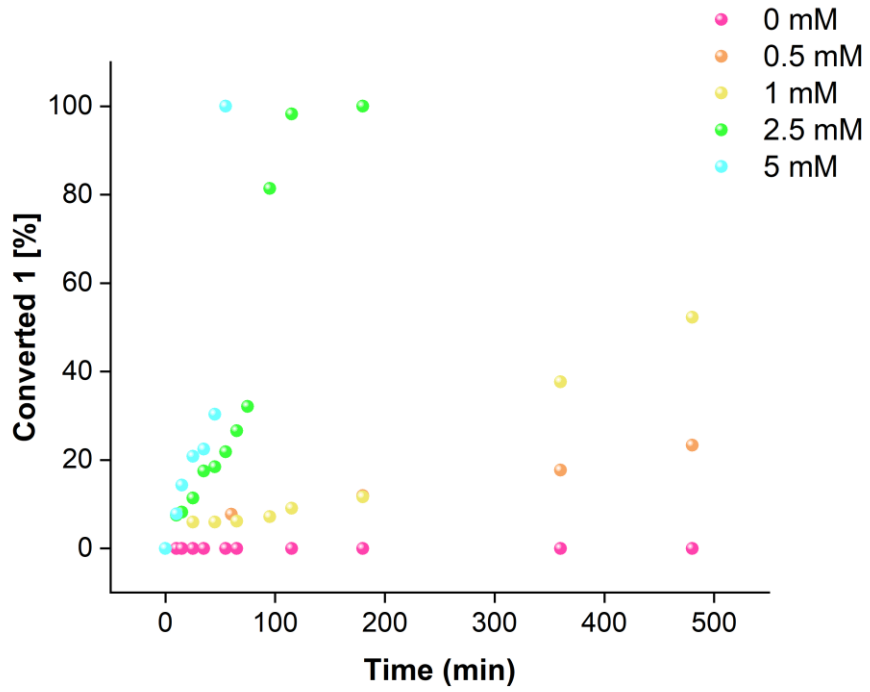

Figure S10. Dark stability of complex **1** (500 µM) in 18 mM PB (pH 7.0, 10% D_2O) in the presence of (a) 0–150 µM **Rf** and 1 mM NADH over time or (b) 25 µM **Rf** and 0–5 mM NADH over time.

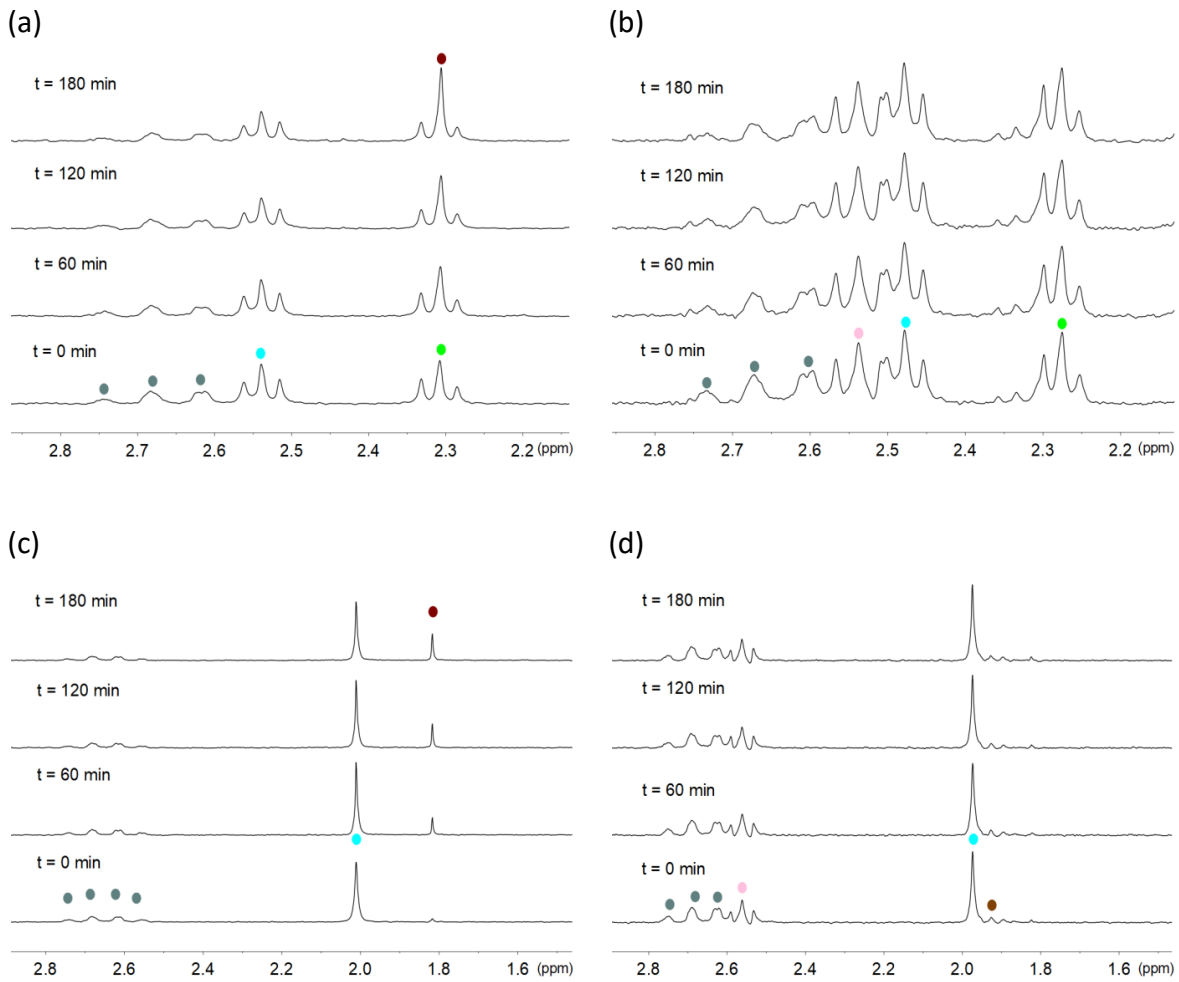

Figure S11. Photostability of complexes **1**–**4** (500 µM) in 18 mM PB (pH 7.0, 10% D_2O) in the presence of 1 mM NADH for 3 hours under 460-nm light irradiation (6 $mW \cdot cm^{-2}$). ^1H NMR signal labelling: ● NADH, (a) **1**, ● Pt–OCO**CH$_2$**$CH_2CO_2^-$, ● Pt–OCOCH_2**CH$_2$**CO_2^-, ● free ^-O_2C**CH$_2$CH$_2$**CO_2^-; (b) **2**, ● Pt–OCO**CH$_2$**$CH_2CO_2^-$, ● Pt–OCOCH_2**CH$_2$**CO_2^-, ● Pt–$[(OCO)_2C($**CH$_2$)$_2$**$CH_2]$; (c) **3**, ● Pt–OCO**CH$_3$**, ● free $^-$OCO**CH$_3$** and (d) **4**, ● Pt–OCO**CH$_3$**, ● Pt–$[(OCO)_2C($**CH$_2$)$_2$**$CH_2]$, ● Pt–$[(OCO)_2C(CH_2)_2$**CH$_2$**$]$.

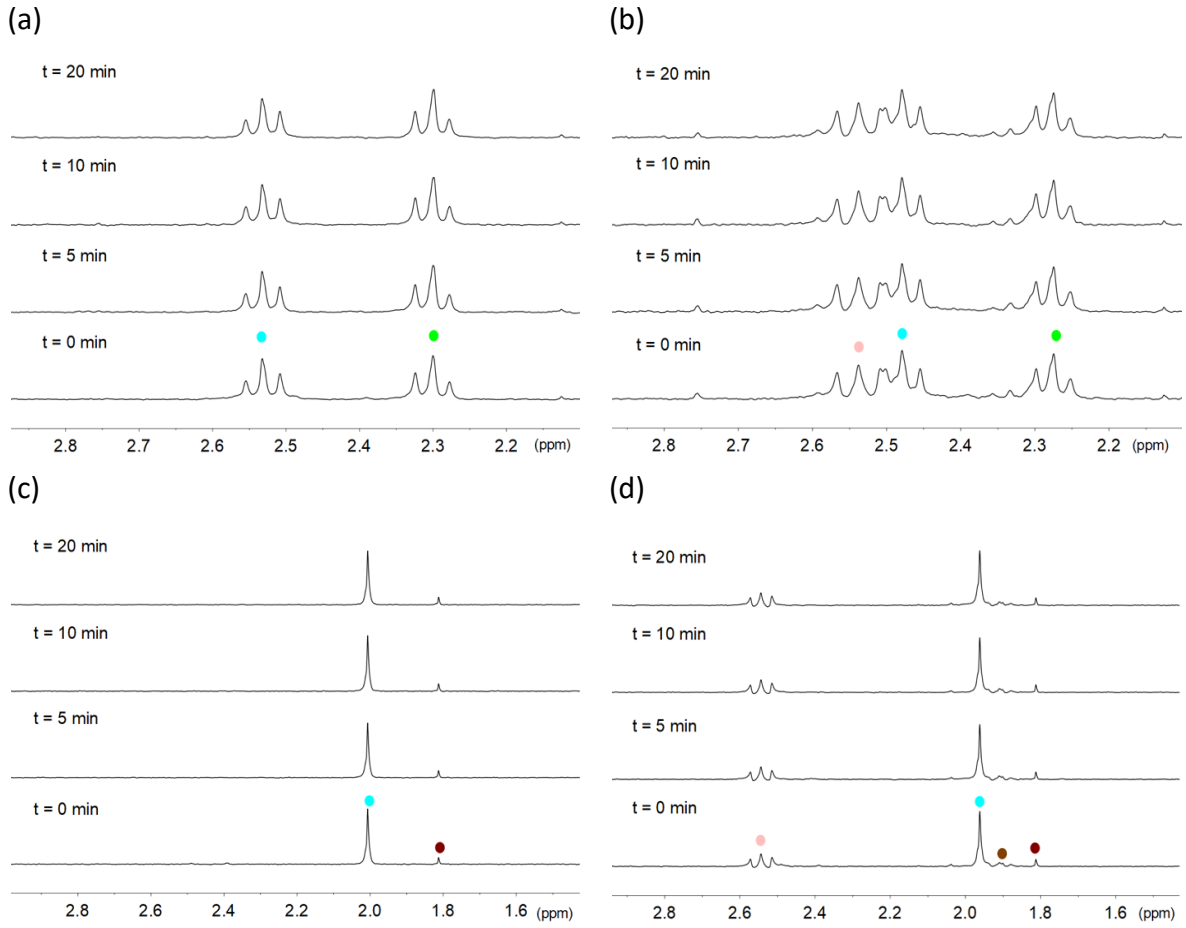

Figure S12. Photostability of complexes **1**–**4** (500 µM) in 18 mM PB (pH 7.0, 10% D_2O) in the presence of 25 µM **Rf** under 460-nm light irradiation (6 $mW \cdot cm^{-2}$).
^1H NMR signal labelling: ● NADH, (a) **1**, ● Pt–OCO**CH_2**$CH_2CO_2^-$, ● Pt–OCOCH_2**CH_2**CO_2^-, ● free ^-O_2C**CH_2CH_2**CO_2^-; (b) **2**, ● Pt–OCO**CH_2**$CH_2CO_2^-$, ● Pt–OCOCH_2**CH_2**CO_2^-, ● Pt–[$(OCO)_2C$(**CH_2**$)_2CH_2$]; (c) **3**, ● Pt–OCO**CH_3**, ● free $^-$OCO**CH_3** and (d) **4**, ● Pt–OCO**CH_3**, ● Pt–[$(OCO)_2C$(**CH_2**$)_2CH_2$], ● Pt–[$(OCO)_2C(CH_2)_2$**CH_2**].

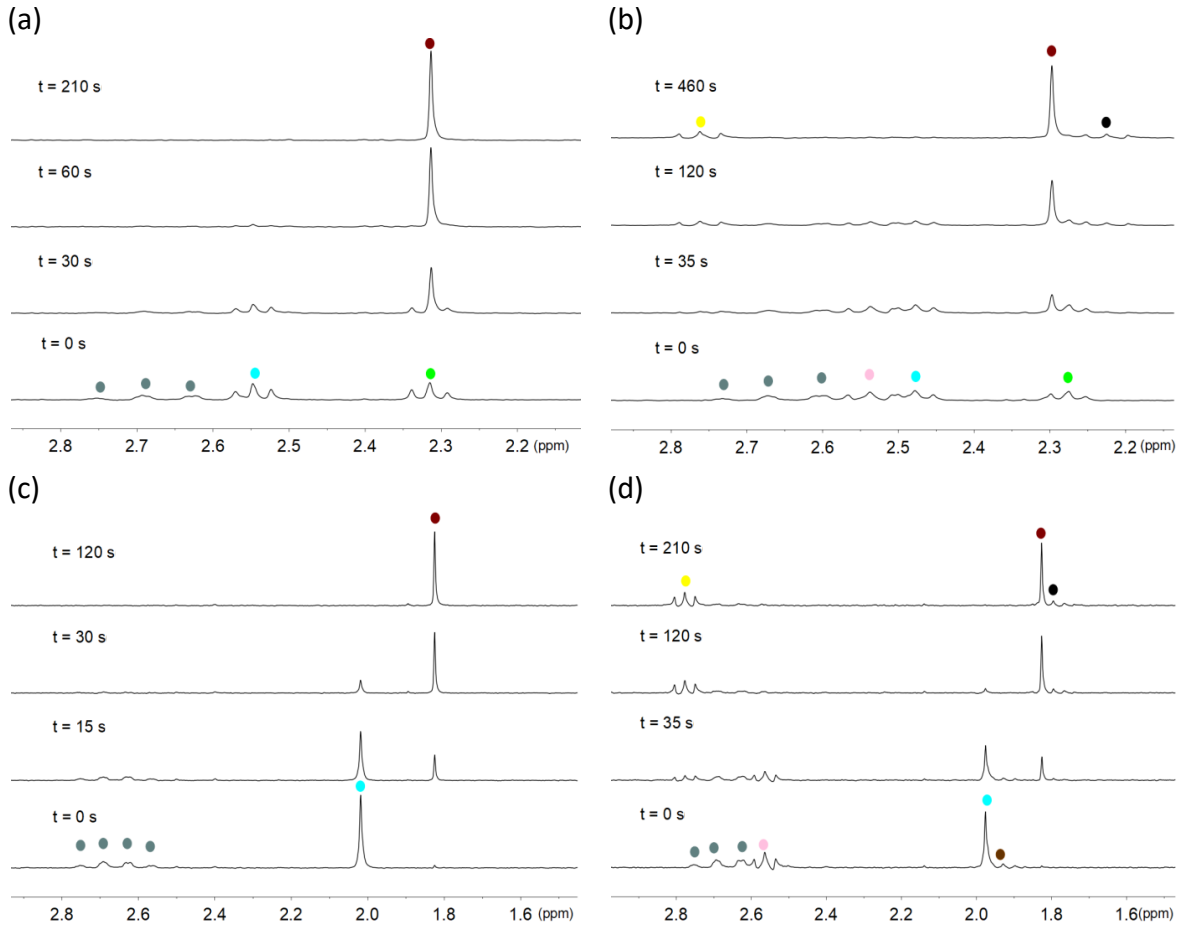

Figure S13. Photocatalytic activation of complexes **1**–**4** (500 µM) in 18 mM PB (pH 7.0, 10% D_2O) in the presence of 1mM NADH and 25 µM **Rf** under 460-nm light irradiation (6 $mW{\cdot}cm^{-2}$).
^1H NMR signal labelling: ● NADH, (a) **1**, ● Pt–OCO**CH$_2$**$CH_2CO_2^-$, ● Pt–$OCOCH_2$**CH$_2$**CO_2^-, ● free ^-O_2C**CH$_2$CH$_2$**CO_2^-; (b) **2**, ● Pt–OCO**CH$_2$**$CH_2CO_2^-$, ● Pt–$OCOCH_2$**CH$_2$**CO_2^-, ● Pt–$[(OCO)_2C($**CH$_2$)$_2$**$CH_2]$, ● free ^-O_2C**CH$_2$CH$_2$**CO_2^-, ● Pt^{II}–$[(OCO)_2C($**CH$_2$)$_2$**$CH_2]$, ● free $[(^-OCO)_2C(CH_2)_2$**CH$_2$**$]$; (c) **3**, ● Pt–OCO**CH$_3$**, ● free $^-$OCO**CH$_3$** and (d) **4**, ● Pt–OCO**CH$_3$**, ● Pt–$[(OCO)_2C($**CH$_2$)$_2$**$CH_2]$, ● Pt–$[(OCO)_2C(CH_2)_2$**CH$_2$**$]$, ● Pt^{II}–$[(OCO)_2C($**CH$_2$)$_2$**$CH_2]$, ● Pt^{II}–$[(OCO)_2C(CH_2)_2$**CH$_2$**$]$, ● free $^-$OCO**CH$_3$**.

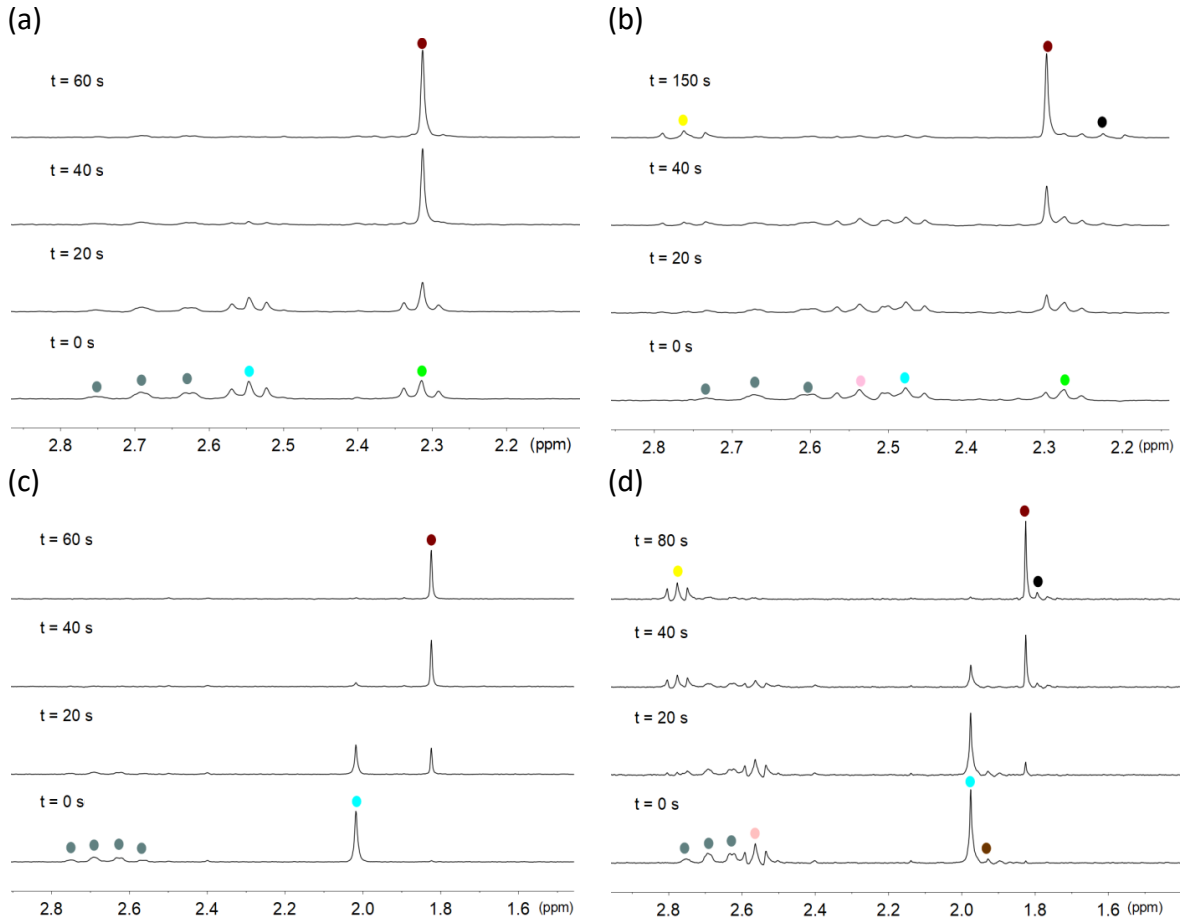

Figure S14. Photocatalytic activation of complexes **1**–**4** (500 µM) in 18 mM PB (pH 7.0, 10% D_2O) in the presence of 1mM NADH and 25 µM **FMN** under 460-nm light irradiation (6 $mW{\cdot}cm^{-2}$).
^1H NMR signal labelling: ● NADH, **1**, (a) ● Pt–OCO**CH$_2$**$CH_2CO_2^-$, ● Pt–$OCOCH_2$**CH_2**CO_2^-, ● free ^-O_2C**CH_2CH_2**CO_2^-; (b) **2**, ● Pt–OCO**CH$_2$**$CH_2CO_2^-$, ● Pt–$OCOCH_2$**CH_2**CO_2^-, ● Pt–$[(OCO)_2C($**$CH_2)_2$**$CH_2]$, ● free ^-O_2C**CH_2CH_2**CO_2^-, ● Pt^{II}–$[(OCO)_2C($**$CH_2)_2$**$CH_2]$, ● free $[(^-OCO)_2C(CH_2)_2$**$CH_2]$**; (c) **3**, ● Pt–OCO**CH$_3$**, ● free ^-OCO**CH_3** and (d) **4**, ● Pt–OCO**CH$_3$**, ● Pt–$[(OCO)_2C($**$CH_2)_2$**$CH_2]$, ● Pt–$[(OCO)_2C(CH_2)_2$**$CH_2]$**, ● Pt^{II}–$[(OCO)_2C($**$CH_2)_2$**$CH_2]$, ● Pt^{II}–$[(OCO)_2C(CH_2)_2$**$CH_2]$**, ● free ^-OCO**CH_3**.

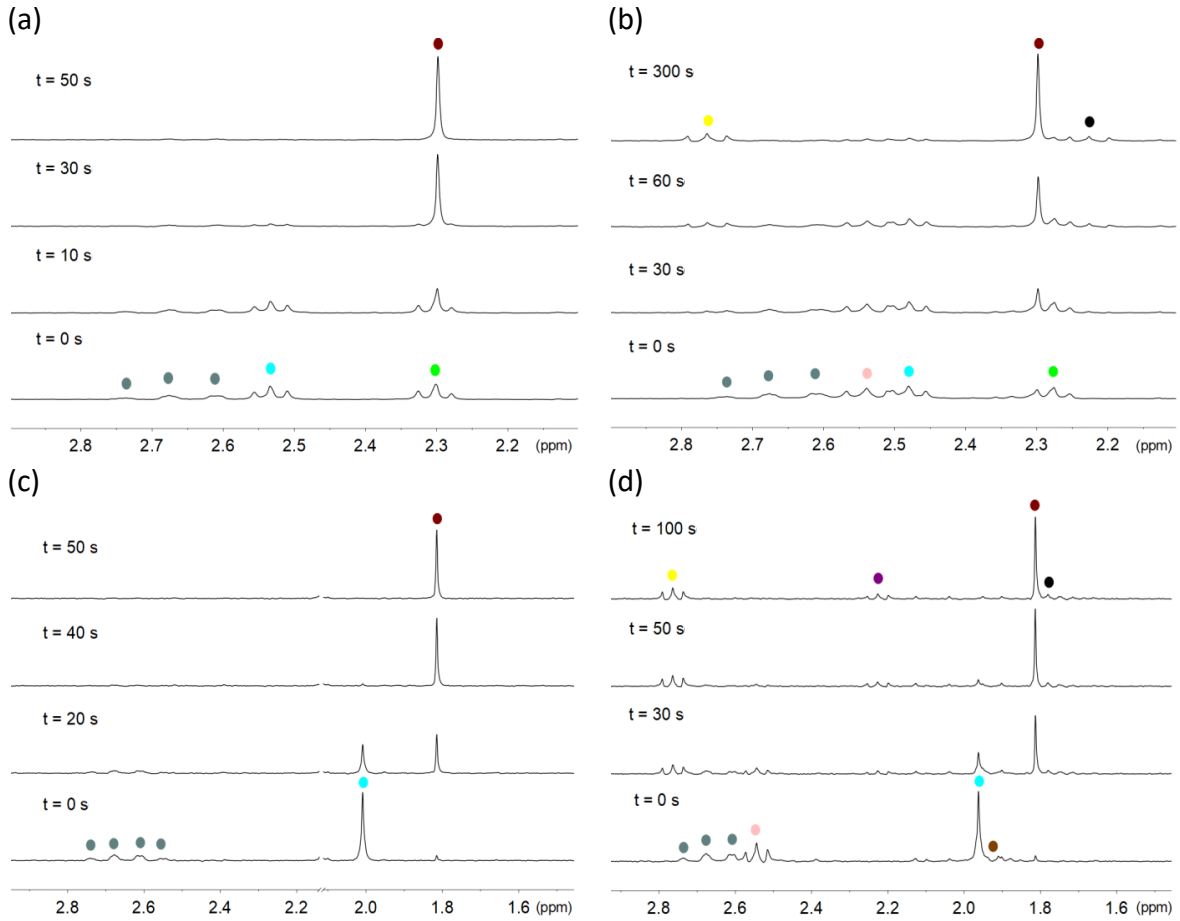

Figure S15. Photocatalytic activation of complexes **1**–**4** (500 µM) in 18 mM PB (pH 7.0, 10% D_2O) in the presence of 1mM NADH and 25 µM **TARF** under 460-nm light irradiation (6 $mW{\cdot}cm^{-2}$).
^1H NMR signal labelling: ● NADH, (a) **1**, ● Pt–OCO**CH$_2$**$CH_2CO_2^-$, ● Pt–$OCOCH_2$**CH_2**CO_2^-, ● free ^-O_2C**CH_2CH_2**CO_2^-; (b) **2**, ● Pt–OCO**CH$_2$**$CH_2CO_2^-$, ● Pt–$OCOCH_2$**CH_2**CO_2^-, ● Pt–$[(OCO)_2C($**$CH_2)_2$**$CH_2]$, ● free ^-O_2C**CH_2CH_2**CO_2^-, ● Pt^{II}–$[(OCO)_2C($**$CH_2)_2$**$CH_2]$, ● free $[(^-OCO)_2C($**$CH_2)_2$**$CH_2]$; (c) **3**, ● Pt–OCO**CH$_3$**, ● free $^-$OCO**CH$_3$** and (d) **4**, ● Pt–OCO**CH$_3$**, ● Pt–$[(OCO)_2C($**$CH_2)_2$**$CH_2]$, ● Pt–$[(OCO)_2C(CH_2)_2$**$CH_2]$, ● Pt^{II}–$[(OCO)_2C($**$CH_2)_2$**$CH_2]$, ● Pt^{II}–$[(OCO)_2C(CH_2)_2$**$CH_2]$, ● free $^-$OCO**CH$_3$**, ● free $[(^-OCO)_2C($**$CH_2)_2$**$CH_2]$.

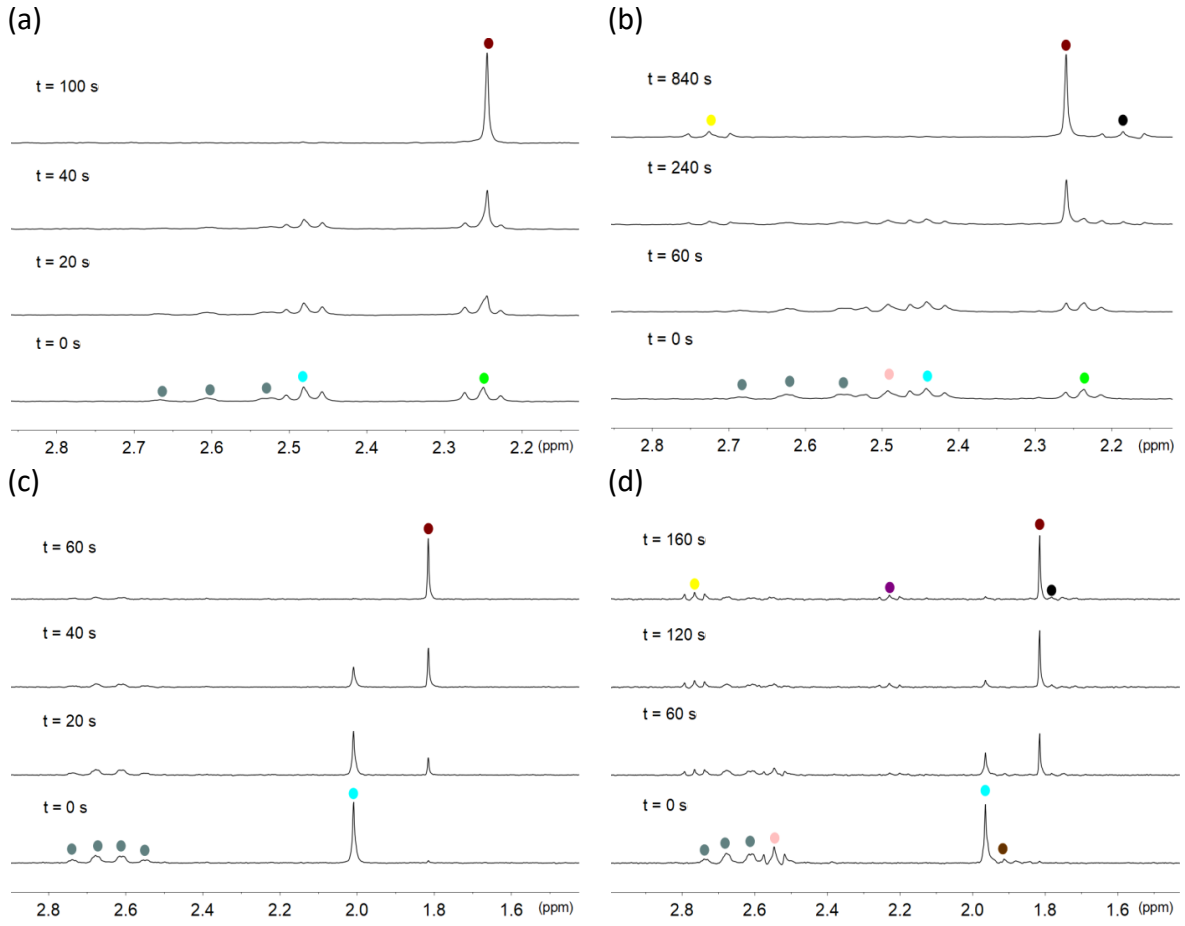

Figure S16. Photocatalytic activation of complexes **1**–**4** (500 µM) in 18 mM PB (pH 7.0, 10% D_2O) in the presence of 1mM NADH and 25 µM **Lf** under 460-nm light irradiation (6 $mW{\cdot}cm^{-2}$).
^1H NMR signal labelling: ● NADH, (a) **1**, ● Pt–OCO**CH_2**$CH_2CO_2^-$, ● Pt–OCOCH_2**CH_2**CO_2^-, ● free ^-O_2C**CH_2CH_2**CO_2^-; (b) **2**, ● Pt–OCO**CH_2**$CH_2CO_2^-$, ● Pt–OCOCH_2**CH_2**CO_2^-, ● Pt–[$(OCO)_2C$(**CH_2**)**$_2$**CH_2], ● free ^-O_2C**CH_2CH_2**CO_2^-, ● Pt^{II}–[$(OCO)_2C$(**CH_2**)**$_2$**CH_2], ● free [($^-$OCO)$_2$C**(CH_2)$_2$**CH_2]; (c) **3**, ● Pt–OCO**CH_3**, ● free $^-$OCO**CH_3** and (d) **4**, ● Pt–OCO**CH_3**, ● Pt–[$(OCO)_2C$(**CH_2**)**$_2$**CH_2], ● Pt–[$(OCO)_2C(CH_2)_2$**CH_2**], ● Pt^{II}–[$(OCO)_2C$(**CH_2**)**$_2$**CH_2], ● Pt^{II}–[$(OCO)_2C(CH_2)_2$**CH_2**], ● free $^-$OCO**CH_3**, ● free [($^-$OCO)$_2$C**(CH_2)$_2$**CH_2].

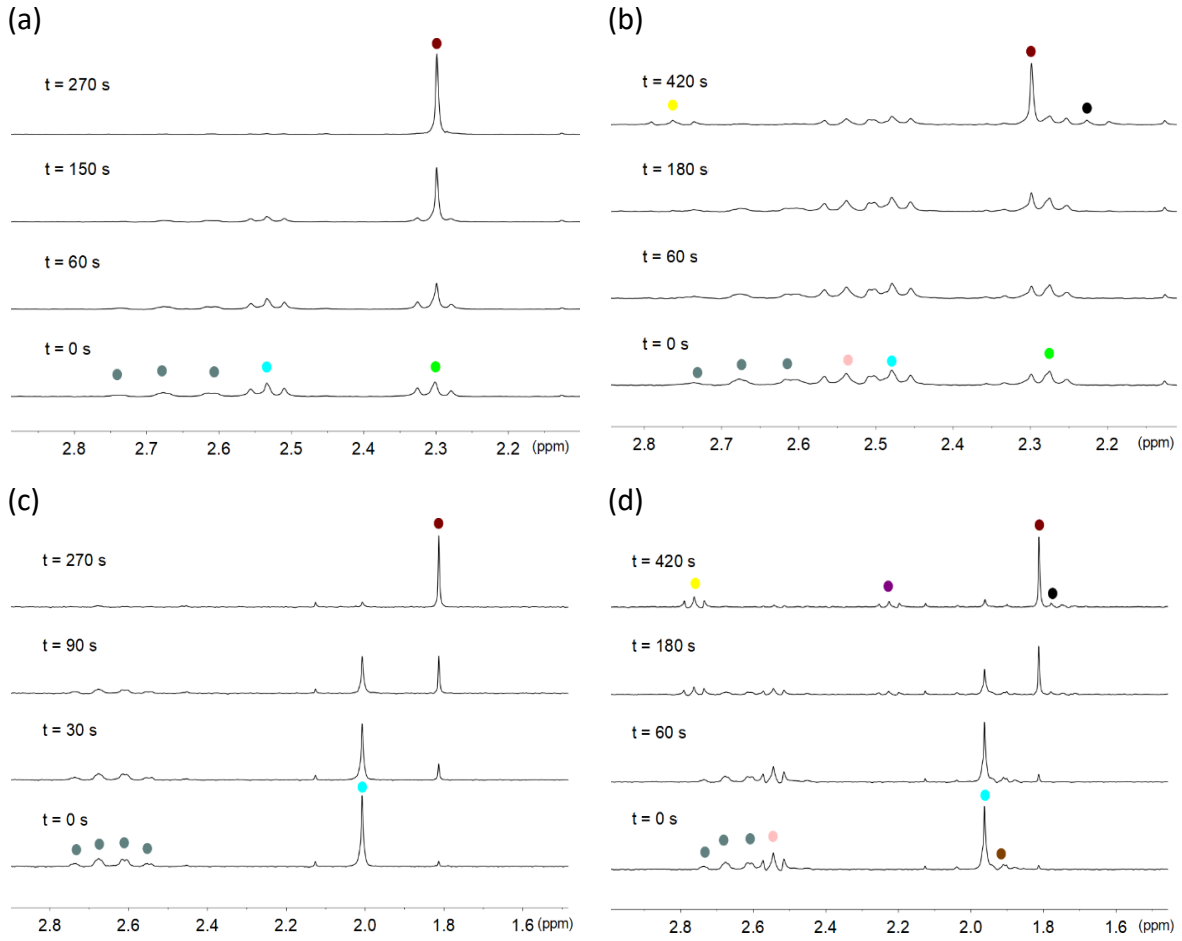

Figure S17. Photocatalytic activation of complexes **1**–**4** (500 µM) in 18 mM PB (pH 7.0, 10% D_2O) in the presence of 1mM NADH and 25 µM **miniSOG** under 460-nm light irradiation (6 $mW{\cdot}cm^{-2}$).
^1H NMR signal labelling: ● NADH, (a) **1**, ● Pt–OCO**CH_2**$CH_2CO_2^-$, ● Pt–$OCOCH_2$**CH_2**CO_2^-, ● free ^-O_2C**CH_2CH_2**CO_2^-; (b) **2**, ● Pt–OCO**CH_2**$CH_2CO_2^-$, ● Pt–$OCOCH_2$**CH_2**CO_2^-, ● Pt–[$(OCO)_2C$(**CH_2**)**$_2$**CH_2], ● free ^-O_2C**CH_2CH_2**CO_2^-, ● Pt^{II}–[$(OCO)_2C$(**CH_2**)**$_2$**CH_2], ● free [($^-$OCO)$_2$C**(CH_2)$_2$**CH_2]; (c) **3**, ● Pt–OCO**CH_3**, ● free $^-$OCO**CH_3** and (d) **4**, ● Pt–OCO**CH_3**, ● Pt–[$(OCO)_2C$(**CH_2**)**$_2$**CH_2], ● Pt–[$(OCO)_2C(CH_2)_2$**CH_2**], ● Pt^{II}–[$(OCO)_2C$(**CH_2**)**$_2$**CH_2], ● Pt^{II}–[$(OCO)_2C(CH_2)_2$**CH_2**], ● free $^-$OCO**CH_3**, ● free [($^-$OCO)$_2$C**(CH_2)$_2$**CH_2].

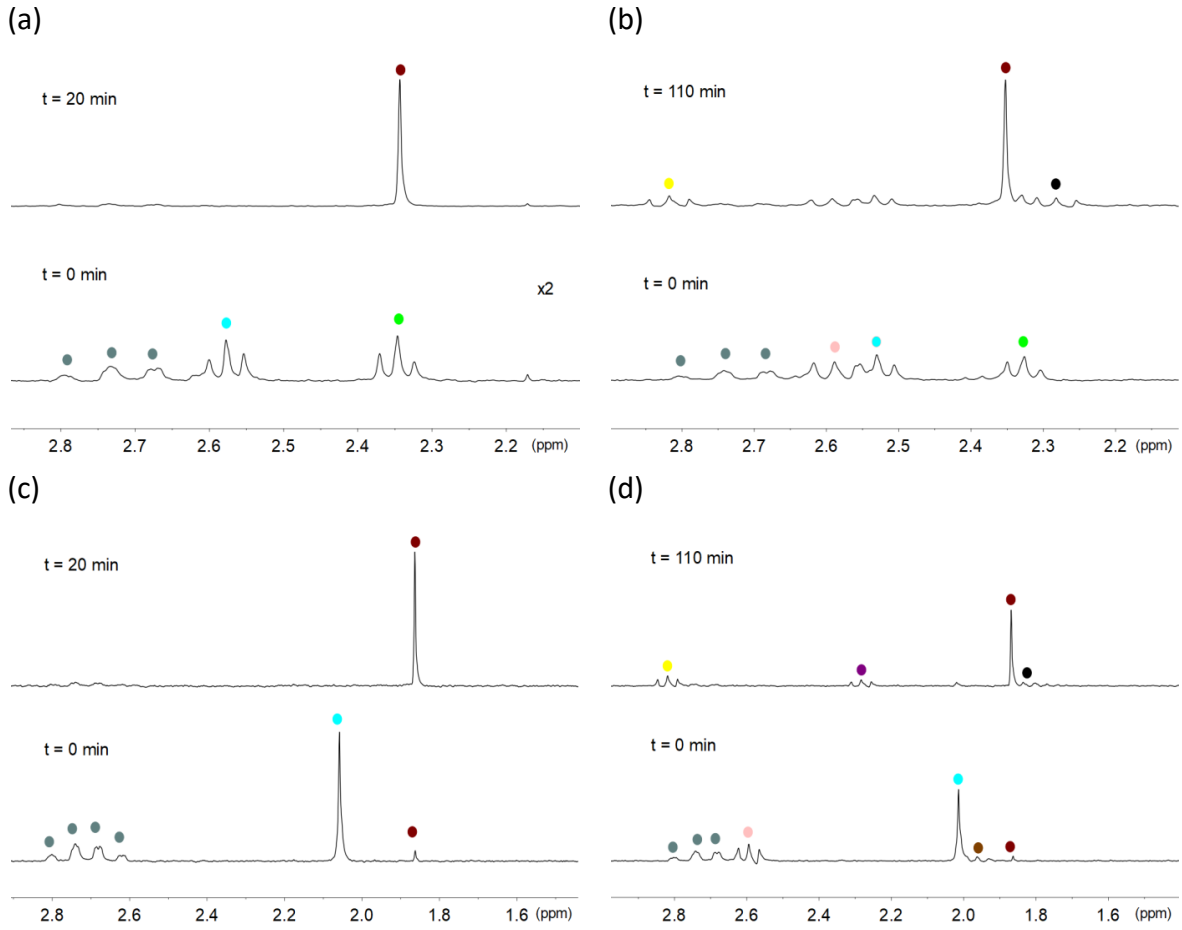

Figure S18. Photocatalytic activation of complexes **1**–**4** (500 µM) in 18 mM PB (pH 7.0, 10% D_2O) in the presence of 1mM NADH and 1 µM **Rf** under 460-nm light irradiation (6 $mW \cdot cm^{-2}$).

^1H NMR signal labelling: ● NADH, (a) **1**, ● Pt–OCO**CH$_2$**$CH_2CO_2^-$, ● Pt–$OCOCH_2$**CH$_2$**CO_2^-, ● free ^-O_2C**CH$_2$CH$_2$**CO_2^-; (b) **2**, ● Pt–OCO**CH$_2$**$CH_2CO_2^-$, ● Pt–$OCOCH_2$**CH$_2$**CO_2^-, ● Pt–[$(OCO)_2C$(**CH$_2$**)$_2$$CH_2$], ● free ^-O_2C**CH$_2CH_2$**CO_2^-, ● Pt^{II}–[$(OCO)_2C$(**CH$_2$**)$_2$$CH_2$], ● free [($^-$OCO)$_2C(CH_2)_2$**CH$_2$**]; (c) **3**, ● Pt–OCO**CH$_3$**, ● free $^-$OCO**CH$_3$** and (d) **4**, ● Pt–OCO**CH$_3$**, ● Pt–[$(OCO)_2C$(**CH$_2$**)$_2$$CH_2$], ● Pt–[$(OCO)_2C(CH_2)_2$**CH$_2$**], ● Pt^{II}–[$(OCO)_2C$(**CH$_2$**)$_2$$CH_2$], ● Pt^{II}–[$(OCO)_2C(CH_2)_2$**CH$_2$**], ● free $^-$OCO**CH$_3$**.

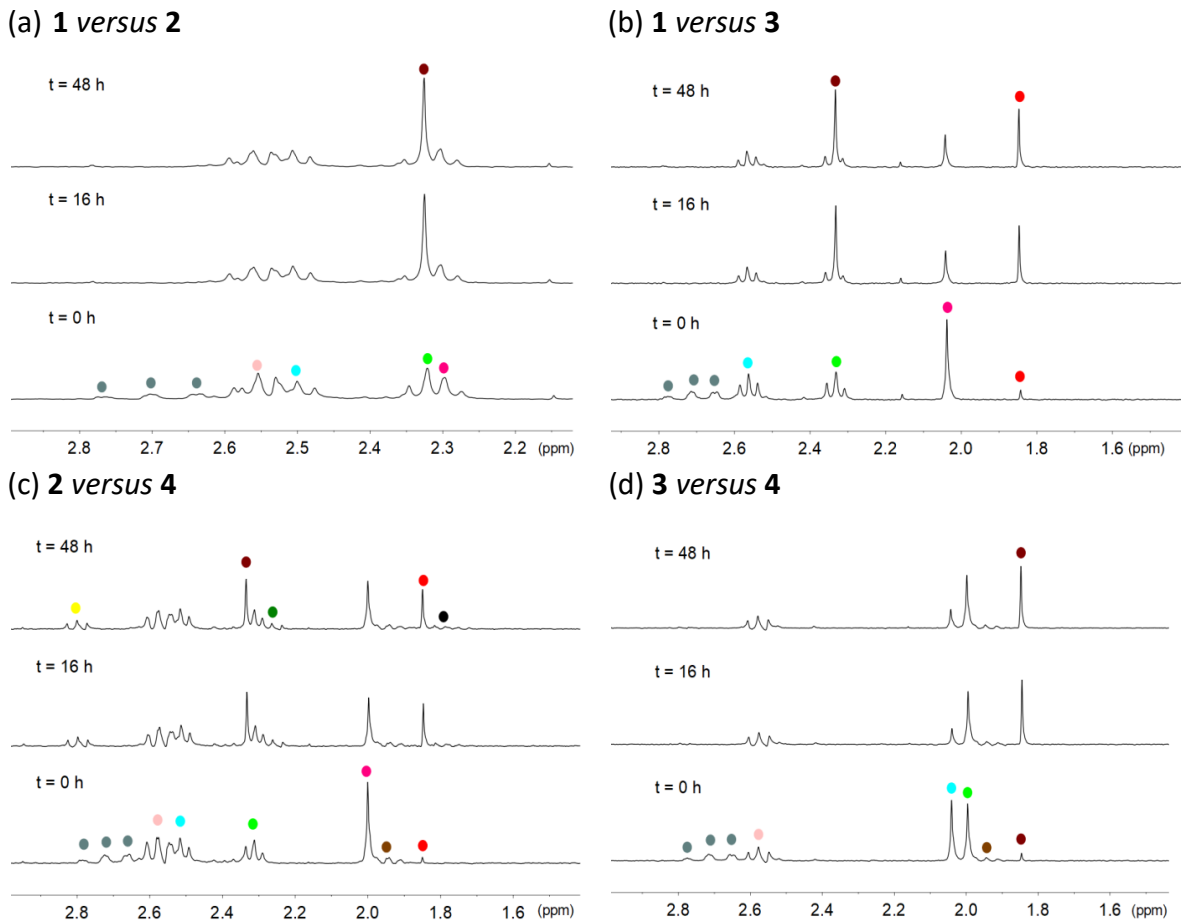

Figure S19. Competitive stability experiments of complexes **1**–**4** (500 µM each substrate) in 18 mM PB (pH 7.0, 10% D_2O) in the presence of 1mM NADH and 25 µM **Rf**.
^{1}H NMR signal labelling: ● NADH, (a) **1**, ● Pt–OCO**CH$_2$**CH$_2$CO$_2^-$, ● Pt–OCOCH$_2$**CH$_2$**CO$_2^-$, ● free $^-$O$_2$C**CH$_2$CH$_2$**CO$_2^-$; **2**, ● Pt–[(OCO)$_2$C(**CH$_2$**)$_2$CH$_2$], ● Pt–OCO**CH$_2$**CH$_2$CO$_2^-$, ● Pt–OCOCH$_2$**CH$_2$**CO$_2^-$; (b) **1**, ● Pt–OCO**CH$_2$**CH$_2$CO$_2^-$, ● Pt–OCOCH$_2$**CH$_2$**CO$_2^-$, ● free $^-$O$_2$C**CH$_2$CH$_2$**CO$_2^-$; **3**, ● Pt–OCO**CH$_3$**, ● free $^-$OCO**CH$_3$**; (c) **2**, ● Pt–[(OCO)$_2$C(**CH$_2$**)$_2$CH$_2$], ● Pt–OCO**CH$_2$**CH$_2$CO$_2^-$, ● Pt–OCOCH$_2$**CH$_2$**CO$_2^-$, ● free [($^-$OCO)$_2$C(CH$_2$)$_2$**CH$_2$**], ● Pt^{II}–[(OCO)$_2$C(**CH$_2$**)$_2$CH$_2$]; ● free $^-$O$_2$C**CH$_2$CH$_2$**CO$_2^-$; **4**, ● Pt–OCO**CH$_3$**, ● Pt–[(OCO)$_2$C(CH$_2$)$_2$**CH$_2$**], ● Pt^{II}–[(OCO)$_2$C(CH$_2$)$_2$**CH$_2$**], ● free $^-$OCO**CH$_3$**, ● Pt^{II}–[(OCO)$_2$C(**CH$_2$**)$_2$CH$_2$] and (d) **3**, ● Pt–OCO**CH$_3$**, ● free $^-$OCO**CH$_3$**; **4**, ● Pt–[(OCO)$_2$C(**CH$_2$**)$_2$CH$_2$], ● Pt–OCO**CH$_3$**, ● Pt–[(OCO)$_2$C(CH$_2$)$_2$**CH$_2$**].

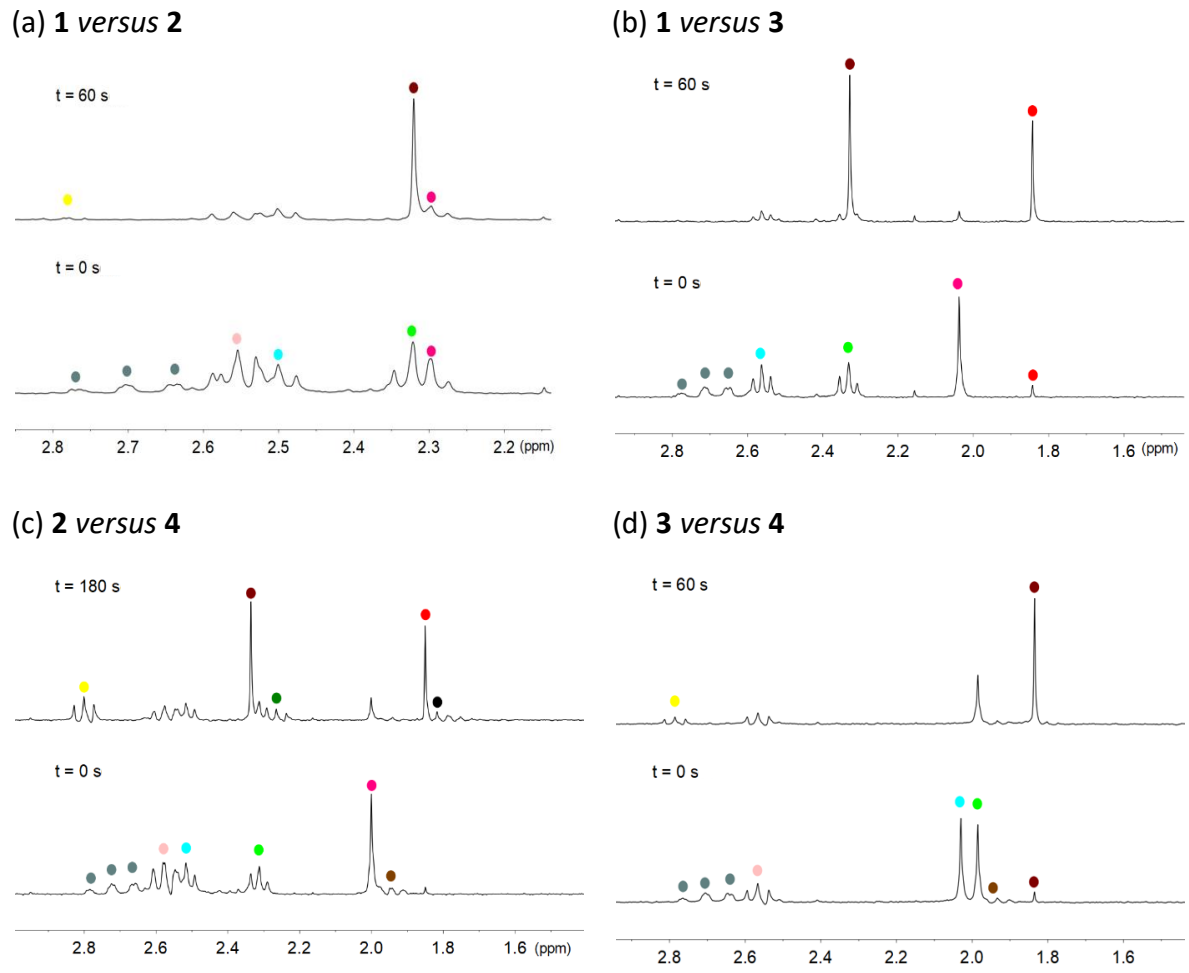

Figure S20. Competitive photocatalytic activation of complexes **1**–**4** (500 µM each substrate) in 18 mM PB (pH 7.0, 10% D_2O) in the presence of 1mM NADH and 25 µM **Rf** under 460-nm light irradiation (6 $mW{\cdot}cm^{-2}$).
^{1}H NMR signal labelling: ● NADH, (a) **1**, ● Pt–OCO**CH_2**$CH_2CO_2^-$, ● Pt–OCOCH$_2$**CH_2**CO_2^-, ● free ^-O_2C**CH_2CH_2**CO_2^-; **2**, ● Pt–[(OCO)$_2$C(**CH_2**)$_2$CH$_2$], ● Pt–OCO**CH_2**$CH_2CO_2^-$, ● Pt–OCOCH$_2$**CH_2**CO_2^-, ● Pt^{II}–[(OCO)$_2$C(**CH_2**)$_2$CH$_2$]; (b) **1**, ● Pt–OCO**CH_2**$CH_2CO_2^-$, ● Pt–OCOCH$_2$**CH_2**CO_2^-, ● free ^-O_2C**CH_2CH_2**CO_2^-; **3**, ● Pt–OCO**CH_3**, ● free $^-$OCO**CH_3**; (c) **2**, ● Pt–[(OCO)$_2$C(**CH_2**)$_2$CH$_2$], ● Pt–OCO**CH_2**$CH_2CO_2^-$, ● Pt–OCOCH$_2$**CH_2**CO_2^-, ● free [($^-$OCO)$_2$C(CH$_2$)$_2$**CH_2**], ● Pt^{II}–[(OCO)$_2$C(**CH_2**)$_2$CH$_2$], ● free ^-O_2C**CH_2CH_2**CO_2^-; **4**, ● Pt–OCO**CH_3**, ● Pt–[(OCO)$_2$C(CH$_2$)$_2$**CH_2**], ● Pt^{II}–[(OCO)$_2$C(CH$_2$)$_2$**CH_2**], ● free $^-$OCO**CH_3**, ● Pt^{II}–[(OCO)$_2$C(**CH_2**)$_2$CH$_2$] and (d) **3**, ● Pt–OCO**CH_3**, ● free $^-$OCO**CH_3**; **4**, ● Pt–[(OCO)$_2$C(**CH_2**)$_2$CH$_2$], ● Pt–OCO**CH_3**, ● Pt–[(OCO)$_2$C(CH$_2$)$_2$**CH_2**], ● free $^-$OCO**CH_3**.

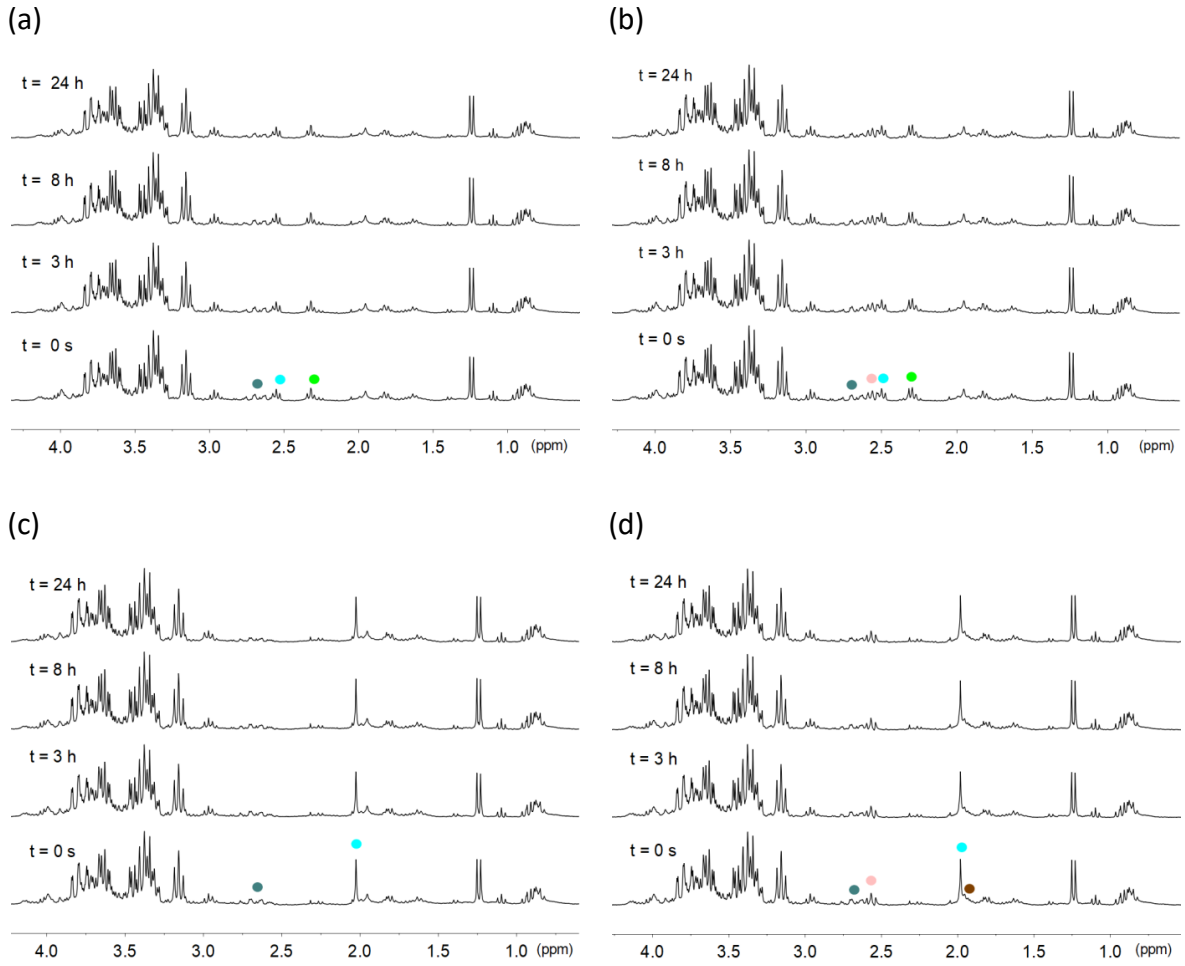

Figure S21. Stability of complexes **1**–**4** (500 µM) in cell culture medium (pH 7.0, 10% D_2O) in the presence of 1mM NADH.
^{1}H NMR signal labelling: ● NADH, (a) **1**, ● Pt–OCO**CH$_2$**CH$_2$CO$_2^-$, ● Pt–OCOCH$_2$**CH$_2$**CO$_2^-$; (b) **2**, ● Pt–OCO**CH$_2$**CH$_2$CO$_2^-$, ● Pt–OCOCH$_2$**CH$_2$**CO$_2^-$, ● Pt–[(OCO)$_2$C(**CH$_2$**)$_2$**$_2$**CH$_2$]; (c) **3**, ● Pt–OCO**CH$_3$** and (d) **4**, ● Pt–OCO**CH$_3$**, ● Pt–[(OCO)$_2$C(**CH$_2$**)$_2$**$_2$**CH$_2$], ● Pt–[(OCO)$_2$C(CH$_2$)$_2$**CH$_2$**].

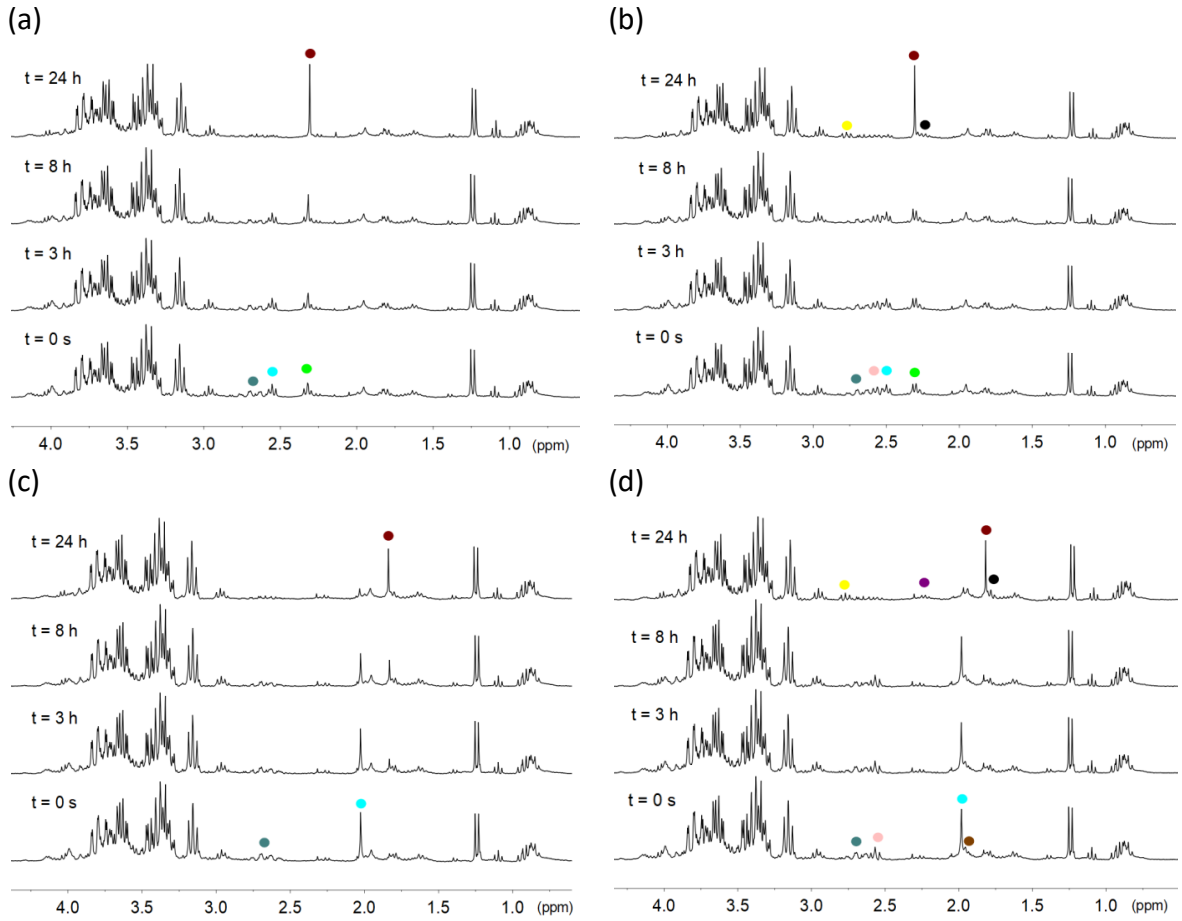

Figure S22. Stability of complexes **1**–**4** (500 µM) in cell culture medium (pH 7.0, 10% D_2O) in the presence of 1mM NADH and 25 µM of **Rf**.
^{1}H NMR signal labelling: ● NADH, (a) **1**, ● Pt–OCO**CH$_2$**CH$_2$CO$_2^-$, ● Pt–OCOCH$_2$**CH$_2$**CO$_2^-$, ● free $^-$O$_2$C**CH$_2$CH$_2$**CO$_2^-$; (b) **2**, ● Pt–OCO**CH$_2$**CH$_2$CO$_2^-$, ● Pt–OCOCH$_2$**CH$_2$**CO$_2^-$, ● Pt–[(OCO)$_2$C(**CH$_2$**)$_2$CH$_2$], ● free $^-$O$_2$C**CH$_2$CH$_2$**CO$_2^-$, ● Pt^{II}–[(OCO)$_2$C(**CH$_2$**)$_2$CH$_2$], ● free [($^-$OCO)$_2$C(CH$_2$)$_2$**CH$_2$**]; (c) **3**, ● Pt–OCO**CH$_3$**, ● free $^-$OCO**CH$_3$** and (d) **4**, ● Pt–OCO**CH$_3$**, ● Pt–[(OCO)$_2$C(**CH$_2$**)$_2$CH$_2$], ● Pt–[(OCO)$_2$C(CH$_2$)$_2$**CH$_2$**], ● Pt^{II}–[(OCO)$_2$C(**CH$_2$**)$_2$CH$_2$], ● Pt^{II}–[(OCO)$_2$C(CH$_2$)$_2$**CH$_2$**], ● free $^-$OCO**CH$_3$**, ● free [($^-$OCO)$_2$C**(CH$_2$)$_2$**CH$_2$].

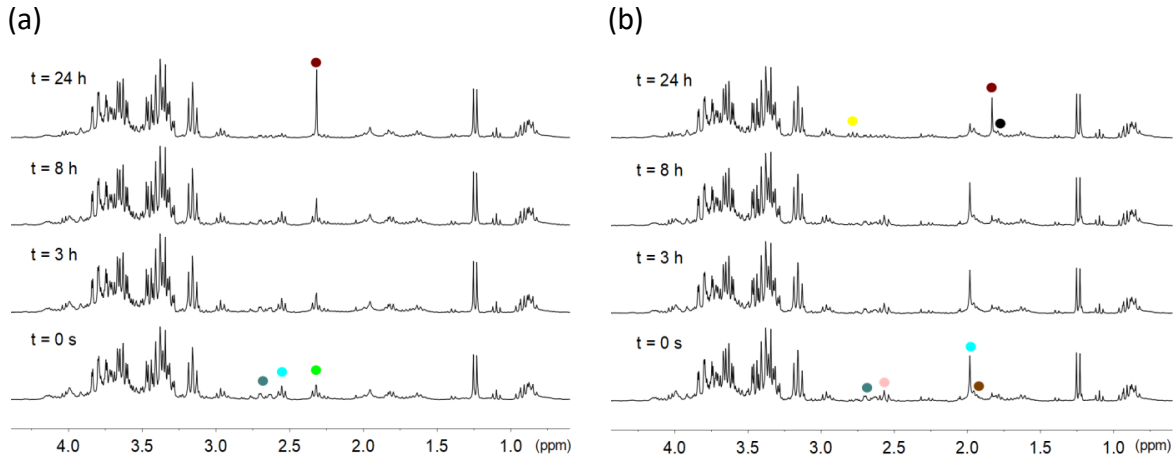

Figure S23. Stability of complexes **1** and **4** (500 µM) in cell culture medium (pH 7.0, 10% D_2O) in the presence of 1mM NADH and 25 µM of **FMN**.
^{1}H NMR signal labelling: ● NADH, (a) **1**, ● Pt–OCO**CH$_2$**CH$_2$CO$_2^-$, ● Pt–OCOCH$_2$**CH$_2$**CO$_2^-$, ● free $^-$O$_2$C**CH$_2$CH$_2$**CO$_2^-$ and (b) **4**, ● Pt–OCO**CH$_3$**, ● Pt–[(OCO)$_2$C(**CH$_2$**)$_2$CH$_2$], ● Pt–[(OCO)$_2$C(CH$_2$)$_2$**CH$_2$**], ● Pt^{II}–[(OCO)$_2$C(**CH$_2$**)$_2$CH$_2$], ● Pt^{II}–[(OCO)$_2$C(CH$_2$)$_2$**CH$_2$**], ● free $^-$OCO**CH$_3$**.

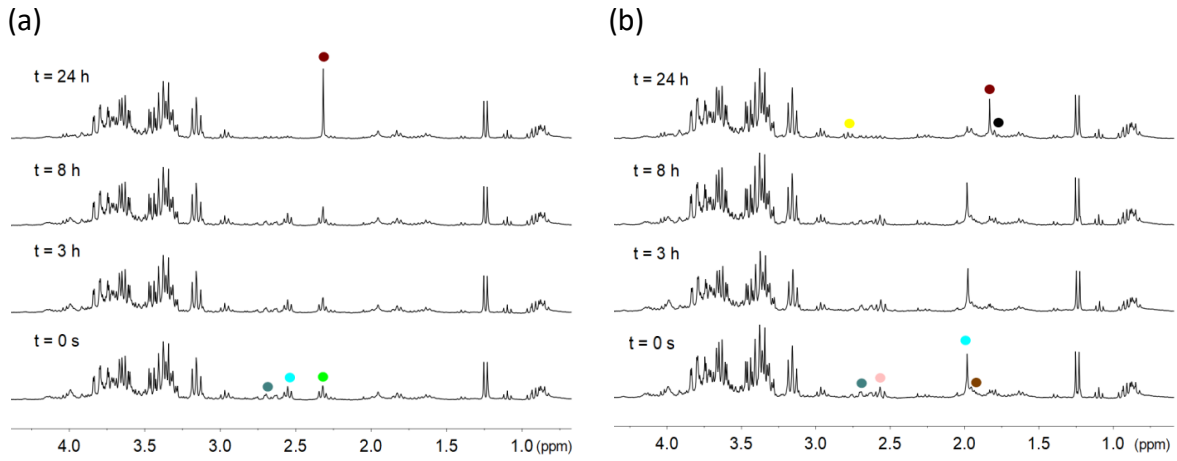

Figure S24. Stability of complexes **1** and **4** (500 µM) in cell culture medium (pH 7.0, 10% D_2O) in the presence of 1mM NADH and 25 µM of **Lf**.
^{1}H NMR signal labelling: ● NADH, (a) **1**, ● Pt–OCO**CH$_2$**CH$_2$CO$_2^-$, ● Pt–OCOCH$_2$**CH$_2$**CO$_2^-$, ● free $^-$O$_2$C**CH$_2$CH$_2$**CO$_2^-$ and (b) **4**, ● Pt–OCO**CH$_3$**, ● Pt–[(OCO)$_2$C(**CH$_2$**)$_2$CH$_2$], ● Pt–[(OCO)$_2$C(CH$_2$)$_2$**CH$_2$**], ● Pt^{II}–[(OCO)$_2$C(**CH$_2$**)$_2$CH$_2$], ● Pt^{II}–[(OCO)$_2$C(CH$_2$)$_2$**CH$_2$**], ● free $^-$OCO**CH$_3$**.

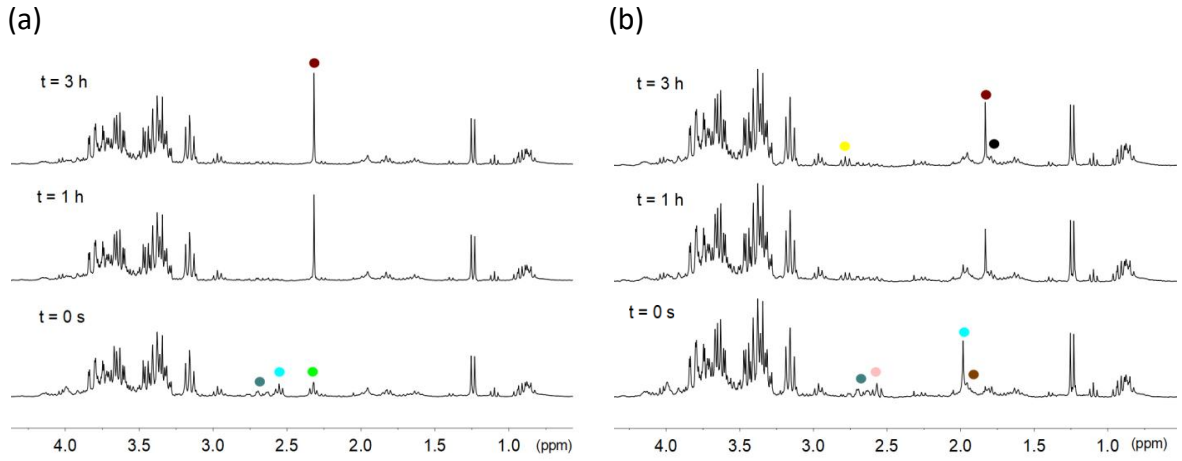

Figure S25. Stability of complexes **1** and **4** (500 µM) in cell culture medium (pH 7.0, 10% D_2O) in the presence of 1mM NADH and 25 µM of **TARF**.
^{1}H NMR signal labelling: ● NADH, (a) **1**, ● Pt–OCO**CH$_2$**CH$_2$CO$_2^-$, ● Pt–OCOCH$_2$**CH$_2$**CO$_2^-$, ● free $^-$O$_2$C**CH$_2$CH$_2$**CO$_2^-$ and (b) **4**, ● Pt–OCO**CH$_3$**, ● Pt–[(OCO)$_2$C(**CH$_2$**)$_2$**$_2$**CH$_2$], ● Pt–[(OCO)$_2$C(CH$_2$)$_2$**CH$_2$**], ● Pt^{II}–[(OCO)$_2$C(**CH$_2$**)$_2$**$_2$**CH$_2$], ● Pt^{II}–[(OCO)$_2$C(CH$_2$)$_2$**CH$_2$**], ● free $^-$OCO**CH$_3$**.

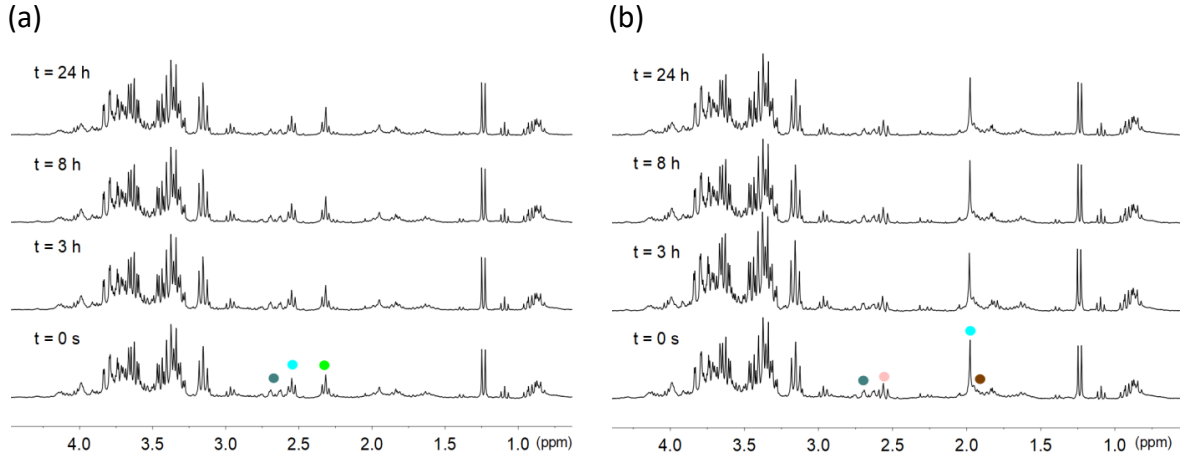

Figure S26. Stability of complexes **1** and **4** (500 µM) in cell culture medium (pH 7.0, 10% D_2O) in the presence of 1mM NADH and 25 µM of **miniSOG**.
^{1}H NMR signal labelling: ● NADH, (a) **1**, ● Pt–OCO**CH$_2$**CH$_2$CO$_2^-$, ● Pt–OCOCH$_2$**CH$_2$**CO$_2^-$, ● free $^-$O$_2$C**CH$_2$CH$_2$**CO$_2^-$ and (b) **4**, ● Pt–OCO**CH$_3$**, ● Pt–[(OCO)$_2$C(**CH$_2$**)$_2$**$_2$**CH$_2$], ● Pt–[(OCO)$_2$C(CH$_2$)$_2$**CH$_2$**], ● Pt^{II}–[(OCO)$_2$C(**CH$_2$**)$_2$**$_2$**CH$_2$], ● Pt^{II}–[(OCO)$_2$C(CH$_2$)$_2$**CH$_2$**], ● free $^-$OCO**CH$_3$**.

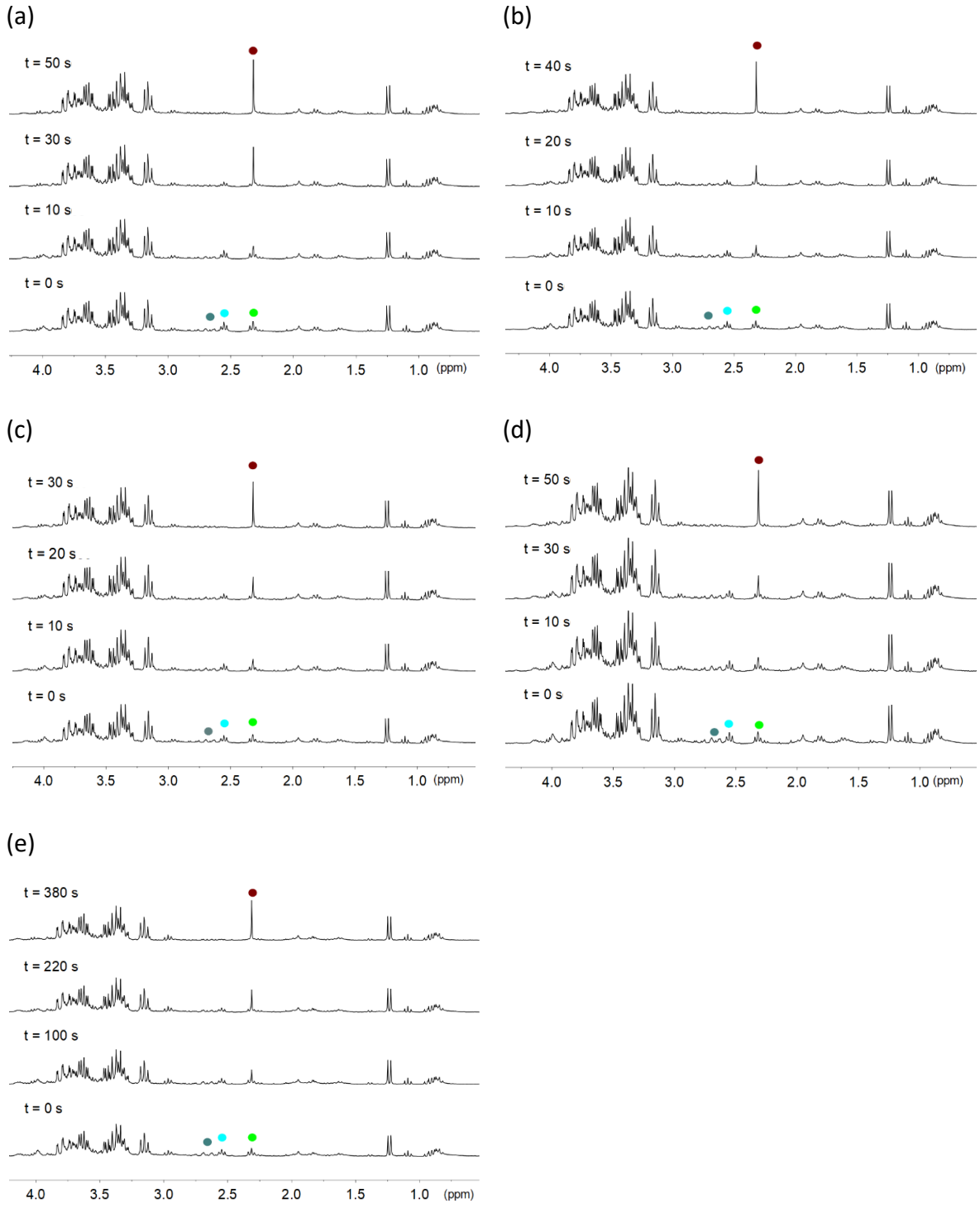

Figure S27. Photocatalytic activation of complex **1** (500 µM) in cell culture medium (pH 7.0, 10% D_2O) in the presence of 1mM NADH and 25 µM of a) **Rf**; b) **FMN**; c) **TARF**; d) **Lf**; e) **miniSOG**, under 460-nm light irradiation (6 mW·cm^{-2}).
^{1}H NMR signal labelling: ● NADH, ● Pt–OCO**CH$_2$**CH$_2$CO$_2^-$, ● Pt–OCOCH$_2$**CH$_2$**CO$_2^-$, ● free $^-$O$_2$C**CH$_2$CH$_2$**CO$_2^-$.

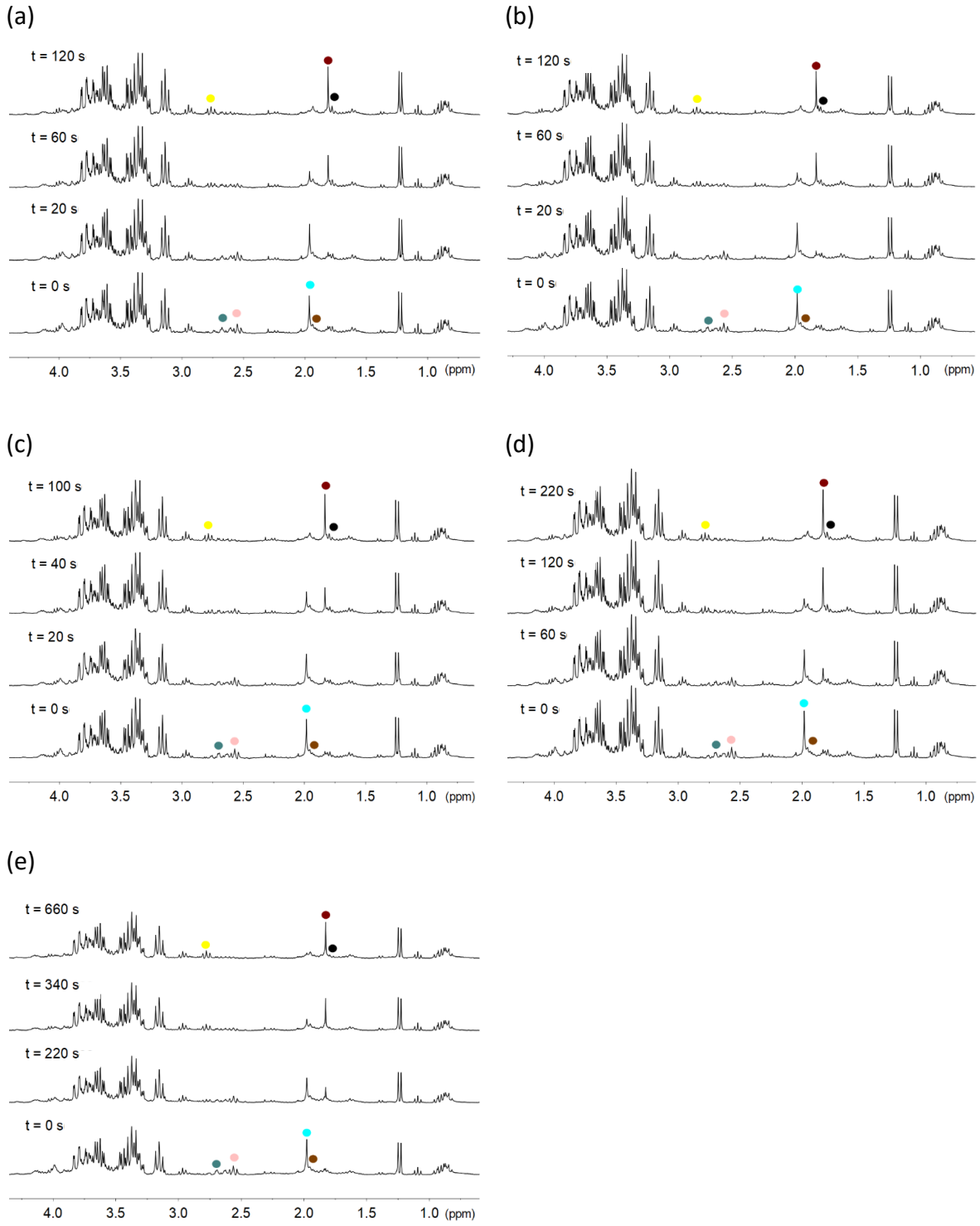

Figure S28. Photocatalytic activation of complex **4** (500 µM) in RPMI-1640 medium (pH 7.0, 10% D_2O) in the presence of 1mM NADH and 25 µM of (a) **Rf**; (b) **FMN**; (c) **TARF**; (d) **Lf**; (e) **miniSOG**, under 460-nm light irradiation (6 $mW{\cdot}cm^{-2}$).
^1H NMR signal labelling: ● NADH, ● Pt–OCO**CH_3**, ● Pt–[$(OCO)_2C(\mathbf{CH_2})_2CH_2$], ● Pt–[$(OCO)_2C(CH_2)_2\mathbf{CH_2}$], ● Pt^{II}–[$(OCO)_2C(\mathbf{CH_2})_2CH_2$], ● Pt^{II}–[$(OCO)_2C(CH_2)_2\mathbf{CH_2}$], ● free $^-$OCO**CH_3**.

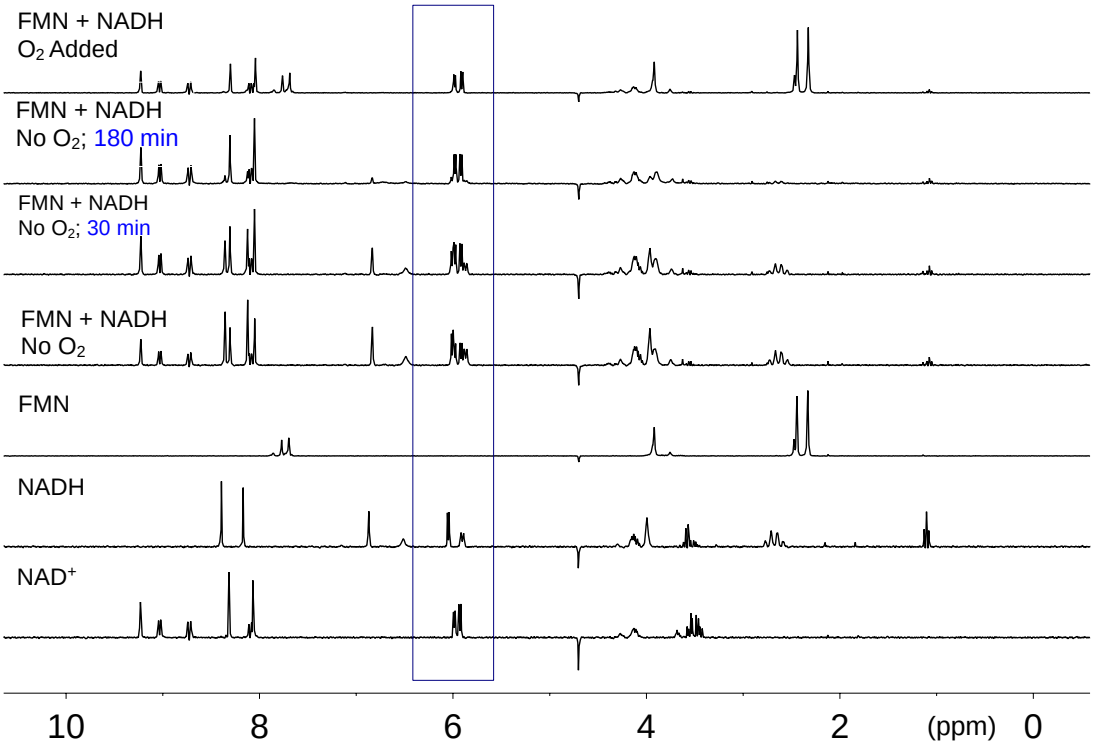

Figure S29. Time course of NADH oxidation in the presence of **FMN** (1:1, 3 mM) in 18 mM PB (pH 7.0, 10% D_2O) under dark. The ribose H1 and H1' diagnostic peaks for NADH-to-NAD^+ conversion are highlighted in the blue box.

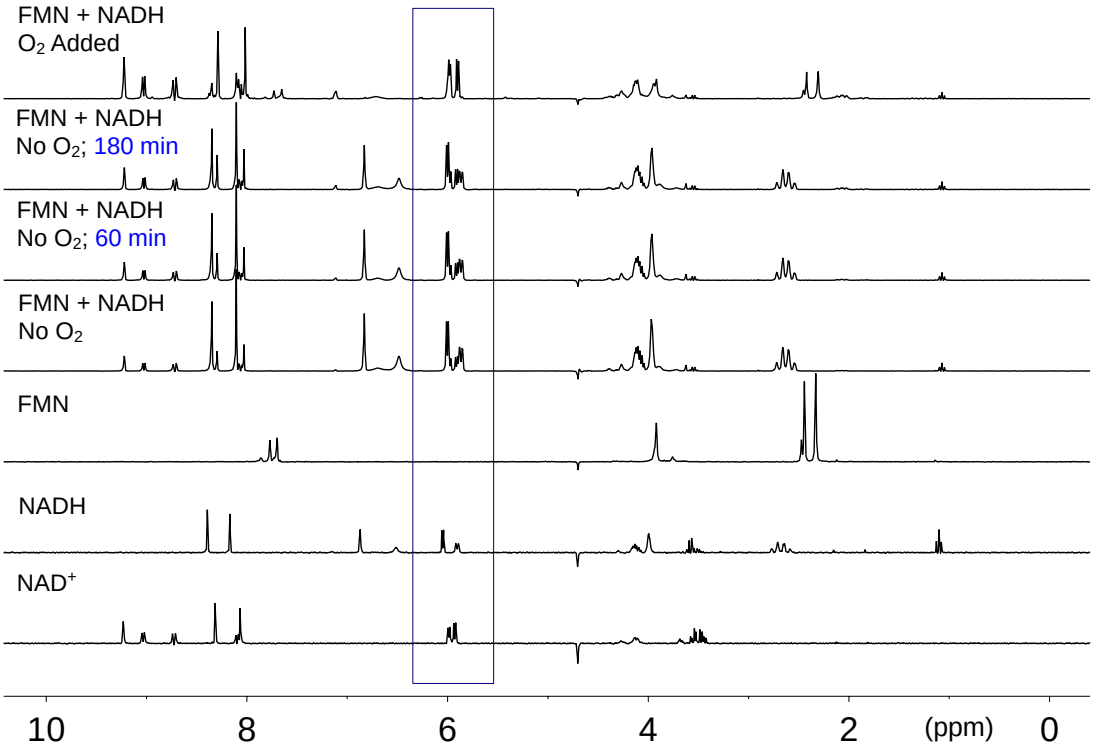

Figure S30. Time course of NADH oxidation in the presence of **FMN** (5:1, 15:3 mM) in 18 mM PB (pH 7.0, 10% D_2O) under dark conditions. The ribose H1 and H1' diagnostic peaks for NADH-to-NAD^+ conversion are highlighted in the blue box.

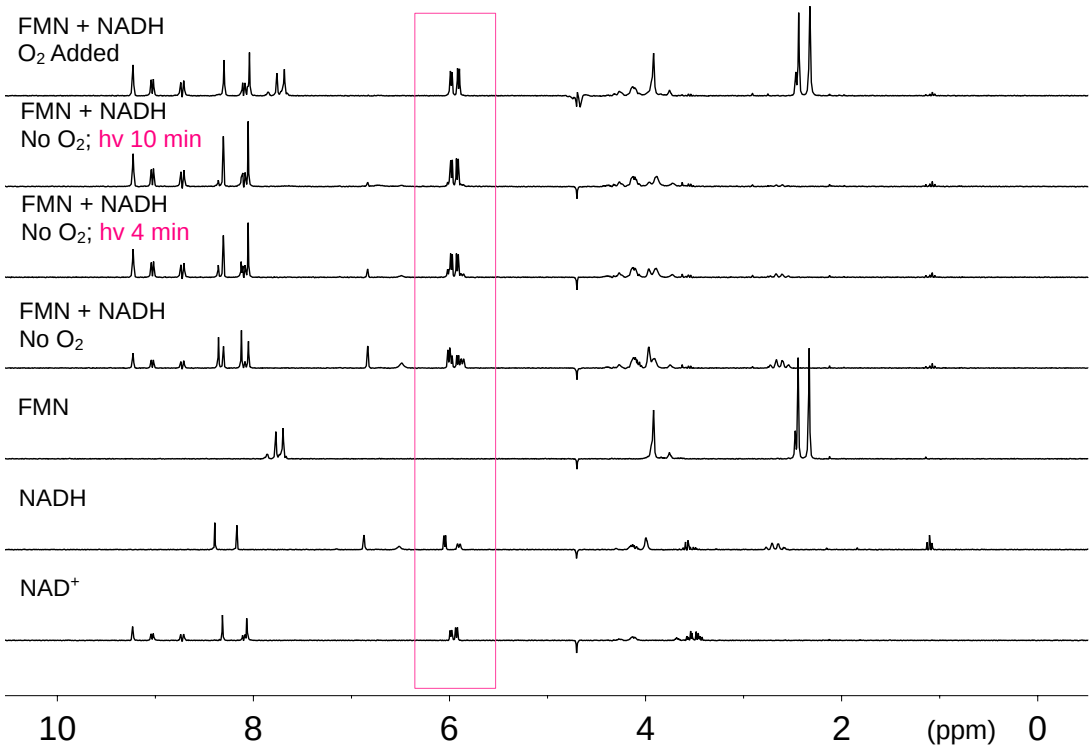

Figure S31. Time course of NADH oxidation in the presence of **FMN** (1:1, 3 mM) in 18 mM PB (pH 7.0, 10% D_2O) under 460-nm light irradiation (6 $mW \cdot cm^{-2}$). The ribose H1 and H1' diagnostic peaks for NADH-to-NAD^+ conversion are highlighted in the blue box.

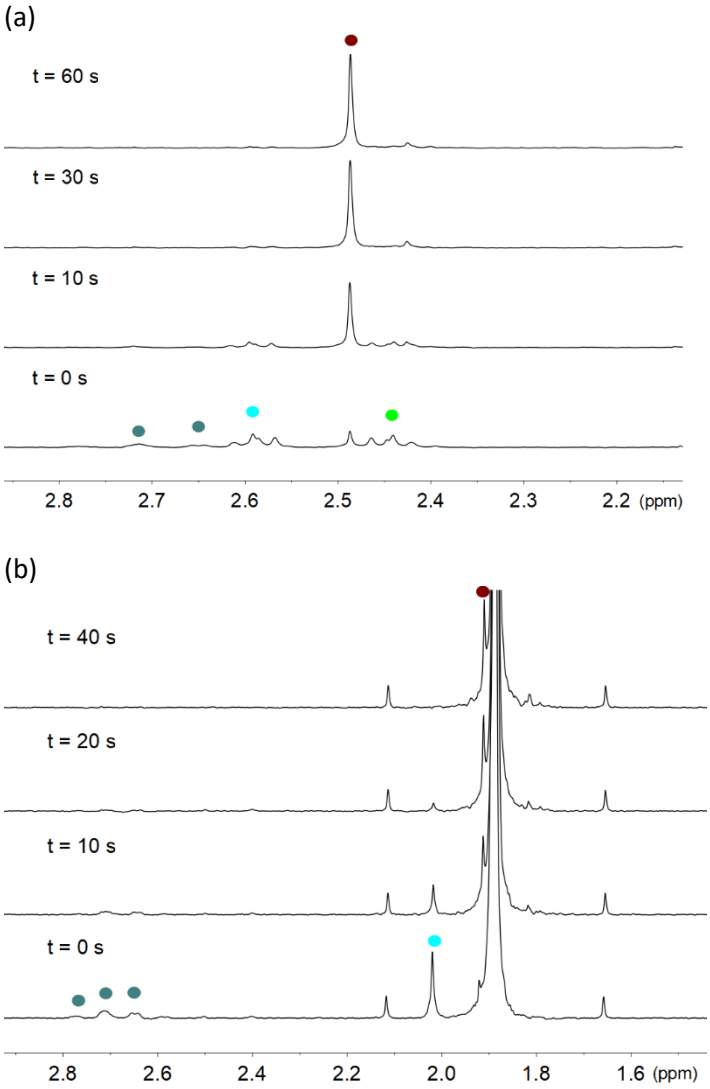

Figure S32. Photocatalytic activation of complexes **1** and **3** (500 µM) in 18 mM cacodylate (pH 4.3, 10% D_2O) in the presence of 1mM NADH and 25 µM **FMN** under 460-nm light irradiation (6 $mW{\cdot}cm^{-2}$). ^1H NMR signal labelling: ● NADH, **1**, (a) ● Pt–OCO**CH_2**$CH_2CO_2^-$, ● Pt–OCOCH_2**CH_2**CO_2^-, ● free ^-O_2C**CH_2CH_2**CO_2^-; (b) **3**, ● Pt–OCO**CH_3**, ● free $^-$OCO**CH_3**.

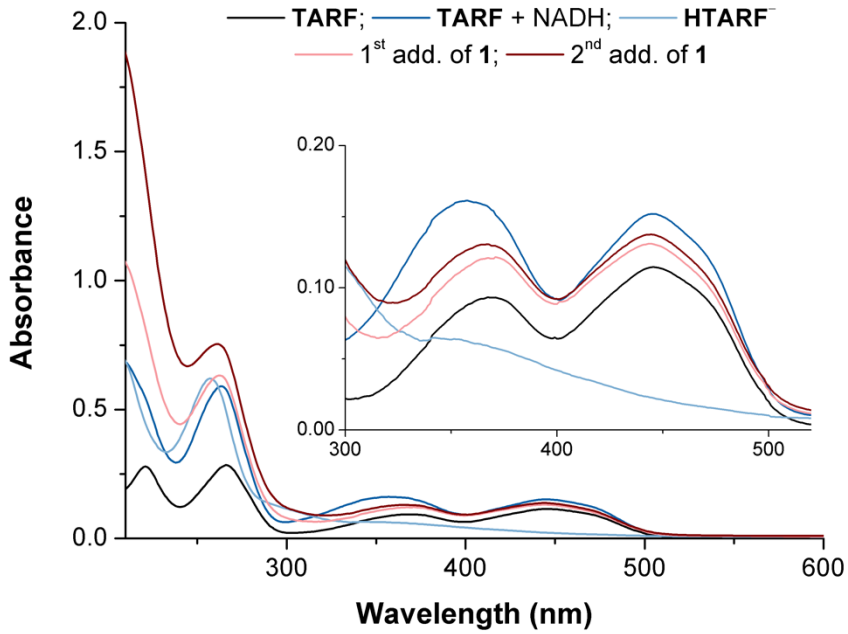

Figure S33. Generation of **HTARF**$^{-}$ and its oxidation by **1** (18 mM PB, pH 7.5) in the absence of O_2 monitored by UV-Vis. **HTARF**$^{-}$ was obtained upon 460-nm irradiation (90 s) of **TARF** (15 µM) in the presence of equimolar NADH under an oxygen-free atmosphere.

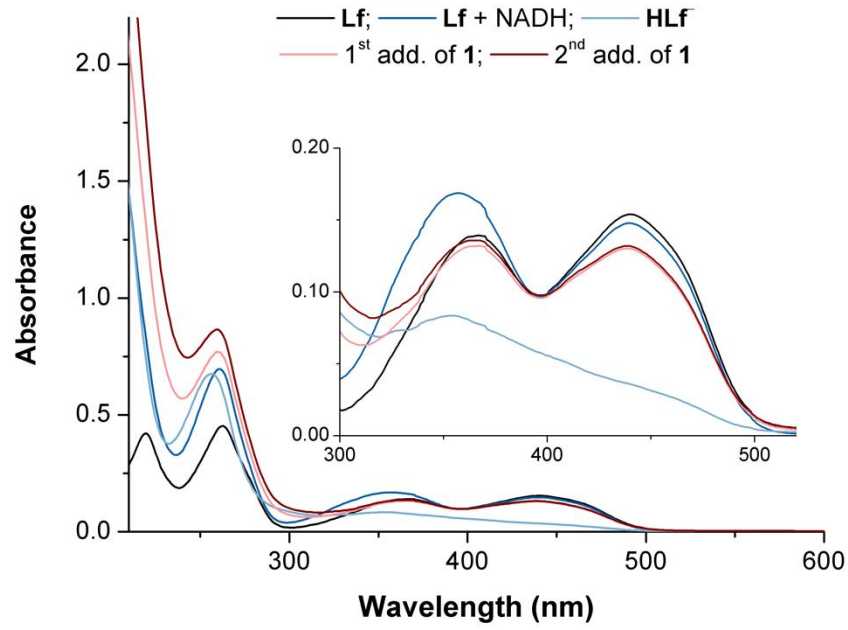

Figure S34. Generation of **HLf**$^{-}$ and its oxidation by **1** (18 mM PB, pH 7.5) in the absence of O_2 monitored by UV-Vis. **HLf**$^{-}$ was obtained upon 460-nm irradiation of **Lf** (15 µM) in the presence of equimolar NADH under an oxygen-free atmosphere.

(a)

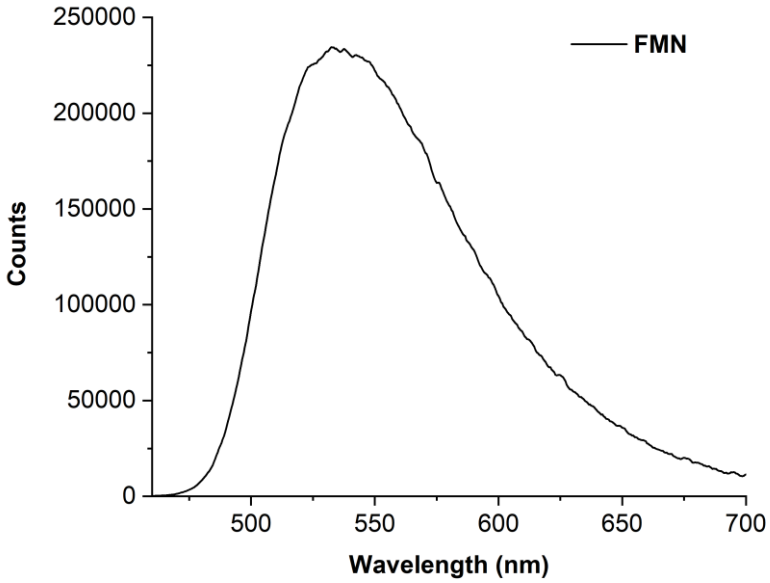

(b)

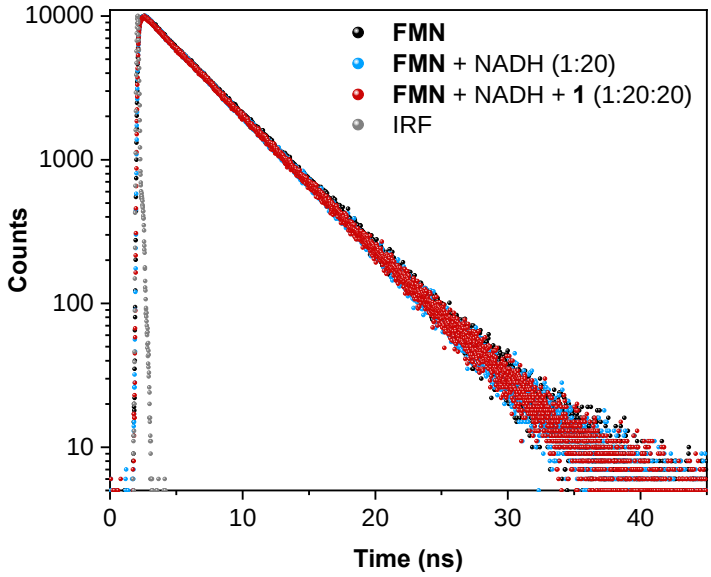

Figure S35. (a) Fluorescence emission spectrum of **FMN** (20 µM) and (b) radiative decay curves (λ_{exc} 445 nm, λ_{em} = 540 nm) for solutions of **FMN** (20 µM), **FMN** (20 µM) and NADH (400 µM), and **FMN** (20 µM), NADH (400 µM) and **1** (400 µM). All decays are monoexponential and show a τ_{Fluo} of 4.7 ns.

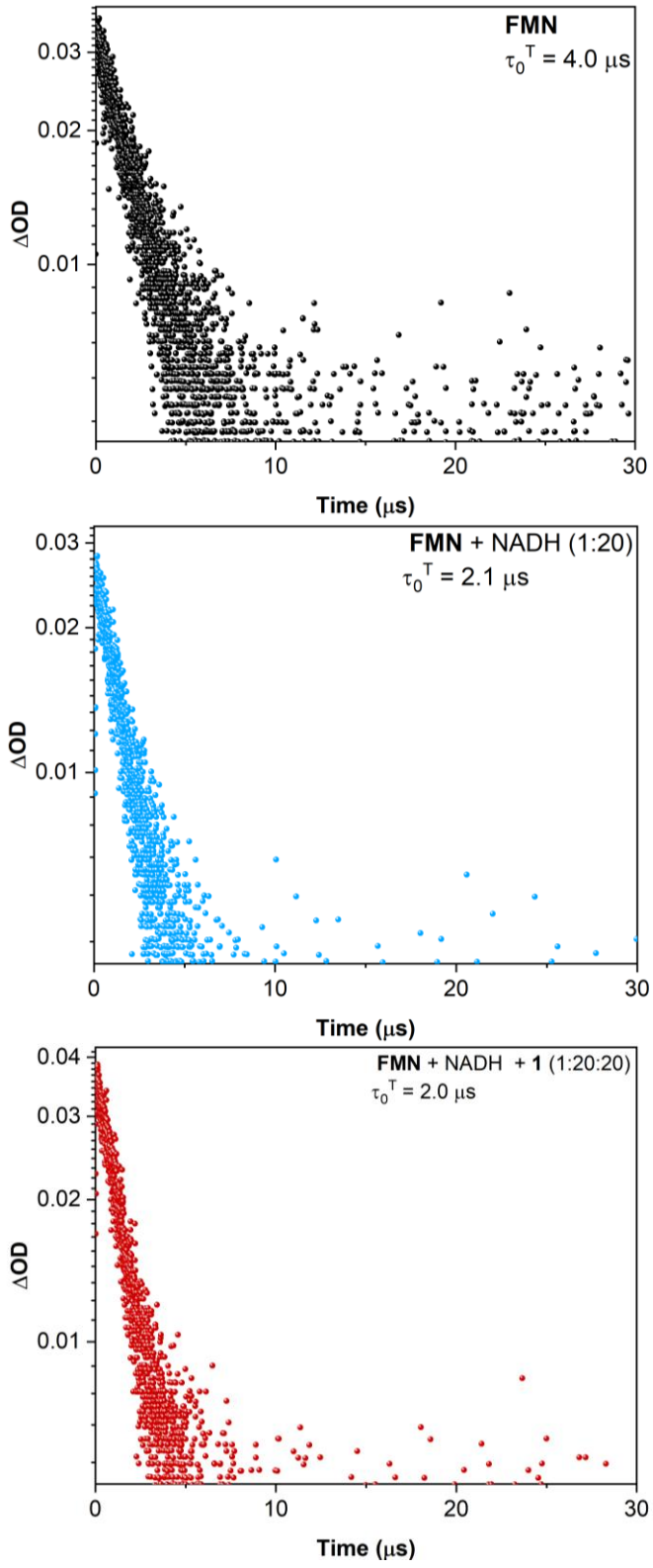

Figure S36. Decay of triplet-triplet absorption of ^{3}**FMN*** (λ_{exc} 445 nm, λ_{abs} = 700 nm) in air saturated solutions of **FMN** (20 µM), **FMN** (20 µM) and NADH (400 µM), and **FMN** (20 µM), NADH (400 µM) and **1** (400 µM).

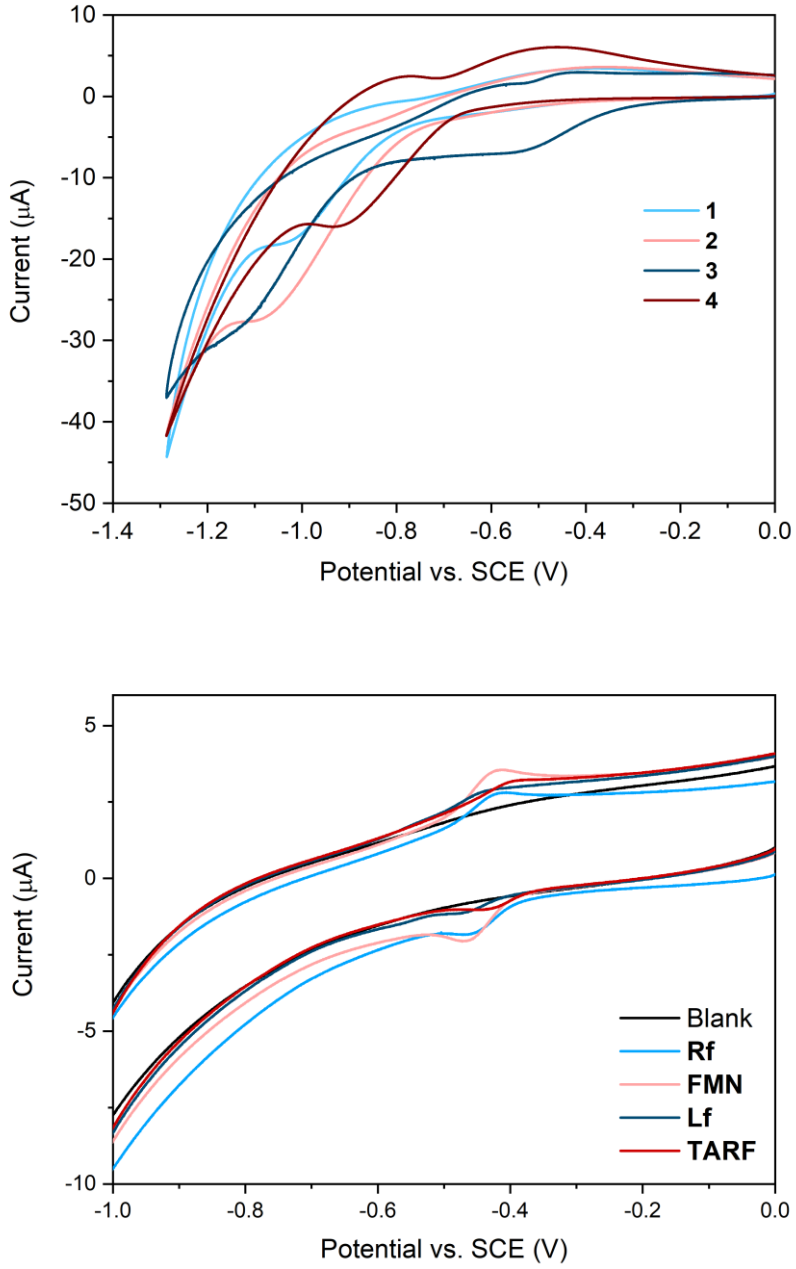

Figure S37. Cyclic voltammograms of **1**–**4** and flavins at 0.2 V s^{-1} in 0.05 M phosphate (pH 7.4, 0.15 M NaCl). Cathodic peak potentials for metal complexes (E_{pc}): **1**, −1.03 V; **2** −1.11 V; **3** −0.56 V; **4**, −0.93 V. $E_{1/2}$ potentials for flavins: **Rf**, −0.44 V; **FMN**, −0.44 V; **Lf**, −0.46 V; **TARF**, −0.42 V.

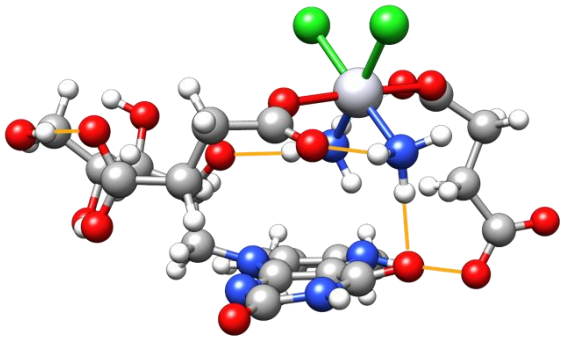

1

ΔE_{wb97xd} = 2.3 kcal/mol
$\Delta E_{cam\text{-}b3lyp}$ = 2.3 kcal/mol

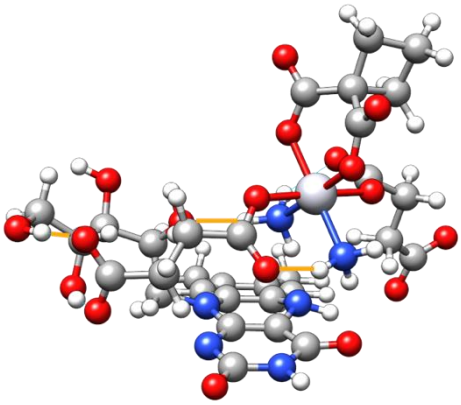

2

ΔE_{wb97xd} = 2.8 kcal/mol
$\Delta E_{cam\text{-}b3lyp}$ = 0.3 kcal/mol

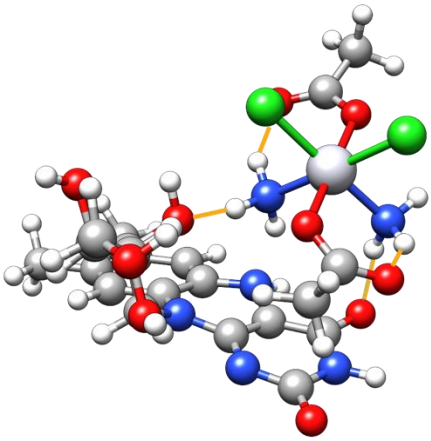

3

ΔE_{wb97xd} = 1.6 kcal/mol
$\Delta E_{cam\text{-}b3lyp}$ = 0.7 kcal/mol

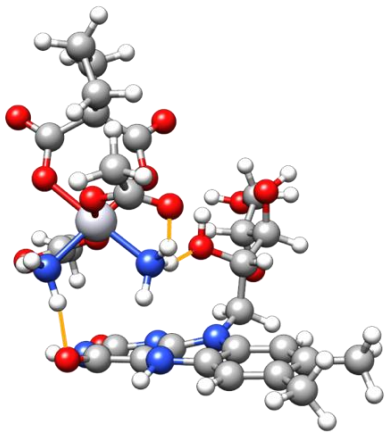

4

ΔE_{wb97xd} =4.5 kcal/mol
$\Delta E_{cam\text{-}b3lyp}$ = -1.1 kcal/mol

Figure S38. Least-stable DFT-optimized (pbe0/def2-SVP) structures of adducts between **1**–**4** and **RfH**$^{-}$ (H-bond contacts highlighted with orange lines). For each structure, ΔE describes the energy difference with the corresponding most stable adduct reported in Figure 4 of the main manuscript (i.e. $E_{Least\text{-}stable} - E_{Most\ stable}$). Energies were calculated using the wb97xd and cam-b3lyp functionals and def2-TZVP basis set with single point calculations.

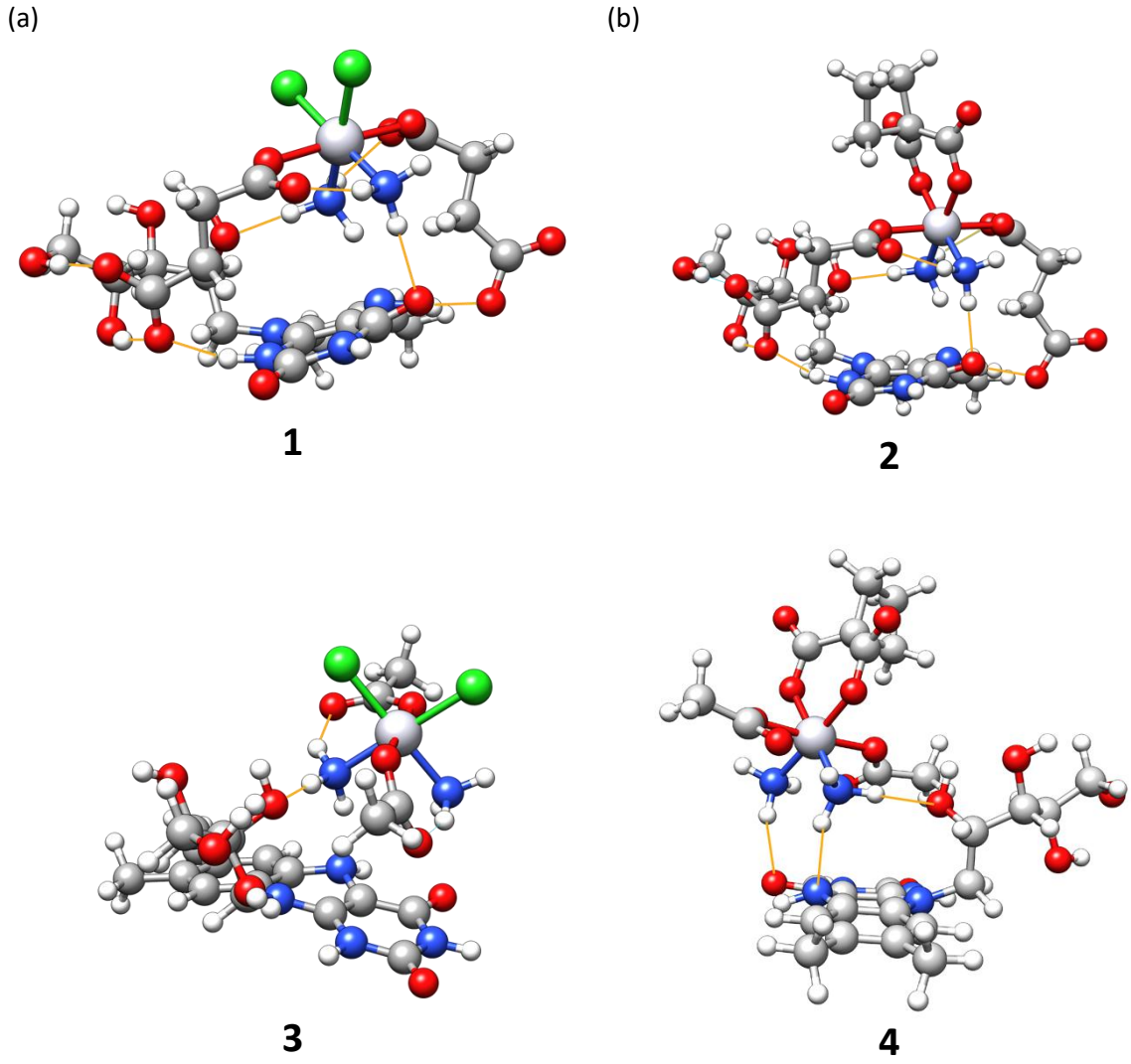

Figure S39. DFT-optimized (pbe0/def2-SVP) structures of adducts between **1**–**4** and **RfH_2** (H-bond contacts highlighted with orange lines).

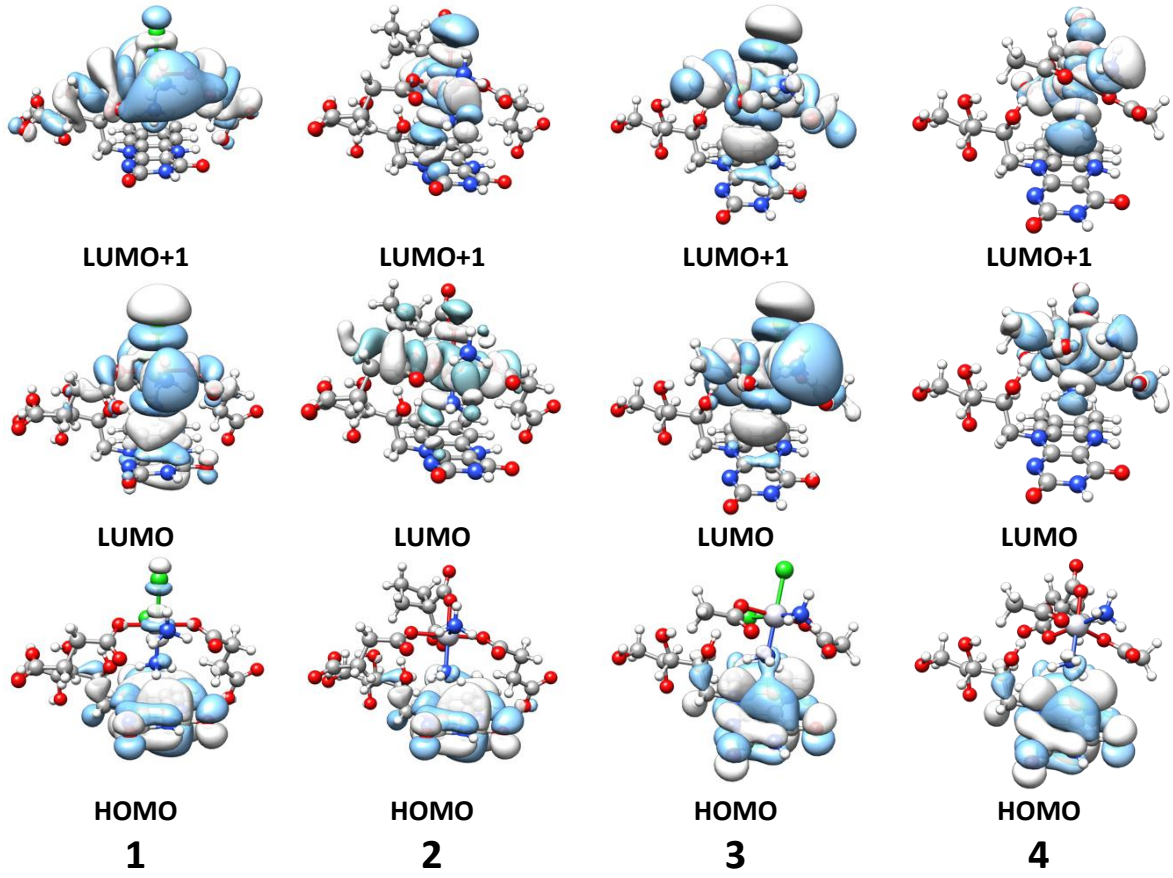

Figure S40. Selected DFT frontier orbitals for the most stable adducts between **1**–**4** and **RfH**$^{-}$ (pbe0/def2-SVP, isodensity surfaces plotted with the isovalue of 0.02 $e^{-}\cdot bohr^{-3}$).

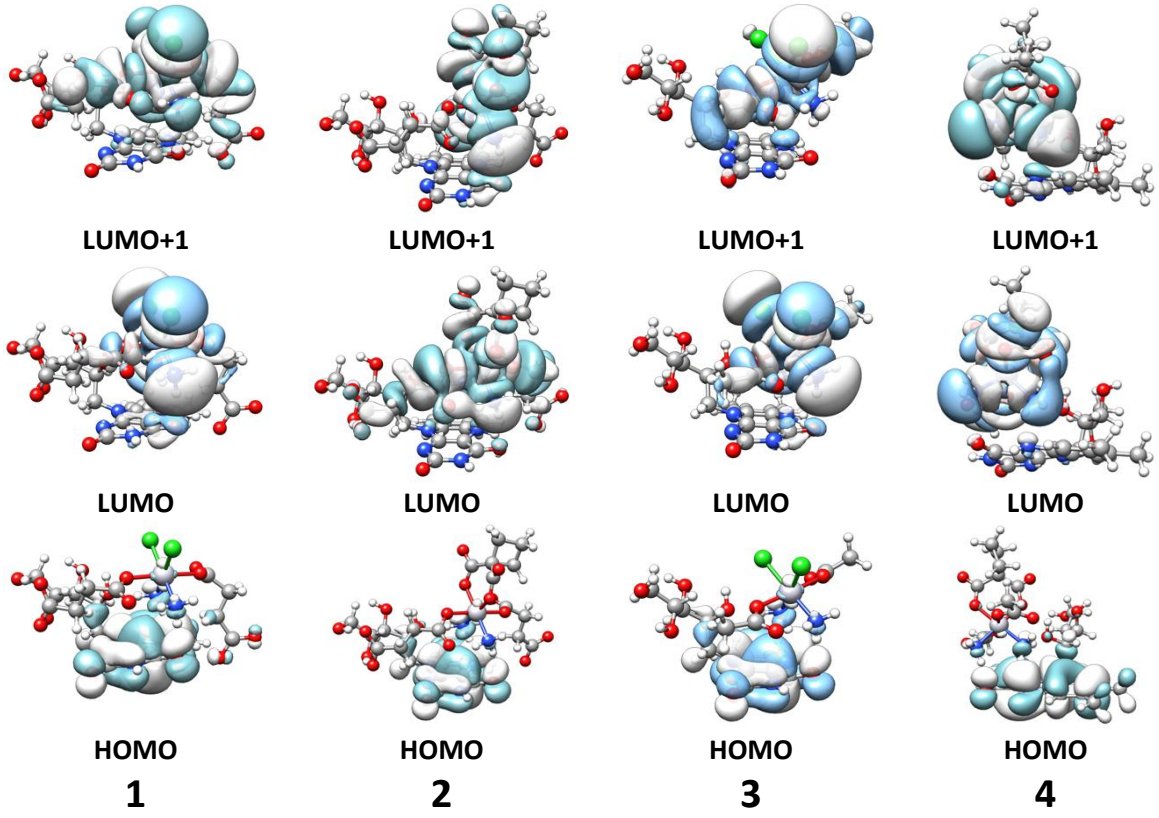

Figure S41. Selected DFT frontier orbitals for the least stable adducts between **1**–**4** and **RfH**$^{-}$ (pbe0/def2-SVP, isodensity surfaces plotted with the isovalue of 0.02 $e^{-}\cdot bohr^{-3}$).

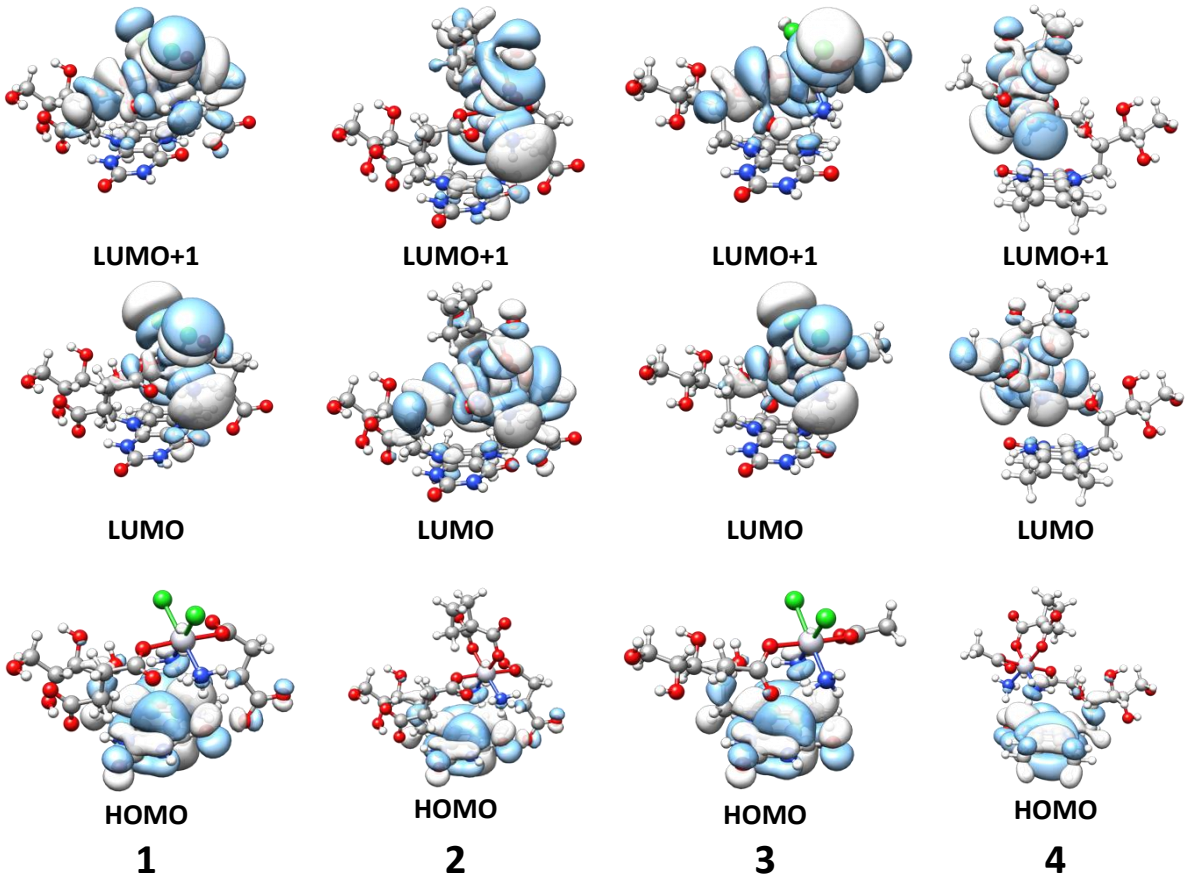

Figure S42. Selected DFT frontier orbitals for the stable adducts between **1**–**4** and **RfH_2** (pbe0/def2-SVP, isodensity surfaces plotted with the isovalue of 0.02 $e^{-}\cdot bohr^{-3}$).

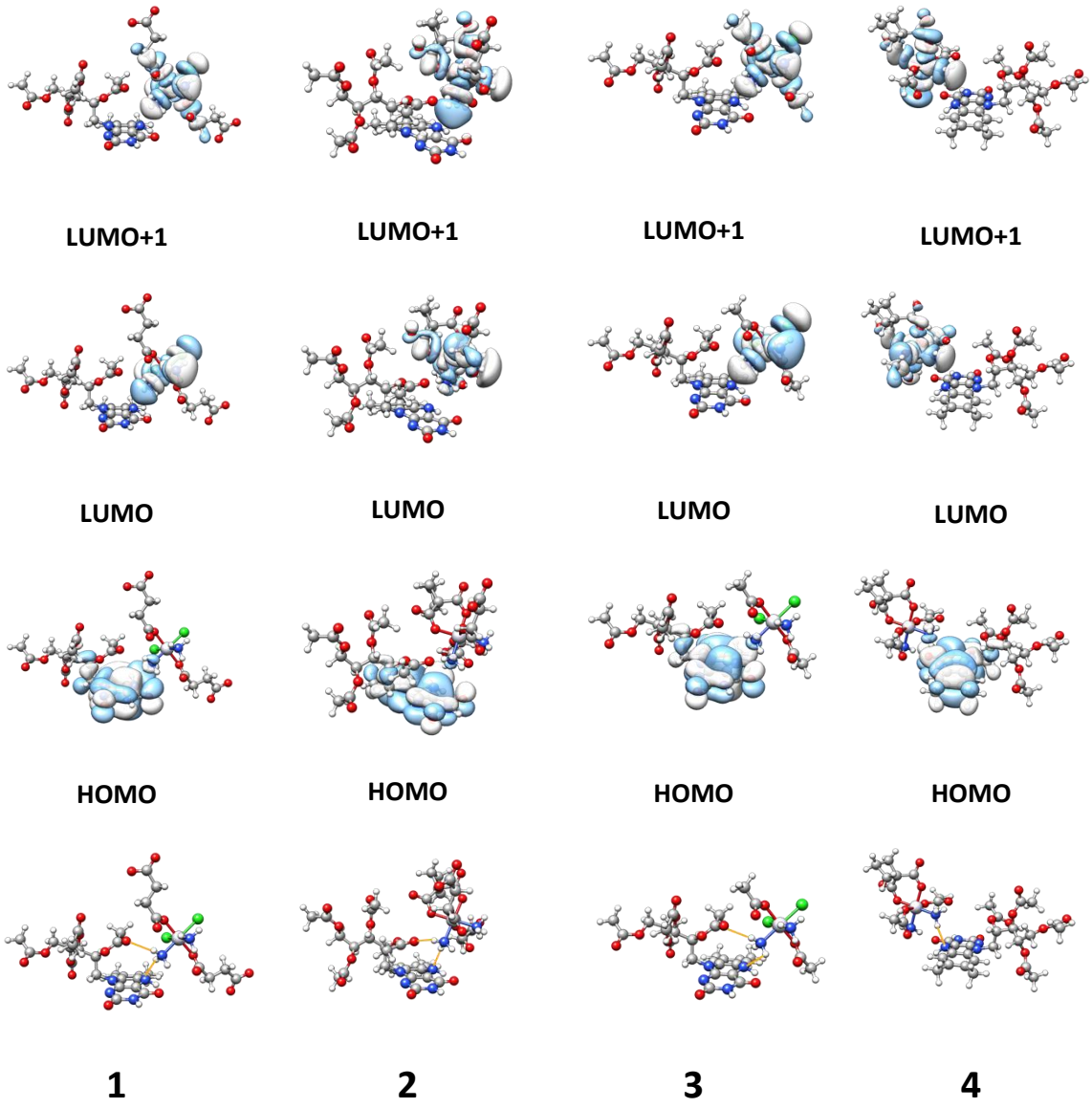

Figure S43. DFT-optimized (pbe0/def2-SVP) structures of adducts between **1**–**4** and **TARFH**$^{-}$ (H-bond contacts highlighted with orange lines) and selected frontier orbitals (isodensity surfaces plotted with the isovalue of 0.02 $e^{-}{\cdot}bohr^{-3}$).

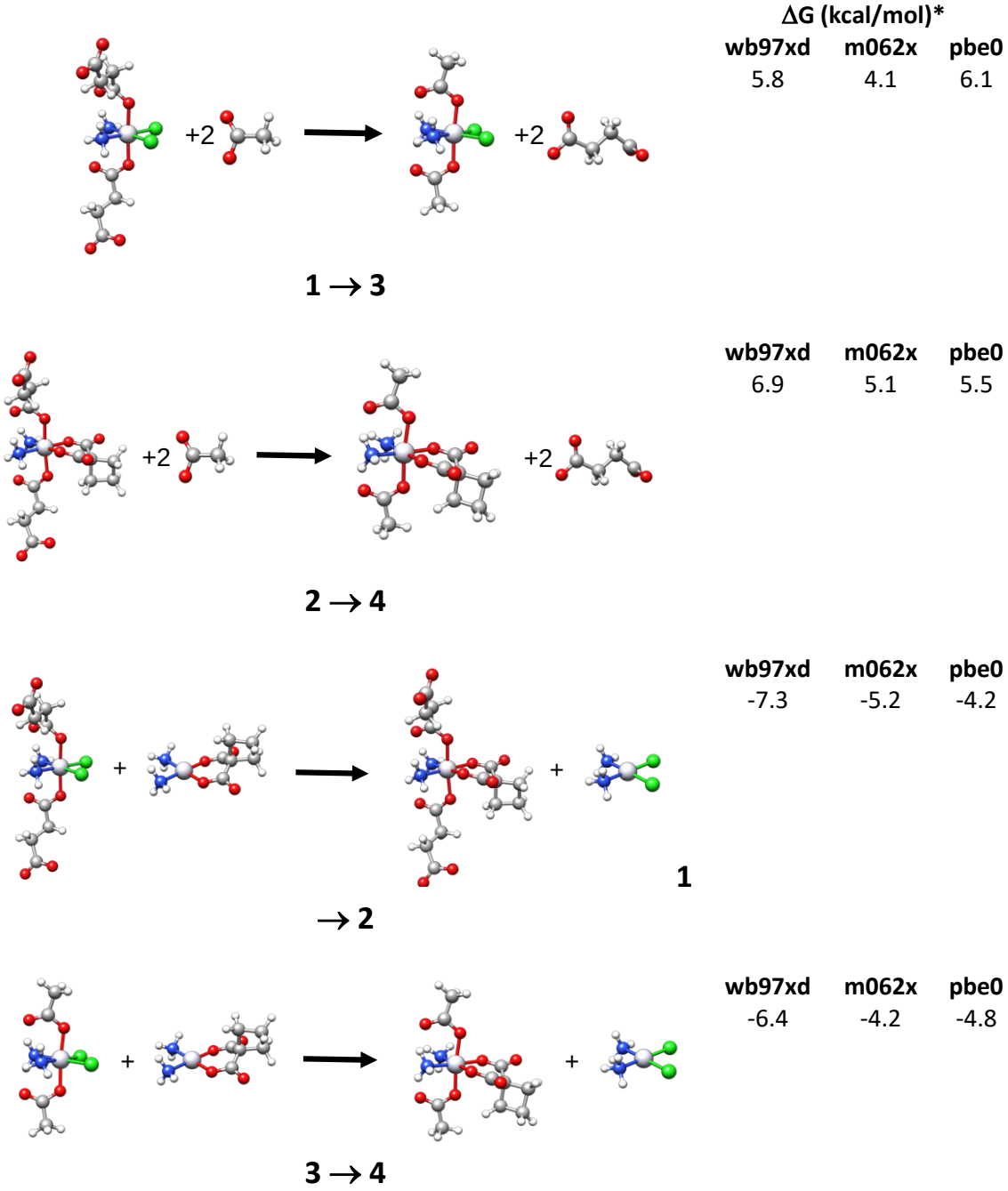

* Free energies (kcal/mol) for the axial and equatorial ligand exchange reactions of **1**–**4**. All calculations were performed using the def2-TZVP basis set at the pbe0/def2-SVP optimized geometries. See Computational Method section for details.

Figure S44. Stability DFT calculations for substrates **1**–**4** using different functionals and the def2-TZVP basis set. Relative stabilities: **1** > **3** and **2** > **4** (ΔG > 0); **1** < **2** and **3** < **4** (ΔG < 0).

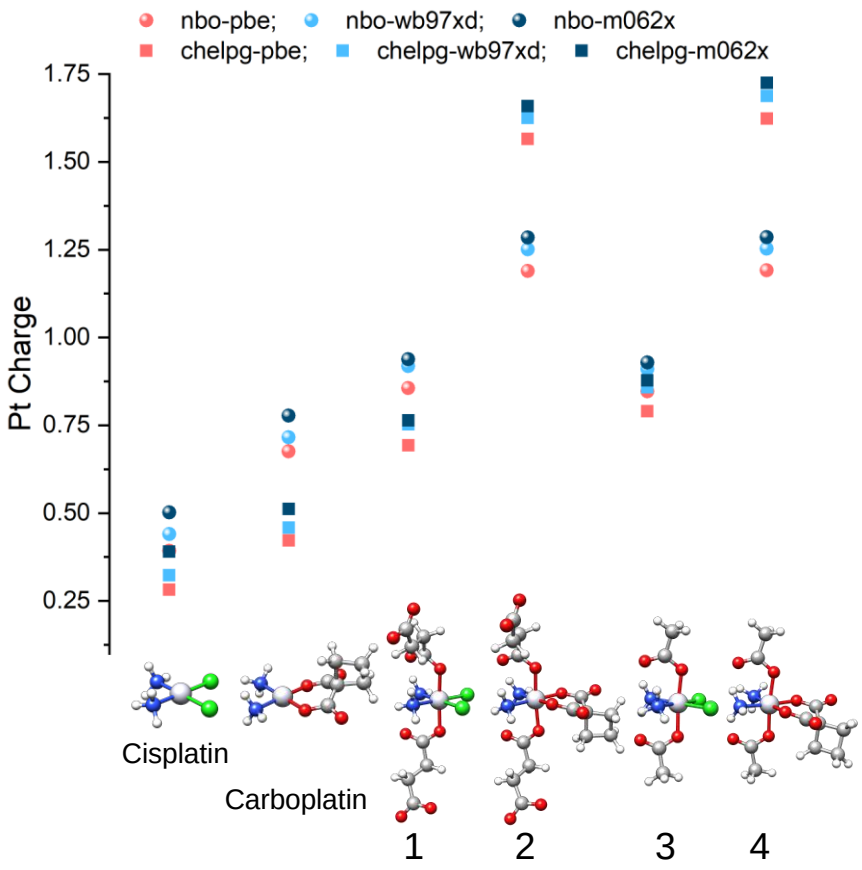

Figure S45. Pt charge for **1**–**4**, cisplatin and carboplatin calculated at the DFT level using the nbo and chelpg methods (pbe0, wb97xd and m062x functionals and the def2-TZVP basis set).

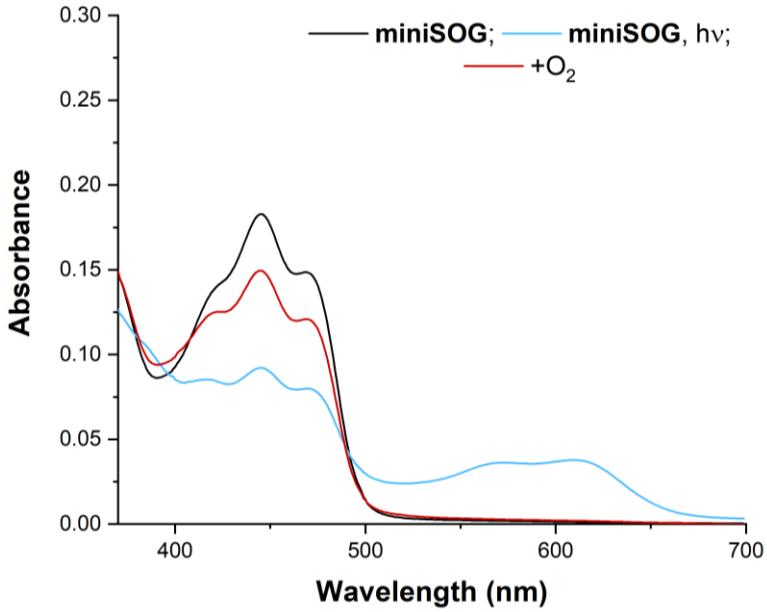

Figure S46. UV-Vis of light-irradiated **miniSOG** under anaerobic conditions in the absence of NADH and response to the addition of O_2. Solutions of **miniSOG** (15 µM, 18 mM PB, pH 7.4) were irradiated (6 mW·cm^{-2}, 600 s) at 460 nm.

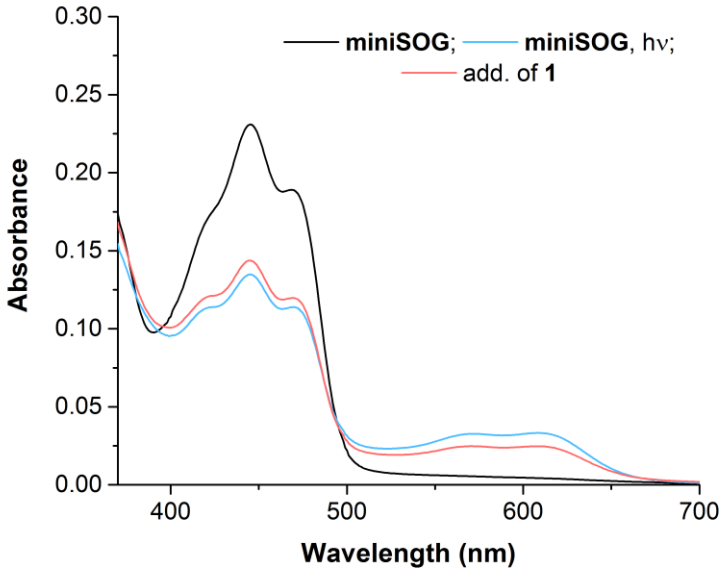

Figure S47. UV-Vis of light-irradiated **miniSOG** under anaerobic conditions in the absence of NADH and response to the addition of **1** (80 µM). Solutions of miniSOG (15 µM, 18 mM PB, pH 7.4) were irradiated (6 mW·cm^{-2}, 600 s) at 460 nm.

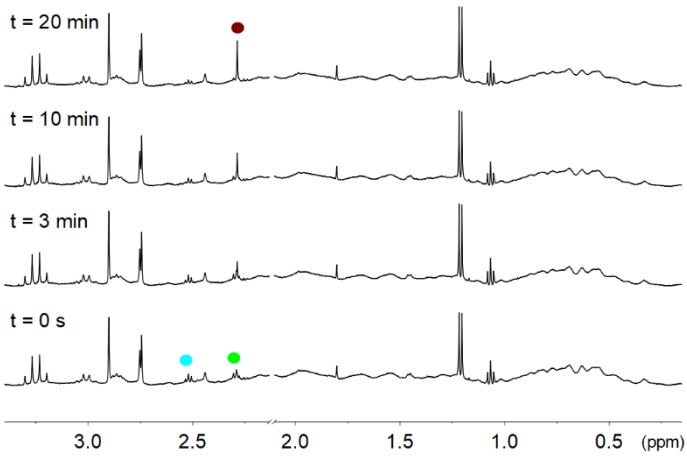

Figure S48. Photocatalytic activation of **1** (50 µM) in 18 mM PB (pH 7.0, 10% D_2O) in the presence of 95 µM **miniSOG** under 460-nm light irradiation (6 mW·cm^{-2}) and anaerobic conditions. Note that **miniSOG** is in excess compared to **1**.
^{1}H NMR signal labelling: **1**, ● Pt–OCO**CH$_2$**CH$_2$CO$_2^-$, ● Pt–OCOCH$_2$**CH$_2$**CO$_2^-$, ● free $^-$O$_2$C**CH$_2$CH$_2$**CO$_2^-$.

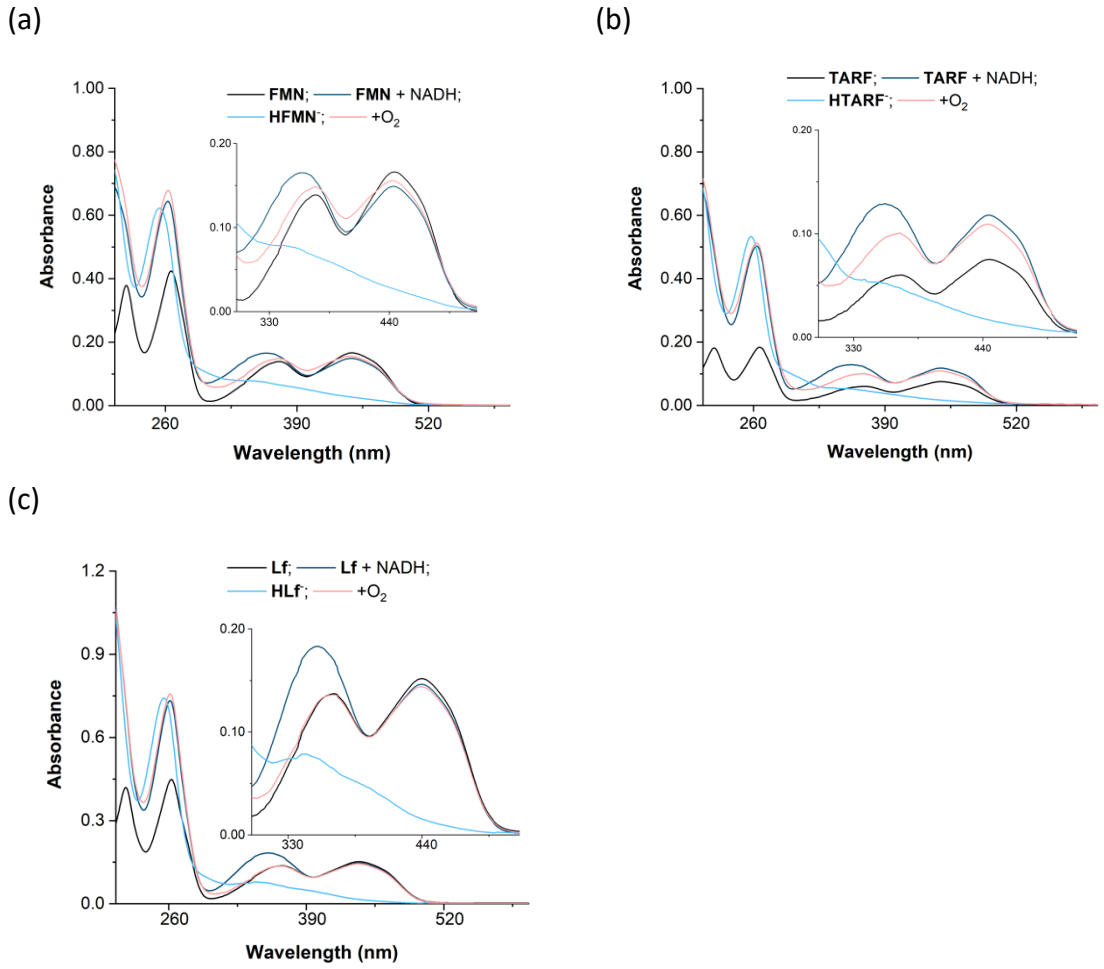

Figure S49. Reduction of **FMN** (a), **TARF** (b) and **Lf** (c) by NADH under light irradiation and re-oxidation by O_2 monitored by UV-Vis. Generation of **HFL**$^{-}$ species (18 mM PB, pH 7.5) in the absence of O_2 was achieved upon 460-nm irradiation of FL (15 µM, 40–90 s) in the presence of equimolar NADH under an oxygen-free atmosphere.

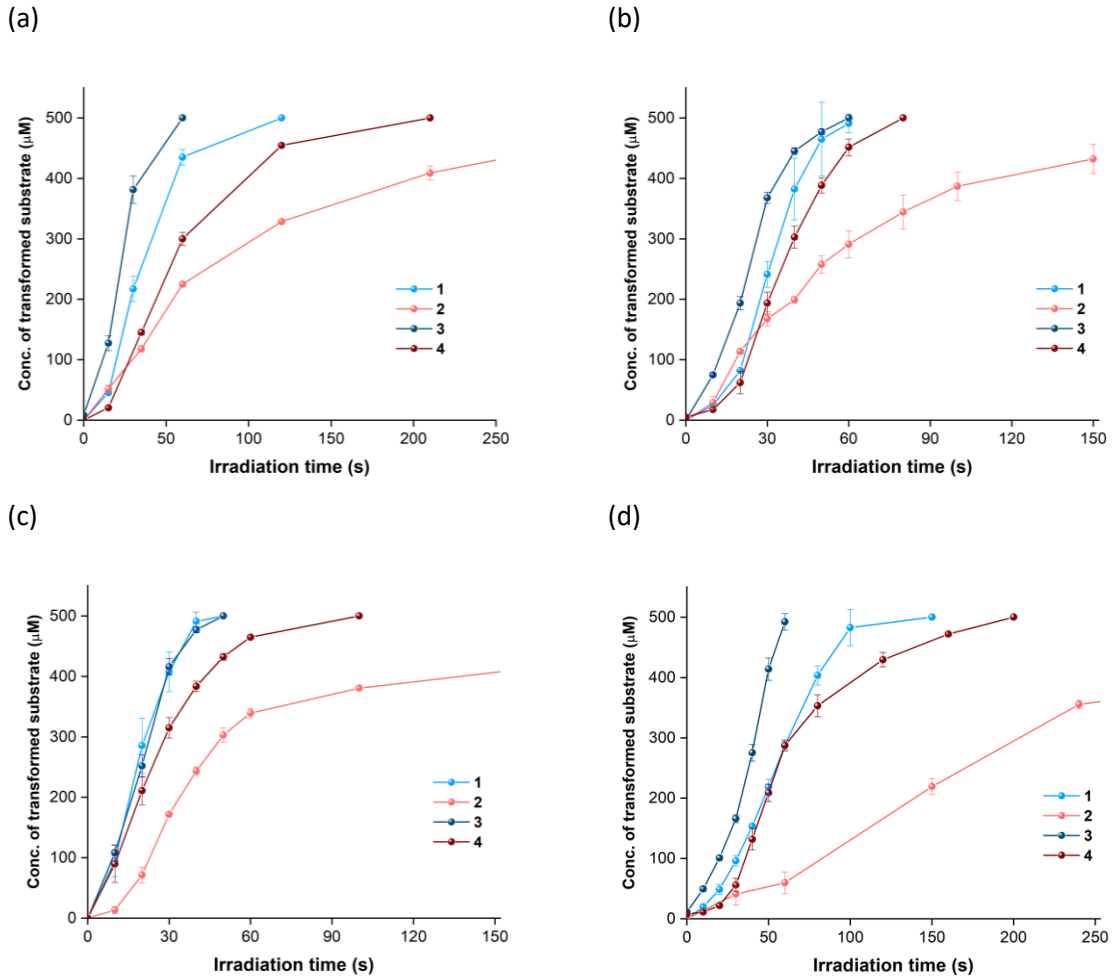

Figure S50. Kinetics profiles for the photocatalytic conversion of **1**–**4** by **Rf** (a), **FMN** (b), **TARF** (c), **Lf** (d). Reactions were monitored by ^{1}H NMR and performed using 500 μM **1**–**4** in the presence of 1 mM NADH and 25 μM FL catalysts (18 mM PB, pH 7.0, 10% D_2O).

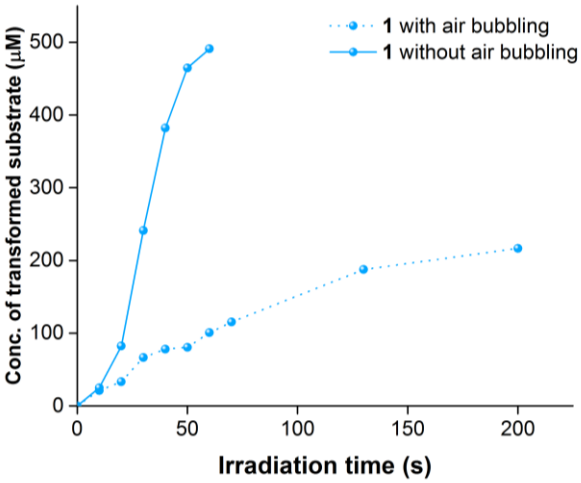

Figure S51. Kinetics profiles for the photocatalytic conversion of **1** by **FMN** with and without air bubbling. Reactions were monitored by ^{1}H NMR and performed using 500 μM **1**–**4** in the presence of 1 mM NADH and 25 μM FL catalyst (18 mM PB, pH 7.0, 10% D_2O).

(a)

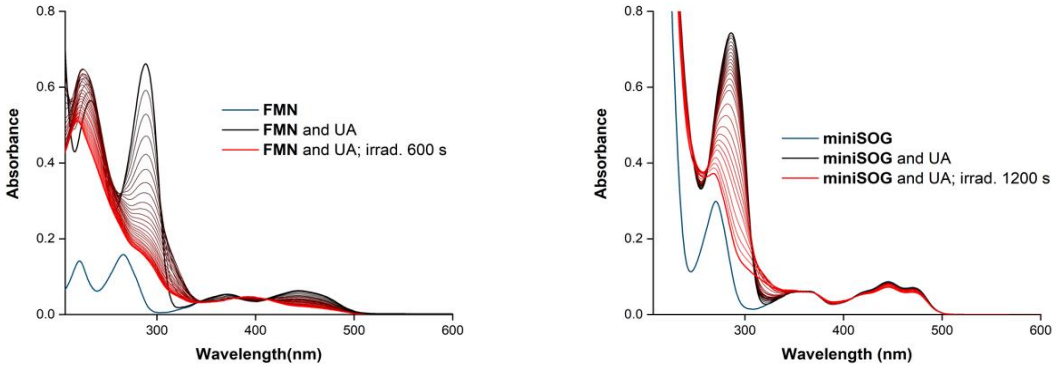

(b)

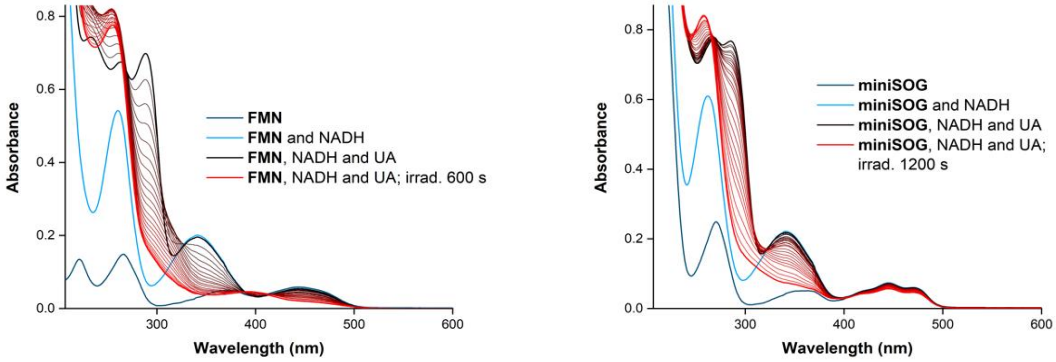

(c)

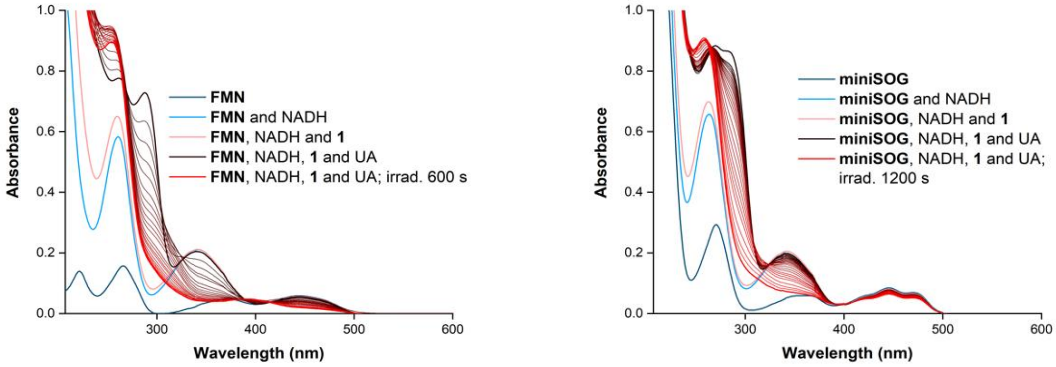

Figure S52. Singlet oxygen sensitization by **FMN** and **miniSOG** determined using uric acid (UA) as probe. Spectral variations of optically-matched solutions of 5 µM **FMN** and **miniSOG** upon excitation at 460 nm (6 $mW \cdot cm^{-2}$) in the presence of (a) 50 µM UA, (b) 50 µM UA and 30 µM NADH, and (c) 50 µM UA, 30 µM NADH and 15 µM **1**.

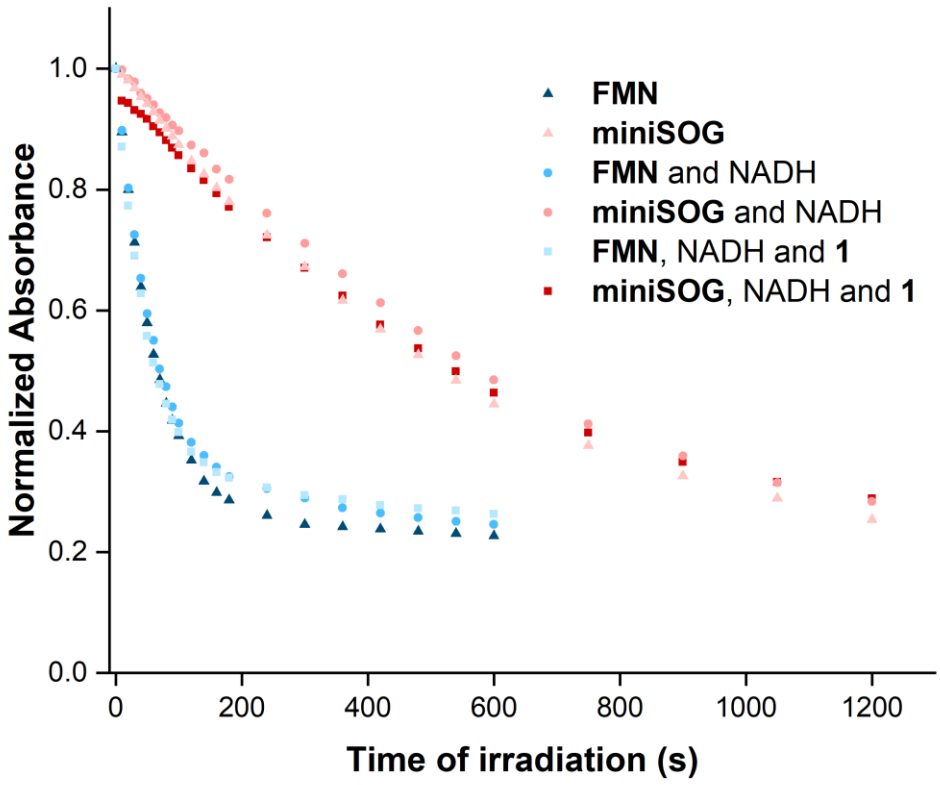

Figure S53. Comparison of uric acid (UA) bleaching rate at 292 nm in the presence of optically-matched solutions of 5 µM **FMN** (blue) and **miniSOG** (red) under different conditions: (▲) 50 µM UA, (●) 50 µM UA and 30 µM NADH, and (■) 50 µM UA, 30 µM NADH and 15 µM **1**.

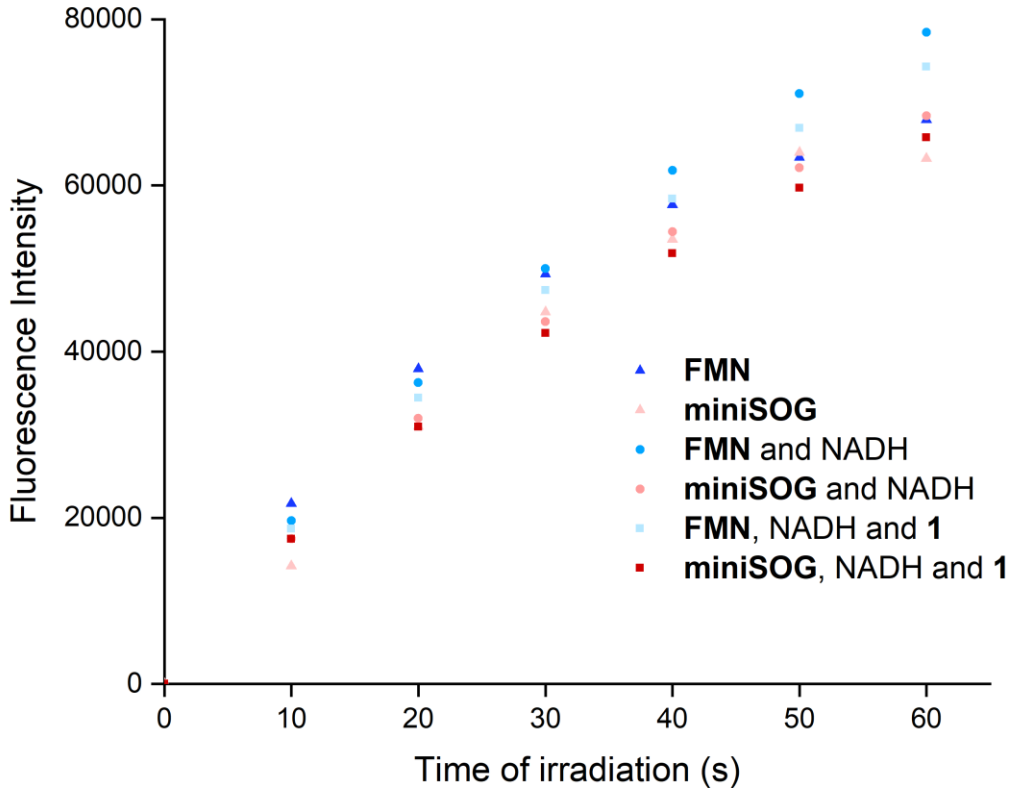

Figure S54. Fluorescence intensity of the hydroethidine (HE) oxidation product formed by light irradiation of HE (50 µM) in the presence of (▲) **FMN**/**miniSOG** (5 µM), (●) **FMN**/**miniSOG** (5 µM) and NADH (30 µM), and (■) **FMN**/**miniSOG** (5 µM), NADH (30 µM) and **1** (15 µM).

Appendix Chapter 4

Enhancing The Photocatalytic Conversion Of Pt^{IV} Substrates By Flavoprotein Engineering

Supporting Information

Appendix Chapter 4

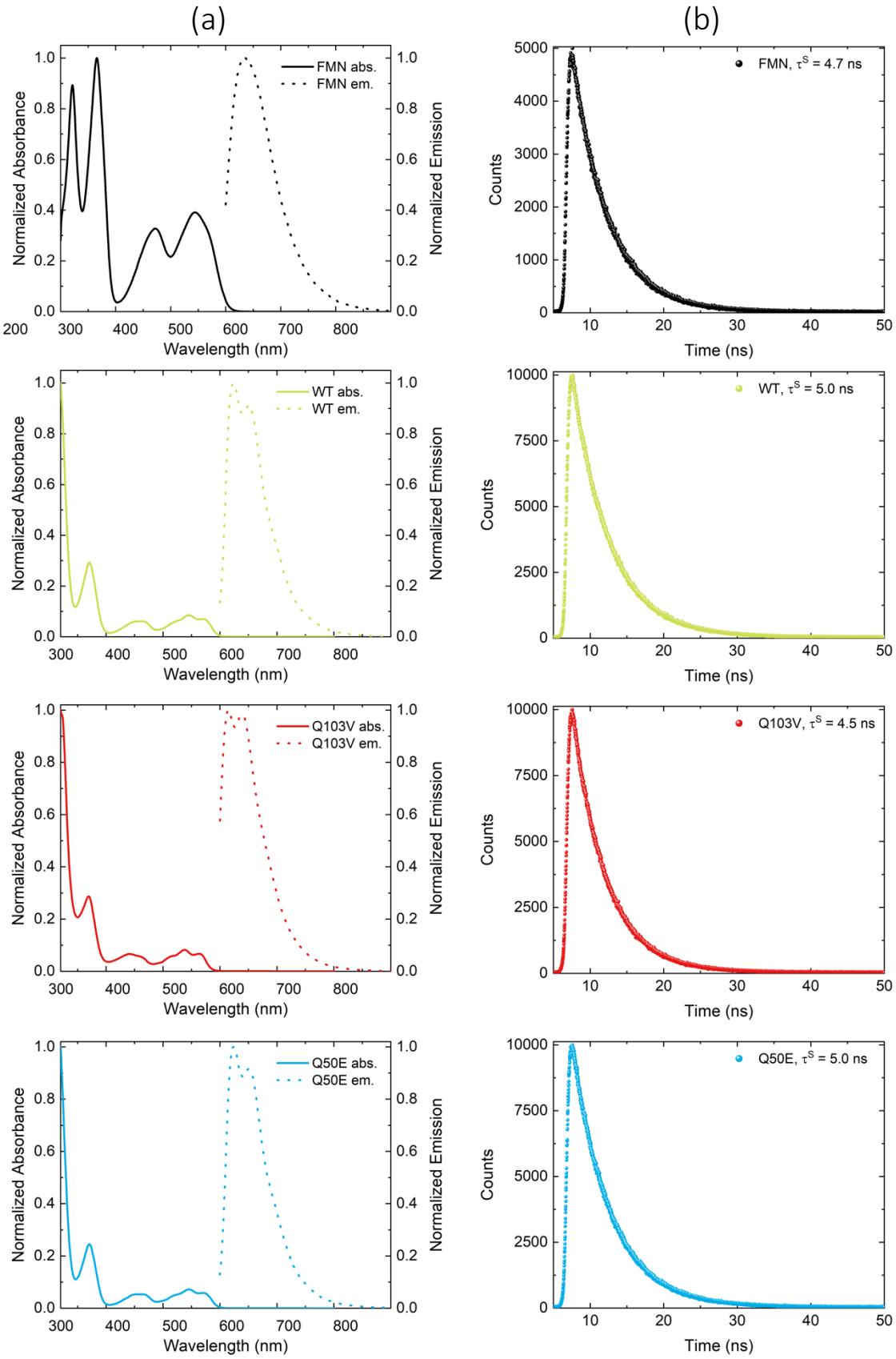

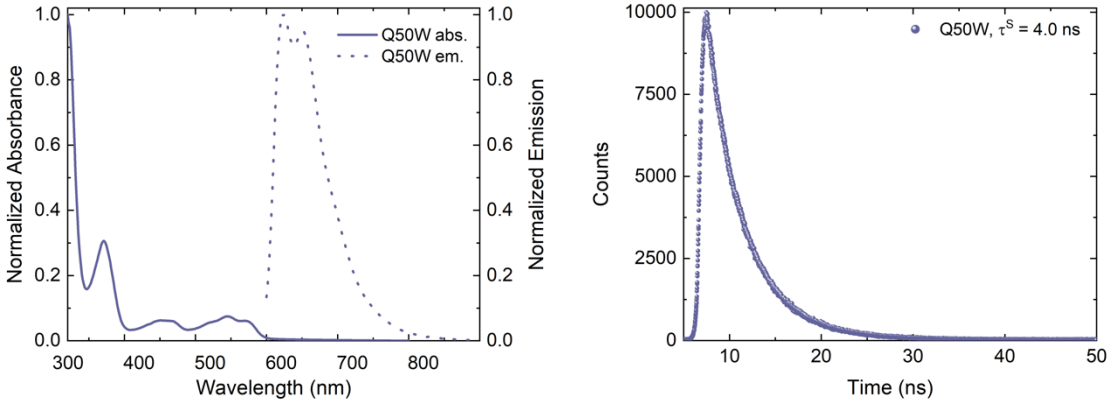

Figure S1. (a) Absorption and emission spectra (λ_{exc} = 450 nm) and (b) fluorescence decay curves (τ^S, λ_{exc} = 485 nm, λ_{em} = 520 nm) of FMN, miniSOG WT, Q103V, Q50E and Q50W in PB (20 mM, pH 7) in the presence of O_2. Steady-state and lifetime measurements were performed using 3 and 6 µM solutions of miniSOG catalysts respectively. In the case of FMN, 15 µM solutions were employed.

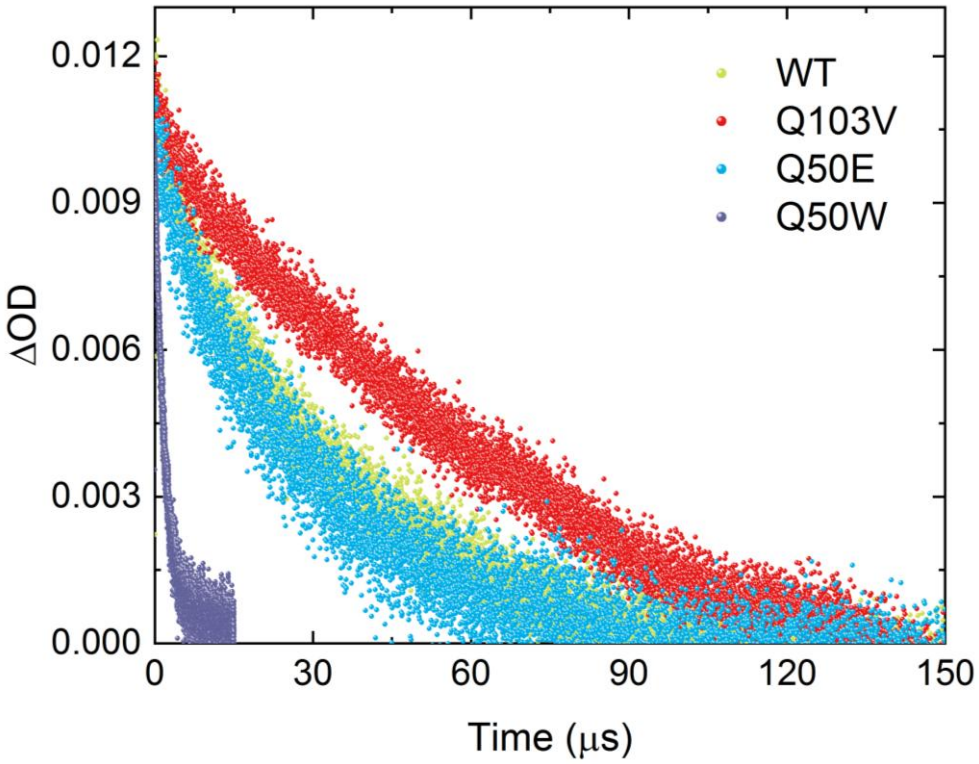

Figure S2. Decays (τ^T) of the triplet−triplet absorption at 720 nm for the miniSOG WT and its Q103V, Q50E and Q50W mutants. All measurements were performed in PB solutions (20 mM, pH 7, air-saturated) containing 20 µM of the miniSOG proteins.

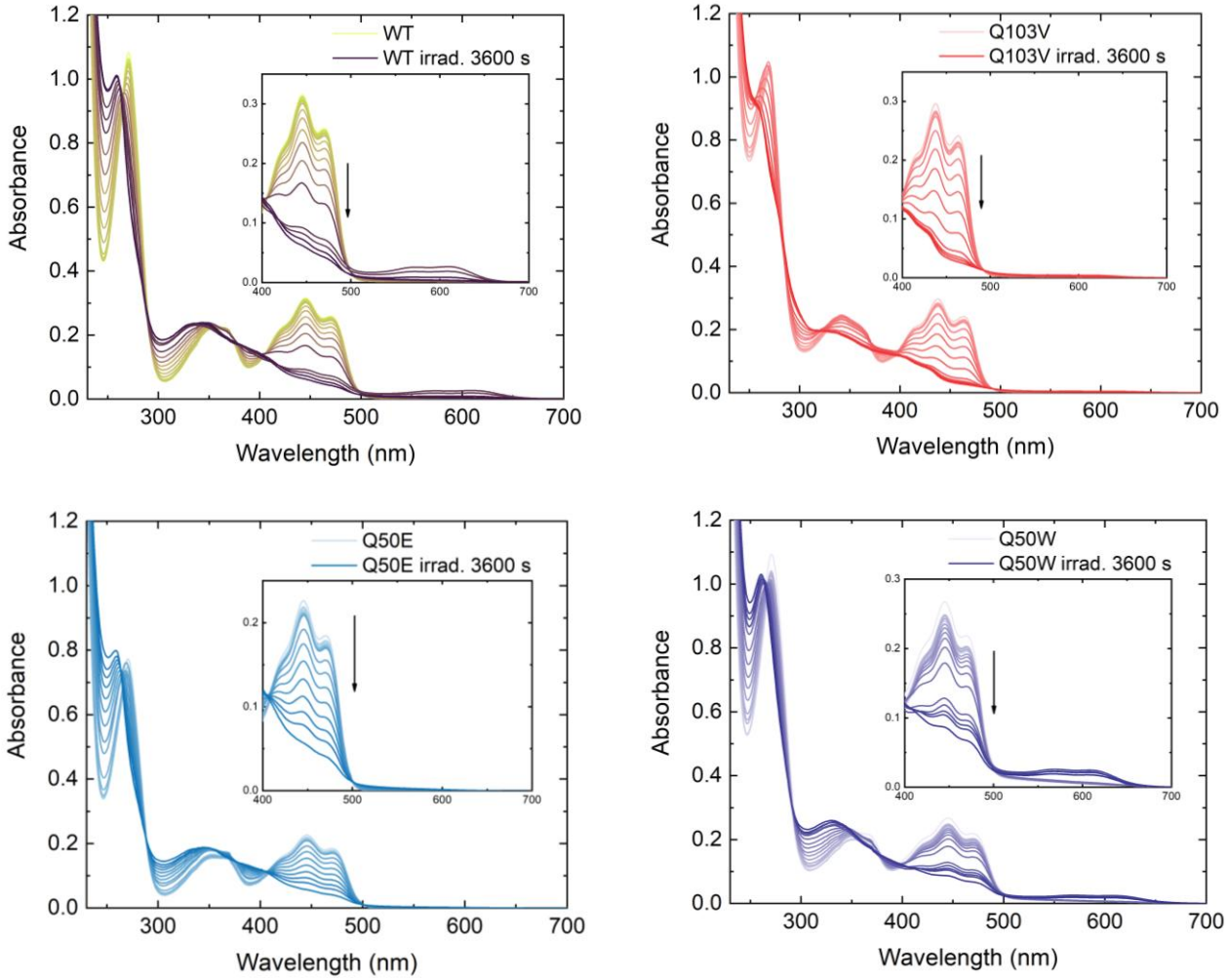

Figure S3. Photostability of miniSOG catalysts (15 µM) in PB (20 mM, pH 7) under blue light irradiation (460 nm, 6 mW·cm^{-2}).

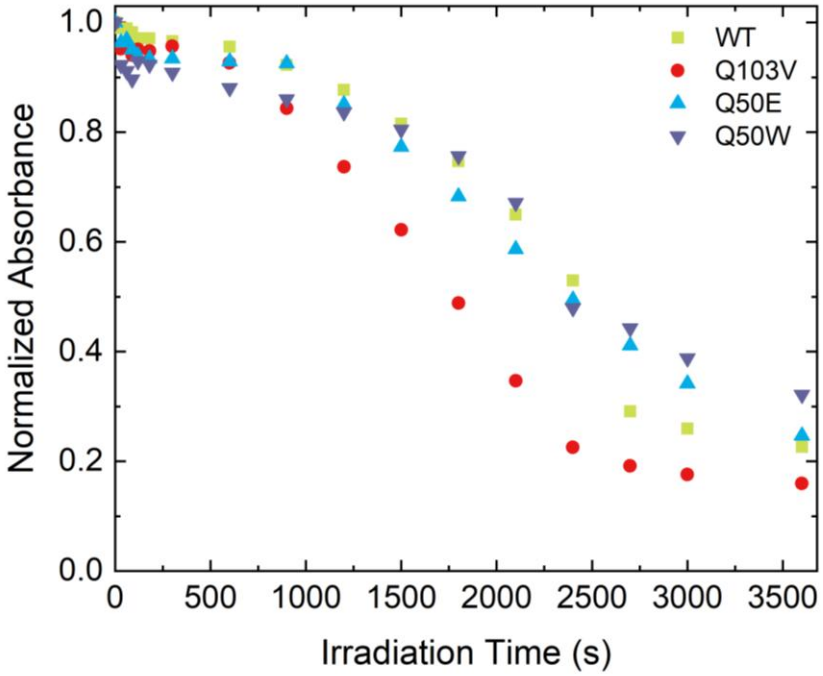

Figure S4. Photostability profiles of miniSOG catalysts (15 µM) in PB (20 mM, pH 7) under blue light irradiation (460 nm, 6 mW·cm^{-2}) obtained monitoring the decrease in absorbance at 450 nm.

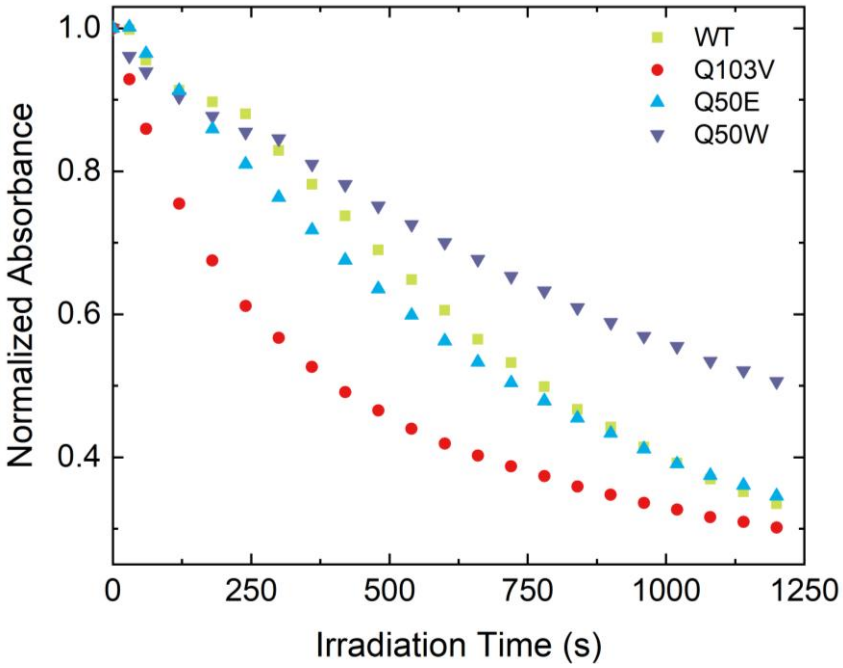

Figure S5. Singlet oxygen formation by miniSOG catalysts (3 µM) under blue light irradiation (460 nm, 6 mW·cm^{-2}) determined using uric acid UA (30 µM) as probe.

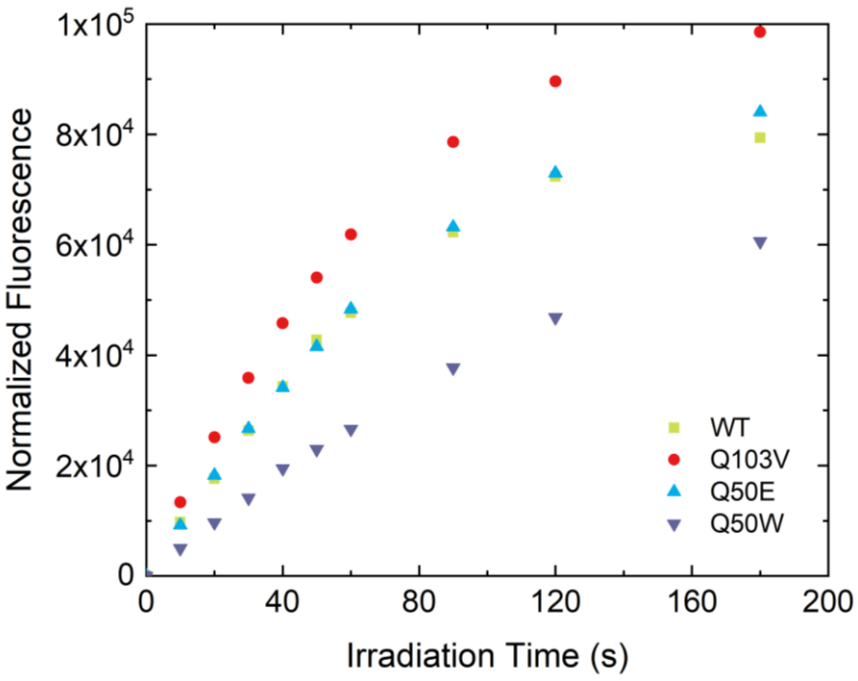

Figure S6. ROS production by miniSOG catalysts determined by monitoring the fluorescence intensity of hydroethidine (HE, 30 µM) oxidation product (λ_{exc} 525 nm, λ_{em} 550–800 nm) formed during blue light irradiation (460 nm, 6 mW·cm^{-2}) in the presence of the miniSOG variants (3 µM).

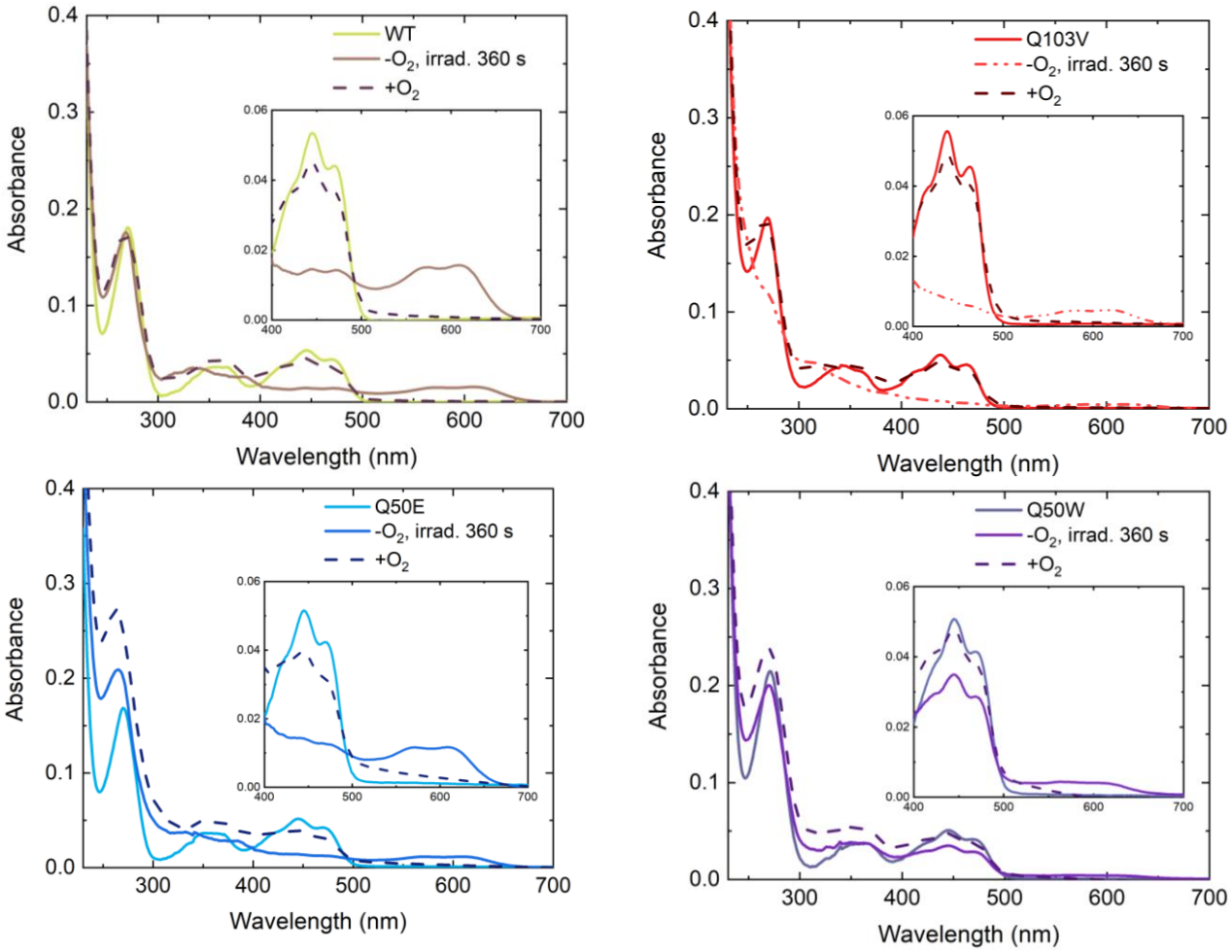

Figure S7. Photostability of miniSOG catalysts (3 µM) in PB (20 mM, pH 7) under blue light irradiation (460 nm, 6 mW·cm^{-2}) in the absence of O_2. After light irradiation, samples were exposed to the oxygen-containing ambient atmosphere to monitor the semiquinone disappearance (dashed line).

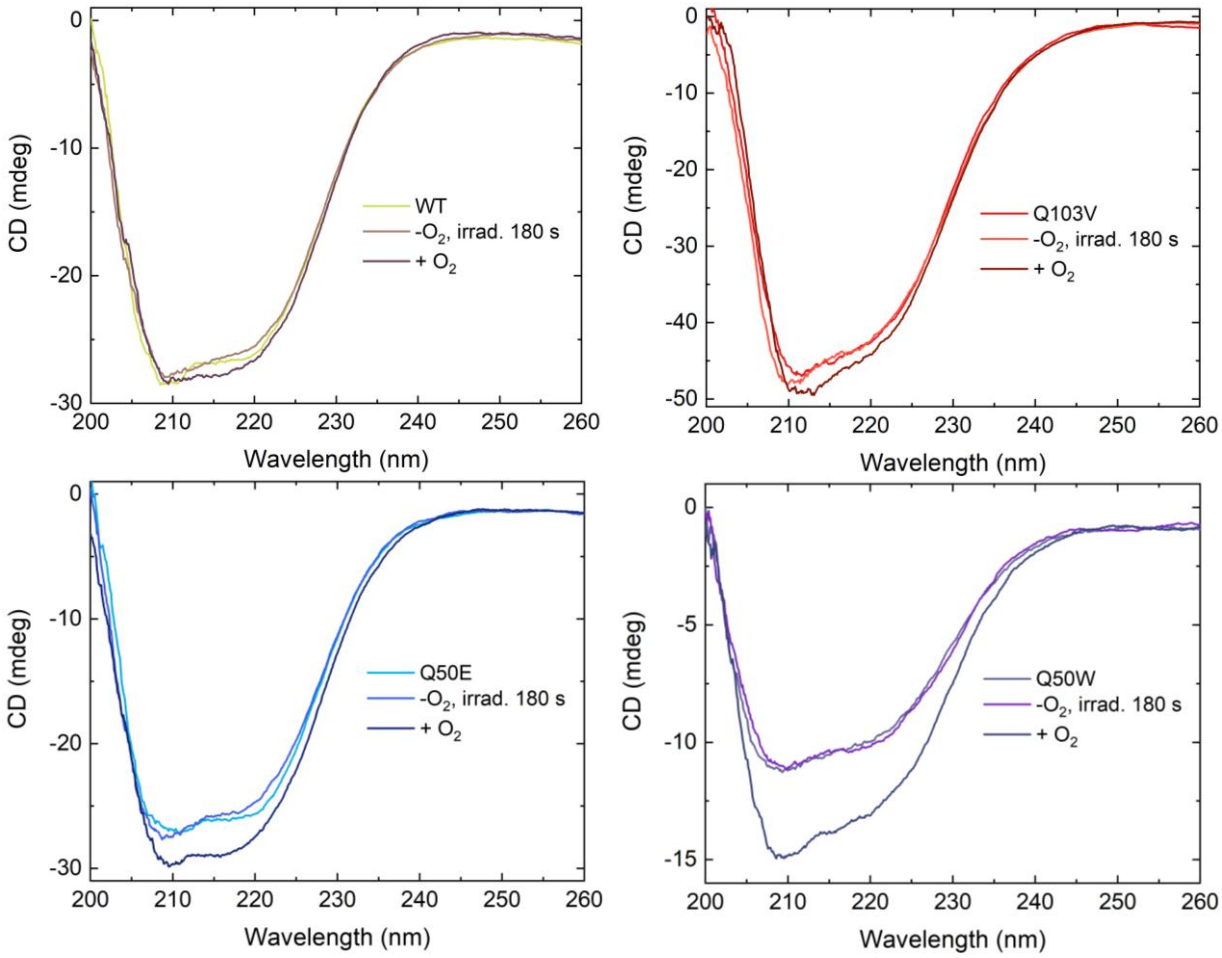

Figure S8. Circular dichroism spectra of miniSOG variants (3 µM) in PB (20 mM, pH 7) irradiated for 180 s (460 nm, 6 mW·cm^{-2}) in the absence of O_2.

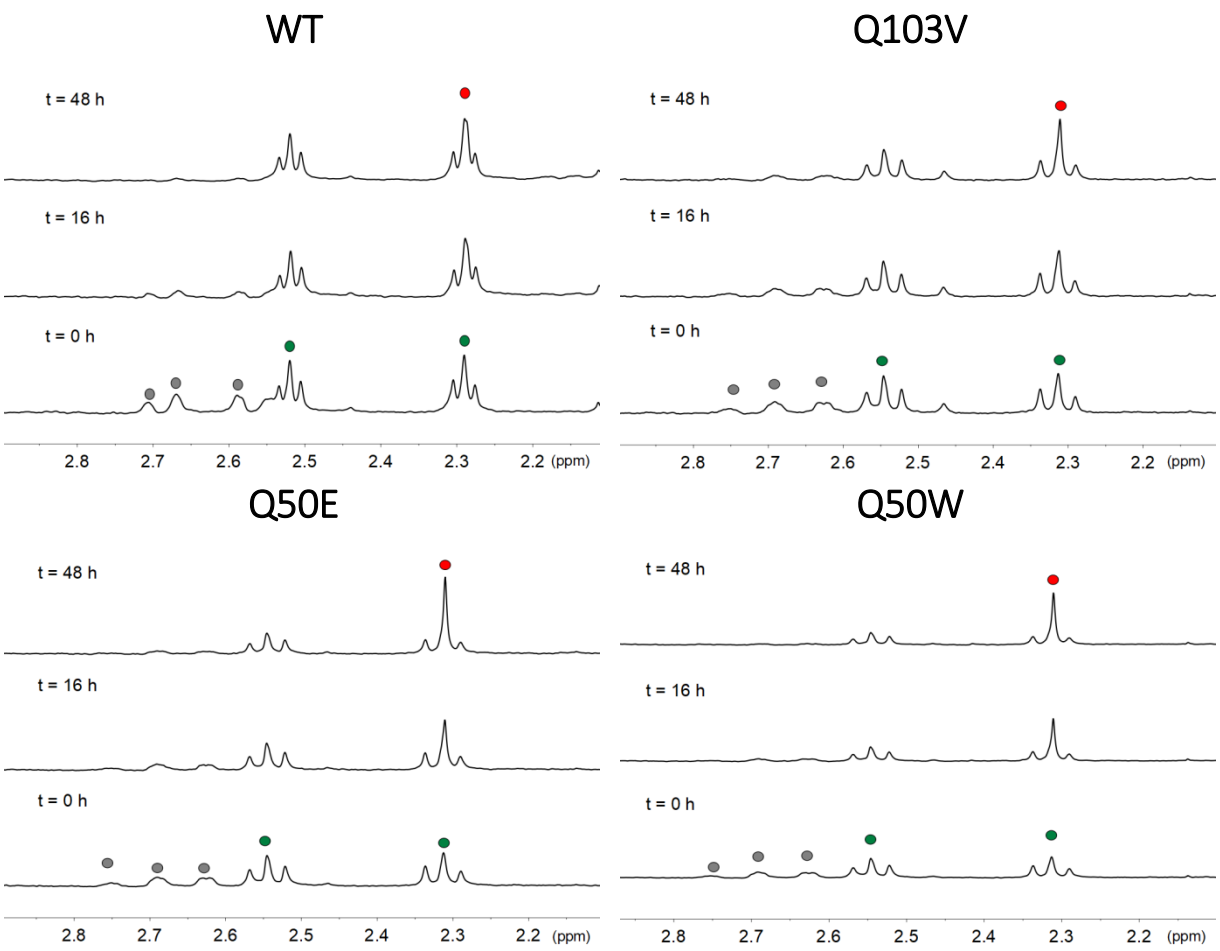

Figure S9. Dark stability of complex **1** (500 µM) in 18 mM PB buffer (pH 7.0, 10% D_2O) in the presence of 1 mM NADH and 25 µM miniSOG proteins for 48 h. ^{1}H NMR signal labelling: ● NADH; **1**: ● Pt–OCO**CH$_2$**$CH_2CO_2^-$, ● Pt–$OCOCH_2$**CH_2**CO_2^-; ● free $^-O_2CCH_2CH_2CO_2^-$.

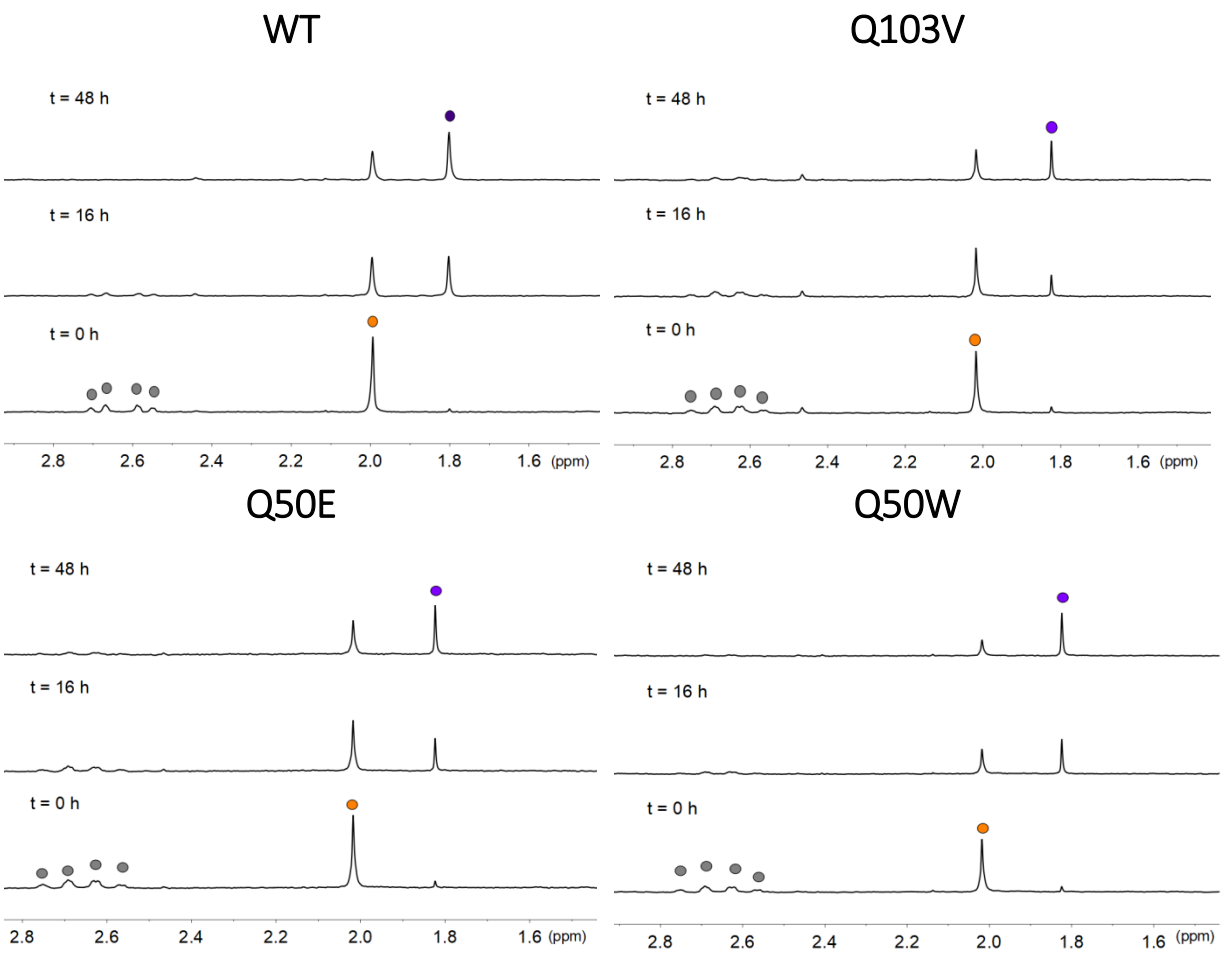

Figure S10. Dark stability of complex **2** (500 µM) in 18 mM PB buffer (pH 7.0, 10% D_2O) in the presence of 1 mM NADH and 25 µM miniSOG proteins for 48 h. ^{1}H NMR signal labelling: ● NADH; **2**: ● Pt–OCO**CH$_3$**; ● free $^-$OCO**CH$_3$**.

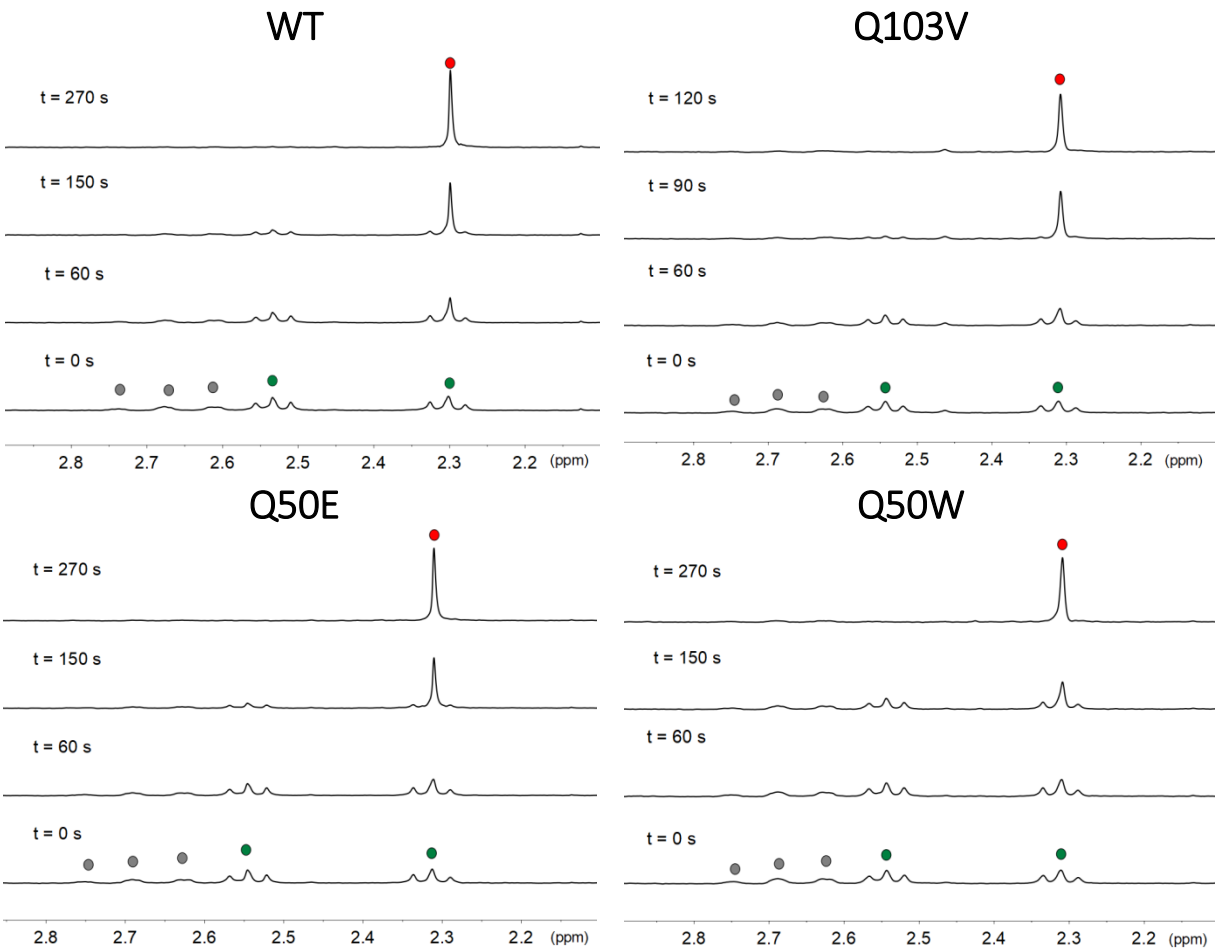

Figure S11. Photocatalytic activation of complex **1** (500 µM) in 18 mM PB buffer (pH 7.0, 10% D_2O) in the presence of 1 mM NADH and 25 µM miniSOG. ^{1}H NMR signal labelling: ● NADH; **1**: ● Pt–OCO**CH$_2$**$CH_2CO_2^-$, ● Pt–OCOCH$_2$**CH$_2$**CO_2^-; ● free $^-O_2CCH_2CH_2CO_2^-$.

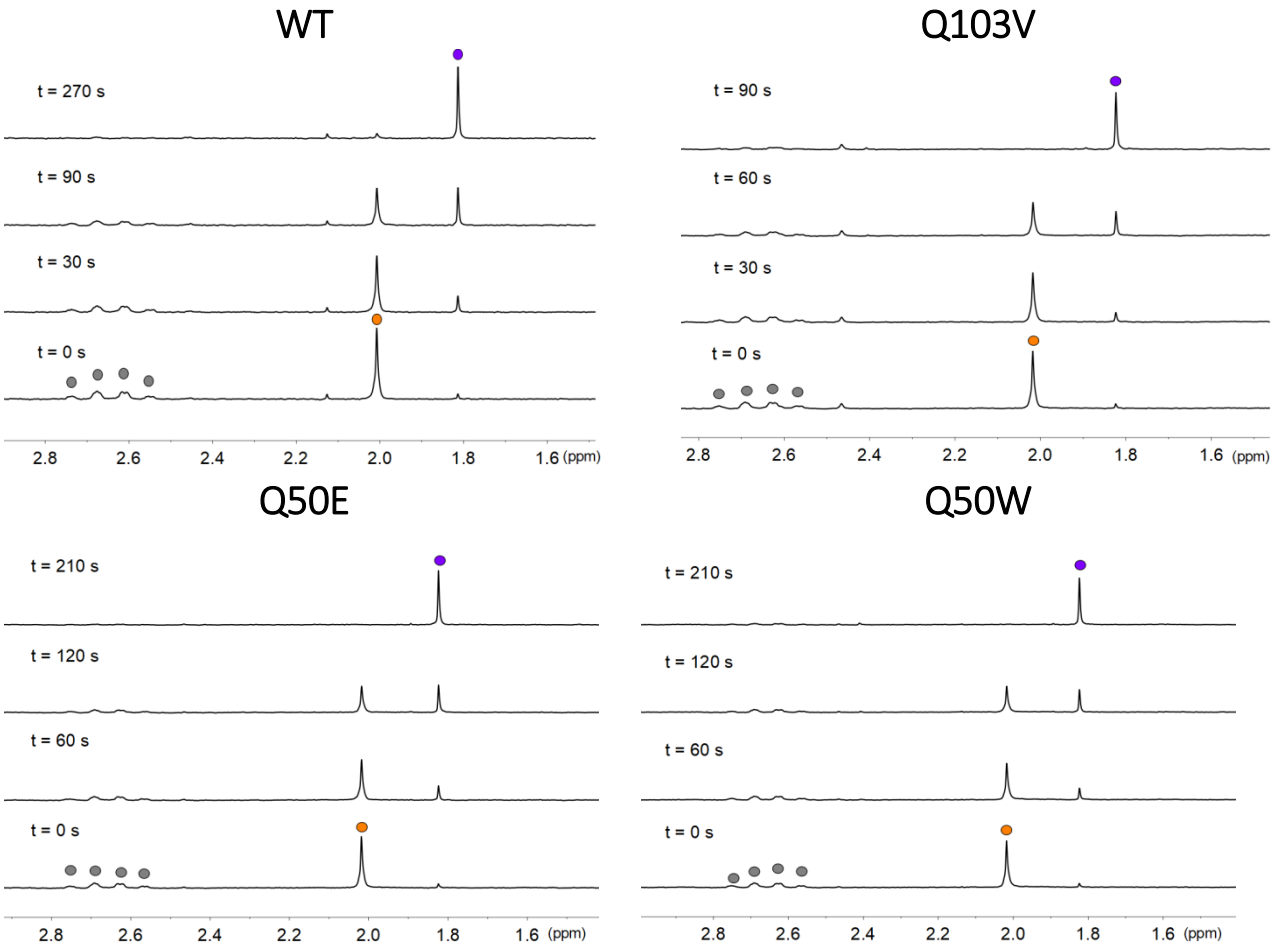

Figure S12. Photocatalytic activation of complex **2** (500 µM) in 18 mM PB buffer (pH 7.0, 10% D_2O) in the presence of 1 mM NADH and 25 µM miniSOG. ^{1}H NMR signal labelling: ● NADH; **2**: ● Pt–OCO**CH$_3$**; ● free $^-$OCO**CH$_3$**.

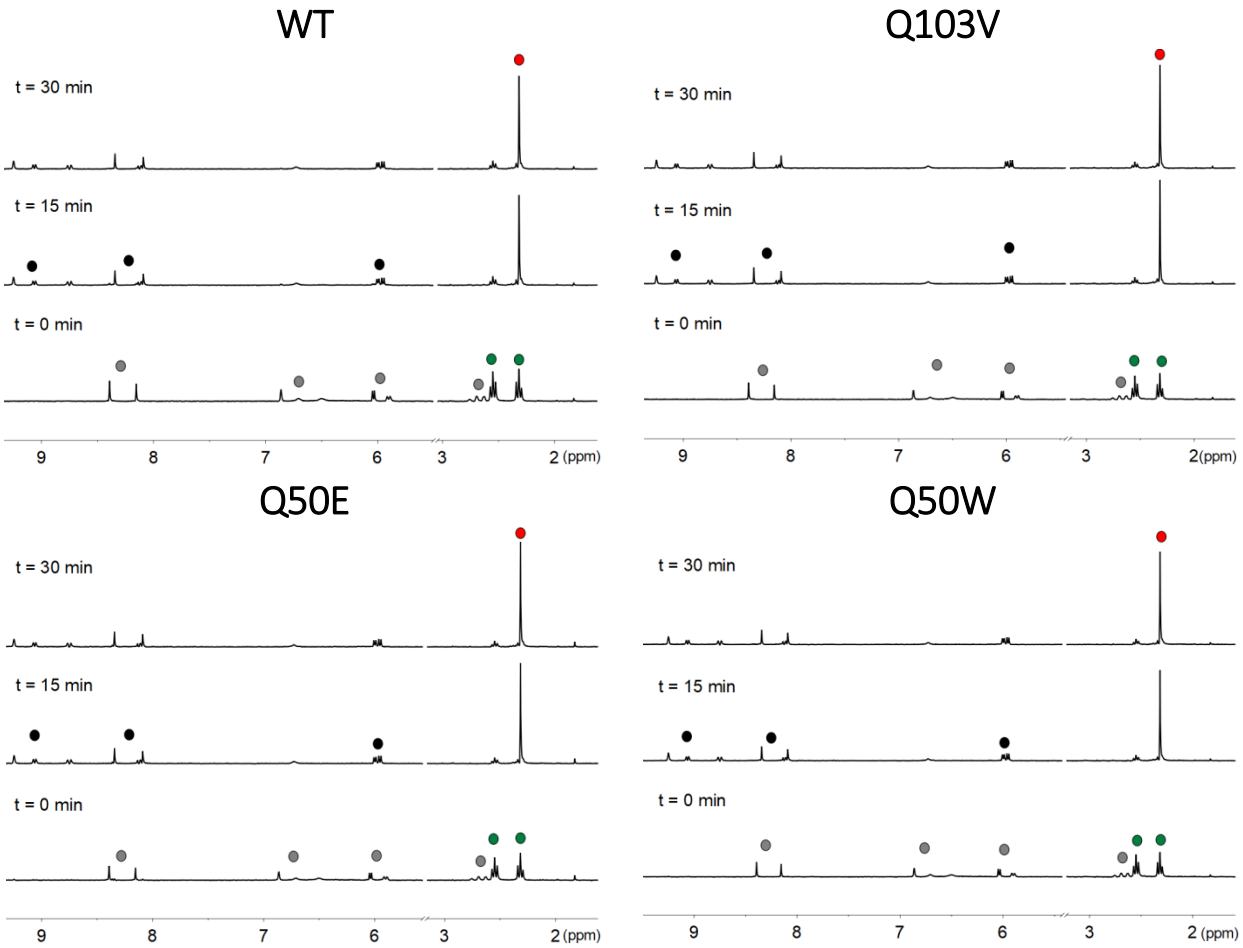

Figure S13. Photocatalytic activation of complex **1** (1 mM) in 18 mM PB buffer (pH 7.0, 10% D_2O) in the presence of 1 mM NADH and 1 µM miniSOG catalysts. ^{1}H NMR signal labelling: ● NADH; ● NAD^+; **1**: ● Pt–OCO**CH$_2$**$CH_2CO_2^-$, ● Pt–OCOCH_2**CH$_2$**CO_2^-; ● free $^-O_2CCH_2CH_2CO_2^-$.

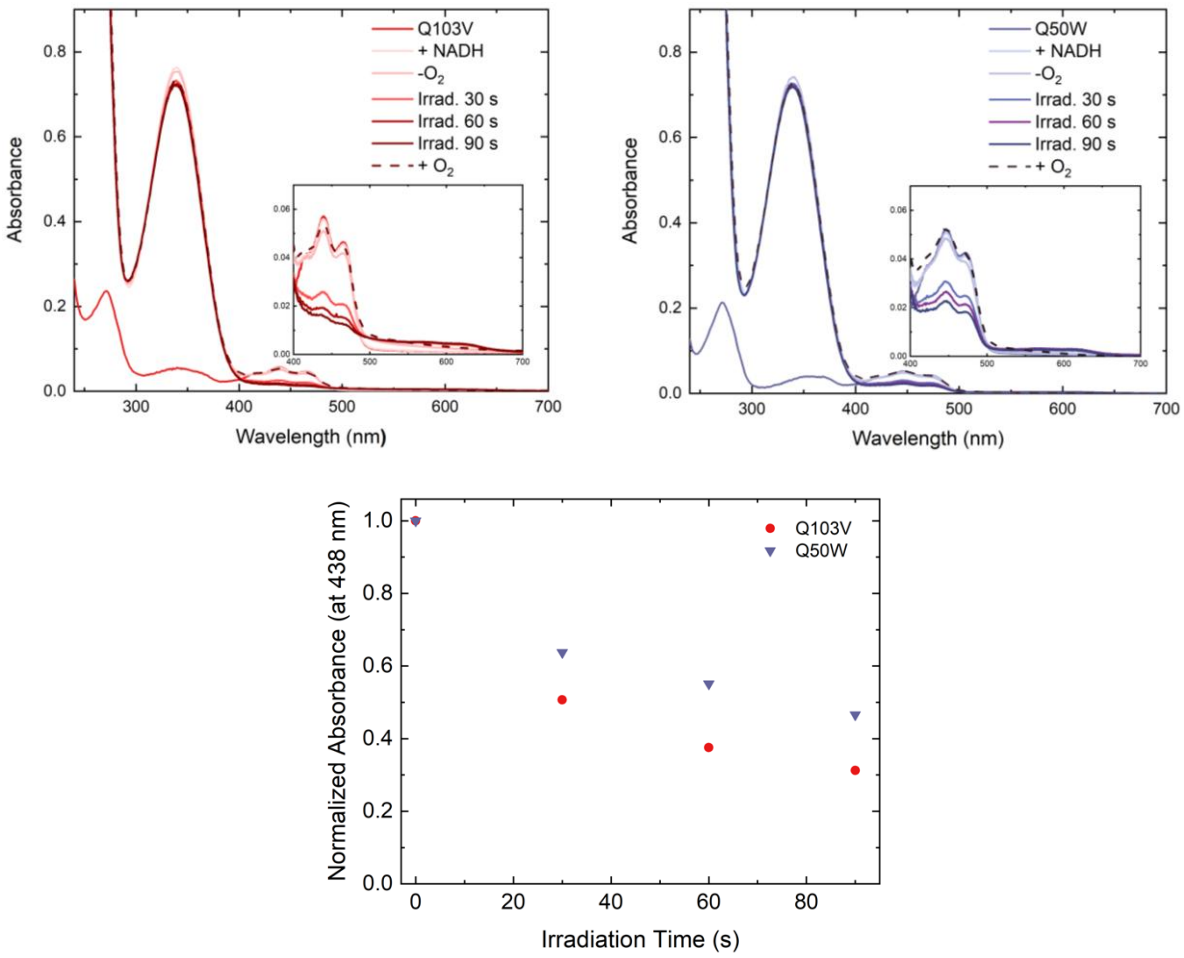

Figure S14. Photoirradiation of miniSOG Q103V and Q50W mutants (3 µM) in PB (20 mM, pH 7) under blue light irradiation (460 nm, 6 mW·cm^{-2}) in the presence of NADH (120 µM) and in the absence of O_2. After light irradiation, samples were exposed to the oxygen-containing ambient atmosphere to monitor the semiquinone disappearance (dashed line).

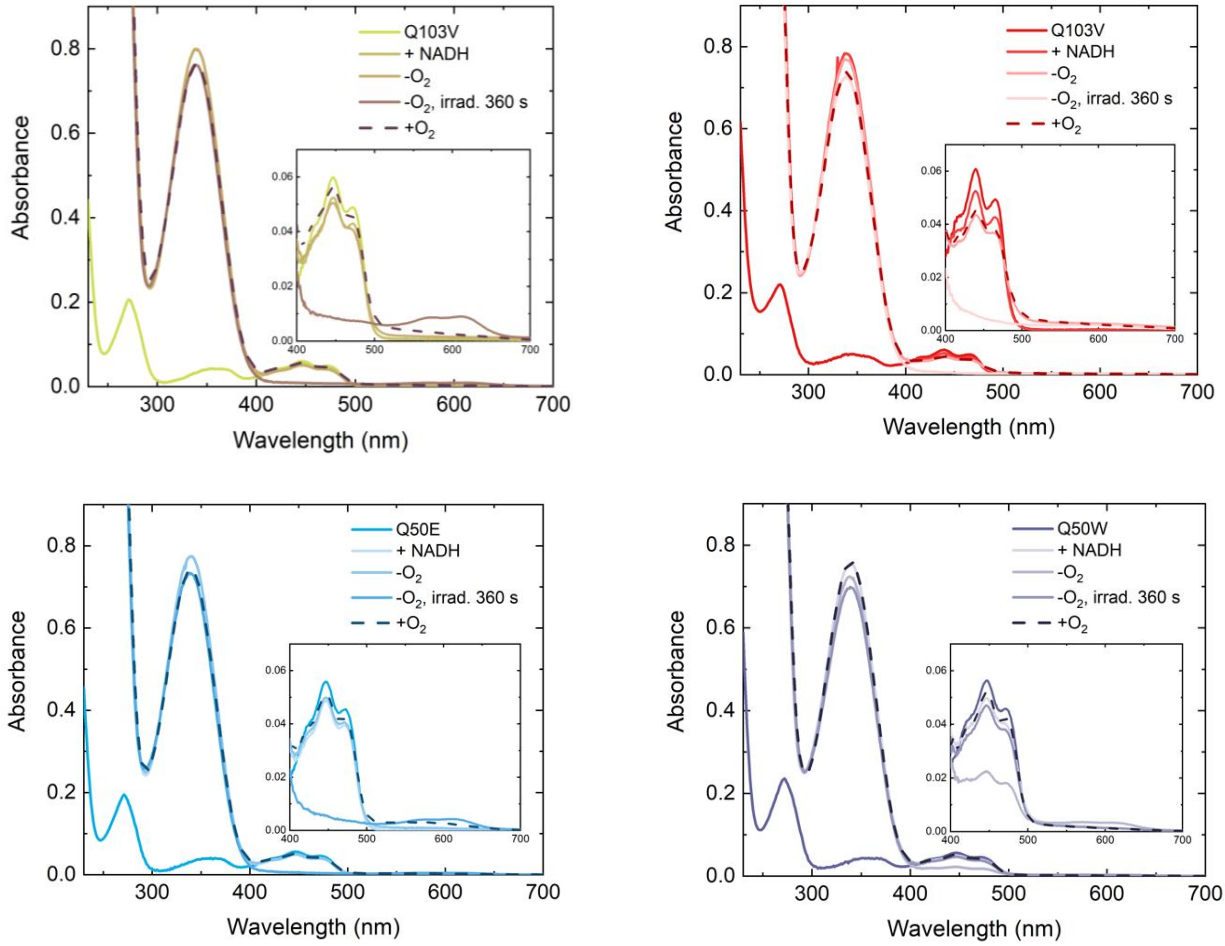

Figure S15. Photostability of miniSOG catalysts (3 µM) in PB (20 mM, pH 7) under blue light irradiation (460 nm, 6 mW·cm^{-2}) in the presence of NADH (120 µM) and in the absence of O_2. After light irradiation, samples were exposed to the oxygen-containing ambient atmosphere to monitor the semiquinone disappearance (dashed line).

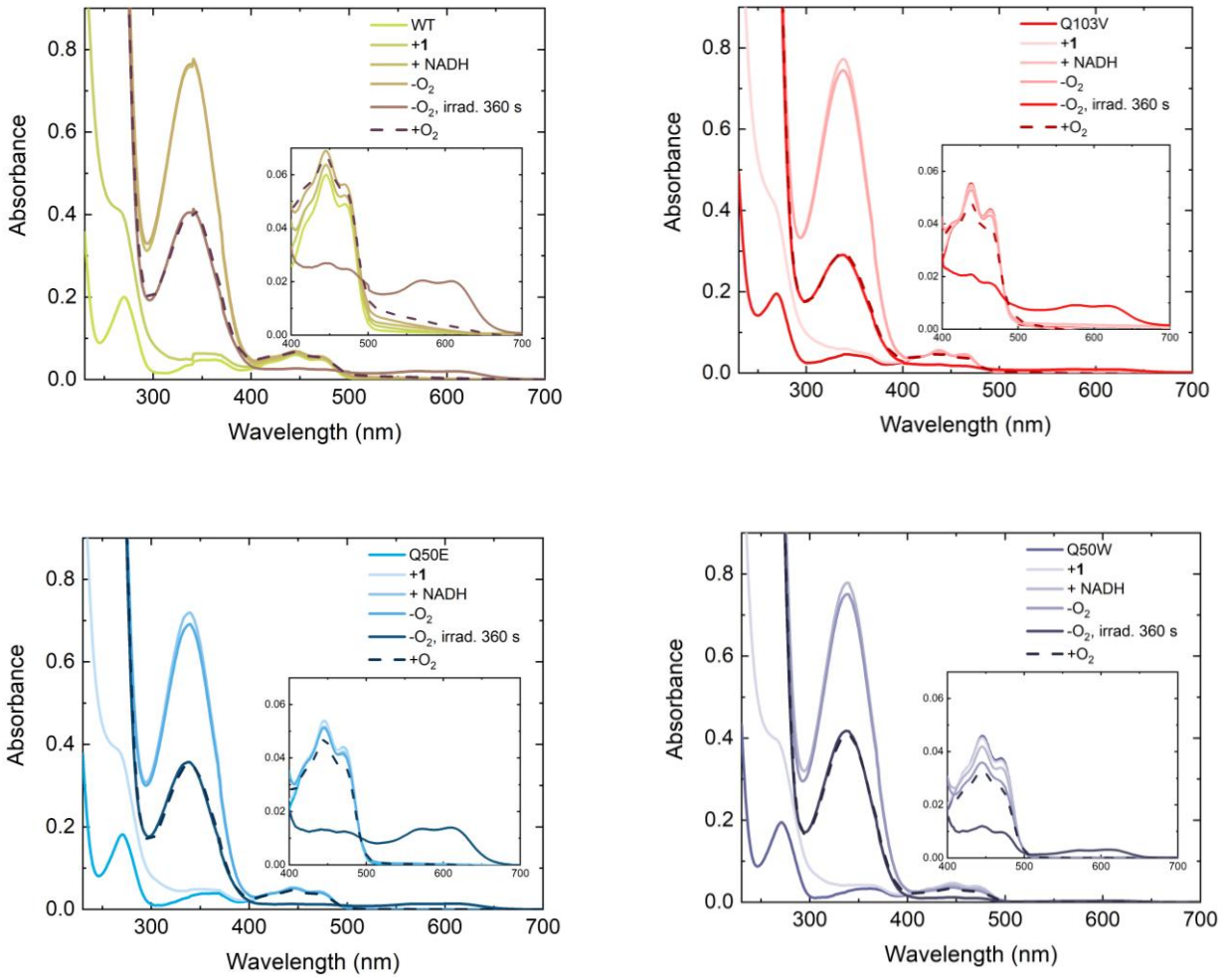

Figure S16. Photostability of miniSOG catalysts (3 µM) in PB (20 mM, pH 7) under blue light irradiation (460 nm, 6 mW·cm^{-2}) in the presence of **1** (60 µM) and NADH (120 µM), and in the absence of O_2. After light irradiation, samples were exposed to the oxygen-containing ambient atmosphere to monitor the semiquinone disappearance (dashed line).

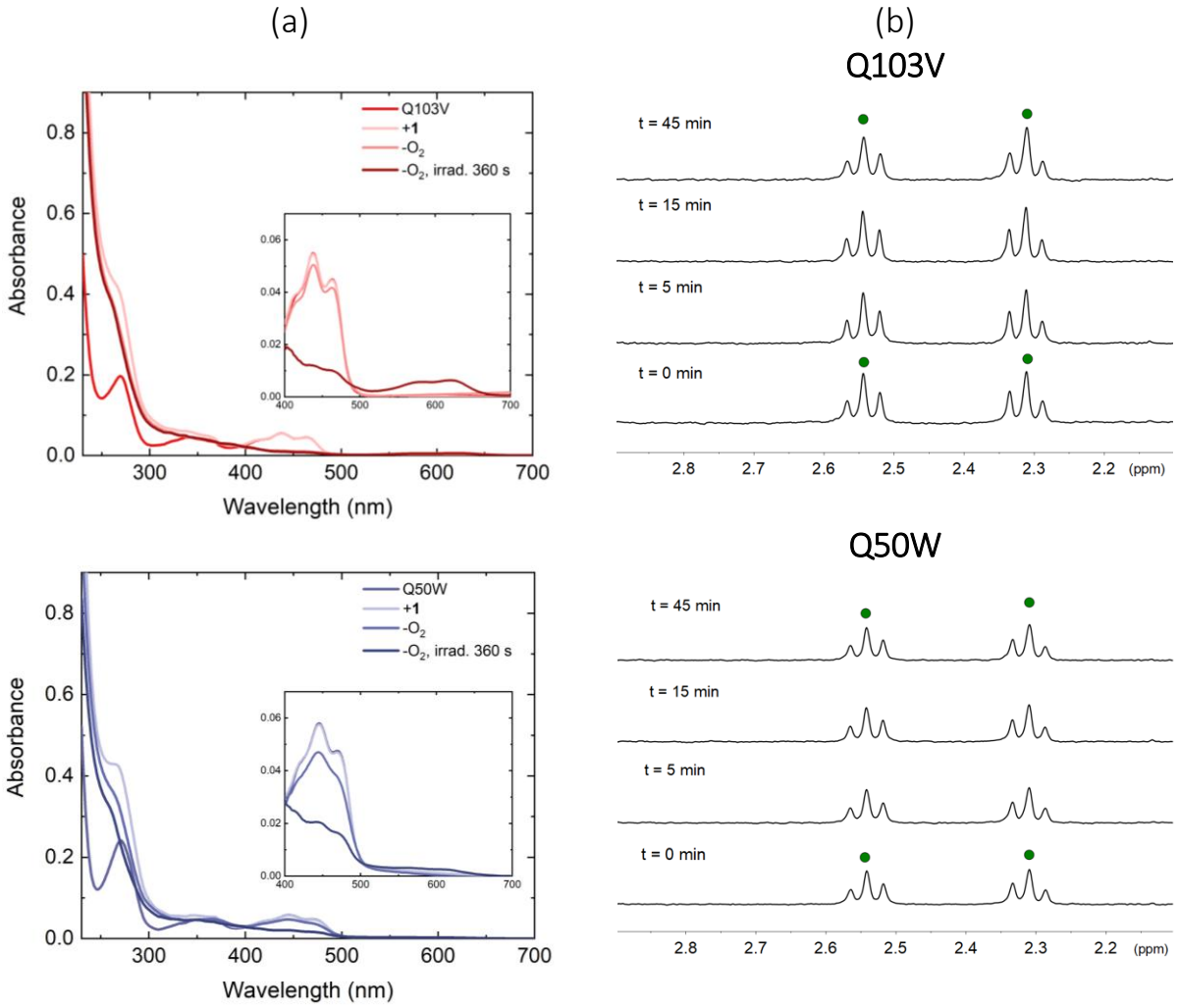

Figure S17. (a) Photostability of miniSOG Q103V and Q50W mutants (3 µM) in PB (20 mM, pH 7) under blue light irradiation (460 nm, 6 mW·cm^{-2}) in the presence of **1** (60 µM) and in the absence of O_2. (b) Photostability of **1** (500 µM) in 18 mM PB buffer (pH 7.0, 10% D_2O) in the presence of 25 µM miniSOG Q103V and Q50W mutants over time. ^{1}H NMR signal labelling: **1**: ● Pt–OCO**CH$_2$**CH$_2$CO$_2^-$, ● Pt–OCOCH$_2$**CH$_2$**CO$_2^-$.

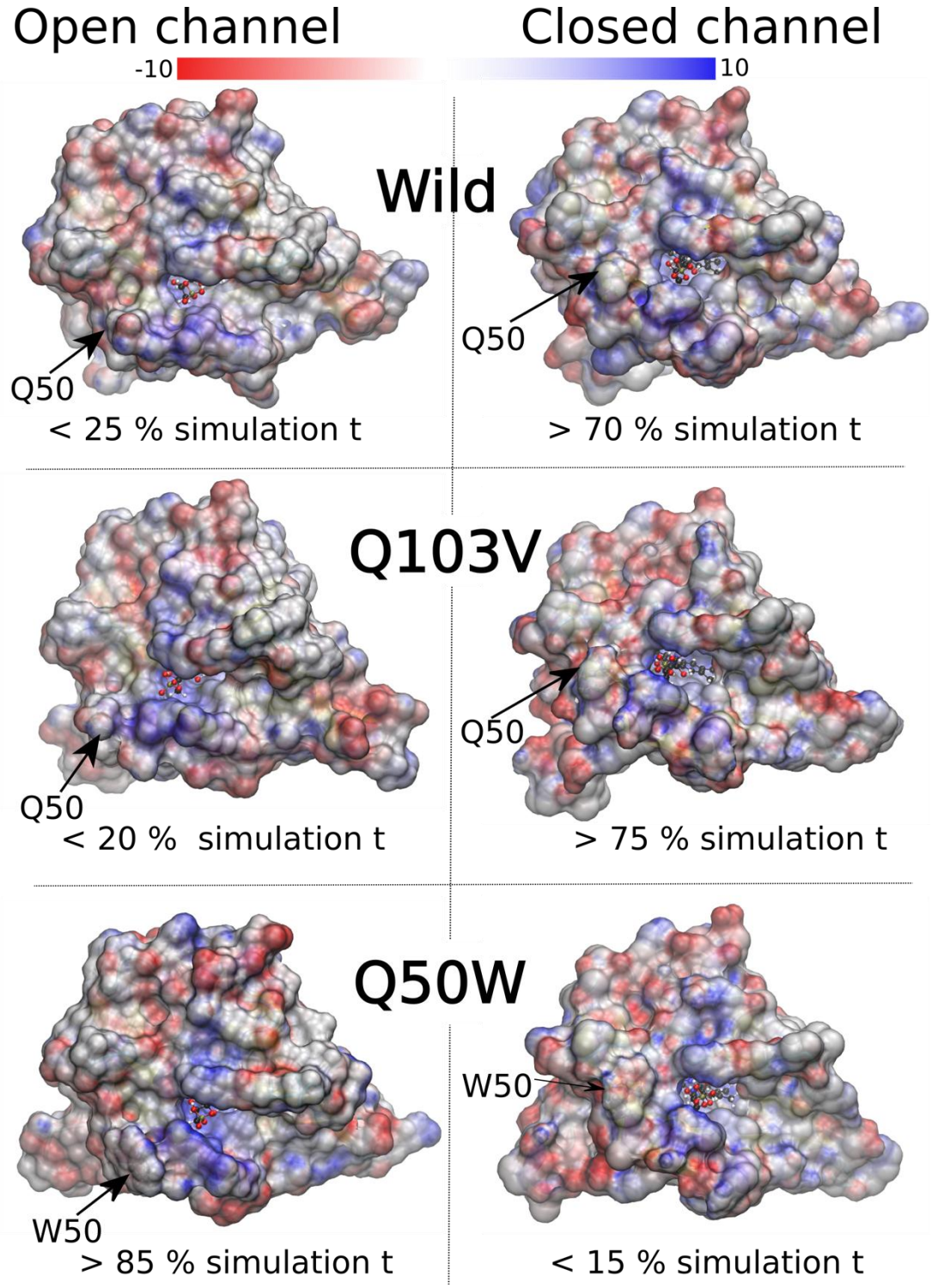

Figure S18. Solvent accessible surface of miniSOG variants in the open and closed conformations colored by Electrostatic Potential Surface (± 10 kT/e), and % of simulation time spent in each conformation.

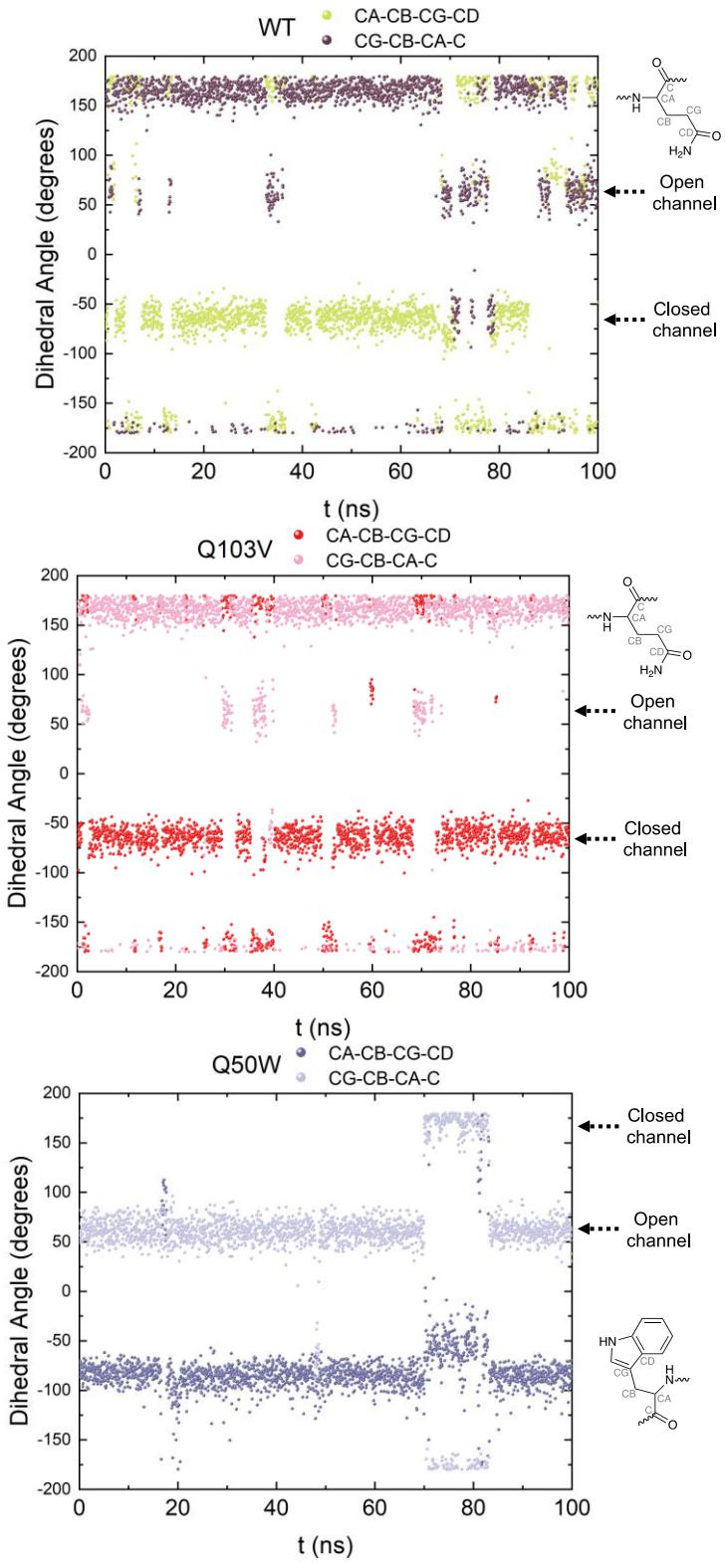

Figure S19. Representation of dihedral angles for residue 50 as function of simulation time. The open or closed channel conformation of miniSOG is determined by the values of these dihedral angles.

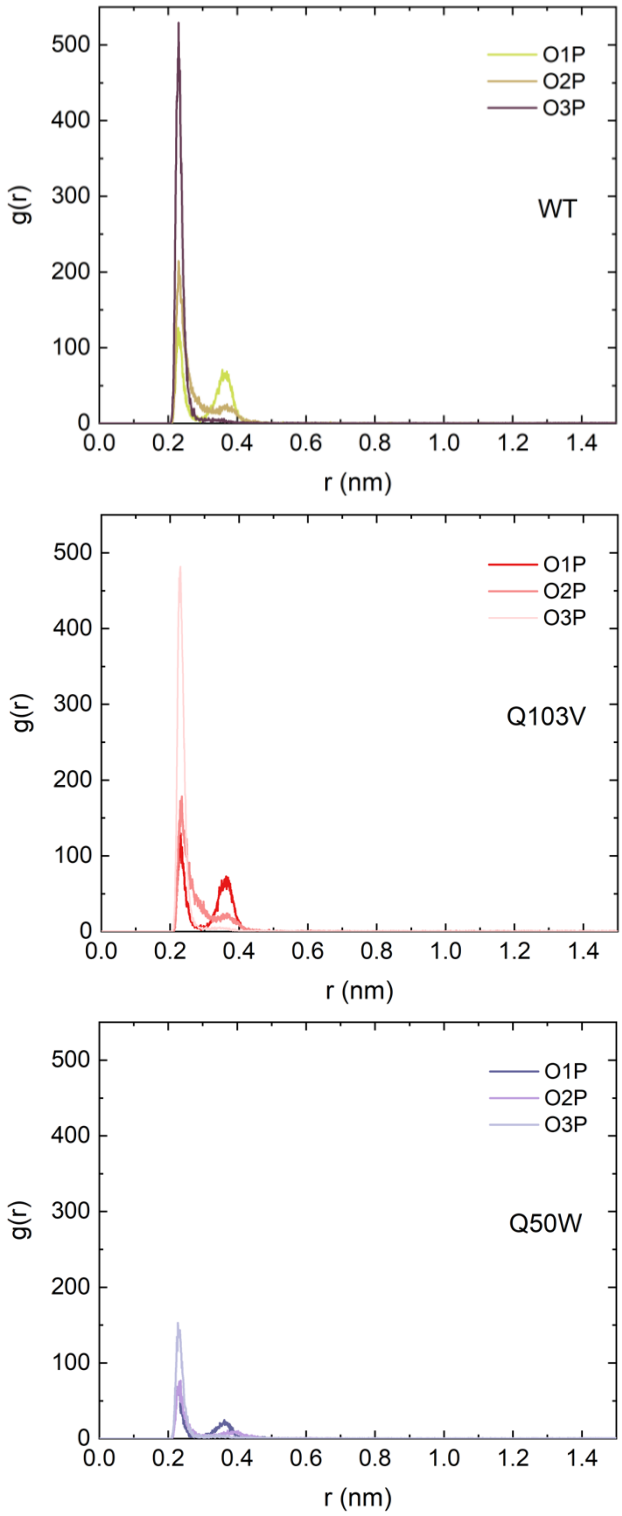

Figure S20. The Radial Distribution Function of Na^+ cations around phosphate oxygens (i.e. the probability distribution to find Na^+ cations at r distance from phosphate oxygens).

Appendix Chapter 5

Dual Bioorthogonal Activation of Prodrugs by Flavin and Palladium Chemistry

Supporting Information

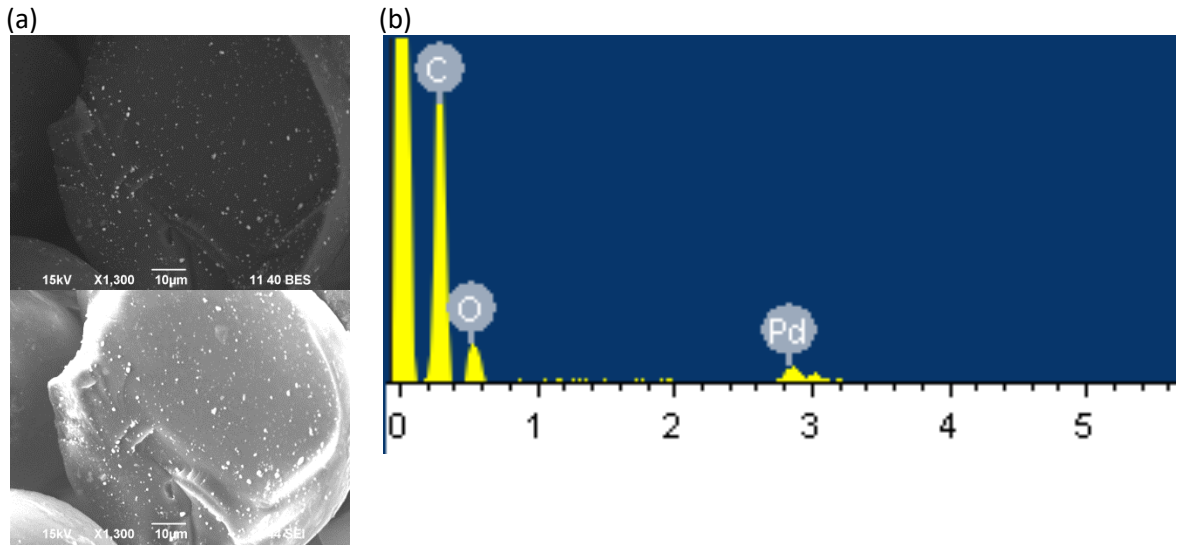

Figure S1. a) SEM Images obtained using Secondary Electron (SE) and Backscattered Electron (BE) detectors and b) EDX spectrum of the surface of **TARF@PdNPs**.

Table S1. Summary of results obtained by ICPMS after acid digestion of **TARF@PdNPs** resins and naked Tentagel resins.

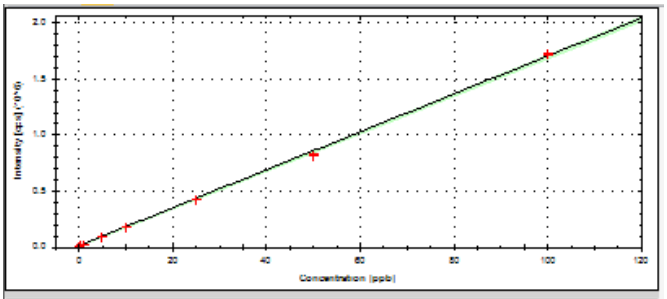

f(x) = b*x + a

Parameter	Value	Confidence Delta a	StdErr	Rel. StdErr [
b	16,908.441	+/-170.121	121.793	0.720
a	4,943.212	+/-0.000	0.000	0.000
R^2	0.999			
BEC	0.292 ppb			
IDL(LOD)	0.092 ppb			

Sample Name	Conc. (µg/L)	SD (µg/L)	RSD (µg/L)
Pd containing Resins	304714	2238.68	0.7
Blank (Tentagel Beads)	15.31	1.39	9.1

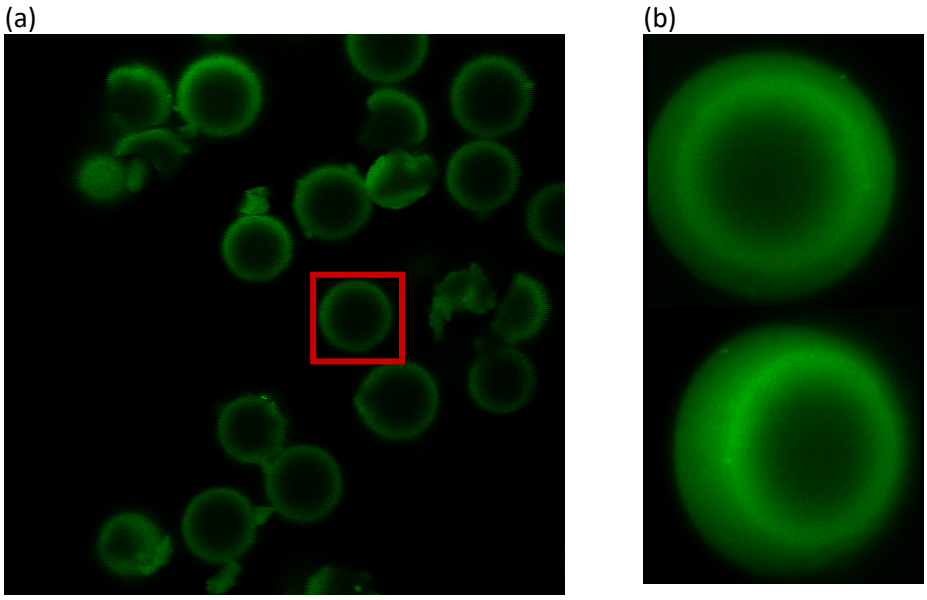

Figure S2. a) Image of **TARF@PdNPs** by fluorescent microscopy and b) 3D representation of fluorophore distribution through the surface.

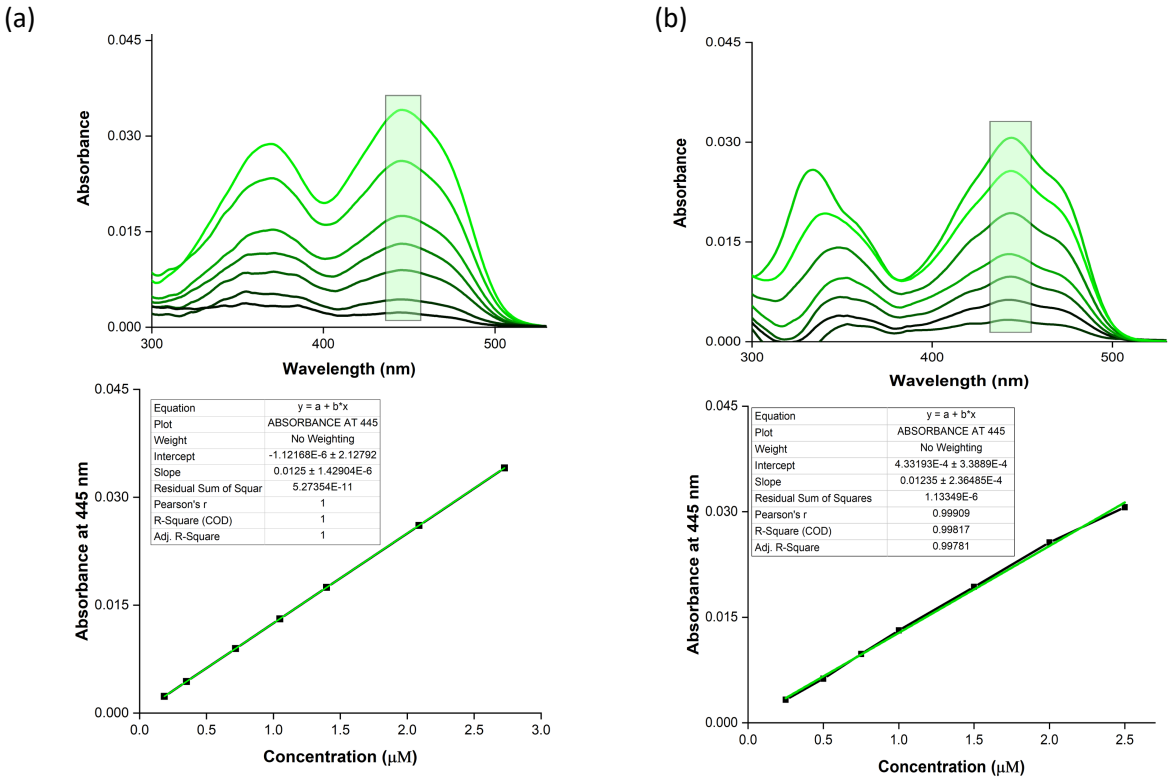

Figure S3. UV-Vis absorption spectra and calibration curve of **TARF** determined at 445 nm in: a) PBS (from 0.18 to 2.7 μM) and b) DCM/DMF (from 0.25 to 2.5 μM).

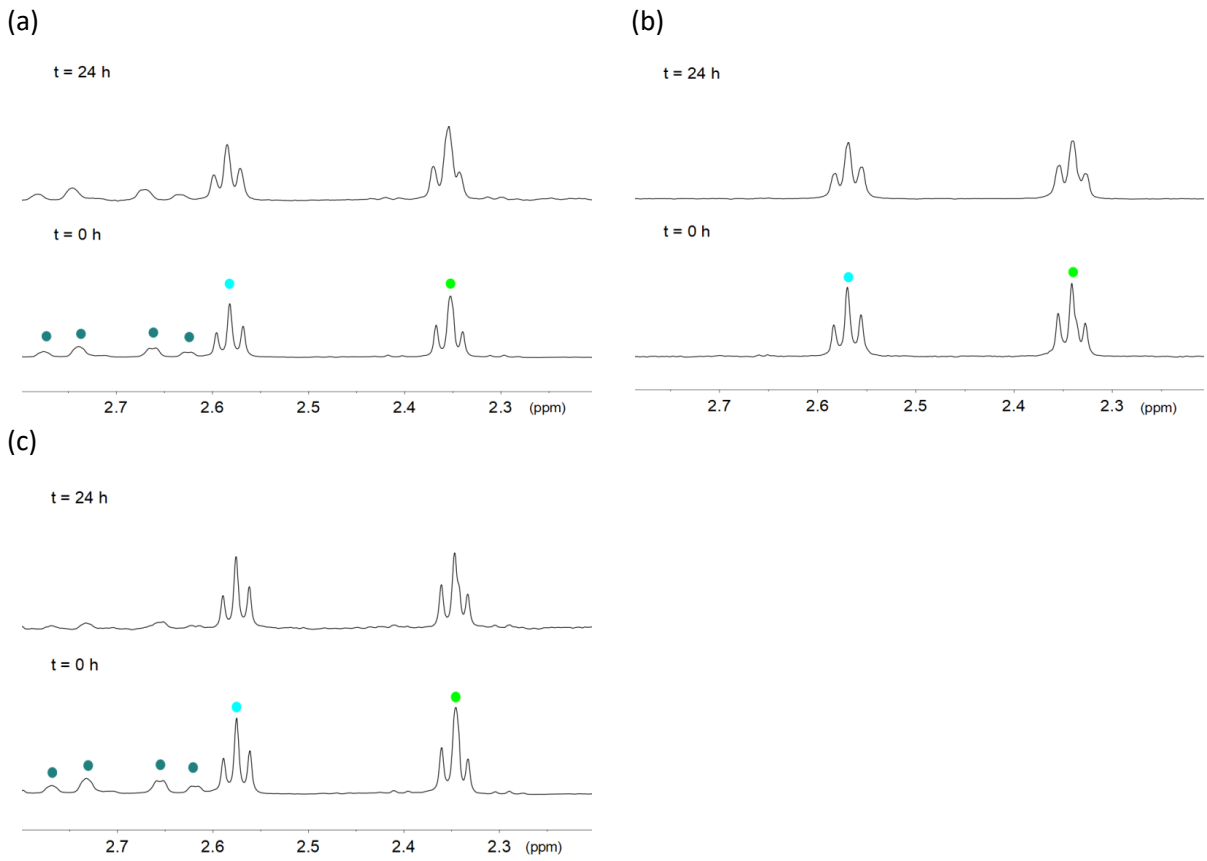

Figure S4. Dark stability of complex **1** (500 µM) in PBS (pH 7.4, 10% D_2O) (a) in the presence of 1 mM of **NADH**; (b) in the presence of 1.2 mg mL^{-1} of **PdNPs** and (c) in the presence of 1 mM of **NADH** and 1.2 mg mL^{-1} of **PdNPs** resins. ^1H NMR labelling: ● NADH, ● Pt–OCO**CH₂**$CH_2CO_2^-$, ● Pt–$OCOCH_2$**CH₂**CO_2^-.

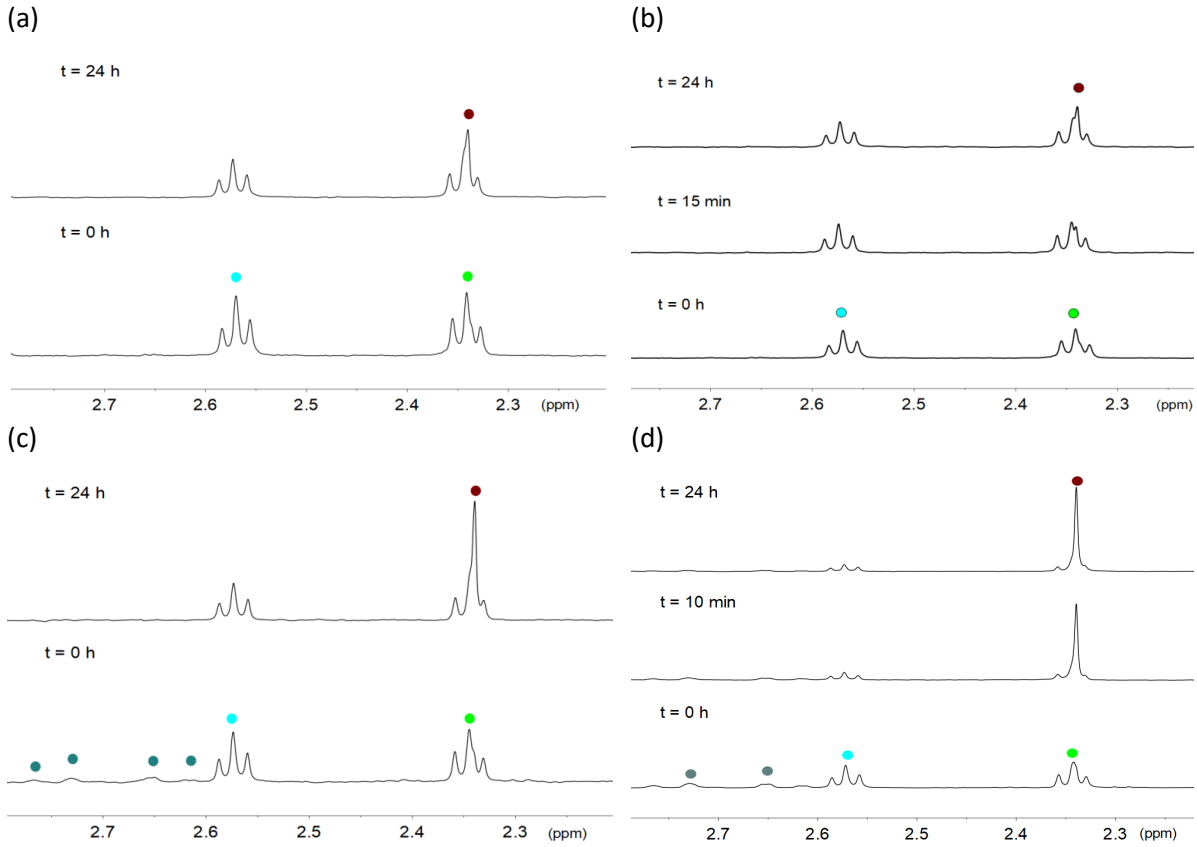

Figure S5. Stability of complex **1** (500 µM) in PBS (pH 7.4, 10% D_2O): (a) in the dark in the presence of 1.2 mg mL^{-1} of **TARF@PdNPs**; (b) in the presence of **TARF@PdNPs** after 10 minutes of 460-nm light irradiation and kept in the dark for 24 hours; (c) in the dark in the presence of 1 mM of **NADH** and 1.2 mg mL^{-1} of **TARF@PdNPs** and (d) in the presence of 1 mM of **NADH** and 1.2 mg mL^{-1} of **TARF@PdNPs** irradiated for 10 minutes upon 460-nm light irradiation (6 mW cm^{-2}). ^1H NMR signal labelling: ● **NADH**, ● Pt–OCO**CH_2**$CH_2CO_2^-$, ● Pt–OCOCH_2**CH_2**CO_2^-, ● free ^-O_2C**CH_2CH_2**CO_2^-.

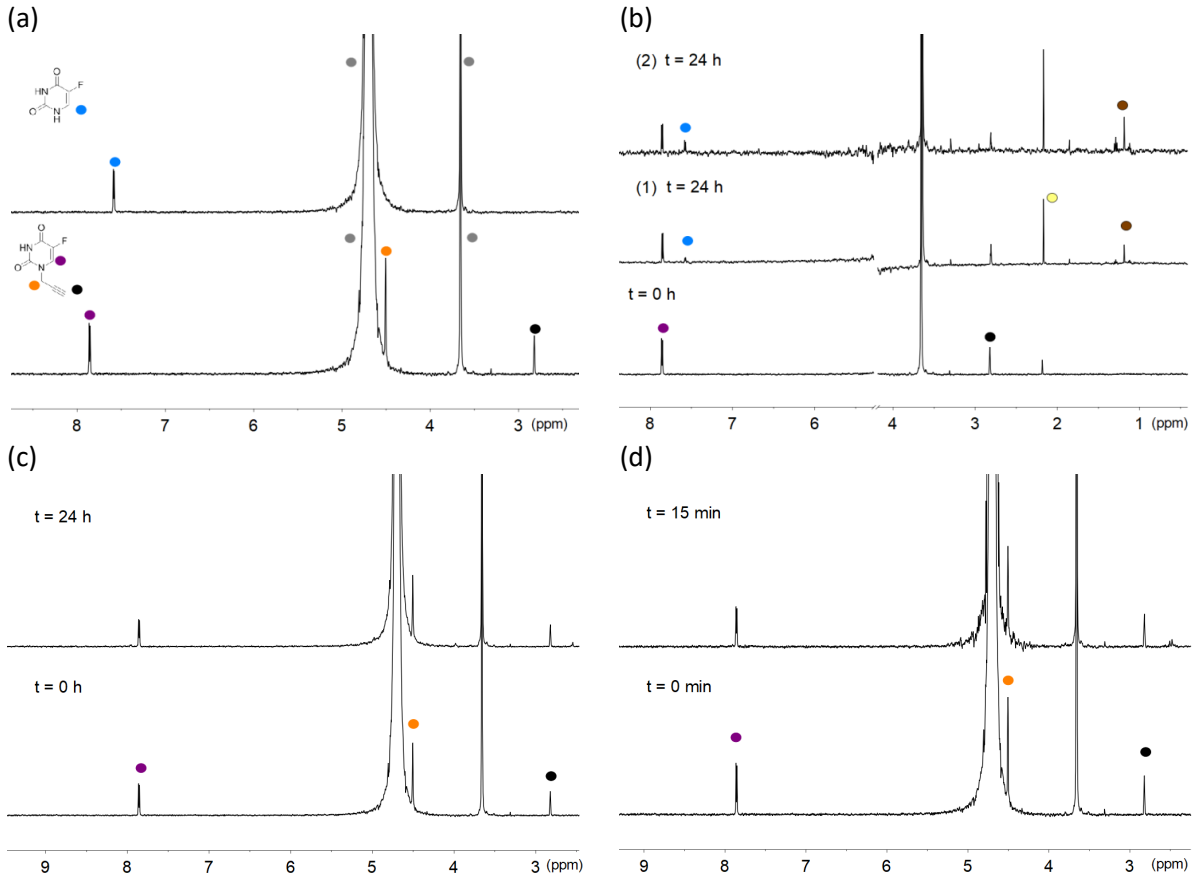

Figure S6. (a) Spectra of **Pro-5FU** (500 µM) and **5FU** (500 µM) in PBS (pH 7.4, 10% D_2O); (b) Stability of **Pro-5FU** (500 µM) in PBS in the presence of (1) 1.2 mg mL^{-1} and (2) 2.4mg mL^{-1} of **TARF@PdNPs** for 24 hours; (c) Dark stability and (d) Photostability of **Pro-5FU** (500 µM) in PBS in the presence of **FMN** (25µM) after 15 minutes of 460-nm light irradiation (6 mW cm^{-2}). ^1H NMR signal labelling: ● **Pro-5FU**, ● Pro-5FU–**CH_2**CCH, ● Pro-5FU–CH_2CC**H**, ● **5FU**, ● solvent residual peak ● Acetone (solvent residual peak).

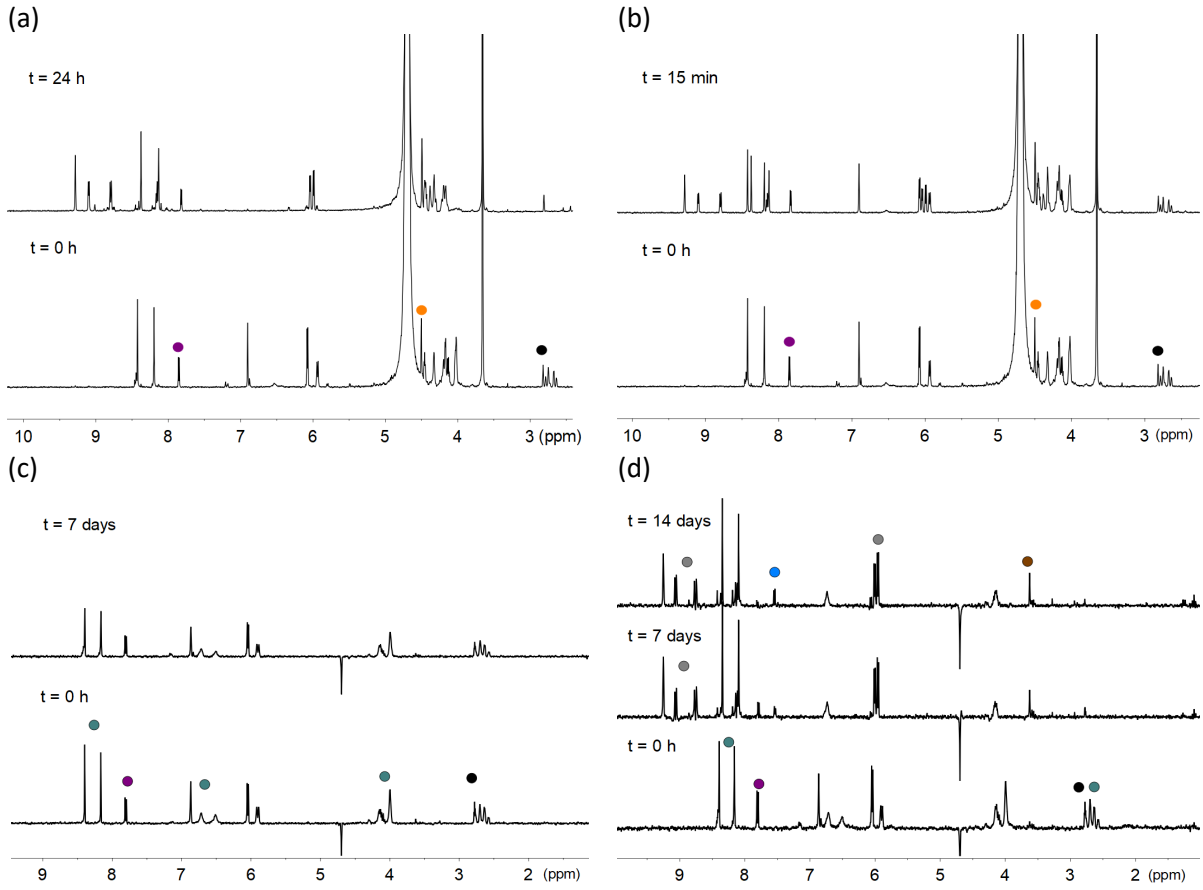

Figure S7. (a) Dark stability and (b) Photostability of **Pro-5FU** (500 µM) in PBS (pH 7.4, 10% D_2O) in the presence of 1 mM **NADH** and **FMN** (25µM) after 15 minutes of 460-nm light irradiation (6 mW cm^{-2}); (c) Dark stability of **Pro-5FU** (500 µM) in PBS in the presence of 1 mM **NADH** shaking for 7 days at 25 °C and (d) **Pro-5FU** activation in the presence of 1.2 mg mL^{-1} of **TARF@PdNPs** for 14 days at 25 °C. ^{1}H NMR signal labelling: ; ● NAD^+, ● **NADH**, ● **Pro-5FU**, ● Pro-5FU–**CH_2**CCH, ● Pro-5FU–CH_2CC**H**, ● **5FU**, ● hydroxyacetone.

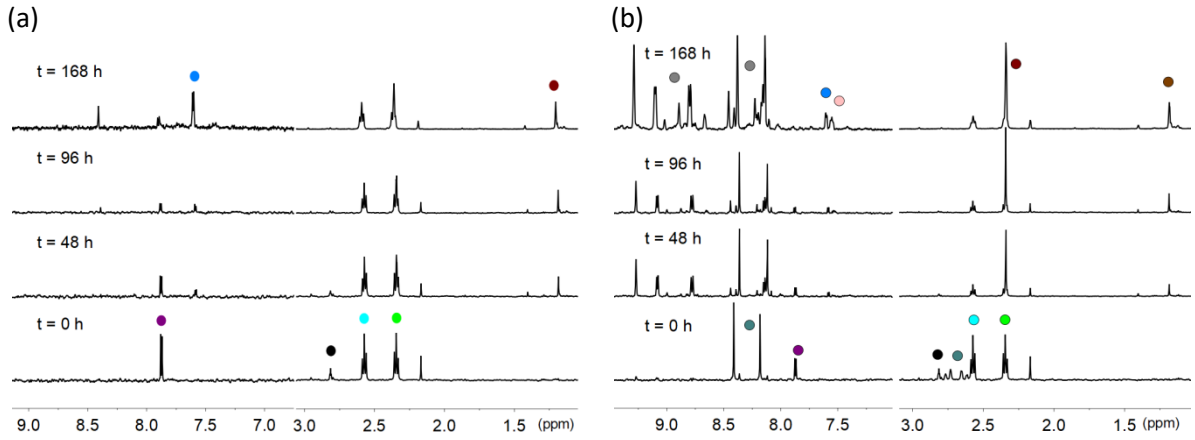

Figure S8. Dark Stability of **Pro-5FU** (500 µM) and **1** (500 µM) in PBS (pH 7.4, 10% D_2O) (a) in the presence of 1.2 mg mL^{-1} of **TARF@PdNPs** and (b) in the presence of 1.2mg mL^{-1} of **TARF@PdNPs** and 1mM **NADH**. ^1H NMR signal labelling: ● NAD^+, ● NADH, ● **Pro-5FU**, ● Pro-5FU–CH_2CCH, ● **5FU**, ● hydroxyacetone, ● Pt–$OCO\mathbf{CH_2}CH_2CO_2^-$, ● Pt–$OCOCH_2\mathbf{CH_2}CO_2^-$, ● free $^-O_2C\mathbf{CH_2CH_2}CO_2^-$ ● 5FU side reaction product$^-$.

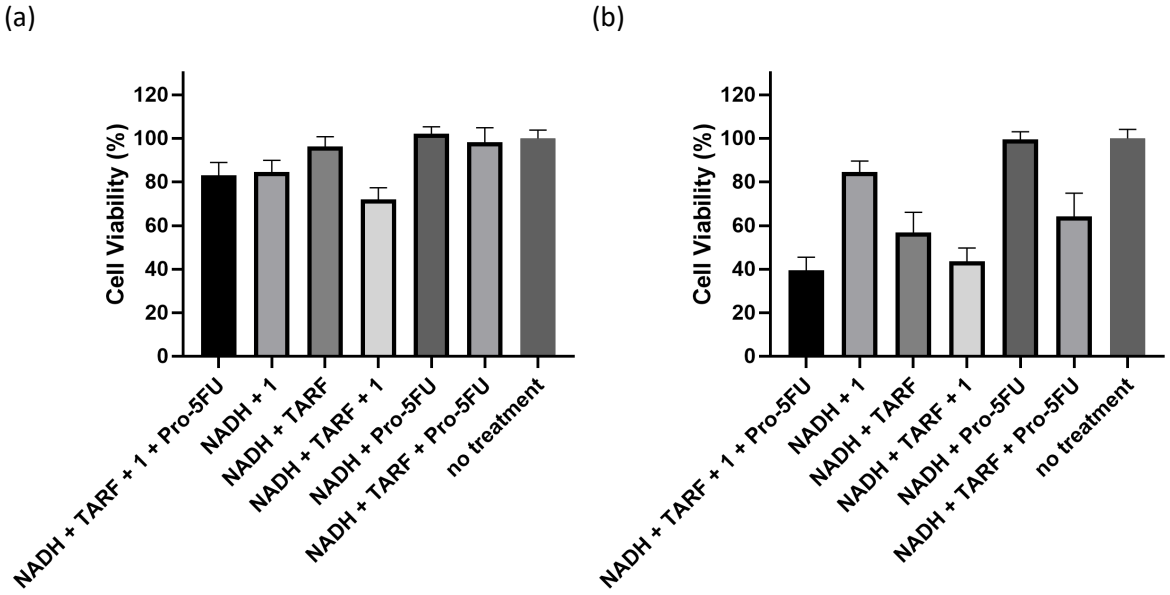

Figure S9. Cell viability results using selected combination of drugs and prodrugs, a) in the dark and b) after 30 seconds of blue light irradiation. Employed concentrations: **NADH** (50 µM), Cisplatin (1 µM), **5FU** (3 µM), **TARF** (1 µM), **1** (1 µM) and **Pro-5FU** (100 µM).

NMR characterization

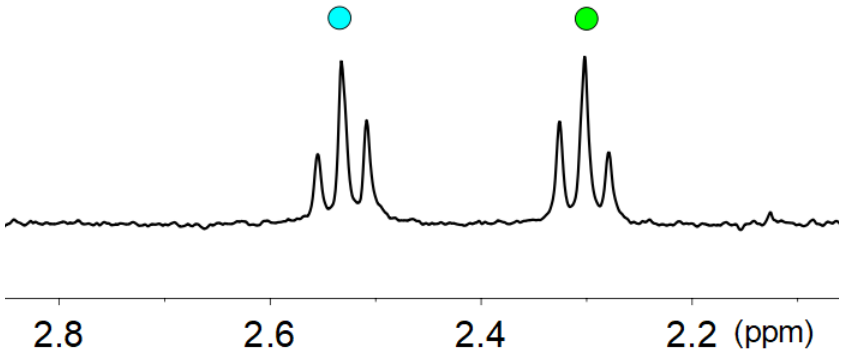

Figure S10. ^{1}H NMR of **1** in PBS (pH: 7.4, 10% of D_2O). ^{1}H NMR signal labelling: ● Pt–OCO**CH₂**$CH_2CO_2^-$, ● Pt–$OCOCH_2$**CH₂**CO_2^-.

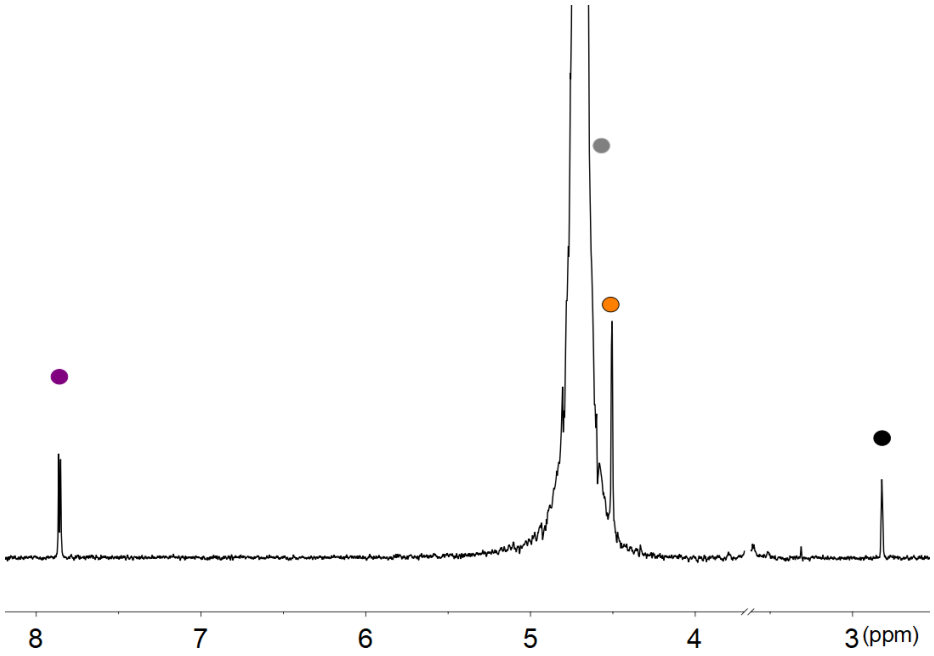

Figure S11. ^{1}H NMR of **Pro-5FU** in PBS (pH: 7.4, 10% of D_2O). ^{1}H NMR signal labelling: ● **Pro-5FU** ● H_2O solvent signal ^{1}H NMR signal labelling: ● **Pro-5FU**, ● Pro-5FU–**CH₂**CCH, ● Pro-5FU–CH_2CC**H**, ● solvent residual peak.

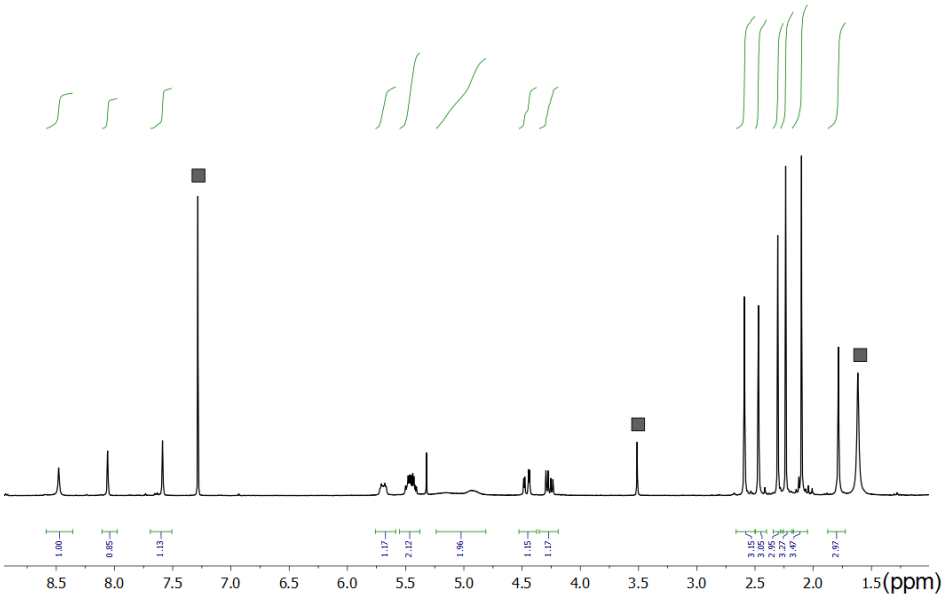

Figure S12. ^{1}H NMR of tetraacetylated riboflavin in deuterated chloroform ($CDCl_3$). Solvent residual peaks that corresponded to $CHCl_3$, MeOH and H_2O were labeled with ■.

Acknowledgements

First of all, I would like to thank Prof. Luca Salassa for providing me the opportunity to develop this Ph.D. thesis under his supervision in the DIPC. I highly appreciate all the knowledge that you share with me, you have made me a better scientist.

I would also like to thank Prof. Aitziber Lopez Cortajarena for providing me the opportunity to develop my research under her supervision in the CIC biomaGUNE. I should like to thank you for all the valuable and constructive discussions. I am also thankful to Prof. Xabier Lopez Pestaña for his assistance as my university tutor.

Obviously, big thanks to all the people from both laboratories and all the people that I met during the thesis. I just want to write some words of encouragement for all the people who need them:

“The world is not perfect for anybody, keep going forward, try to do the best with what you have”

Simplemente quiero dar las gracias a todas esas personas que sin esperar nada a cambio, han colaborado para que esto haya llegado a buen puerto.

Gracias Ama y Javier por estar a mi lado. Quiero acabar dando las gracias a la persona que me ha acompañado en esta aventura. Mila esker Maritxu! Zu gabe hau ezinezkoa izango litzateke.

Para acabar, Mil gracias a tod@s con l@s que he compartido algo más que ciencia.

Mila esker!

Curriculum Vitae

Juantxo_gurru@hotmail.com
0034 659 778841

Academic Profile

Chemistry Ph.D in *Bioorthogonal activation of platinum anticancer complexes* **(2017-2021).**

Research Groups: Inorganic Photochemistry Lab. & Biomolecular Nanotechnlogy Lab.

Supervisor: Dr. Luca Salassa & Dr. Aitziber L. Cortajarena

Donostia Interantional Physics Center and CIC BiomaGUNE, San Sebastián, Spain

Ph.D research stay (3 months 2019)

Research Group: Innovative Therapeutics Lab

Supervisor: Asier Unciti-Broceta

Institute of Cancer Research UK, Edinburgh Centre, MRC Institute of Genetics & Molecular Medicine (University of Edinburgh)

Experimental project: Dual Bioorthogonal Activation of Anticancer Drugs

Other short research stays

Research Group: Organic Nanotechnology Lab

Supervisor: Fabrizio Mancin

Department of Chemistry, University of Padova, Italy (*3 weeks in 2017*)

Experimental project: Synthesis of Flavin Derivatives

Research Group: Medicinal inorganic Chemistry

Supervisor: Chiara Gabbiani

Department of Chemistry, University of Pisa , Pisa, Italy (*3 weeks in 2019*)

Experimental project: Unconventional Photocatalytic activation of Platinum Terpyridine Complexes

Master of Science in Environmental Nanotechnology (2016)

Master thesis: *Variation of interfacial tension between water and toluene, due to the presence of gold nanoparticles*

Research Group: Bionanoplasmonics Lab

Supervisor: Dr. Javier Reguera

University of Zaragoza, Zaragoza, Spain

Degree in Environmental Sciences (2014)

University of the Basque Country (UPV/EHU) Vitoria, Spain.

Techniques and Practical skills

Language skills: **Spanish and Basque** (Mother tongues) and **English** (good).

Technical skills:

- Spectroscopy: UV-Vis, Fluorescence, Nuclear Magnetic Resonance (**NMR**) and Circular Dichroism (**CD**).
- Biology: Protein expression in E. Coli bacteria and cell viability experiments.
- Software: Microsoft Office™ tools such as Word™, Excel™ and PowerPoint™, ChemDraw™and MestreNova™.

Publications

1. Alonso-de Castro, S.; Terenzi, A.; Gurruchaga-Pereda, J.; Salassa, L.; "Catalysis Concepts In Medicinal Inorganic Chemistry", Chem. Eur. J., 2019, 25, 6651-6660.

2. Gurruchaga-Pereda, J.; Martínez, Á.; Terenzi, A.; Salassa, L.; "Anticancer Platinum Agents and Light",Inorg. Chim. Acta, 2019, 495, 118981.

3. Gurruchaga-Pereda, J.; Martínez-Martínez, V.; Rezabal, E.; Lopez, X.; Garino, C.; Mancin, F.; Cortajarena, A. L.; Salassa, L.; "Flavin Bioorthogonal Photocatalysis Toward Platinum Substrates", ACS Catal. 2020, 10, 187-196.

4. Gurruchaga-Pereda J.; Martínez-Martínez V.; Formoso E.; Azpitarte O.; Rezabal E.; Lopez X.; Cortajarena L. A.; Salassa L.; "Enhancing The Photocatalytic Conversion Of Pt(IV) Substrates By Flavoprotein Engineering", J. Phys. Chem. Lett. 2021, 12, 4504–4508**.**

Oral Presentations

1. Contribution with an oral communication to the "8th early stage researchers workshop in nanoscience" on June 13rd-14th 2018.
2. Contribution with an oral communication to the "II Jornadas Españolas de Biocatálisis" on June 25th-26th 2018.
3. Contribution with a flash communication to the "XXXVII Reunión Bienal De La Real Sociedad Española De Química" on May 26th-30th 2019.

Poster Presentations/Courses / Workshops

Course online "Buenas Prácticas en el Laboratorio (II): Gestión de Residuos".

Contributed 3 hours to practical activity "Química para ti" for high school students.

Poster presentation on March 3rd on the "2020 #RSCPoster Twitter Conference".

Summer Course: AEBIN Photochemistry School 2020. Attendant and part of the organizing committee.

Video presentation on RSC Photophysics and Photochemistry Online meeting 1st-3rd December 2020.

Poster presentation on December 16th on the 10th Early Stage Researchers Workshop in Nanoscience.

Flabinen Bidez Gauzatutako Katalisi Bioortogonala Sendagaien Aktibaziorako

Doktorego Tesia

JUAN GURRUCHAGA PEREDA

Donostia, 2021

Zuzendariak	Prof. Luca Salassa Prof. Aitziber L. Cortajarena
Unibertsitateko Tutorea	Xabier Lopez Pestaña

Aurkibidea

Laburpena

Kimioterapian erabiltzen diren farmako ez espezifikoen mugak gainditzeko eta bigarren mailako ondorioak saihesteko, katalisi metalikoa deritzona sortu da aukera baliagarri gisa. Erreakzio katalitiko ez natural askok, substratuarekiko selektibitate handia eta anplifikazio gaitasuna erakusten dute. Hori dela eta, sistema biologikoen barnean farmakoen efektua hobeto kontrolatzeko erabiliak izan dira.
Erreakzio ez naturalek, sistema biologiko bizidunen barnean ostalariaren ohiko funtzioak oztopatu gabe gauzatzeko duten gaitasuna, bioortogonal moduan definitu da. Bioortogonal kontzeptua garatzen zihoan heinean, metaletan oinarritutako katalisiarekin batera ikertu zen, bi ikerketa alor nagusi sorraraziz:

Farmako katalitiko metalikoen erabilera biomolekula garrantzitsuen eraldaketa eragiteko. Orokorrean, farmako katalitiko metalikoek, hainbat biomolekulen eraldaketa egiteko gai dira. Beraz, katalizatzailearen kontzentrazio txikia nahikoa izango litzateke zeluletan erantzun kaltegarria eragiteko. Minbiziaren kontrako ekintza eta toxikotasuna, biomolekula garrantzitsuen degradazioaren ondorioz, edo zelulen homeostasia mantentzen duten biomolekulen aldaketen ondorioz sortzen da.

Metaletan oinarritutako katalisia profarmakoen aktibazioa gauzatzeko. Normalean, trantsizio metal katalizatzaile batek, farmako inerte baten eraldaketa eragiten du, honen bikote toxikoa sortuz. Hurbilketa honen bitartez, espezie toxikoak katalizatzailearen inguruan sortzen dira, kalte zelularra ehun edo organo zehatz batean kokatuz.

Tesi honetan, erreakzio katalitiko mota berri bat ikertu dut. Non, **konplexu metalikoek, katalizatzaile moduan erabili beharrean, substratu moduan erabiltzen dira minbiziaren kontrako Pt^{IV} profarmakoen aktibazio fotokatalitiko bioortogonala gauzatzeko**. Hurbilketa katalitiko honetan, flabinen ezaugarri fotokimikoak, energia baxuko argiaren menpe profarmako metalikoak aktibatzeko erabili dira. Erreakzio hauen mekanismo katalitikoaren xehetasunak ikertu ditut, Pt^{IV} konplexuen erredukzioa eragiten duten espezie katalitiko nagusiak identifikatuz. Horretaz gain, egitura katalitikoaren eraldaketa arinek (flabina askeetan eta flabina barnean duten proteinetan) ekintza katalitikoan nolako eragina duten aztertu dut, ikusitako ezberdintasunak arrazionalizatuz.

Lehenengo bi kapituluek, nire ikerketa lanaren testuingurua deskribatzen dute. Hurrengo hiru kapituluek berriz, doktoregoan egindako lan esperimentala deskribatzen dute.

1. Kapituluak minbiziaren kontrako platino agente fotoaktibagarrien adibide adierazgarrienak laburbiltzen ditu. Kapituluak, argiaren bidez Pt konplexuen toxikotasuna menderatzeko egin diren ikerketak kronologikoki deskribatzen ditu, Rosenbergen

aurkikuntzatik gaur egunera arte. Kapituluaren amaieran, farmako askatze eta aktibazio estrategia moderno eta interesgarrienak azpimarratu ditut.

"Anticancer platinum agents and light" Gurruchaga-Pereda, J.; Martinez, Á.; Terenzi, A.; Salassa, L.; Inorg. Chim. Acta, 2019, 495, 118981.

2. Kapituluak kimioterapia helburuetarako metaletan oinarritutako katalisi bioortogonalaren erabilera laburbiltzen du. Kapituluan, estrategia katalitikoen arteko desberdintasun nagusiak nabarmentzen saiatu naiz. Eztabaida hiru ataletan antolatu da: Zelulen homeostasia mantentzeko garrantzitsuak diren biomolekulekin erreakzionatzen duten konplexu metalikoak, profarmakoen aktibazioa katalizatzaile metaliko heterogenoen bidez, eta Pt^{IV} profarmakoak ez-ohiko substratu gisa erabiltzen dituen aktibazio fotokalitiko bioortogonala.

3. Kapituluak flabinek egindako Pt^{IV} substratuen aktibazio fotokatalitikoaren xehetasun mekanistikoak ikertzen ditu. Riboflabina (Rf), flabina mononukleotidoa (FMN), tetra-O-azetilatutako riboflabina (TARF) eta lumiflabina (Lf) flabina askeak eta miniSOG (mini Singlet Oxygen Generator) flaboproteina eta lau Pt^{IV} profarmako erabiliz, katalizatzaileen eta substratuen bilduma ikertu eta zabaldu zen. Pt^{IV} profarmakoak Pt^{II} farmakoetan bihurtzen zituen espeziea, erreduzitutako flabina zela frogatu zen.

"Flavin Bioorthogonal Photocatalysis Toward Platinum Substrates" Gurruchaga-Pereda, J.; Martínez-Martínez, V.; Rezabal, E.; Lopez, X.; Garino, C.; Mancin, F.; Cortajarena, A. L.; Salassa, L., ACS Catal. 2020, 10, 187-196.

4. Kapituluak mutagenesi guneratuaren erabilera ikertzen du miniSOG flaboproteinaren ezaugarri fotokatalitikoak aldatzeko. Q103V, Q50E eta Q50W mutanteen ezaugarri katalitikoak, jatorrizko tipoarekin (WT) alderatu zirenean, Q103V mutanteak bizitza denbora triplete luzeena azaldu zuen. Horren ondorioz, bi Pt^{IV} profarmako ereduen eraldaketa katalitiko handiena erakutsi zuen mutante honek.

"Enhancing The Photocatalytic Conversion Of Pt(IV) Substrates By Flavoprotein Engineering" Gurruchaga-Pereda, J.; Martínez-Martínez, V.; Formoso, E.; Azpitarte, O.; Rezabal, E.; Lopez, X.; Cortajarena, L. A.; Salassa, L., J. Phys. Chem. Lett. 2021, 12, 4504–4508.

Aurreko lanez gain, proiektu eta berrikusketa artikulu ezberdinetan lagundu dut. Esfortzu kooperatibo hauen ondorioz, artikulu bat gehiago argitaratu nuen:

"Catalysis Concepts In Medicinal Inorganic Chemistry" Alonso-de Castro, S.; Terenzi, A.; Gurruchaga-Pereda, J.; Salassa, L., Chem. Eur. J., 2019, 25, 6651-6660.

1

Minbiziaren Aurkako Platino Agenteak eta Argia

Kapitulu honetan deskribatutako lanaren atal bat, Chim. Acta, 2019, 495, 118981 (egileak: Gurruchaga-Pereda, J.; Martínez, Á.; Terenzi, A.; Salassa, L.) aldizkarian argitaratu zen.

1.1 Sarrera

Minbiziaren aurkako Pt konplexuen eta argiaren arteko harremana cisplatinoaren aurkikuntzarekin batera hasi zen. Eremu elektrikoen eraginpean, Pt espezieak, *Escherichia coli* bakterioen ezohiko hazkuntza haritsuaren erantzuleak zirela identifikatu ostean,[1] Rosenbergek eta lankideek ultramore (UV) argiarekin irradiatutako $(NH_4)_2[PtCl_6]$ disoluziotik lortutako *cis*-$[PtCl_4(NH_3)_2]$ neutrala, zelula zatiketaren inhibitzaile eraginkorra zela frogatu zuten.[2,3] Aurkikuntza horrek, Pt konplexuak minbiziaren aurkako farmako gisa berretsi eta cisplatinoaren finkapena sendagai lider bezala sustatu zuen.[4–6]

Horren ondoren, ikerkuntza arlo honek Pt konplexuen alderdi biologiko-kimikoak aztertu zituen eta argiaren erabilera urte askoz alde batera utzi zen. Bigarren mailako efektuak gutxitzeko, Pt^{IV} profarmakoen kontzeptua ezarri ondoren, ikertzaileek, Pt agenteen fotokimikak zer nolako eragina zuen toxikotasuean aztertzera bueltatu ziren. Terapia fotodinamikoan erabiltzeko (PDT, Photodynamic Therapy) klinikoki onartutako lehen sendagaiaren (photofrin, 1993) onarpenak, arlo honen ikerketa bultzatu zuen ere.[7]

Berriskusketa motz honen helburua, minbiziaren aurkako Pt konplexu fotoaktibagarrien adibiderik arrakastasuenak aurkeztea da. Kapitulu hau, hiru atal nagusietan banatuta dago. Lehenengo eta bigarren ataletan, argiaren eragina minbiziaren aurkako Pt^{II} eta Pt^{IV} konplexuen biologian eztabaidatzen da. Hirugarren atalean ordea, azken urteotan Pt konplexuen ekintza biologikoa pizteko helburuarekin garatutako sendagai askatze eta fotokimika estrategia berriak nabarmendu dira. Pt konplexuek eragindako efektu biologikoa, argi irradiazioaren menpe, espezie metalikoek eragindako erradikal ekoizpen handipenarengatik (metal-enhanced phototoxicity) edota konplexu metalikoen fotoaktibazioarengatik (photo-enhanced toxicity) sor daiteke. Testu honetan, fototoxikotasun hitzak, bi kontzeptuak bat egiten ditu. Hemen deskribatutako sistemak hobeto ulertu ahal izateko, lehenik eta behin Pt^{II} eta Pt^{IV} konplexuen ezaugarri elektronikoak laburbildu dira. Helburu hori lortzeko, gure arreta Rosenbergen lehen ikerketetan jarri eta *cis*-$[PtCl_2(NH_3)_2]$ eta *cis*-$[PtCl_4(NH_3)_2]$ konplexuak, eredu adierazgarri gisa hartu dira.

1.2 Pt^{II} eta Pt^{IV} konplexuen fotokimika

Minbiziaren aurkako terapian interesagarriak izan daitezkeen Pt^{II} eta Pt^{IV} konplexuen fotokimikan, fotodisoziazio (Pt^{II} eta Pt^{IV}) edota fotoerredukzio (Pt^{IV}) erreakzioak dira garrantzitsuenak. Adibide gehienetan, konplexu hauek ez dira lumineszenteak eta horren ondorioz, zaila da teknika espektroskopiko arrunten bidez, propietate elektroniko kitzikatuak aztertzea. Orain dela gutxi, zenbait Pt^{IV} gatz[8,9] eta konplexuekin[10] (azidak ere[11,12]) frogatu den moduan, ezaugarri espektroskopiko bereizgarririk ez edukitzeak, hauen egoera kitzikatuen bilakaera aztertzeko, teknika ultra-azkarren (adib. ebazpen temporala duen absortzio-espektroskopia eta infragorrri-espektroskopia) erabilera beharrezkoa egiten du.

Hala ere, 60-90. hamarkadetan zenbait ikerketa argitaratu ziren, non kimioterapian aplikagarri izan daitezkeen Pt konplexuen fotokimika aztertu zen. Bestalde, Pt^{II} konplexuak 2,2´-bipiridina moduko diamino estekatzaile aromatikoekin, emisio propietate altuak dituzte eta hauen propieta fotofisiko eta fotokimikoak sakonki ikertu dira sentsore, katalisi eta biologia aplikazioetarako.[13]

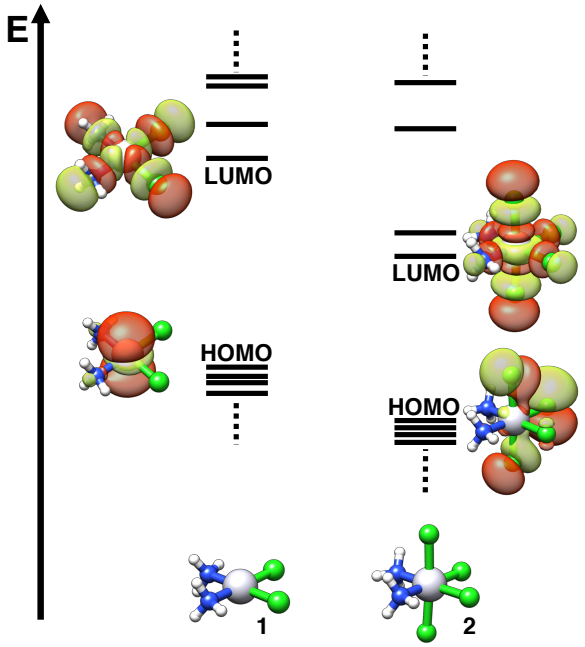

1. Irudia. 1) *cis*-$[Pt^{II}(NH_3)_2Cl_2]$ eta (**2**) *cis*-$[Pt^{IV}(NH_3)_2Cl_4]$ konplexuen egitura elektroniko eskematikoa eta DFT (dentsitate funtzionalaren teoria) bidez kalkulatutako muga orbitalak SDD mailan.[14] Atomoen kolore kodea: grisa = Pt, berdea = Cl, urdina = N, zuria = H. HOMO = Betetako orbital molekular altuena; LUMO = Betetako orbital molekular baxuena.

1. Irudian ikus daitekeen moduan, Pt^{II} (*cis*-$Pt^{II}(NH_3)_2Cl_2$, cisplatinoa, **1**) eta Pt^{IV} (*cis*-$[PtCl_4(NH_3)_2]$, **2**) konplexuen egitura elektronikoen LUMO orbitalek, izaera σ-antilotzailea erakusten dute. Argi irradiazioaren menpe, orbital hauek bete egiten dira disoziazio egoera kitzikatuak lortzeko; konplexuen erreaktibitatea piztuz. **1**, **2** eta antzeko sistemen egoera kitzikatuek, estekatzailetik-metalera karga transferentzia (LMCT) edo estekatzaile eremu (LF edo d-d) izaera dute. LMCT trantsizioak, fotoerredukzio eta estekatzaile ordezpen (estekatzailearen arabera) erreakzioekin lotzen dira. LF trantsizioak ordea, fotoisomerizazio eta fotoerrazemizaio erreakzioekin lotzen dira. Pt^{II} eta Pt^{IV} konplexuen (**1**, **2** eta antzeko konplexuak) ezaugarri bereizgarria, HOMO-LUMO orbitalen arteko jauzi energetiko handia da. Horren ondorioz, nekez aurkitzen dira absortzio bandak 400 nm baino handiagoko uhin-luzeretan.

Pt konplexu fotoaktibagarrien diseinu zentzudunek, konplexuen egonokortasuna ilunpean eta erreduktore biologikoen aurrean kontuan hartu behar dute, baita haren fotokimika ahal den moduan aurreratu ere. Pt^{II} eta Pt^{IV} konplexuen kasuan, iragarpen hori ez da gauza

erraza eta askotan, erreakzioaren fotoproduktuak, ordezkapen, erredukzio eta isomerizazio espezieen nahasteak dira.

1.3 Pt^{II} konplexu fotoaktiboak

Minbiziaren kontrako Pt^{II} konplexuen irradiazio zuzenak, hauen aktibitate biologikoa areagotzeko baliogarritasun murriztua duela frogatuta dago. Brabecek eta kolaboratzaileek, UV-rekin argiztatutako carboplatinoren (5 ordutik gora, 365 nm, 4.3 $mW \cdot cm^{-2}$) DNA-ra lotzeko gaitasuna, cisplatinoarekin alderagarriak diren mailetara handitzen zela deskribatu zuten.[15] Era berean, transplatino inaktiboak argi irradiazioaren menpe (365 nm, 50 min, 1.77 $mW \cdot cm^{-2}$), ugaltze zelularraren aurkako ekintza erakutsi zuen DNA interharia eta DNA-proteina gurutzamendua bultzatuz.[16] Quirogak, Malinak eta Bednarskik, isopropil, dimetil edo metilamina estekatzaileak zituzten *trans*-diioduro konplexuak, energi baxuko (0.12 $mW \cdot cm^{-2}$) argiarekin 350 nm-tara irradiatzerakoan, ilupetan baino 1.5–3 aldiz toxikotasun handiagoa azaltzen zutela deskribatu zuten. Bestalde, isopropilamina eratorriaren *cis* isomeroa baldintza berdinen menpe frogatzerakoan, ez zen efektu biologikorik erakutsi.[17]

Energia altuko irradiazio erregimen luzeek eragindako efektu biologiko mugatuak ikusita, cisplatinoren antzeko sendagaiak argi irradiazioarekin batera erabiltzea eragotzi zuten. Hori dela eta, ikertzaileen arreta, Pt^{II} konplexuekin koordina daitezkeen estekatzaile fotoaktiboen diseinuan jarri zen. Estekatzaile hauek, PDT fotosortzaile gisa jarduteko gai ziren. Argi irradiazioaren menpe oxigeno singletea eta beste oxigeno espezie erreaktiboak (ROS) sortzeko ahalamena zuten. sustatzailearen eta metalaren arteko koordinazioak banakako osagaien konbinazioak baino propietate hobeak erakusten dituzten konplexuak, “agente dual” bezala izendatu dira. Bestalde, irradiazioaren ondoren espezie aktiboak askatzen dituzten konplexuak, “kaiola konposatu” moduan izendatu dira.

1.3.1 Pt^{II} konplexu fotoaktibagarrariak PDT agente edota kaiola konposatu bezala

Brabecek, Kašpárkovák eta kolaboratzaileek, cisplatino analogo baten ekintza mekanismoa ikertu zuten. Konplexu honen aminetako bat, 1-metil-7azaindola atalarengatik ordezkatu zen (**3**, 2. Irudia).

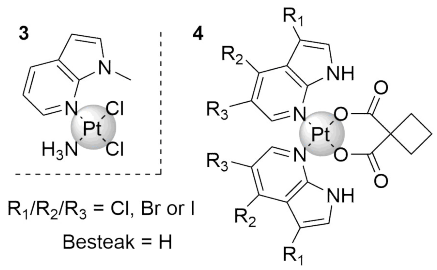

2. Irudia. Minbiziaren aurkako azaindola-Pt^{II} konplexuen egitura kimikoak.

3 Konplexuak, ez zuen toxikotasunik erakutsi ilunpetan. 365 nm-ko argiarekin (3.5 $mW \cdot cm^{-2}$) irradiatu zenean ordea, mikromolar IC_{50} balioak erakutsi zituen cisplatinoaren aurrean sentikorrak diren A2780 (obulutegi kartzinoma) eta erresistenteak diren LNCaP (prostata adenokartzinoma) zeluletan. Konplexu honek, agente dual moduan jokatu zuen minbiziaren kontra. Toxikotasuna oxigeno singlete formakuntzaren eta DNA interhari gurutzamenduren ondorioz sortuz.[18] Mekanismo berdinaren bitartez, irradiatu ondoren **4** konpleaxuak (halogenoz ordezkatutako 7-azaindola zuen karboplatino eratorria, 2. Irudia), **3** konplexuak bezalako toxikotasuna erakutsi zuen cisplatinoaren aurrrean sentikorrak eta erresistenteak diren zeluletan.[19]

Chakravartyk eta kideek Pt^{II} atomoak, antrazeno eta pireno atal fluoreszenteekin apaindutako katekolato edo dizetonato estekatzaileekin lotu zituzten (3. Irudia). **5** eta **6** katekolato konplexuak haien estekatzaileekin alderatuz gero, ilunpetan toxikotasun handiagoa erakutsi zuten (IC_{50} ~ 30-50 μM) eta antzeko IC_{50} balioak (5-20 μM) argi irradiazioren menpe (400-700 nm, 10 $J \cdot cm^{-2}$), azal keratinozito HaCaT eta bular minbizi MCF-7 zeluletan. Datuek erakutsi zutenez, fototoxikotasuna ROS-ek eragindako apoptosi bidez sortu zen, baina, ilunpetan neurtutako toxikotasun altuagoaren zergatia ez zen argitu. Argirik gabe, ez zen konplexuaren hidrolisia behatu, ezta 5'-guanosina monofosfatorekin (GMP) koordinazioa ere. Dena den, ilunpetan glutationa (GSH) askorekin inkubatu zenean, estekatzaileen askapena hauteman zen.[20] **7** eta **8** Azetilzetona eratorriek, **5** eta **6** konplexuek bezala jokatu zuten. Egonkorrak ziren 24 orduz, baina, ingurunean GSH asko zegoenean, estekatzaileen askapena gertatzen zen. Piridinaren edo antrazenoaren presentzia dela eta, konplexu hauek DNA egitura tartean sartzeko ahalmena erakutsi zuten. Ondorengo argi irradiazioren ondorioz, kaltea sortzen zen. HaCaT zeluletan **7** eta **8** konplexuek, **5** eta **6** konplexuek bezalako toxikotasun balioa eta ekintza-mekanismoa erakutsi zuten, ROS-en sorkutzaren bitartez apoptosia eraginez (3. irudia).[21]

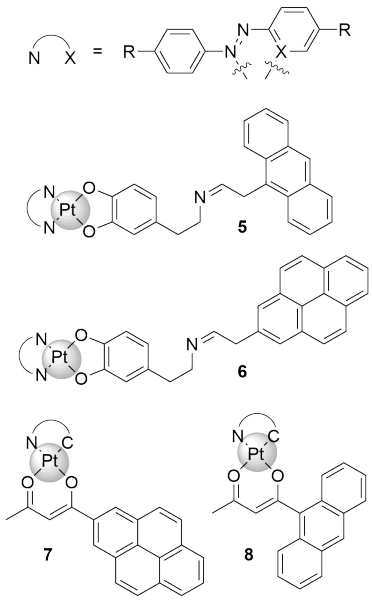

3. Irudia. Katekolato-Pt^{II} (**5**,**6**) eta azetilzetona-Pt^{II} (**7**,**8**) konjokatu fluoreszenteen egitura kimikoak. **5** eta **6**: X=N, R=H; **7** eta **8**: X=C, R=OMe.

Chakravartyk eta kolaboratzaileek, kurkumina atal fotoaktiboarekin koordinatutako diaminoplatino konplexu baten berri eman zuten (4. Irudia). Produktu natural hau, hantura eta minbiziaren kontrako agente eraginkorra da nahiz eta hidrolisi eta metabolizazio azkarrerako joera azaldu. Platicur (**9**) bezala izendatutako Pt^{II} eratorria, kurkumina hidrolisitik babesteko eta aldi berean argi ikuskorraren menpe (400–700 nm, 10 $J \cdot cm^{-2}$) DNA-ra lotzeko gai dire Pt^{II} espezieen sorrera kontrolatua baimentzeko diseinatu zen. **9.** Konplexuak ez zuen toxikotasunik erakutsi ilunpetan (IC_{50} > 200 µM) eta argiztatzerakoan 15 µM-eko IC_{50} balioa erakutsi zuen HaCaT zeluletan; kurkumina soilik bezala. Balio hau 30 µM-era igo zen hilezkorrak bihurtutako ez-transformatutako giza birika epitelio periferiko (HPL1D) zeluletan.[22] Aminen ordez diazobenzeno estekatzatilea duen kurkumina eratorriak (**10**) eta **9** konplexuak (11 µM IC_{50} balioa HaCaT zeluletan, 400-700 nm, 10 $J \cdot cm^{-2}$) antzeko fototoxikotasuna azaldu zuten. Ilunpetan aldiz, **10** konplexuak toxikotasuna altuagoa erakutsi zuen (56 µM IC_{50}). Eratorri hauen toxikotasuna, hidroxilo erradikalen sorkuntzari atxikitu zitzaion gehienbat, baina oxigeno singletearen sorrera behatu zen ere (4. Irudia).[21]

Infragorri gertuko (NIR) argia (700-100 nm) ehunetan sakonago barneratzen da eta UV argiak baino kalte gutxiago eragiten ditu. NIR lehioan aktiba daitezkeen agenteak garatzeko helburuarekin, Harten taldeak NIR (720–740 nm, 3.5 $mW \cdot cm^{-2}$) argiaren aurrean sentikorra zen profarmakoa sintetizatu zuten. Horretarako, IR797 kromoforoa Pt diamino atal batekin koordinatu zuen (**11**). NIR argiaren menpe, **11** konplexuak agente dual izaera erakutsi zuen. Alde batetik, oxigeno singletea sortu zuen eta bestetik, Pt-ura konplexua (*cis*-$[Pt(NH_3)_2(H_2O)_2]^{2+}$) fotoaskatu zuen. Nahiz eta ilunpetan utero eta bular minbizi C-33 and MCF-7 zeluletan toxikotasun altua erakutsi (8-18 µM), IC_{50} balioak nanomolarrrera gutxitu ziren argi aktibazioaren menpe (0.14-0.65 µM), 57 eta 27 fototoxikotasun indizea erakutsiz hurrenez hurren.[23]

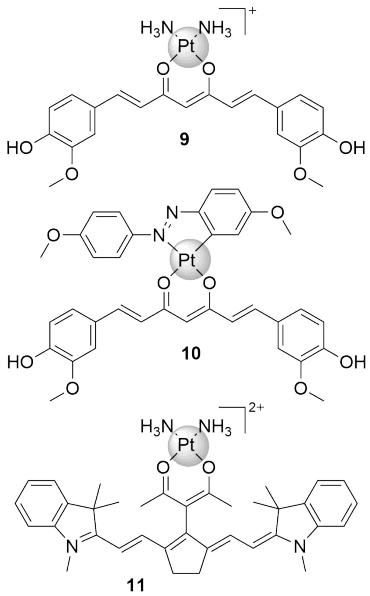

4. Irudia Platicur (**9**), Pt-kurkumina azetoazetato (**10**) eta Pt-IR797 konjokatuaren egitura kimikoak.

PDT sistema klasikoek, oxigeno espezie erreaktiboen bidez sortzen dituzte kalteak, oxigeno molekularraren presentzia muga nagusia izanik.[7] Hau, oinarrizko arazoa da minbizi ehunetan oxigeno maila ehun osasuntsuetan baino baxuagoa delako. Orain dela gutxi, Palaciosek eta lankideek, amida-karratuan oinarrituriko farmakoak (**12**, 5. Irudia) fototoxikotasuna soilik, oxigenorik gabeko baldintzetan erakutsi zuela deskribatu zuten (IC_{50} 69 µM cisplatinoaren aurrean erresistenteak diren giza adenokarzinoma HeLa zeluletan). Amida karratu fotobanaketa mekanismoa zen toxizitate ezberdinen erantzulea ikertzaileen arabera. Oxigenorik gabe, amino-sulfuro zatiak sortu ziren, toxikotasun altuko **13** konplexua eratuz (5. Irudia). Estekatzaile hauen oxidazioa baldintza normaletan (oxigenoarekin) aztertu zenean ordea, **14** konplexu ez toxikoa sortzen zela frogatu zen (5. Irudia).[24]

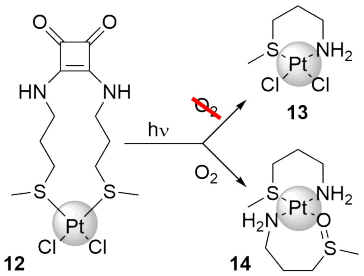

5. Irudia. Amida karratu konplexuaren (**12**) eta honen fotoprodukturen egitura kimikoak, hipoxia (**13**) edo normoxia (**14**) baldintzetan

1.3.2 Pt^{II} unitate funtzional heterometalikoekin

Estekatzaile fotoaktiboez gain, Pt^{II} agenteak beste egitura metalikoekin lotu dira ezaugarri fotofisiko eta fotokimikoak hobetzeko asmoarekin.

Chakravartyk eta kolaboratzaileek, sakonki ikertu zuten hurbilketa hau. Pt^{II} zentruak, fotoaktiboak ziren ferrozeno eta DNA tartekari N,N,N-pintza estekatzaileekin lotu zituzten, konplexu heterobimetalikoak diseinatuz (6. Irudia). Familia honetako lehen belaunaldiko konplexuek, fenantrolinatik (phen) eta dipiridofenazinatik (dppz) eratorritako polipiridilo estekatzaileetan oinarritu ziren. Phen eratorriek **15a** eta **15b**, ez zuten toxikotasunik erakutsi ilunpetan edo argi irradiazioaren menpe (365 nm, 6 W). Dppz klorido **16a** konplexuak ordea, mikromolarreko toxikotasuna (2-3 µM IC_{50}) erakutsi zuen HeLa eta MCF-7 zeluletan argi irradiazioaren menpe (365 nm, 6 W). MCF-10A zeluletan aldiz, zuhurki eraginkorra (19 µM IC_{50}) izan zen. Hala ere, ilunpetan, **16a** konplexuak toxikotasun apala erakutsi zuen HeLa zeuletan (18 µM IC_{50}). Klorido estekatzailea ferrozenoarengatik ordezkatzerakoan (**16b**) MCF-10A zeluletan fototoxikotasuna handitu zen (13 µM IC_{50}) baina HeLa eta MCF-7 zeluletan (13-16 µM IC_{50}) txikitu zen. Ilunpetan ordea, toxikotasuna kasu guztietan txikitu zen (> 25 µM).[25]

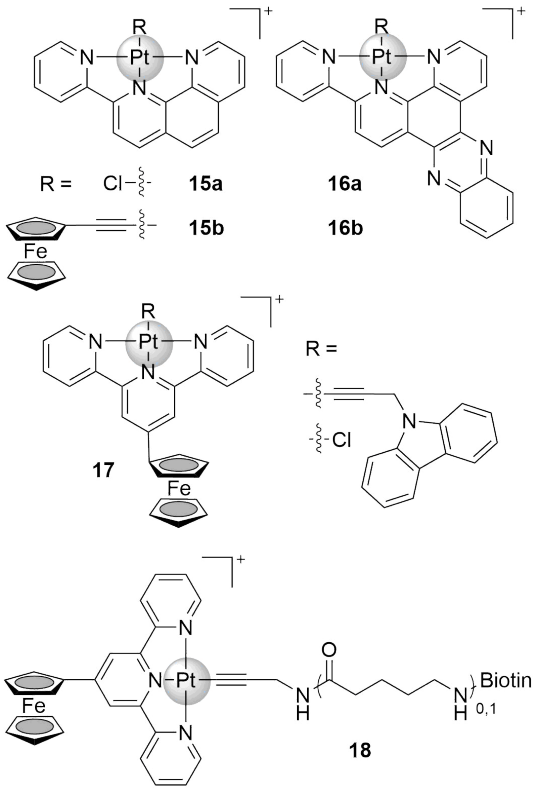

6. Irudia. Minbiziaren kontrako ferrozenilo phen (**15**), dppz (**16**) edo tpy (**17**,**18**) pintza konplexuen liburutegi kimikoa.

Sistema hauek hobetzeko helburuarekin, ferrozeno-terpiridina estekatzaileak zituzten konplexuak sintetizatu zituzten (**17**). Haien erredox eta ezaugarri fotofisikoengatik eta terpiridina-Pt^{II} konplexuek erakusten duten toxikotasun altua dela eta aukeratu ziren konplexu horiek. Hauek, toxikotasun egokia (10-18 µM IC_{50}) erakutsi zuten argi ikusgaiarekin argiztatzerakoan (400-700 nm, 2.4 $mW \cdot cm^{-2}$) eta toxikotasun baxua ilunpetan (> 65 µM) HaCaT zeluletan. Zelulen nukleora iritsi arren, konplexu hauek DNA-n tartekatzeko gaitasun baxua erakutsi zuten.[26] Ikerketa berri batean, absortzio zelularra handitzeko, biotina unitate bat konposatu analogo batzuetara (**18**) lotu zen. Minbizi zelula batzuetan gertatzen den biotina zehazki ezagutzen duten estreptavidina errezeptoreen gehiegizko adierazpenaz baliatu ziren helburu hori lortzeko. Absortzio zelular altua erakutsi arren, antzeko ilun/argi toxikotasun profilak (IC_{50} 8-17 µM argi irradiazioaren menpe, > 50 µM iluntasunean) azaldu zituzten giza bular karzinoma minibizi zeluletan (BT474). Hala ere, argiarekin irradiatzerakoan IC_{50} balioak 40 µM-tik gora igo ziren giza bular epitelio HBL-100 zelula normaletan.[27]

Platinoa eta unitate funtzional heterometalikoen konbinazioa, PDT-tik haratago doan efektua eragiteko ikertu da (7.Irudia). Esate baterako, sistema optiko eta erradioaktibo batzuk irudi propietateak eta minbiziaren kontrako aktibitatea bateratzeko diseinatu ziren. Diaminokloruroplatinato unitatea BODIPY batekin konbinatzerakoan, fototoxikotasun eta emisio altuko agente teranostikoak (**19a** and **19b**) garatzera gidatu zuen. **19a** konplexuaren emisioa jarraitzerakoan, gehienbat zelulen mitokondrioan metatzen zela ikusi zen. Funtsean, biak (**19a** eta **19b**) ez ziren toxikoak ilunpetan eta heriotza apoptotikoa eragin zuten argi

ikusgaiarekin argiztatzerakoan (400-700 nm, 10 J·cm^{-2}). 100-150 nM-eko IC_{50} balioak lortu zitren HaCaT zeluletan eta 3-6 µM-eko balioak MCF-7 zeluletan.[28] 9-etilguanina ereduarekin egindako DNA-lotura ikasketek, klorido atomo baten ordez, amina baten monoordezkapen ez-ohikoa gertatzen zela erakutsi zuten. Guok, Hek eta lankideek, antzeko estruktura bat (**20**) deskribatu zuten. Pt eta BODIPY unitateen arteko lotura aldatzerakoan, BODIPY-ak baino ROS produkzioa eta pilaketa intrazelularra handiagoa eragiten zela frogatu zuten. Hau, argi irradiazio laburren ondorioz mintz zelularrean sortutako kalteen ondorio zela azaldu zuten (5 min, 532 nm, 3.5 mW·cm^{-2}). Osagai ezberdinek banaka, 40 µM-etik gorako IC_{50} balioak erakutsi zituzten. Hala eta guztiz ere, Pt-BODIPY konjokatuak (**20**) 4–10 µM bitarteko IC_{50} balioak erakutsi zituen hainbat minibizi zelula lerroetan argi aktibazioaren menpe.[29]

Pt zentrutik fotodisoziatutako Eu konplexu baten emisio naturala erabili zen, cisplatinoa askatzeko gai zen molekula jarraigarri eta kontrolagarria sintetizatzeko (**21**). Konplexu honek ez zuen toxikotasunik erakutsi eta ez zuen emisio propietaterik adierazi, baina bi-fotoi kitzikapenaren ondorioz fotobanaketa pairatu zuen (730 nm), *cis*-[Pt(NH$_3$)$_2$(H$_2$O)Cl]$^+$ eta emisio altuko Eu unitatea aldi berean askatuz. Honek, prozesuaren jarraipena baimendu zuen. Hala ere, **21** konplexuak toxikotasun arina azaldu zuen HeLa (22 µM) eta A549 (50 µM) zeluletan.[30]

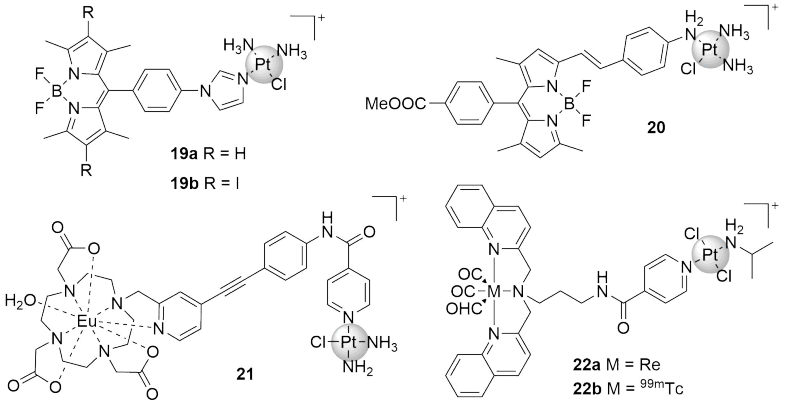

7.Irudia. Cisplatino antzeko BODIPY konjokatuen (**19** eta **20**), askapen jarraipenerako Eu-an oinarritutako profarmakoen (**21**) eta konplexu teranostiko optikoen eta erradioetiketadunen (**22**) estruktura kimikoak.

Orain dela gutxi, metalaren arabera, gaitasun optiko edota erradiokimikoak dituzten konposatu teranostikoak eraikitzeko eredu berri bat deskribatu zen. Konjokatuak, *trans* geometria zuen eta Pt zentru batez eta renio igorle edo teknezio trikarbonilo erradiaktiboa duen pintza unitate batez osatuta zegoen. Renio **22a** konposatuak, ilunpetan argiztatzerakoan (350 nm, 2.58 J·cm^{-2}), baino toxikotasun baxuagoa (> 60 µM) erakutsi zuen. Argi irradiazioaren menpe 10 eta 20 µM arteko IC_{50} balioak azaldu zituen HeLa eta cisplatinoaren aurrean sentiberak eta erresistenteak diren A2780 zeluletan. Konplexuak, ez zuen DNA-ra lotzeko gaitasunik erakutsi eta kalte zelularra oxigeno singlete sorkuntzari atxikitu zitzaion. Ez zen CO askapen azterketarik egin baina oxigeno singletearen eraketa baieztatu eta kuantifikatu zen. **22b** Teknezio erradiaktibo anagoaren *in vivo* biobanaketa

esperimentuek, odol jarioan konplexua egonkorra zela (ordu baten ostean) eta gibel eta giltzurrunetan metatu zela frogatu zuten.[31]

1.4 Minbiziaren aurkako Pt^{IV} konplexuak eta argi aktibazioa

Pt^{II} sendagaiekin lotutako arazo klinikoak gutxitzeko, azken 20 urteetan, komunitate zientifikoak gero eta interes handiagoa izan du hidrolisiaren aurrean inerteak diren Pt^{IV} konplexuetan. Orokorrean, Pt^{IV} agenteak ez dute hidrolisi azkarrik pairatzen ingurumen biologikoetan (nahiz eta dogma hau orain dela gutxi ezeztatu den[32]) eta horren ondorioz toxikotasun ez-espezifikoa gutxitzen da. Konposatu oktaedriko familia honek, estekatzaile axialak gehitzen dituzte haien egitura kimikoetan, disolbagarritasun ezaugarriak eta zeluletan efektu biologikoak modulatzen laguntzeaz gain, minbizi zeluletara zuzentzeko bektore-molekularrak eta nano-bektoreak gehitzeko aukera eskaintzen dute.[33–35]

Pt^{II} baliokideekin alderatuta, Pt^{IV} konplexu oktaedrikoek aktibazio pauso bat gehiago behar dute. Aktibazio pauso honetan, konplexuek estekatzaileen eliminazio erreduktiboa sufritzen dute, barne edo kanpo esfera elektroi transferentzia mekanismoa bidez.[36] Aktibazio prozesua batez ere zelulen barnean gertatzen dela uste da, Pt^{IV} konplexu inerteak Pt^{II} eratorrietan eraldatzeko gai diren agente erreduktore intrazelularren eraginez. Horren ondoren, ur espezie erreaktiboak sortu, DNA-rekin elkatu eta ondorioz heriotza zelularra gertatzen da (8. Irudia).[37]

Pt^{IV} konplexuei buruz egindako ikerketa asko, Pt farmakoen propietate farmakologikoak hobetzeko, $Pt^{IV} \rightarrow Pt^{II}$ aktibazioaren xehetasunak eta efektu bilogikoak ezagutzeko, *in vitro* toxikotasun profil arrakastatsuak lortzeko eta aurreko tratamenduek eragindako farmako erresistentzia gainditzeko helburuarekin egin dira.

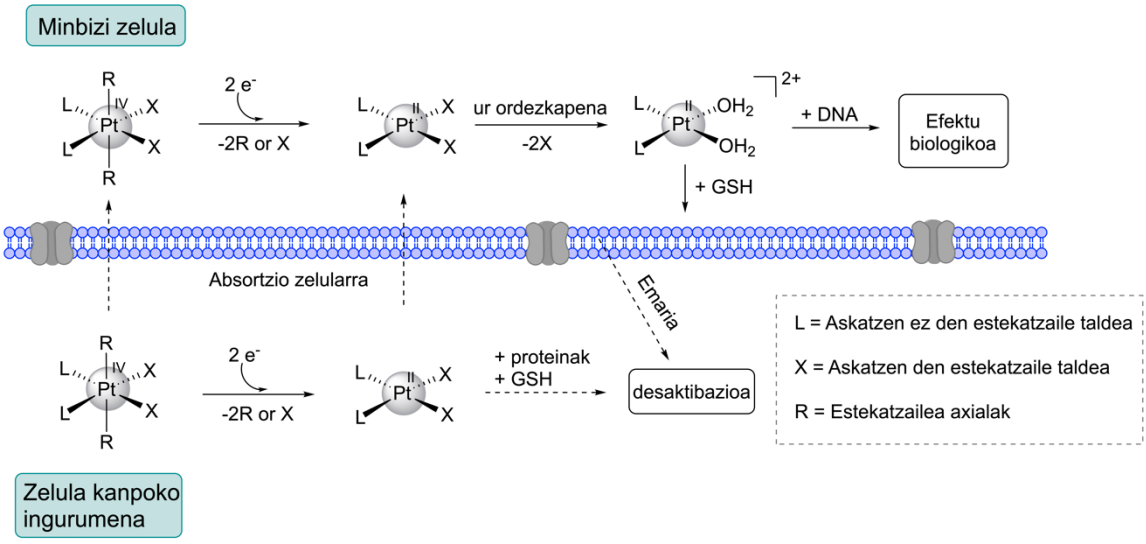

8. Irudia. Pt^{IV} profarmakoen aktibazio mekanismoa eta zeluletan duten ekintza biologikoaren irudikapen eskematikoa. Eskema [37] erreferentziatik moldatu zen.

Hainbat Pt^{IV} profarmako froga klinikoetan sartu ziren; ormaplatinoa, iproplatinoa eta satraplatinoa adibide bikainak izanik (9. Irudia).[38–40] Zoritxarrez, 3 konposatu hauek onartutako Pt^{II} sendagaiek baino eraginkortasun txikiagoa erakutsi zuten minibiziaren aurka eta horren ondorioz ez zuten janari eta sendagaien administrazioaren (FDA) onespenik jaso.

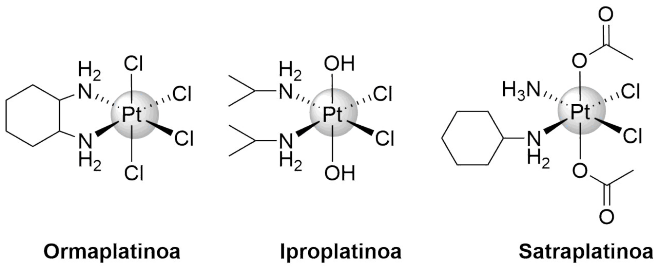

9. Irudia. Froga klinikoetan sartu ziren Pt^{IV} profarmakoak.

Hala ere, Pt^{IV} konplexuak minbiziaren kontrako Pt^{II} farmakoen ohiko eragozpenak gainditzeko sistema interesgarriak dira. Gainera, fotoaktibazioa, Pt^{IV} profarmakoen efektu biologikoak zorroztasunez kontrolatzeko estrategia alternatibotzat eta potentzialki arrakastatsutzat hartu izan da. Fotokimioterapiaren alorrean, lehen ikerketen helburua, iluntasunean egonkorrak, ez toxikoak eta argi irradiazioaren menpe bidegarrritasun biologikoa gutxitzen zuten konplexuak garatzea zen. Berriki, ikerketa esparru honen arreta, askapen eta zuzendutako hurbilketera eta kitzikapen uhin-luzera handiagoko argia erabiltzera mugitu da (espektroaren eremu gorri edo infragorri hurbilean irradiatzen duten argi iturriak). Hemen jarraian, Pt^{IV} konplexuak Pt^{II} espezie aktiboen profarmako gisa erabili diren adibide adierazgarrien bidez arlo horiek eztabadaitu dira.

1.4.1 Diiodo-Pt^{IV} konplexuak

Bednarskiren laborategiak 1990eko hamarkadan, Pt^{IV} konplexuen toxikotasuna argi aktibazioaren menpe ikertu zuen lehen taldea izan zen (10. Irudia).[41,42] **23**–**25** konplexuetan (10. Irudia), iodoak askatze estekatzaile bezela eta etilendiamina (en) askatzen ez den talde bezala aukeratu ziren, 380-400 nm inguruan azaltzen zituzten LMCT bandak faboragarriak direlako ($\varepsilon \approx 1 \times 10^3$ M^{-1} cm^{-1}). Horretaz gain, iodo estekatzaileen *cis* geometriak, **23**–**25** konplexuen fotoerredukzioa sustatu zuen fotoordezkapen erreakzioen ordez. Etilendiamina kelatoak berriz, fotoisomerizazio erreakzioak gutxitu zituen, trans Pt^{II} espezie inaktiboak potentzialki sortuz.

410 nm-ko argiarekin argiztatzerakoan, **23** konplexuak fotodeskonposizioa pairatu zuen, [$PtCl_2$(en)] sortuz. Produktu hau, DNA-rekin elkartzeko gai zen. Zoritxarrez, **23** konplexuak ilunpetan ere deskonposatzeko eta DNA-rekin elkatzeko gaitasuna erakutsi zuen. Hori dela eta, ez zen desbedintasunik aurkitu mibizi zeluletan (giza maskuria eta melanoma zelulak,

TCCSUP eta SK-MEL-24, hurrenez hurren) argiztatutako edo iluntasunean gordetako laginen artean.[42]

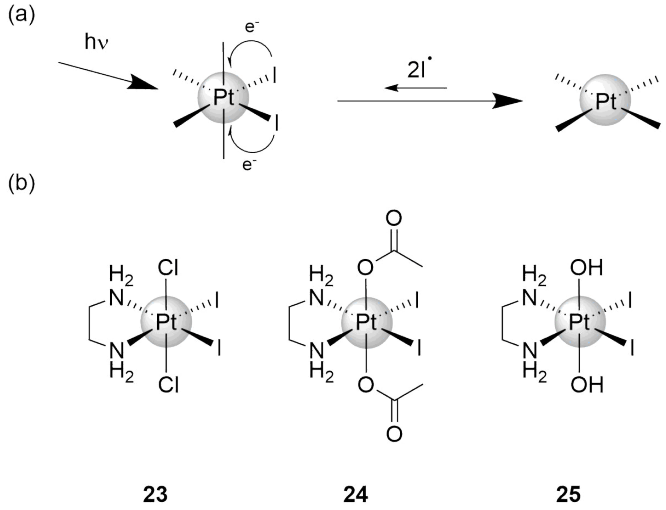

23 **24** **25**

10. Irudia. (a) Iodoan oinarrituriko Pt^{IV} konposatuen fotoerredukzioa azaltzeko proposatutako mekanismoa. (b) Iodo estekatzaileetan oinarritako Pt^{IV} profarmakoen lehen belaunaldia.

Mota honetako konposatuen egonkortasuna iluntasunean hobetzeko, Bednarskik eta kolaboratzaileek, **23** konplexuaren kloro estekatzaile axialak, azetato (**24**) eta hidroxidoengatik (**25**) ordezkatu zituzten.[41] **24** eta **25** eratorriak, Ingurumen zelularrarekin inkubatu zirenean, 6.6 eta 46.8 h ordu ondoren deskonposatu ziren hurrenez hurren. Prozesu hau, askoz ere bizkorrago gertatzen zen (≈ 1 h) argi kitzikapenaren menpe (> 375 nm). Disoluzio ingargetzailean, **24** konplexuaren % 60-a DNA-rekin lotu zen 6 h orduz argiztatu ondoren. Iluntasunean aldiz, interakzio hori mespretxagarria zen. Bestalde, **25** konplexuak, ez zuen DNA-rekin elkartzeko ahalmenik azaldu 6 h ordu argiztatu ondoren, fotoproduktuak batez ere Pt^{IV} espezieak zirela iradokiz. Argi irradiazioaren menpe **24** eta **25** konplexuek iluntasunean baino toxikotasun handiagoa erakutsi zuten minibizi zeluletan (TCCSUP). Bi konplexuen fotoproduktuek izaera ezberdina zutenez, fototoxikotasuna ekintza mekanismo desberdinetatik eratorri zela iradoki zuten. Hala ere, iluntasunean **24** eta **25** konplexuek, toxikotasuna erakutsi zuten mikromolar kontzertrazio baxuetan minibizi zeluletan. Izan ere, N-azetlizisteina eta GSH bezalako biotiolen presentzian, bi konplexuen erredukzioa barne esfera mekanismo bidez gertatzen zela erakutsi zuten NMR esperimentuek.[43]

Nahiz eta diiodo-Pt^{IV} konplexuak farmako fotoaktibagarritzat ulertu, Bednaskik eta kolaboratzaileek zuzendutako kontzeptu frogak, Pt^{IV}-an oinarrituriko profarmakoak argiaren bidez aktiba zitekeela egiaztatu zuten, eratorri berri eta hobeen diseinua bultzatuz.

1.4.2 Diazida-Pt^{IV} konplexuak

2000ko hamarkadaren hasieran, Sadlerrek, azidetan oinarrituriko Pt^{IV} konplexuak garatu zituen. Konplexu hauek, ilunpeko egonkortasunarekin eta biotiolen eraginez gertatutako

erreduzioekin loturiko arazoak arrakasta handiz gainditu zituzten.[44] Azidek beren izaera elektroi emailearengatik, ingurumen erreduktibo zelularrean egonkortasuna ematen diete Pt^{IV} konplexuei. Azida estekatzaileak dituzten Pt^{IV} konplexuen fotokimika, 1970eko hamarkadaren amaieratik ezagutzen da. Vogler *et al.*, *trans*-$[Pt(N_3)_2(CN)_4]^{2-}$ konplexua irradiatu ondoren, aziden askapena eta fotoerredukzioa gertatzen zela frogatu zuten.[45] Proposatutako mekanismoaren arabera, azida erradikalak sortu ondoren, nitrogeno molekularrean bihurtzen ziren (11. Irudia).[45,46] Erradikal haluroak uretan egonkorrak eta Pt^{II}-ak Pt^{IV}-ean birraldatzeko gaitasuna erakutsi zuten bitartean (ikusi 10. Irudia), azida estekatzaileek, Pt^{IV} konplexuen fotoerredukzio azkarra eta itzulezina sustatu zuten.[47]

Sadlerrek eta kolaboratzaileek, azidetan oinarrituriko konplexuak ikertu zituztenean, lehenengo konplexuak, *cis,trans*-$[Pt(en)(N_3)_2(OH)_2]$ eta *cis,trans,cis*-$[Pt(N_3)_2(OH)_2(NH_3)_2]$ izan ziren (**26** eta **27**, 11. Irudia). Bi eratorriek, antzeko izaera erakutsi zuten, ilunpean (90 egun baino gehiago) egonkorrak ziren, baita GSH bezalako erreduktore biologikoen presentzian ere (asteak baino gehiago).

Soilik argi irradiazioaren menpe, **26** eta **27** konplexuek, 5'-GMP edo d(GpG) DNA nukleobase ereduetara lotzeko gai ziren espezieak sortu zituzten.[44,48] Biek, antzeko absortzio ezaugarriak zituzten, 256 nm-tan ($\varepsilon \approx 1 \times 10^4$ $M^{-1}\cdot cm^{-1}$) kokatutako LMCT banda partekatuz. **26** konplexua 5'-GMP-ren presentzian eta 458 nm-tan irradiatu ostean, bi DNA eredu molekurrarekin lotzeko gaitasuna erakutsi zuen $[Pt(en)(5'\text{-GMP-N7})_2]$. Gainera dGpG eredua erabili zenean, gauza bera gertatu zen. **26** konplexua 3 orduz 458 nm-ko argiarekin argiztatu ondoren, fotoprodukuek DNA plasmidoarekin GG elkargutzamendua sortzeko gaitasuna erakutsi zuten. Horren ondorioz, RNA polimerasa bidez egiten den RNA sintesia amatatu zen *in vitro*.[48] Azpimarragarria da, nahiz eta **26** eta **27** konplexuek 350 nm-taraino absortzio ezaugarriak erakutsi, eremu ikusgarrian (> 400 nm) fotoaktibitatea jasateko gaitasuna erakutsi zutela. DFT modelizazioek, 400–500 nm artean agertzen diren transferentzia elektroniko ahulen bidez azaldu zuten fotoaktibitate hori.[49]

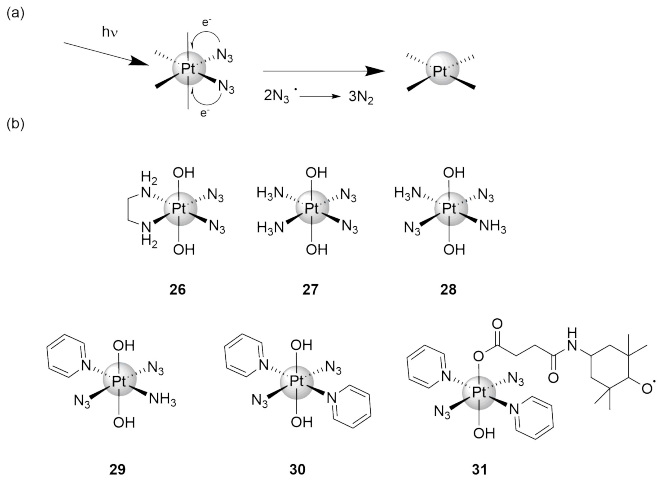

11. Irudia. (a) Azidetan oinarrituriko Pt^{IV} konposatuen fotoerredukzioa azaltzeko proposatutako mekanismoa. (b) Azida estekatzaileetan oinarrituriko Pt^{IV} profarmakoen bigarren belaunaldia.

26 eta **27** konplexuak giza maskuri minbizi zelulen aurka (cisplatioaren aurrean erresistenteak direnak barne) aktiboak ziren soilik ,366 nm-ko argiarekin irradiatu ondoren, 50 μM-eko IC_{50} balioak azalduz.[50] Fluoreszentzia mikroskopio azterketek frogatu zuten moduan, zelulen morfologi aldaketak ez ziren alderagarriak cisplatinoak eragindakoekin. Beraz, fotoaktibatutako **26** eta **27** konplexuen ekintza mekanismoa desberdina zela ondorioztatu zuten. Geroago, Salderren taldeak, *trans,trans,trans*-$[Pt(N_3)_2(OH)_2(NH_3)_2]$ (**28**, **27** konplexuaren *trans* isomeroa) konplexuaren fotokimika eta minbiziaren aurkako ekintza ikertu zuen.[51,52] Ilunpetan, **28** konplexua egonkorra zen, baina 5'-GMP-ren presentzian eta 365nm-ko argiarekin argiztatu ondoren, sortutako *trans* egiturak $[Pt(NH_3)_2(5'\text{-GMP-N7})_2$, bi DNA eredu ezberdinekin elkarrekintzak azaldu zituen. Prozesu hau, **27** konplexuak gauzatutako fotoerredukzioa baino eraginkorragoa izan zen. **28** konplexuaren kasuan, gutxienez fotoproduktuen % 75-a baino gehiago, 5'-GMP eredu molekularrera lotu ziren ordu baten ostean. **28** konplexuaren fotoaktibazioa disoluzioan, *trans*-$[Pt(NH_3)_2(OH_2)_2$ eta beste fotoerredukzio eta fotoisomerizazio produktuen sorrera eragin zuen. DNA-ren presentzian, **28** konplexuaren irradiazioak, interhari gurutzamendua eragin zuen, transplatinoaren kasuan frogatu zen bezala.[16] Konparaketa ikerketa batean, **27**, **28**, cisplatinoa eta transplatinoa, giza keratinozitoen (HaCaT zelulak) aurka frogatu ziren. IIrradiatu ostean, **28** konplexuak, aktibitaterik altuena azaldu zuen.[51]

28 konplexuaren aurkikuntzaren ondoren, Sadlerrek eta kolaboratzaileek, piridina (Py) estekatzaileak zituzten bi *trans* azida eratorri sintetizatu zituzten (11. Irudia): *trans,trans,trans*-$[Pt(N_3)_2(OH)_2(NH_3)(py)]$ (**29**)[50] eta *trans,trans,trans*-$[Pt(N_3)_2(OH)_2(py)_2]$ (**30**)[52] konplexuak hain zuzen ere. Piridinek, hainbat abantaila azaltzen dituzte NH_3 taldeen aldean: i) bolumen gehiago betetzen dute, Pt^{IV} konplexuak eta honen fotoprodutuek sor ditzaketen ez desiratutako interakzioak potentzialki saihestuz; ii) DNA-rekin π metaketa interakzioak sustatzen dituzte, Pt^{IV} konplexuaren eta bere objektiboaren arteko interakzioak lagunduz eta iii) absortzio espektroan efektu batokromikoak eragiten dituzte. **29** eta **30** konplexuak egonkorrak ziren ilunpetan (20 egun baino gehiago), baita GSH eta askorbatoa bezalako erreduktoreen presentzian ere.[52,53] Irradiatu ondoren (365 eta 420 nm-ko argiarekin egin zitekeena), bi konposatuen fotoproduktuek **28** konplexuaren fotoproduktuek baino eraginkortasun handiz elkartu ziren DNA ereduekin (5'-GMP and ct-DNA adibidez).[54] Adibide gisa, **30** konposatua DNA-rekin inkubatu eta 365 nm-ko argiarekin irradiatu zenean (4.6 $mW \cdot cm^{-2}$), cisplatinoak baino 16 aldiz interakzio bakar eta bikoitz gehiago eragin zituen.[55]

Berriki, tioredoxina (Trx); hainbat minbizi zeluletan gehiegi espresatzen den entzima,[56] irradiatutako **30** konplexuaren (eta potentzialki beste Pt^{IV} profarmakoen) objektibo potentziala zela proposatu zen. Konplexuaren fotoproduktuek Trx-ren histidina, azido glutamiko eta glutamina hondakinetara lotu zitekeen argi urdinarekin argiztatzerakoan (460 nm).[57] Are gehiago, Sadlerrek beste eskuizkribu berri batean, **30** konplexuaren fotoproduktuek, bi neuropeptido ezberdinekin interakzionatzen zutela frogatu zuen.

Oxidatutako edo platinoari lotutako fotoproduktuen jatorria, peptidoaren aminoazido konposizioaren araberakoa zen.[58]

29 eta **30** piridina eratorriak hainbat minbizi zelula lerroen aurka frogatu ziren eta oraindik ere, fototoxikotasunari dagokionez, probatutako konposatu arrakastatsuenetarikoak dira. **29** konplexua adibidez, ilunpetan ez zen aktiboa. Soilik 366 nm-ko argiarekin argiztatu zenean A2780 giza obulutegi karzinoma zelulak eta cisplatinoaren aurrean erresistenteak ziren zelula analogoak, mikromolar kontzentrazioan hiltzeko gaitasuna erakutsi zuen (2 eta 16 μM, hurrenez hurren). Toxikotasun balio hauek cisplatinoarekin lortutako balioak baino 80 aldiz altuagoak ziren. Esperimentu hauek burutzeko, argi dosi baxuen menpe jarri ziren zelulak (5 $J \cdot cm^{-2}$ for 30 min).[54] **29** konposatuak, toxikotasuna erakutsi zuen 420 nm-ko argiarekin irradiatzerakoan ere. Argi aktibitatearen ondorioz, konplexu honek eta cisplatinoak mibizi zeluletan eragindako heriotz zelularra, mekanismo apoptotiko desberdinen bidez gertatu zen. LC3B-II eta p62 proteina autofagikoen maila aldaketek, autofagia izan zitekeela mekanismo nagusia iradoki zuten. Izan ere, OE19 (hestegorri) tumoreak zituen sagu konpuru bat (estatistikoki esanguratsua dena), **29** konplexuarekin eta argiarekin (420 nm, 100 $J \cdot cm^{-2}$) tratatu eta 35 egun ostean bizizirik ziraun. Kontrol saguak ordea (tratamendurik gabe edo ilunpetan), hil egin ziren denbora tarte berdinean.[59] Duela gutxi, **30** konplexuaren fototoxikotasun bortitza, azida erradikalen eta Pt^{II} fotoproduktuen sorreraren araberakoa zela frogatu zen.[60] Xehetasunez, Sadlerren taldeak, minbizi zeluletan L-triptofanoa kontzentrazio baxuak (500 μM) gehituz, **30** konplexuaren ekintza gelditu zitekeela frogatu zuten EPR eta NMR tekniken bidez. L-triptofanoa, proteinen elektroi transferenzia bitartekari ezaguna da.

26–**30** konplexuen egitura aktibitate harremanean oinarriturik, talde berberak, azidetan oinarrituriko zenbait Pt^{IV} profarmako garatu zituen. Profarmako hauek, estekatzaile ezberdinak zituzten (adibizez: posizio axialean azetatoa edo N-koordinazio estekatzaile ezbedinak posizio ekuatorialean).[61–63] Egonkortasunari, DNA-ra lotzeko ahalmentari eta ilunpean edo argi iradiazioaren menpe erakutsitako toxikotasunari (HaCaT eta A2780 zelulen kontra) zegokienez, **29** eta **30** konplexuekin lortutako emaitzekin konparagarriak ziren. Honek ondorio orokor batera gidatu zituen ikertzaileak: *trans* eratorriak, *cis* eratorriak baino aktibitate handiagoa dute.

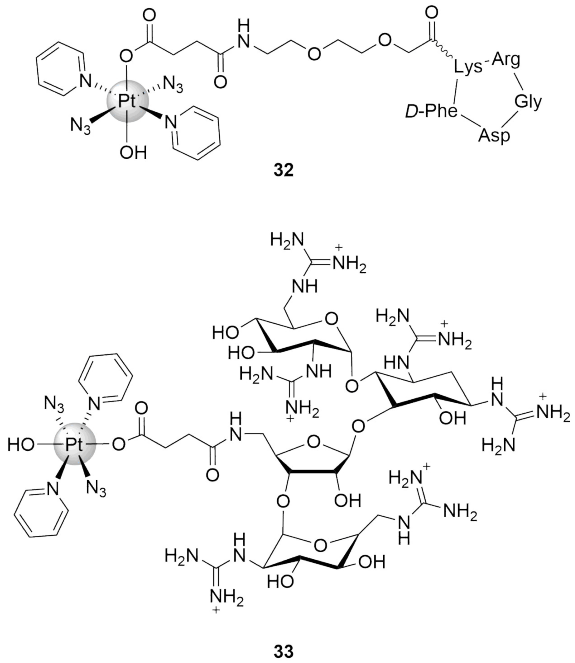

32

33

12. Irudia. Xurgapen zelularra hobetzeko gida estekatzaileekin apaindutako azida-Pt^{IV} profarmakoak.

Orain dela gutxi, V. Venkateshek *et al*. spin-markatutako nitroxido Pt^{IV} profarmako fotoaktibagarria *trans,trans,trans*-$[Pt(N_3)_2(OH)(OCOCH_2CH_2CONH\text{-}TEMPO)(py)_2]$ (TEMPO = 2,2,6,6-tetrametilpiperidina 1-oxiloa) deskribatu zuten (**31**, 11. Irudia).[64] **31** konposatua, *in vivo* EPR bidez jarraitu ahal izateko eta erradikalen bidez minibiziaren kontrako aktbitatea azaltzeko helburuarekin sintetizatu zen. Konposatu hau sortzeko, **30** konposatuaren posizio axialean kokatutako hidroxiloetako bat, eraldatutako TEMPO erradiakalaregatik ordezkatu zen. Irradiazio urdinaren menpe (465 nm, 50 mW) soluzioan dagoen **31** konplexuak, azidilo eta nitroxilo erradiakalen sorrera eragin zuela frogatu zuten EPR esperimentuek. Fenomeno hau toxikotasun altuan bihurtu zen A2780 giza obuluteko kartzinoma zeluletan (cisplatinoa baino 10 aldiz altuagoa.).[64]

Ahalegin kolaboratibo batean, Marchanek eta Sadlerrek, **30** eratorriak azaldutako izaera biologikoaren antzekoa zuten agente fotoaktibagarri berriak diseinatu zituzten. Eratorri berri hauek absortzio zelular hobea erakutsi zuten. **32** konposatuaren kasuan (12. Irudia) adibidez, Pt^{IV} profarmakoa, RGD sekuentzia (–Arg–Gly–Asp–) zuen peptide zikliko batera lotu zen. Hainbat minibizi zeluletan gehiegi azaltzen diren mintz zeharreko glikoproteinek ($\alpha_V\beta_3$ eta $\alpha_V\beta_5$ integrinak) peptido hau modu zehatz batean ezagutzen dute.[65] **33** Konplexua ordea, zelulen barnean zenbait egitura proteoglikanoen menpeko garraio selektiboan parte hartzen duen guanidinoglikosidoarekin (guanidinoneomizinoa) elkartu zen.[66] Bi kasuetan konplexu metalikoek, nolabaiteko selektibitatea erakutsi zuten giza melanoma gaizto zelulengatik (SK-MEL-28). Gainera, argi urdinaren menpe, konplexu hauek eta **30** konplexuak, 5'-GMP DNA eredura lotzeko ahalmen berdintsua erakutsi zuten.[65,66] Pt^{IV} agente fotoaktibagarri hauek, platinoak minbiziaren kontra azaldutako ekintzaren kontrol bikoitza eskaini zezaketeela azpimarratu zuten: aukeratutako estekatzaile axialek

profarmakoari emandako gida ezaugarrietan oinarritutakoa eta kitzikapen arinaren bidez Pt^{II} espezieak selektiboki sortzeko aukeran oinarritutakoa.

1.4.3 Porfirina Pt konplexuarekin lotuta

70eko hamarkaditik, porfirinak PDT helburuetarako erabili dira.[67,68] Konposatu makrozikliko organiko hauek, absortzio espektroaren eremu gorrian xurgapen indartsua eta ROS ekoizpen altua erakusten dutenez, fotosentsitizatzaile gisa aztertu izan dira. Komposatu organiko hauek argi gorriarekin argiztatzerakoan kalte zelularrak eragiteko hautagai bikainak dia. 13a Irudian azaltzen den moduan, uhin-luzera handiagoko argia, ehunetan gehiago barneratzen da. Hortaz, ehun sakonetan kokatutako agente kimioterapeutikoak aktibatzeko egokiak dira. Duela gutxi, Wangek, Zhuk eta kolaboratzaileek, argi gorriarekin kitzikagarria zen porfirina bat, minbiziaren kontrako Pt^{IV} konplexu batekin elkartu zuten, molekula txiki berri bat sintetizatuz.[69] Phorbiplatin bezala izendatutako molekula txikia, pirofeoforbida a (PPA) eta oxaliplatino Pt^{IV} profarmako batez osaturik zegoen (13b Irudia). 1 mM askorbatoaren presentzian eta argi irradiazioaren ondoren (10 min, λ = 650 nm, 7 mW cm^{-2}), 10 µM phorbiplatinoaren % 80 inguru, oxiplatinoan bihurtu zen. Ikertzaileek proposatutako mekanismoa hurrengoa zen: irradiazioaren menpe, PPA-k kitzikapen egoera singletera iritsi ondoren tripletera jaisten zen. Askorbatoaren presentzian, kitzikapen egoera tripletetik PPA-k, erredukzioa jasan eta erreduzitutako PPA, zentru metalikora elektroi bat garraitzen zuen, Pt^{III} espezie erreaktiboak sortuz. Azkenik, espezie erreaktibo hauek, Pt^{II} oxaliplatino farmako toxikoan bihurtzen ziren.

Azterketa zelularrek, ilunpetan phorbiplatinoa apalki aktiboa zela (10 µM-etik gorako IC_{50} balioekin) erakutsi zuten. Argi irradiazioaren menpe ordea, haren fototoxikotasuna oxaliplatinoarekin alderatuta, 974 eta 1786 aldiz handitu zen obulutegi minibizi erresistente (A2780cisR) eta giza bular minbizi (MCF-7) zelula lerroetan hurrenez hurren. Zitotoxikotasun esperimentuek, toxikotasuna bi mekanismo ezberdinen bidez sortzen zela frogatu zuten: i) fotosentsitizatzailearen eraginez sortutako ROS-en bidez eta ii) *in situ* askatutako oxaliplatinoak DNA-rekin lotzeko duen gaitasunaren bidez. Phorbiplatinoa A2780 zeluletan argiztatu ondoren, DNA-ri lotutako kantitatea, ilunpean baino 4 aldiz handiagoa zen. Horrela, DNA-ra lotzeko gai diren espezieak sortzen zirela frogatu zuten.

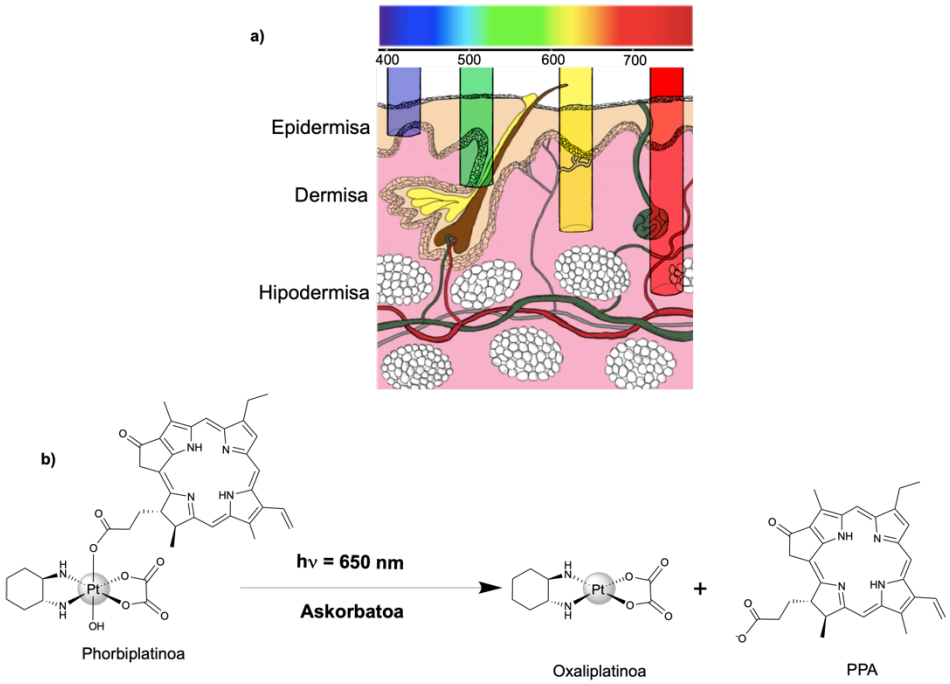

13. Irudia. a) Argi barneraketaren irudikapena azalean. b) Phorbiplatinaren fotoaktibazioa argi gorriaren bidez.[69]

Orokorrean, minbizi askotan dagoen oxigeno faltak, fotosentsitizatzaileen eraginkortasuna txikitzen du, hauen efektu toxikoa ROS-en sorreraren bidez eragiten delako. Hala ere, phorbiplatinoaren kasuan, sortutako Pt^{II} espezie zitotoxikoek, PDT-ren mugak gaindi ditzake. Ideia hori frogatzeko helburuarekin, Wangen eta Zhuren taldeek, ugaztun adenokartzinoma murinoa 4T1 zuten saguak, phorbiplatinoarekin, PPA-rekin eta oxaliplatinoarekin tratatu zituzten. Phorbiplatinoaren irradiazio arinak (660 nm, 100 mW/cm^{-2}), minbizi hazkundearen (65%) eta minbizi pisuaren (60%) murrizketa esanguratsua eragin zuela frogatu zuten emaitzek (kontrol taldearekin alderatuta).[69]

1.5 Pt profarmako fotoaktibagarrien nanoaskapena

Ahalegin asko egin dira argiaren bidez minbiziaren kontrako Pt konplexuen askapena hobetzeko. Hainbat sistemetan, Pt^{IV} konpexu oktaedrikoak mizela polimerikoetan kargatu ziren eta UVA argiaren ondorioz, Pt^{II} espezie zitotoxikoak askatzen ziren.[70–72] Esate baterako, Zhengek eta lankideek monometoxi poli(ethilen glikol)-blokea-poli(ε-kaprolaktona)-blokea-poli(L-lisina) kopolimeroez egindako mizelen barnean **34** konplexua kargatu zuten garraio egitura berri bat eraikiz (14. Irudia). Mizela hauek UVA argiarekin irradiatu ostean (18 $mW{\cdot}cm^{-2}$), gibel hepatozelular kartzinoma (HepG2) eta obulutegi adenokartzinoma (SKOV3) zeluletan cisplatinoak baino minbiziaren kontrako efektu bortitzagoa erakutsi zuten. Argiaren menpe, **34** konplexuak erredukzioa pairatu zuen eta Pt^{II} espezieak mizela polimerikoetatik askatu ziren. Absortzio zelular azterketen bidez, konplexua mizelen barnean zegoenean zeluletan aurkitutako Pt kantitatea igo zela frogatu zuten ikertzaileek.[70]

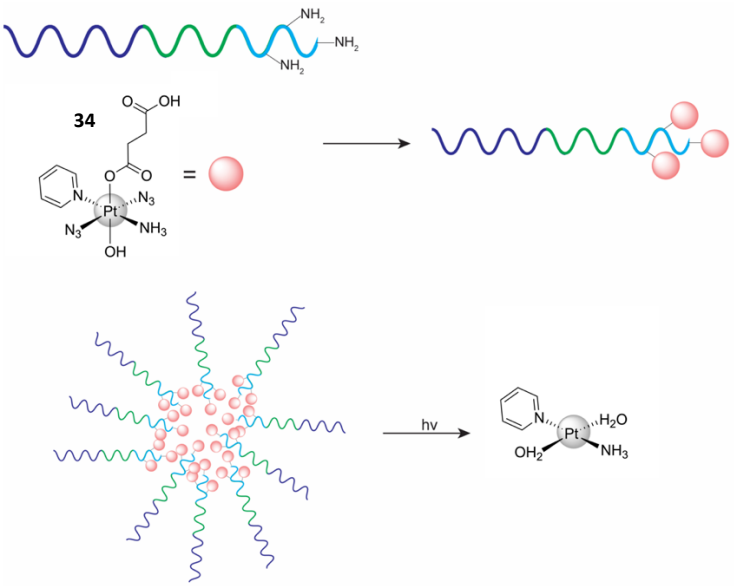

14. Irudia. Zhengen askapen nanopolimeriko hurbilketaren ilustrazioa.[70]

Huangek eta lankideek beste hurbilketa baten bidez, bat edo bi amino apaindutako laktosa molekula hidrofilikoa, **35** eta **36** konpleuexara lotu zituzten hurrenez hurren (15. Irudia). Egitura konjokatu hauek, mizelak (laktosa eratorri bat) eta besikulak (bi laktosa eratorri) eratu zituzten. Laktosan oinarriturako anfifiloak, farmako garraiatzaile moduan lan egiteko diseinatu zituzten. Horretaz gain, estruktura hauek, asialoglikoproteina errezeptoreak gehiegi espresatzen dituzten HepG2 zeluletara zuzentzeko ahalmena erakutsi zuten. Errezetore hau, gibel zelulen mintz plasmatikoan aurki daitekeen lektina da.[73] UVA argi irradiazioaren menpe (10 $mW \cdot cm^{-2}$), **35** eta **36** konplexuek fotoerredukzioa jasan zuten, laktosa garraiatzaileen apurketa eraginez eta Pt^{II} espezieak azkatuz.

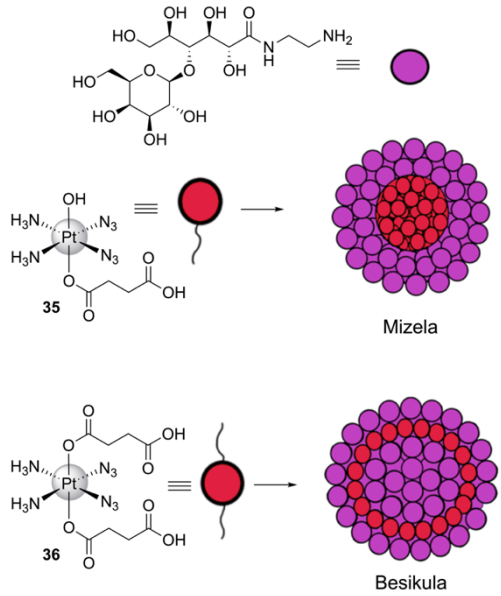

15. Irudia. Huangek diseinatutako laktosan anfifiloen irudikapena.[71]

In vitro esperimentuetan argiztatutako besikulak, mizelak baino Pt-DNA egitura gehiago sortu zituzten. Gainera, asialoglikoproteina errezeptorea gehiegi adierazten zuten zelula lerroek, HepG2 zelulelak adibidez, Pt xurgapen handiagoa azaldu zuten. Horretaz gain, NIR argia xurgatzen duen Cy7.5 tindatzailearekin apaindutako besikulak, irudi fluoreszenteen bidez jarraitu zituzten sagu ereduetan. Gibel minbizi subkutaneo ereduan egindako *in vivo* azterketek, besikulak gehienbat gibeletan metatzen zirela frogatu zuten, argi irradiazioaren menpe, cisplatinoak baino toxikotasun sistemiko txikiagoa eraginez.[71] Sadlerren laborategiak guanosina eratorrien ezaugarriak erabili zituzten, **37** konplexua, biobateragarriak diren hidrogeletan barneratzeko. Dopamina molekula batekin konjokatutako konplexua monoborato esterren bidez G-quadruplexean oinarritutako hidrogelean kargatu zen (16. Irudia). Argi irradiazioaren menpe hidrogel egiturek, toxikotasun altuko Pt^{II} espezieen askapen kontrolatu eta mantsoa baimendu zuen. Argi urdinarekin irradiatzerakoan (465 nm 50 $mW \cdot cm^{-2}$), Pt^{II} eta Pt^{IV} fotoprodukTuak G-quadruplex hidrogeletik askatzen ziren. Argiztatutako hidrogel egiturek, **38** jatorri konposatuak baino toxikotasun altuagoa erakutsi zuen (IC_{50} 3 µM and 74 µM hurrenez hurren) minibizi eta zelula osasuntsuetan. Aipagarria da, irradiatutako hidrogelek, cisplatinoaren aurrean erresistenteak diren A2780 giza obulutegi kartzinoma zeluletan (IC_{50} 3 µM), MRC-5 zelula osasuntsuetan (IC_{50} > 50µM) baino 18 aldiz toxikotasun altuagoa erakutsi zutela.[74]

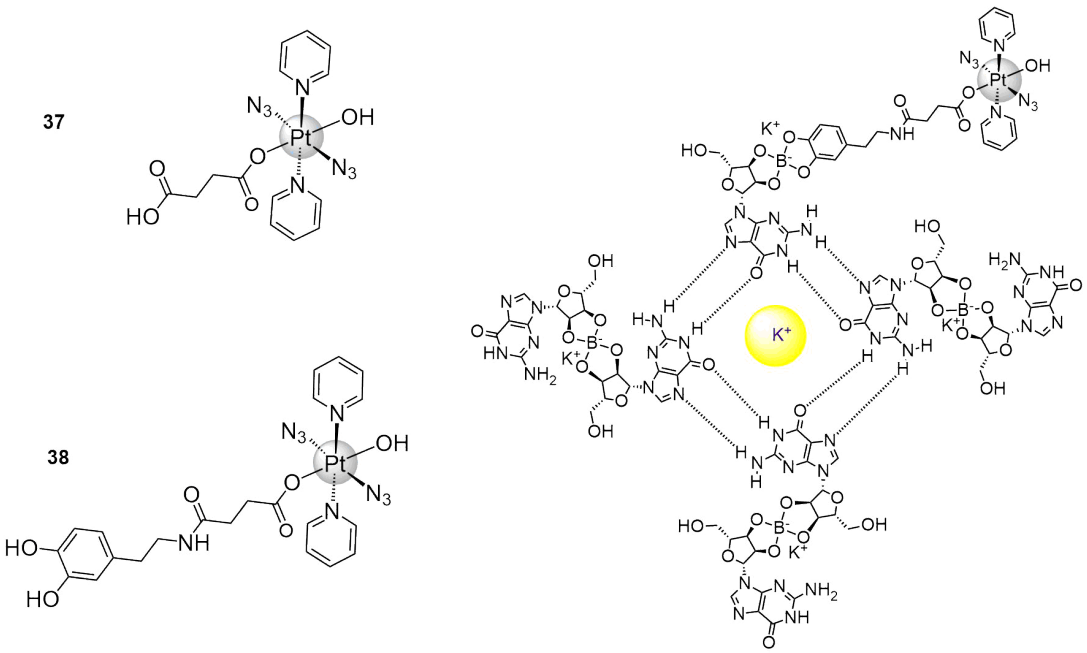

16. Irudia. Pt^{IV}-guanosina borato hidrogelaren irudikapen eskematikoa.[74]

Minbiziaren kontrako Pt agente fotoaktibarrarriak aztertzen dituzten ikertzaileek, uhin-luzera egoki batekin irradiatzerakoan (espektroaren eremu gorrian edo NIR-ean), erreakzio fotokimiko zehatzak eragiteko ezaugarri fotofisiko egokiak dituzten zenbait nano-eskala materialak ikertu dituzte ere.

Mareque-Rivasen taldeak, **39** konplexuarekin kargatutako CdSe@ZnS nukleo-oskol puntu kuantikoak (17. Irudia) eta teknezio trikarbonil konplexu erradiaktiboa *fac*-

$[^{99m}Tc(OH_2)_3(CO)_3]^+$, mizelen barnean enkapsulatu zituzten helburu teranostikoekin. 630 nm-ko argi kitzikapenaren menpe (30 $mW \cdot cm^{-2}$), nanoegiturek **39** konplexuaren erredukzioa eragin zuten elektroi transferentzia bidez, Pt^{II} espezie toxikoak sortuz. *In vitro* esperimentuek azaldu zuten moduan, irradiatutako mizelak, giza maskuri PC-3 minbizi zelulen kontra aktiboak ziren (IC_{50} 25 µM), iluntasunean ez toxikoak ziren bitartean. Gainera, **39** bakarrik argiztatzerakoan ez zuen toxikotasunik erakutsi PC-3 zeluletan (IC_{50} ≈ 500 µM).[75] Ondoren egindako lan batean, Infantek *et al*. QD-en bidez edo UVA irradiaketa zuzenaren bidez **39** konplexuaren fotoerredukzioak, fotoprodukturu ezberdinak ematen zituela frogatu zuten.[76]

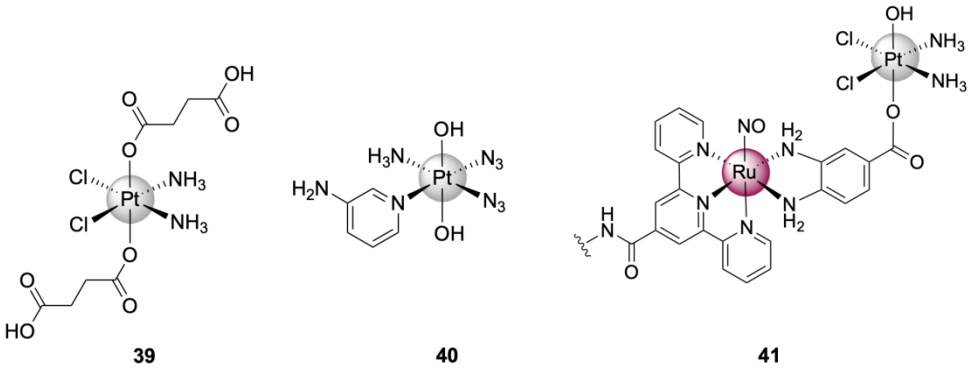

17. Irudia. QD (**39**), CD (**40**) eta GQD (**41**) egiturekin elkartutako Pt^{IV} profarmakoen estruktura kimikoak.

Argiaren arurrean sentiberak diren karbono puntuak (CD), Pt farmakoak garraiatzeko ere erabili izan dira. **40** konplexuarekin eta azido folikoarekin apaindutako CD fluoreszenteak (17. Irudia), folato errezeptoreak gehiegi adierazten dituzten hainbat minibizi zeluletara zuzentzeko ahalmena erakutsi zuten. Argi ikusgarriarekin irradiatu ostean (> 400 nm, 200 $mW \cdot cm^{-2}$), heriotza zelularra apoptosi bitartez eragiten zituzten Pt^{II} espezieak askatu ziren.[77] Era berean, Liuk eta lankideek, **41** konplexu heterobimetalikoa, folatoarekin apaindutako aminekin dopatutako grafeno puntu kuantikoetan (GQD) kargatu zuten. HeLa eta MCF-7 minbizi zeluletan eta HUVEC zelula osasuntsuetan egindako *in vitro* esperimentuek, egitura konposatu hauek, gehienbat HeLa minbizi zeluletan metatzen zirela frogatu zuten. NIR argi irradiaziarioaren menpe (808 nm, 1 $W \cdot cm^{-2}$), **41** konplexuak, NO molekula eta Pt^{II} sendagaiak askatu zituen eta horren ondorioz, minibiziaren aurkako ekintza azaldu zuen (17. Irudia).[78]

Goranzko kobertsioa egiten duten nanopartikulak (Upconverting nanoparticles, UCNP) ere erabili dira infragorri hurbileko argiaren bidez Pt^{IV} konplexuen fotoaktibazioa lortzeko. Bere emisio ezaugarriengatik, nanomaterial inerte mota hau tresna interesagarri bihurtu da medikuntzan irudiak egiteko.[79] Lantanido ioiez dopatutako nano-eskala materialek, energi baxuko bi fotoi edo gehiago jarraian xurgatu eta uhin laburragoko argi emisioara (ikuskorra eta UV) daramaten prozesu optiko ez linealak (anti-Stokes) jasateko gaitasuna dute.[79] UCNP-en ezaugarri luminiszenteak aproposak dira metaletan oinarrituriko minibizaren kontrako agenteen aktibazio fotokimikoa gauzatzeko.

Esate baterako, gure taldeak aurreko lan batean $NaYF_4$:Yb,Tm@$NaYF_4$ nukleo-oskol UCNP-etan amino PEG fosfolipido batekin apaindutako Pt^{IV} konplexua kargatu (**42** 18a Irudia) zuen. 42 konplexua lau orduz 980 nm-ko argiarekin argiztatu (4.9 $W \cdot cm^{-2}$) ondoren, biologikoki aktiboak ziren Pt^{IV} eta Pt^{II} (%30) konplexuetan eraldatzen zen.[80]

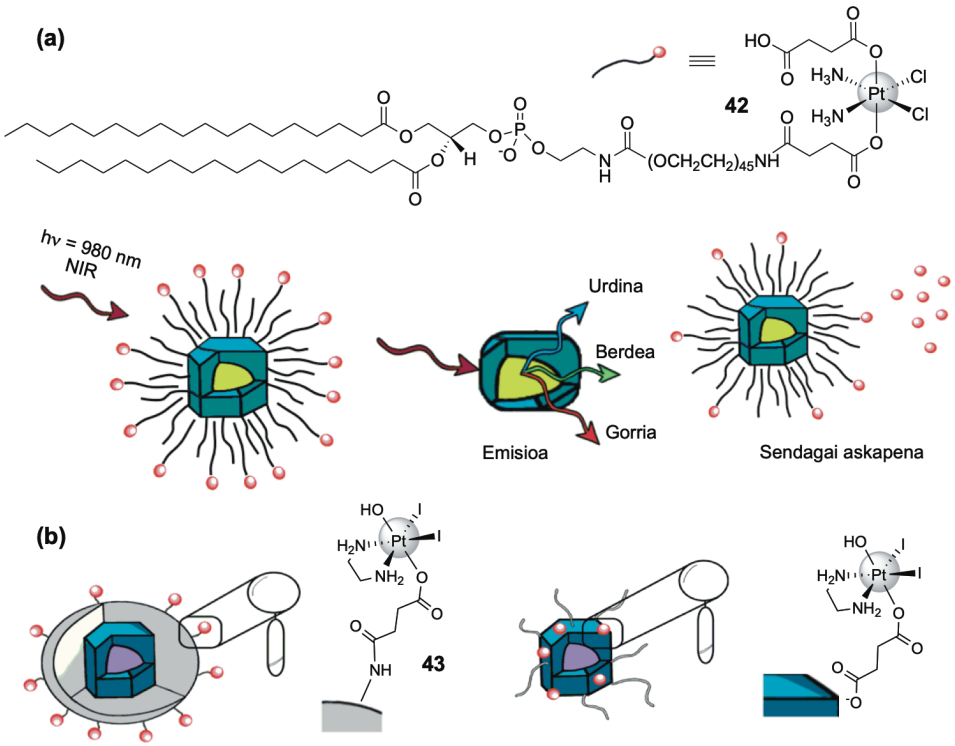

18. Irudia. UCNP-en bidez gauzatutako Pt^{IV} profarmakoen NIR fotoaktibazioa.[80,81]

Bednarskik eta lankideek, argiaren aurrean sentibera zen diiodo monokarboxilatu eratorria (**43**), $NaGdF_4$:Yb,Er UCNP-etara itsatsi zuten bi estrategia ezberdin erabiliz (18b Irudia). Lehenengo kasuan, UCNP aminadun silika oskol batekin apaindu ziren eta konplexuak amida lotura bidez kobalenteki itsatsi ziren gainazalean. Beste kasuan, estekatzaile elkartruketaren bitartez, **43** konplexua elektrotatikoki lotu zen gainazalean. Pt kantitate konparagarria aurkitu zen bi estrategien bidez sintetizatutako UCNP-en gainazalean. Pt espezieen askatzeari zegokionez, konplexua kobalenteki itsatsita zeukaten egiturek elektrostatikoki itsatsita zeukaten egiturek baino argi sentikortasun handiagoa erakutsi zuten. Horretaz gain, UCNP-Pt^{IV} konjokatu kobalenteak konjonkatu elektrostatikoak baino zitotoxikotasun altuagoa erakutsi zuen ilunpetan eta NIR argi irradiazioaren menpe (980 nm, 1.2 $W \cdot cm^{-2}$) HL60 giza leuzemia zeluletan. Bestalde, XPS neurketen bidez, bi estrategietan gainazaleko platinoaren % 20 inguru Pt^{IV} oxidazio egoeran zegoela eta % 80 Pt^{II} oxidazio egoeran zegoela frogatu zen.[81]

Daikek *et al*.[82] eta Minek *et al*.[83] **29** eta **30** Pt^{IV} azida konplexuen eratorriak UCNP-nanomaterialetara lotu zituzten. Konplexuek, minbiziaren kontrako ekintza erakutsi zuten *in vitro* esperimentuetan eta horretaz gain, lehenengo konplecuak, *in vivo* esperimentuetan tumoreen murrizketa eragin zuenn NIR argiarekin irradiatzerakoan. Nahiz eta lan honek,

aipamen kopuru handia jaso duen, karakterizazio sakonagoa eta hainbat esperimentu kontrol gako falta dira. Gainera NIR irradiazioak eragindako Pt^{IV} konplexuen fotoaktibazioaren eta ikusitako efektu bologikoarekin arteko harremana ez da xehetasunez azaltzen. Bestalde, garrantzitsua da azpimarratzea UNCP-en bidez gauzatutako Pt agenteen aktibazioa lortzeko 980 nm-ko intentsitate altuko kitzikapen argi iturriak erabili zirela. Uhin-luzera honetako irradiazioaren menpe, uraren berotzea gertatzen da eta ondorioz, osagai biologiko ezberdinetan kalte zuzena eragin daiteke.[84] Gaur egun muga horiek gainditzeko, Nd-rekin dopatutako UCNP eta 808 nm-ko argi kitzikapena, PDT aplikazioaren alternatiba gisa aztertzen ari dira.[85]

1.6 Laburpena

Azken urteotan, arreta handia jaso du fotokimikaren erabilpena minbiziaren kontrako agenteak eta farmako askapen estrategia berriak garatzeko. Testuinguru honetan, Sadlerrek eta lankideek sintetizatutako Pt^{IV} azida konplexuak, eredu moduan agertu ziren ikerketa eremu honetan. Gainera, ikerketa arlo honek, aurrerapauso adierazgarriak eman ditu aktibitate biologiko desberdina, minbizi zeluletara zuzentzeko gaitasuna edo ezaugarri fotokimiko hobeak dituzten Pt agenteen garapenari dagokionez. Hala ere, Pt agente fotoaktibagarrien *in vivo* azterketen kopuru txikiak, oraindik ere eremu honetan asko aztertzeko dagoela adierazten du.

Esate baterako, Pt konplexuen aktibazioa argi gorriaren bidez lortzeari eskainitako ahaleginak ekarpen handiak egin ditzake ikerketa eremu honetan. Gainera, mota honetako konposatuak PDT-ren alternatiba edo sinergia tresna gisa ikertzea pena merezi du. Neurri batean, nanomaterialetan oinarritutako egitura fotoaktibagarri berriek helburu hau lortu zuten (puntu kuantikoak eta UCNP adibidez). sistema horiek, farmakoen askapen helburuetarako sofistikatuegiak dira, sistemen onespena eta erabilera klinikoa zailduz. Ezaugarri fotofisiko bereziak eduki arren, UCNP-en bidez gauzatutako farmakoen aktibazioak, fotokonbertsio eraginkortasun baxua erakutsi du. Horretaz gain lantanidoen lixibiazioaren inguruan kezkak sortu dira.

Gaur egun, metaletan oinarritutako farmakoek, farmazia-sektorearen interes falta dute. Hau noski, minbiziaren kontrako Pt agente fotoaktibagarrietara hedatzen da. Beraz, zaila da iragartzea zer behar duen ikerketa eremu honek, minbiziaren kontrako Pt agente aktibagarrien hurrengo belaunaldia garatzeko. Segur aski, Pt konposatu berrien sintesi hutsa eta *in vitro* azterketak irradiatuz ez dira ahalegin nahikoak. Hortaz, argiaren bidez aktibatzeko estrategia egokiak eta hauen inplementazioa askapen sistema biobatergarrietan, Pt agente fotoaktibagarrien diseinuan barneratu behar da hasierako hurratsetatik. Pt profarmakoak antigorputzei edo suero proteinei bezalako bektoreei lotzeak (tumoreetara zuzentzeko) adibidez, metaketa ez-selektiboa eta Pt profarmakoek eragindako

efektu sistemiko kaltegarriak murriztu ditzakete. Horretaz gain, klinikoki onartutako aitzindariak, estekatzaileak, sensitizatzaileak edo gehigarriak Pt konplexuen egituran gehitzeak, farmakoen onespenean lagundu dezake eta ondorioz, industria farmakologikoaren atentzioa erakarri dezake. Zorionez, orain dela gutxi TLD-1433 Ru PDT agenteak giza proba klinikoetan lortutako emaitzek, minbiziaren kontrako Pt agente fotoaktibagarrien ikerketa eremua susta dezakete.[7]

1.7 Erreferentziak

(1) Rosenberg, B.; Van Camp, L.; Krigas, T. Inhibition of Cell Division in Escherichia Coli by Electrolysis Products from a Platinum Electrode. *Nature* **1965**, *205*, 698–699.

(2) Rosenberg, B.; Van, C. L.; Grimley, E. B.; Thomson, A. J.; Van Camp, L.; Grimley, E. B.; Thomson, A. J. The Inhibition of Growth or Cell Division in Escherichia Coli by Different Ionic Species of Platinum(IV) Complexes. *J. Biol. Chem.* **1967**, *242*, 1347–1352.

(3) Rosenberg, B.; Renshaw, E.; Vancamp, L.; Hartwick, J.; Drobnik, J. Platinum-Induced Filamentous Growth in Escherichia Coli. *J. Bacteriol.* **1967**, *93*, 716–721.

(4) Rosenberg, B.; VanCamp, L.; Trosko, J. E.; Mansour, V. H. Platinum Compounds: A New Class of Potent Antitumour Agents. *Nature* **1969**, *222*, 385–386.

(5) Rosenberg, B.; VanCamp, L. The Successful Regression of Large Solid Sarcoma 180 Tumors by Platinum Compounds. *Cancer Res.* **1970**, *30*, 1799–1802.

(6) Harder, H. C.; Rosenberg, B. Inhibitory Effects of Anti-Tumor Platinum Compounds on DNA, RNA and Protein Syntheses in Mammalian Cells in Vitro. *Int. J. Cancer* **1970**, *6*, 207–216.

(7) Monro, S.; Colón, K. L.; Yin, H.; Roque, J.; Konda, P.; Gujar, S.; Thummel, R. P.; Lilge, L.; Cameron, C. G.; McFarland, S. A. Transition Metal Complexes and Photodynamic Therapy from a Tumor-Centered Approach: Challenges, Opportunities, and Highlights from the Development of TLD1433. *Chem. Rev.* **2019**, *119*, 797–828.

(8) Matveeva, S. G.; Pozdnyakov, I. P.; Grivin, V. P.; Plyusnin, V. F.; Mereshchenko, A. S.; Melnikov, A. A.; Chekalin, S. V.; Glebov, E. M. Primary Photochemical Processes for $PtCl_6^{2-}$ Complex in Acetonitrile Solutions. *J. Photochem. Photobiol. A.* **2016**, *325*, 13–21.

(9) Matveeva, S. G.; Grivin, V. P.; Plyusnin, V. F.; Vasilchenko, D. B.; Glebov, E. M. Mechanism of Chain Photochemical Reaction of $(n\text{-}Bu_4N)_2[PtCl_6]$ in Chloroform. *J. Photochem. Photobiol. A.* **2018**, *359*, 80–86.

(10) Glebov, E. M.; Pozdnyakov, I. P.; Vasilchenko, D. B.; Zadesenets, A. V.; Melnikov, A. A.; Magin, I. M.; Grivin, V. P.; Chekalin, S. V.; Plyusnin, V. F. Photochemistry of cis,trans-$[Pt(En)(I)_2(OH)_2]$ Complex in Aqueous Solutions. *J. Photochem. Photobiol. A.* **2018**, *354*, 78–85.

(11) Shushakov, A. A.; Pozdnyakov, I. P.; Grivin, V. P.; Plyusnin, V. F.; Vasilchenko, D. B.; Zadesenets, A. V.; Melnikov, A. A.; Chekalin, S. V.; Glebov, E. M. Primary Photochemical Processes for Pt(IV) Diazido Complexes Prospective in Photodynamic Therapy of Tumors. *Dalton Trans.* **2017**, *46*, 9440–9450.

(12) Vernooij, R. R.; Joshi, T.; Horbury, M. D.; Graham, B.; Izgorodina, E. I.; Stavros, V. G.; Sadler, P. J.; Spiccia, L.; Wood, B. R. Spectroscopic Studies on Photoinduced Reactions of the Anticancer Prodrug, trans,trans,trans-$[Pt(N_3)_2(OH)_2(Py)_2]$. *Chem. Eur.*

J. **2018**, *24*, 5790–5803.

(13) Li, K.; Tong, G. S. M.; Wan, Q.; Cheng, G.; Tong, W.-Y.; Ang, W.-H.; Kwong, W.-L.; Che, C.-M.; Ming Tong, G. S.; Wan, Q.; et al. Highly Phosphorescent Platinum(II) Emitters: Photophysics, Materials and Biological Applications. *Chem. Sci.* **2016**, *7*, 1653–1673.

(14) T. H. Dunning Jr. and P.J.Hay. Gaussian Basis Sets for Molecular Calculations, in *Modern Theoretical Chemistry, Volume 3: Methods of Electronic Structure Theory*; Plenum, **1977**; pp 1–28.

(15) Mlcouskova, J.; Stepankova, J.; Brabec, V. Antitumor Carboplatin Is More Toxic in Tumor Cells When Photoactivated : Enhanced DNA Binding. *J. Biol. Inorg. Chem.* **2012**, *17*, 891–898.

(16) Heringova, P.; Woods, J.; Mackay, F. S.; Kasparkova, J.; Sadler, P. J.; Brabec, V. Transplatin Is Cytotoxic When Photoactivated: Enhanced Formation of DNA Cross-Links. *J. Med. Chem.* **2006**, *49*, 7792–7798.

(17) Navas, F.; Perfahl, S.; Garino, C.; Salassa, L.; Novakova, O.; Navarro-Ranninger, C.; Bednarski, P. J.; Malina, J.; Quiroga, A. G. A. G. Increasing DNA Reactivity and in Vitro Antitumor Activity of trans Diiodido Pt(II) Complexes with UVA Light. *J. Inorg. Biochem.* **2015**, *153*, 211–218.

(18) Prachařová, J.; Intini, F. P.; Natile, G.; Kasparkova, J.; Brabec, V. Potentiation of Cytotoxic Action of cis-[$PtCl_2(NH_3)$(1M7AI)] by UVA Irradiation. Mechanistic Insights. *Inorg. Chim. Acta.* **2018**, *472*, 199–206.

(19) Štarha, P.; Trávníček, Z.; Dvořák, Z.; Radošová-Muchová, T.; Prachařová, J.; Vančo, J.; Kašpárková, J. Potentiating Effect of UVA Irradiation on Anticancer Activity of Carboplatin Derivatives Involving 7-Azaindoles. *PLoS One.* **2015**, *10*, e0123595.

(20) Mitra, K.; Patil, S.; Kondaiah, P.; Chakravarty, A. R. 2-(Phenylazo)Pyridineplatinum(II) Catecholates Showing Photocytotoxicity, Nuclear Uptake, and Glutathione-Triggered Ligand Release. *Inorg. Chem.* **2015**, *54*, 253–264.

(21) Raza, M. K.; Mitra, K.; Shettar, A.; Basu, U.; Kondaiah, P.; Chakravarty, A. R. Photoactive Platinum(II) β-Diketonates as Dual Action Anticancer Agents. *Dalton Trans.* **2016**, *45*, 13234–13243.

(22) Mitra, K.; Gautam, S.; Kondaiah, P.; Chakravarty, A. R. The cis-Diammineplatinum(II) Complex of Curcumin: A Dual Action DNA Crosslinking and Photochemotherapeutic Agent. *Angew. Chem., Int. Ed.* **2015**, *54*, 13989–13993.

(23) Mitra, K.; Lyons, C. E.; Hartman, M. C. T. T. A Platinum(II) Complex of Heptamethine Cyanine for Photoenhanced Cytotoxicity and Cellular Imaging in Near-IR Light. *Angew. Chem., Int. Ed.* **2018**, *57*, 10263–10267.

(24) Morales, K.; Samper, K. G.; Peña, Q.; Hernando, J.; Lorenzo, J.; Rodríguez-Diéguez, A.; Capdevila, M. M.; Figueredo, M.; Palacios, Ò.; Bayón, P.; et al. Squaramide-Based Pt(II) Complexes as Potential Oxygen-Regulated Light-Triggered Photocages. *Inorg. Chem.* **2018**, *57*, 15517–15525.

(25) Maity, B.; Gadadhar, S.; Goswami, T. K.; Karande, A. A.; Chakravarty, A. R. Photo-Induced Anticancer Activity of Polypyridyl Platinum(II) Complexes. *Eur. J. Med. Chem.* **2012**, *57*, 250–258.

(26) Mitra, K.; Basu, U.; Khan, I.; Maity, B.; Kondaiah, P.; Chakravarty, A. R. Remarkable Anticancer Activity of Ferrocenyl-Terpyridine Platinum(II) Complexes in Visible Light with Low Dark Toxicity. *Dalton Trans.* **2014**, *43*, 751–763.

(27) Mitra, K.; Shettar, A.; Kondaiah, P.; Chakravarty, A. R. Biotinylated Platinum(II) Ferrocenylterpyridine Complexes for Targeted Photoinduced Cytotoxicity. *Inorg. Chem.* **2016**, *55*, 5612–5622.

(28) Raza, M. K.; Gautam, S.; Garai, A.; Mitra, K.; Kondaiah, P.; Chakravarty, A. R. Monofunctional BODIPY-Appended Imidazoplatin for Cellular Imaging and Mitochondria-Targeted Photocytotoxicity. *Inorg. Chem.* **2017**, *56*, 11019–11029.

(29) Xue, X.; Zhu, C.; Chen, H.; Bai, Y.; Shi, X.; Jiao, Y.; Chen, Z.; Miao, Y.; He, W.; Guo, Z. A New Approach to Sensitize Antitumor Monofunctional Platinum(II) Complexes via Short Time Photo-Irradiation. *Inorg. Chem.* **2017**, *56*, 3754–3762.

(30) Li, H.; Lan, R.; Chan, C.-F. F.; Jiang, L.; Dai, L.; Kwong, D. W. J. J.; Lam, M. H.-W. W.; Wong, K.-L. L. Real-Time in Situ Monitoring via Europium Emission of the Photo-Release of Antitumor Cisplatin from a Eu-Pt Complex. *Chem. Commun.* **2015**, *51*, 14022–14025.

(31) Quental, L. L.; Raposinho, P.; Mendes, F.; Santos, I.; Navarro-Ranninger, C.; Alvarez-Valdes, A.; Huang, H.; Chao, H.; Rubbiani, R.; Gasser, G.; et al. Combining Imaging and Anticancer Properties with New Heterobimetallic Pt(II)/M(I) (M = Re, 99mTc) Complexes. *Dalton Trans.* **2017**, *46* (42), 14523–14536.

(32) Kastner, A.; Poetsch, I.; Mayr, J.; Burda, J. V.; Roller, A.; Heffeter, P.; Keppler, B. K.; Kowol, C. R. Doubt on a Dogma: Aquation of Equatorial Ligands of Pt(IV) Complexes under Physiological Conditions. *Angew. Chem., Int. Ed.* **2019**, *58*, 7464-7469.

(33) Johnstone, T. C.; Suntharalingam, K.; Lippard, S. J. The Next Generation of Platinum Drugs: Targeted Pt(II) Agents, Nanoparticle Delivery, and Pt(IV) Prodrugs. *Chem. Rev.* **2016**, *116*, 3436–3486.

(34) Gibson, D. Platinum(IV) Anticancer Prodrugs-Hypotheses and Facts. *Dalton Trans.* **2016**, *45*, 12983–12991.

(35) Hall, M. D.; Hambley, T. W. Platinum(IV) Antitumour Compounds: Their Bioinorganic Chemistry. *Coord. Chem. Rev.* **2002**, *232*, 49–67.

(36) Sinisi, M. M.; Intini, F. P.; Natile, G. Dependence of the Reduction Products of Platinum(IV) Prodrugs upon the Configuration of the Substrate, Bulk of the Carrier Ligands, and Nature of the Reducing Agent. *Inorg. Chem.* **2012**, *51*, 9694–9704.

(37) Varbanov, H. P.; Jakupec, M. A.; Roller, A.; Jensen, F.; Galanski, M.; Keppler, B. K. Theoretical Investigations and Density Functional Theory Based Quantitative Structure-Activity Relationships Model for Novel Cytotoxic Platinum(IV) Complexes.

J. Med. Chem. **2013**, *56*, 330–344.

(38) Gibbons, G. R.; Wyrick, S.; Chaney, S. G. Rapid Reduction of Tetrachloro(D,L-trans)1,2-Diaminocyclohexaneplatinum(IV) (Tetraplatin) in RPMI 1640 Tissue Culture Medium. *Cancer Res.* **1989**, *49*, 1402–1407.

(39) Brown, D.; Swindell, R.; Timms, M. S.; Wagstaff, J.; Crowther, D.; Palmer, P.; Lind, M. J.; McGregor, J.; Anderson, H. Comparative Toxicity of Cisplatin, Carboplatin (CBDCA) and Iproplatin (CHIP) in Combination with Cyclophosphamide in Patients with Advanced Epithelial Ovarian Cancer. *Eur. J. Cancer Clin. Oncol.* **1988**, *24*, 1471–1479.

(40) Sternberg, C. N.; Whelan, P.; Hetherington, J.; Paluchowska, B.; Slee, P. H. T. J.; Vekemans, K.; Van Erps, P.; Theodore, C.; Koriakine, O.; Oliver, T.; et al. Phase III Trial of Satraplatin, an Oral Platinum plus Prednisone vs. Prednisone Alone in Patients with Hormone-Refractory Prostate Cancer. *Oncology* **2005**, *68*, 2–9.

(41) Kratochwil, N. A.; Zabel, M.; Range, K.-J. J.; Bednarski, P. J. Synthesis and X-Ray Crystal Structure of trans,cis-[Pt(OAc)$_2$I$_2$(En)]: A Novel Type of Cisplatin Analog That Can Be Photolyzed by Visible Light to DNA-Binding and Cytotoxic Species in Vitro. *J. Med. Chem.* **1996**, *39*, 2499–2507.

(42) Kratochwil, N. A.; Bednarski, P. J.; Mrozek, H.; Vogler, A.; Nagle, J. K. Photolysis of an Iodoplatinum(IV) Diamine Complex to Cytotoxic Species by Visible Light. *Anticancer. Drug Des.* **1996**, *11*, 155–171.

(43) Parkinson, J. A.; Sadler, P. J.; Kratochwil, N. A.; Bednarski, P. J.; Guo, Z.; del Socorro Murdoch, P. Electron-Transfer-Driven Trans-Ligand Labilization: A Novel Activation Mechanism for Pt(IV) Anticancer Complexes. *J. Am. Chem. Soc.* **1998**, *120*, 8253–8254.

(44) Müller, P.; Schröder, B.; Parkinson, J. A.; Kratochwil, N. A.; Coxall, R. A.; Parkin, A.; Parsons, S.; Sadler, P. J. Nucleotide Cross-Linking Induced by Photoreactions of Platinum(IV)–Azide Complexes. *Angew. Chem., Int. Ed.* **2003**, *42*, 335–339.

(45) Vogler, A.; Kern, A.; Hüttermann, J. Photochemical Reductive trans-Elimination from trans-Diazidotetracyanoplatinate(IV). *Angew. Chem., Int. Ed. Engl.* **1978**, *17*, 524–525.

(46) Weber, W.; Van Eldik, R. Charge-Transfer Photochemistry under High Pressure: Reductive Elimination from Trans-Diazidotetracyanoplatinate(IV). *Inorg. Chim. Acta.* **1986**, *111*, 129–131.

(47) Vogler, A.; Kern, A.; Fußeder, B.; Hüttermann, J. Photochemical Reductive Trans-Elimination from trans-Diacidotetracyanoplatinate(IV) Complexes. *Zeitschrift für Naturforsch. B.* **1978**, *33*, 1352–1356.

(48) Kašpárková, J.; Mackay, F. S.; Brabec, V.; Sadler, P. J.; Kasparkova, J.; Mackay, F. S.; Brabec, V.; Sadler, P. J. Formation of Platinated GG Cross-Links on DNA by Photoactivation of a Platinum(IV) Azide Complex. *J. Biol. Inorg. Chem.* **2003**, *8*, 741–745.

(49) Salassa, L.; Phillips, H. I. A. A.; Sadler, P. J. Decomposition Pathways for the Photoactivated Anticancer Complex cis,trans,cis-[$Pt(N_3)_2(OH)_2(NH_3)_2$]: Insights from DFT Calculations. *Phys. Chem. Chem. Phys.* **2009**, *11*, 10311–10316.

(50) Bednarski, P. J.; Grünert, R.; Zielzki, M.; Wellner, A.; Mackay, F. S.; Sadler, P. J. Light-Activated Destruction of Cancer Cell Nuclei by Platinum Diazide Complexes. *Chem. Biol.* **2006**, *13*, 61–67.

(51) Mackay, F. S.; Woods, J. A.; Moseley, H.; Ferguson, J.; Dawson, A.; Parsons, S.; Sadler, P. J. A Photoactivated trans-Diammine Platinum Complex as Cytotoxic as Cisplatin. *Chem. Eur. J.* **2006**, *12*, 3155–3161.

(52) Farrer, N. J.; Woods, J. A.; Salassa, L.; Zhao, Y.; Robinson, K. S.; Clarkson, G.; MacKay, F. S.; Sadler, P. J. A Potent trans-Diimine Platinum Anticancer Complex Photoactivated by Visible Light. *Angew. Chem., Int. Ed.* **2010**, *49*, 8905–8908.

(53) Westendorf, A. F.; Bodtke, A.; Bednarski, P. J. Studies on the Photoactivation of Two Cytotoxic trans,trans,trans-Diazidodiaminodihydroxo-Pt(IV) Complexes. *Dalton Trans.* **2011**, *40*, 5342–5351.

(54) Mackay, F. S.; Woods, J. A.; Heringová, P.; Kašpárková, J.; Pizarro, A. M.; Moggach, S. A.; Parsons, S.; Brabec, V.; Sadler, P. J. A Potent Cytotoxic Photoactivated Platinum Complex. *Proc. Natl. Acad. Sci.* **2007**, *104*, 20743–20748.

(55) Novakova, O.; Zerzankova, L.; Pracharova, J.; Kasparkova, J.; Stepankova, J.; Brabec, V.; Farrer, N. J.; Sadler, P. J.; Zerzankova, L.; Stepankova, J.; et al. Interactions of DNA with a New Platinum(IV) Azide Dipyridine Complex Activated by UVA and Visible Light: Relationship to Toxicity in Tumor Cells. *Chem. Res. Toxicol.* **2012**, *25*, 1099–1111.

(56) Zhang, J.; Li, X.; Han, X.; Liu, R.; Fang, J. Targeting the Thioredoxin System for Cancer Therapy. *Trends Pharmacol. Sci.* **2017**, *38*, 794–808.

(57) Du, J.; Wei, Y.; Zhao, Y.; Xu, F.; Wang, Y.; Zheng, W.; Luo, Q.; Wang, M.; Wang, F. A Photoactive Platinum(IV) Anticancer Complex Inhibits Thioredoxin-Thioredoxin Reductase System Activity by Induced Oxidization of the Protein. *Inorg. Chem.* **2018**, *57*, 5575–5584.

(58) Wootton, C. A.; Sanchez-Cano, C.; Lopez-Clavijo, A. F.; Shaili, E.; Barrow, M. P.; Sadler, P. J.; O'Connor, P. B. Sequence-Dependent Attack on Peptides by Photoactivated Platinum Anticancer Complexes. *Chem. Sci.* **2018**, *9*, 2733–2739.

(59) Westendorf, A. F.; Woods, J. A.; Korpis, K.; Farrer, N. J.; Salassa, L.; Robinson, K.; Appleyard, V.; Murray, K.; Grünert, R.; Thompson, A. M.; et al. trans,trans,trans-[$Pt^{IV}(N_3)_2(OH)_2(Py)(NH_3)$]: A Light-Activated Antitumor Platinum Complex That Kills Human Cancer Cells by an Apoptosis-Independent Mechanism. *Mol. Cancer Ther.* **2012**, *11*, 1894–1904.

(60) Butler, J. S.; Woods, J. A.; Farrer, N. J.; Newton, M. E.; Sadler, P. J. Tryptophan Switch for a Photoactivated Platinum Anticancer Complex. *J. Am. Chem. Soc.* **2012**, *134*, 16508–16511.

(61) Mackay, F. S.; Farrer, N. J.; Salassa, L.; Tai, H.-C.; Deeth, R. J.; Moggach, S. A.; Wood, P. A.; Parsons, S.; Sadler, P. J. Synthesis, Characterisation and Photochemistry of Pt(IV) Pyridyl Azido Acetato Complexes. *Dalton Trans.* **2009**, 13, 2315–2325.

(62) Mackay, F. S.; Moggach, S. A.; Collins, A.; Parsons, S.; Sadler, P. J. Photoactive trans Ammine/Amine Diazido Platinum(IV) Complexes. *Inorg. Chim. Acta* **2009**, *362*, 811–819.

(63) Farrer, N. J.; Woods, J. A.; Munk, V. P.; Mackay, F. S.; Sadler, P. J. Photocytotoxic trans-Diam(m)Ine Platinum(IV) Diazido Complexes More Potent than Their cis Isomers. *Chem. Res. Toxicol.* **2010**, *23*, 413–421.

(64) Venkatesh, V.; Wedge, C. J.; Romero-Canelón, I.; Habtemariam, A.; Sadler, P. J.; Romero-Canelon, I.; Habtemariam, A.; Sadler, P. J.; Wedge, C. J.; Romero-Canelon, I.; et al. Spin-Labelled Photo-Cytotoxic Diazido Platinum(IV) Anticancer Complex. *Dalton Trans.* **2016**, *45*, 13034–13037.

(65) Gandioso, A.; Shaili, E.; Massaguer, A.; Artigas, G.; González-Cantó, A.; Woods, J. A.; Sadler, P. J.; Marchán, V. An Integrin-Targeted Photoactivatable Pt(IV) Complex as a Selective Anticancer pro-Drug: Synthesis and Photoactivation Studies. *Chem. Commun.* **2015**, *51*, 9169–9172.

(66) Shaili, E.; Fernández-Giménez, M.; Rodríguez-Astor, S.; Gandioso, A.; Sandín, L.; García-Vélez, C.; Massaguer, A.; Clarkson, G. J.; Woods, J. A.; Sadler, P. J.; et al. A Photoactivatable Platinum(IV) Anticancer Complex Conjugated to the RNA Ligand Guanidinoneomycin. *Chem. Eur. J.* **2015**, *21*, 18474–18486.

(67) Dougherty, T. J.; Grindey, G. B.; Fiel, R.; Weishaupt, K. R.; Boyle, D. G. Photoradiation Therapy. II. Cure of Animal Tumors with Hematoporphyrin and Light. *J. Natl. Cancer Inst.* **1975**, *55*, 115–121.

(68) Granelli, S. G.; McDonagh, A. F.; Wilson, C. B.; Nielsen, S. L. Photochemotherapy of Glioma Cells by Visible Light and Hematoporphyrin. *Cancer Res.* **1975**, *35*, 2567–2570.

(69) Wang, Z.; Wang, N.; Cheng, S. C.; Xu, K.; Deng, Z.; Chen, S.; Xu, Z.; Xie, K.; Tse, M. K.; Shi, P.; et al. Phorbiplatin, a Highly Potent Pt(IV) Antitumor Prodrug That Can Be Controllably Activated by Red Light. *Chem* **2019**, *5*, 3151–3165.

(70) Song, H.; Kang, X.; Sun, J.; Jing, X.; Wang, Z.; Yan, L.; Qi, R.; Zheng, M. Nanoparticle Delivery of Sterically Hindered Platinum(IV) Prodrugs Shows 100 Times Higher Potency than That of Cisplatin upon Light Activation. *Chem. Commun.* **2016**, *52*, 2281–2283.

(71) He, S.; Li, C.; Zhang, Q.; Ding, J.; Liang, X.-J.; Chen, X. X.; Xiao, H.; Chen, X. X.; Zhou, D.; Huang, Y. Tailoring Platinum(IV) Amphiphiles for Self-Targeting All-in-One Assemblies as Precise Multimodal Theranostic Nanomedicine. *ACS Nano* **2018**, *12*, 7272–7281.

(72) Guo, D.; Xu, S.; Huang, Y.; Jiang, H.; Yasen, W.; Wang, N.; Su, Y.; Qian, J.; Li, J.; Zhang, C.; et al. Platinum(IV) Complex-Based Two-in-One Polyprodrug for a Combinatorial Chemo-Photodynamic Therapy. *Biomaterials* **2018**, *177*, 67–77.

(73) D'Souza, A. A.; Devarajan, P. V. Asialoglycoprotein Receptor Mediated Hepatocyte Targeting—Strategies and Applications. *J. Control. Release* **2015**, *203*, 126–139.

(74) Venkatesh, V.; Mishra, N. K.; Romero-Canelón, I.; Vernooij, R. R.; Shi, H.; Coverdale, J. P. C. C.; Habtemariam, A.; Verma, S.; Sadler, P. J.; Romero-Canelon, I.; et al. Supramolecular Photoactivatable Anticancer Hydrogels. *J. Am. Chem. Soc.* **2017**, *139*, 5656–5659.

(75) Maldonado, C. R.; Gómez-Blanco, N.; Jauregui-Osoro, M.; Brunton, V. G.; Yate, L.; Mareque-Rivas, J. C. QD-Filled Micelles Which Combine SPECT and Optical Imaging with Light-Induced Activation of a Platinum(IV) Prodrug for Anticancer Applications. *Chem. Commun.* **2013**, *49*, 3985–3987.

(76) Infante, I.; Azpiroz, J. M.; Blanco, N. G.; Ruggiero, E.; Ugalde, J. M.; Mareque-Rivas, J. C.; Salassa, L. Quantum Dot Photoactivation of Pt(IV) Anticancer Agents: Evidence of an Electron Transfer Mechanism Driven by Electronic Coupling. *J. Phys. Chem. C* **2014**, *118*, 8712–8721.

(77) Yang, X. D.; Xiang, H. J.; An, L.; Yang, S. P.; Liu, J. G. Targeted Delivery of Photoactive Diazido Pt(IV) Complexes Conjugated with Fluorescent Carbon Dots. *New J. Chem.* **2015**, *39*, 800–804.

(78) Shi, S.-W.; Li, Y.-H.; Zhang, Q. Q.-L.; Yang, S.-P. S.; Liu, J.-G. Targeted and NIR Light-Controlled Delivery of Nitric Oxide Combined with a Platinum(IV) Prodrug for Enhanced Anticancer Therapy. *J. Mater. Chem. B* **2019**, *7*, 1867–1874.

(79) Haase, M.; Schäfer, H. Upconverting Nanoparticles. *Angew. Chem., Int. Ed.* **2011**, *50*, 5808–5829.

(80) Ruggiero, E.; Hernández-Gil, J.; Mareque-Rivas, J. C.; Salassa, L. Near Infrared Activation of an Anticancer Pt(IV) Complex by Tm-Doped Upconversion Nanoparticles. *Chem. Commun.* **2015**, *51*, 2091–2094.

(81) Perfahl, S.; Natile, M. M.; Mohamad, H. S.; Helm, C. A.; Schulzke, C.; Natile, G.; Bednarski, P. J. Photoactivation of Diiodido-Pt(IV) Complexes Coupled to Upconverting Nanoparticles. *Mol. Pharm.* **2016**, *13*, 2346–2362.

(82) Dai, Y.; Xiao, H.; Liu, J.; Yuan, Q.; Ma, P.; Yang, D.; Li, C.; Cheng, Z.; Hou, Z.; Yang, P.; et al. In Vivo Multimodality Imaging and Cancer Therapy by Near-Infrared Light-Triggered Trans-Platinum Prodrug-Conjugated Upconverison Nanoparticles. *J. Am. Chem. Soc.* **2013**, *135*, 18920–18929.

(83) Min, Y.; Li, J.; Liu, F.; Yeow, E. K. L.; Xing, B. Near-Infrared Light-Mediated Photoactivation of a Platinum Antitumor Prodrug and Simultaneous Cellular Apoptosis Imaging by Upconversion-Luminescent Nanoparticles. *Angew. Chem., Int. Ed.* **2014**, *53*, 1012–1016.

(84) Wu, S.; Blinco, J. P.; Barner-Kowollik, C. Near-IR Photoinduced Reactions Assisted by Upconverting Nanoparticles. *Chem. Eur. J.* **2017**, *23*, 8325–8332.

(85) Wang, D.; Xue, B.; Kong, X.; Tu, L.; Liu, X.; Zhang, Y.; Chang, Y.; Luo, Y.; Zhao, H.;

Zhang, H. 808 Nm Driven Nd3+-Sensitized Upconversion Nanostructures for Photodynamic Therapy and Simultaneous Fluorescence Imaging. *Nanoscale* **2015**, *7*, 190–197.

2

Aktibazio kimioterapeutiko Bioortogonala

2.1 Sarrera

Gaur egun minbizia, gaixotasun larri sarrienetakoa da eta populazioaren zahartzearekin, ingurumen kutsatzaileekin eta bizi ohiturekin lotuta dago.[1] Minibizi hitzak, hazkuntza eta zelula banaketa ez-ohikoa, desberdindugabea eta geldiezina ezaugarri orokor bezala partekatzen duten gaixotasun talde bati egiten dio erreferentzia. Ezohiko zelula hauek, inbaditzaileak dira, zelula normalen funtzionamenduan aldaketak sortzen dituzte eta programatutako heriotz zelularra saihesteko gai dira.[2] Minbizi zelula gaizto hauek inguruko ehunetara zabaltzeko gaitasuna dute, gorputzeko beste lekuetan errepikatuz. Mota askotako minbiziak daude; kartzinoma, melanoma eta meuzemia adibidez, eta bakoitzak bere ezaugarri bereizgarriak ditu.[2] Giza minbiziaren lehenengo ebidentzia, kristo aurreko hiru mila urte inguruan azaldu zen Egipton, baina minibizi hitza Hippocratesek erabili zuen lehen aldiz antzinako Grezian.[3,4]

Gaur egungo gaixotasun hilgarrienetako bat izanik, minbizia sakonki ikertu da eta mota askotako tratamenduak garatu dira. Hurbilketa terapeutiko bakoitzaren erabilgarritasuna, minbizi egoera eta motaren araberakoa da. Minbizia jasaten duten gaixoetako gehienek, ondorengo tratamenduetako bat edo konbinazioa jasotzen dute:[5]

- ***Kirurgia***: minibizi ehunak kentzeko prozedura fisikoa.
- ***Erradiazio bidezko terapia***: minbizi zelulak hiltzeko erradiazio dosi altuak, X-izpiak normalean, erabiltzen dituen terapia.
- ***Kimioterapia***: minbizi zelulak hiltzeko sendagai toxikoak erabiltzen dituen tratamendua. Kimioterapia dosi altuen ondoren, gaixoek zelula ama transplantea behar izaten dute kimioterapiak hildako hezur muineko zelulak berrezartzeko.
- ***Inmunoterapia***: Hurbilketa honetan, gaixoen immunitate sistema minbiziaren aurka estimulatzen den. Tratamendu honen adibiderik adierazgarrienak, immunitate sistema intrinsekoa pizten duten zitokinak edo antigorputzak eta immunitate sistema antigenoen aurka prestatzen dituzten txertoak eta inibitzaileak dira.
- ***Hormona terapia***: tumore zehatzen hazkuntza moteltzeko edo ezabatzeko, gaixoari hormonak ematen zaizkio.
- ***Terapia genetikoa***: bektore bat, normalean birus bat, minbizidun zelulei informazio genetiko zehatz bat emateko erabiltzen da, euren jatorrizko ezaugarriak aldatuz. Informazio hori baliagarria izan daiteke immunofagia bezalako beste tratamendu batzuen ekintza hobetzeko. Nahiz eta tratamendu hau erakargarria eta esperantzagarria izan, garapen goiztiarrean dago eta etorkizuneko aplikazioetarako optimizatu behar da.

Gaur arte munduan zehar minbiziaren kontrako tratamendu erabilienak, kirurgia, erradioterapia eta kimioterapia izan dira. Minbiziaren biologia sakonago ulertzen den heinean, immunoterapia bezalako tratamenduak garrantzia hartzen ari dira, nahiz eta gaur egung kimioterapia baino hedapen gutxiago duten. Testuinguru honetan, tratamendu

berrriek garapena jasan arte, ahalegin handiak egin dira kimioterapia eta tratamendu klasikoak hobetzeko. Konposatu organiko eta inorganiko anitz diseinatu eta sintetizatu dira azkeneko hamarkadetan minbiziaren koontrako agente bezala, baina gutxi batzuk lortu dute Janari eta Sendagai Administrazioaren (FDA) edo Europar Sendagai Agentziaren (EMA) onespena.

Onartutako minbiziaren kontrako konposatu gehienak, zatiketa zelularra etetean eragiten duten toxikotasuna. Minbizi zelulak, zelula normalak baino azkarrago zatitzen direnez, sendagaiek minbizi zelulenganako lehentasuna erakusten dute.[6] Hala ere, efektu hau selektibitate baxuarekin gertatzen da eta horren ondorioz, nefro eta neuro toxikotasun bezalako albo ondorio larriak eragiten dira.[7]

Efektu horri aurre egiteko eta albo ondorioak sahiesteko, farmakologikoki aktiboak diren sendagaien eraldaketa fisikokimikoa egitea estrategia alternatibo bezela agertu zen. Profarmakoak, inerte edo toxikotasun gutxiko farmako atzindarien eratorriak dira. Hauek, baldintza zehatzen menpe aktiboak bilakatzen dira.[8] Profarmakoen erabilera, sendagai aitzindarien xurgapen, banaketa, metabolismo, eskrezio eta nahi gabeko efektu toxikoak gainditzeko hasi zen.[9] Profarmakoen diseinuan bi estrategia nagusi desberdindu daitezke. Alde batetik, garraiatzaile bati lotutako profarmakoak, non molekula aktiboa garraiatzaile bati lotutako dago eta ostean, lotura hori apurtzen da farmakoa askatuz. Bestalde, egitura eraldatuta duten farmakoak daude. Profarmako hauek, osagai biologikoek eragindako eraldaketa kimikoen bidez farmako aktiboetan bilakatzen dira.[8] Orokorrean, profarmakoen erabilerak, nahi ez diren efektu toxikoak gutxitu ditzake. Aldi berean, tratamenduaren eraginkortasuna handitu dezake, soilik behar den gunean efektu farmakologikoa azalduz.

Aktibazio prozesuen selektibitate maximoa lortzeko, kimika bioortogonala tresna interesagarri bezala sortu da. Bertozzik eta lankideek, jatorrizko prozesu biologikoak oztopatu gabe, ingurune biologikoetan gertatzen diren erreakzioak, kimika biolortogonal bezala definitu zituzten. Termino hau, ingurumen zelularrean Straudinger loturaren bidez azida zuen glikoproteinen etiketatze selektiboa fosfina zundekin deskribatzeko sortu zen (1. Irudia).[10] Nahiz eta kimika bioortogonal terminoa proteinen etiketatze erreakzioa deskribatzeko sortu, gaur egun, zelulen barnean selektibitate maila altuarekin gertatzen diren erreakzio ez naturaletara hedatzen da, hala nola proteina, lipido eta glikano eraldaketa, azida alkano erreakzioak, profarmako askapen eta aktibazio erreakzioak besteak beste.[11]

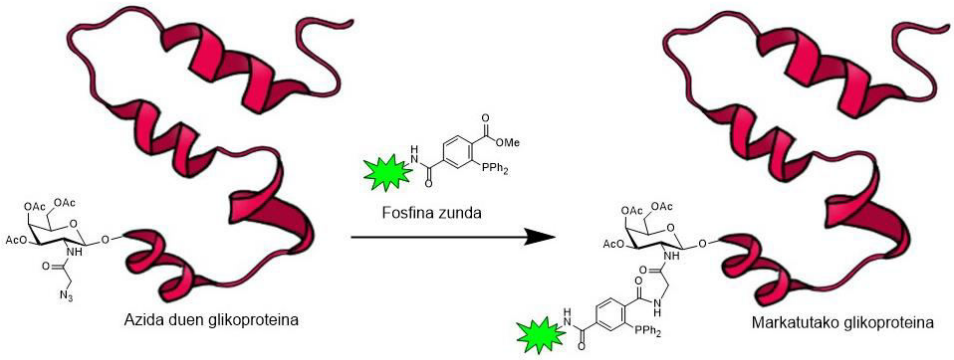

1. Irudia. Bertozzik eta lankideek deskribatutako glikoproteina etiketatzearen irudikapen eskematikoa.[10]

Kimikari eta biologoek bizitzari buruzko ulermen sakonagoa lortzeko helburuarekin jakintza elkartrukatzen hasi zirenetik, entzimek arreta handia erakarri zuten. Entzimak, organismo biologikoen barnean erreakzio katalitiko selektibo eta eraginkorrak egiteko ahalmena duten proteinak dira. Ezagutzen diren entzimen herenak, ioi metalikoak behar dituzte haien jarduera egiteko.[12] Gertaera honek, entzima naturalen moduan jarduten duten katalizatzaile metalikoak sintetizatzera bultzatu zituen kimikariak. Katalizatzaile hauen helburua, zelulen barnean substratu zehatz baten kopia askorekin erreakzionatzea da. Helburu kimioterapeutikoetarako aproposak diren erreakzio katalitikoek, tresna berriak ekar ditzakete minbiziaren kontrako farmakoen aktibazio estrategiak garatzeko. Izan ere, erreakzio bioortogonal katalitikoek, erantzun biologiko bat anplikatu dezakete eta gainera, selektibitate handiko efektu terapeutikoa eragin dezakete.[13] Erreakzio bioortogonal guztiak biobateragarriak, selektiboak eta ur ingurunean gertatzen dira. Horregatik, katalizatzaile bioortogonalak, ez toxikoak izan behar dira desiratutako kontzentrazioetan eta selektiboak izan behar dira ingurune konplexu batean (azukreak, aminoazidoak, lipidoak eta mota askotariko biomolekulak duituen ingurune zelularra), bigarren mailako erreakzioa eman ez daitezen.[14] Organismo multizelularren konplexutasunaren ondorioz, katalisi bioortogonalaren helbururik zailenetakoa oraindik ere, katalizatzaileen askapen eta erreaktibitate kontrolatua da.

Kapitulu honetan, kimioterapian erabiltzeko helburuarekin diseinatutako katalisi bioortogonalen hurbilketa ezberdinen adibiderik adierazgarrienak aurkeztu dira. Katalizatzailearen arabera hiru estrategia nagusi desberdindu dira:

- Konplexu metalikoen bidez gauzatutako katalisi bioortogonala
- Nanoboten bidez gauzatutako aktibazio katalitikoa
- Fotokatalisi bioortogonala metal konplexuak substratu moduan erabiliz

2.2 Konplexu metalikoen bidez gauzatutako katalisi bioortogonala

Katalisia, katalizatzaile deritzon bitartekari baten presentzian gertatzen den erreakzio kimikoaren tasa handipena bezala define daiteke. Prozesu honetan zehar, katalizatzailearen zebatekoan, ez da aldaketarik gertatzen.[15] Katalizatzaile metalikoak sarritan, btartekari gisa erabili dira molekula organikoak balio handiagoko molekuletan bihurtzeko.[16] Hala ere, azkeneko hamarkadan, medikuntza kimiko ez organikoan lan egiten duten talde batzuk, katalizatzaile metalikoak kimioterapia helburuentzako erabili dituzte haien ezaugarri fisikokimiko bereizagarrietaz baliatuz. Gaur egun, katalizatzaile metalikoek, ingurune biologikoetan metodo klasikoen bidez ezinezkoak diren hainbat transformazio egiteko aukera ematen dute.[17] Atal honetan ingurune biologikoetan gertatzen den katalisi metalikoa, medikuntza kimikoaren erabileraren arabera, bi talde ezberdinetan desberdindu da. Efektu toxikoa eragiten duten farmako katalitiko metalikoak eta irudi edo aplikazio terapeutikoetarako substratuak eraldatzen dituzten katalizatzaile metalikoak.

2.2.1 Farmako katalitiko metalikoak

Hemen, farmako katalitiko metalikoen adibide aipagarrienak laburbildu dira. Farmako hauek zelulen funtzio normalak aldatzen dituzte, erredox sistema eraldatzen dute edo zelulentzako ezinbestekoak diren biomolekulen degradazioa eragiten dute.

Zelula homeostasia erregulatzeko erredox sistema funtsezkoa da. Oreka fina dago espezie oxidatzaile eta antioxidatzaileen artean eta oreka horren aldeketak ondorio hilgarriak eragin ditzake.[18] Terapia fotodinamikoan (PDT), argi irradiazioaren menpe fotosensitizatzaile batek, oxigeno espezie erreaktiboen (ROS) sorrera eragiten du, erredox oreka horretan aldaketa eraginez eta kalte oxidatiboa eraginez. Terapia hau, minbizi zehatz batzuen tratamendurako onartuta dago eta munduan mailan onartutako agente bakarra Photofrin da.[19] Duela gutxi, Ru^{II} polipiridilo konplexuak, PDT fotosensitizatzaile agente potentzial gisa berrikusi dira haien ezaugarri fotokimiko bereizgarriengatik. Esate baterako, McFarlanden taldeak sintetizatutako TLD-1433 konposatuak (**1**, 2. Irudia), efektu kimioterapeutiko esperantzagarriak adierazi zituen eta maskuri minbiziaren tratamendurako, Ib fasea burutu zuen. [20]

Salderren taldeak, zelulen erredox orekaren sentikortasuna erabili zuten kimioterapia helburuetarako. Talde honek, zelulen barnean glutationa tripeptidoa glutationa (GSH) disulfitoan (GSSG) oxidatzen zuen fenilazopirinato Ru^{II} katalizatzailea (**2**a eta **2**b, 2. Irudia) aurkeztu zuten. GSH, zelulen barnean eskuragarri dagoen pisu molekular gutxiko antioxidatzaile garrantzitsuena da.[21] **2**a eta **2**b katalizatzaileek 0.33 h^{-1} eta 40 inguruko berraldatze frekuentziak (TOF) eta berraldatze zenbakiak (TON) lortu zituzten. Alde batetik, denbora unitate bakoitzeko eraldatutako substratu mol kopuru handiena TOF bezala

definitu da. Bestetik, TON erreakzioaren bukaren eraldatutako substratu mol zenbakia adierazen du. Komposatu hauek, minbiziaren kontrako efektua erakutsi zuten A549 giza birika eta A2780 giza obulutegi minbizi zeluletan, 2-6 µM arteko IC_{50} balioak lortuz. GSH/GSSG mailen desorekak eragindako toxikotasunaz gain, rutenio katalizatzaile honek ROS sortu zituen.[22]

Talde berdinak, **3** (2. Irudia) bezalako Noyori motako Ru^{II} sulfonamida etilenamina konplexuak, formato kantitate ez toxikoekin inkubatzerakoan, oxidatutako eta erreduzitutako nikotina adenida dinukleotidoen (NAD^+/NADH) erredox oreka aldatzeko gai zirela frogatu zuen. Nikotina adenina dinukleotidoa, zelulen barneko erredox erreakzio askotan oinarrizko kofaktorea da.[23] **3** konplexuak, NAD^+ NADH-ra 0.2-7 h^{-1} arteko TOF balioekin erreduzitzeko gai zela erakutsi zuten ikertzaileek. Konplexuak 13.6 µM-eko IC_{50} balioa erakutsi zuen A2780 zeluletan. **3** konplexuak NAD^+ erreduzitzeaz gain, zetona edo imina bezalako biomolekulak erreduzitzeko gai zela erakutsi zuten. Hortaz, farmako katalitiko metalikoa, ez zen guztiz selektiboa.[24]

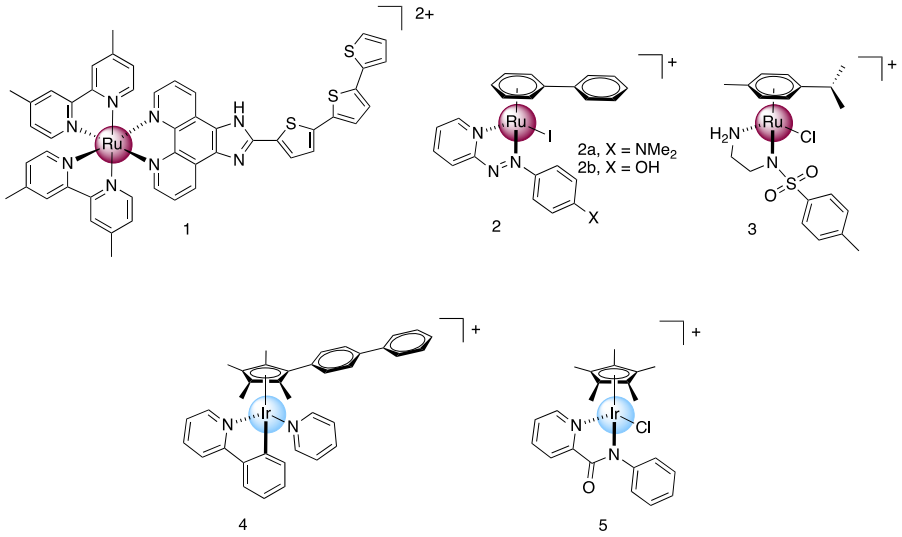

2. Irudia. Estres oxidatiboa sortzeko erabili ziren Ru^{II} eta Ir^{III} katalizatzaileen egitura kimikoak.

Talde berak 2014. urtean, H_2O_2 sortzeko gai zen Ir^{III} katalizatzailea sintetizatu zuen (**4**, 2. Irudia). Katalizatzaile honek NADH hidruro iturri moduan erabiltzen zuen erreakzioa aurrera eramateko. Erreaktibitate hori, funtsezkoa zen zelulen erredox orekan eragina izateko, azkenik efektu toxiko bortitza erakutsiz (120 nM-eko IC_{50} balioa).[25] Handik gutxira, Dok eta kolaboratzaileek, aldehidoak alkoholetan bihurtzeko gai zen Ir^{III} katalizatzailea diseinatu zuten (**5**, 2. Irudia). Katalizatzaileak, aldehido batekin babaestutako fluoroforoa askatzeko gaitasuna zuen. **5** Konplexuak, NADH-tik babestutako koloragarrira hidruro tranferentzia katalizatzen zuen. Transferentzia honen bidez, babestutako koloragarriaren fluoreszentzia piztu zen ingurune biologikoan. Zenbait aldehido prozesu metabolikoetan sortzen dira eta hainbat gaixotasun metaboliko, desorden degeneratibo, eta minbizi ezberdinekin lotzen dira.[26] Doren taldearen aurkikuntzek, katalizatzaile metalikoen bidez gaixotasunak sortzen dituzten agenteen detoxifikazio katalitikoa egitea posible dela iradokitzen dute.[26,27]

1990eko hamarkadatik ezaguna den beste farmako katalitiko metaliko mota bat, zelulen funtzionamendu egokirako funtsezkoak diren proteinak, peptidoak eta azido nukleikoak deskonposatzeko edo apurtzeko gai diren konplexuez osatuta dago.[28,29] Hala ere, katalizatzaile metaliko hauen muga nagusia, substratu zehatzenganako selektibitate falta da. Selektibitate hori hobetzeko aukeretako bat, substratu zehatz batera lotzen den atal bat gehitzea izango litzateke, katalizatzailearen selektibitate falta txikituz.

Perrinen taldeak, 90eko hamarkadan biomolekulak apurtzen zituzten katalizatzaile metalikoen lehengo adibideak argitaratu zituen. Cu 1,10-fenantrolina eta Fe etilendiaminatetraazetato konplexuak nukleasa artifizial moduan jokatuz DNA/RNA apurketa eragiteko gai ziren.[28] Ondoren, Sigmanen taldeak, **6** katalizatzailea sintetizatu zuen (3. Irudia). Horretarako, fenantrolina atala sulfonamida inhibitzaile batekin koordinatu zen. Konjokatu hau, anhidrasa karbonikoaren gune katalitikora lotzeko gai zen eta askorbatoaren eta O_2-ren presentzian entzima zati diskretuetan apurtu zuen.[30] Bitartean, Schultzen taldeak, merkaptoetanol eta O_2-ren presentzian estreptavidinara lotu eta polipeptidoaren bizkarrezurraren apurketa oxidatiboa egiteko gai ziren Cu eta Fe EDTA biotina konjokatuak (**7**, 3. Irudia) sintetizatu zituen.[31] Suk eta lankideek sintetizatutako CO^{III} cyclen katalizatzailea (**8**, 3. Irudia), peptido defolmilasa entzima katalitikoki apurtu zuen hidrolisi bidez. Konposatu hau, ß-amiloideen eta beste gaixotasunekin lotutako proteinen hidrolisirako ikertu zen.[32]

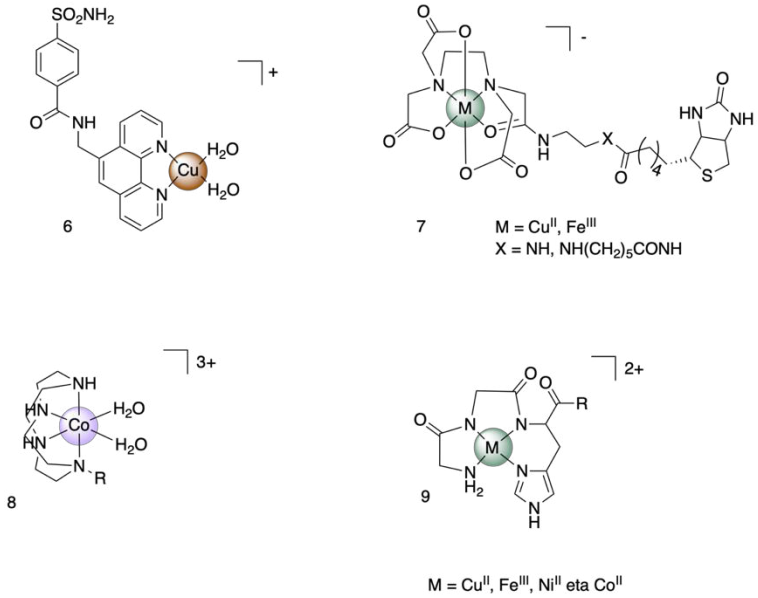

3. Irudia. Biomolekulen apurketa eragiten duten farmako katalitiko metalikoen egitura kimikoak.[30-38]

ATCUN (amino terminal Cu^{II} eta Ni^{II} lotzailea) péptido, atala proteina natural batzuetan agertzen da eta Cu^{2+}-ra eta Ni^{2+}-ra afinitate handiarekin lotzeko gaitasuna duela frogatu da. Cowanek eta lankideek ATCUN atala, metal ioi ezberdinak koodinatzeko (Cu^{II}, Ni^{II}, Fe^{III} eta Co^{II}) eta biomolekula zehatzen oxidazio edo apurketa hidrolitikoa eragiteko (**9**, 3. Irudia) erabili zuten. Talde honek angiotensina eraldatzen duen entzimaren[33], Hepatitis C-aren[34,35] eta VIH-aren[36,37] RNA eta fukosaren[38] apurketa deskribatu zuen.

2.2.2 Babestutako substratuen eraldaketa eragiten duten katalizatzaile metalikoak

Transformazio bioortogonal katalitikoen adibide gehienak, babestutako substratuen eta hauen akoplamendu gurutzatu erreakzioak deskribatzen dituzte. 2006an Meggersek eta Streuk, HeLa zelulen barnean, alilokarbamato (alloc) taldearekin babestutako rodamina fluoroforoaren aktibazio katalitikoa deskribatu zuten lehen aldiz. Lan horretan, fluoroforoaren aktibazioa Ru^{II} sandwich erdi katalizatzailearen (**10**, 4. Irudia) bitartez lortu zen. Tiofenolaren presentzian, **10** konplexuak, babestutako fluoroforoa apurtu eta fluoroforo askearen fluoreszentzia piztu zuen 4 balioko TON lortuz.[39]

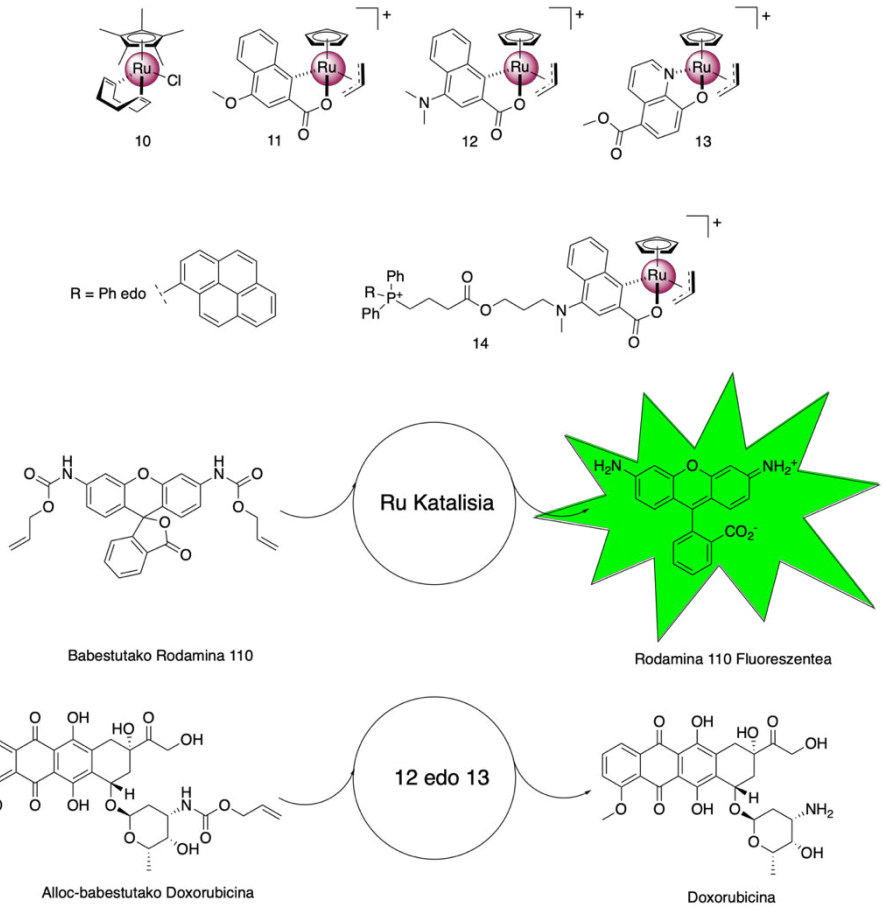

4. Irudia. Zelulen barnean erabili ziren rutenio katalizatzaileen egitura kimikoak eta babestutako rodamina 110 fluoroforoaren eta doxorubicina profarmakoen aktibazio katalitikoa.[39-40]

Beranduago, Meggersek eta lankideek Ru katalizatzaileen diseinua hobetzeko helburuarekin, apurketa katalitiko erreakzio berdina gauzatzeko gai ziren Ru^{IV} kinolina komplexu talde bat sintetizatu zuten. Glutationa bezalako nukleofilo ahulen presentzian, konplexu berri hauek, azkarrago eragin zuten apurketa erreakzioa.[40,41] Kinolina estekatzaileak, egonkortasun eta erreaktibitate handiagoa ematen zien katalizatzaileei, berraldatze zenbakia 150 eta 270 balioetara handituz **11** eta **12** konplexuen kasuan hurrenez hurren (4. Irudia).[40] Horretaz gain, kinolina-2-karboxilatoa 8-hidroxikinolinatoarengatik ordezkatu zuten, **13** katalizatzailea sortuz (4. Irudia). Ordezkapen honen ondorioz, TON 300-etik gora igo zen, 580 M^{-1} s^{-1} erreakzio abiadurarekin.[41] **12** eta **13** konplexuak erabiliz,

Meggersen taldeak N-(aliloxikarbonil) babestutako doxorubicinaren (alloc-babestutako doxorubicina, 3.Irudia) aktibazio katalitikoa eragin zuten HeLa zelulen barnean. Lan honen bitartez, hurbilketa honen potentziala kimioterapia helburuentzako frogatu zen.[40,41] Doxorubicina DNAn sartu eta topoisomerasa-II-aren DNA konponketa ekintza eragotzi edota ROS sorreraren bidez kalte zelularrak eragin ditzakeen antraziklina taldeko farmakoa da.[42] **13** konplexuaren kantitate katalitikoetan (% 2.5 karga) alloc-babestutako doxorubicinarekin inkubatu zenean, farmako aitzindariaren antzeko IC_{50} balioak erakutsi zituen.[40]

2014ean Mascareñasen taldeak alloc-babestutako 4´,6-diamidina-2´-fenilindola (DAPI) edo etidio bromuroa (EtBr) bezalako DNA lotzaileen aktibazio katalitikoa zelulen barnean deskribatu zuten. Aktibazio hori **10** katalizatzailearen bidez gauzatu zuten ikertzaileek.[43] Ostean, talde berak, ugaztuen zelulen mitokondrioetan profluoroforoak askatzeko trifenilfosfonio (TPP) rutenio konjokatua (**14**, 4. Irudia) diseinatu zuen. TPP ituraketa taldeak, mitokondioetan metatzeko lehentasuna erakusten dutela ezaguna da eta horri esker organo zehatz batera zuzendu daiteke katalizatzailea.[44]

Testuinguru honetan, metal entzima artifizialen (ArM) diseinuak aipatzea pena merezi du. Hemen aztertutako egitura artifizial hauek, Ru katalizatzaileak eta protein egiturak elkartze dituzte. 2018an, Wardek eta lankideek alloc-babestutako triiodotironina tiroide hormona, HEK-293T zeluletan aktibatu zuten rutenio estreptavidina katalizatzaile hibrido baten (5. Irudia). Aktibazioaren ondorioz, tiroide hormonaren erantzun genea pizten zen. Gainera, hormona hori, ehun guztietako termogenesi, karbohidrato metabolismo, eta lipido homeostasi prozesuetan inplikatuta dago. Estreptavidinaren izaera homotetramerikoak, biotinilatutako Ru **15** katalizatzailearen eta zelula iragazkorra den poli(disulfuro)(CPD) atalera lotutako tetrametilrodamina (TAMRA) zundaren elkartzea baimendu zuen. Proteinak babes egitura moduan jokatzen zuen, Ru katalizatzaileak babestutako hormonaren aktibazioa gauzatzen zuen bitartean. Gainera poli(disulfuro) atalak, zelulen xurgapena handitu zuen bitartean, lotutako fluoroforoa ArM-ren jarraipena ahalbidetu zuen.[45]

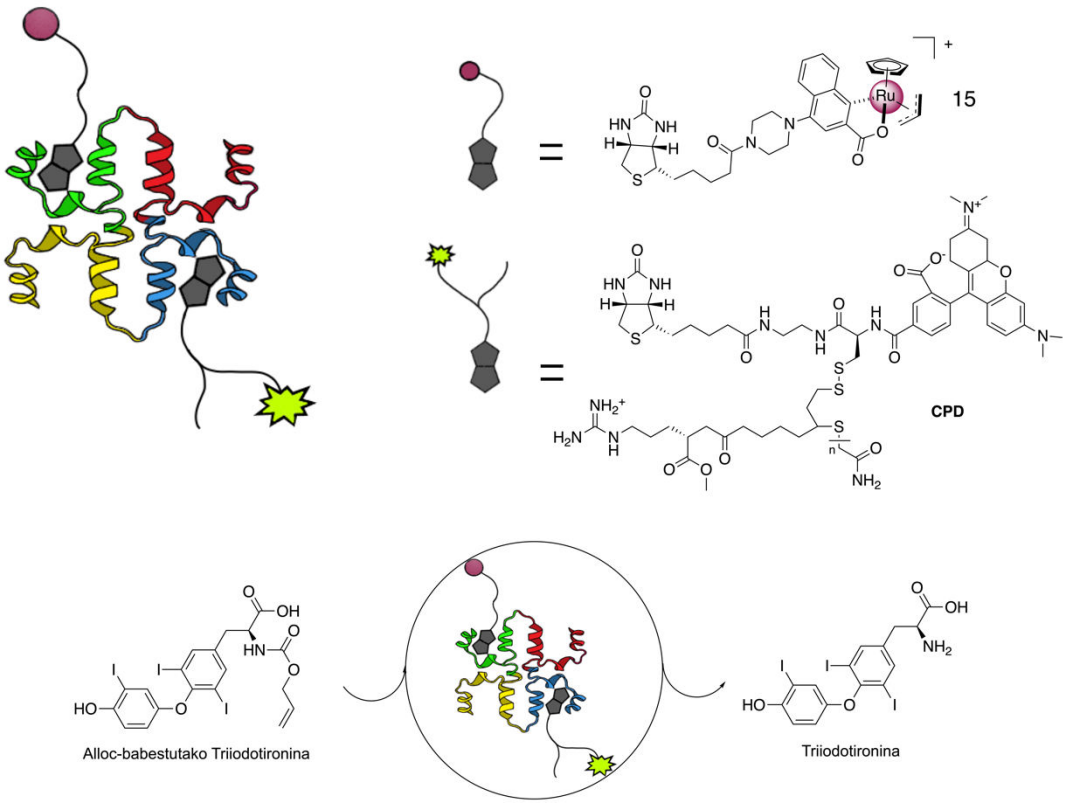

5. Irudia. Estreptadivina katalizatzaile hibridoaren, biotinilatutako CPD-aren irudikapen eskematikoa eta rutenio katalizatzailea eta triodotironina hormonaren babesgabetze katalitikoa.[45]

Urte bete beranduago, Tanakak eta lankideek, glikoalbumina artifizial bat garatu zuten. Proteinaren poltsikoan barneratutako Ru **16** konplexuak (6. Irudia), eraztun itxiera metatesi bidez, minbiziaren kontrako umbelliprenina agentearen profarmakoaren aktibazio katalitikoa gauzatu zuen. Egitura proteikoak **16** konplexuaren aktibitatea mantendu zuen 20 mM glutationaren aurrean ere. ArM, SW620 kolon adenokartzinoma, A549 eta HeLa zelua lerroetan metatzen den N-glikano gida atal batekin apaindu zen. Metaketa fenomeno hau, galaktina-8 errezeptorearen gehiegizko adierazpenarekin lotuta dago.[46] Entzima metaliko artifizial profarmako sistema hau *in vitro* SW620, A549 eta HeLa zelula lerroetan frogatu zen. ArM eta fromarmakoa batera inkubatu zirenean, farmako aitzindariak erakutsitako toxikotasunarekin konparagarriak ziren balioak lortu ziren.[47]

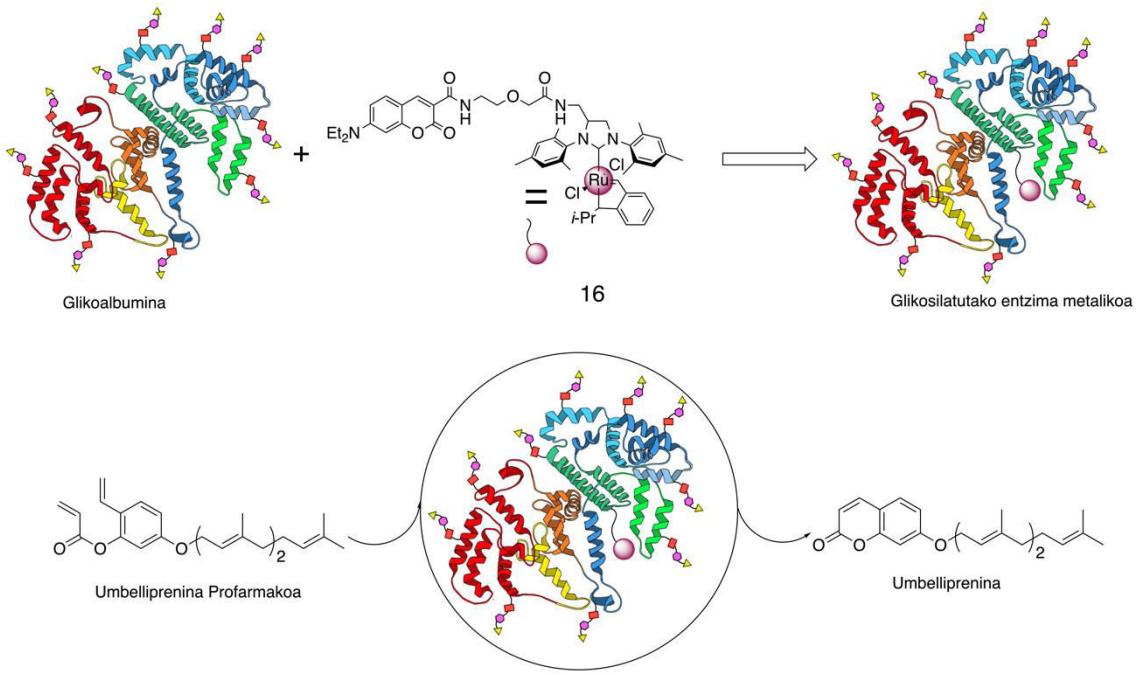

6. Irudia. Tanakak eta lankideek diseinatutako ArM-ren irudikapen eskematikoa, **16** Ru katalizatzailearen egitura kimikoa eta umbelliprenina profarmakoaren aktibazio katalitikoa.[47]

Paladioak (Pd), zenbait erreakzio bioortogonal gauzatu ditzake. Zelulen barnean, biomolekulen eraldaketa edo profarmakoen aktibazioa egin dezake adibidez. 2014an, Chenek eta lankideek Pd^0 **17** eta Pd^{II} **18** katalizatzaileen bitartez, alloc edo propargiloxikarbonilo (proc) babestutako lisina aminoazidoaren babesgabetzea deskribatu zuten *in vitro* (7. Irudia). Estrategia honen bidez, gune katalitikoetan lisinek funtsezko papera jokatzen duten entzima batzuen aktibitatea kontrolatu daiteke. Bakteria patogeniko gram negatiboek sarritan zelula ostalarietan OspF fosfotreonina liasa askatzen dute Honek seinaleen bidea modulatu eta patogenoaren infekzioa bultzatzen du.[48] Mitogenoek aktibatutako kinasaren defosforilazio itzulezina gauzatzen du fosforilatutako ErK (p-Erk) bezalako entzimetan. Proteina hau erantzun inflamatorioan parte hartzen du.[49] OspF-ren lisinak proc atalarekin babestu zirenean bere defosforilazio ekintza p-Erk entziman itzali zen. Hala ere, **17** edo **18** katalizatzaileekin inkubatzerakoan, defosforilazioa berrezarri zen.[50] Urte pare bat beranduago, Pd bitartez gauzatutako kimika bioortogonalak, beste entzima batzuk aktibatzeko aukera eskaintzen duela frogatu zen. Entzima hauetan, tirosinak dira aktibitate katalitikoa gauzatzen zuten funtsezko aminoazidoak.[51]

Duela gutxi, Bradleyren taldeak, **19** bezalako (7. Irudia) karbeno N-heteroziklikoetan oinarritutako paladio katalizatzaileek zunda fluoreszenteen eta proc-babestutako 5-Fluorouraziloaren (5FU, 7.Irudia) akibazioa gauzatzeko ahalmena zutela frogatu zuen. Aipatu beharra dago, proc-5FU profarmakoaren aktibazioak, 5FU-rekin alderagarria zen toxikotasun efektua erakutsi zuela.[52]

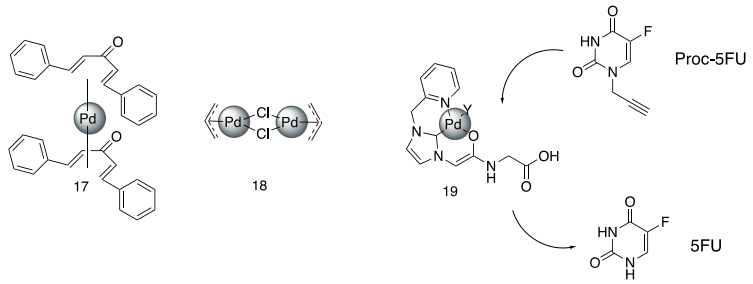

7. Irudia. Chenek, Linek eta Bradleyek erabilitako paladio katalizatzaileen egitura kimikoak.[50-52]

2.3 Nanoboten bidez gauzatutako aktibazio katalitikoa

Trantsizio metaletan oinarritutako katalizatzaileen administrazio zuzena kimioterapia helburuetarako sakonki ikertu den, oraindik ere disolbagarritasunari, egonkortasunari eta biobateragarritasunari lotutako mugak, erronka handia suposatzen dute.[53] Muga horiek gainditzeko, trantsizio metaletan oinarrituriko katalizatzaileak, nano eskala egitura artifizialetan txertatzea estrategia esperantzagarritzat sortu da. Nanobot deituriko egitura hauek, sistema bizien barnean erreakzio katalikoak gauzatzeko diseinatutako nano gailu artifizialak dira.[53] Atal honetan, nanobotak 3 mota desberdinetan sailkatu dira haien ezaugarrien arabera.

2015ean Rotellok eta lankideek lehenengo belaunaldiko nanobotak diseinatu eta sortu zituzten.[54] Ru **10** eta Pd **20** katalizatzaileak, urre nanopartikula (NP) txikietan (2 nm inguru) txertatu zituzten zunda fluoreszentea eta minbiziaren kontrako profarmakoa aktibatzeko helburuarekin (8. Irudia). NP-en estaldura, tiolak zituen alkano kate hidrofobo geruza batek osatzen zuen eta bertan katalizatzaileak kapsulatu zituzten. Estekatzaile kateak, urrungailu hidrofobo moduan jokatzen zuen tetraetilen glikol geruza batek osatzen zuen. Honen muturrean, dimetilbenzilamonio taldea zegoen eta azkeneko hau, atezain moduan jokatzen zuen cucurbit uriloari (CB[7]) lotuz. Lotutako CB[7]-k, efektu esterikoaren ondorioz, babestutako substratuaren sarbidea katalizatzailearen kokalekura oztopatzen zuen. Nolanahi ere, CB[7] molekularen ostalari lehiakorra, 1-adamantilamina (ADA) gehitu zenean, babestutako substratuen aktibazioa gertatu zen (8. Irudian aurkeztu den moduan). Izan ere, **10** edo **20** katalizatzaileak barnean zituzten nanobotek, HeLa zelulen barnean alloc-babestutako rodamina 110 kromoforoa aktibatu zuten. Are gehiago, **20** katalizatzaileak, propargilo taldearekin babestutako 5FU profarmakoa aktibatu zuen (8. Irudia). Honen ondorioz, zelula bideragarritasun murrizketa bortitza neurtu zen.[54]

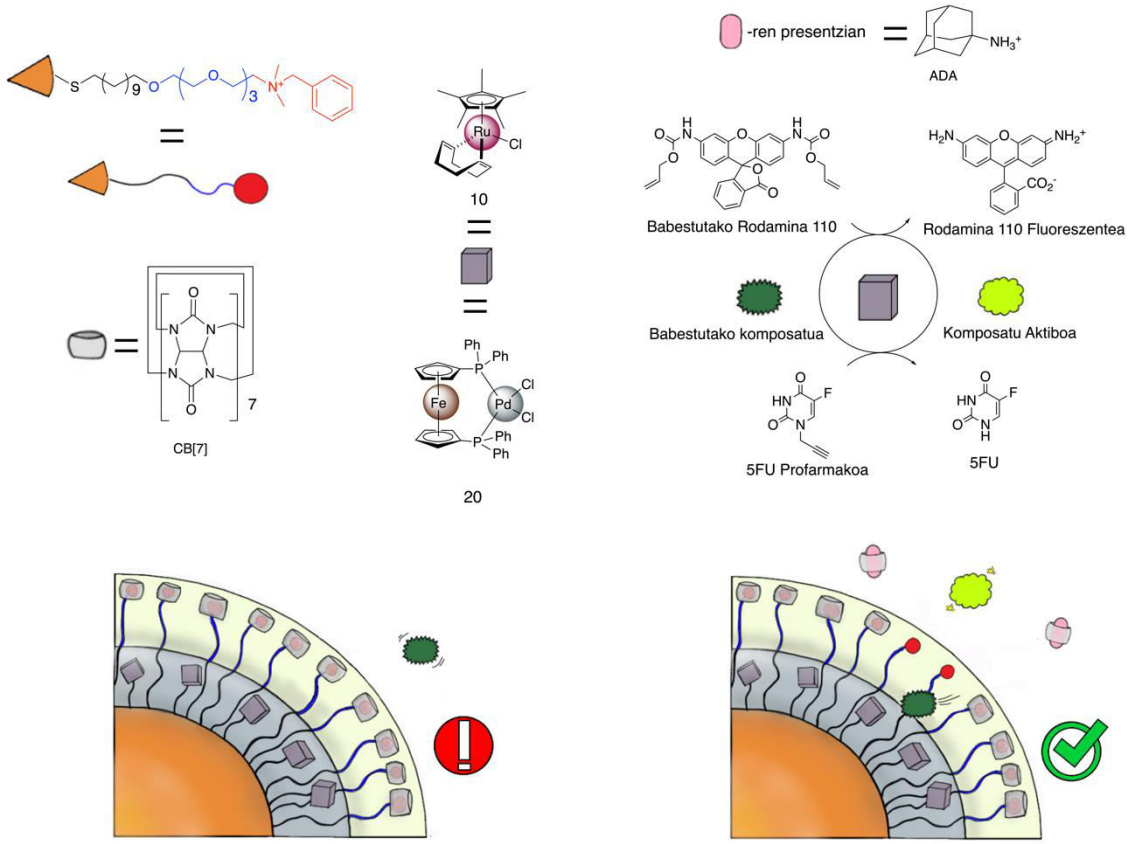

8. Irudia. Rotelloren taldeak diseinatutako Au nanobotaren irudikapen eskematikoa. Disoluzioan ADA-rik ez zegoenean, babestutako substratuek ez zuten inolako eraldaketarik jasan (ezkerrra). ADA disoluzioan zegoenean berriz, CB[7] askatu eta substratuaren eraldaketa gertatzen zen.[54]

Talde honek hiru urte beranduago, Au NP-en estalduraren muturreko taldea aldatzeak NP-en lokalizazioa modulatu dezakela frogatu zuen. Hortaz, nanoboten aktibitate katalitikoa ere erregulatu daiteke. Ru katalizatzailea **10**, Au nano egituraren estalduran barneratu zen alloc babestutako **21** doxorubicina profarmakoa aktibatzeko. NP-en estalduran erabilitako mutur taldearen arabera, aktibazioa zelulen barnealdean edo kanpoaldean gertatzen zen. Ikertzaileek bi estaldu ezberdin zituzten Au NP sintetizatu zituzten. Alde batetik, estekatzaile kationikoarekin apaindutako NP (Pos 9. Irudian), zeluletan barneratu ziren eta ondorioz **21** profarmakoaren aktibazioa zelulen barnean gertatu zen. Bestalde, zwitterioi estekatzaileekin apaindutako NP (ZW 9. Irudian), zeluletan gutxiago barneratu ziren eta ondorioz, aktibazioa zelula kanpoko ingurumenean gauzatu zen.[55] Rotellok eta lankideek nanoboten mekanismoari buruzko ikerketa sakona egin zuten arren, berraldatze zenbakia eta frekuentzia bezalako katalizatzaileen ezaugarri katalitikoei buruzko informazio falta somatzen da.

2017an, Weisslederren taldeak bigarren motako nanobota deskribatu zuen.[56] Babestutako substratua eta katalizatzailea banaka kapsulatu zituzten, poli(azido laktiko-co-glikolikoa)-b-polietilenglikolez (PLGA-PEG) osatutako NP polimeriko biobateragarrietan. PLGA-PEG NP, **21** profarmakoa eta **22** Pd katalizatzailea ingurune zelularrean zehar aldi berean garraiatzeko erabili ziren. NP-ek zama askatu ondoren, **22** katalizatzailea **21** profarmakoa aktibatzeko gai zen; honen efektu toxikoa piztuz. Frogatutako Pd katalizatzaileen artean, **22**-ak erakutsi

zuen eraginkortasun handiena babestutako susbtratuen aktibazioa gauzatzeko, baldintza fisiologikoetan eta HT1080 fibrosarkoma minbizi zelula lerroa. Gainera, **21**-ren aktibazioa saguetan frogatu zen bi tumore eredu ezberdinetan (ES2 obulutegi minbizian eta H1080 epitelio minbizian). Tratamendu honen bidez, minbizi hazkundearen inhibizioa lortu zen.[56]

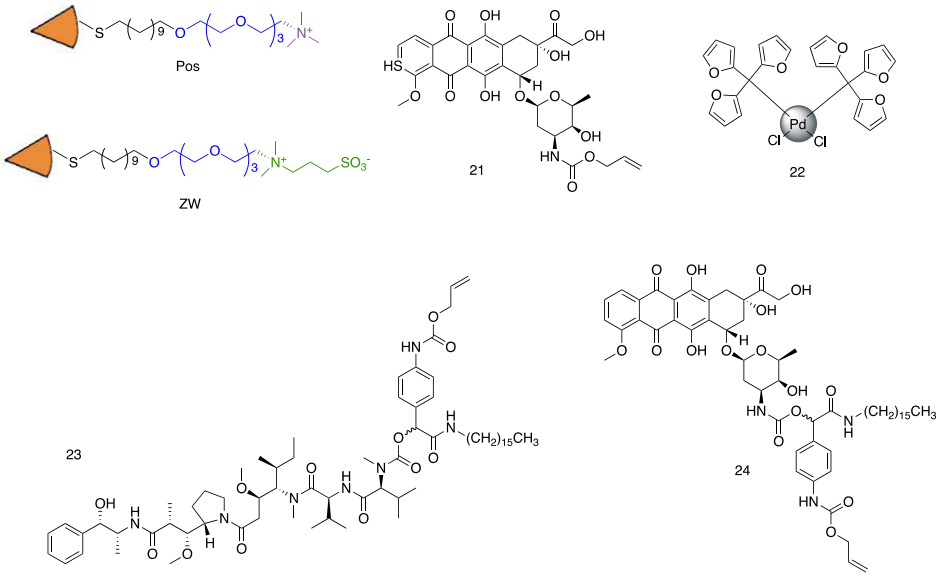

9.Irudia. Rotellok bere diseinuan erabilitako estaldura muturreko taldeak eta alloc-babestutako doxorubicina profarmakoa (**21**)[55] eta Weissleiderrek erabilitako Pd prekatalizatzailea (**22**), MMAE (**23**) eta doxorubicina profarmakoak (**21** eta **24**).[56,57]

Urte bete beranduago talde berdinak, **22** katalizatzailea, zehazki diseinatutako bi profarmakoekin kapsulatu zen, hauen aktibazioa ingurune biologikoan gauzatuz. Aingura alifatiko batekin apaindutako alilo babestutako estekatzaile auto immolatiboa, monometil auristatina E-ra (MMAE) (**23**) edo doxorubicinara (**24**) konjokatu zen profarmako berriak sortzeko. MMAE, zelulak banatzen ari direnean tubulinaren polimerizazioa inhibitzen duen agente antimitotiko indartsua da.[58] Aktibazio estrategia hau, ES2 (obulutegi), 4T1 (bular), MC38 (kolon) eta HT1080 (epitelio) zelula lerroetan frogatu zen *in vitro*. Esperimentu hauetan, profarmakoek, farmako aitzindariek baino toxikotasun txikiagoa erakutsi zuten. Hala ere, profarmakoak **22**-rekin inkubatu zirenean, farmakoak erakutsitako toxikotasunarekin alderagarriak ziren toxikotasun balioak lortu ziren. Kapsulatutako MMAE profarmakoa, Pd katalizatzailearekin batera *in vivo* esperimentuetan MC38 eta HT1080 minbizi ereduetan erabili zenean, tumorearen hazkuntza gelditzen zela erakutsi zuten emaitzek. Edozein modutan ere, tratamendua sendagarria ez zela esan beharra dago.[57] Ikerketa hauek, ez zuten inongo ezaugarri katalitikorik azaldu eta gehienbat efektu terapeutikoan fokuratu ziren. Dena den, ikertzaileen emaitzetan oinarrituz, katalizatzaileak, substratuaren kantitate estekiometrikoa eralda zitzakeen.

Hirugarren nanobot mota, Bradleyek eta Unciti-Brocetak deskribatu zuten.[59] Ikertzaileek NP metalikoz betetako egitura polimeriko heterogenoak erabili zituzten erreakzio organometaliko bioortogonal (BOOM) bezela izendatu zutena ikertzeko. Lehengo lanean, poliestirenoz egindako erretxina mikrometrikoetan barneratutako Pd NP (5 nm inguru),

alilokarbamatoaren apurketa katalizatu zuten HeLa zelulen barnean. Pd NPekin kargatutako erretxinek, alloc-babestutako rodamina 110 kromoforoa eta minbiziaren kontrako alloc-babestutako amsacrina profarmakoa *in vitro* aktibatu zituzten.[59] Erretxinak mM-eko glutationa kontzentrazioarekin inkubatu zirenean 30-eko berraldatze zenbakia lortu zen babestutako kromoforoaren aktibaziorako.

Erretxina hauek, propargilo taldearekin babestutako 5FU profarmakoa (10. Irudia) eraginkortasun handiarekin aktibatu zuten HCT116 eta BxPC-3 minibizi zelula lerroetan. Horren ondorioz, zelula bideragarritasuna, farmako aitzindariarekin konparagarriak diren balioetara gutxitu zen. Ikertzaileek gainera, erretxinek zebra arrainen zaku bitelinoan inongo kalterik sortu gabe, babestutako kromoforo (10. Irudia) baten fluoreszentzia piztu zezaketela frogatu zuten.[60] Geroago, zenbait lanetan erretxinen itzulkortasuna frogatu zen. Lan horietan, gemcitabina,[61] floxuridina,[62] vorinostatoa,[63] doxorubicina[64] eta irinotecan[65] profarmakoen aktibazioa (10. Irudia) hainbat minbizi zelula lerroetan frogatu zen.

Bradleyren taldeak, Pd NP barnean zituzten erretxinak minizi zeluletara gidatzeko, RGD peptido zikliko atalarekin (gehiegi adiezten den $\alpha_v\beta_3$ errezeptorearen antagonista) apaindu zituzten.[66,67] RGD-z apaindutako Pd erretxina fluoreszenteak, Suzuki-Miyaura elkargurutzamendu erreakzioaren bidez, toxikoak ez diren erreaktibo aitzindarietatik (10. Irudia) PP-121 konposatua sortu zuten (fosfatidilinositol-3-OH kinasa inhibitzailea). Ikerketa horretan, propargilo babaestutako 5FU profarmakoaren aktibazioa gertatzen zen aldi berean. Absortzio zelularre emaitzen arabera, $\alpha_v\beta_3$ errezeptoreak gehiegi adierazten zituzten U87-MG zelulek era selektiboan barneratu zituzten erretxinak. Errezeptore hori gehiegi adieazten ez zuten MCF-7 zeluletan ordea, ia ez zen erretxinarik aurkitu.[68]

Pd NP-en bidez gauzatutako profarmako aktibazioaren adibide berrienetakoa, Unciti-Brocetak eta lankideek, 2019an argitaratu zuten.[69] Minbizi exosoma eratorrietan, Pd xaflak barneratu zituzten exosomen minbizi zelula lerroetara zuzentzeko. Exosomak, zelulen arteko komunikazioa modulatzen duten zelula kanpoko besikulak dira. Minbizi zeluletatik askatutako exosomak minbizi garapenarekin lotuta daudela frogatuta dago.[70] Egitura bioartifizial horiek A549 zelula lerrora zuzentzeko garraio bezala erabili zitezkeela frogatu zuten ikertzaileek, panobinostato profarmakoaren aktibazio era selektiboan gauzatuz (10. Irudia).[69]

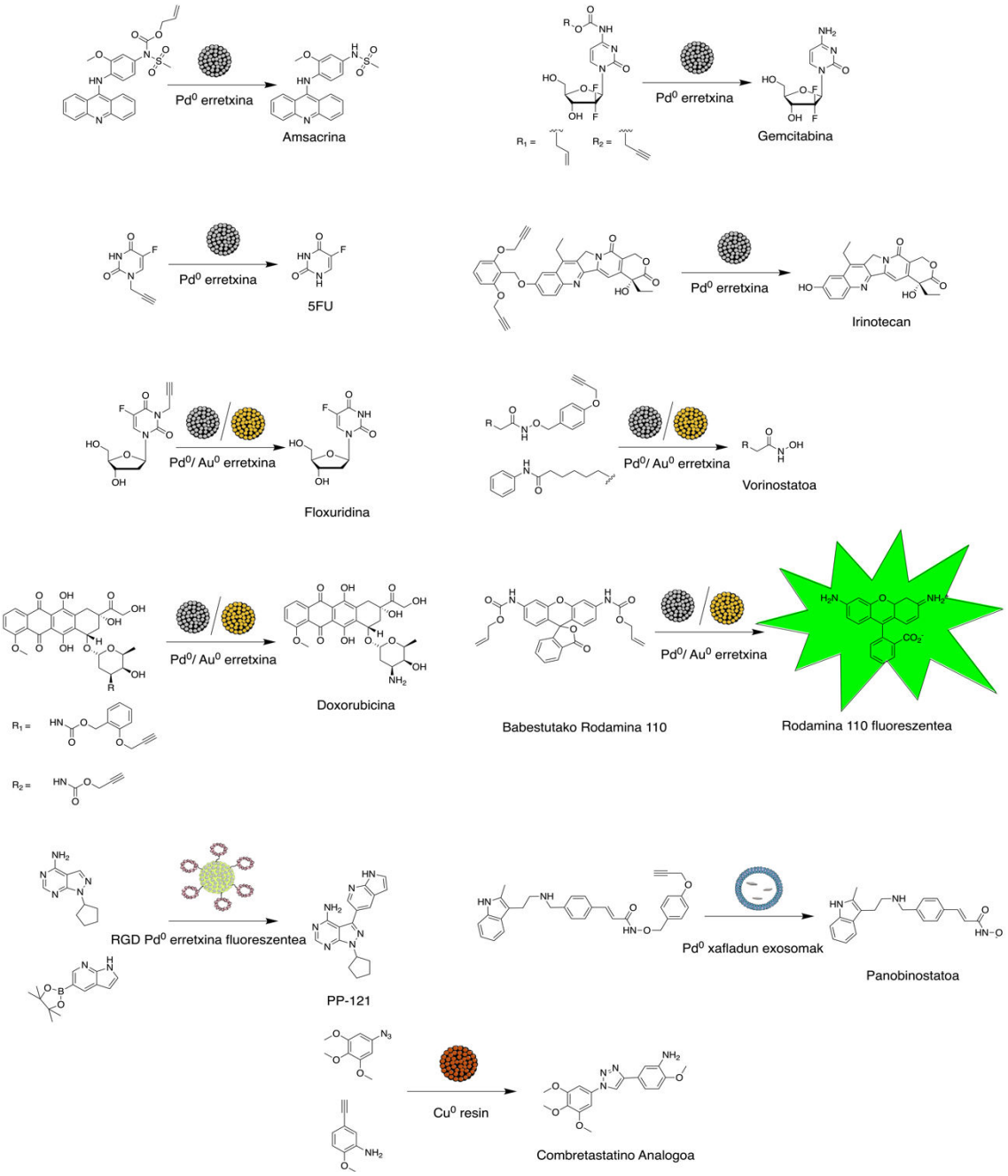

10. Irudia. NP metalikoen bidez gauzatutako Amsacrina,[59] 5FU,[60], Gemcitabina,[61] Floxuridina,[62,71] Vorinostato,[63,71] doxorbicina,[64,71] Irinotecan[65] eta Panobinostato[69] profarmakoen aktibazioa, babestutako Rodamina 110 zundaren fluoreszentzia piztea eta minbiziaren kontrako PP-121[68] eta Combrestatino[72] farmakoen sorrera.

2017an, talde berdinak, Au NP-ak (30 nm inguru) erretxina polimerikoen barnean txertatu zituzten. Katalizatzaile heterogeneo hauen bidez A549 birika minbizi zeluletan minbiziaren kontrako floxuridina, vorinostatoa eta doxorubicina (10. Irudia) profarmakoen aktibazioa gauzatu zen. Au erretxina biobateragarriek, zebra arrainen garunean rodamina zundaren fluoreszentzia pizteko ahalmena erakutsi zuten, ostalariari inongo kalterik sortu gabe.[71]

Nanobot mota honen azken adibide gisa, Bradleyren taldeak aurkeztutako amino apaindutako erretxina polimerikoentan kargatutako Cu NP deskribatu dira. Katalizatzaileek

gauzatutako azida-alkino zikloadizio erreakzioaren bidez, bi komposatu ez toxikoetatik, konposatu toxikoa sortu zen (10. Irudia). Erreakzio honen bidez, minbiziaren kontrako combrestatino analogoaren sorrera lortu zen HeLa eta SKOV-3 zelula lerroetan.[72] Combrestatinoak tubulina polimerizazioa inhibitzen du.[73] Nahiz eta, analogo honek efektu toxiko nabaria erakutsi (IC_{50} 1.3µM) ez zuen antitubulina efektu handirik azaldu K562 leuzemia zelula lerroan.[72,74]

Hiru nanobot mota hauek, zelula ingurunean, profarmako ezberdinen aktibazio bioortogonala lortzeko arrakasta handiarekin erabili dira. Ikerketa hauek estrategia honen potentziala erakusten dute. Hala ere, kasu hauetako askotan, xehetasun mekanistikoen falta larria somatzen da. Esperimentu askotan, katalizatzailearen kontzentrazioa substratuarena baino handiagoa da. Gertaera honek, profarmakoen aktibaziorako berraldatze zenbaki eta berraldatze frekuentzia txikiak lortu zirela adierazten du. Azken finean, nanobotak, katalitikoak baino gehiago estekiometrikoak ziren. Horregatik, nanobot bioortogonalen potentziala erabii ahal izateko, azpi mekanismoa deskribatzen duten oinarrizko ikerketak behar dira benetan eraginkorrak diren sistema katalizatzaileak diseinatu eta sortu ahal izateko.

2.4 Fotokatalisi bioortogonala metal konplexuak susbtratu moduan erabiliz

Aurreko kapituluan azaldu zen moduan, Pt^{IV} profarmakoen fotoaktibazio ikerketa arloa sakonki ikertu da. Azkeneko hiru urteetan, bitaminak eta proteinak bezalako zenbait biomolekulek minbiziaren kontrako Pt konposatuen fotoaktibazioa gauzatu dezaketela deskribatu da.[75–78] Hurbilketa berri honek, Pt-an oinarritutako farmakoen efektu terapeutikoa modulatzeko tresna berriak ekar ditzake.

2017an, Salassaren taldeak arlo honetan egin zuen lehengo lanean, ingurune biologikoan, *cis,cis,trans*-[$Pt(NH_3)_2(Cl)_2(O_2CCH_2CH_2CO_2H)_2$] (**25**) profarmakoa fotokatalitikoki cisplatinoan eraldatu zen riboflabinaren (Rf) bidez 460 n-ko argi irradiazioaren menpe (11. Irudia a).[75] Rf-ren fotoerredox ezaugarri bereizgarriei esker,[79] argi urdin dosi baxuen menpe (0.75 J cm^{-2}) Rf-ren kontzentrazio subestekiometrikoak **25** konplexuaren erredukzioa fotokatalizatzeko gai ziren. Horretarako, azido 2-morfolinoetanosulfonikoa (MES), elektroi iturri moduan erabili zen. Forgatutako baldintza esperimentalen menpe, Rf-k 0.22 s^{-1}-ko TOF balioa eta 38-ko TON balioa azaldu zuen.

Rf edo B2 bitamina, janari askotan aurki daitekeen antiooxidatzaile naturala da eta Flabina Adenina Dinukleotidoaren (FAD) eta Flabina Mononukleotidoaren (FMN) aitzindaria da (11. Irudia b). Naturan, flabina kofaktore hauek proteinei eta entzimei lotuta daude. Hauek, animali eta landare bizidunen barnean gertatzen diren bi elektroi transferentzia erreakzio askotan parte hartzen dute.[80–82] Honek, FMN eta FAD barnean zuten proteinak Pt^{IV}

profarmakoen eraldaketa egiteko fotokatalizatzaile bioortogonal moduan ikertzera bultzatu zuen taldea. FAD, FMN eta mini singlet oxygen generator proteina (miniSOG), NADH oxidasa (NOX) (11.Irudia b), Glucose Oxidasa (GOX) eta Glutationa Reductasa (GR) minbiziaren kontrako Pt^{IV} (**25**, **26** eta **27**) eta Ru^{II} (**28** eta **29**) profarmakoen aktibazioa gauzatzeko fotokatalizatzaile gisa aztertu ziren mM-eko MES edo NADH kontzentrazioaren presentzian.

mM-eko NADH kontzentrazioaren presentzian, FAD askeak, **25**, **27** eta **28** konplexuen eraldaketa fotokatalitiko eraginkorra eragin zuen. TOF balio altuenak 5–9 min^{-1} artean lortu ziren, 20-eko TTN balioarekin; susbstratutaren eraldaketa totala dierazi zuena. Flaboproteinekin gauzatutako ikerketa fotokatalitikoa, **25** eta **27** konplexuekin egin zen. Azken hauek, minbiziaren kontra onartutako Pt farmakoen eratorriak izateagatik aukeratu ziren. Bestalde, flaboproteina bakoitzean, flabina kofaktorea inguratzen duen ingurune kimikoa ezberdina da. NOX eta GR flaboproteinen kasuan, poltsiko aktiboaren inguruko gainazal elektrostatikoa neutrala da. MiniSOG eta GOX flaboproteinen kasuan aldiz, gainazal elektrostatikoa positiboa eta negatiboa da hurrenez hurren. Gainera, NOX, GOX eta GR flaboproteinek FAD flabina kofaktorea duten bitartean, miniSOG flavoproteinak, FMN du.

MiniSOG eta NOX flavoproteinak, FAD askea bezain eraginkorrak ziren erreakzio fotokatalitikoa gauzatzeko. GR eta GOX flaboproteinek berriz, eraginkortasun baxuagoa erakutsi zuten. Azpimarratu beharra dago, ilunpetan eta NADH-ren presentzian, NOX flaboproteinak, **25** eta **27** konplexuak 4.3 eta 8.3 TOF balioekin eraldatzeko gai zela hurrenez hurren. MiniSOG flaboproteinak ordea, argiarekiko menpekotasun handia erakutsi zuen eta iluntasunean profarmakoak egonkorrak ziren. Proteina egituren konplexutasuna eta flabina kofaktoreen inguru kimiko ezberdinek, prozesu katalitiko osoaren ulermena zailtzen dute.[77] Hala ere, lan honek, flabina askeen eta flaboproteinen bitartez Ru^{II} eta Pt^{IV} substratuen eraldaketa lor ziteekelaren lehen froga esperimentalak azaldu zituen. Ikerketa honek, argiarekin kontrolatu daitezkeen entzimen bidez minbiziaren kontra onartutako agenteen profarmako aktibazioa diseinatzeko aukerak, ikaragarri zabaldu zituen.

Estrategia honen erabilgarritasuna minbiziaren tratamendurako egiaztatzeko, lehenik eta behin, **25** konplexuaren aktibazio katalitikoa Rf-ren bitartez, PC-3 maskuri minbizi zelula lerroan frogatu zen. Zelula bideragarritasun emaitzek, ilunpetan Rf/**25** katalizatzaile-substratu bikotea toxikoa ez zela erakutsi zuten. Argi urdinarekin irradiatzerakoan ordea, cisplatinoarekin alderagarria zen efektu antiproferatiboa azaldu zuten. Rf/**25** eta argia elkartzearen ondorioz sortutako efektu toxikoa, gehienbat Pt^{II} espezieen eraginez sortu zen. Hala ere, O_2-ren presentzian, irradiatutako flabinek, kaltegarriak diren ROS-en sorrera eragiten dutela deskribatuta dago.[81,83] Hurbilketa honek, aldi bereko bi mekanismoen bidez sor dezake kalte zelularra: O_2 dagoen ehunetan, ROS sorrerak egindako estres oxidatiboaren bitartez eta Pt^{II} espezieen sorrerak eragindako DNA kaltearen bidez. Errreakzio katalitikoan O_2-ren efektua aztertu zenean, O_2-ren gabeziak Pt profarmakoen eraldaketa katalitikoa hobetu zuela aurkitu zen.[77] Aurkikuntza honek, Rf-ren bidez gauzatutako Pt^{IV} konplexuen

aktibazio fotokatalitikoa, ehun hipoxikoetan eraginkortasun altuagoarekin burutzeko balio dezakeela iradokitzen du.

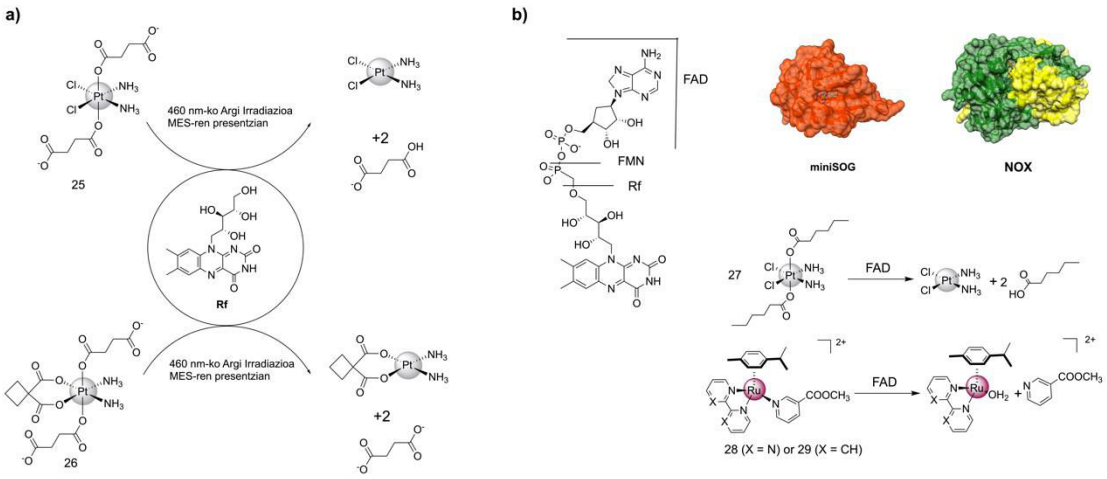

11. Irudia. a) Cisplatino (**25**) eta Carboplatino (**26**) profarmakoen aktibazio fotokatalitikoa; eta b) FAD, FMN, RF; mini Singlet Oxygen Generator, miniSOG; NADH Oxidasa, NOX katalizatzaileen eta Pt^{IV} (**27**) eta Ru^{II} (**28** eta **29**) substratuen egiturak

Hurrengo lan batean, **25** eta **26** (11. Irudia a) substratuen aktibazio fotokatalitikoa Rf-ren bitartez, Capan-1 pankreako minbizi zelula lerroan frogatu zen. Zelula lerro honek, ROS-ek eragindako kalte zelularraren aurrean tolerantzia handia erakusten duelako aukeratu zen.[84–86] Xurgapen esperimentuen arabera, Pt^{IV} profarmakoen aktibazioa zelulen barnean gertatu zen neurri batean. Rf, **25** edo **26** substratuekin irradiatzerakoan, cisplatino eta carboplatino farmakoek eragindako toxikotasun maila eragin zuten. *Cis*-Pt^{II} farmakoak, DNA-ra lotzerakoan, DNA egituran aldaketak eragiten ditu, azkenik heriotza zelularra sortuz.[87] Rf/**25** bikotea argiztatzerakoan, DNA ereduan (ODN ds26) interhari gurutzamenduak eragiten zituzten Pt espezieak sortzen zirela erakutsi zuen dikroismo zirkularrak. Zenbait minbizi zelula lerroek, Pt farmkoen kontrako erresistentzia garatu dezakete, farmakoaren efektu kimioterapeutikoa eragotziz. MVP-ren (*Major Vault Protein*) gehiegizko adierazpena, cisplatinoaren aurkako erresistentziarekin lotura duela deskribatuta dago.[88] **25** substratuaren aktibazio katalitikoa, MVP-ren adierazpena gutxitu zuen. Estrategia honek, MVP erresistentzia gainditzeko ekintza mekanismo bat zuela iradoki zuen gertakizun honek.[76]

Gure taldeak minbiziaren kontrako Pt konplexuen aktibazio fotokatalitikoa deskribatu eta urte gutxi batzuk beranduago, Bradleyek eta lankideek, rutenio fotosensitizatzaile baten bitartez gauzatutako oxaliplatino Pt^{IV} profarmakoaren aktibazioa deskribatu zuten. Mitokondriora zuzentzen zen rutenio polipiridilo potosensitizatzailea (12. Irudia, **31**) argi urdinarekin irradiatzerakoan (58 mW cm^{-2}), **30** konplexua aktibatu zuen. Argi irradiazioaren menpe, **31** konplexuak 45-eko TON balioa erakutsi zuen ur disoluzioetan. Dena den, **31** konplexuak, ordu bete behar izan zuen 45 µM substratu eraldatzeko; TOF balio baxuetan bihurtzen zena. SKOV-3 obulutegi minbizi zeluletan neurtutako toxikotasuna, oxaliplatinoaren eta **31** konplexuak sortutako ROS-en ondorio zela adierazi zuten

ikertzaileek.[78] Ikertzaileek ez zuten aztertu O_2-ren gabeziak eta ondorioz ROS-en absentziak, zer nolako eragina zuen emaitza biologikoetan.

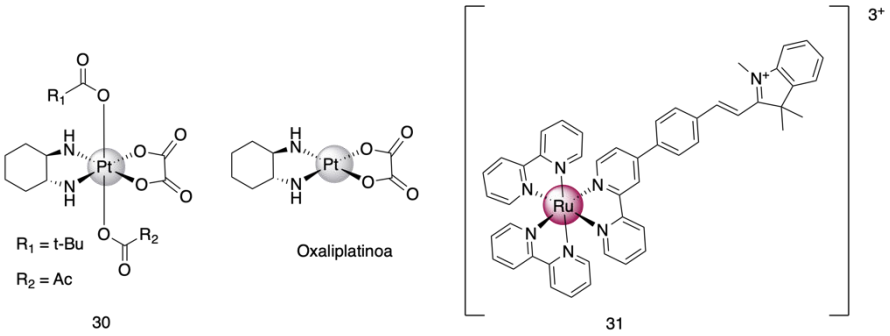

12. Irudia. Bradleyek sintetizatutako rutenio katalizatzailearen eta oxaliplatino farmakoaren eta profarmakoaren egitura kimikoak.[78]

2.5 Laburpena eta etorkizuneko ikuspegiak

Profarmakoen aktibazio bioortogonala, minbiziaren kontrako sendagaien efektua kontrolatzeko tresna interesgarri moduan sortu da. Kapitulu honetan erakutsi den moduan, hainbat estrategia garatzen eta aztertzen ari dira profarmakoen aktibitatea zelulen barnean kontrolatzeko. Hauetako askok in vitro eraginkortasun handia erakutsi arren, muga nagusia oraindik ere, bizidun konplexuetan ehun normal eta berezien artean bereiztea da. Edonola ere, erreakzio bioortogonal hauen espektroa zabaltzeko eta xehetasunak mekanistikoak ulertzeko beharra dago, gaixotasun zehatzetan, estrategien diseinu eta ebaluazio egokia egiteko. Estrategia hauek, minbizi gaixotasunaren tratamendurako diseinatu ziren, baina honek ez du esan nahi beste gaixotasun batzuen botiken askapen edo tratamendua hobtzeko aplikagarriak ez direnik. Beraz, komunitate zientifikoak, kimika medizinalaren alor jaio berri honetan ahaleginak egiten jarraitu behar du.

2.6 Erreferentziak

(1) Cancer Research UK. Causes of cancer and reducing your risk. https://www.cancerresearchuk.org/about-cancer/causes-of-cancer.

(2) National Cancer Institute. What is Cancer? https://www.cancer.gov/about-cancer/understanding/what-is-cancer.

(3) Faguet, G. B. A Brief History of Cancer: Age-Old Milestones Underlying Our Current Knowledge Database. *Int. J. Cancer* **2015**, *136*, 2022–2036.

(4) The American Cancer Society. Early History of Cancer. https://www.cancer.org/cancer/cancer-basics/history-of-cancer/what-is-cancer.

(5) National Cancer Institute. Types of Cancer Treatment https://www.cancer.gov/about-cancer/treatment/types.

(6) Freres, P.; Jerusalem, G.; Moonen, M. Categories of Anticancer Treatments. In *Anti-Cancer Treatments and Cardiotoxicity*; Elsevier, **2017**, pp 7–11.

(7) Cancer Research UK. Side effects of cancer drugs https://www.cancerresearchuk.org/about-cancer/cancer-in-general/treatment/cancer-drugs/side-effects.

(8) Zawilska, J. B.; Wojcieszak, J.; Olejniczak, A. B. Prodrugs: A Challenge for the Drug Development. *Pharmacol. Rep.* **2013**, *65*, 1–14.

(9) Huttunen, K. M.; Raunio, H.; Rautio, J. Prodrugs-from Serendipity to Rational Design. *Pharmacol. Rev.* **2011**, *63*, 750–771.

(10) Hang, H. C.; Yu, C.; Kato, D. L.; Bertozzi, C. R. A Metabolic Labeling Approach toward Proteomic Analysis of Mucin-Type O-Linked Glycosylation. *Proc. Natl. Acad. Sci.* **2003**, *100*, 14846–14851.

(11) Sletten, E. M.; Bertozzi, C. R. Bioorthogonal Chemistry: Fishing for Selectivity in a Sea of Functionality. *Angew. Chem., Int. Ed.* **2009**, *48*, 6974–6998.

(12) Punekar, N. S. *ENZYMES: Catalysis, Kinetics and Mechanisms*; Springer Singapore, **2018**, pp 33–34.

(13) Alonso-de Castro, S.; Terenzi, A.; Gurruchaga-Pereda, J.; Salassa, L. Catalysis Concepts in Medicinal Inorganic Chemistry. *Chem. Eur. J.* **2019**, *25*, 6651–6660.

(14) Thiel, Z.; Nguyen, J.; Rivera-Fuentes, P. Genetically Encoded Activators of Small Molecules for Imaging and Drug Delivery. *Angew. Chem., Int. Ed.* **2020**, *59*, 7669–7677.

(15) Muller, P. Glossary of Terms Used in Physical Organic Chemistry. *Pure & Appl. Chem.* **1994**, *66*, 1077–1184.

(16) Gurruchaga-Pereda, J.; Martínez-Martínez, V.; Rezabal, E.; Lopez, X.; Garino, C.; Mancin, F.; Cortajarena, A. L.; Salassa, L. Flavin Bioorthogonal Photocatalysis Toward

Platinum Substrates. *ACS Catal.* **2020**, *10*, 187–196.

(17) Martínez-Calvo, M.; Mascareñas, J. L. Organometallic Catalysis in Biological Media and Living Settings. *Coord. Chem. Rev.* **2018**, *359*, 57–79.

(18) Trachootham, D.; Lu, W.; Ogasawara, M. A.; Valle, N. R. Del; Huang, P. Redox Regulation of Cell Survival. *Antioxid. Redox Signal.* **2008**, *10*, 1343–1374.

(19) McFarland, S. A.; Mandel, A.; Dumoulin-White, R.; Gasser, G. Metal-Based Photosensitizers for Photodynamic Therapy: The Future of Multimodal Oncology? *Curr. Opin. Chem. Biol.* **2020**, *56*, 23–27.

(20) Monro, S.; Colón, K. L.; Yin, H.; Roque, J.; Konda, P.; Gujar, S.; Thummel, R. P.; Lilge, L.; Cameron, C. G.; McFarland, S. A. Transition Metal Complexes and Photodynamic Therapy from a Tumor-Centered Approach: Challenges, Opportunities, and Highlights from the Development of TLD1433. *Chem. Rev.* **2019**, *119*, 797–828.

(21) Forman, H. J.; Zhang, H.; Rinna, A. Glutathione: Overview of Its Protective Roles, Measurement, and Biosynthesis. *Mol. Aspects Med.* **2009**, *30*, 1–12.

(22) Dougan, S. J.; Habtemariam, A.; McHale, S. E.; Parsons, S.; Sadler, P. J. Catalytic Organometallic Anticancer Complexes. *Proc. Natl. Acad. Sci.* **2008**, *105*, 11628–11633.

(23) Sorci, L.; Kurnasov, O.; Rodionov, D. A.; Osterman, A. L. Genomics and Enzymology of NAD Biosynthesis. *Comprehensive Natural Products II*; Elsevier, **2010**, pp 213–257.

(24) Soldevila-Barreda, J. J.; Romero-Canelón, I.; Habtemariam, A.; Sadler, P. J. Transfer Hydrogenation Catalysis in Cells as a New Approach to Anticancer Drug Design. *Nat. Commun.* **2015**, *6*, 6582.

(25) Liu, Z.; Romero-Canelón, I.; Qamar, B.; Hearn, J. M.; Habtemariam, A.; Barry, N. P. E. E.; Pizarro, A. M.; Clarkson, G. J.; Sadler, P. J. The Potent Oxidant Anticancer Activity of Organoiridium Catalysts. *Angew. Chem., Int. Ed.* **2014**, *53*, 3941–3946.

(26) Ngo, A. H.; Ibañez, M.; Do, L. H. Catalytic Hydrogenation of Cytotoxic Aldehydes Using Nicotinamide Adenine Dinucleotide (NADH) in Cell Growth Media. *ACS Catal.* **2016**, *6*, 2637–2641.

(27) Bose, S.; Ngo, A. H.; Do, L. H. Intracellular Transfer Hydrogenation Mediated by Unprotected Organoiridium Catalysts. *J. Am. Chem. Soc.* **2017**, *139*, 8792–8795.

(28) Sigman, D. S.; Mazumder, A.; Perrin, D. M. Chemical Nucleases. *Chem. Rev.* **1993**, *93*, 2295–2316.

(29) Stadtman, E. R. Metal Ion-Catalyzed Oxidation of Proteins: Biochemical Mechanism and Biological Consequences. *Free Radical Biol. Med.* **1990**, *9*, 315–325.

(30) Gallagher, J.; Zelenko, O.; Walts, A. D.; Sigman, D. S. Protease Activity of 1,10-Phenanthroline-Copper(I). Targeted Scission of the Catalytic Site of Carbonic Anhydrase. *Biochemistry.* **1998**, *37*, 2096–2104.

(31) Cuenoud, B.; Tarasow, T. M.; Schepartz, A. A New Strategy for Directed Protein Cleavage. *Tetrahedron Lett.* **1992**, *33*, 895–898.

(32) Lee, T. Y.; Suh, J. Target-Selective Peptide-Cleaving Catalysts as a New Paradigm in Drug Design. *Chem. Soc. Rev.* **2009**, *38*, 1949–1957.

(33) Joyner, J. C.; Hocharoen, L.; Cowan, J. A. Targeted Catalytic Inactivation of Angiotensin Converting Enzyme by Lisinopril-Coupled Transition-Metal Chelates. *J. Am. Chem. Soc.* **2012**, *134*, 3396–3410.

(34) Bradford, S. S.; Ross, M. J.; Fidai, I.; Cowan, J. A. Insight into the Recognition, Binding, and Reactivity of Catalytic Metallodrugs Targeting Stem Loop IIb of Hepatitis C IRES RNA. *ChemMedChem.* **2014**, *9*, 1275–1285.

(35) Bradford, S.; Cowan, J. A. Catalytic Metallodrugs Targeting HVC IRES RNA. *Chem. Commun.* **2012**, *48*, 3118–3120.

(36) Jin, Y.; Cowan, J. A. Cellular Activity of Rev Response Element RNA Targeting Metallopeptides. *J. Biol. Inorg. Chem.* **2007**, *12*, 637–644.

(37) Joyner, J. C.; Keuper, K. D.; Cowan, J. A. Kinetics and Mechanisms of Oxidative Cleavage of HIV RRE RNA by Rev-Coupled Transition Metal–Chelates. *Chem. Sci.* **2013**, *4*, 1707–1718.

(38) Yu, Z.; Cowan, J. A. Design of Artificial Glycosidases: Metallopeptides That Remove H Antigen from Human Erythrocytes. *Angew. Chem., Int. Ed.* **2017**, *56*, 2763–2766.

(39) Streu, C.; Meggers, E. Ruthenium-Induced Allylcarbamate Cleavage in Living Cells. *Angew. Chem., Int. Ed.* **2006**, *45*, 5645–5648.

(40) Völker, T.; Meggers, E. Chemical Activation in Blood Serum and Human Cell Culture: Improved Ruthenium Complex for Catalytic Uncaging of Alloc-Protected Amines. *ChemBioChem.* **2017**, *18*, 1083–1086.

(41) Völker, T.; Dempwolff, F.; Graumann, P. L.; Meggers, E. Progress towards Bioorthogonal Catalysis with Organometallic Compounds. *Angew. Chem., Int. Ed.* **2014**, *53*, 10536–10540.

(42) Thorn, C. F.; Oshiro, C.; Marsh, S.; Hernandez-Boussard, T.; McLeod, H.; Klein, T. E.; Altman, R. B. Doxorubicin Pathways: Pharmacodynamics and Adverse Effects. *Pharmacogenet. Genomics.* **2011**, *21*, 440–446.

(43) Sánchez, M. I.; Penas, C.; Vázquez, M. E.; Mascareñas, J. L. Metal-Catalyzed Uncaging of DNA-Binding Agents in Living Cells. *Chem. Sci.* **2014**, *5*, 1901–1907.

(44) Tomás-Gamasa, M. M.; Martínez-Calvo, M.; Couceiro, J. R.; Mascarenãs, J. L.; Mascareñas, J. L. Transition Metal Catalysis in the Mitochondria of Living Cells. *Nat. Commun.* **2016**, *7*, 12538.

(45) Okamoto, Y.; Kojima, R.; Schwizer, F.; Bartolami, E.; Heinisch, T.; Matile, S.; Fussenegger, M.; Ward, T. R. A Cell-Penetrating Artificial Metalloenzyme Regulates a Gene Switch in a Designer Mammalian Cell. *Nat. Commun.* **2018**, *9*, 1943.

(46) Ogura, A.; Urano, S.; Tahara, T.; Nozaki, S.; Sibgatullina, R.; Vong, K.; Suzuki, T.; Dohmae, N.; Kurbangalieva, A.; Watanabe, Y.; et al. A Viable Strategy for Screening the Effects of Glycan Heterogeneity on Target Organ Adhesion and Biodistribution in Live Mice. *Chem. Commun.* **2018**, *54*, 8693–8696.

(47) Eda, S.; Nasibullin, I.; Vong, K.; Kudo, N.; Yoshida, M.; Kurbangalieva, A.; Tanaka, K. Biocompatibility and Therapeutic Potential of Glycosylated Albumin Artificial Metalloenzymes. *Nat. Catal.* **2019**, *2*, 780–792.

(48) Li, H.; Xu, H.; Zhou, Y.; Zhang, J.; Long, C.; Li, S.; Chen, S.; Zhou, J.-M.; Shao, F. The Phosphothreonine Lyase Activity of a Bacterial Type III Effector Family. *Science.* **2007**, *315*, 1000–1003.

(49) Arbibe, L.; Kim, D. W.; Batsche, E.; Pedron, T.; Mateescu, B.; Muchardt, C.; Parsot, C.; Sansonetti, P. J. An Injected Bacterial Effector Targets Chromatin Access for Transcription Factor NF-KB to Alter Transcription of Host Genes Involved in Immune Responses. *Nat. Immunol.* **2007**, *8*, 47–56.

(50) Li, J.; Yu, J.; Zhao, J.; Wang, J.; Zheng, S.; Lin, S.; Chen, L.; Yang, M.; Jia, S.; Zhang, X.; et al. Palladium-Triggered Deprotection Chemistry for Protein Activation in Living Cells. *Nat. Chem.* **2014**, *6*, 352–361.

(51) Wang, J.; Zheng, S.; Liu, Y.; Zhang, Z.; Lin, Z.; Li, J.; Zhang, G.; Wang, X.; Li, J.; Chen, P. R. Palladium-Triggered Chemical Rescue of Intracellular Proteins via Genetically Encoded Allene-Caged Tyrosine. *J. Am. Chem. Soc.* **2016**, *138*, 15118–15121.

(52) Cherukaraveedu, D.; Cowling, P. T.; Birch, G. P.; Bradley, M.; Lilienkampf, A. Solid-Phase Synthesis of Biocompatible N-Heterocyclic Carbene-Pd Catalysts Using a Sub-Monomer Approach. *Org. Biomol. Chem.* **2019**, *17*, 5533–5537.

(53) Zhang, X.; Huang, R.; Gopalakrishnan, S.; Cao-Milán, R.; Rotello, V. M. Bioorthogonal Nanozymes: Progress towards Therapeutic Applications. *Trends Chem.* **2019**, *1*, 90–98.

(54) Tonga, G. Y.; Jeong, Y.; Duncan, B.; Mizuhara, T.; Mout, R.; Das, R.; Kim, S. T.; Yeh, Y. C.; Yan, B.; Hou, S.; et al. Supramolecular Regulation of Bioorthogonal Catalysis in Cells Using Nanoparticle-Embedded Transition Metal Catalysts. *Nat. Chem.* **2015**, *7*, 597–603.

(55) Das, R.; Landis, R. F.; Tonga, G. Y.; Cao-Milán, R.; Luther, D. C.; Rotello, V. M. Control of Intra- versus Extracellular Bioorthogonal Catalysis Using Surface-Engineered Nanozymes. *ACS Nano.* **2019**, *13*, 229–235.

(56) Miller, M. A.; Askevold, B.; Mikula, H.; Kohler, R. H.; Pirovich, D.; Weissleder, R. Nano-Palladium Is a Cellular Catalyst for in Vivo Chemistry. *Nat. Commun.* **2017**, *8*, 15906.

(57) Miller, M. A.; Mikula, H.; Luthria, G.; Li, R.; Kronister, S.; Prytyskach, M.; Kohler, R. H.; Mitchison, T.; Weissleder, R. Modular Nanoparticulate Prodrug Design Enables Efficient Treatment of Solid Tumors Using Bioorthogonal Activation. *ACS Nano.* **2018**, *12*, 12814–12826.

(58) Francisco, J. A.; Cerveny, C. G.; Meyer, D. L.; Mixan, B. J.; Klussman, K.; Chace, D. F.; Rejniak, S. X.; Gordon, K. A.; DeBlanc, R.; Toki, B. E.; et al. CAC10-VcMMAE, an Anti-CD30-Monomethyl Auristatin E Conjugate with Potent and Selective Antitumor Activity. *Blood.* **2003**, *102*, 1458–1465.

(59) Yusop, R. M.; Unciti-Broceta, A.; Johansson, E. M. V.; Sánchez-Martín, R. M.; Bradley, M. Palladium-Mediated Intracellular Chemistry. *Nat. Chem.* **2011**, *3*, 239–243.

(60) Weiss, J. T.; Dawson, J. C.; Macleod, K. G.; Rybski, W.; Fraser, C.; Torres-Sánchez, C.; Patton, E. E.; Bradley, M.; Carragher, N. O.; Unciti-Broceta, A. Extracellular Palladium-Catalysed Dealkylation of 5-Fluoro-1-Propargyl-Uracil as a Bioorthogonally Activated Prodrug Approach. *Nat. Commun.* **2014**, *5*, 3277.

(61) Weiss, J. T.; Dawson, J. C.; Fraser, C.; Rybski, W.; Torres-Sánchez, C.; Bradley, M.; Patton, E. E.; Carragher, N. O.; Unciti-Broceta, A. Development and Bioorthogonal Activation of Palladium-Labile Prodrugs of Gemcitabine. *J. Med. Chem.* **2014**, *57*, 5395–5404.

(62) Weiss, J. T.; Carragher, N. O.; Unciti-Broceta, A. Palladium-Mediated Dealkylation of N-Propargyl-Floxuridine as a Bioorthogonal Oxygen-Independent Prodrug Strategy. *Sci. Rep.* **2015**, *5*, 9329.

(63) Rubio-Ruiz, B.; Weiss, J. T.; Unciti-Broceta, A. Efficient Palladium-Triggered Release of Vorinostat from a Bioorthogonal Precursor. *J. Med. Chem.* **2016**, *59*, 9974–9980.

(64) Bray, T. L.; Salji, M.; Brombin, A.; Pérez-López, A. M.; Rubio-Ruiz, B.; Galbraith, L. C. A.; Patton, E. E.; Leung, H. Y.; Unciti-Broceta, A. Bright Insights into Palladium-Triggered Local Chemotherapy. *Chem. Sci.* **2018**, *9*, 7354–7361.

(65) Adam, C.; Pérez-López, A. M.; Hamilton, L.; Rubio-Ruiz, B.; Bray, T. L.; Sieger, D.; Brennan, P. M.; Unciti-Broceta, A. Bioorthogonal Uncaging of the Active Metabolite of Irinotecan by Palladium-Functionalized Microdevices. *Chem. Eur. J.* **2018**, *24*, 16783–16790.

(66) Zitzmann, S.; Ehemann, V.; Schwab, M. Arginine-Glycine-Aspartic Acid (RGD)-Peptide Binds to Both Tumor and Tumor-Endothelial Cells in Vivo. *Cancer Res.* **2002**, *62*, 5139–5143.

(67) Danhier, F.; Breton, A. Le; Préat, V. RGD-Based Strategies to Target Alpha(v) Beta(3) Integrin in Cancer Therapy and Diagnosis. *Mol. Pharm.* **2012**, *9*, 2961–2973.

(68) Clavadetscher, J.; Indrigo, E.; Chankeshwara, S. V.; Lilienkampf, A.; Bradley, M. In-Cell Dual Drug Synthesis by Cancer-Targeting Palladium Catalysts. *Angew. Chem., Int. Ed.* **2017**, *56*, 6864–6868.

(69) Sancho-Albero, M.; Rubio-Ruiz, B.; Pérez-López, A. M.; Sebastián, V.; Martín-Duque, P.; Arruebo, M.; Santamaría, J.; Unciti-Broceta, A. Cancer-Derived Exosomes Loaded with Ultrathin Palladium Nanosheets for Targeted Bioorthogonal Catalysis. *Nat. Catal.* **2019**, *2*, 864–872.

(70) Osaki, M.; Okada, F. Exosomes and Their Role in Cancer Progression. *Yonago Acta*

Med. **2019**, *62*, 182–190.

(71) Pérez-López, A. M.; Rubio-Ruiz, B.; Sebastián, V.; Hamilton, L.; Adam, C.; Bray, T. L.; Irusta, S.; Brennan, P. M.; Lloyd-Jones, G. C.; Sieger, D.; et al. Gold-Triggered Uncaging Chemistry in Living Systems. *Angew. Chem., Int. Ed.* **2017**, *56*, 12548–12552.

(72) Clavadetscher, J.; Hoffmann, S.; Lilienkampf, A.; Mackay, L.; Yusop, R. M.; Rider, S. A.; Mullins, J. J.; Bradley, M. Copper Catalysis in Living Systems and In Situ Drug Synthesis. *Angew. Chem., Int. Ed.* **2016**, *55*, 15662–15666.

(73) Tron, G. C.; Pirali, T.; Sorba, G.; Pagliai, F.; Busacca, S.; Genazzani, A. A. Medicinal Chemistry of Combretastatin A4: Present and Future Directions. *J. Med. Chem.* **2006**, *49*, 3033–3044.

(74) Odlo, K.; Fournier-Dit-Chabert, J.; Ducki, S.; Gani, O. A. B. S. M.; Sylte, I.; Hansen, T. V. 1,2,3-Triazole Analogs of Combretastatin A-4 as Potential Microtubule-Binding Agents. *Bioorg. Med. Chem.* **2010**, *18*, 6874–6885.

(75) Alonso-de Castro, S.; Ruggiero, E.; Ruiz-de-Angulo, A.; Rezabal, E.; Mareque-Rivas, J. C.; Lopez, X.; López-Gallego, F.; Salassa, L. Riboflavin as a Bioorthogonal Photocatalyst for the Activation of a Pt(IV) Prodrug. *Chem. Sci.* **2017**, *8*, 4619–4625.

(76) Alonso-de Castro, S.; Terenzi, A.; Hager, S.; Englinger, B.; Faraone, A.; Martínez, J. C.; Galanski, M.; Keppler, B. K.; Berger, W.; Salassa, L. Biological Activity of Pt(IV) Prodrugs Triggered by Riboflavin-Mediated Bioorthogonal Photocatalysis. *Sci. Rep.* **2018**, *8*, 17198.

(77) Alonso-de Castro, S.; Cortajarena, A. L.; López-Gallego, F.; Salassa, L.; Lopez-Gallego, F.; Salassa, L.; López-Gallego, F.; Salassa, L. Bioorthogonal Catalytic Activation of Platinum and Ruthenium Anticancer Complexes by FAD and Flavoproteins. *Angew. Chem., Int. Ed.* **2018**, *57*, 3143–3147.

(78) Norman, D. J.; Gambardella, A.; Mount, A. R.; Murray, A. F.; Bradley, M. A Dual Killing Strategy: Photocatalytic Generation of Singlet Oxygen with Concomitant Pt(IV) Prodrug Activation. *Angew. Chem., Int. Ed.* **2019**, *58*, 14189–14192.

(79) Brondani, P. B.; Fraaije, M. W.; de Gonzalo, G. Recent Developments in Flavin-Based Catalysis. In *Green Biocatalysis*; John Wiley & Sons, **2016**, pp 149–164.

(80) Saedisomeolia, A.; Ashoori, M. *Riboflavin in Human Health: A Review of Current Evidences*; Elsevier, **2018**, pp 57–81.

(81) Heelis, P. F. The Photophysical and Photochemical Properties of Flavins (Isoalloxazines). *Chem. Soc. Rev.* **1982**, *11*, 15–39.

(82) Bates, C. J. Riboflavin. In *Encyclopedia of Human Nutrition*; Elsevier, **2013**, pp 158–165.

(83) Oster, G.; Bellin, J. S.; Holmström, B. Photochemistry of Riboflavin. *Experientia,* **1962**, *18*, 249–253.

(84) Bown, S. G. Photodynamic Therapy for Cancer of the Pancreas. *Acta Endoscopica,* **2003**, *33*, 531–538.

(85) Celli, J. P.; Solban, N.; Liang, A.; Pereira, S. P.; Hasan, T. Verteporfin-Based Photodynamic Therapy Overcomes Gemcitabine Insensitivity in a Panel of Pancreatic Cancer Cell Lines. *Lasers Surg. Med.* **2011**, *43*, 565–574.

(86) Ouyang, G.; Liu, Z.; Huang, S.; Li, Q.; Xiong, L.; Miao, X.; Wen, Y. Gemcitabine plus Cisplatin versus Gemcitabine Alone in the Treatment of Pancreatic Cancer: A Meta-Analysis. *World J. Surg. Oncol.* **2016**, *14*, 59.

(87) Dasari, S.; Bernard Tchounwou, P. Cisplatin in Cancer Therapy: Molecular Mechanisms of Action. *Eur. J. Pharmacol.* **2014**, *740*, 364–378.

(88) Steiner, E.; Holzmann, K.; Elbling, L.; Micksche, M.; Berger, W. Cellular Functions of Vaults and Their Involvement in Multidrug Resistance. *Curr. Drug Targets.* **2006**, *7*, 923–934.

3

Flabinen Fotokatalisi Bioortogonala Platino Substratuentzako

Kapitulu honetan deskribatutako lana *ACS Catal.* 2020, 10, 187-196 (egileak: Gurruchaga-Pereda, J.; Martínez-Martínez, V.; Rezabal, E.; Lopez, X.; Garino, C.; Mancin, F.; Cortajarena, A. L.; Salassa, L.). aldizkarian argitaratu zen.

3.1 Sarrera

Katalisiaren arloan ohikoa da koordinazio eta konplexu organometalikoak katalizatzaile gisa erabiltzea, substratu organikoak balio handiagoko produktuetan bihurtuz zinetikoki azkarragoa den prozesu baten bitartez. Duela gutxi, paradigma horri buelta eman genion, metaletan oinarrituriko minbiziaren aurkako profarmakoen aktibazioa, hurbilketa berrien bidez lortzeko (1. Irudia).[1–4] Argi irradiaziopean, flabinek (FL), katalizatzaile moduan jardun dezaketela eta trantsizio metal substratuak, biologikoki aktibo diren homologoetan eralda ditzaketela frogatu genuen. Ingurumen biologikoetan agente elektroi-emaileak eskuragarri daudenean, flabina kofaktoreek eta zenbait flaboproteinek, Pt^{IV} aitzindariak cisplatino eta carboplatino sendagaietan fotoeraldatzeko gaitasuna erakutsi dute, Pt^{II} katioiean oinarrituriko printzipio aktibo hauen *in vitro* ekintza antiproliferatiboa sustatuz. Ez ohikoa den ikuspegi honek, sendagaien garapenean eskuragarri dauden erreakzio katalitiko bioortogonalen substratu sorta eta aldakortasuna zabaldu du.[1,5,6] Gainera, azken hamarkadetan, bai kimioterapian bai eta bakterien aurka erabilitako agente biologiko ez-organikoen erabilera berriak sortzeko ahalmena du pentsamolde honek. Bioortogonal hitzak, biologikoki konplexua den ingurune batean, flabina katalizatzaileek substratuen eraldatze anitz burutzeko gaitasuna, hala nola Pt^{IV}-Pt^{II} eraldaketa selektibitate handiz burutzeko ahalamena adierazten du.

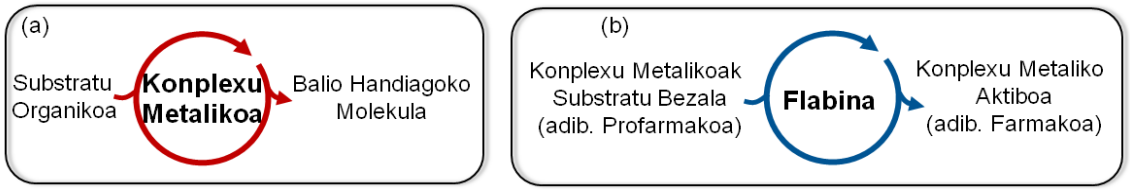

1.Irudia (a) Metaletan oinarrituriko katalisia eta (b) substratu metalikoen katalisia

Dakigula, konplexu metalikoak substratu moduan erabiltzen dituzten erreakzio katalitikoen adibide bakarrak flabinen kontestuan erabilita, Meggers-en $[Ru(bpy)_3]^{2+}$ sintesi enantioselektiboa organokatalisi bidez[7] eta, orain dela gutxi, Leonorik[8] deskribatutako Ru^{II} eta Rh^{III} konplexu oktaedrikoen aminazio aromatikoa dira. Lurralde ezezagun honek, aukera interesagarriak eskaini ditzake kimika organiko sintetikoa zabaltzeko eta koordinazio eta konplexu organometalikoen katalisian oinarrituriko aplikazio berriak susta ditzake.

Ikuspegi horri begira, ikerketa honen helburua, flabinen bidez Pt^{IV} konplexuen aktibazio fotokatalitikoaren xehetasun mekanistikoen ulermena hornituz, substratu metalikoak erabiltzen dituen prozesu katalitikoen mugak zabaltzea da. Lan honetan, mekanismo katalitiko honen xehetasun berriak eta flabinen eta Pt^{IV} konplexuen zenbait eraldaketa estrukturalek, erreakzioaren azken produktuetan zer nolako eragina duten ikertu eta laburbildu ditugu.

Gainera, lan honek, trantsizio metal eta flabinen arteko erredox kimikaren oinarrizko informazioa azaltzen du. Esate baterako, flaboentzima erreduktasa merkurikoak, zenbait organismoen Hg erresistentziaren erregulazioan parte hartzen du, toxikotasun altuko Hg^{II} espezieak, arrisku txikiagoko Hg^{0} espezieetan eraldatuz.[9] Hortaz, eskuidatzi honetan deskribatutako aurkikuntzek, zelulen homeostasi metalikoan eta biokimikan eragina izan dezakete.

3.2 Emaitzak eta eztabaida

3.2.1 Azterketa katalitikoak

Minbiziaren kontra erabiltzen diren konplexu metalikoen erredukzioa burutzen duten katalizatzaile eta subtratu sorta ikertzeko, bost flabina eta lau Pt^{IV} profarmako erabili genituen (2. Irudia). Ribitilo albo-katearen eragina substratu metalikoen eraldaketa katalitikoan aztertzeko, riboflabina (**Rf**), flabina mononukleotidoa (**FMN**), 2',3',4',5'-tetraazetilriboflabina (**TARF**) eta lumiflabina (**Lf**) aukeratu genituen. IO 1. Irudian eta aurreko ikerketetan[10] azaldu zen moduan, flabina eratorrien fotoegonkortasuna, egitura osoaren zati edo atal honen menpekoa da (**TARF** ~ **Lf** > **Rf** ~ **FMN**). Horretaz gain, **MiniSOG** (mini Singlet Oxygen Generator)[11] flaboproteina katalizatzaile gisa aukeratu genuen kromoforoaren inguruan aminoazido agitura batek katalisian duen eragina aztertzeko. **MiniSOG**, **FMN** kromoforoa barnean duen proteina fluoreszente txikia da. Proteina hau, CLEM (correlative light and electron microscopy) etiketa[11] moduan garatu zen eta fotosentsibilizazio agente bezala[12,13] terapia fotodinamikoan (PDT) erabiltzeko,[14,15] ikertu da.

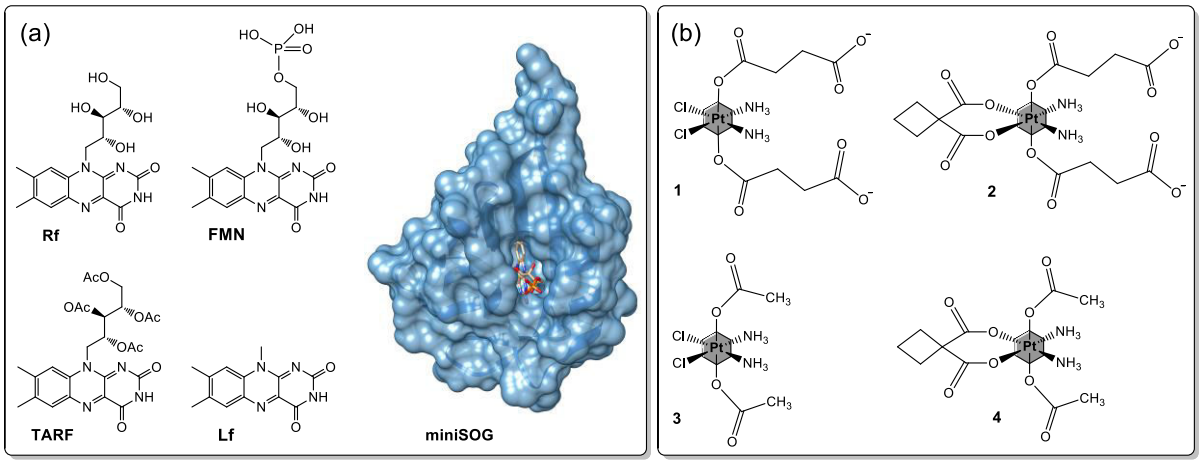

2. Irudia. Lan honetan erabilitako (a) katalizatzaileen eta (b) Pt^{IV} substratuen egiturak. Katalizatzaileak: riboflabina (**Rf**), Flabina mononukleotidoa (**FMN**), 2',3',4',5'-tetraacetilriboflabina (**TARF**), lumiflabina (**Lf**), mini Singlet Oxygen Generator (**miniSOG**). Substratuak: *cis,cis,trans*-$[Pt(NH_3)_2(Cl_2)(O_2CCH_2CH_2CO_2)_2]^{2-}$ (**1**), *cis,cis,trans*-$[Pt(NH_3)_2(O_4C_6H_6)(O_2CCH_2CH_2CO_2)_2]^{2-}$ (**2**), *cis,cis,trans*-$[Pt(NH_3)_2(Cl_2)(O_2CCH_3)_2]$ (**3**), *cis,cis,trans*-$[Pt(NH_3)_2(O_4C_6H_6)(O_2CCH_3)_2]$ (**4**).

3. Kapitulua

Cis,cis,trans-$[Pt(NH_3)_2(Cl_2)(O_2CCH_2CH_2CO_2)_2]^{2-}$ (**1**), *cis,cis,trans*-$[Pt(NH_3)_2(O_4C_6H_6)(O_2CCH_2CH_2CO_2)_2]^{2-}$ (**2**), *cis,cis,trans*-$[Pt(NH_3)_2(Cl_2)(O_2CCH_3)_2]$ (**3**), *cis,cis,trans*-$[Pt(NH_3)_2(O_4C_6H_6)(O_2CCH_3)_2]$ (**4**) Pt^{IV} substratu moduan aukeratu genituen, egitura aldetik antzekoak direlako eta katalisi prozesuan eragina izan dezaketen zenbait ezaugarri dituztelako. Estekatzaile ekuatorialen (kloruroa *versus* ziklobutano dikarboxilatoa) eta axialen (sukzinato *versus* azetato) ezberdintasunek katalisian eragina izan lezaketela aurre ikusi genuen. Horretaz gain, konplexu hauek, izugarrizko garrantzia dute kimika ez-organikoan oinarrituriko medikuntza arloan, cisplatino (**1** eta **3**) edo carboplatino (**2** eta **4**) sendagaien profarmakoak direlako.[16,17] Cisplatino eta carboplatino konplexu metalikoak mundu mailan minbiziaren aurka onartutako sendagaiak dira.

Bestela adierazi ezean, fotokatalisi esperimentu guztiak, fosfato disoluzioan (PB, 18 mM pH 7) egin ziren, 25 µM katalizatzaile (%5 karga), 500 µM substratu (**1**–**4**) eta 1 mM NADH (nikotinamida adenina dinucleotido erreduzitua) elektroi emaile gisa erabiliz. NADH kofaktoreak, flaboproteinek burututako erredox erreakzio biokimiko ugaritan parte hartzen du. [18] Hori dela eta, NADH elektroi emaile moduan aukeratu zen. Hala ere, askorbatoa eta glutationa (GSH) elektroi emaile biologikoak ordezko elektroi iturri gisa frogatu genituen. Askorbatoa eraginkorra zen erreakzio hauek burutzen, baina glutationa berriz ez (IO 2. eta IO 3. Irudiak). Laginak, 460 nm-ko LED argi iturri batekin (6 $mW \cdot cm^{-2}$) irradiatu ziren O_2-ren presentzian. Erreakzioaren jarraipena ^1H NMR bidez egin zen, seinale esanguratsuen agerpena eta desagerpena behatuz. Seinale esanguratsu edo diagnostikorako erabilitako gailur hauek, sukzinato edo azetato estekatzaile koordinatu edo askeei zegokie. Estekatzaile hauen askatzeak, bilogikoki aktibo diren Pt^{II} espezieen sorrerarekin bat dator.[2]

Lehenik, **1**–**4** (500 µM) konplexuen ilunpeko egonokortasuna frogatu zen 48 orduz, PB (18 mM) dizoluzioan eta NADH (1 mM) kofaktorearen presentzian. Flabinarik gabe, ez zen Pt^{IV} substratuen deskonposiziorik eman (IO 4. Irudia). Bestalde, flabinak (25 µM) PB disoluzioari gehitu eta 16 ordu igaro ondoren, **1**–**4** substratuen eraldaketa mantsoa eta %40-100 bitartekoa gertatu zen. **MiniSOG** flaboproteina zuten laginek aldiz, ia ez zuten aldaketarik erakutsi 48 ordu ostean (IO 5–9. Irudiak). Ilunpetan **Rf** eta **1** erabiliz burututako esperimentuek agerian utzi zuten, **Rf** (50 – 150 µM) eta NADH (2,5 eta 5 mM) kontzentrazio altuagoak erabiltzen zirenean substratuaren konbertsioa azkarragoa gertatzen zela (IO 10. Irudia).

Ilunpetan, katalizatzaileen erreaktibitateak ez zuen joera argirik jarraitu. **2** eta **4** konplexuek **FMN**, **TARF** eta **Lf** katalizatzaileen presentzian, (% 5–40) ziklobutano dikarboxilatoa (CBDA) estekatzaile askea eman zuten erreakzio produktu gisa. Horrez gain, **1**–**4** substratu metalikoen fotoegonkortasuna 1 mM NADH-ren presentizian (18 mm PB, pH 7) eta 460 nm-ko argiaren irradiaziopean frogatu zen. **1** eta **3** konplexuek, % 20 inguruko eraldaketa jasan zuten 3 ordu ostean. Carboplatino eratorriek aldiz, ez zuten erreaktibotasunik aurkeztu argi irradiazioaren eraginez (IO 11. Irudia). Era berean, **1**–**4**, **Rf** (kopuru katalitikoetan) eta elektroi emailerik gabeko laginek, ez zuten substratuaren eraldaketa esanguratsurik

aurkeztu baldintza horietan. Katalisia gerta dadin, elektroi emaile baten beharra berretsi zuten esperimentu hauek (IO 12. Irudia).

1. Taulak eta 3. Irudiak, goian deskribatutako baldintzetan, flabina katalizatzaile eta substratu metaliko ezberdinek lortutako katalisi emaitzak biltzen ditu (ikusi, IO 13–17. Irudiak).

Konplexua	TOF (min^{-1})	TON	Konb. [%]
Rf			
1	17.3 ± 0.6	20	100
2	8.1 ± 0.4	20	100
3	20.3 ± 2.0	20	100
4	10.0 ± 0.3	20	100
FMN			
1	19.3 ± 1.7	20	100
2	13.4 ± 0.9	17.9 ± 0.2	89.9 ± 0.9
3	23.2 ± 1.7	20	100
4	15.5 ± 1.4	20	100
TARF			
1	24.1 ± 5.1	20	100
2	13.7 ± 0.2	18.5 ± 0.2	92.4 ± 1.0
3	26.0 ± 1.1	20	100
4	22.7 ± 5.6	20	100
Lf			
1	9.2 ± 0.1	20	100
2	2.6 ± 1.6	20	100
3	13.3 ± 0.5	20	100
4	7.9 ± 1.0	20	100
miniSOG			
1	3.7 ± 0.2	20	100
2	1.3 ± 0.3	14.7 ± 0.7	73.4 ± 3.8
3	5.6 ± 0.3	18.7 ± 1 .1	93.7 ± 5.5
4	2.6 ± 0.4	17.5 ± 0.6	87.7 ± 3.1

* TOF: Berraldatze frekuentzia; ziklo kopurua denbora unitate bakoitzeko (TOFs, min^{-1}), TON: Berraldatze zenbakia, ziklo kopuru totala, eta Konb. [%]: **1**–**4** substratuen konbertsio ehunekoa amaieran.

Erreakzio fotokatalitiko guztiek, **1**–**4** substratuen eraldaketa osoa lortu zuten; minutu batzuen ondoren, eskuraturiko berraldatze zenbakia (TON, ingelesetik TurnOver Number) 20-ekoa zelarik. Salbuespen bakarrak, **2** substratua **FMN** eta **TARF** katalizatzaileentzako eta **2** eta **4** substratuak **miniSOG** katalizatzailearentzako izan ziren. Berraldatze frekuentzia balioak (TOF, ingelesetik TurnOver Frequency) 4-6 aldiz altuagoak ziren **FMN** askearentzako **miniSOG** katalizatzailearentzako baino eta **2** substratuaren kasuan 10 aldiz altuagoak. Aipagarria da, TON balio adierazgarri altuagoak lortu zirela, katalizatzaile karga jaitsi (% 0.2, 1 µM) eta irradiazio epe luzeagoak erabili zirenean. **Rf**-ren kasuan, **1** eta **3** substratuentzako

500-eko TON balioa lortu zen. **2** eta **4** substratuentzako aldiz, 423 eta 469-eko TON balioak lortu ziren hurrenez hurren, 2 orduz irradiatu ostean (IO 18. Irudia).

Orokorrean, **1** eta **3** cisplatino profarmakoak, modu eraginkorragoan eraldatu ziren bere **2** eta **4** carboplatino analogoekin alderatuta. Hori dela eta, Berraldatze frekuentzia (TOF, min^{-1}) balio altuagoak lortu ziren. Lehiaketa esperimentuen bidez, cisplatino profarmakoen lehentasuna baieztatu zen. Esperimentu hauetan, substratu bikoteak lagin berean aztertu ziren (IO 19. eta 20. Irudiak).

3 konplexuak TOF balio altuena erakutsi zuen flabina katalizatzaile guztientzako. **Lf**-ren aktibitate katalitikoak, beste flabinek baino TOF balio nabarmen baxuagoetan bihurtu ziren. Emaitza hauek, ribitilo albo-kateak prozesu katalitikoan zeregin garrantzitsua duela iradokitzen dute (*vide infra*). Gainera, **miniSOG** katalizatzaileak eraginkortasun baxuena azaldu zuen. Flaboproteinak, 1.3–5.6 min^{-1} bitarteko TOF balioak erakutsi zituen. **2** substratuaren kasuan **Lf**-k eta flaboproteinak antzeko erreaktibitatea erakutsi zuten. Bataz beste, **miniSOG** proteinaren egiturak 6.4 aldiz gutxitu zuen erreakzioaren abiadura **FMN** askearekin alderatuz. Gertakizun hau, **FMN**-ren inguruko egitura proteikoak, Pt^{IV} substratuen eta **FMN** kromoforaren arteko hurbilketa oztopatzen duelako azal daiteke.

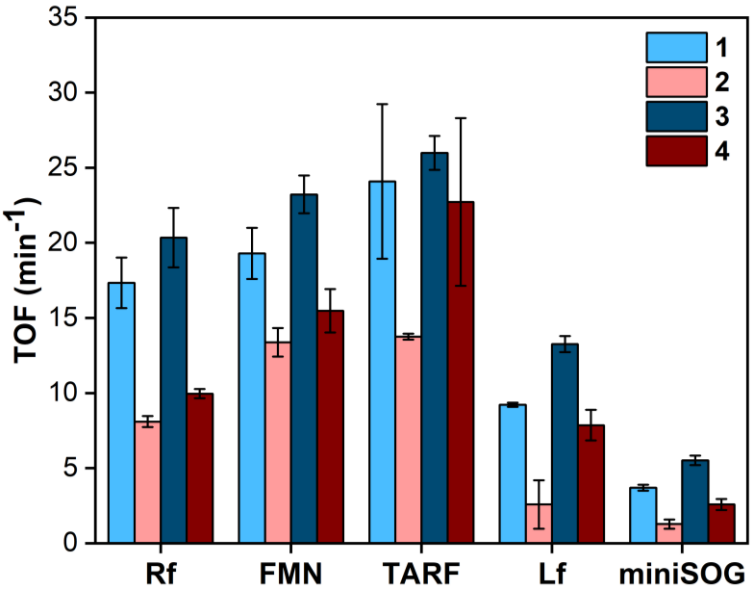

3. Irudia. Flabinek katalizatutako **1**–**4** substratuen fotoaktibaziorako berraldatze frekuentzia balioak (TOF, min^{-1}).

3.2.1 Katalisia ingurune zelularrean

substratu metalikoen eraldaketa sustatzen duten katalisiaren garapena kimika ez-organikoan oinarritzen den medikuntzaren arloan, flabinek ingurune biologikoan Pt^{IV} profarmakoak Pt^{II} espezieetan modu selektibo batean bihurtzeko duten gaitasunean oinarritzen da; bai zelulen barnean edota bestelako ingurune biologiko batean.[2,3] Horregatik, behi-suero fetala gehigarritzat zuen ingurune zelular batean, flabina

katalizatzaileek, Pt^{IV} substratuen aktibazioa nola gauzatzen zuten ikertu genuen. Horrelako inguruneek, katalisian traba eragin dezaketen produktu kimiko eta molekula biologiko ugari dituzte.

1mM NADH-ren presentzian, **1**–**4** substratuak 24 ordu ondoren egonkorrak ziren (IO 21. Irudia). **Rf**-ren adizioak (25 μM), substratuen eraldaketa motela euren erreakzio produktuetan eragin zuen, argi kitzikapen beharrik gabe. Erreakzioak motelak ziren eta % 40-eko konbertsioa neurtu zen lehenengo 8 orduetan (IO 22. Irudia). Gainontzeko flabina katalizatzaileen portaera, **1** eta **4** substratuekin ikertu zen, haien arteko egitura ezberdintasunak direla eta. Ilunpetan, **FMN**-k eta **Lf**-k, **Rf**-ren antzera jokatu zuten; 8 orduren ostean substratuen eraldaketa partziala sustatuz eta 24 orduren ostean konbertsio osoa (IO 23. eta 24. Irudiak). **TARF** katalizatzaileak aldiz, ordu baten ostean, **1** eta **4** substratuen konbertsio osoa lortu zuen ilunpetan (IO 25. Irudia). **MiniSOG** katalizatzaileak ordea, ez zuen substratuen (24 ordu) aktibazioa burutzeko gaitasuna erakutsi argirik ezean (IO 26. Irudia). Hau, abantaila moduan ikus daiteke zelulen barnean Pt^{IV} profarmakoen aktibazioak eragindako efektuak menderatzeko.

Argi irradiaziopean, flabina guztiak oso eraginkorrak izan ziren **1** eta **4** substratuak eraldatzen. Katalizatzaile guztiek Pt^{IV} profarmakoak erabat aktibatu zituzten minutu baten ostean **miniSOG**-aren kasuan izan ezik, 6-10 minuntu artean behar izan zituela (IO 27. eta 28. Irudia). Ingurune zelularrean, erreakzioren eraginkortasunaren kuantifikazioa konplexua eta zaila da, seinaleen gainjartzearen ondorioz. Hala ere, ^{1}H espektroek, erreakzio katalitikoak ingurune zelularrean disoluzio arruntetan baino azkarragoak zirela erakutsi zuten. Konposatu kimiko eta biologiko asko zituen ingurune zelular batean, katalizatzaileak desaktibatzen ez zirela eta Pt^{IV} substratuak ezagutzeko eta eraldatzeko gai zirela iradokiz. Beraz, flabinek gauzatutako Pt substratuen eraldaketa katalitikoa, selelektibitate bioortogonala erakutsi eta ingurunean egon daitezkeen elektroi emaileek katalisian lagundu dezaketela azpimarratu zuten emaitza hauek.

3.2.1 Mekanismo Katalitikoa

Flabinek, Pt^{IV} substratuak Pt^{II} sendagaietan eraldatzeko jarraitzen duten mekanismo katalitikoa azaltzea zaila da. Hori dela eta, zenbait prozesu eta fenomeno onartu behar dira. Argi irradiazioaren menpe, flabinek egoera singlete kitzikatua ($^{1}FL^{*}$) lortzen dute. Hemendik sistemen arteko gurutzamendua gertatzen da eta flabinek egoera triplete kitzikatua ($^{3}FL^{*}$) lortzen dute. $^{3}FL^{*}$ oxidatzaile indartsua da eta NADH bezalako elektroi emaileei bi elektroi kentzeko gai da. Disoluzioaren pH-aren arabera, erreakzio honek H_2FL edo HFL^{-} ematen ditu produktu gisa.[18] Flabina erreduzitu hauek, espezie aktibo katalitikoak dira eta **1**–**4** susbtratuen transformazio bioortogonala burutzen dute (1. Eskema). Argirik ez dagoenean, H_2FL/HFL^{-} espezieen sorrera eraginkortasun gutxiagoarekin gertatzen da. Izan ere, oxigenorik gabeko baldintzetan egindako esperimentuak alderatuz gero, **FMN**-k NADH motelago kontsumitzen du ilunpetan argipean baino (IO 29-31. Irudiak). Horretaz gain,

baldintza aerobikoetan oxigenoaren presentzian, flabina erreduzituak erraz oxidatzen dira, H_2O_2 sortuz.[19] Hori dela eta, argi irradiaziorik ez dagoenean, Pt^{IV} substratuen konbertsioa motelagoa da, izan ere, H_2FL/HFL^- espezieen kontzentrazioa baxuagoa da.

Hipotesi mekanistiko hau balioztatzeko, H_2FL/HFL^- espezieen errekatibitatea **1** substratuarekiko O_2-rik gabeko baldintzetan ikertu genuen. N_2-rekin purgatutako **FMN** eta **NADH** (1:1, 15 µM in PB, pH 7.4) disoluzioa, 460 nm-ko argiarekin argiztatu zen epe labur batez, **HFMN**$^-$ espezia lortuz. Espezie honen sorrera, bereizgarria den absortzio espektroa eta **FMN**-ren banden desagerpenak 400-500 nm artean (4. Irudia), baieztatu zuten. [20] Lan honetan ikertutako katalizatzaileen artean, HFL^- espeziea da ugariena, pH 7-tik gora. [18] Hala ere, pH ezberdinetan egindako esperimentuek, **FMN**, **1** eta **3** erabiliz, H_2FL eta HFL^- espezieek katalisia antzeko eraginkortasunarekin egin zezaketela frogatu zuten (IO 14. eta 32. Irudiak).

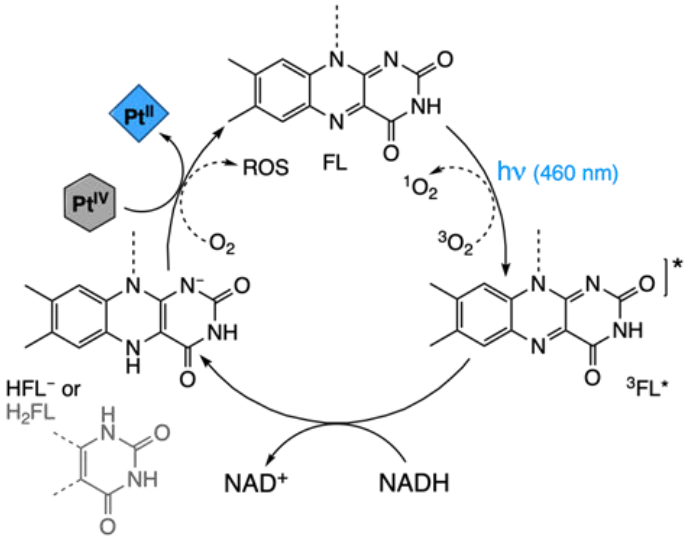

1. Eskema. Flabina katalizatzaileek gauzatutako **1**–**4** substratuen eraldaketa azaltzeko proposaturiko mekanismoa.

Hollmannek bere lanetan,[21,22] flabina katalizatzaileen argi irradiazioak nikotinamida kofaktore erreduzituen oxidazio aerobikoa bizkortu zezaketela frogatu zuen. Hortaz, NADH-ren eta argi ikuskorraren erabilera oxigenorik gabeko baldintzetan, bi aldiz erreduzituriko flabina askeak sortzeko era eraginkorra zela plazaratu zuten gure emaitzek. Onartutako beste prozedura batzuekin alderatuta,[23] hurbilketa hau onuragarria da, erreduktore indartsuen (adib. Sodio ditionitoa edo borohidruroa) kontzentrazio altuak edo fotoerredukzio erreakzio luzeen beharra oxalatoa eta argi ultramorearekin sahiesten dituelako.

Espezie katalitiko aktiboa, **HFMN**$^-$ zela frogatu genuen. Horretarako, katalizatzailearen absortzio espektroaren eboluzioa jarraitu genuen baldintza anaerobikoetan, **1** substratua gehitzen gindoazen heinean (54 µM, kontzentrazio finala). 4a Irudian erakusten den moduan, **HFMN**$^-$ berehala biroxidatu zen eta **FMN**-ren absortzio ezaugarriak berreskuratu

ziren Pt^{IV} substratua gehitu zenean. Antzeko baldintzetan (O_2-rik gabe, 3.3 mM **FMN** eta NADH, PB, pH 7.4), argi irradiazioaren menpe, **FMN**-ren ^1H erresonantziak desagertu egin ziren (4b Irudia); $\mathbf{HFMN}^-$-ren sorrerarekin bat datorrena. **1** substratua gehitu ondoren (4 mM kontzentrazio finala) seinaleak berragertu ziren. Singlete seinalea, sukzinato askeari dagokio eta honek Pt^{IV} substratuaren eraldaketa frogatzen du. Behar adina substratu gehitu ostean (4b Irudia), erreakzionatu gabeko **1** substratuaren seinale erlatiboak berrikusi daitezke. Lehenago Gschwindek eta kideek argitaratu zuten moduan,[24,25] protoi trukeen ondorioz, ur disoluzioetan ezinezkoa da flabina erreduzituen ^1H NMR seinaleak antzematea. UMore-Ikus espektroskopia bidez, emaitza baliokideak lortu ziren **TARF** eta **Lf** katalizatzaileentzako **1** subtratua gehitu zenean (IO 33. eta 34. Irudiak).

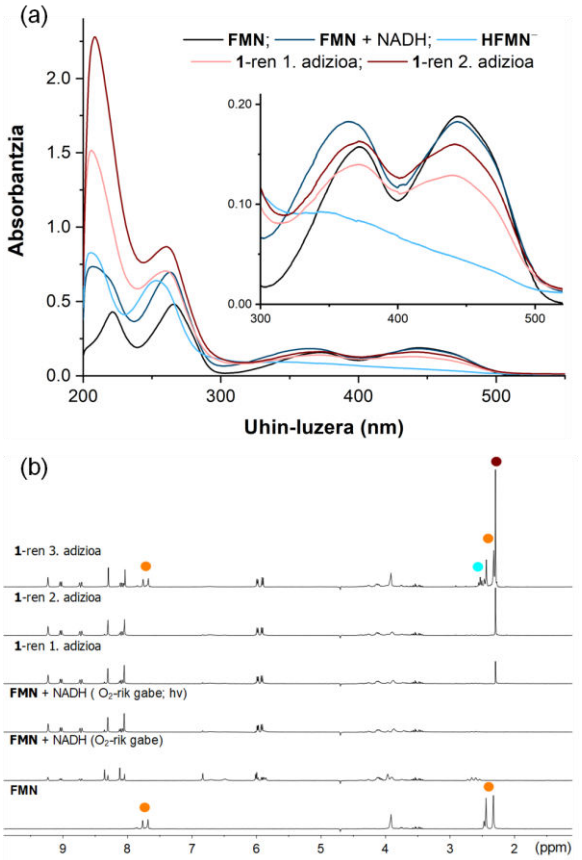

4. Irudia. $\mathbf{HFMN}^-$ espezie katalitikoaren karakterizazio eta erreaktibotasuna 1 substratuarekiko: (a) UMore-Ikus eta (b) NMR. $\mathbf{HFMN}^-$ (a: 15 µM; b: 3.3 mM) NADH-ren balikokide bat erabiliz eta 460 nm-ko argi irradiaziopean sortuta (6 $mW{\cdot}cm^{-2}$, a: 40 s; b: 360 s), oxigenorik gabe (18 mM PB, pH 7.4). **1** substratuaren kontzentrazio finalak UMore-Ikus eta NMR esperimentuetarako, 54 µM eta 4 mM izan ziren hurrenez hurren. ^1H NMR Seinaleen etiketak: ● **FMN**; ● $^-O_2CCH_2CH_2CO_2^-$ askea; ● **1** (Pt–$OCOCH_2CH_2CO_2^-$).

HFL^- espeziearen sorrera, NADH-k eragindako, $^3FL^*$ egoera kitzikatuaren iraungipen erreduktiboaren ondorioz gertatzen zela frogatu zen ebazpen tenporala duen espektroskopia optikoaren bidez. Lehenik, **FMN**-ren (λ_{kitz} = 445 nm, λ_{em} = 540 nm, IO 35. Irudia) fluoreszentzia emisioaren bizitza-denbora neurketek, egoera kitzikatu singletearen beheraldi balioa (τ_{Fluo} = 4.7 ns) NADH (1:20) edo NADH eta **1** (1:20:20) substratuaren presentzian berdin mantendu zela plazaratu zuten. Beraz, egoera kitzikatu horrek prozesu

katalitikoan parte hartzen ez zuela ondorioztatu genuen. Flash fotolisi esperimentuek frogatu zuten moduan, ^{3}**FMN*** egoera kitzikatuaren kasua, alabaina, ezberdina da (5. Irudia, IO 36. Irudia). Aurreko lanek,[26] **Rf**-ren egoera tripletearen eboluzioa iraungipen eragile ezberdinen presentzian, triplete-triplete absortzio banda karakteristikoaren beheraldia aztertuz neurtu zitekeela erakutsi zuten. Horregatik, **FMN**-ren (λ_{kitz} = 445 nm) bitarteko absortzio espektro, oxigenorik gabeko baldintzetan neurtu zen eta egoera triplete kitzikatuaren bizitza-denbora NADH-ren eta **1** substratuaren presentzian zehaztu genuen. Literaturan aurki daitekeen moduan, ^{3}**FMN***-k kontribuzio negatibo esanguratsua erakusten du 420–480 nm artean. Kontribuzio hau, $S_0 \rightarrow S_1$ trantsizioari lotutako oinarrizko egoeraren zuritzeari dagokio. 600–720 nm inguruan agertzen den banda positiboa, T_1 egoera kitzikatuaren absortzioari dagokio. Oxigenoaren presentzian ikusten den bandaren desagerpen edo suntsipenak, egoera kitzikatu tripletea berretsi zuen. **FMN** tripletearen bizitza-denbora oxigenorik gabeko disoluzioetan (τ_0^T) 14 µs-koa zen (5. Irudia), oxigenoak iraugipen eraginkorra eragiteko nahikoa. Izan ere, aireztatutako laginetan τ^T 4 µs-tara murriztu zen (IO 36. Irudia). Disoluzioan NADH soberan (1:20) zegoenean, τ_0^T 14 µs-etatik 2.3 µs-etara murriztu egiten zela ikusi genuen. Elektroi emaileek, ^{3}**FMN***-ren erredukzio iraungipena eragiten zutela baieztatuz. Bestalde, ez zen τ_0^T-ren aldaketa nabarmenik neurtu **FMN**, NADH eta **1** (1:20:20) zuten dizoluzioetan. Emaitza hauek, Pt^{IV} substratuen konbertsio prozesuan ^{3}**FMN*** egoerak parte hartzen ez duela azatzen dute. Izan ere, **HFMN**$^-$ espeziea egoera elementalean da katalizatzaile nagusia, UMore-Ikus eta NMR esperimentuekin bat datorrena (4. Irudia). Airearekin saturatutako laginetan, antzeko emaitzak lortu ziren egoera triplete kitzikatuaren bizitza-denbora neurtu zenean (IO 36. Irudia).

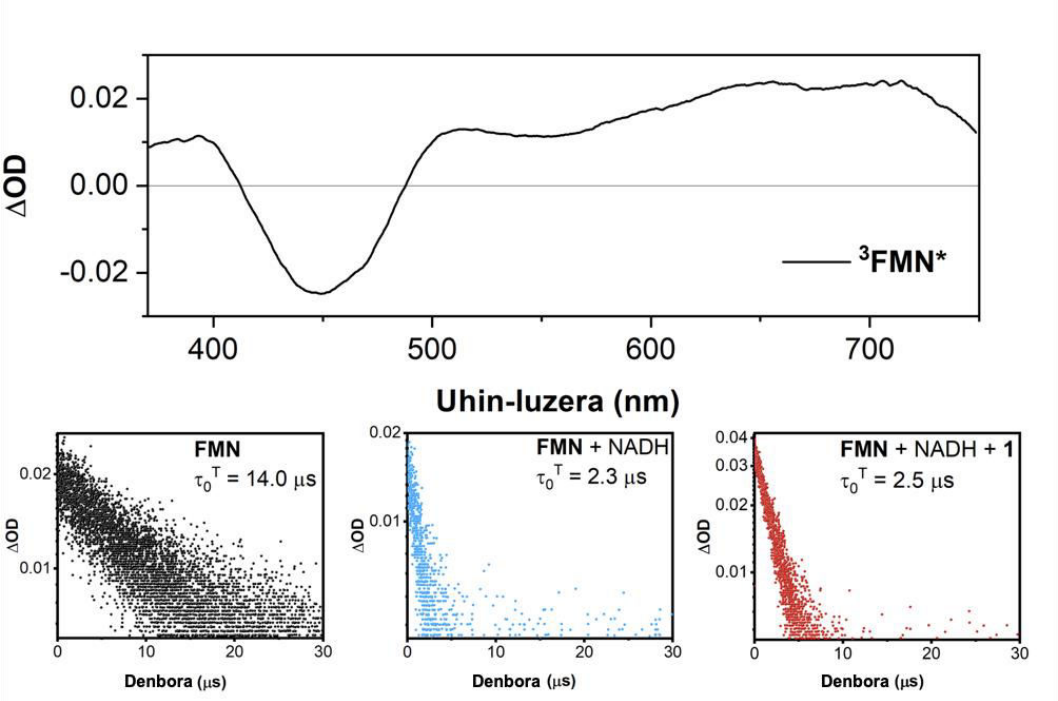

5. Irudia. FMN (20 µM), **FMN** (20 µM) + NADH (400 µM), eta **FMN** (20 µM) + NADH (400 µM) + **1** (400 µM), oxigenorik gabeko baldintzetan, ^{3}**FMN***-ren bitarteko absortzio espektroa (λ_{kitz} 445 nm) eta 700 nm-tan neurtutako triplete- triplete absortzioaren bizitza-denbora (τ_0^T).

1–**4** substratuen erredukzio potetziala flabinena baino negatiboagoa (IO 37. Irudia) dela kontuan hartuta, substratuen kanpo esferaren erredukzioa, erreakzio erlatiboki eragotzia izango litzateke. Hortaz, substratu-H_2FL/HFL^- bitartekarien formakuntzak eta estekatzaile bidezko barne esfera mekanismoak, flabina bidezko Pt^{IV} konplexuen erredukzioa susta dezakete.[27] Bitartekari hauek, **1**–**4** substratuen eraldaketa Pt^{II} baliokideetan, potentzial negatibo baxuagoetan eragin dezakete.[12] Are gehiago, katalizatzaile-substratu interakzio espezifikoek, erreakzio hauen selektibitate bioortogonala azaldu dezakete.

Dentsitate funtzionalaren teorian (DFT, *Density Functional Theory*) oinarritutako kalkuluek, egoera hori gertagarria zela azaldu zuten. Horrela, hidrogeno loturek egonkortutako Pt konplexuen estekatzaileen eta flabinen isoalloxazina eta ribitilo zatien arteko interakzioek sortutako zenbait substratu-$\mathbf{H_2Rf/HRf^-}$ bitartekarien egiturak optimizatu genituen (6. Irudia, IO 38. eta 39. Irudiak). Optimizatutako geometrietan, HOMO (betetako orbital molekular altuena) orbital molekularra, $\mathbf{H_2Rf/HRf^-}$ katalizatzailean aurkitzen da batez ere. Bestetik, LUMO (hutsik dagoen orbital molekular baxuena) eta LUMO+1, **1**–**4** substratuetan aurkitzen diren σ orbital molekular-antilotzaileak dira (IO 40–42. Irudiak). Emaitza konputazional hauek, bat datoz erredukzio eliminazio erreakzioekin. Optimizatutako estruktura guztiek, Pt-estekatzaileen eta ribitilo katearen arteko interakzioa erakutsi zuten. Atal honen gabeziak, **Lf** katalizatzailearen kasuan ikusi zen moduan, aktibitate katalitikoaren gutxitzea eragin zuen (1. Taula eta 3. Irudia). Gainera, DFT kalkuluek, **TARF**-ren eta substratuen arteko hidrogeno loturak posible zirela nabarmendu zuten, nahiz eta katalizatzailearen ribitilo kateak azetil taldeak eduki. Katalizatzaile honen kasuan, **1**–**4** substratuen NH_3 estekatzaileek ribitilo katearen C=O(2'C)-rekin edota **TARF**-ren isoalloxazina unitatearen N(5)-rekin, hidrogeno loturak sor zitzaketen zenbait bitartekarien geometriak optimizatu genituen (IO 43. Irudia).

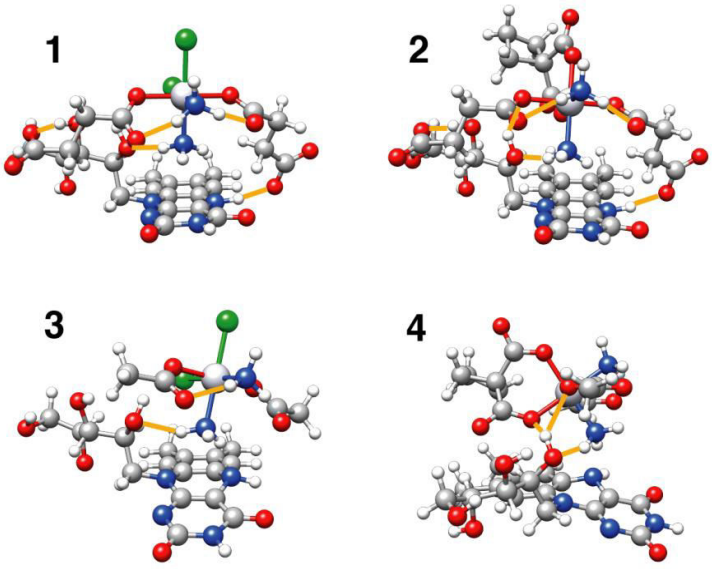

6. Irudia. 1–**4** substratuen eta $\mathbf{RfH^-}$-ren (H-lotura elkarrekintzak marra laranjez adierazita) artean sortutako bitartekarien DFT (pbe0/def2-SVP) estruktura optimizatuak.

Orokorrean, **2** eta **4** carboplatino substratuen konbertsioa baxuagoa da euren cisplatino homologoekin (1 eta 3) alderatuta. Hau, Pt konplexuen egonkortasun termodinamiko intrintsekoaren bidez azaldu daiteke. Izan ere, estekatzaile axial eta ekuatorialen trukatze energiak; DFT funtzional ezberdinen bidez kalkulatuta (IO 4. Irudia), **1** eta **3**, **2** eta **4** substratuak baino ez-egonkorragoak zirela erakutsi zuten. Berdina gertatu zen sukzinato eta azetato estekatzaileak alderatzerakoan. **3** eta **4** substratuek **1** eta **2** substratuek baino egonkortasun txikiagoa erakustsi zuen hurrenez hurren. Joera hau, konplexuen erredukzio potentzialarekin bat dator (IO 37. Irudia).

Cisplatino eratorrien egonkortasun txikiagoa arrazionalizatzeko, **1**–**4** subtratuen eta hauetatik sortutako Pt^{II} farmako aktiboen, Pt atomoen DFT karga atomikoa analizatu genuen. Edozer funtzional edo karga atomikoaren ebaluazio metodo erabilita ere, cisplatinoak eta honen eratorriek, carboplatinoak eta bere eratorriek baino karga positibo txikiago adierazgarria erakutsi zuten (IO 37. Irudia). Beraz, Cisplatino eratorrietan, Pt atomoaren eta estekatzaile ekuatorialen arteko interakzio elektrostatikoa, carboplatino eratorrietan baino ahulagoa da. Horregatik, **1** eta **3**, **2** eta **4** konplexuak baino errazago eralda daitezke. Bestalde, pH neutroan, sukzinato estekatzaileek karga negatibo bikoitza dute (pK_{a1} = 4.2 eta pK_{a2} = 5.6), azetato estekatzaileek (pK_a = 5.5) karga negatibo bakarra duten bitartean. Hori dela eta, Pt-azetato lotura Pt-sukzinato lotura baino ahulagoa da eta errazago aktiba daitezke. **1**–**4** subtratuen egonkortasun joera azaltzeko, Pt-estekatzaileen arteko loturen egonkortasunari erreparatu behar zaio. Lotura hauen egonkortasunak, substratuen eraldaketa eraginkortasun ezberdinak azal dezakete.

MiniSOG-ek, **FMN** kromoforoa du egitura proteikoaren barnean eta fotokimika zailagoa erakusten du. **MiniSOG**, elektroi emaile eta O_2-rik gabeko ingurunean irradiatzerakoan, $\mathbf{FMN}^{\bullet-}$ erradikala (semikinona) sortzen da. Honek, absortzio-banda zabala aurkezten du (IO 46. Irudia) 600 nm inguruan. Prozesu hau, aminoazido batzuen oxidazioari egotzi zitzaien eta $^1O_2$ erredimendu handietan sortzeko gaitasunarekin lehiatzen duela jakina da.[28–30] Oxigenorik gabe irradiatutako **miniSOG** soluzioak oxigenoarekin kontaktuan jartzerakoan, $\mathbf{FMN}^{\bullet-}$-aren ezaugarri espektralak desagertu eta absortzioa 450 nm inguru ia guztiz berreskuratu zen (IO 46. Irudia). **1** substratua erreakzio eskasa erakutsi zuen **miniSOG** flaboproteinak sortutako erradikalarekin inkubatu zenean. Efektu hau, UMore-Ikus eta RMN esperimentuen bidez behatu zen. Oxigenorik gabe irradiatutako **miniSOG** eta **1** kantitate estekiometrikoetan, substratuaren eraldaketa baldintza estadarretan baino motelago gertatu zen (IO. 47 eta 48).

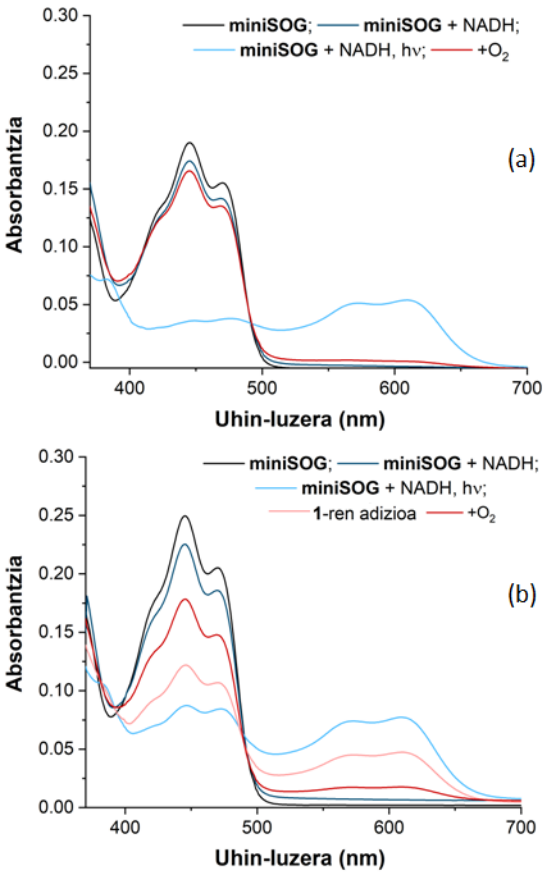

7. Irudia. Oxigenorik gabe irradiatutako **miniSOG**-aren UMore-Ikus jarraipena elektroi-hartzaile ezberdinak gehitzerakoan: (a) O_2 eta (b) **1** (120 µM). **miniSOG** soluzioak (15 µM, 18 mM PB, pH 7.4) NADH-ren baliokide batekin eta oxigenorik gabe irradiatu ziren (6 $mW{\cdot}cm^{-2}$, 180 s).

NADH soluzioan zegoenean, egitura proteikoan sortutako elektroi-transferentzia ez zen amatatu eta **FMN**$^{\bullet-}$ erradikala antzeman zitekeen (7a eta b Irudiak). Bestalde, UMore-Ikus espektroek bi aldiz erreduzitutako **FMN** lortu zela erakutsi zuten, 400–500 nm artean absorbantzia gutxitze nabarmenak adierazten duen moduan. Soluzio horiei O_2 edo **1** (120 µM) gehitzerakoan, **FMN**-ren banda espektrala berreskuratu zen. Hortaz, **miniSOG**-aren kasuan ere, **1** substratuaren eraldaketa eragiten duen katalizatzaile aktibo nagusia, H**FMN**$^{-}$ espeziea zela ondorioztatu zen. Beraz, aminoazidoen fotooxidazioak eragindako **FMN**-ren egoera kitzikatuaren iraungipena, katalizatzaile aktiboaren sorrerarekin lehiatzen zuen, $^1O_2$-ren eraketan hauteman zen moduan. Lan honetan aztertutako beste flabinekin alderatuta, **miniSOG**-ak aurkeztutako TOF balioak eta substratu konbertsio baxuagoa, **FMN**-ren eskuragarritasun murriztuari egotzi behar zaio.

IO 49. Irudian ikus daitekeen moduan, O_2-k elektroi isurtegi moduan jokatzen du behin eta bi aldiz erreduzitutako **miniSOG** eta beste flabina katalizatzaileak desaktibatuz. Ez da harritzekoa izaera hau, flabinen eta flaboproteinen biokimika aintzat hartuz. Honek, **1**–**4** substratuen konbertsio katalitikoa hobeto ulertzeko, O_2-ren papera sakonago aztertu behar dela iradokitzen du. Horrez gain, lan honetan azterturiko flabinak, oxigeno singlete ($^1O_2$) fotosortzaile ezagunak dira. [3,31]

Aireztatutako **1**–**4** disoluzioen fotoaktibazio zinetikak aztertu zirenean, indukzio epea behatu zen irradiazio epe laburretan flabina guztientzako (IO 50. Irudia). Aurkikuntza hauek, O_2, $^1O_2$-n eta oxigeno espezie erreaktiboetan (ROS) eraldatzea dakarten ziklo katalitiko lehiakorren presentziarekin bat datoz. Oxigenorik gabeko baldintzetan, substratuen konbertsioa berehala gertatu zen. Alabaina, **FMN** eta **1** substratua zituen disoluzio batean aire burbuilak egiterakoan, erreakzioa ez zen guztiz burutu eta zinetika nabarmen motelagoa zen (IO 51. Irudia).

Flabina katalizatzaileen ^{3}FL* egoera kitzikatuak, O_2-rekin interakzionatu dezakete $^1O_2$ emateko edo HFL^- espezie erreduzitua lortu ostean, $O_2^{\bullet-}$ eta H_2O_2 bezalako ROS-k sortzeko (1. Eskema). Bi bideen existentzia, **FMN**-rentzako eta **miniSOG**-arentzako aldez aurretik onartutako metodo optiko ez zuzenen bidez egiaztatu genuen.[12,29] Azido urikoa eta dihidroetidiuma, zunda molekular moduan erabili genituen $^1O_2$ eta ROS-en sorrera frogatzeko hurrenez hurren. **1** eta **NADH** soberan zuten, **FMN** eta **miniSOG** disoluzioak irradiatzerakoan, bi oxigeno espezie erreaktiboen sorkuntza antzeman genuen (IO 52–54. Irudiak). Aldez aurretik deskribatu zen bezala,[12,29] **FMN** askea, egitura proteikoan sartutakoa baino $^1O_2$ fotosortzaile hobea da. Gertaera hau, estruktura proteikoak kromoforoan eragiten duen egoera triplete kitzikatuaren autoiraungipenarekin bat dator. Hala ere, **miniSOG**-aren eta **FMN**-ren ROS sorkutza konparagarria zen, proteina barnean foto eragindako elektroi transferentzia erreakzioen bidez, $O_2^{\bullet-}$ berehala sortzen zelako (adib. $\mathbf{FMN}^{\bullet-}$-tik). NADH eta **1** gabe egindako esperimentu kontrolek, ez zuten $^1O_2$-ren eta ROS-en gutxitze nabarmenik erakutsi. Flabinek, Pt substratuen katalisia gauzatu aurretik, O_2 fotoprodukturu horietan berehala eraldatzen dituela iradokitzen du honek.

3.3 Ondorioak

Lan honek, flabinen bidez gauzatutako platino substratuen fotokatalisi esparrua zabaltzen du, oinarrizko zehaztapen mekanistiko berriak hornituz. Oxigenorik gabeko baldintzetan erreduzitutako H_2FL/HFL^- espezieak, katalizatzaile aktibo gisa identifikatu ziren espektroskopia optiko eta NMR bidez. H_2FL/HFL^- eta Pt^{IV} substratuen arteko H-lotura elkarrekintzak funtsezkoak izan daitezke Pt^{II} sendagaien eraldaketa eragiteko, segur aski, estekatzaile-zubi barne esfera erredukzio mekanismoa bidez. Ribitilo kateak, usteko bitartekari hauek egonkortu ditzake eta erreakzioen eraginkortasun katalitikoa areagotu. Horregatik, frogatutako flabina askeen artean, **Lf**-k erakutsi zuen TOF-ik baxuena. Egitura proteikoaren aminoazidoek eragindako **miniSOG**-aren egoera kitzikatuen auto-iraungipenak, katalizatzaile honen eraginkortasuna gutxitzen dute, $^1O_2$-ren fotosorkuntza ahalmenerako ikusi zen moduan. Etorkizunean, **FL** askeen ribitilo taldearen eraldaketa estrukturalak eta **miniSOG**-aren lekuko mutagenesia ikertzea merezi dute; euren aktibitate katalitikoa eta kimika berri hau metal sorta ezberdinekin erabiltzeko.

3.4 Xehetasun esperimentalak

Materialak. Riboflabina (**Rf**), flabina-mononukleotidoa (**FMN**), potasio fosfato monobasikoa, potasio fosfato dibasikoa, β-nikotinamida adenina dinukleotidoa, erreduzitutako disodio gatz hidratatua, sodio ditionitoa, RPMI-1640 ingurumena Sigma-Aldrichen erosi ziren eta Potasio tetrakloroplatinatoa (II) Precious Metals Online-tik lortu ziren. Erreaktibo guztiak, jaso bezala eta purifikazio gehigarririk gabe erabili ziren. RPMI-1640 ingurumenera gehitu zitzaion behi suero fetala (10%) Invitrogen-en erosi zen.

Substratu eta katalizatzaileen prestakuntza. *cis,cis,trans*-$[Pt(NH_3)_2(Cl_2)(O_2CCH_2CH_2CO_2)_2]^{2-}$ (**1**), *cis,cis,trans*-$[Pt(NH_3)_2(O_4C_6H_6)(O_2CCH_2CH_2CO_2)_2]^{2-}$ (**2**), *cis,cis,trans*-$[Pt(NH_3)_2(Cl_2)(O_2CCH_3)_2]$ (**3**), *cis,cis,trans*-$[Pt(NH_3)_2(O_4C_6H_6)(O_2CCH_3)_2]$ (**4**) konplexuak, lehenago azaldu zen moduan sintetizatu eta karakterizatu ziren.[32–34] Tetra-O-azetil riboflabina (**TARF**) eta lumiflabina (**Lf**) I. Jhulkik *et al*.[35] azaldu zuten prozedura jarraituz sintetizatu ziren. Bestalde, **MiniSOG** katalizatzailea aurretik azaldu genuen moduan prestatu eta purifikatu zen.[3]

Metodoak

Erresonantzia magentiko nuklearra (NMR). Laginen ^{1}H NMR espektroak, Fourier TM Bruker 300 NMR eta AVANCE III Bruker 500 NMR espektrometroetan pultsu estandarreko programak erabiliz lortu ziren. Lekualdaketa kimikoak, milioiko parteetan (δ, ppm) azaldu eta disolbatzailearen aztarnen seinalearekiko erreferentziatu ziren.

Esperimentu katalitikoak. Besterik aipatu ezean, erreakzio guztiak atmosfera normalean, 298 K-etan eta pH 7-an, 25 μM katalizatzaile, 500 μM substratu (1–4) eta 1 mM NADH erabiliz egin ziren. Argi irradiazio esperimentuak, LED argi iturria (λ_{max} = 460 nm, 6 $mW{\cdot}cm^{-2}$) erabiliz gauzatu ziren.[4] Berraldatze frekuentzia (TOF), berraldatze zenbakia (TON) eta erreakzio katalitikoen % konbertsioa, ^{1}H NMR bidez 1–4 substrauen eraldaketa kuantifikatuz neurtu ziren. Sukzinato eta azetato estekatzaile askeen seinaleen (singleteak 2.25–2.35 ppm artean eta 1.80 ppm inguru hurrenez hurren) integrazioaren bidez, erreakzioaren garapena jarraitu zen. TOF balioak, substratuen konbertsioa %25–35 inguru zeudenean lortu ziren.

Argi ultramore-ikuskorreko absortzio-espektroskopia (UMore-Ikus). Espektro guztiak, JASCO V-730 espektrofotometroa erabiliz lortu ziren. Laginak, ur soluzio edo tampoi disoluzioetan disolbatu eta kuartzozko kubeta optikoetan neurtu ziren.

Emisio fluoreszentea eta bizitza-denbora. FMN-ren (20 μM) emisio espektroa Edinburgh instruments espektrofluorimetroan (FL920 modeloa) neurtu zen. 450W-ko flash lanpara erabili zen, kitzikapen iturri bezala. Beheraldi erradiatibo fluorezentearen kurba λ_{em} = 540 nm-tara neurtu zen, denbora korrelatibo fotoi bakar zenbatzaile teknikarekin (Edinburgh instrumentua, FL920 modeloa), λ_{kitz} = 445 nm-tan kitzikatu ostean. Pikosegundoko (ps) ebazpen tenporala duen mikrokanal plaka detektagailua (Hamamatsu C4878), uhin luzera

aldagarriko 150 ps FWHM pultsuko Fianium laser superjarraia erabiliz egin ziren neurketa hauek. Iterazio-metodoen bidez neurtutako beheraldi kurben seinale erantzun instrumentalaren dekonboluzioa egin ostean, bizitza-denbora fluoreszenteak lortu ziren. Doiketa esponentzialaren egokitasuna, parametro estatistikoen (χ^2 eta hondarren analisia) bidez kontrolatu zen. Neurketak, airez asetutako (a) **FMN** (20 μM), (b) **FMN** (20 μM) eta NADH (400 μM), eta (c) **FMN** (20 μM), NADH (400 μM) eta **1** (400 μM) disoluzioetan egin ziren.

Bitarteko absortzioa eta bizitza-denbora tripleteak. Nano segundoko bitarteko absortzio neurketak, LP980 laser flash fotolisi espektrometro (Edinburgh Instruments, Livingston, UK) batean egin ziren. Laginak, absortzio maximoan (445 nm) nanosegundoko laser pultsatuaren (Nd:YAG laser/OPO, LOTIS TII 2134) bidez kitzikatu ziren, 1Hz, 7 ns pultsu amplitudearekin eta 10 mJ-ko kitzikapen potentziarekin. Kitzikapen uhin luzeeran 0.3 absortzio optikoa zuten disoluzioei, nitrogenoa edo airea 10 minutuz pasarazi zitzaien baldintza anaerobiko edo aerobikoak lortzeko. Bitarteko espektroak, ICCD detektoreakin lortu ziren (DH320T TE hoztuta, Andor Technology). Triplete-triplete absortzioen beheraldiak, oxigenoaren presentzian edo gabezian (nitrogeno edo airez asetutako soluzioak) 700 nm-tara neurtu ziren, detektagailu bakarrean (PMT R928P) eta osziloskopioan. Oxigenoaren presentzian edo gabezian neurtutako bizitza-denbora tripleteak (τ_0^T eta τ^T), beheraldi kurben maldetatik lortu ziren, LP 900 software-n iterazio-metodoen bitartez. Doiketa esponentzialaren egokitasuna, parametro estatistikoen (χ^2 eta hondarren analisia) bidez kontrolatu zen. (a) **FMN** (20 μM), (b) **FMN** (20 μM) eta NADH (400 μM), eta (c) **FMN** (20 μM), NADH (400 μM) eta **1** (400 μM) disoluzioak erabili ziren esperimentu multzo hau osatzeko.

Oxigeno singletearen eta ROS-en formakuntza. $^1O_2$ eta ROS-en kuantifikazioa, aurretik **FMN** eta **miniSOG**-entzako onartutako metodoak erabiliz gauzatu zen.[12,29] Azido urikoa (UA), zunda moduan erabili zen $^1O_2$-aren zeharkako neurketak egiteko. Absorbantzia aldaketak 292 nm-tan jarraitu ziren, argi irradiazio denbora aurrera joan ahala. Optikoki bat zetozen UA (50 μM) eta (a) **FMN**/**miniSOG** (5 μM), (b) **FMN**/**miniSOG** (5 μM) eta NADH (30 μM), eta (c) **FMN**/**miniSOG** (5 μM), NADH (30 μM) eta **1** (15 μM) disoluzioak, 460 nm-ko argi (6 $mW \cdot cm^{-2}$) iturriaren eraginpean jarri genituen.

Bestalde, beste ROS-en sorkuntza neurtzeko ($O_2^{\bullet -}$ bereziki), hidroetidiumaren (HE) fotooxidazioa erabili zen. Zunda honek $^1O_2$-rekin interakzionatuz gero, ez du eraldaketarik jasaten. [29,37] Kasu honetan ere, HE (50 μM) (a) **FMN**/**miniSOG** (5 μM), (b) **FMN**/**miniSOG** (5 μM) eta NADH (30 μM), eta (c) **FMN**/**miniSOG** (5 μM), NADH (30 μM) eta **1** (15 μM) disoluzioak 460 nm-ko argi iturriarekin irradiatu ziren eta aurretik deskribatu zen bezala, haien fluoreszentzia intentsitatea (λ_{ex} = 525 nm, λ_{em} = 550–800 nm) denbora puntu ezberdinetara neurtu zen. [29]

Elektrokimika. Voltametria ziklikoko esperimentuak Metrohm Autolab 302 N potentziostatoan gauzatu ziren. Zelda elektrokimikoa, konpartimentu bakarreko zelda bat zen, hiru elektrodoz hornituta: beirazko karbono lan elektrodoa (Ø = 1 mm), platinozko hari

kontra-elektrodoa eta kalomelez asetutako elektrodoa (SCE) erreferetzia moduan. Neurketa guztiak, oxigenorik gabeko baldintzetan argon atmosferapean egin ziren. Neurketak, 0.15 M NaCl zuen 0.05 M fosfato tampoi (pH 7.4) disoluzioetan burutu ziren. $5.0\cdot10^{-4}$ M-eko disoluzioak erabili ziren konplexu metalikoak neurtzeko. **FMN** eta **Rf** neurtzeko $2.7\cdot10^{-4}$ eta $2.0\cdot10^{-4}$ M-eko disoluzioak erabili ziren hurrenez hurren. Aseturiko disoluzioak erabili ziren **TARF** eta **Lf**-aren kasuan, disolbagarritasun baxua dela eta. Lan elektrodoa aluminarekin leundu, ur distilatuarekin garbitu eta lehortu egin zen potentzial bilaketa bakoitzaren aurretik, esperimentu guztietan azalera berdina zela bermatzeko.

Metodo konputazionalak. Kalkulu guztiak, Gaussian 16 programaren B01 errebisioarekin gauzatu ziren.[38] Riboflabina-substratu aduktuen optimizazio geometrikoak, DFT mailan egin ziren pbe0/def2-SVP konbinazioaren bitartez.[39,40] Ura, eredu jarrai polarizatuaren (PCM) bidez disolbatzaile inplizitu moduan ezarri zen. Becke eta Johnsonen indargetzea (moteltzea) duen Grimeren dispertsiorako zuzenketa erabili zen dispertsio elkarrekintzak kontuan hartzeko.[41] Ondoren, frekuentziak, zero-puntuko bibrazio-energia (ZPVE) eta bibrazio-termiko (T = 298 K) zuzenketak, entalpia eta Gibbs-en energi askeak, oszilatzaile harmonikoaren hurbilpenaren barnean ebaluatzeko erabili ziren. Entropia kalkulatzeko, partizio funtzioaren ekarpen ezberdinak, multzo kanonikoaren, eta osziladore armonikoaren eta errotore zurrunaren hurbilpenaren barnean, adierazpen estatistiko mekaniko estandarrak erabiliz aztertu ziren. **1**–**4** sustratuen egonkortasun eraltiboaren energia kalkuluak egiteko, def2-TVP oinarrizko base multzoa[40] eta pbe0, wb97xd[42] eta m062x[43] deituriko hiru funtzional ezberdinak erabili ziren. Karga atomikoak kalkulatzeko, funtzional eta oinarrizko base multzoaren konbinazio berdina erabili zen nbo[44] eta chelpg[45] metodoekin batera.

3.5 Erreferentziak

(1) Alonso-de Castro, S.; Terenzi, A.; Gurruchaga-Pereda, J.; Salassa, L. Catalysis Concepts in Medicinal Inorganic Chemistry. *Chem. Eur. J.* **2019**, *25*, 6651–6660.

(2) Alonso-de Castro, S.; Terenzi, A.; Hager, S.; Englinger, B.; Faraone, A.; Martínez, J. C.; Galanski, M.; Keppler, B. K.; Berger, W.; Salassa, L. Biological Activity of Pt^{IV} Prodrugs Triggered by Riboflavin-Mediated Bioorthogonal Photocatalysis. *Sci. Rep.* **2018**, *8*, 17198.

(3) Alonso-de Castro, S.; Cortajarena, A. L.; López-Gallego, F.; Salassa, L. Bioorthogonal Catalytic Activation of Platinum and Ruthenium Anticancer Complexes by FAD and Flavoproteins. *Angew. Chem., Int. Ed.* **2018**, *57*, 3143–3147.

(4) Alonso-de Castro, S.; Ruggiero, E.; Ruiz-de-Angulo, A.; Rezabal, E.; Mareque-Rivas, J. C.; Lopez, X.; López-Gallego, F.; Salassa, L. Riboflavin as a Bioorthogonal Photocatalyst for the Activation of a Pt(IV) Prodrug. *Chem. Sci.* **2017**, *8*, 4619–4625.

(5) Ngo, A. H.; Bose, S.; Do, L. H. Intracellular Chemistry: Integrating Molecular Inorganic Catalysts with Living Systems. *Chem. Eur. J.* **2018**, *24*, 10584–10594.

(6) Martínez-Calvo, M.; Mascareñas, J. L. Organometallic Catalysis in Biological Media and Living Settings. *Coord. Chem. Rev.* **2018**, *359*, 57–79.

(7) Gong, L.; Lin, Z.; Harms, K.; Meggers, E. Isomerization-Induced Asymmetric Coordination Chemistry : From Auxiliary Control to Asymmetric Catalysis. *Angew. Chem., Int. Ed.* **2010**, *49*, 7955–7957.

(8) Ruffoni, A.; Juliá, F.; Svejstrup, T. D.; McMillan, A. J.; Douglas, J. J.; Leonori, D. Practical and Regioselective Amination of Arenes Using Alkyl Amines. *Nat. Chem.* **2019**, *11*, 426–433.

(9) Barkay, T.; Miller, S. M.; Summers, A. O. Bacterial Mercury Resistance from Atoms to Ecosystems. *FEMS Microbiol. Rev.* **2003**, *27*, 355–384.

(10) Edwards, A. M.; Bueno, C.; Saldaño, A.; Silva, E.; Kassab, K.; Polo, L.; Jori, G. Photochemical and Pharmacokinetic Properties of Selected Flavins. *J. Photochem. Photobiol. B Biol.* **1999**, *48*, 36–41.

(11) Shu, X.; Lev-Ram, V.; Deerinck, T. J.; Qi, Y.; Ramko, E. B.; Davidson, M. W.; Jin, Y.; Ellisman, M. H.; Tsien, R. Y. A Genetically Encoded Tag for Correlated Light and Electron Microscopy of Intact Cells, Tissues, and Organisms. *PLoS Biol.* **2011**, *9*, e1001041.

(12) Agut, M.; Ruiz-González, R.; Cortajarena, A. L.; Flors, C.; Mejias, S. H.; Nonell, S. Singlet Oxygen Generation by the Genetically Encoded Tag MiniSOG. *J. Am. Chem. Soc.* **2013**, *135*, 9564–9567.

(13) Rodríguez-Pulido, A.; Cortajarena, A. L.; Torra, J.; Ruiz-González, R.; Nonell, S.; Flors, C. Assessing the Potential of Photosensitizing Flavoproteins as Tags for Correlative Microscopy. *Chem. Commun.* **2016**, *52*, 8405–8408.

(14) Proshkina, G. M.; Shramova, E. I.; Shilova, O. N.; Ryabova, A. V.; Deyev, S. M. Phototoxicity of Flavoprotein MiniSOG Induced by Bioluminescence Resonance Energy Transfer in Genetically Encoded System NanoLuc-MiniSOG Is Comparable with Its LED-Excited Phototoxicity. *J. Photochem. Photobiol. B Biol.* **2018**, *188*, 107–115.

(15) Souslova, E. A.; Mironova, K. E.; Deyev, S. M. Applications of Genetically Encoded Photosensitizer MiniSOG: From Correlative Light Electron Microscopy to Immunophotosensitizing. *J. Biophotonics* **2017**, *10*, 338–352.

(16) Varbanov, H. P.; Jakupec, M. A.; Roller, A.; Jensen, F.; Galanski, M.; Keppler, B. K. Theoretical Investigations and Density Functional Theory Based Quantitative Structure–Activity Relationships Model for Novel Cytotoxic Platinum(IV) Complexes. *J. Med. Chem.* **2013**, *56*, 330–344.

(17) Englinger, B.; Pirker, C.; Heffeter, P.; Terenzi, A.; Kowol, C. R.; Keppler, B. K.; Berger, W. Metal Drugs and the Anticancer Immune Response. *Chem. Rev.* **2019**, *119*, 1519–1624.

(18) Weber, S.; Walker, J. M. *Flavins and Flavoproteins.; Springer,* ***2014***

(19) Chaiyen, P.; Fraaije, M. W.; Mattevi, A. The Enigmatic Reaction of Flavins with Oxygen. *Trends Biochem. Sci.* **2012**, *37*, 373–380.

(20) Ghisla, S.; Massey, V.; Lhoste, J.-M.; Mayhew, S. G. Fluorescence and Optical Characteristics of Reduced Flavines and Flavoproteins. *Biochemistry.* **1974**, *13*, 589–597.

(21) Gargiulo, S.; Arends, I. W. C. E.; Hollmann, F. A Photoenzymatic System for Alcohol Oxidation. *ChemCatChem.* **2011**, *3*, 338–342.

(22) Rauch, M.; Schmidt, S.; Arends, I. W. C. E.; Oppelt, K.; Kara, S.; Hollmann, F. Photobiocatalytic Alcohol Oxidation Using LED Light Sources. *Green Chem.* **2017**, *19*, 376–379.

(23) Kao, Y.-T.; Saxena, C.; He, T.-F.; Guo, L.; Wang, L.; Sancar, A.; Zhong, D. Ultrafast Dynamics of Flavins in Five Redox States. *J. Am. Chem. Soc.* **2008**, *130*, 13132–13139.

(24) Feldmeier, C.; Bartling, H.; Magerl, K.; Gschwind, R. M. LED-Illuminated NMR Studies of Flavin-Catalyzed Photooxidations Reveal Solvent Control of the Electron-Transfer Mechanism. *Angew. Chem., Int. Ed.* **2015**, *54*, 1347–1351.

(25) Bartling, H. Dissertation: NMR Spectroscopic Investigations on Photocatalytic Reactions and Photochromic Materials., Ph.D. Thesis Universität Regensburg, **2016**.

(26) Cardoso, D. R.; Franco, D. W.; Olsen, K.; Andersen, M. L.; Skibsted, L. H. Reactivity of Bovine Whey Proteins, Peptides, and Amino Acids toward Triplet Riboflavin as Studied by Laser Flash Photolysis. *J. Agric. Food Chem.* **2004**, *52*, 6602–6606.

(27) Dabbish, E.; Ponte, F.; Russo, N.; Sicilia, E. Antitumor Platinium(IV) Prodrugs: A Systematic Computational Exploration of Their Reduction Mechanism by l -Ascorbic Acid. *Inorg. Chem.* **2019**, *58*, 3851–3860.

(28) Torra, J.; Lafaye, C.; Signor, L.; Aumonier, S.; Flors, C.; Shu, X.; Nonell, S.; Gotthard, G.; Royant, A. Tailing MiniSOG: Structural Bases of the Complex Photophysics of a Flavin-Binding Singlet Oxygen Photosensitizing Protein. *Sci. Rep.* **2019**, *9*, 2428.

(29) Westberg, M.; Holmegaard, L.; Pimenta, F. M.; Etzerodt, M.; Ogilby, P. R. Rational Design of an Efficient, Genetically Encodable, Protein-Encased Singlet Oxygen Photosensitizer. *J. Am. Chem. Soc.* **2015**, *137*, 1632–1642.

(30) Pimenta, F. M.; Jensen, R. L.; Breitenbach, T.; Etzerodt, M.; Ogilby, P. R. Oxygen-Dependent Photochemistry and Photophysics of "MiniSOG," a Protein-Encased Flavin. *Photochem. Photobiol.* **2013**, *89*, 1116–1126.

(31) Silva, A. V.; López-Sánchez, A.; Junqueira, H. C.; Rivas, L.; Baptista, M. S.; Orellana, G. Riboflavin Derivatives for Enhanced Photodynamic Activity against Leishmania Parasites. *Tetrahedron.* **2015**, *71*, 457–462.

(32) Varbanov, H. P.; Valiahdi, S. M.; Kowol, C. R.; Jakupec, M. A.; Galanski, M.; Keppler, B. K. Novel Tetracarboxylatoplatinum(IV) Complexes as Carboplatin Prodrugs. *Dalton. Trans.* **2012**, *41*, 14404–14415.

(33) Gramatica, P.; Papa, E.; Luini, M.; Monti, E.; Gariboldi, M. B.; Ravera, M.; Gabano, E.; Gaviglio, L.; Osella, D. Antiproliferative Pt(IV) Complexes: Synthesis, Biological Activity, and Quantitative Structure–Activity Relationship Modeling. *J. Biol. Inorg. Chem.* **2010**, *15*, 1157–1169.

(34) Tetko, I. V; Varbanov, H. P.; Galanski, M.; Talmaciu, M.; Platts, J. A.; Ravera, M.; Gabano, E. Prediction of LogP for Pt(II) and Pt(IV) Complexes: Comparison of Statistical and Quantum-Chemistry Based Approaches. *J. Inorg. Biochem.* **2016**, *156*, 1–13.

(35) Jhulki, I.; Chanani, P. K.; Abdelwahed, S. H.; Begley, T. P. A Remarkable Oxidative Cascade That Replaces the Riboflavin C8 Methyl with an Amino Group during Roseoflavin Biosynthesis. *J. Am. Chem. Soc.* **2016**, *138*, 8324–8327.

(36) Rabello, B. R.; Gerola, A. P.; Pellosi, D. S.; Tessaro, A. L.; Aparício, J. L.; Caetano, W.; Hioka, N. Singlet Oxygen Dosimetry Using Uric Acid as a Chemical Probe: Systematic Evaluation. *J. Photochem. Photobiol. A.* **2012**, *238*, 53–62.

(37) Gomes, A.; Fernandes, E.; Lima, J. L. F. C. Fluorescence Probes Used for Detection of Reactive Oxygen Species. *J. Biochem. Biophys. Methods* **2005**, *65*, 45–80.

(38) Frisch, M. J.; Trucks, G. W.; Schlegel, H. B.; Scuseria, G. E.; Robb, M. A.; Cheeseman, J. R.; Scalmani, G.; Barone, V.; Petersson, G. A.; Nakatsuji, H.; Li, X.; Caricato, M.;

Marenich, A. V; Bloino, J.; Janesko, B. G.; Gomperts, R.; Mennucci, B.; Hratchian, H. P.; Ortiz, J. V; Izmaylov, A. F.; Sonnenberg, J. L.; Williams-Young, D.; Ding, F.; Lipparini, F.; Egidi, F.; Goings, J.; Peng, B.; Petrone, A.; Henderson, T.; Ranasinghe, D.; Zakrzewski, V. G.; Gao, J.; Rega, N.; Zheng, G.; Liang, W.; Hada, M.; Ehara, M.; Toyota, K.; Fukuda, R.; Hasegawa, J.; Ishida, M.; Nakajima, T.; Honda, Y.; Kitao, O.; Nakai, H.; Vreven, T.; Throssell, K.; Montgomery Jr., J. A.; Peralta, J. E.; Ogliaro, F.; Bearpark, M. J.; Heyd, J. J.; Brothers, E. N.; Kudin, K. N.; Staroverov, V. N.; Keith, T. A.; Kobayashi, R.; Normand, J.; Raghavachari, K.; Rendell, A. P.; Burant, J. C.; Iyengar, S. S.; Tomasi, J.; Cossi, M.; Millam, J. M.; Klene, M.; Adamo, C.; Cammi, R.; Ochterski, J. W.; Martin, R. L.; Morokuma, K.; Farkas, O.; Foresman, J. B.; Fox, D. J. Gaussian 16, Revision B.01. **2016**.

(39) Adamo, C.; Barone, V. Toward Reliable Density Functional Methods without Adjustable Parameters: The PBE0 Model. *J. Chem. Phys.* **1999**, *110*, 6158–6170.

(40) Weigend, F.; Ahlrichs, R. Balanced Basis Sets of Split Valence, Triple Zeta Valence and Quadruple Zeta Valence Quality for H to Rn: Design and Assessment of Accuracy. *Phys. Chem. Chem. Phys.* **2005**, *7*, 3297–3305.

(41) Grimme, S.; Ehrlich, S.; Goerigk, L. Effect of the Damping Function in Dispersion Corrected Density Functional Theory. *J. Comput. Chem.* **2011**, *32*, 1456–1465.

(42) Chai, J.-D.; Head-Gordon, M. Long-Range Corrected Hybrid Density Functionals with Damped Atom–Atom Dispersion Corrections. *Phys. Chem. Chem. Phys.* **2008**, *10*, 6615–6620.

(43) Zhao, Y.; Truhlar, D. G. The M06 Suite of Density Functionals for Main Group Thermochemistry, Thermochemical Kinetics, Noncovalent Interactions, Excited States, and Transition Elements: Two New Functionals and Systematic Testing of Four M06-Class Functionals and 12 Other Function. *Theor. Chem. Acc.* **2008**, *120*, 215–241.

(44) Reed, A. E.; Curtiss, L. A.; Weinhold, F. Intermolecular Interactions from a Natural Bond Orbital, Donor-Acceptor Viewpoint. *Chem. Rev.* **1988**, *88*, 899–926.

(45) Chirlian, L. E.; Francl, M. M. Atomic Charges Derived from Electrostatic Potentials: A Detailed Study. *J. Comput. Chem.* **1987**, *8*, 894–905.

4

Pt^{IV} Substratuen Konbertsio Fotokatalitikoaren Hobekuntza Ingeniaritza Proteikoaren Bidez

Kapitulu honetan deskribatutako lana *J. Phys. Chem. Lett.* 2021, 12, 4504–4508 (egileak: Gurruchaga-Pereda J.; Martínez-Martínez V.; Formoso E.; Azpitarte O.; Rezabal E.; Lopez X.; Cortajarena L. A.; Salassa L.) aldizkarian argitaratu zen.

4.1 Sarrera

Elektroi emaileen presentzian, flaboproteinek eta flaboentzimek, konplexu metalikoeen erredukzioa katalizatzeko gai dira.[1] Orain dela gutxi gure taldeak, NOX (NADH oxidasa) entzima eta miniSOG (mini Singlet Oxygen Generator) bezalako flaboproteinek, minbiziaren kontrako Pt^{IV} agenteak euren Pt^{II} baliokideetan berraldatze zenbaki (TON) eta frekuentzia (TOF) adierazgarriekin bihurtzeko ahalmena zutela erakutsi zuen (ingurumen zelularrean ere).[2–4] Erreakzio katalitiko honetan, argiaren eraginez, flabinek, egoera triplete kitzikatua (^{3}FL*) lortzen dute. Elektroi emaileen presentzian, egoera triplete kitzikatua duten flabinek, iraungipen erreduktiboa jasaten dute eta ondorioz, Pt^{IV} substratuak erreduzitzeko gai den flabina hidroquinona egoera (adibidez HFL^-) sortzen da (1a Irudia).

Ez-ohiko kimika hau, metal konplexuak substratu gisa erabiltzen dituen erreakzio katalitiko bakanetakoa da.[5,6] Gainera, kimika berri honek, metaletan oinarritutako profarmako kimioterapeutikoen (foto)aktibazioa gauzatzeko estrategia berriak diseinatu nahi ditu.[4,7]

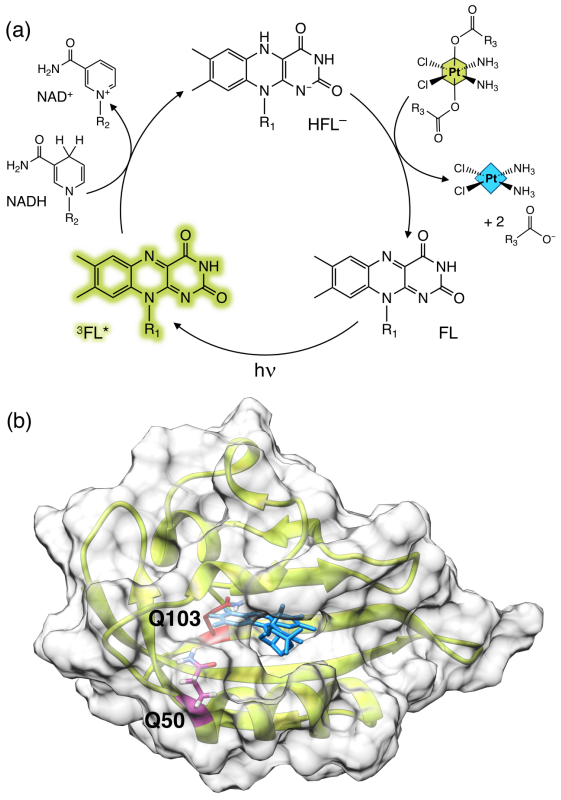

1. Irudia. (a) Flabinen bidez gauzatutako Pt^{IV} profarmakoen aktibazio mekanismo fotokatalitiko orokorra; R_1 = adibidez: ribitilo, ribitilo fosfatoa, R_2 = adenosina difosfato erribosa eta R_3 = CH_2CH_2COOH (**1**) edo CH_3 (**2**). (b) iLOV proteinaren (PBD ID: 6GPU) egituran ionarritutako miniSOG-aren eredu molekularra. miniSOG-aren bizkarrezurra zinta horiz, FMN makil urdinez, eta mutazioa eragindako aminoazido posizioa morez (Q50) eta gorriz (Q103) irudikatu dira.

Ingeniaritza proteikoak katalisian lortu dituen emaitza harrigarriak kontuan hartuz,[8,9] flaboproteinen egitura aldaketek, Pt^{IV} substratuak katalitikoki eraldatzeko duten

gaitasunean nola eragin zezaketen eta mutagenesi guneratuak argi irradiazio arinen menpe aktibazio eraginkortasuna hobetu zezakeen galdetu genion geure bururuari. Hori ikertzeko, FMN barnean zuen miniSOG flaboproteina aukeratu zen, eta Q103V, Q50E eta Q50W mutanteen eta jatorrizko tipoaren (WT) gaitasun katalitikoak alderatu ziren. miniSOG eredu aproposa da helburu honetarako, proteina honen mutanteak eta hauen fotofisika, argi korrelatibo eta mikroskopio elektroniko (CLEM) eta $^1O_2$ sorkutza helburuetarako sakonki ikertu delako.[10–15]

Hainbat taldek, Q103V mutantearen eta honen Q103L (SOPP, oxigeno singlete proteina fotosentsibilizatzailea) analogoaren fotofisika ikertu dute.[12,14,15] 103 posizioan dagoen glutamina aminoazidoa, FMN-rekin hidrogeno lotura osatzen zuela proposatu zen (1b Irudia), ^{3}FMN*-ren bizitza-denbora eta $O_2^{\bullet-}$ sorkuntza txikituz.[15] Q hondakina, albo kate hidrofobikoa duen aminoazido batengatik (hala nola balina edo leuzina) ordezkatzeak, ^{3}FMN*-ren bizitza denbora eta miniSOG-ak $^1O_2$ sortzeko duen gaitasuna nabarmen handitu zuen.[12,14,15] Bestalde, Q50E eta Q50W mutante berriak dira, Q50 posizioaren eta FMN-ren arteko hurbilatsunean oinarrituz sortu ziren. Mutazio hauen helburua, karga negatibo (azido glutamiko, E, pKa 4.5) eta tamaina handiko aminoazido aromatiko (triptofanoa, W) batek katalisian, zer nolako eragina zuen aztertzea zen. Gainera, W optikoki aktiboa eta flabinen egoera kitzikatuen iraungipen eragilea dela ezaguna da.[16,17]

4.2 Emaitzak eta eztabaida

Mutante ezberdinek, Pt^{IV} konplexuen konbertsioa katalizatzeko zuten gaitasuna aztertzeko, *cis,cis,trans*-[$Pt(NH_3)_2(Cl)_2(O_2CCH_2CH_2CO_2H)_2$] (**1**) eta *cis,cis,trans*-[$Pt(NH_3)_2(Cl)_2(O_2CCH_3)_2$] (**2**) cisplatino profarmakoak erabili ziren NADH elektroi emailearen presentzian (1a Irudia).

Dakigula, ingeniaritza proteikoaren bidez konposatu metalikoen eraldaketa katalitikoa hobetzeko lehen saiaketa da hau. Ikerketa hauek, eragin garrantzitsuak ekar ditzakete bai biologian, eta bai medikuntzarako teknologia berrien garapenean ere.

4.2.1 Azterketa fotofisiko eta fotokimikoak

Lehenik eta behin, lau flaboproteina ezberdinen ezaugarri fotofisiko eta fotokimikoak aztertu ziren metodo optiko eta baldintza esperimental desberdinak erabiliz (IO 1–8. Irudiak). Lau proteinek, FMN kromoforoaren absortzio eta emisio profil bereizgarria erakutsi zuten, floureszentzia bizitza-denbora 4–5 ns artean egonik (IO 1. Irudia). Q50W mutanteak, fluoreszentzia bizitza-denbora motzena erakutsi zuen (4 ns), W hondakinak ^{1}FMN egoera kitzikatuaren desaktibazioa laguntzen zuela adieraziz. Honek, W eta FMN-ren arteko elkarrekintza frogatu zuen, jatorrizko hipotesia baieztatuz. miniSOG mutante eta WT flaboproteinen bitarteko absortzio espektroek, ^{3}FMN-ren bereizgarri den irudia azaldu zuten. Flaboproteinak guztiek, 420−480 nm artean funtsezko egoeraren zuritzeari zegokion

banda negatiboa eta 550−750 nm artean, T1 egoeraren absortzioari zegokion banda positiboa erakutsi zuten (2. Irudia).[2,16] ^{3}FMN-ren bizitza-denbora aireztatutako disoluzioetan, 720 nm-tan triplete−triplete absortzioaren beheraldi mono-esponentziala jarraituz neurtu zen (2. Irudia eta IO 2. Irudia). miniSOG WT-arekin alderatuta (35 µs), Q103V eta Q50W mutanteek, bizitza-denbora triplete luzeago eta motzago erakutsi zuten hurrenez hurren (102 *vs* 1.8 µs). Q50W mutantearen kasuan neurtutako τ^T murrizketa bortitza, ^{3}FMN eta triptofano atalen arteko elektroi transferentzia prozesuei esleitu zitzaien, erradikal bikoteen sorkuntza barne.[16,17] Bestalde, Q50E mutanteak 31 µs-ko bizitza-denborarekin, WT-aren antzeko ^{3}FMN beheraldia erakutsi zuen. Lan honetan WT eta Q103V mutanteentzako lortutako bizitza-denbora balioak, aurretik argitaratutako datuekin bat datoz.[11]

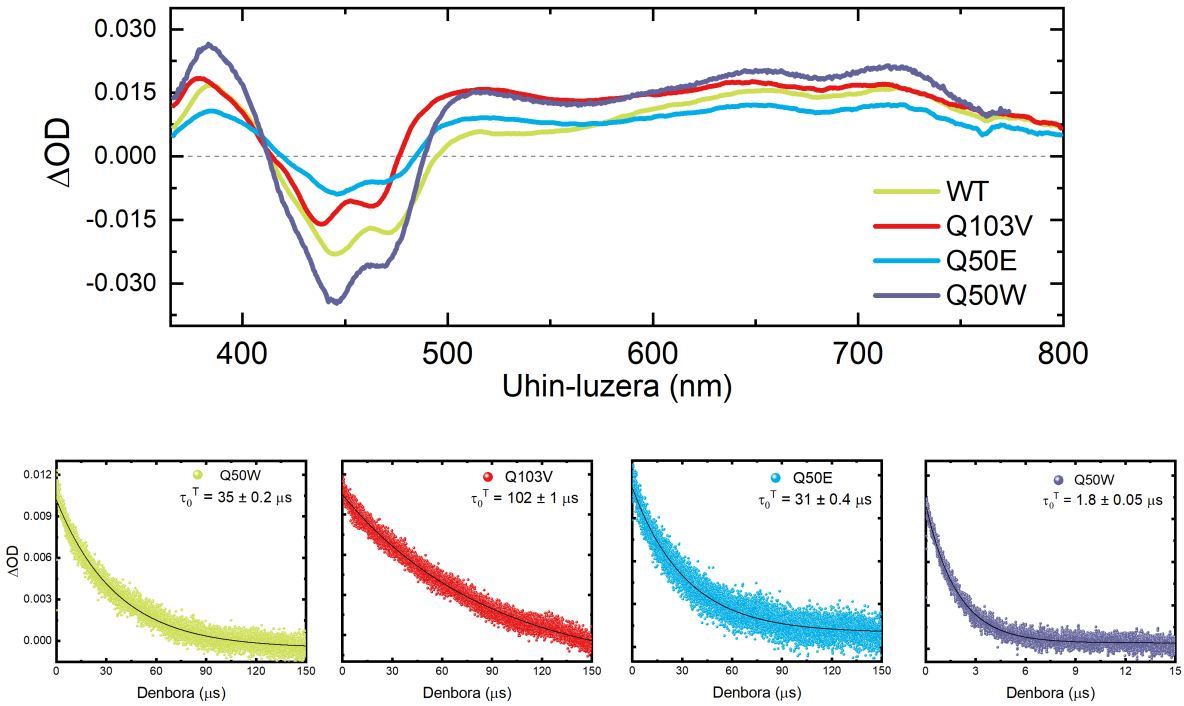

2. Irudia. miniSOG WT eta Q103V, Q50E eta Q50W mutanteen bitarteko absortzio espektroak (λ_{exc} = 445 nm) eta 720 nm-tan neurtutako triplete−triplete absortzioen beheraldiak (τ^T). Neurketa guztiak PB (20 mM, pH 7, airez asetuta) disoluzio indargetzailean egin ziren.

Fotoegonkortasuna, funtsezkoa da fotokatalisian. Hori dela eta, lau mutanteen izaera aztertu zen irradiaziopean (460 nm, 6 mW·cm^{-2}) eta baldintza esperimental desberdinen menpe. Laginak oxigenatutako disoluzioetan irradiatzerakoan, FMN-ren degradazioari zegokion 450 nm inguru agertzen zen absortzio bandaren txikitzea neurtu zen (IO 3. eta 4. Irudiak). [11,14,15,18] Flaboproteina guztiek antzeko fotodeskonposaketa pairatu zuten irradiazio denbora motzen ostean (< 10 min); katalisi esperimentuek dirauen denbora tartean (*vide infra*). WT eta Q50W laginak argi urdinarekin denbora luzeagoz irradiatu ostean, banda berri bat agertu zen 600 nm inguruan. Banda berri hori, FMN erradikal sorkuntzari egotzi zitzaion (semikinona).[18] Espezie hau, oxigenorik gabeko disoluzioetan ikus daiteke bereziki, non miniSOG-aren aminoazido egiturak ^{3}FMN*egoera eraginkortasunez desaktiba dezake eletroi

transferentzia prozesuen bitartez.[15] Gainera, denbora luzez argiztatu ondoren (> 20 min), Q103V mutanteak beste mutanteek baino fotodeskonposizio nabarmenagoa erakutsi zuen. Emaitza horiek, $^1O_2$ eta beste ROS ($O_2^{\bullet-}$ bereziki) sortzeko gaitasun handiagoarekin bat datoz, aurretik miniSOG flaboproteinarentzako erabili ziren zeharkako metodoen bitartez frogatu zen bezala (IO 5. eta 6. Irudia).[11,13] Gainera duela gutxi Bregnhøjek *et al.*, $^1O_2$ antzemateko, azido urikoa zunda moduan erabiltzea, muga garrantzitsuak dituela frogatu zuten.[19]

Oxigenorik ez zegoenean, FMN erradikalen sorkuntza nabarmenagoa zen flaboproteina guztietan (IO 7. Irudia). O_2-k, FMN-ren elektroi bakar erreduzituaren iraungipengile moduan jardun zuen (semikinona edo egoera anionikoan),[18] bigarren mailako elektroi transferentzia bidez $O_2^{\bullet-}$ emateko. FMN erradikal hauek, azkar desagertu ziren oxigenoa zuen atmosfera baten menpe berriz jartzerakoan. Aldi berean, 400–500 nm arteko FMN-ren banda ia osorik berreskuratu zen, nahiz eta hau, zati batean lumikromaren sorkuntzari eratxiki zekiokeen.[15] miniSOG proteinen artean, Q103V eta Q50W mutanteek azaldu zuten FMN erradikal sorkutza txikiena. Lehenengoaren kasuan, lehenago argitaratu zen moduan; Q103 posizioaren mutazioak, proteinatik FMN-ra gertatzen den elektroi transferentzia txikitzen du.[11,14] Bigarrenaren kasuan, $FMN^{\bullet-}/Trp^{\bullet+}$ erradikal bikoteen sorkuntza eta kontrako elektroi transferentzia prozesuek, 600 nm-ko banden intentsitate baxuagoa azaldu dezakete. Hau bitarteko absortzioaren bidez neurtutako ^{3}FMN* egoeraren bizitza-denbora motzagoarekin bat dator.[17] Hala ere, Trp-k eragindako ^{1}FMN egoera kitzikatuaren desaktibazioak ere ezaugarri espektral ezberdin hauen eragilea izan daiteke Q50W-ren kasuan, fluoreszentzia bizitza-denbora esperimentuen bidez ikusi zen moduan. Argiztatutako miniSOG eratorrien dikroismo zirkularrak, FMN erradikalaren sorkuntzak, egitura proteikoan aldaketa handirik eragin ez zuela frogatu zuen (IO 8. Irudia).

4.2.2 Azterketa katalitikoak

Ondoren, miniSOG proteinen ezaugarri fotofisiko eta kimiko bereizgarriek, nolako eragina zuten **1** eta **2** konplexuen tranformazio katalitikoan aztertu zen. Katalisi esperimentuetan, 25 µM miniSOG (karga: % 5-a), 500 µM Pt^{IV} substratu eta 1 mM NADH erabili ziren PB disoluzio indargetzailean. Aurreko lanean azaldu zen moduan, elektroi emaile kontzetrazio horiek ez zuten Pt^{IV} substratuen deskonposizio nabarmenik eragin.[2] Erreakzioaren jarraipena ilunpetan edo argi irradiazioaren menpe, ^{1}H NMR bidez egin zen, Pt^{IV} atomoari lotutako estekatzaile axialen askapena jarraituz (Xehetasun experimentalak), cisplatinoaren sorrerarekin bat datorrena.[4]

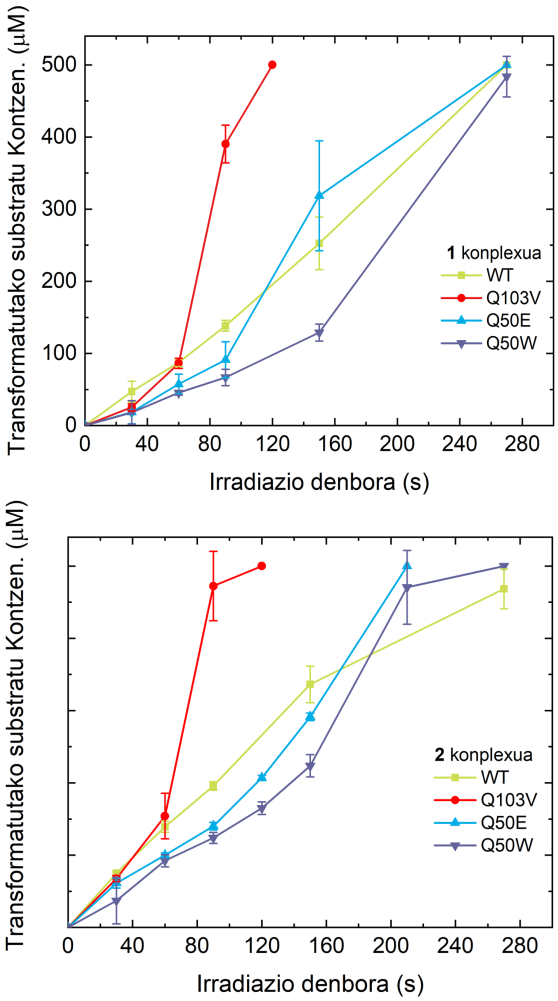

3. Irudia. miniSOG ezberdinek gauzatutako **1** eta **2** konplexuen konbertsio fotokatalitikoen profil zinetikoak. Erreakzioak NMR bidez jarraitu ziren eta 25 μM miniSOG katalizatzaile, 500 μM **1** edo **2** eta 1 mM NADH zituen PB disoluzio indargetzailea erabili zen (18 mM PB, pH 7.0, 10% D_2O).

Ilunpetan substratuen konbertsioa nekez gertatzen zela erakutsi zuten lehengo esperimentu kontrolek (IO 9. eta 10. Irudiak). Ez zen aktibitaterik neurtu lehenengo orduetan eta **1** substratuaren % 20-a eta **2** substratuaren % 60–80 inguru eraldatu ziren 48h ilunpetan miniSOG eratorrien presentzian egon ondoren. Bestetik, argi irradiazioaren menpe, erreakzioa nabarmen azkartu zen **1** eta **2** substratuentzako (3. Irudia, IO 11. eta 12. Irudiak). 1. Taulan laburbildu den moduan, fotokatalizatzaileen presentzian eta 5 minutuz argiztatu ondoren (1.8 $J \cdot cm^{-2}$) substratuen konbertsio osoa lortu zen, 20-eko berraldatzen zenbakian (TON) bihurtu zena. Horretaz gain, fotokatalizatzaile karga txikitu zenean (% 0.1) 610 eta 738 TON_{max} balioak lortu ziren 30 minutuz argiztatu ondoren (IO 13. Irudia).

Nolanahi ere, azterketa fotofisikoetatik espero zen bezala, aktibitate katalitiko handiena Q103V mutanteak erakutsi zuen. Mutante honek, Pt^{IV} substratuen % 80 inguru eraldatu zuen 90 segundoz argiztatu ostean. **1** profarmakoaren kasuan esate baterako, gertakizun hori 2.8 eta 5.8 aldiz berraldatze frekuentzia (TOF) areagotzean bihurtu zen WT eta Q50W mutanteekin alderatuta hurrenez hurren. Q50E eta WT flaboproteinen eraginkortasun katalitikoari zegokionez, biek antzeko izaera azaldu zuten (1. Taula).

1. Taula. NADH-ren presentzian miniSOG flaboproteinek katalizatutako **1** eta **2** konplexuen fotoaktibazioaren berraldatze frekuentziak (TOF, min^{-1}), berraldatze zenbakiak (TON), eta ehuneko konbertsioak (Konber.).

Konplexua	TOF (min^{-1})	TON	Konb. (%)	TON_{max}
		WT		
1	3.7±0.2	20	100	610
2	5.2±0.2	19	94	-
		Q103V		
1	10.4±0.7*	20	100	673
2	12.6±1.3*	20	100	-
		Q50E		
1	2.4±0.7	20	100	738
2	3.7±0.1	20	100	-
		Q50W		
1	1.8±0.3	20	100	734
2	3.3±0.2	20	100	-

* % 79-94 substratu konbertsio artean zehaztuta (90 segundoz irradiatuta)

Q103V mutanteak erakutsitako ^{3}FMN*-ren bizitza-denbora luzea erabakigarria da, NADH bidez gertatzen iraungipen erreduktiboa errazteko.[2] Erredukzio prozesu berezi horren ondorioz, Pt^{IV} profarmakoen eraldaketan katalitikoki aktiboa den flabina hidrokinona HFL^- espeziearen kontzentrazio altuagoa sortu zen. Izan ere, irradiazio epe laburrek (30–90 segundo), Q103V mutantean Q50W-an baino beherakada bortitzagoa eragiten zuten 450 nm inguru agertzen zen bandan. Q103V mutanteak, flabina hidrokinona eraginkortasun handiagoz sortzen zuela iradokiz (IO 14. Irudia). Azpimarratu behar da, Pt^{IV} substratuen edota NADH-ren presentzian, elektroi transferentzia erreakzioak eta erradikal espezieak sortzeko gaitasuna, aldaketa esanguratsurik ez zuela jasan (IO 15. eta 16. Irudiak). Salbuespen bakarra Q103V eratorria izan zen. **1** konplexuaren presentzian (NADH-rekin edo gabe), mutante honek, beste mutanteek baino absorbantzia intetsitate handiagoa erakutsi zuen 600 nm-tan (IO 16. eta 17. Irudiak). Hau, FMN barnean duen egitura proteikoaren eta konplexuaren arteko albo erreakzio (erradikal) baten ondorioz gerta liteke. Aurkikuntza horiek, katalisi baldintzetan, proteinak gauzatutako ^{3}FMN*-ren iraungipena aktibo zegoela eta substratu eraldaketarekin lehiatzen zuela frogatu zuten

Oxidatutako FMN barnean zuten WT, Q103V eta Q50W mutanteen simulazio molekular dinamikoen bidez ikuspegia zabaldu zen. miniSOG eratorri guztiek antzeko egitura eta FMN proteina elkarrekintza patroia erakutsi zuten. FMN-ren isoalloxazina eraztuna eta ribitilo katea proteinen poltsikoan barneratuta zeuden, fosfato taldea sarrerako kanalaren bidez eskuragarri utziz. Orokorrean, simulazioan zehar 50 posizioan kokatutako hondakina (Q edo W) bi konformazio ezberdinen artean txandakatu zen (IO 18. eta 19. Irudia). Konformazio

horiek, kanaleran barnealderantz (“itxita”) edo kanpoalderantz (“irekita”) zuzenduta zeuden. Q103V eta WT mutanteen kasuetan, konformazio horiek ez zuten kanal igarotzea oztopatzeko gaitasunik erakutsi. Horregatik, Q103V mutanteak azaldutako aktibitate katalitiko handiagoa, ^{3}FMN* egoera kitzikatuaren ezaugarrien eta 103 posizian kokatutato hondakinak eragindako iraungipen gabeziaren bidez azaldu daiteke.

Bestalde, desberdintasun gutxi batzuk ikusi ziren Q50W mutantearen kasuan. Nahiz eta mutante honen sarrera kanala zabalik egon simulazioan zehar (103V-ren eta WT-ren kontrakoa), bere konformazio “itxita” oztopatuagoa zegoen, W hondakinaren izaera handiagoagatik. Garrantzitsuago, W-ren albo katearen izaera ez polarrak, Na^{+} ioiak bezalako partikula kargatuen hedapena kanalean zehar FMN-ren fosfato talderaino murriztu zuen, baita “irekita” konformazioan ere (IO 20. Irudia). Hondakin honek, FMN-ren fosfato taldera sarrera ahalbidetzen duten elkarrekintza erakargarriak ezartzen zituela adierazi zuten aurkikuntza horiek. Antzeko izaera espero daiteke kargatutako edo molekula polarrekin (Pt^{IV} substratuak edo NADH, esate baterako). Hortaz, Q50W-ren aktibitate katalitikoa, honen egoera kitzikatuen ezaugarrietara ez ezik, guztiz eraginkorra ez zen sarrera kanal bati ere lotuta egon zitekeela iradoki zuen emaitzek.

4.3 Ondorioak

Kontzeptu froga ikerketa honek, mutagenesi guneratua, metal konplexuak substratu gisa erabiltzen dituen erreakzio artifizialetan flaboproteinen ekintza katalitikoa aldatu edo handitzeko balio zuela frogatu zuen. Emaitza horiek, ingeniaritza proteikoaren bidez miniSOG-aren fotofisika ezaugarriak aldatuz lortu ziren. Gainera, erreakzio katalitikoetan substratuaren loturan edo produktu askapen pausoetan eragina izan dezaketen egitura aldaketek hobekuntza handiagoak ekar ditzaketela uste da. Gaur egun, helburu horiek lortzeko, miniSOG-ak baino funtzionamendu eta egitura konplexutasun handiagoa duten flaboentzimen eraldaketak ikertu behar direla uste da.

4.4 Xehetasun esperimentalak

Materialak eta Metodoak

Riboflabina 5´-monofosfato sodio gatz hidratatua (FMN), potasio fosfato monobasikoa, potasio fosfato dibasikoa, β-nikotinamida adenina dinukleotidoa, erreduzitutako disodio gatz hidratatua Sigma-Aldrichen erosi ziren eta Potasio tetrakloroplatinatoa(II) Precious Metals Online-tik lortu ziren. Guztiak, jaso bezala eta purifikazio gehigarririk gabe erabili ziren.

Pt^{IV} konplexuen prestakuntza. *cis,cis,trans*-[$Pt(NH_3)_2(Cl_2)(O_2CCH_2CH_2CO_2H)_2$] (**1**) eta *cis,cis,trans*-[$Pt(NH_3)_2(Cl_2)(O_2CCH_3)_2$] (**2**) konplexuak, aurretik azaldu zen bezala sintetizatu eta karakterizatu ziren.[20]

Mutagenesi guneratua, proteinen adierazpena eta purifikazioa. QuikChange mutagenesi guneratua erabili zen pPRO-EX-HTA kodifitzen zuen plasmidoan Q50W eta Q50E mutazioak barneratzeko. Erreakzioak, *Escherichia coli* DH10b zelula konpetenteetan transformatu ziren, hautatutako kolonien DNA plasmidoak miniprep kita (Omega Bio-Tek) bidez atera ziren eta mutanteen identifikazioa sekuenziazio bidez egiaztatu zen (IO 1. Taula). Aurretik deskribatutako 103V mutantea, Pbad-Myc-His plasmidoan klonatu zen. Plasmidoak barnean zituzten bakteriak −80 °C-tan eta % 20 glizerolean (v/v) gorde ziren. WT, Q50W eta Q50E proteinak *E. coli* (C41) bakterietan adierazi ziren eta aurreko lanean bezala purifikatu ziren.[1] Q103V mutantea ordea, DH10β zeluletan, Florsek eta kolaboratzaieleek deskribatu zuten moduan egin zen.[14]

IO 1. Taula. miniSOG sekuentzien zatiak pDRAW bidez ikusita.

Izena	Mutatutako posizioa	Jatorrizko hondakina	Ordezko hondakina	Primer(5'-3') (Rev)
Q50E	50	Q	E	CTGAACAGTTGCTTCATCGGTTTCCGG
Q50W	50	Q	W	CTGAACAGTTGCCCAATCGGTTTCCGG
WT sekuentzia				
M E K S F V I T D P R L P D N P I I F A S D G F L E L T E Y S R E E I L G R N G R F L Q G P E T D Q A T V Q K I R D A I R D Q R E I T V Q L I N Y T K S G K K F W N L L H L Q P M R D Q K G E L Q Y F I G V Q L D G				
Q50E sekuentzia				
M E K S F V I T D P R L P D N P I I F A S D G F L E L T E Y S R E E I L G R N G R F L Q G P E T D **E** A T V Q K I R D A I R D Q R E I T V Q L I N Y T K S G K K F W N L L H L Q P M R D Q K G E L Q Y F I G V Q L D G				
Q50W sekuentzia				
M E K S F V I T D P R L P D N P I I F A S D G F L E L T E Y S R E E I L G R N G R F L Q G P E T D **W** A T V Q K I R D A I R D Q R E I T V Q L I N Y T K S G K K F W N L L H L Q P M R D Q K G E L Q Y F I G V Q L D G				

Argi ultramore-ikuskorreko absortzio-espektroskopia (UMore-Ikus). Espektro guztiak, JASCO V-730 espektrofotometroa erabiliz lortu ziren. Laginak PB disoluzio indargetzailean disolbatu eta kuartzozko kubeta optikoetan neurtu ziren.

Emisio fluoreszentea eta bizitza-denbora. FMN-ren (20 µM) emisio espektroa Edinburgh instruments espektrofluorimetroan (FL1000 modeloa) neurtu zen. 450W-ko Xenon flash lanpara erabili zen, kitzikapen iturri bezala. Fluoreszentzia beheraldien kurba (τ^S) denbora korrelatibo fotoi bakar zenbatzaile teknikarekin λ_{em} = 540 nm-tan neurtu zen 100 ps FWHM pultsuko EPL-485 laserrarekin (Edinburgh) λ_{kitz} = 485nm-tara kitzikatu ostean, pikosegundoko (ps) ebazpen tenporala duen mikrokanal plaka detektagailua erabiliz. Iterazio-metodoen bidez neurtutako beheraldi kurben seinale erantzun instrumentalaren

dekonboluzioa egin ostean, bizitza-denbora fluoreszenteak lortu ziren. Doiketa esponentzialaren egokitasuna, parametro estatistikoen (χ^2 eta hondarren analisia) bidez kontrolatu zen. Neurketak, WT eta honen Q103V, Q50E and Q50W mutanteak PB disoluzio indargetzailean disolbatuz egin ziren (20 mM, pH 7, airez asetuta). Emisio eta bizitza-denbora neurketak miniSOG proteinen 3 eta 15 µM erabiliz egin ziren hurrenez hurren.

Bitarteko absortzioa eta bizitza-denbora tripleteak. Nano segundo bitarteko absortzio neurketak, LP980 laser flash fotolisi espektrometro (Edinburgh Instruments, Livingston, UK) batean egin ziren. Laginak, absortzio maximoan (445 nm) nanosegundoko laser pultsatuaren (Nd:YAG laser/OPO, LOTIS TII 2134) bidez kitzikatu ziren, 1Hz, 7 ns pultsu amplitudearekin eta 6.5 mW-ko kitzikapen potentziarekin (10 mW Q50W mutantearen kasuan). Kitzikapen uhin-luzeran 0.3 absortzio optikoa zuten airez asetutako disoluzioak erabili ziren neurketa horietarako. Bitarteko espektroak, ICCD detektoreakin lortu ziren(DH320T airez hoztuta, Andor Technology). Triplet-triplete absortzioaren beheraldia, oxigenoaren presentzian (airez asetutako disoluzioak) 720 nm-tara lortu ziren PMT detektagailuan eta osziloskopioan. Oxigenoaren presentzia bizitza-denbora tripleteak (τ^T) beheraldi kurben maldetatik lortu ziren LP 900 software-n iterazio-metodoen bitartez. Doiketa esponentzialaren egokitasuna, parametro estatistikoen (χ^2 eta hondarren analisia) bidez kontrolatu zen. 20 µM miniSOG proteina (31 µM Q50W-ren kasuan) PB disoluzio indargetzailean (20 mM, pH 7, airez asetuta) disolbatu zen esperimentu talde hau egiteko.

Oxigeno singletearen eta ROS-en formakuntza. $^1O_2$ eta ROS-en kuantifikazioa, aurretik **FMN** eta **miniSOG**-entzako onartutako metodoak erabiliz gauzatu zen.[11,13] Azido urikoa (UA), zunda moduan erabili zen $^1O_2$-aren zeharkako neurketak egiteko.[21] Absorbantzia aldaketak 292 nm-tan jarraitu ziren, argi irradiazio denbora aurrera joan ahala. Optikoki bat zetozen UA (30 µM) eta miniSOG proteina (3 µM), disoluzioak, 460 nm-ko argi (6 $mW \cdot cm^{-2}$) iturriaren eraginpean jarri ziren.
Beste ROS-en (zehazki $O_2^{\bullet -}$) ebaluazioa odea, hidroetidiumaren (HE) fotooxidazioaren bidez egin zen. Zunda hau, $^1O_2$ erreakzionatzen ez duelako aukeratu zen.[11,22] Kasu honetan HE (30 µM) disoluzioak, miniSOG (3 µM) katalizatzailaerekin batera 460 nm-tara irradiatu ziren eta haien fluoresnzentzia intentsiatea denbora puntu ezberdinetan neurtu zen (λ_{ex} = 525 nm, λ_{em} = 550–800 nm); aurretik deskribatu zen moduan.[11]

Dikroismo zirkularra (CD). J-1500 espectrofotometro batean egin ziren neurketak. CD espektroak, tenperatura baldintza normaletan egin ziren, 0.1 cm bide optikoa zuen kubetarekin eta hurrengo parametroekin: sentikortasuna 200 mdeg; 0.1 nm-ko datu neurria; 50 nm/min-ko eskaneatze abiadura; 8 segundoko erantzuna; 1nm-ko banda zabalera. Espektroaren 190–260 nm eskualdean neurketak egiteko, 3 µM miniSOG flaboproteina erabili zen

Erresonantzia magentiko nuklearra (NMR). Lagin ezberdinen ^1H NMR espektroak, Fourier TM Bruker 300 NMR espektrometro batean pultsu estandarreko programak erabiliz egin

ziren. Lekualdaketa kimikoak milioiko partetan (δ, ppm) adierazi ziren eta disolbatzaile hondakin seinalearekiko erreferentziatu ziren

Esperimentu katalitikoak. Erreakzio guztiak 298 K-etan eta pH 7.0-an egin ziren, 25 µM katalizatzaile, 500 µM substratu (**1** eta **2**) eta 1 mM NADH erabiliz. Irradiazioak LED argi iturri batekin (λ_{max} = 460 nm, 6 $mW{\cdot}cm^{-2}$) egin ziren. ^{1}H NMR bidez neurtutako **1** eta **2** substratuen konbertsio kantitatea kuantifikatuz berraldatze frekuentzia, (TOF), berraldatze zenbakia (TON) eta erreakzio katalitikoen % konbertsioa zehaztu ziren. Sukzinato eta azetato estekatzaile askeen seinaleak integratuz (2.25–2.35 ppm-tara eta 1.80 ppm inguru azaltzen diren singleteak hurrenez hurren) erreakzioaren jarraipena egin zen. TOF balioak, substratu konbertsioa % 25–35 artean (90 s argi irradiazio ostean) zegoenean zehaztu ziren, Q103V mutantearen kasuan izan ezik, substratuen konbertsioa % 80–94 artean zegoen kasu honetan. TON_{max} balioak 1 µM miniSOG flaboproteina, 1 mM NADH eta 1 mM **1** erabiliz lortu ziren.

Metodo konputazionalak. Barnean, FMN kromoforoa oxidatutako egoeran zuten miniSOG WT, Q50W eta Q103V flaboproteinen atomo guztien simulazio dinamiko molekularra (MD) egin zen. MD simulazioak egiteko, FMN-rekin konplexutako miniSOG egitura Proteina Data Bankutik (PDB: 6GPU) lortu zen.[15] X-izpi egitura hau atomo guztiak dituen MD simulazioentzat prestatu zen, hidrogeno atomoak gehituz eta bi orientazio posibleen artean hondakinen orientazioa aukeratuz. Proteinekin erabili ziren parametroak TIP3P ur ereduari hedapena zuen atomo guztien indar atomiko AMBER99SB-ILDN eremuari lotuta zeuden.[23] FMN-rentzat, AMBER parametro datu-basea erabili zen.[24] Q50W eta Q103V mutazioak VMD softwarearen bidez egin ziren.[25] Ur solbatazio ingurunea kutxa dodekaedriko erronboa zuen solbatazio sistema batekin sortu zen,[26] non proteina eta ur kutxaren azkeneko geruzaren arteko distantzia 12 Å ziren. Ondoren, Na^{+} eta Cl^{-} ioiak ausazko posizioetan jarri ziren sistemak neutralizatzeko eta zelula kanpoan aurkitzen den 0.15 M-eko kontzetrazio fisiologikoa irudikatzeko.

Ekoizpen fasean zehar, aldizkako mugalde-bandintzak erabili ziren isoterma-isokoriko taldearekin (NVT) batera oreka epealdian eta isoterma-isokoriko taldea (NPT) 1 atm eta 300 K-etan Parrinello-Rahman barostatoa[27] eta Nosé-Hoover termostatoaren[28] bidez. Newtonen mugimendu ekuazioak zenbakiz integratu ziren Verlet algoritmo[29] jauzia erabiliz 2 fs denbora pausuarekin. Hidrogenoa barne hartzen zuten lotura konbalenteen luzeerak, LINCS algoritmoarekin mugatu ziren.[30] Hasiera batean, ur molekulak, 10000 mailatan erlaxatu ziren[31] atomo solutu guztiak mantenduz eta ioi posizioak jatorrizko koordinatuak 5,000 kJ/mol^{-1} nm^{-1} potentzial harmoniko konstatea erabiliz egin ziren. Orduan, ioien mugak erlaxatu ziren eta disolbentea (ura eta ioiak) 10000 aldiz erlaxatu zen, solutu atomoak mantenduz. Hasiera puntu honetatik, 4 ns-ko oreka fase hasi zen. Lehenengo 2 ns-tan, dinamika molekularra 300K-tan egin zen NVT taldea erabiliz Bussi termostatoaren bitartez. Solutu atomoen muga harmonikoak pixkanaka askatzen joan ziren simulazioan zehar. Oreka fasearen azkeneko 2 ns-tan NPT taldea 1 atm eta 300K-etan erabili zen. Azkenik, ekoizpen

fase dinamika molekularrak 100 ns iraun zuen. Simulazio guztiak GROMACS molkula dinamika paketearekin egin ziren, 2018ko bertsioarekin hain zuzen ere.[32]
FMN fosforil oxigenoen inguruko Na^+ katioien distribuzio erradial funtzioak (RDF)[33] GROMACS RDF tresnarekin kalkulatu ziren. Disolbentearentzat eskuragarri dagoen area (SAS) eta sistemen gainazaleko potentzial elektrostatikoa, PDB2PQR eta Adaptive Poisson-Boltzmann Solver (APBS) softwarearen bidez kalkulatu ziren.[33,34]

4.5 Erreferentziak

(1) Alonso-de Castro, S.; Cortajarena, A. L.; López-Gallego, F.; Salassa, L.; Lopez-Gallego, F.; Salassa, L.; López-Gallego, F.; Salassa, L. Bioorthogonal Catalytic Activation of Platinum and Ruthenium Anticancer Complexes by FAD and Flavoproteins. *Angew. Chem., Int. Ed.* **2018**, *57*, 3143–3147.

(2) Gurruchaga-Pereda, J.; Martínez-Martínez, V.; Rezabal, E.; Lopez, X.; Garino, C.; Mancin, F.; Cortajarena, A. L.; Salassa, L. Flavin Bioorthogonal Photocatalysis Toward Platinum Substrates. *ACS Catal.* **2020**, *10*, 187–196.

(3) Alonso-de Castro, S.; Ruggiero, E.; Ruiz-de-Angulo, A.; Rezabal, E.; Mareque-Rivas, J. C.; Lopez, X.; López-Gallego, F.; Salassa, L. Riboflavin as a Bioorthogonal Photocatalyst for the Activation of a Pt(IV) Prodrug. *Chem. Sci.* **2017**, *8*, 4619–4625.

(4) Alonso-de Castro, S.; Terenzi, A.; Hager, S.; Englinger, B.; Faraone, A.; Martinez, J. C.; Galanski, M.; Keppler, B. K.; Berger, W.; Salassa, L. Biological Activity of Pt(IV) Prodrugs Triggered by Riboflavin-Mediated Bioorthogonal Photocatalysis. *Sci. Rep.* **2018**, *8*, 1–10.

(5) Ruffoni, A.; Juliá, F.; Svejstrup, T. D.; McMillan, A. J.; Douglas, J. J.; Leonori, D. Practical and Regioselective Amination of Arenes Using Alkyl Amines. *Nat. Chem.* **2019**, *11*, 426–433.

(6) Gong, L.; Lin, Z.; Harms, K.; Meggers, E. Isomerization-Induced Asymmetric Coordination Chemistry: From Auxiliary Control to Asymmetric Catalysis. *Angew. Chem., Int. Ed.* **2010**, *49*, 7955–7957.

(7) Mazzei, L. F.; Martínez, Á.; Trevisan, L.; Rosa-Gastaldo, D.; Cortajarena, A. L.; Mancin, F.; Salassa, L. Toward Supramolecular Nanozymes for the Photocatalytic Activation of Pt(IV) Anticancer Prodrugs. *Chem. Commun.* **2020**, *56*, 10461–10464.

(8) Chen, K.; Arnold, F. H. Engineering New Catalytic Activities in Enzymes. *Nat. Catal.* **2020**, *3*, 203–213.

(9) Arnold, F. H. Innovation by Evolution: Bringing New Chemistry to Life (Nobel Lecture). *Angew. Chem., Int. Ed.* **2019**, *58*, 14420–14426.

(10) Shu, X.; Lev-Ram, V.; Deerinck, T. J.; Qi, Y.; Ramko, E. B.; Davidson, M. W.; Jin, Y.; Ellisman, M. H.; Tsien, R. Y. A Genetically Encoded Tag for Correlated Light and Electron Microscopy of Intact Cells, Tissues, and Organisms. *PLoS Biol.* **2011**, *9*, e1001041.

(11) Westberg, M.; Holmegaard, L.; Pimenta, F. M.; Etzerodt, M.; Ogilby, P. R. Rational Design of an Efficient, Genetically Encodable, Protein-Encased Singlet Oxygen Photosensitizer. *J. Am. Chem. Soc.* **2015**, *137*, 1632–1642.

(12) Westberg, M.; Bregnhøj, M.; Etzerodt, M.; Ogilby, P. R. Temperature Sensitive Singlet Oxygen Photosensitization by LOV-Derived Fluorescent Flavoproteins. *J. Phys. Chem. B* **2017**, *121*, 2561–2574.

(13) Ruiz-González, R.; Cortajarena, A. L.; Mejias, S. H.; Agut, M.; Nonell, S.; Flors, C. Singlet Oxygen Generation by the Genetically Encoded Tag Minisog. *J. Am. Chem. Soc.* **2013**, *135*, 9564–9567.

(14) Rodríguez-Pulido, A.; Cortajarena, A. L. L.; Torra, J.; Ruiz-González, R.; Nonell, S.; Flors, C. Assessing the Potential of Photosensitizing Flavoproteins as Tags for Correlative Microscopy. *Chem. Commun.* **2016**, *52*, 8405–8408.

(15) Torra, J.; Lafaye, C.; Signor, L.; Aumonier, S.; Flors, C.; Shu, X.; Nonell, S.; Gotthard, G.; Royant, A. Tailing MiniSOG: Structural Bases of the Complex Photophysics of a Flavin-Binding Singlet Oxygen Photosensitizing Protein. *Sci. Rep.* **2019**, *9*, 1–10.

(16) Cardoso, D. R.; Franco, D. W.; Olsen, K.; Andersen, M. L.; Skibsted, L. H. Reactivity of Bovine Whey Proteins, Peptides, and Amino Acids toward Triplet Riboflavin as Studied by Laser Flash Photolysis. *J. Agric. Food Chem.* **2004**, *52*, 6602–6606.

(17) Bialas, C.; Barnard, D. T.; Auman, D. B.; McBride, R. A.; Jarocha, L. E.; Hore, P. J.; Dutton, P. L.; Stanley, R. J.; Moser, C. C. Ultrafast Flavin/Tryptophan Radical Pair Kinetics in a Magnetically Sensitive Artificial Protein. *Phys. Chem. Chem. Phys.* **2019**, *21*, 13453–13461.

(18) Pimenta, F. M.; Jensen, R. L.; Breitenbach, T.; Etzerodt, M.; Ogilby, P. R. Oxygen-Dependent Photochemistry and Photophysics of "MiniSOG," a Protein-Encased Flavin. *Photochem. Photobiol.* **2013**, *89*, 1116–1126.

(19) Bregnhøj, M.; Dichmann, L.; McLoughlin, C. K.; Westberg, M.; Ogilby, P. R. Uric Acid: A Less-than-Perfect Probe for Singlet Oxygen. *Photochem. Photobiol.* **2019**, *95*, 202–210.

(20) Gramatica, P.; Papa, E.; Luini, M.; Monti, E.; Gariboldi, M. B. B.; Ravera, M.; Gabano, E.; Gaviglio, L.; Osella, D. Antiproliferative Pt(IV) Complexes: Synthesis, Biological Activity, and Quantitative Structure-Activity Relationship Modeling. *J. Biol. Inorg. Chem.* **2010**, *15*, 1157–1169.

(21) Rabello, B. R.; Gerola, A. P.; Pellosi, D. S.; Tessaro, A. L.; Aparício, J. L.; Caetano, W.; Hioka, N. Singlet Oxygen Dosimetry Using Uric Acid as a Chemical Probe: Systematic Evaluation. *J. Photochem. Photobiol. A.* **2012**, *238*, 53–62.

(22) Gomes, A.; Fernandes, E.; Lima, J. L. F. C. Fluorescence Probes Used for Detection of Reactive Oxygen Species. *J. Biochem. Biophys. Methods* **2005**, *65*, 45–80.

(23) Jorgensen, W. L.; Chandrasekhar, J.; Madura, J. D.; Impey, R. W.; Klein, M. L. Comparison of Simple Potential Functions for Simulating Liquid Water. *J. Chem. Phys.* **1983**, *79*, 926–935.

(24) Schneider, C.; Sühnel, J. A Molecular Dynamics Simulation of the Flavin Mononucleotide–RNA Aptamer Complex. *Biopolymers* **1999**, *50*, 287–302.

(25) Humphrey, W.; Dalke, A.; Schulten, K. VMD: Visual Molecular Dynamics. *J. Mol. Graph.* **1996**, *14*, 33–38.

(26) Bekker, H.; Van Den Berg, J. P.; Wassenaar, T. A. A Method to Obtain a Near-Minimal-Volume Molecular Simulation of a Macromolecule, Using Periodic Boundary Conditions and Rotational Constraints. *J. Comput. Chem.* **2004**, *25* (8), 1037–1046.

(27) Parrinello, M.; Rahman, A. Polymorphic Transitions in Single Crystals: A New Molecular Dynamics Method. *J. Appl. Phys.* **1981**, *52*, 7182–7190.

(28) Nosé, S. A Molecular Dynamics Method for Simulations in the Canonical Ensemble. *Mol. Phys.* **1984**, *52*, 255–268.

(29) Hockney, R. W.; Goel, S. P.; Eastwood, J. W. Quiet High-Resolution Computer Models of a Plasma. *J. Comput. Phys.* **1974**, *14*, 148–158.

(30) Hess, B.; Bekker, H.; Berendsen, H. J. C.; Fraaije, J. G. E. M. LINCS: A Linear Constraint Solver for Molecular Simulations. *J. Comput. Chem.* **1997**, *18*, 1463–1472.

(31) Abraham, M. J.; van der Spoel, D.; Lindahl, E.; Hess, B. and the G. development team. GROMACS User Manual Version **2018**.

(32) Abraham, M. J.; Murtola, T.; Schulz, R.; Páll, S.; Smith, J. C.; Hess, B.; Lindahl, E. GROMACS: High Performance Molecular Simulations through Multi-Level Parallelism from Laptops to Supercomputers. *SoftwareX* **2015**, *1–2*, 19–25.

(33) Verlet, L. Computer “Experiments” on Classical Fluids. II. Equilibrium Correlation Functions. *Phys. Rev.* **1968**, *165*, 201–214.

(34) Jurrus, E.; Engel, D.; Star, K.; Monson, K.; Brandi, J.; Felberg, L. E.; Brookes, D. H.; Wilson, L.; Chen, J.; Liles, K.; et al. Improvements to the APBS Biomolecular Solvation Software Suite. *Protein Sci.* **2018**, *27*, 112–128.

Ondorioak

Azkeneko hamarkadan, hurbilketa katalitiko bioortogonalek arreta handia erakarri dute terapien mugak gainditzeko aukera bideragarri gisa. Doktorego tesi honetan eztabaidatutako hiru estrategia katalitiko bioortogonal nagusien artean, nire lanak, konplexu metalikoak katalizatzaile moduan erabili beharrean substratu moduan erabiltzen dituen erreakzio fotokatalitiko bioortogonal ez-ohikoak garatu eta zabaldu nahi ditu. Riboflabinak gauzatutako Pt^{IV} konplexuen eraldaketa katalitikoaren aurkikuntzak, erreakzio ez-natural berezi hau xehetasun handiagoz ikertzea motibatu zuen. Disoluzioan, flabina askeek eta kapsulatutakoek, Pt^{IV} profarmako inerteak Pt^{II} espezie toxikoetan eraginkortasun eta selektibitate handiarekin eraldatzeko ahalmena azaldu zuten. Gainera, biomolekula ugari zituen zelula kultibo ingurunean, errakzio fotokatalitikoaren eraginkortasuna mantendu zen.

Doktoregoan zehar, flabinen bitartez gauzatutako platino substratuen fotokatalisi bilduma zabaldu dut. Lau platino substratu eta bost flabina katalizatzaile ikertu ziren, erreakzio fotokatalitiko berezi honen katalogoa handituz. Metodo konputazionalek, datu esperimentalekin batera, ribitilo kateak eraginkortasun katalitikoan eragin zuzena zuela erakutsi zuten. Albo kate honek, erreduzitutako flabinaren (espezie katalitiko aktiboa) eta substratu metalikoaren arteko elkarrekintza errazten du. Aztertutako katalizatzaileen artean, MiniSOG (mini Singlet Oxygen Generator) flaboproteinak eraginkortasun txikiena erakutsi zuen. Fenomeno hau, FMN kromoforoaren inguruko proteina egiturak, egoera kitzikatu tripletearen iraungipenarekin lotu daiteke. Horretaz gain, Pt^{IV} konplexuen fotoerredukzioa gauzatzen zuten espezie katalitiko aktiboak identifikatu ziren. Oinarrizko xehetasun mekanistikoak, O_2-rik gabeko baldintzetan, NMR espektroskopia bidez argitu ziren.

Doktorego proiektu honetan , miniSOG flaboproteina eta honen hiru eratorri (Q103V, Q50E eta Q50W) baldintza ezberdinen menpe aztertu ziren. Ikerketan, NADH bezalako elektroi emaileen presentzian, flaboproteina hauek bi cisplatino profarmako eraldatzeko zuten gaitasuna aztertu zen. 103 posizioan balina (V) bezalako amino azido hidrofobo batekin egindako mutazioak, FMN-ren egoera kitzikatu tripletearen bizitza denbora 35 µs-etatik (WT) 102 µs-etara handitu zuen. Beste flaboproteina mutanteekin alderatuta, Q103V mutanteak aktibitate katalitiko handiena erakutsi zuen. 50 posizioan bolumen handiko triptofanoarekin egindako mutazioa egoera kitzikatu tripletearen bizitza denbora 35 µs-etatik (WT) 1.8 µs-etara txikitu zuen; eraginkortasun txikieneko katalizatzailea izanik. Guneratutako mutagenesia prozesu katalitiko entzimatiko asko hobetzeko erabili den arren, guneratutako mutagenesiaren erabilera Pt^{IV} profarmakoen (i.e. substratu metalikoak) aktibazio katalitikoa eraldatzeko ez da inoiz ikertu.

Orokorrean, tesi honek, flabinek gauzatutako Pt^{IV} substratuen fotokatalisi eraldaketa mekanismoa hobeto ulertzen lagundu du. Metal konplexuak ez-ohiko substratu bezala

erabiltzen dituen erreakzio katalitikoen epe luzeko garapenean, aurrera pauso bat besterik ez da. Flabinek katalizatutako Pt profarmakoen eraldaketaren alderdi asko argitu behar dira oraindik, sistema biologikoen barnean profarmakoen aktibazio eraginkorrena lortzeko.

Testuinguru horretan, helburu terapeutikoetarako diseinatutako profarmako metalikoen aktibazio fotokatalitiko bioortogonala garatu dadin, hurrengo faktoreak ezinbestekoak direla usted dut:

- Flabinak argi urdinarekin kitzikatzerakoan, hauek sortutako albo erreakzioen eragin erreala zehaztea. Argi irradiazioran menpe, kromoforoak, oxigeno espezie erreaktiboen sorrera eragiten du. Espezie erreaktibo hauek kuantifikatu egin behar dira prozesu katalitikoa sakonago ulertzeko eta azkenik optimizatzeko. Horretaz gain, metodo konputazionalek eta esperimentalek azaldu zuten moduan, carboplatino eratorrien estekatzaile disoziazioa ez da soilik posizio axialetara murrizten. Hau ez da cisplatino analogoen kasuen gertatzen. Hala ere, horren eraginez, eraginkortasuna gutxitu daiteke eta beraz, profarmakoen egitura aldaketak lagungarriak izan daitezke disoziazio eta aktibazio selektiboagoa lortzeko.
- Argi urdinak flaboproteinen amino azidoetan eragindako aldaketa kimikoak teknika ezberdinen bidez (NMR edo erresonantzia paramagnetiko elektronikoa esate baterako) ikertzea. Teknika hauek, eraginkortasun katalitikoa hobetzeko helburuarekin, guneratutako mutagenesiaren kokalekua zehazten lagundu dezakete (erradikalen sorrera edo atzerako elektroi transferentzia prozesuak saihestuz).
- Profarmakoak aktibatzeko estrategia katalitiko bikoitzen bidez, zenbait itu dituzten farmakoek, zelula erresistentzia mekanismoak saihesten edo txikitzen lagundu dezakete. Kalte zelularra mekanismo ezberdinen bidez gauzatzeak, minbiziaren kontrako agenteen efektu toxikoa handitu dezake. Gainera, sistema katalitikoek, profarmakoen aktibazioaren kontrol espazio-tenporala hobetu dezakete.
- Kromoforoaren egitura aldaketak (porfirinak esate baterako), eta honekin batera ezaugarri fotokimikoak, fotokatalizatzaileen absortzio ahalmena uhin-luzera handiagotara aldatzea baimendu dezake. Uhin-luzera hauek, helburu terapeutikoetarako aproposak dira, sistema biologikoetan kalte txikiagoak eragiten dituztelako eta horretaz gain, ehunetan sakonago barneratzen direlako.

3. Kapituluaren Eranskina

Flabinen Fotokatalisi bioortogonala Platino Substratuentzako

Informazio Osagarria

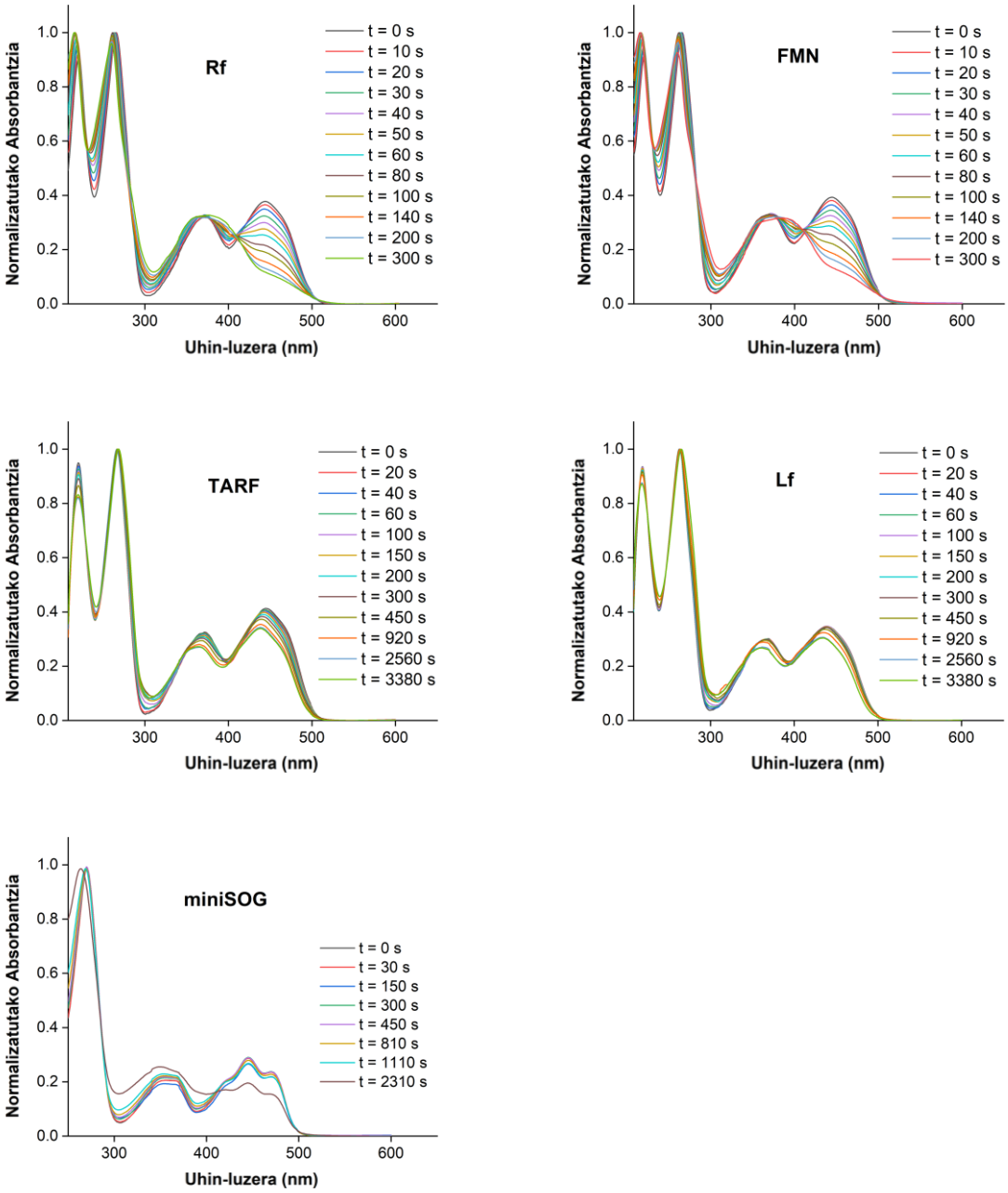

IO 1. Irudia. Flabina katalizatzaileen (13 µM) fotoegonkortasuna PB disoluizioan (20 mM, pH 7), argi urdinaren irradiazioaren menpe (460 nm, 6 $mW \cdot cm^{-2}$).

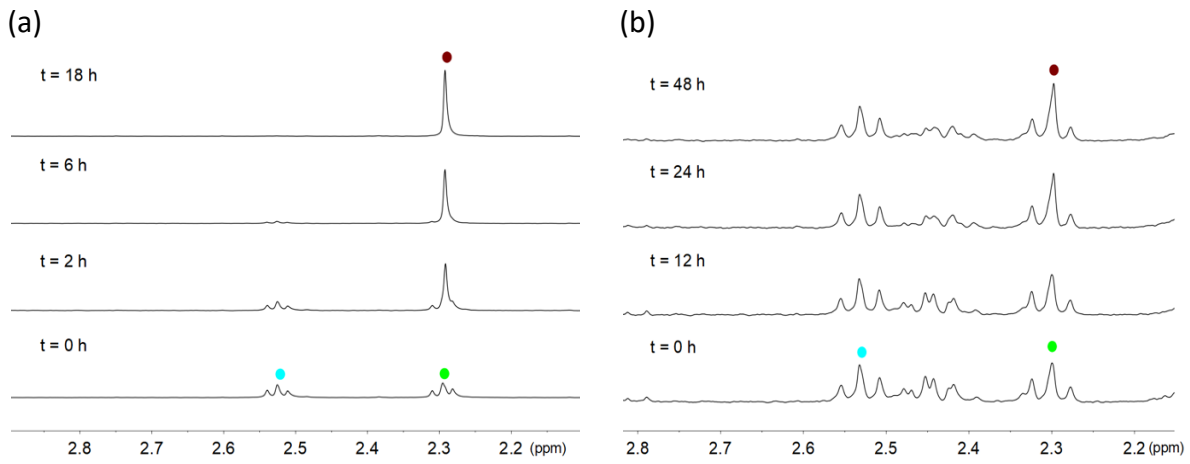

IO 2. Irudia. 1 konplexuaren (500 µM) egonkortasuna ilunpetan 18 mM PB (pH 7.0, % 10 D_2O) disoluzioan, 1 mM askorbatoren (a) eta glutationaren (b) presentzian.
^{1}H NMR seinaleen etiketak ● NADH, ● Pt–OCO**CH$_2$**CH$_2$CO$_2^-$, ● Pt–OCOCH$_2$**CH$_2$**CO$_2^-$, ●$^-$ O$_2$C**CH$_2$CH$_2$**CO$_2^-$ askea.

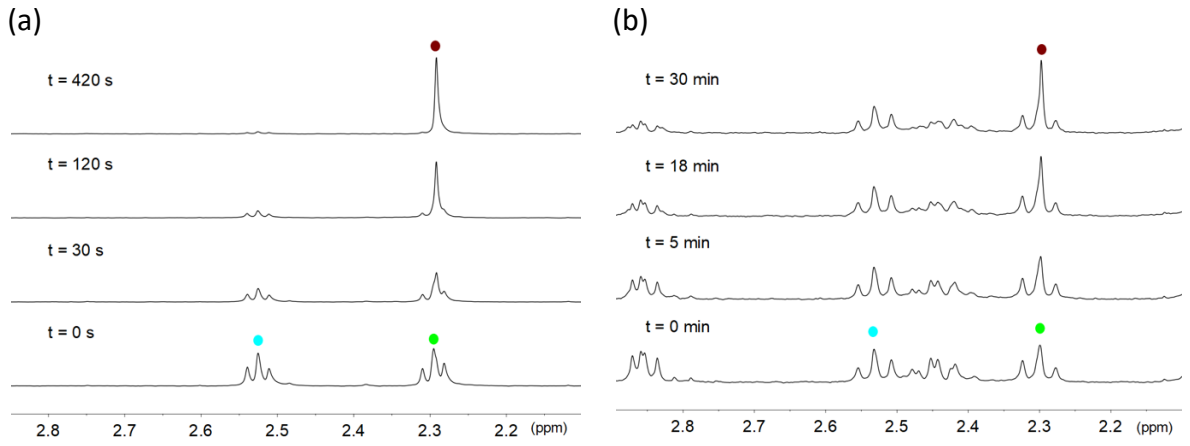

IO 3. Irudia. 1 konplexuaren (500 µM) aktibazio fotokatalitikoa 18 mM PB (pH 7.0, % 10 D_2O) disoluzioan, 1 mM askorbatoaren (a), glutationaren (b) eta 1 µM **Rf**-ren presentzian, 460 nm-ko argi irradiazioaren menpe (6 mW·cm^{-2}).
^{1}H NMR seinaleen etiketak ● NADH, ● Pt–OCO**CH$_2$**CH$_2$CO$_2^-$, ● Pt–OCOCH$_2$**CH$_2$**CO$_2^-$, ●$^-$ O$_2$C**CH$_2$CH$_2$**CO$_2^-$ askea.

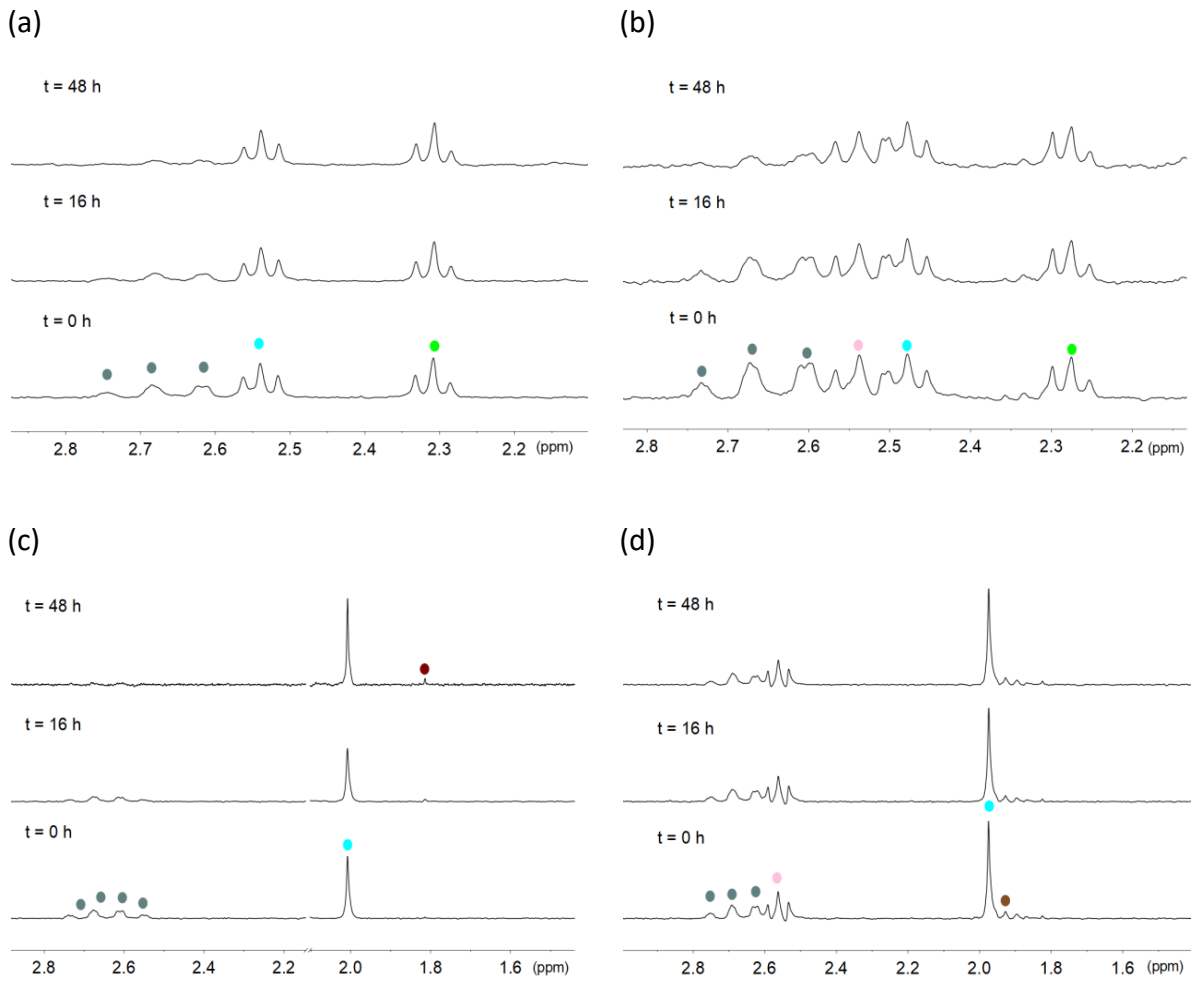

IO 4. Irudia. 1–4 konplexuen (500 µM) egonkortasuna 48 orduz ilunpetan 18 mM PB (pH 7.0, % 10 D_2O) disoluzioan, 1 mM NADH-ren presentzian.
^{1}H NMR seinaleen etiketak: ● NADH, (a) **1**, ● Pt–OCO**CH$_2$**CH$_2$CO$_2^-$, ● Pt–OCOCH$_2$**CH$_2$**CO$_2^-$; (b) **2**, ● Pt–OCO**CH$_2$**CH$_2$CO$_2^-$, ● Pt–OCOCH$_2$**CH$_2$**CO$_2^-$, ● Pt–[(OCO)$_2$C(**CH$_2$**)$_2$**$_2$**CH$_2$]; (c) **3**, ● Pt–OCO**CH$_3$**, ● $^-$OCO**CH$_3$** askea eta (d) **4**, ● Pt–OCO**CH$_3$**, ● Pt–[(OCO)$_2$C(**CH$_2$**)$_2$**$_2$**CH$_2$], ● Pt–[(OCO)$_2$C(CH$_2$)$_2$**CH$_2$**].

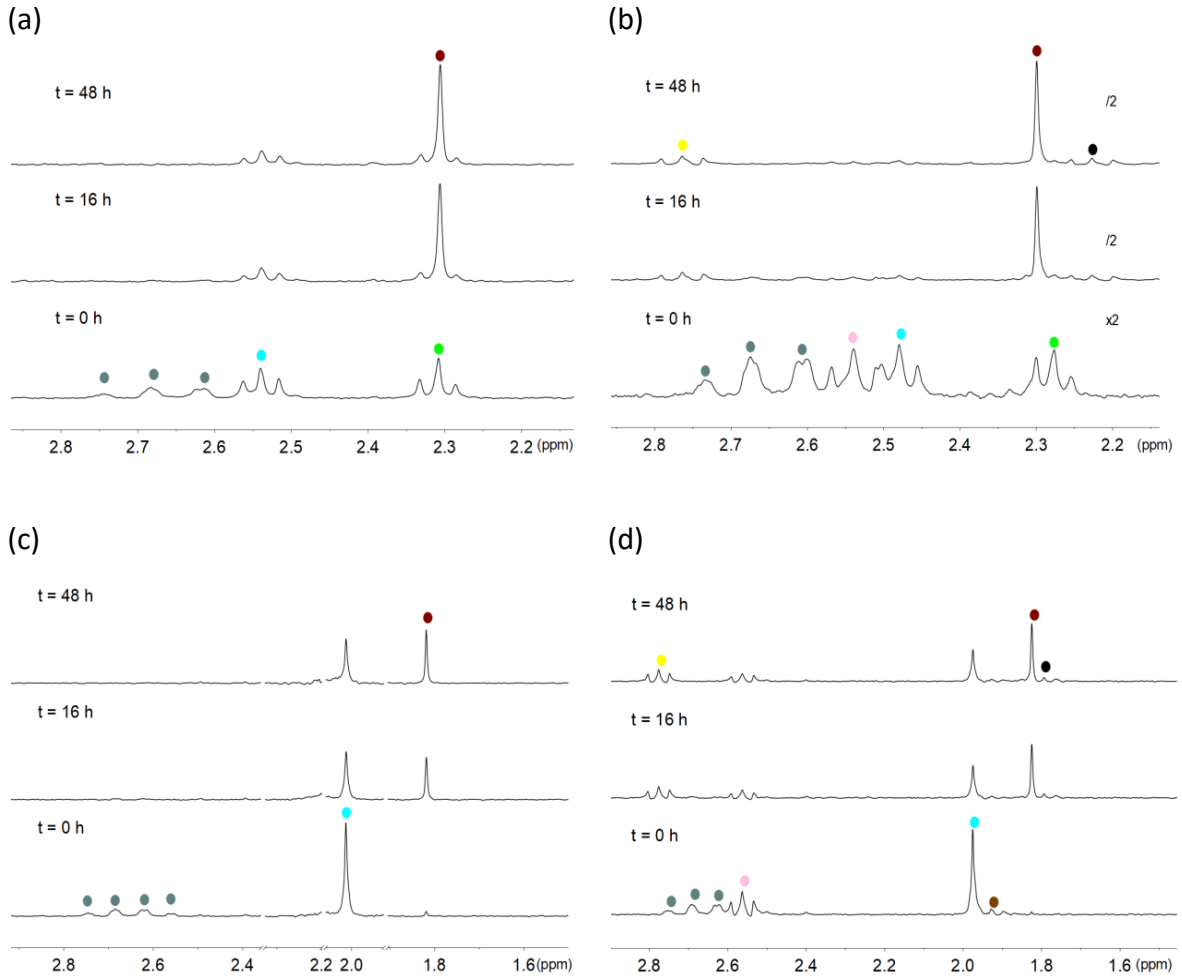

IO 5. Irudia. 1–4 konplexuen (500 µM) egonkortasuna 48 orduz ilunpetan 18 mM PB (pH 7.0, % 10 D_2O) disoluzioan, 1 mM NADH-ren eta 25 µM **Rf**-ren presentzian.
^{1}H NMR seinaleen etiketak: ● NADH, (a) **1**, ● Pt–OCO**CH$_2$**CH$_2$CO$_2^-$, ● Pt–OCOCH$_2$**CH$_2$**CO$_2^-$, ● $^-$O$_2$C**CH$_2$CH$_2$**CO$_2^-$ askea; (b) **2**, ● Pt–OCO**CH$_2$**CH$_2$CO$_2^-$, ● Pt–OCOCH$_2$**CH$_2$**CO$_2^-$, ● Pt–[(OCO)$_2$C(**CH$_2$**)$_2$CH$_2$], ● $^-$O$_2$C**CH$_2$CH$_2$**CO$_2^-$ askea, ● Pt^{II}–[(OCO)$_2$C(**CH$_2$**)$_2$CH$_2$], ● [($^-$OCO)$_2$C**(CH$_2$)$_2$**CH$_2$] askea; (c) **3**, ● Pt–OCO**CH$_3$**, ●$^-$OCO**CH$_3$** askea eta (d) **4**, ● Pt–OCO**CH$_3$**, ● Pt–[(OCO)$_2$C(**CH$_2$**)$_2$CH$_2$], ● Pt–[(OCO)$_2$C(CH$_2$)$_2$**CH$_2$**], ● Pt^{II}–[(OCO)$_2$C(**CH$_2$**)$_2$CH$_2$], ● Pt^{II}–[(OCO)$_2$C(CH$_2$)$_2$**CH$_2$**], ●$^-$OCO**CH$_3$** askea.

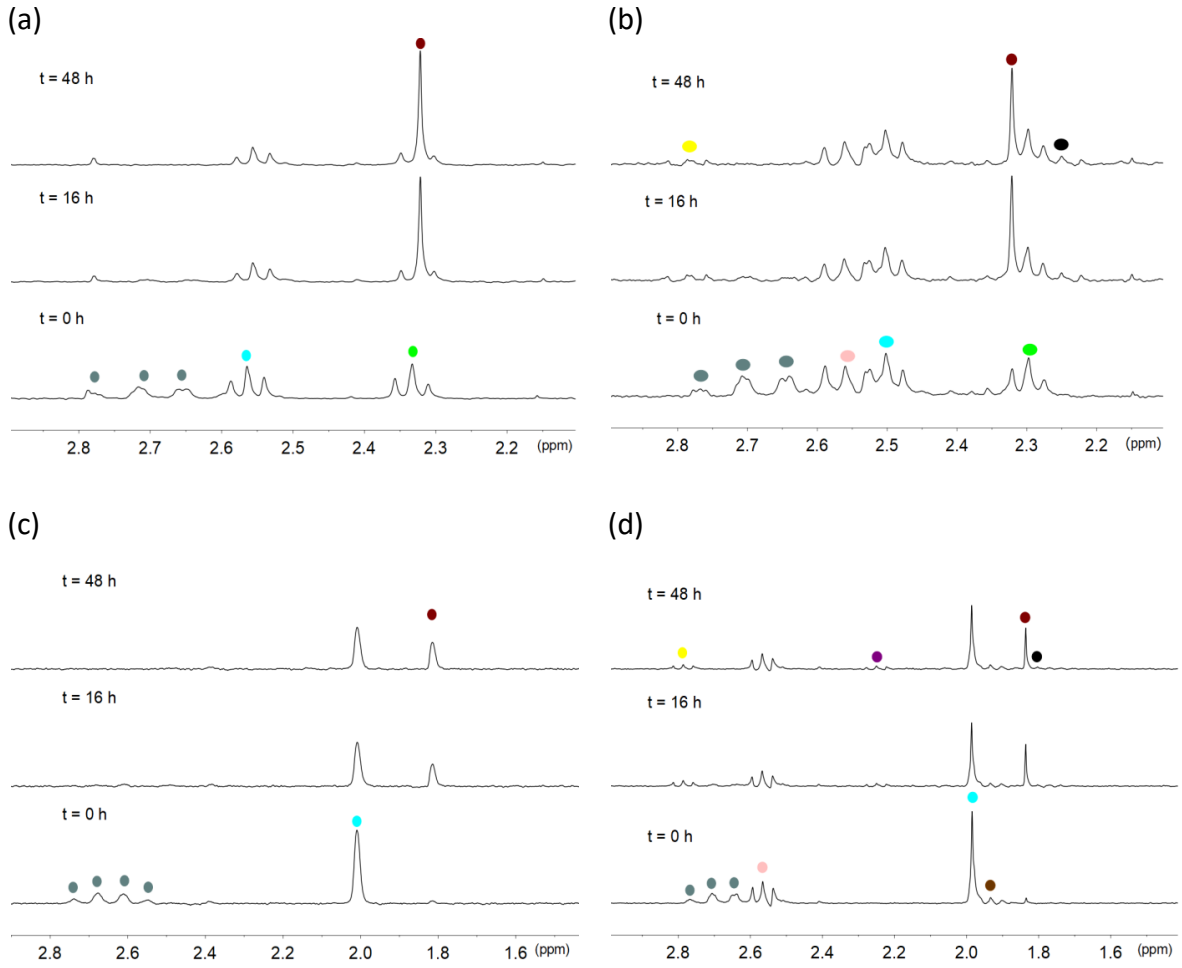

IO 6. Irudia. 1–4 konplexuen (500 µM) egonkortasuna 48 orduz ilunpetan 18 mM PB (pH 7.0, % 10 D_2O) disoluzioan, 1 mM NADH-ren eta 25 µM **FMN**-ren presentzian. ^{1}H NMR seinaleen etiketak: ● NADH, (a) **1**, ● Pt–OCO**CH$_2$**CH$_2$CO$_2^-$, ● Pt–OCOCH$_2$**CH$_2$**CO$_2^-$, ● free $^-$O$_2$C**CH$_2$CH$_2$**CO$_2^-$; (b) **2**, ● Pt–OCO**CH$_2$**CH$_2$CO$_2^-$, ● Pt–OCOCH$_2$**CH$_2$**CO$_2^-$, ● Pt–[(OCO)$_2$C(**CH$_2$**)$_2$CH$_2$], ● $^-$O$_2$C**CH$_2$CH$_2$**CO$_2^-$ askea ● Pt^{II}–[(OCO)$_2$C(**CH$_2$**)$_2$CH$_2$], ● [($^-$OCO)$_2$C**(CH$_2$)$_2$**CH$_2$] askea; (c) **3**, ● Pt–OCO**CH$_3$**, ● $^-$OCO**CH$_3$** askea eta (d) **4**, ● Pt–OCO**CH$_3$**, ● Pt–[(OCO)$_2$C(**CH$_2$**)$_2$CH$_2$], ● Pt–[(OCO)$_2$C(CH$_2$)$_2$**CH$_2$**], ● Pt^{II}–[(OCO)$_2$C(**CH$_2$**)$_2$CH$_2$], ● Pt^{II}–[(OCO)$_2$C(CH$_2$)$_2$**CH$_2$**], ● $^-$OCO**CH$_3$** askea, ● [($^-$OCO)$_2$C**(CH$_2$)$_2$**CH$_2$] askea.

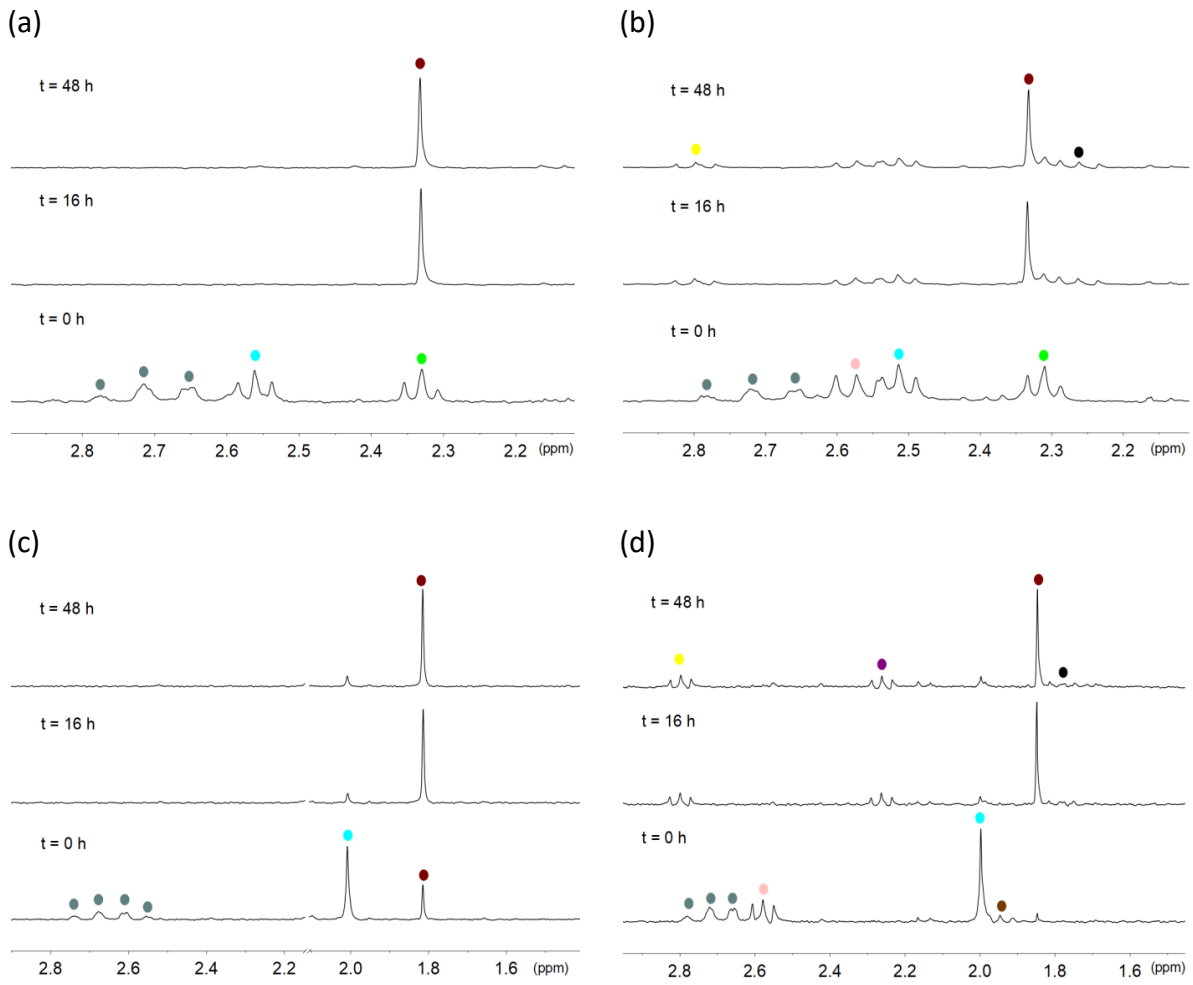

IO 7. Irudia. 1–4 konplexuen (500 µM) egonkortasuna 48 orduz ilunpetan 18 mM PB (pH 7.0, % 10 D_2O) disoluzioan, 1 mM NADH-ren eta 25 µM **TARF**-ren presentzian.
^{1}H NMR seinaleen etiketak: ● NADH, (a) **1**, ● Pt–OCO**CH$_2$**CH$_2$CO$_2^-$, ● Pt–OCOCH$_2$**CH$_2$**CO$_2^-$, ● $^-$O$_2$C**CH$_2$CH$_2$**CO$_2^-$ askea; (b) **2**, ● Pt–OCO**CH$_2$**CH$_2$CO$_2^-$, ● Pt–OCOCH$_2$**CH$_2$**CO$_2^-$, ● Pt–[(OCO)$_2$C(**CH$_2$**)$_2$**$_2$**CH$_2$], ● $^-$O$_2$C**CH$_2$CH$_2$**CO$_2^-$ askea, ● Pt^{II}–[(OCO)$_2$C(**CH$_2$**)$_2$**$_2$**CH$_2$], ● [($^-$OCO)$_2$C**(CH$_2$)$_2$**$_2$**CH$_2$] askea; (c) **3**, ● Pt–OCO**CH$_3$**, ● $^-$OCO**CH$_3$** askea eta (d) **4**, ● Pt–OCO**CH$_3$**, ● Pt–[(OCO)$_2$C(**CH$_2$**)$_2$**$_2$**CH$_2$], ● Pt–[(OCO)$_2$C(CH$_2$)$_2$**CH$_2$**], ● Pt^{II}–[(OCO)$_2$C(**CH$_2$**)$_2$**$_2$**CH$_2$], ● Pt^{II}–[(OCO)$_2$C(CH$_2$)$_2$**CH$_2$**], ● $^-$OCO**CH$_3$** askea, ● [($^-$OCO)$_2$C**(CH$_2$)$_2$**$_2$**CH$_2$] askea.

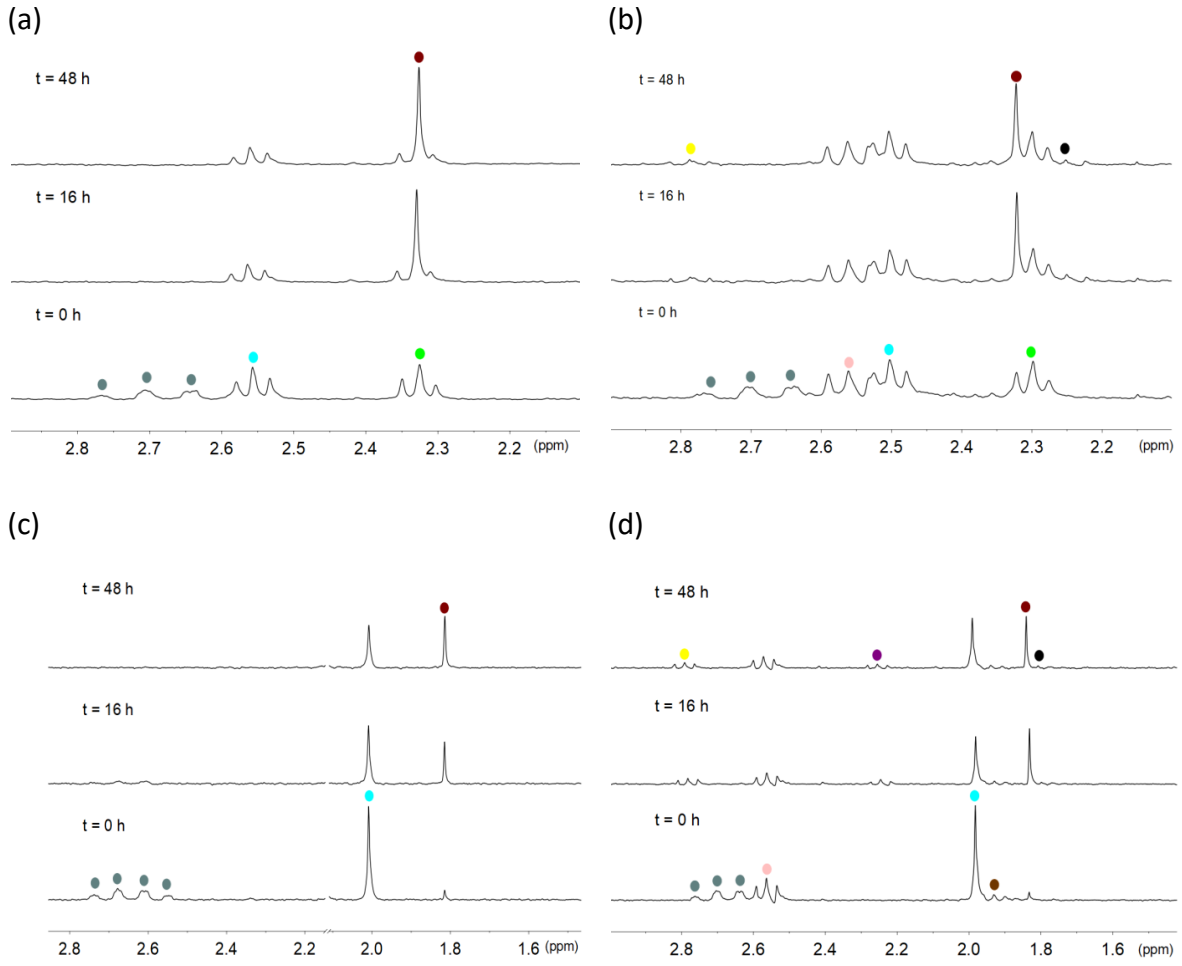

IO 8. Irudia. 1–4 konplexuen (500 µM) egonkortasuna 48 orduz ilunpetan 18 mM PB (pH 7.0, % 10 D_2O) disoluzioan, 1 mM NADH-ren eta 25 µM **Lf**-ren presentzian.
^{1}H NMR seinaleen etiketak: ● NADH, (a) **1**, ● Pt–OCO**CH$_2$**CH$_2$CO$_2^-$, ● Pt–OCOCH$_2$**CH$_2$**CO$_2^-$, ● $^-$O$_2$C**CH$_2$CH$_2$**CO$_2^-$ askea; (b) **2**, ● Pt–OCO**CH$_2$**CH$_2$CO$_2^-$, ● Pt–OCOCH$_2$**CH$_2$**CO$_2^-$, ● Pt–[(OCO)$_2$C(**CH$_2$**)$_2$CH$_2$], ● $^-$O$_2$C**CH$_2$CH$_2$**CO$_2^-$ askea, ● Pt^{II}–[(OCO)$_2$C(**CH$_2$**)$_2$CH$_2$], ● [($^-$OCO)$_2$C**(CH$_2$)$_2$**CH$_2$] askea; (c) **3**, ● Pt–OCO**CH$_3$**, ● $^-$OCO**CH$_3$** askea eta (d) **4**, ● Pt–OCO**CH$_3$**, ● Pt–[(OCO)$_2$C(**CH$_2$**)$_2$CH$_2$], ● Pt–[(OCO)$_2$C(CH$_2$)$_2$**CH$_2$**], ● Pt^{II}–[(OCO)$_2$C(**CH$_2$**)$_2$CH$_2$], ● Pt^{II}–[(OCO)$_2$C(CH$_2$)$_2$**CH$_2$**], ● $^-$OCO**CH$_3$** askea, ● [($^-$OCO)$_2$C**(CH$_2$)$_2$**CH$_2$] askea.

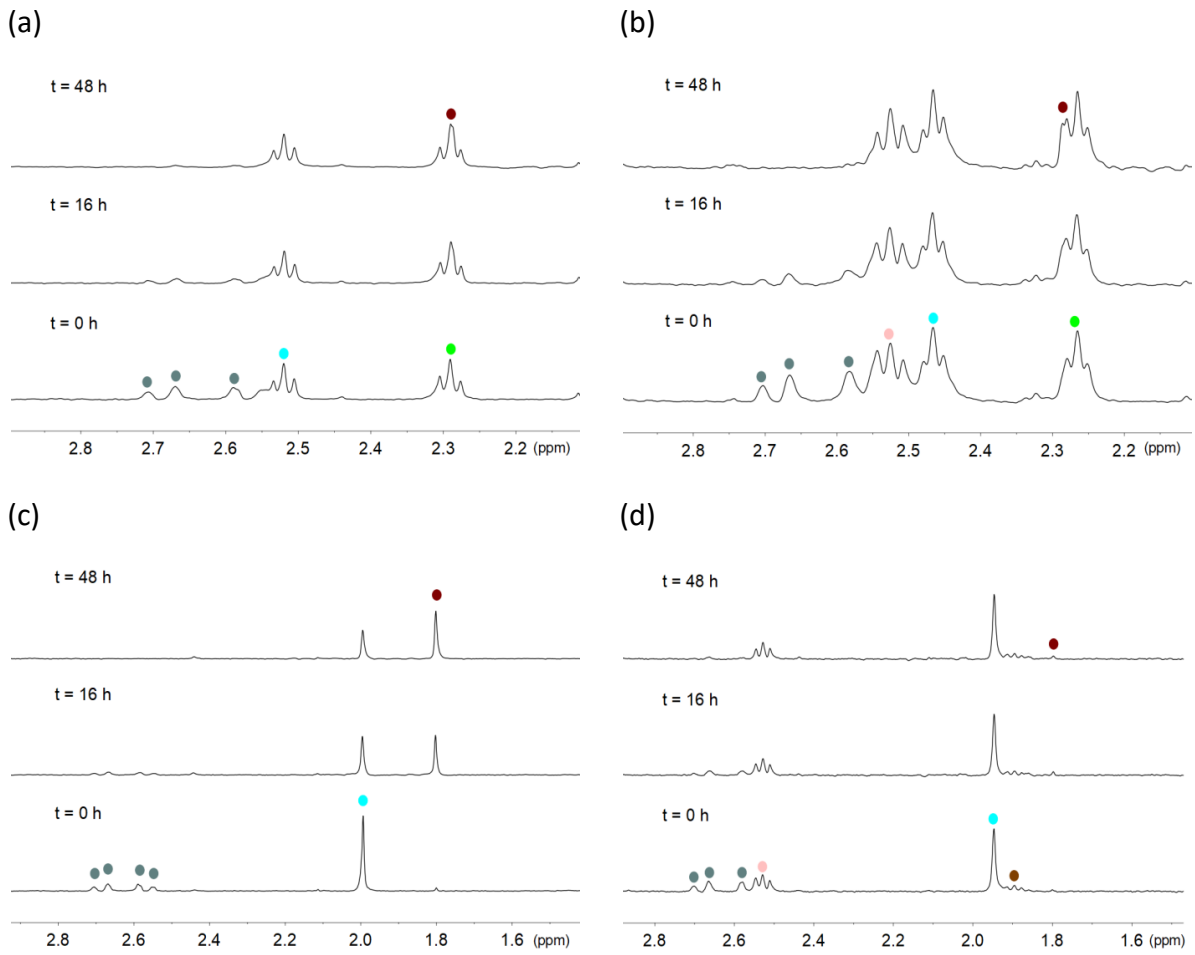

IO 9. Irudia. 1–4 konplexuen (500 µM) egonkortasuna 48 orduz ilunpetan 18 mM PB (pH 7.0, % 10 D_2O) disoluzioan, 1 mM NADH-ren eta 25 µM **miniSOG**-en presentzian. ^{1}H NMR seinaleen etiketak: ● NADH, (a) **1**, ● Pt–OCO**CH$_2$**CH$_2$CO$_2^-$, ● Pt–OCOCH$_2$**CH$_2$**CO$_2^-$, ● $^-$O$_2$C**CH$_2$CH$_2$**CO$_2^-$ askea; (b) **2**, ● Pt–OCO**CH$_2$**CH$_2$CO$_2^-$, ● Pt–OCOCH$_2$**CH$_2$**CO$_2^-$, ● Pt–[(OCO)$_2$C(**CH$_2$**)$_2$CH$_2$], ● $^-$O$_2$C**CH$_2$CH$_2$**CO$_2^-$ askea; (c) **3**, ● Pt–OCO**CH$_3$**, ● $^-$OCO**CH$_3$** askea eta (d) **4**, ● Pt–OCO**CH$_3$**, ● Pt–[(OCO)$_2$C(**CH$_2$**)$_2$CH$_2$], ● Pt–[(OCO)$_2$C(CH$_2$)$_2$**CH$_2$**], ● $^-$OCO**CH$_3$** askea.

(a)

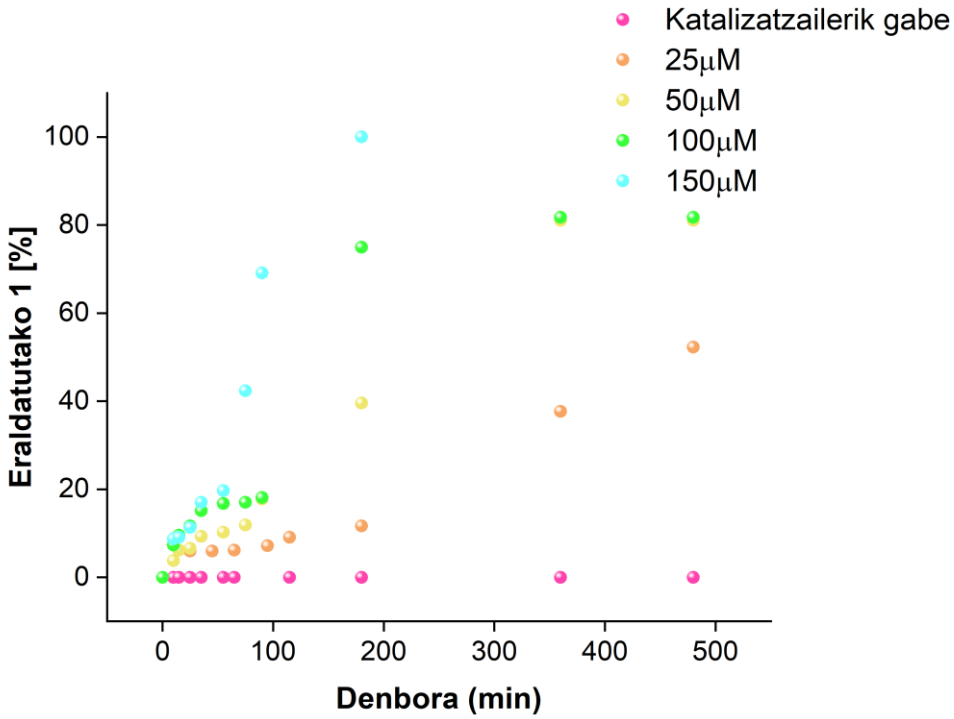

(b)

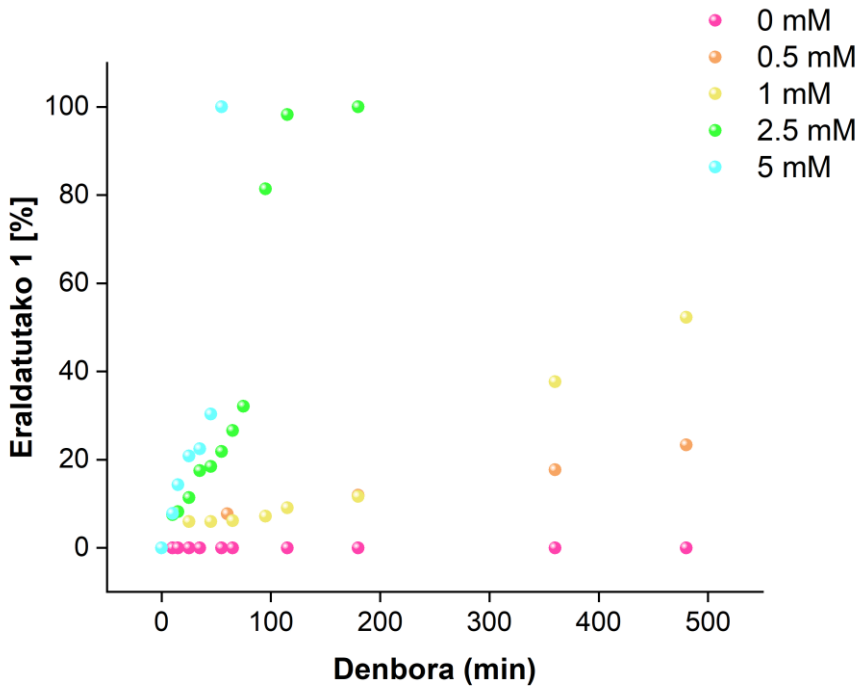

IO 10. Irudia. 1 konplexuaren (500 µM) egonkortasuna ilunpetan 18 mM PB (pH 7.0, % 10 D_2O) disoluzioan, (a) 0–150 µM **Rf**-ren eta 1 mM NADH-ren presentzian denboran zehar edo (b) 25 µM **Rf**-ren eta 0–5 mM NADH-ren presentzian denboran zehar.

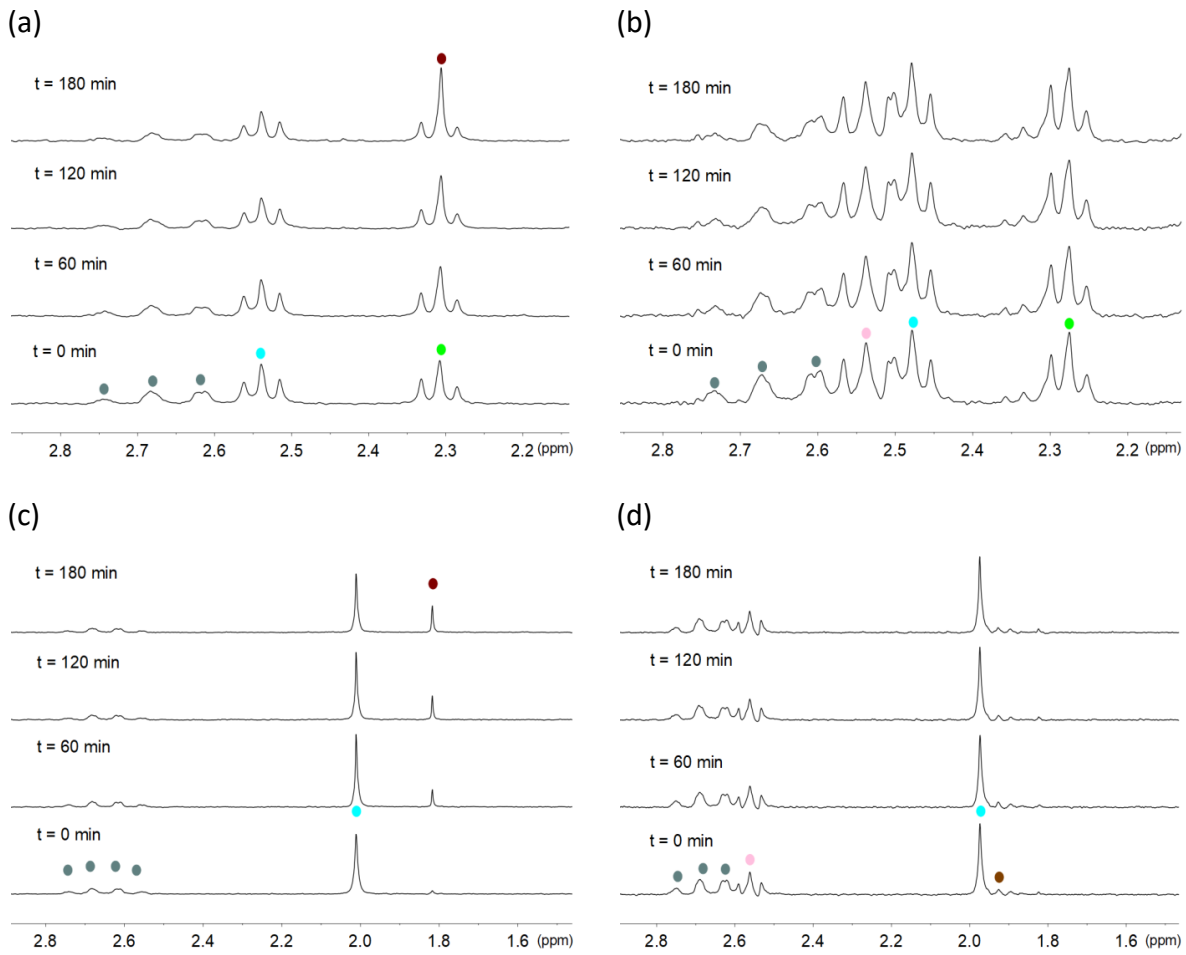

IO 11. Irudia. 1–4 konplexuen (500 µM) fotoegonkortasuna 3 orduz 18 mM PB (pH 7.0, % 10 D_2O) disoluzioan, 1 mM NADH-ren presentzian eta 460 nm-ko argi irradiazioaren menpe (6 $mW{\cdot}cm^{-2}$).
^{1}H NMR seinaleen etiketak: ● NADH, (a) **1**, ● Pt–OCO**CH$_2$**CH$_2$CO$_2^-$, ● Pt–OCOCH$_2$**CH$_2$**CO$_2^-$, ● $^-$O$_2$C**CH$_2$CH$_2$**CO$_2^-$ askea; (b) **2**, ● Pt–OCO**CH$_2$**CH$_2$CO$_2^-$, ● Pt–OCOCH$_2$**CH$_2$**CO$_2^-$, ● Pt–[(OCO)$_2$C(**CH$_2$**)$_2$CH$_2$]; (c) **3**, ● Pt–OCO**CH$_3$**, ● $^-$OCO**CH$_3$** askea eta (d) **4**, ● Pt–OCO**CH$_3$**, ● Pt–[(OCO)$_2$C(**CH$_2$**)$_2$CH$_2$], ● Pt–[(OCO)$_2$C(CH$_2$)$_2$**CH$_2$**].

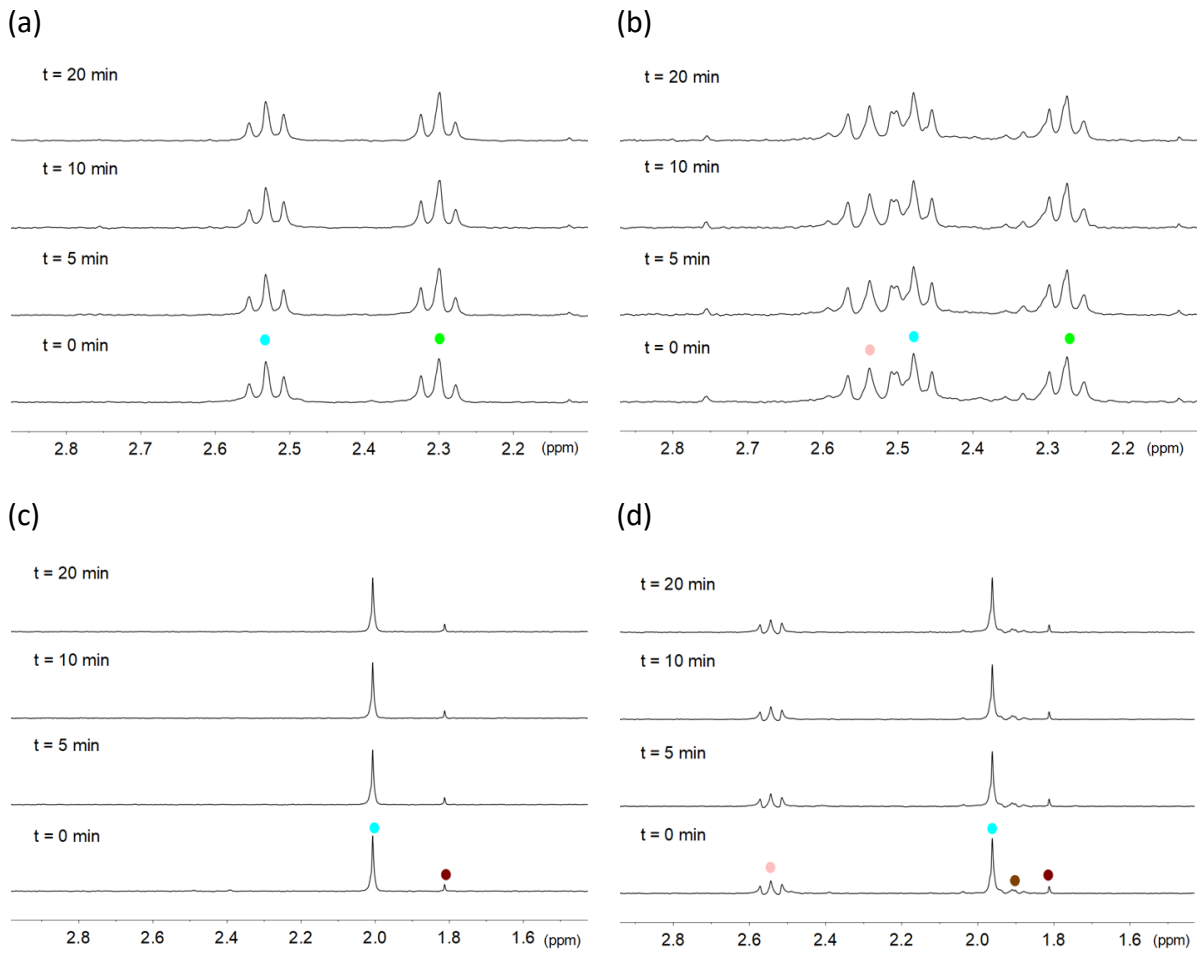

IO 12. Irudia. 1–4 konplexuen (500 µM) fotoegonkortasuna 18 mM PB (pH 7.0, % 10 D_2O) disoluzioan, 25 µM **Rf**-ren presentzian eta 460 nm-ko argi irradiazioaren menpe (6 $mW{\cdot}cm^{-2}$). ^1H NMR seinaleen etiketak: ● NADH, (a) **1**, ● Pt–OCO**CH_2**$CH_2CO_2^-$, ● Pt–OCOCH_2**CH_2**CO_2^-, ● ^-O_2C**CH_2CH_2**CO_2^- askea; (b) **2**, ● Pt–OCO**CH_2**$CH_2CO_2^-$, ● Pt–OCOCH_2**CH_2**CO_2^-, ● Pt–[$(OCO)_2C$(**CH_2**$)_2CH_2$]; (c) **3**, ● Pt–OCO**CH_3**, ● $^-$OCO**CH_3** askea eta (d) **4**, ● Pt–OCO**CH_3**, ● Pt–[$(OCO)_2C$(**CH_2**$)_2CH_2$], ● Pt–[$(OCO)_2C(CH_2)_2$**CH_2**].

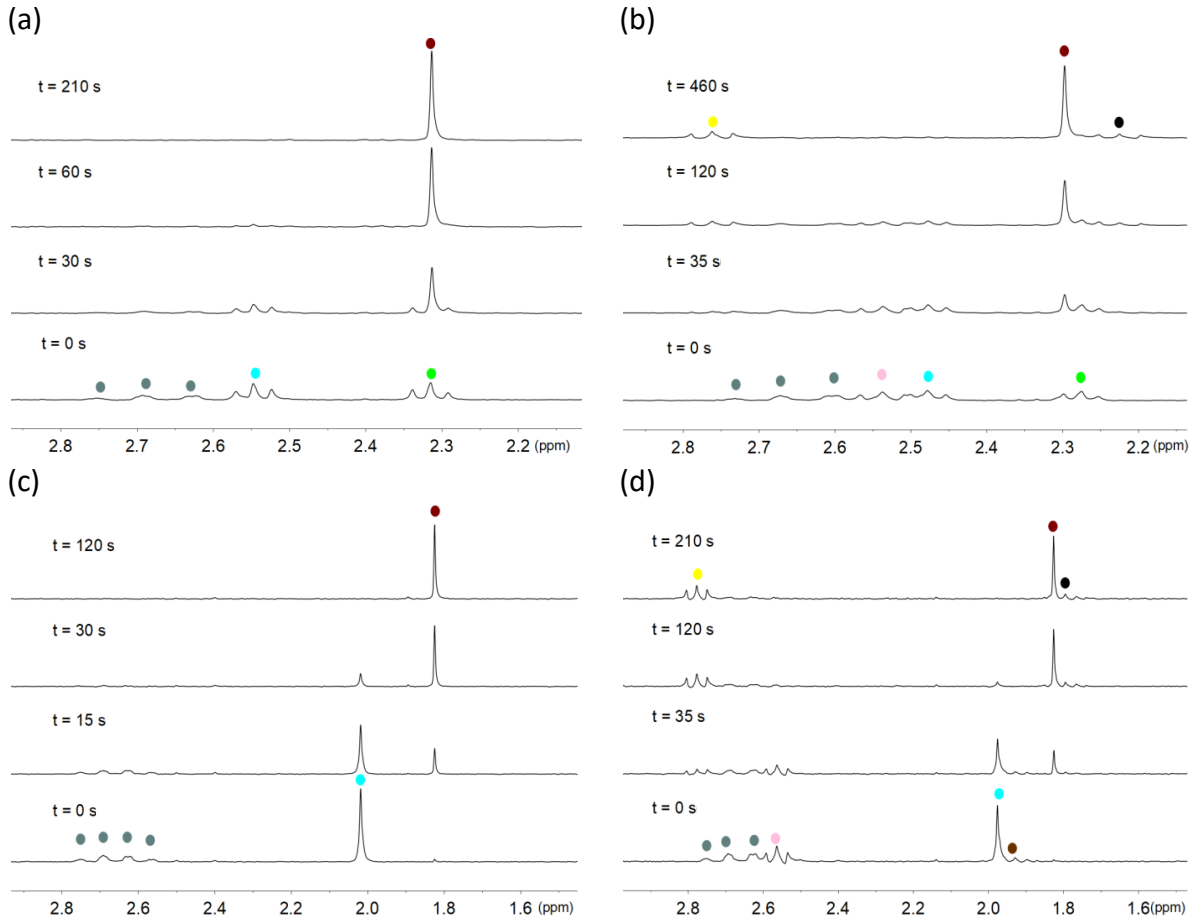

IO 13. Irudia. 1–4 konplexuen (500 µM) aktibazio fotokatalitikoa 18 mM PB (pH 7.0, % 10 D_2O) disoluzioan, 1mM NADH-ren eta 25 µM **Rf**-ren presentzian, 460 nm-ko argi irradiazioaren menpe (6 $mW{\cdot}cm^{-2}$).
^{1}H NMR seinaleen etiketak: ● NADH, (a) **1**, ● Pt–OCO**CH$_2$**CH$_2$CO$_2^-$, ● Pt–OCOCH$_2$**CH$_2$**CO$_2^-$, ● $^-$O$_2$C**CH$_2$CH$_2$**CO$_2^-$ askea; (b) **2**, ● Pt–OCO**CH$_2$**CH$_2$CO$_2^-$, ● Pt–OCOCH$_2$**CH$_2$**CO$_2^-$, ● Pt–[(OCO)$_2$C(**CH$_2$**)$_2$CH$_2$], ● $^-$O$_2$C**CH$_2$CH$_2$**CO$_2^-$ askea, ● Pt^{II}–[(OCO)$_2$C(**CH$_2$**)$_2$CH$_2$], ● [($^-$OCO)$_2$C(CH$_2$)$_2$**CH$_2$**] askea; (c) **3**, ● Pt–OCO**CH$_3$**, ●$^-$OCO**CH$_3$** askea eta (d) **4**, ● Pt–OCO**CH$_3$**, ● Pt–[(OCO)$_2$C(**CH$_2$**)$_2$CH$_2$], ● Pt–[(OCO)$_2$C(CH$_2$)$_2$**CH$_2$**], ● Pt^{II}–[(OCO)$_2$C(**CH$_2$**)$_2$CH$_2$], ● Pt^{II}–[(OCO)$_2$C(CH$_2$)$_2$**CH$_2$**], ●$^-$OCO**CH$_3$** askea.

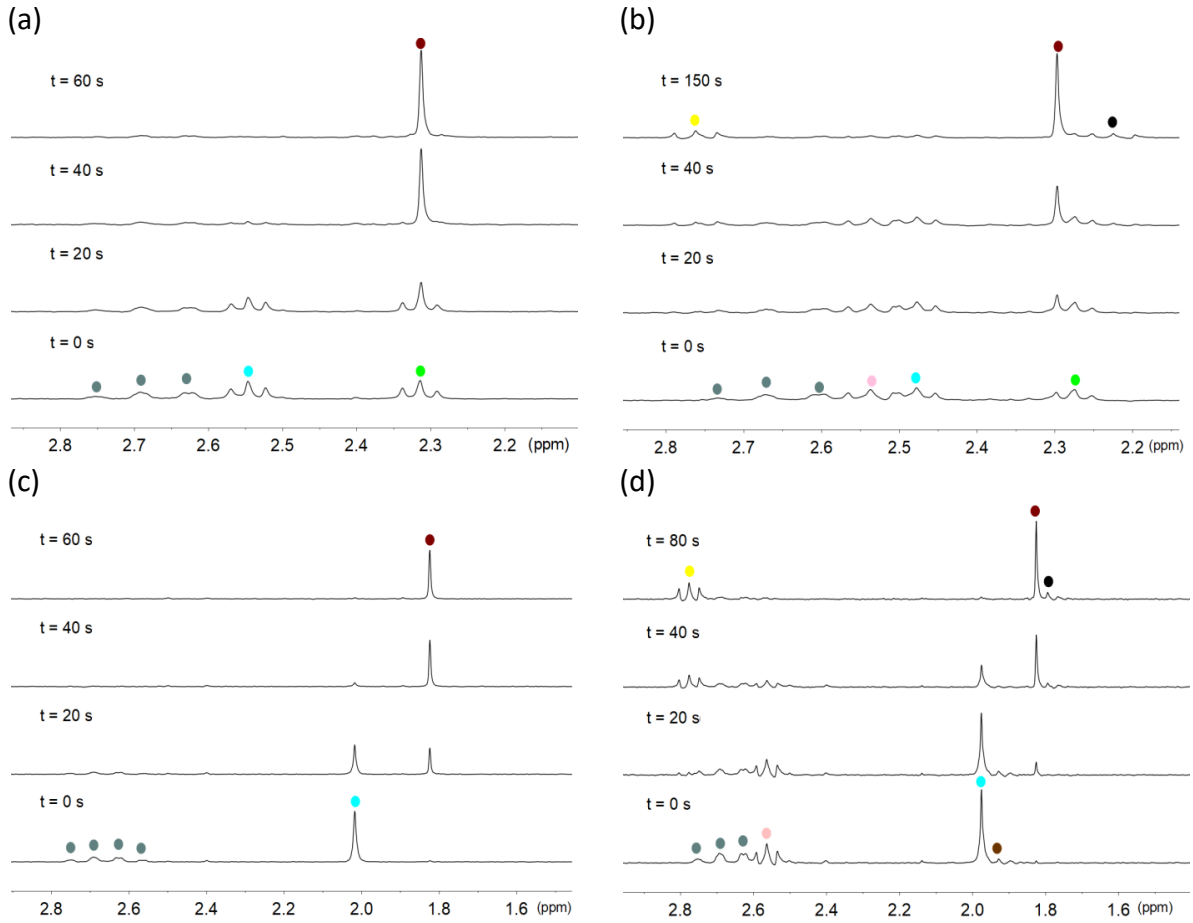

IO 14. Irudia. 1–4 konplexuen (500 µM) aktibazio fotokatalitikoa 18 mM PB (pH 7.0, % 10 D_2O) disoluzioan, 1mM NADH-ren eta 25 µM **FMN**-ren presentzian, 460 nm-ko argi irradiazioaren menpe (6 $mW{\cdot}cm^{-2}$).
^1H NMR seinaleen etiketak: ● NADH, **1**, (a) ● Pt–OCO**CH$_2$**$CH_2CO_2^-$, ● Pt–$OCOCH_2$**CH_2**CO_2^-, ● ^-O_2C**CH_2CH_2**CO_2^- askea; (b) **2**, ● Pt–OCO**CH$_2$**$CH_2CO_2^-$, ● Pt–$OCOCH_2$**CH_2**CO_2, ● Pt–[$(OCO)_2C$(**CH_2**)$_2$$CH_2$], ● ^-O_2C**CH_2CH_2**CO_2^- askea, ● Pt^{II}–[$(OCO)_2C$(**CH_2**)$_2$$CH_2$], ● [($^-$OCO)$_2$C($CH_2$)$_2$**$CH_2$**] askea; (c) **3**, ● Pt–OCO**CH$_3$**, ● $^-$OCO**CH$_3$** askea eta (d) **4**, ● Pt–OCO**CH$_3$**, ● Pt–[$(OCO)_2C$(**CH_2**)$_2$$CH_2$], ● Pt–[$(OCO)_2C(CH_2)_2$**$CH_2$**], ● Pt^{II}–[$(OCO)_2C$(**CH_2**)$_2$$CH_2$], ● Pt^{II}–[$(OCO)_2C(CH_2)_2$**CH_2**], ● $^-$OCO**CH$_3$** askea.

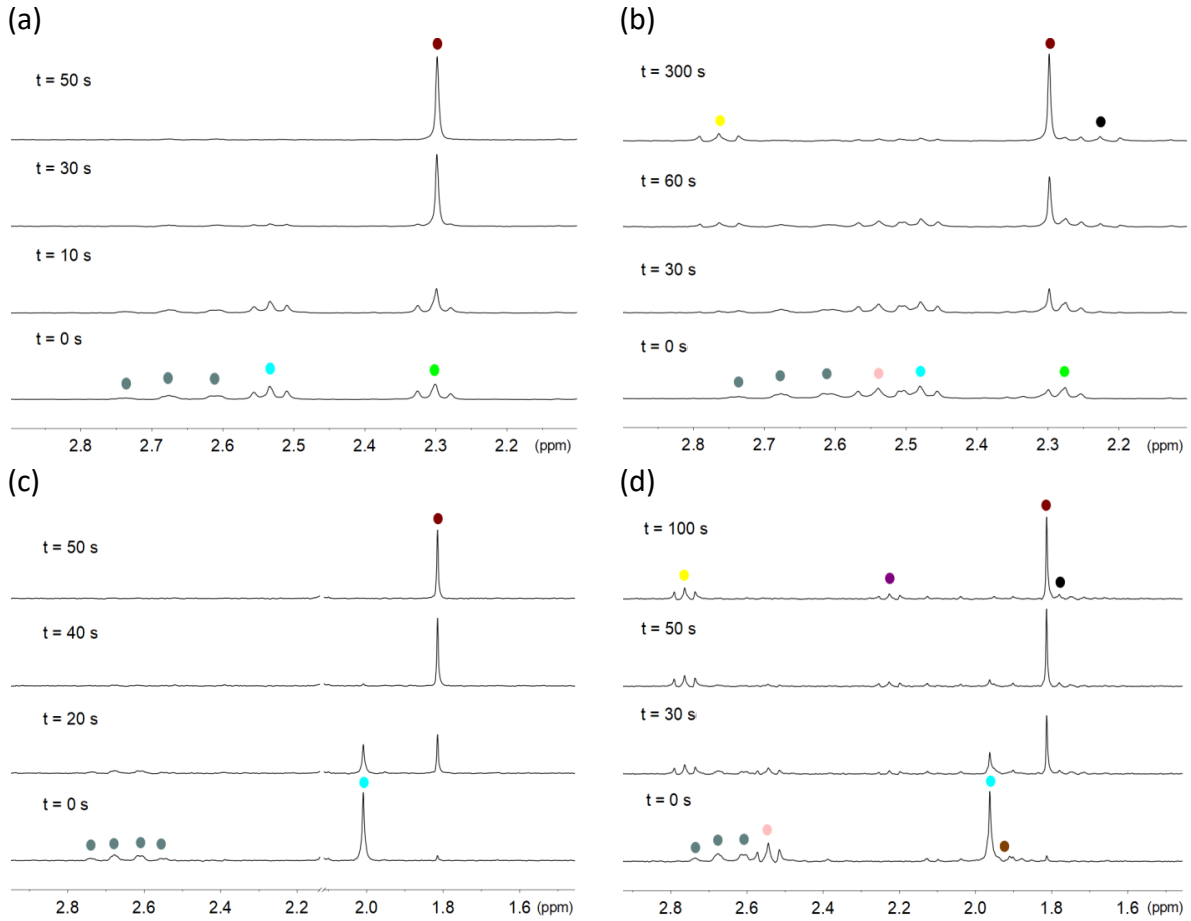

IO 15. Irudia. 1–4 konplexuen (500 µM) aktibazio fotokatalitikoa 18 mM PB (pH 7.0, % 10 D_2O) disoluzioan, 1mM NADH-ren eta 25 µM **TARF**-ren presentzian, 460 nm-ko argi irradiazioaren menpe (6 $mW{\cdot}cm^{-2}$).
^1H NMR seinaleen etiketak: ● NADH, (a) **1**, ● Pt–OCO**CH_2**$CH_2CO_2^-$, ● Pt–OCOCH_2**CH_2**CO_2^-, ● ^-O_2C**CH_2CH_2**CO_2^- askea; (b) **2**, ● Pt–OCO**CH_2**$CH_2CO_2^-$, ● Pt–OCOCH_2**CH_2**CO_2^-, ● Pt–[$(OCO)_2C$(**CH_2**)**$_2$**CH_2], ● ^-O_2C**CH_2CH_2**CO_2^- askea, ● Pt^{II}–[$(OCO)_2C$(**CH_2**)**$_2$**CH_2], ● [($^-$OCO)$_2$C**(CH_2)$_2$**CH_2] askea; (c) **3**, ● Pt–OCO**CH_3**, ● $^-$OCO**CH_3** askea eta (d) **4**, ● Pt–OCO**CH_3**, ● Pt–[$(OCO)_2C$(**CH_2**)**$_2$**CH_2], ● Pt–[$(OCO)_2C(CH_2)_2$**CH_2**], ● Pt^{II}–[$(OCO)_2C$(**CH_2**)**$_2$**CH_2], ● Pt^{II}–[$(OCO)_2C(CH_2)_2$**CH_2**], ● $^-$OCO**CH_3** askea, ● [($^-$OCO)$_2$C**(CH_2)$_2$**CH_2] askea.

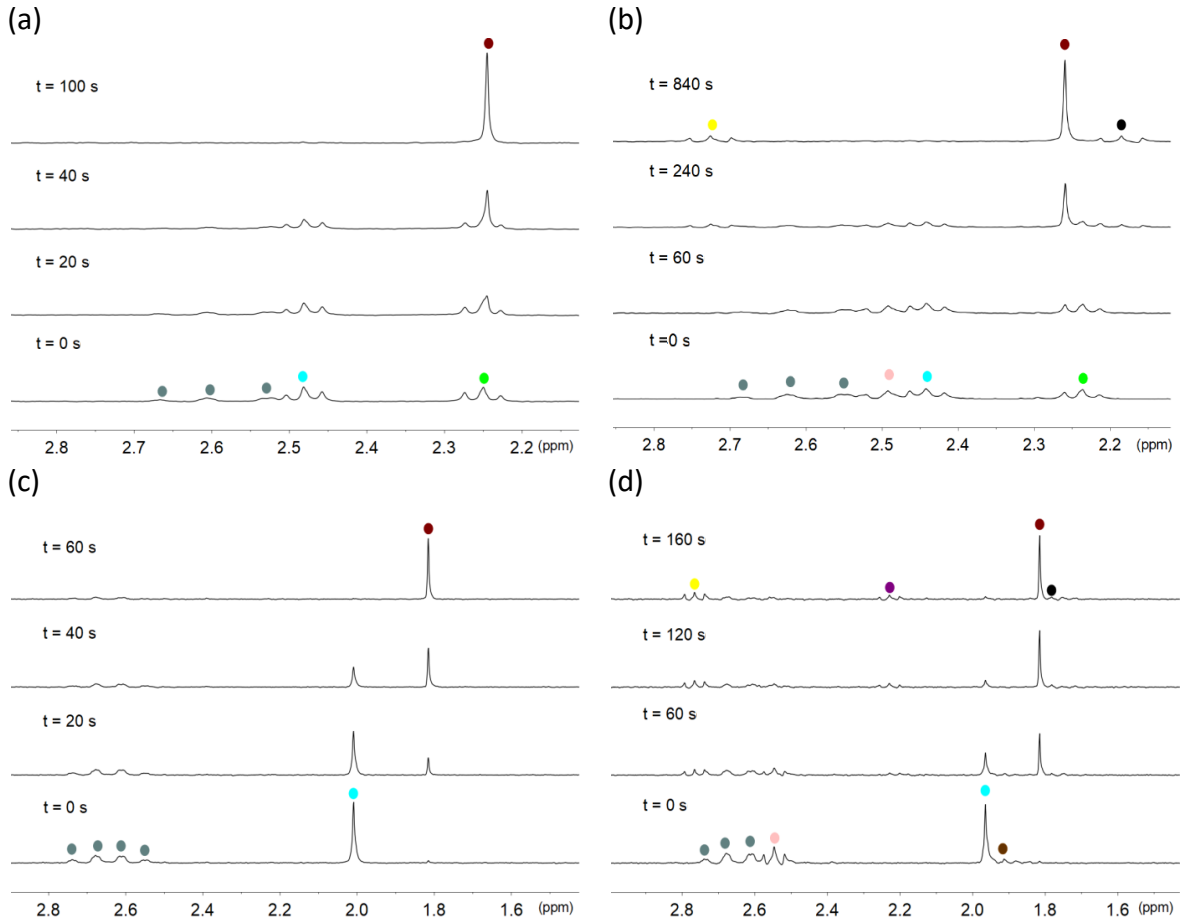

IO 16. Irudia. 1–4 konplexuen (500 µM) aktibazio fotokatalitikoa 18 mM PB (pH 7.0, % 10 D_2O) disoluzioan, 1mM NADH-ren eta 25 µM **Lf**-ren presentzian, 460 nm-ko argi irradiazioaren menpe (6 $mW{\cdot}cm^{-2}$).
^{1}H NMR seinaleen etiketak: ● NADH, (a) **1**, ● Pt–OCO**CH$_2$**CH$_2$CO$_2^-$, ● Pt–OCOCH$_2$**CH$_2$**CO$_2^-$, ● $^-$O$_2$C**CH$_2$CH$_2$**CO$_2^-$ askea; (b) **2**, ● Pt–OCO**CH$_2$**CH$_2$CO$_2^-$, ● Pt–OCOCH$_2$**CH$_2$**CO$_2^-$, ● Pt–[(OCO)$_2$C(**CH$_2$**)$_2$CH$_2$], ● $^-$O$_2$C**CH$_2$CH$_2$**CO$_2^-$ askea, ● Pt^{II}–[(OCO)$_2$C(**CH$_2$**)$_2$CH$_2$], ● [($^-$OCO)$_2$C**(CH$_2$)$_2$**CH$_2$] askea; (c) **3**, ● Pt–OCO**CH$_3$**, ● $^-$OCO**CH$_3$** askea eta (d) **4**, ● Pt–OCO**CH$_3$**, ● Pt–[(OCO)$_2$C(**CH$_2$**)$_2$CH$_2$], ● Pt–[(OCO)$_2$C(CH$_2$)$_2$**CH$_2$**], ● Pt^{II}–[(OCO)$_2$C(**CH$_2$**)$_2$CH$_2$], ● Pt^{II}–[(OCO)$_2$C(CH$_2$)$_2$**CH$_2$**], ● $^-$OCO**CH$_3$** askea, ● [($^-$OCO)$_2$C**(CH$_2$)$_2$**CH$_2$] askea.

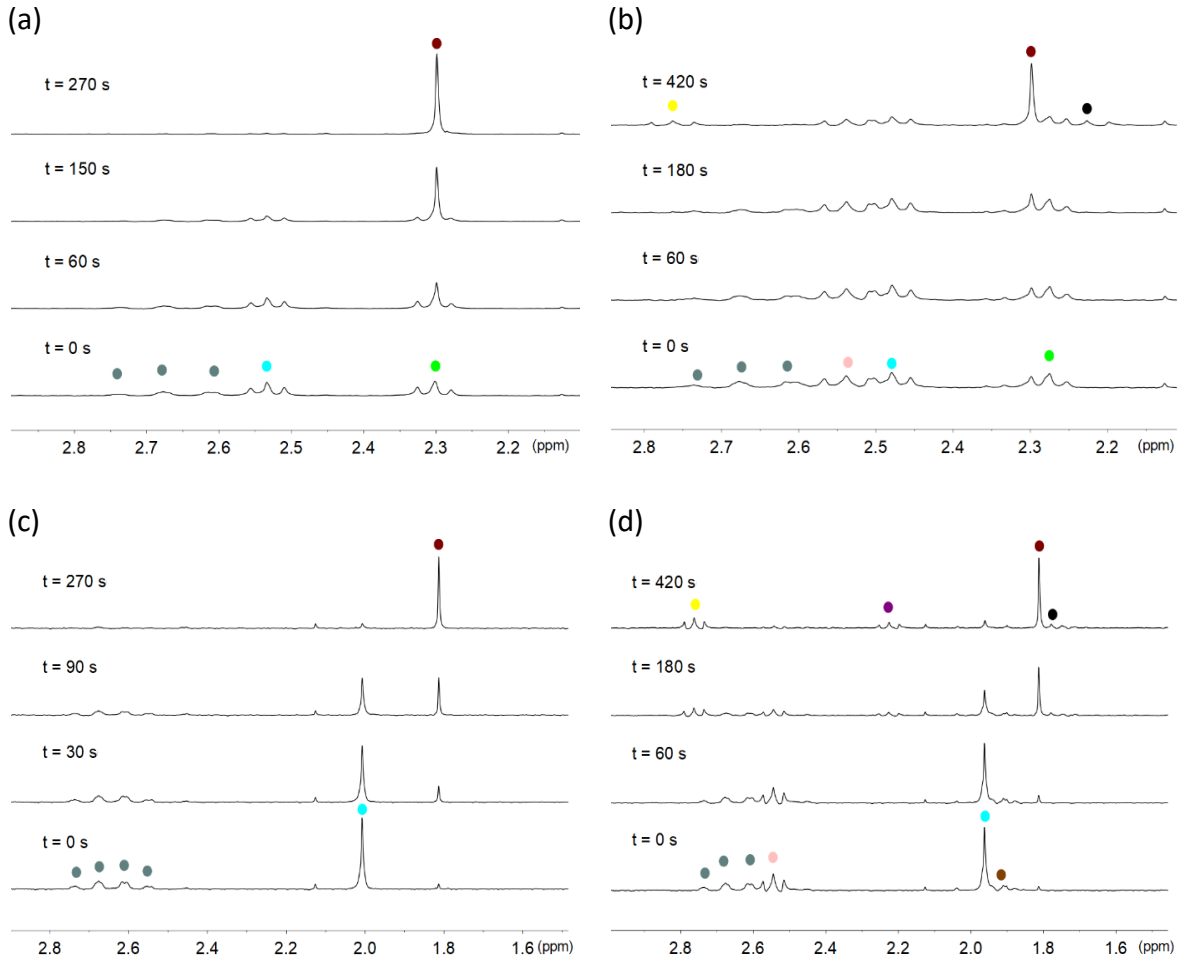

IO 17. Irudia. 1–4 konplexuen (500 µM) aktibazio fotokatalitikoa 18 mM PB (pH 7.0, % 10 D_2O) disoluzioan, 1mM NADH-ren eta 25 µM **miniSOG**-aren presentzian, 460 nm-ko argi irradiazioaren menpe (6 $mW{\cdot}cm^{-2}$).
^1H NMR seinaleen etiketak: ● NADH, (a) **1**, ● Pt–OCO**CH_2**$CH_2CO_2^-$, ● Pt–OCOCH$_2$**CH_2**CO_2^-, ● ^-O_2C**CH_2CH_2**CO_2^- askea; (b) **2**, ● Pt–OCO**CH_2**$CH_2CO_2^-$, ● Pt–OCOCH$_2$**CH_2**CO_2^-, ● Pt–[(OCO)$_2$C(**CH_2)$_2$**CH$_2$], ● ^-O_2C**CH_2CH_2**CO_2^- askea, ● Pt^{II}–[(OCO)$_2$C(**CH_2)$_2$**CH$_2$], ● [($^-$OCO)$_2$C**(CH_2)$_2$**CH$_2$] askea; (c) **3**, ● Pt–OCO**CH_3**, ● $^-$OCO**CH_3** askea eta (d) **4**, ● Pt–OCO**CH_3**, ● Pt–[(OCO)$_2$C(**CH_2)$_2$**CH$_2$], ● Pt–[(OCO)$_2$C(CH$_2$)$_2$**CH_2**], ● Pt^{II}–[(OCO)$_2$C(**CH_2)$_2$**CH$_2$], ● Pt^{II}–[(OCO)$_2$C(CH$_2$)$_2$**CH_2**], ● $^-$OCO**CH_3** askea, ● [($^-$OCO)$_2$C**(CH_2)$_2$**CH$_2$] askea.

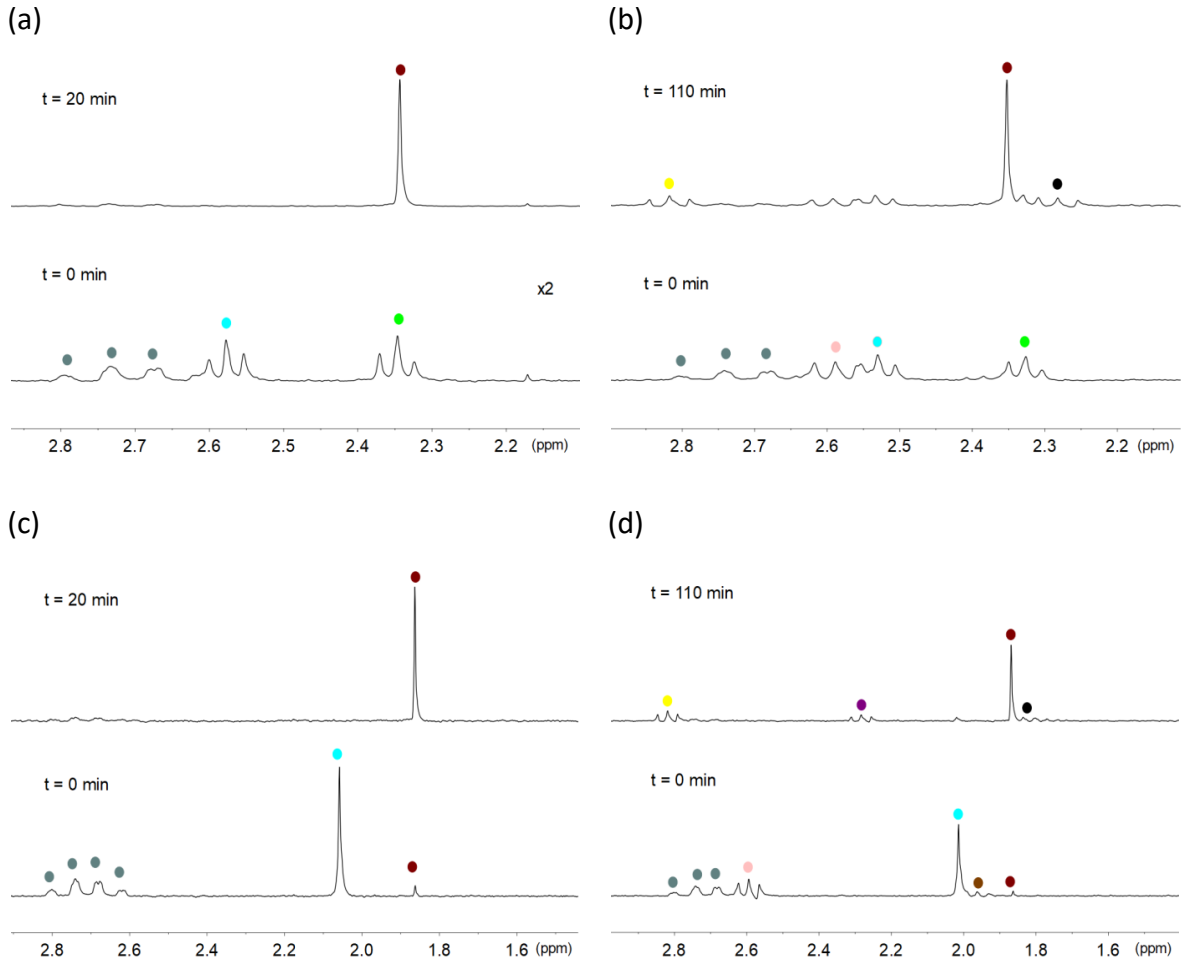

IO 18. Irudia. 1–4 konplexuen (500 µM) aktibazio fotokatalitikoa 18 mM PB (pH 7.0, % 10 D_2O) disoluzioan, 1mM NADH-ren eta 1 µM **Rf**-ren presentzian, 460 nm-ko argi irradiazioaren menpe (6 $mW{\cdot}cm^{-2}$).
^1H NMR seinaleen etiketak: ● NADH, (a) **1**, ● Pt–OCO**CH$_2$**$CH_2CO_2^-$, ● Pt–OCOCH$_2$**CH$_2$**CO_2^-, ● ^-O_2C**CH$_2$CH$_2$**CO_2^- askea; (b) **2**, ● Pt–OCO**CH$_2$**$CH_2CO_2^-$, ● Pt–OCOCH$_2$**CH$_2$**CO_2^-, ● Pt–[(OCO)$_2$C(**CH$_2$**)$_2$CH$_2$], ● ^-O_2C**CH$_2$CH$_2$**CO_2^- askea, ● Pt^{II}–[(OCO)$_2$C(**CH$_2$**)$_2$CH$_2$], ● [($^-$OCO)$_2$C(CH$_2$)$_2$**CH$_2$**] askea; (c) **3**, ● Pt–OCO**CH$_3$**, ● $^-$OCO**CH$_3$** askea eta (d) **4**, ● Pt–OCO**CH$_3$**, ● Pt–[(OCO)$_2$C(**CH$_2$**)$_2$CH$_2$], ● Pt–[(OCO)$_2$C(CH$_2$)$_2$**CH$_2$**], ● Pt^{II}–[(OCO)$_2$C(**CH$_2$**)$_2$CH$_2$], ● Pt^{II}–[(OCO)$_2$C(CH$_2$)$_2$**CH$_2$**], ● $^-$OCO**CH$_3$** askea.

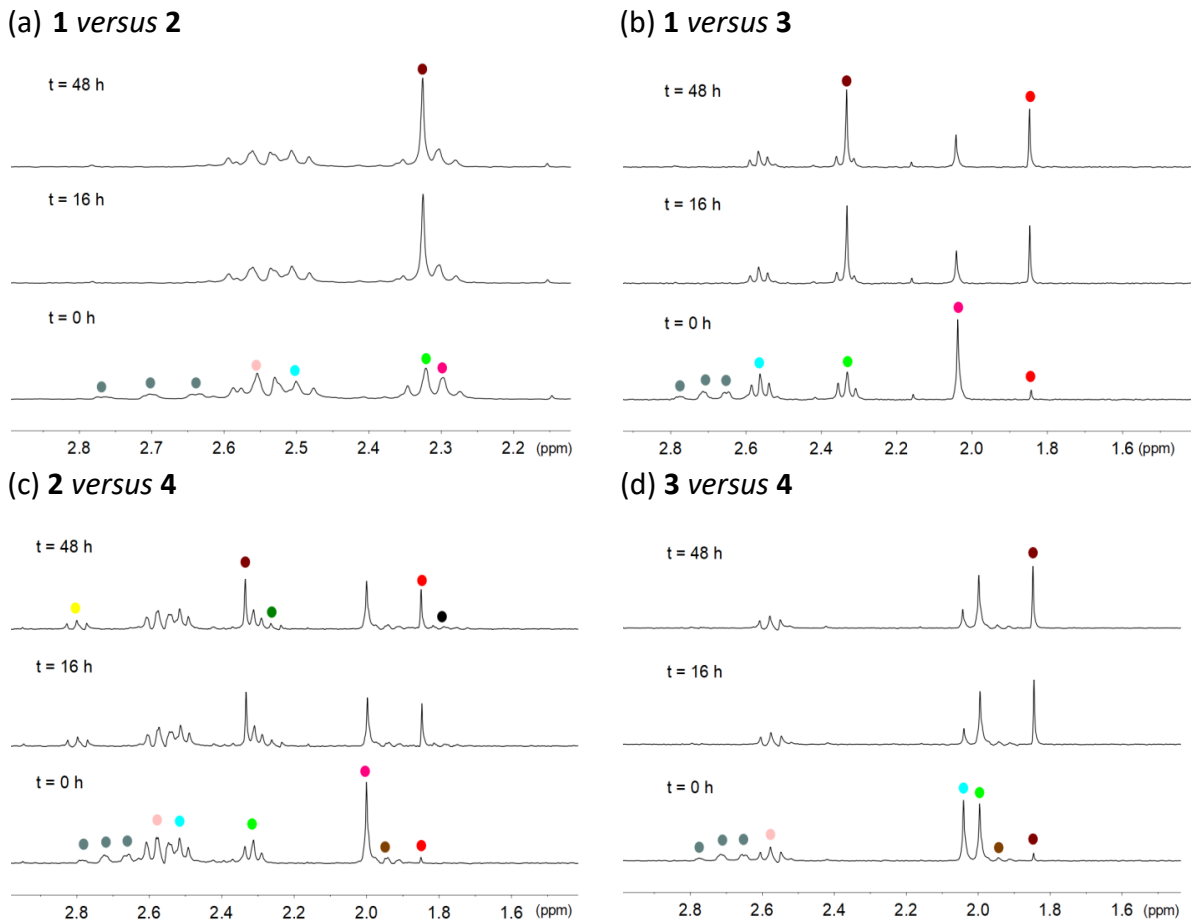

IO 19. Irudia. 1–4 konplexuen (500 µM substratu bakoitzeko) egonkortasun esperimentuak lehiaketa baldintzetan, 18 mM PB (pH 7.0, % 10 D_2O) disoluzioan, 1mM NADH-ren eta 25 µM **Rf**-ren presentzian.
^{1}H NMR seinaleen etiketak: ● NADH, (a) **1**, ● Pt–OCO**CH$_2$**CH$_2$CO$_2^-$, ● Pt–OCOCH$_2$**CH$_2$**CO$_2^-$, ● $^-$O$_2$C**CH$_2$CH$_2$**CO$_2^-$ askea; **2**, ● Pt–[(OCO)$_2$C(**CH$_2$**)$_2$CH$_2$], ● Pt–OCO**CH$_2$**CH$_2$CO$_2^-$, ● Pt–OCOCH$_2$**CH$_2$**CO$_2^-$; (b) **1**, ● Pt–OCO**CH$_2$**CH$_2$CO$_2^-$, ● Pt–OCOCH$_2$**CH$_2$**CO$_2^-$, ● $^-$O$_2$C**CH$_2$CH$_2$**CO$_2^-$ askea; **3**, ● Pt–OCO**CH$_3$**, ● $^-$OCO**CH$_3$** askea; (c) **2**, ● Pt–[(OCO)$_2$C(**CH$_2$**)$_2$CH$_2$], ● Pt–OCO**CH$_2$**CH$_2$CO$_2^-$, ● Pt–OCOCH$_2$**CH$_2$**CO$_2^-$, ● [($^-$OCO)$_2$C(CH$_2$)$_2$**CH$_2$**]askea, ● Pt^{II}–[(OCO)$_2$C(**CH$_2$**)$_2$CH$_2$]; ● $^-$O$_2$C**CH$_2$CH$_2$**CO$_2^-$ askea; **4**, ● Pt–OCO**CH$_3$**, ● Pt–[(OCO)$_2$C(CH$_2$)$_2$**CH$_2$**], ● Pt^{II}–[(OCO)$_2$C(CH$_2$)$_2$**CH$_2$**], ● $^-$OCO**CH$_3$** askea, ● Pt^{II}–[(OCO)$_2$C(**CH$_2$**)$_2$CH$_2$] eta (d) **3**, ● Pt–OCO**CH$_3$**, ● $^-$OCO**CH$_3$** askea; **4**, ● Pt–[(OCO)$_2$C(**CH$_2$**)$_2$CH$_2$], ● Pt–OCO**CH$_3$**, ● Pt–[(OCO)$_2$C(CH$_2$)$_2$**CH$_2$**].

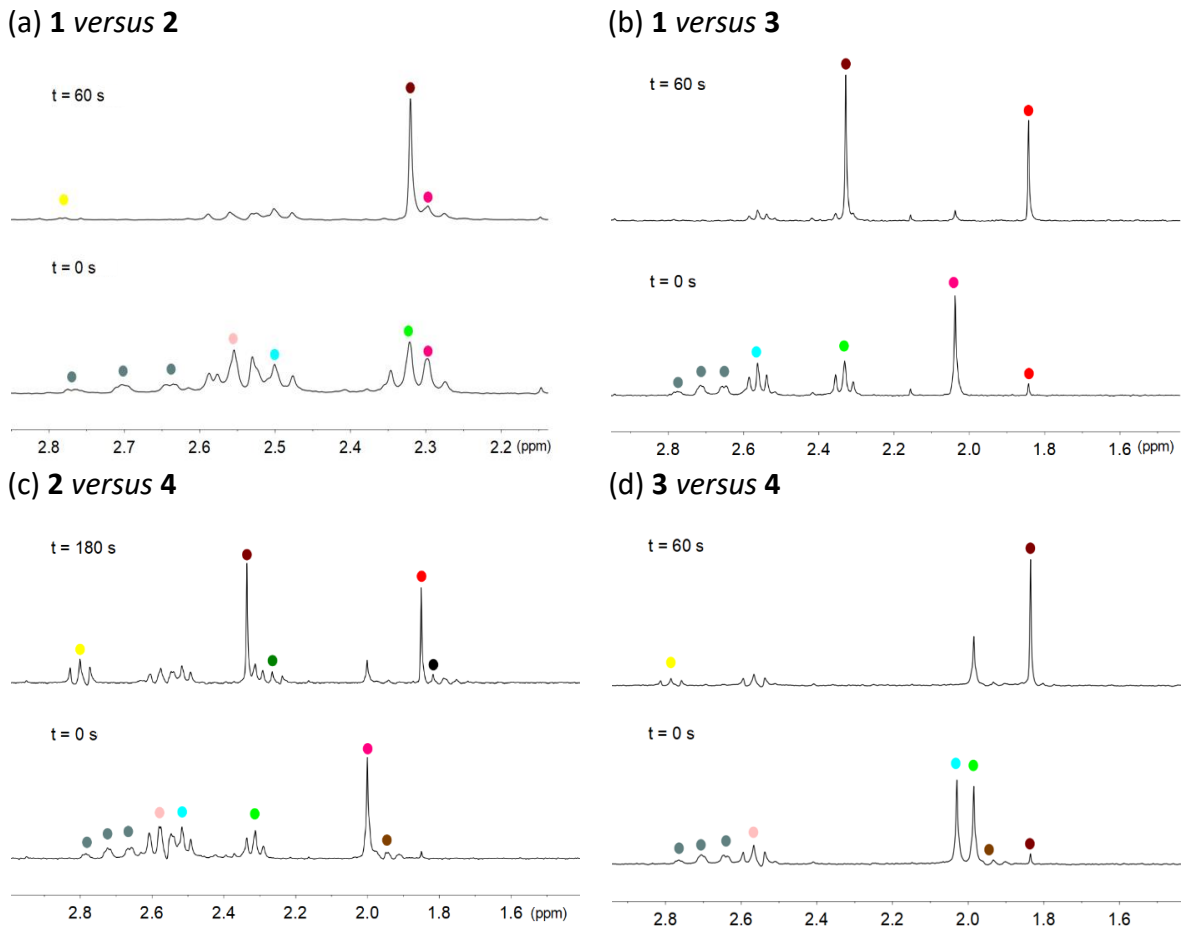

IO 20. Irudia. 1–4 konplexuen (500 µM substratu bakoitzeko) aktibazio fotokatilitiko esperimentuak lehiaketa baldintzetan, 18 mM PB (pH 7.0, % 10 D_2O) disoluzioan, 1mM NADH-ren eta 25 µM **Rf**-ren presentzian, 460 nm-ko argi irradiazioaren menpe (6 $mW{\cdot}cm^{-2}$). ^1H NMR seinaleen etiketak: ● NADH, (a) **1**, ● Pt–OCO**CH$_2$**CH$_2$CO$_2^-$, ● Pt–OCOCH$_2$**CH$_2$**CO$_2^-$, ● $^-$O$_2$C**CH$_2$CH$_2$**CO$_2^-$ askea; **2**, ● Pt–[(OCO)$_2$C(**CH$_2$**)$_2$CH$_2$], ● Pt–OCO**CH$_2$**CH$_2$CO$_2^-$, ● Pt–OCOCH$_2$**CH$_2$**CO$_2^-$, ● Pt^{II}–[(OCO)$_2$C(**CH$_2$**)$_2$CH$_2$]; (b) **1**, ● Pt–OCO**CH$_2$**CH$_2$CO$_2^-$, ● Pt–OCOCH$_2$**CH$_2$**CO$_2^-$, ● $^-$O$_2$C**CH$_2$CH$_2$**CO$_2^-$ askea; **3**, ● Pt–OCO**CH$_3$**, ● $^-$OCO**CH$_3$** askea; (c) **2**, ● Pt–[(OCO)$_2$C(**CH$_2$**)$_2$CH$_2$], ● Pt–OCO**CH$_2$**CH$_2$CO$_2^-$, ● Pt–OCOCH$_2$**CH$_2$**CO$_2^-$, ● [($^-$OCO)$_2$C(CH$_2$)$_2$**CH$_2$**] askea, ● Pt^{II}–[(OCO)$_2$C(**CH$_2$**)$_2$CH$_2$], ● $^-$O$_2$C**CH$_2$CH$_2$**CO$_2^-$ askea; **4**, ● Pt–OCO**CH$_3$**, ● Pt–[(OCO)$_2$C(CH$_2$)$_2$**CH$_2$**], ● Pt^{II}–[(OCO)$_2$C(CH$_2$)$_2$**CH$_2$**], ● $^-$OCO**CH$_3$** askea, ● Pt^{II}–[(OCO)$_2$C(**CH$_2$**)$_2$CH$_2$] and (d) **3**, ● Pt–OCO**CH$_3$**, ● $^-$OCO**CH$_3$** askea; **4**, ● Pt–[(OCO)$_2$C(**CH$_2$**)$_2$CH$_2$], ● Pt–OCO**CH$_3$**, ● Pt–[(OCO)$_2$C(CH$_2$)$_2$**CH$_2$**], ● $^-$OCO**CH$_3$** askea.

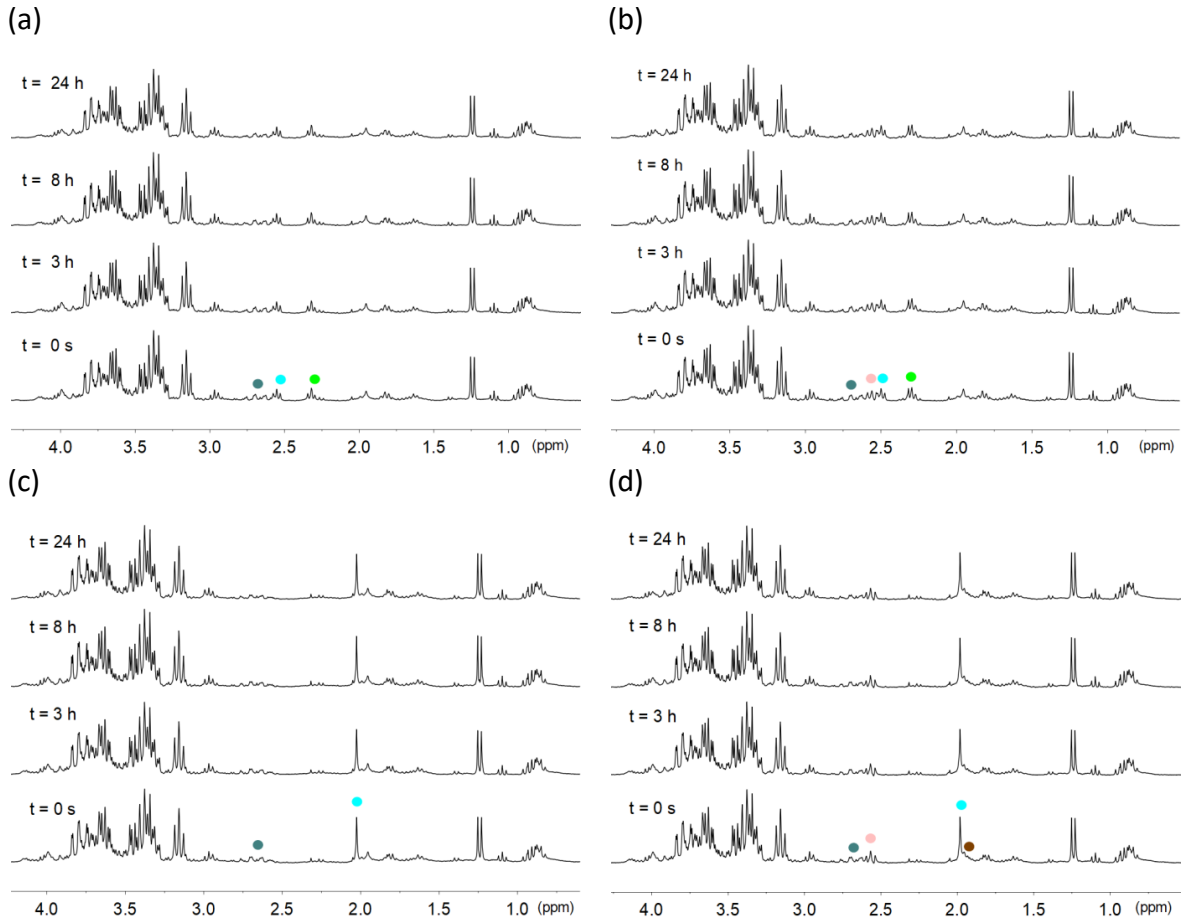

IO 21. Irudia. 1–4 konplexuen (500 µM) egonkortasuna RPMI-1640 ingurune zelularrean (pH 7.0, % 10 D_2O) eta 1 mM NADH-ren presentzian.
^{1}H NMR seinaleen etiketak: ● NADH, (a) **1**, ● Pt–OCO**CH$_2$**CH$_2$CO$_2^-$, ● Pt–OCOCH$_2$**CH$_2$**CO$_2^-$; (b) **2**, ● Pt–OCO**CH$_2$**CH$_2$CO$_2^-$, ● Pt–OCOCH$_2$**CH$_2$**CO$_2^-$, ● Pt–[(OCO)$_2$C(**CH$_2$**)$_2$**$_2$**CH$_2$]; (c) **3**, ● Pt–OCO**CH$_3$** and (d) **4**, ● Pt–OCO**CH$_3$**, ● Pt–[(OCO)$_2$C(**CH$_2$**)$_2$**$_2$**CH$_2$], ● Pt–[(OCO)$_2$C(CH$_2$)$_2$**CH$_2$**].

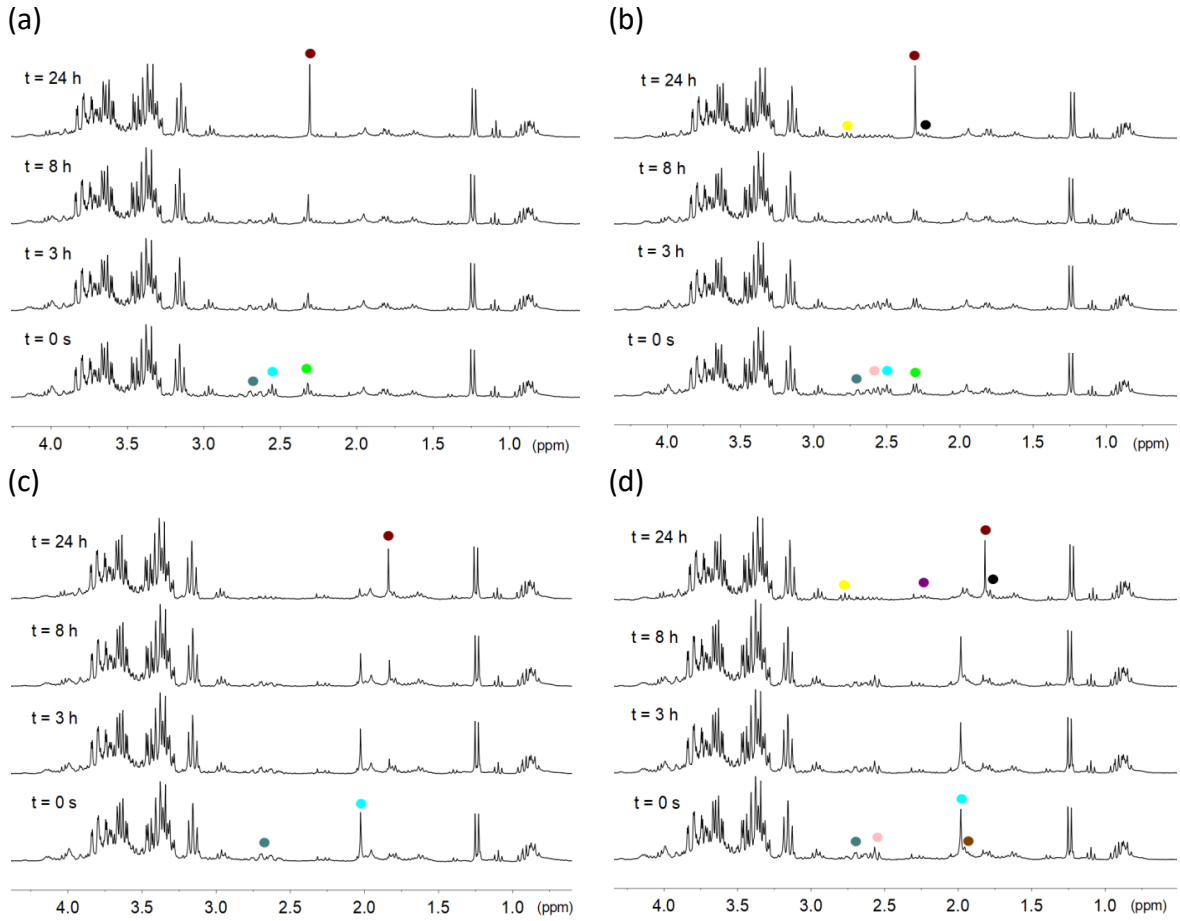

IO 22. Irudia. 1–4 konplexuen (500 µM) egonkortasuna RPMI-1640 ingurune zelularrean (pH 7.0, % 10 D_2O), 1 mM NADH-ren eta 25 µM **Rf**-ren presentzian.
^{1}H NMR seinaleen etiketak: ● NADH, (a) **1**, ● Pt–OCO**CH_2**$CH_2CO_2^-$, ● Pt–OCOCH_2**CH_2**CO_2^-, ● ^-O_2C**CH_2CH_2**CO_2^- askea; (b) **2**, ● Pt–OCO**CH_2**$CH_2CO_2^-$, ● Pt–OCOCH_2**CH_2**CO_2^-, ● Pt–[$(OCO)_2C$(**CH_2**)**$_2$**CH_2], ● ^-O_2C**CH_2CH_2**CO_2^- askea, ● Pt^{II}–[$(OCO)_2C$(**CH_2**)**$_2$**CH_2], ● [($^-$OCO)$_2$C$(CH_2)_2$**CH_2**] askea; (c) **3**, ● Pt–OCO**CH_3**, ● $^-$OCO**CH_3** askea eta (d) **4**, ● Pt–OCO**CH_3**, ● Pt–[$(OCO)_2C$(**CH_2**)**$_2$**CH_2], ● Pt–[$(OCO)_2C(CH_2)_2$**CH_2**], ● Pt^{II}–[$(OCO)_2C$(**CH_2**)**$_2$**CH_2], ● Pt^{II}–[$(OCO)_2C(CH_2)_2$**CH_2**], ● $^-$OCO**CH_3** askea, ● [($^-$OCO)$_2$C**(CH_2)$_2$**CH_2] askea.

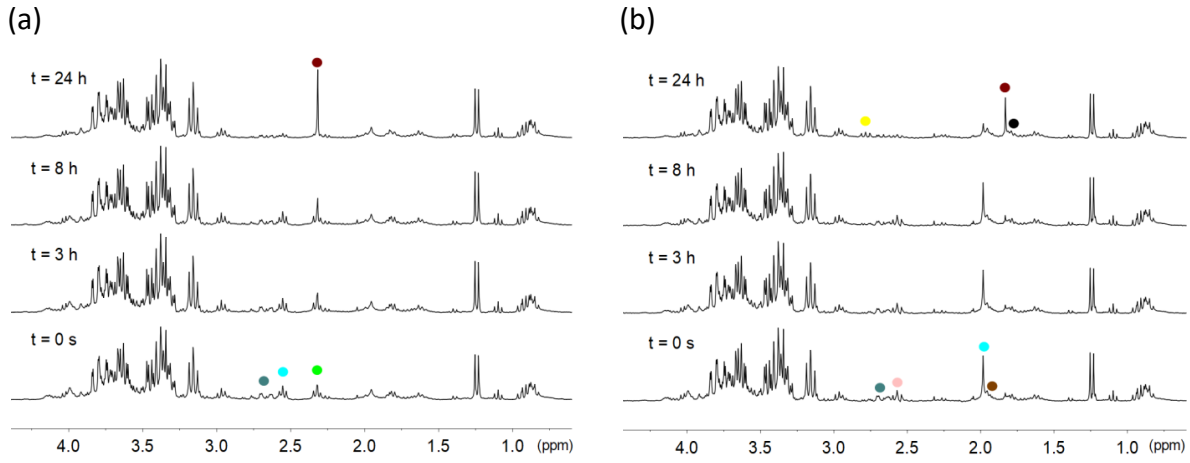

IO 23. Irudia. 1 eta **4** konplexuen (500 µM) egonkortasuna RPMI-1640 ingurune zelularrean (pH 7.0, 10% D_2O), 1 mM NADH-ren eta 25 µM **FMN**-ren presentzian.
^{1}H NMR seinaleen etiketak: ● NADH, (a) **1**, ● Pt–OCO**CH$_2$**CH$_2$CO$_2^-$, ● Pt–OCOCH$_2$**CH$_2$**CO$_2^-$, ● $^-$O$_2$C**CH$_2$CH$_2$**CO$_2^-$ askea eta (b) **4**, ● Pt–OCO**CH$_3$**, ● Pt–[(OCO)$_2$C(**CH$_2$**)$_2$CH$_2$], ● Pt–[(OCO)$_2$C(CH$_2$)$_2$**CH$_2$**], ● Pt^{II}–[(OCO)$_2$C(**CH$_2$**)$_2$CH$_2$], ● Pt^{II}–[(OCO)$_2$C(CH$_2$)$_2$**CH$_2$**], ● $^-$OCO**CH$_3$** askea.

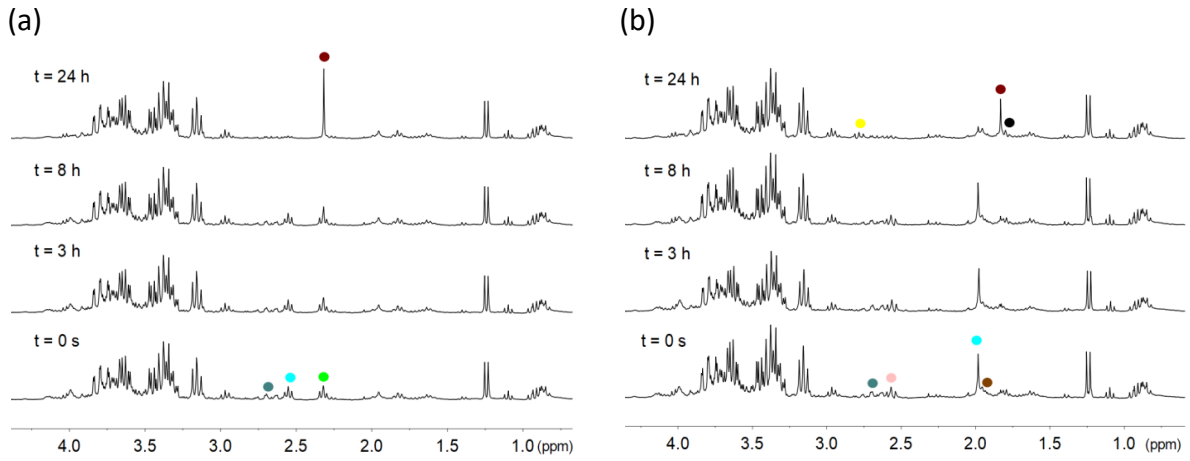

IO 24. Irudia. 1 eta **4** konplexuen (500 µM) egonkortasuna RPMI-1640 ingurune zelularrean (pH 7.0, 10% D_2O), 1 mM NADH-ren eta 25 µM **Lf**-ren presentzian.
^{1}H NMR seinaleen etiketak: ● NADH, (a) **1**, ● Pt–OCO**CH$_2$**CH$_2$CO$_2^-$, ● Pt–OCOCH$_2$**CH$_2$**CO$_2^-$, ● $^-$O$_2$C**CH$_2$CH$_2$**CO$_2^-$ askea eta (b) **4**, ● Pt–OCO**CH$_3$**, ● Pt–[(OCO)$_2$C(**CH$_2$**)$_2$CH$_2$], ● Pt–[(OCO)$_2$C(CH$_2$)$_2$**CH$_2$**], ● Pt^{II}–[(OCO)$_2$C(**CH$_2$**)$_2$CH$_2$], ● Pt^{II}–[(OCO)$_2$C(CH$_2$)$_2$**CH$_2$**], ● $^-$OCO**CH$_3$** askea.

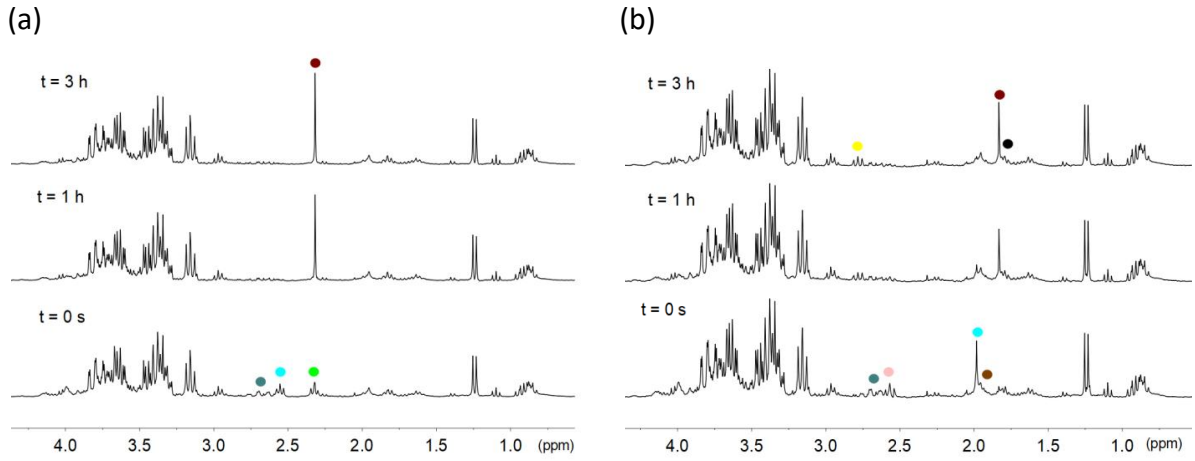

IO 25. Irudia. 1 eta **4** konplexuen (500 µM) egonkortasuna RPMI-1640 ingurune zelularrean (pH 7.0, 10% D_2O), 1 mM NADH-ren eta 25 µM **TARF**-ren presentzian.
^{1}H NMR seinaleen etiketak: ● NADH, (a) **1**, ● Pt–OCO**CH$_2$**CH$_2$CO$_2^-$, ● Pt–OCOCH$_2$**CH$_2$**CO$_2^-$, ● $^-$O$_2$C**CH$_2$CH$_2$**CO$_2^-$ askea eta (b) **4**, ● Pt–OCO**CH$_3$**, ● Pt–[(OCO)$_2$C(**CH$_2$**)$_2$CH$_2$], ● Pt–[(OCO)$_2$C(CH$_2$)$_2$**CH$_2$**], ● Pt^{II}–[(OCO)$_2$C(**CH$_2$**)$_2$CH$_2$], ● Pt^{II}–[(OCO)$_2$C(CH$_2$)$_2$**CH$_2$**], ● $^-$OCO**CH$_3$** askea.

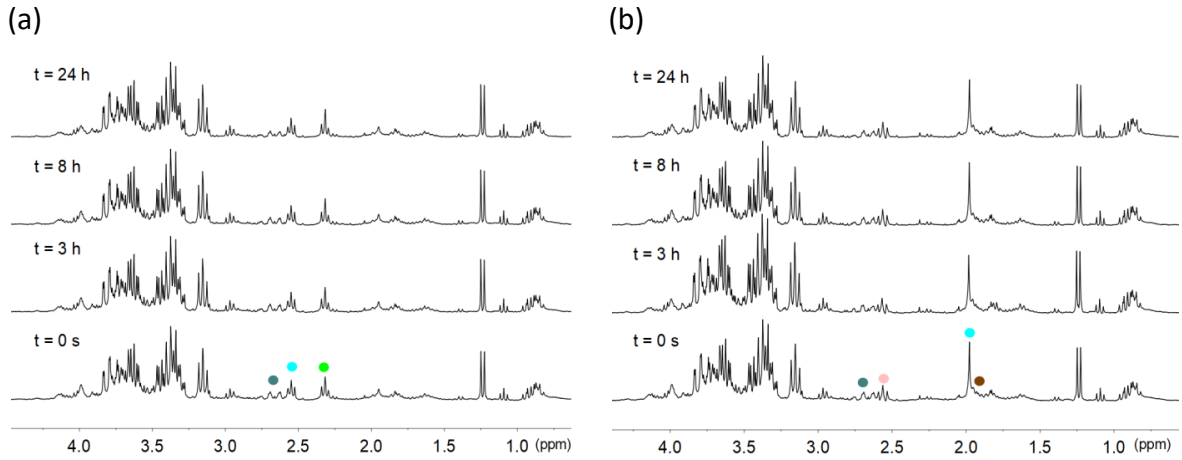

IO 26. Irudia. 1 eta **4** konplexuen (500 µM) egonkortasuna RPMI-1640 ingurune zelularrean (pH 7.0, 10% D_2O), 1 mM NADH-ren eta 25 µM **miniSOG**-ren presentzian.
^{1}H NMR seinaleen etiketak: ● NADH, (a) **1**, ● Pt–OCO**CH$_2$**CH$_2$CO$_2^-$, ● Pt–OCOCH$_2$**CH$_2$**CO$_2^-$, ● $^-$O$_2$C**CH$_2$CH$_2$**CO$_2^-$ askea eta (b) **4**, ● Pt–OCO**CH$_3$**, ● Pt–[(OCO)$_2$C(**CH$_2$**)$_2$CH$_2$], ● Pt–[(OCO)$_2$C(CH$_2$)$_2$**CH$_2$**], ● Pt^{II}–[(OCO)$_2$C(**CH$_2$**)$_2$CH$_2$], ● Pt^{II}–[(OCO)$_2$C(CH$_2$)$_2$**CH$_2$**], ● $^-$OCO**CH$_3$** askea.

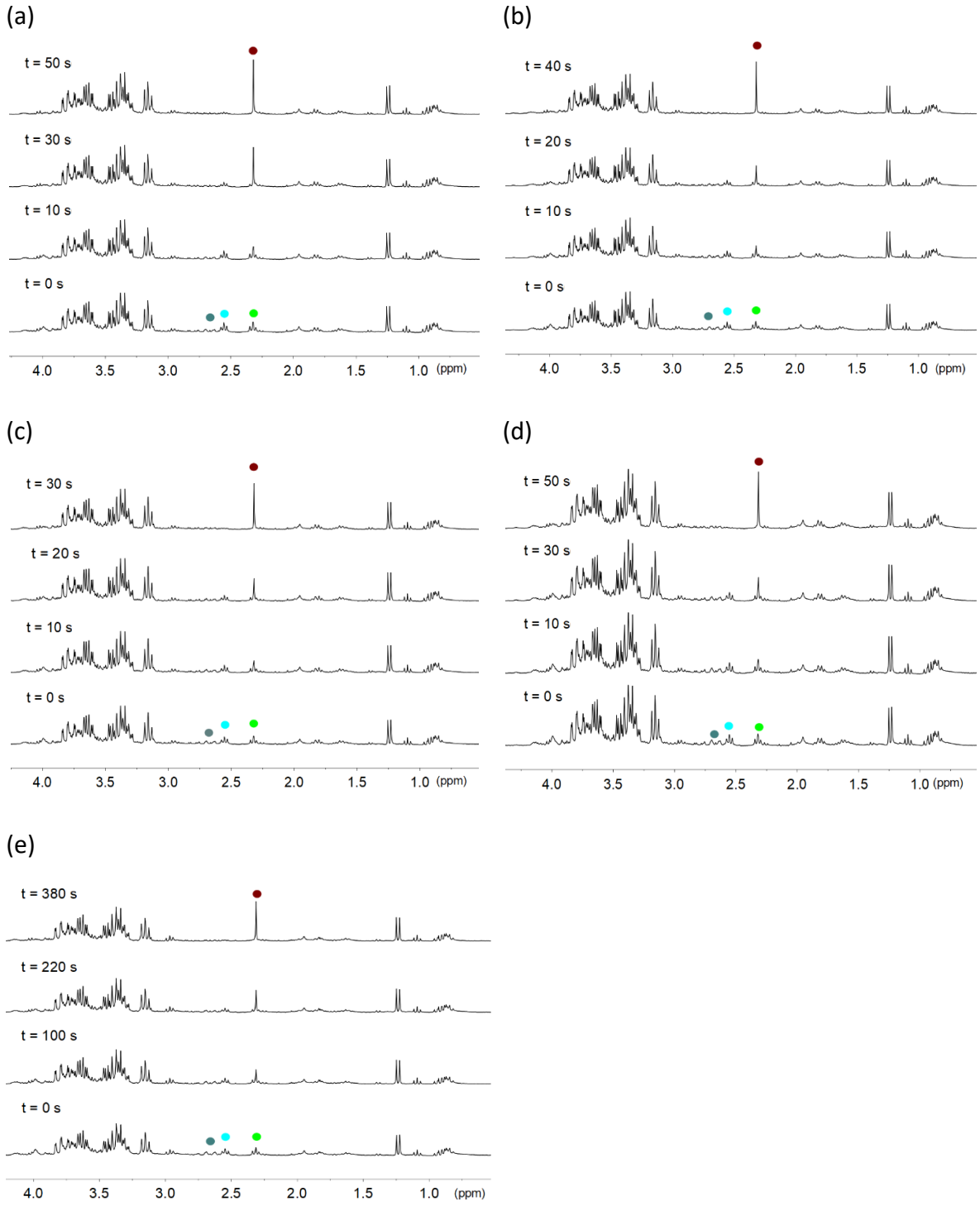

IO 27. Irudia. 1 konplexuaren (500 µM) aktibazio fotokatalitikoa RPMI-1640 ingurune zelularrean (pH 7.0, % 10 D_2O), 1 mM NADH-ren eta 25 µM a) **Rf**; b) **FMN**; c) **TARF**; d) **Lf**; e) **miniSOG**-ren presentzian, 460 nm-ko argi irradiazioaren menpe (6 $mW{\cdot}cm^{-2}$).
^1H NMR seinaleen etiketak: ● NADH, ● Pt–OCO**CH_2**$CH_2CO_2^-$, ● Pt–OCOCH_2**CH_2**CO_2^-, ● ^-O_2C**CH_2CH_2**CO_2^- askea.

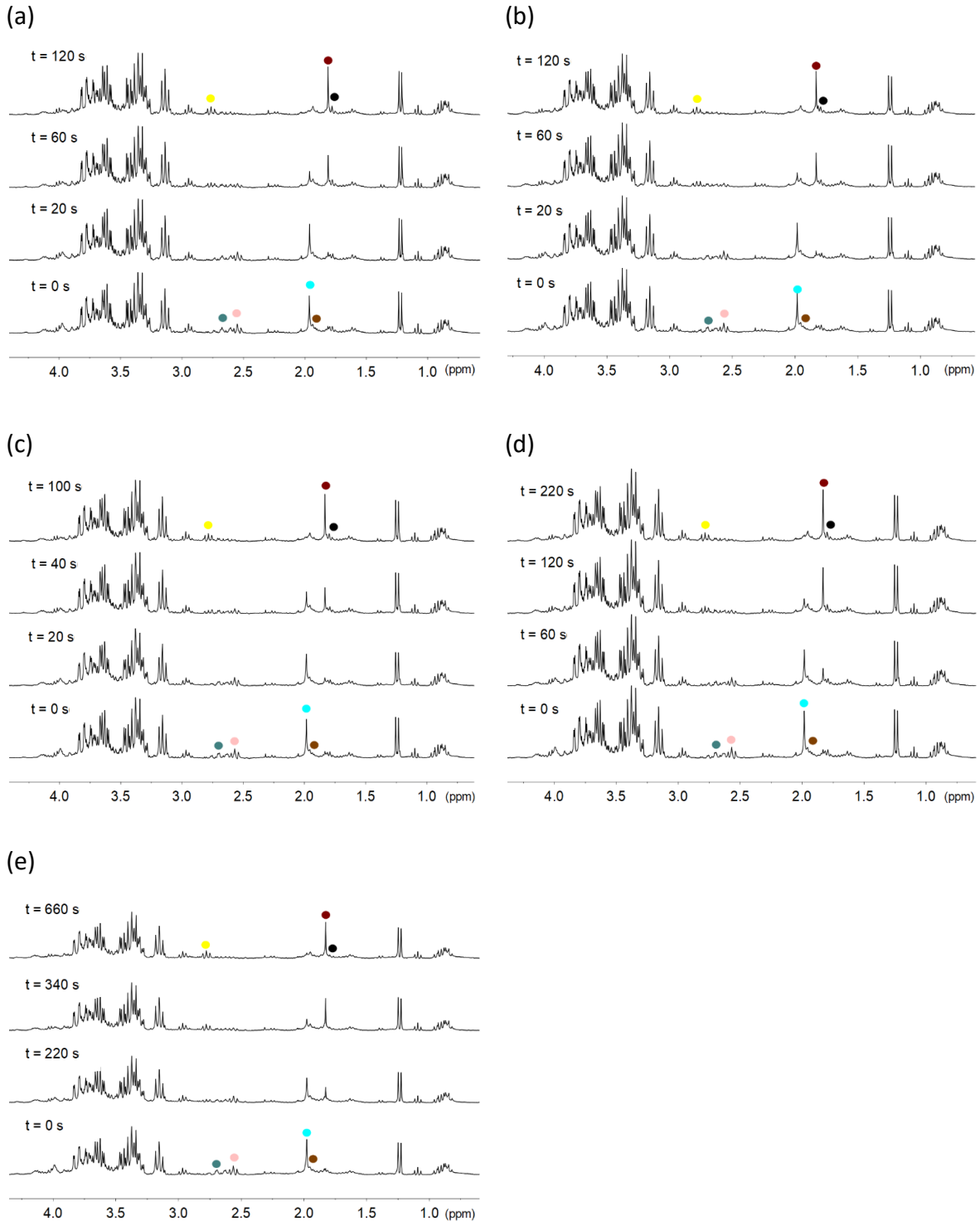

IO 28. Irudia. 4 konplexuaren (500 µM) aktibazio fotokatalitikoa RPMI-1640 ingurune zelularrean (pH 7.0, % 10 D_2O), 1 mM NADH-ren eta 25 µM a) **Rf**; b) **FMN**; c) **TARF**; d) **Lf**; e) **miniSOG**-ren presentzian, 460 nm-ko argi irradiazioaren menpe (6 $mW \cdot cm^{-2}$).
^1H NMR seinaleen etiketak: ● NADH, ● Pt–OCO**CH_3**, ● Pt–[$(OCO)_2C(\mathbf{CH_2})_2CH_2$], ● Pt–[$(OCO)_2C(CH_2)_2\mathbf{CH_2}$], ● Pt^{II}–[$(OCO)_2C(\mathbf{CH_2})_2CH_2$], ● Pt^{II}–[$(OCO)_2C(CH_2)_2\mathbf{CH_2}$], ● $^-$OCO**CH_3** askea.

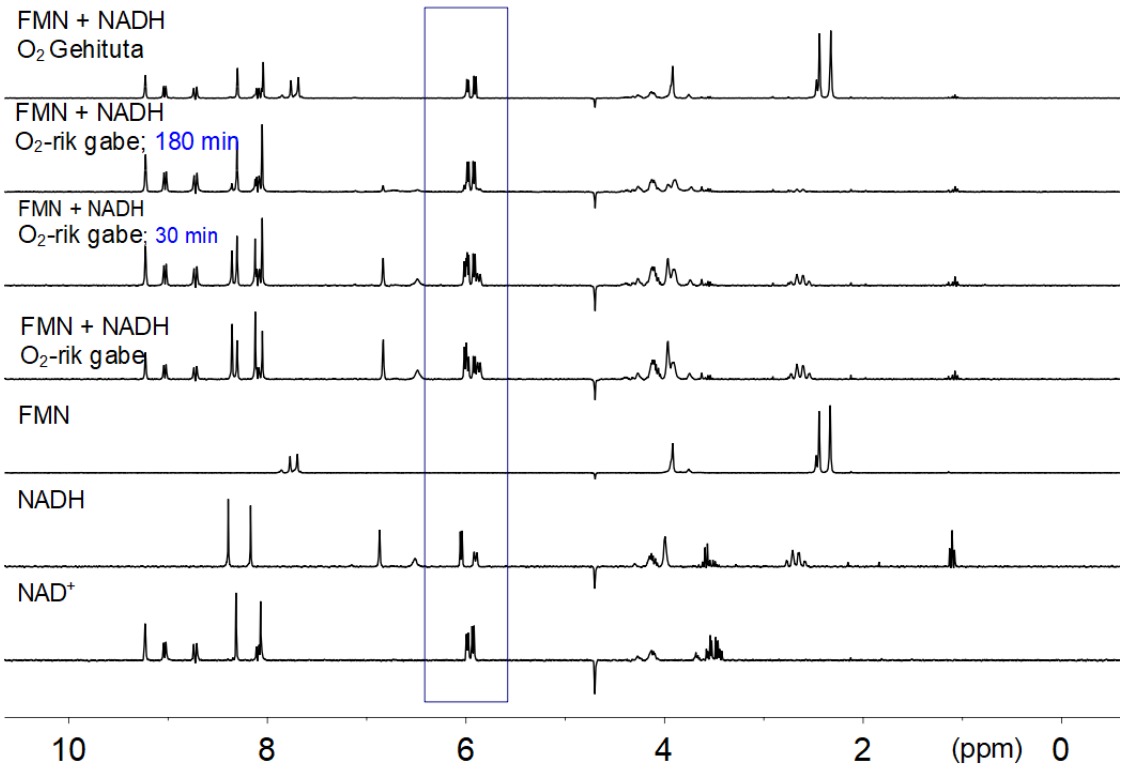

IO 29. Irudia. NADH-ren oxidazio kronologikoa ilunpetan **FMN**-ren presentzian (1:1, 3 mM) 18 mM PB (pH 7.0, % 10 D_2O) disoluzioan. NADH-NAD^+ konbertsioaren jarraipena egiteko erabilitako ribosaren H1 eta H1´gailur diagnostikoak lauki urdinean nabarmendu dira

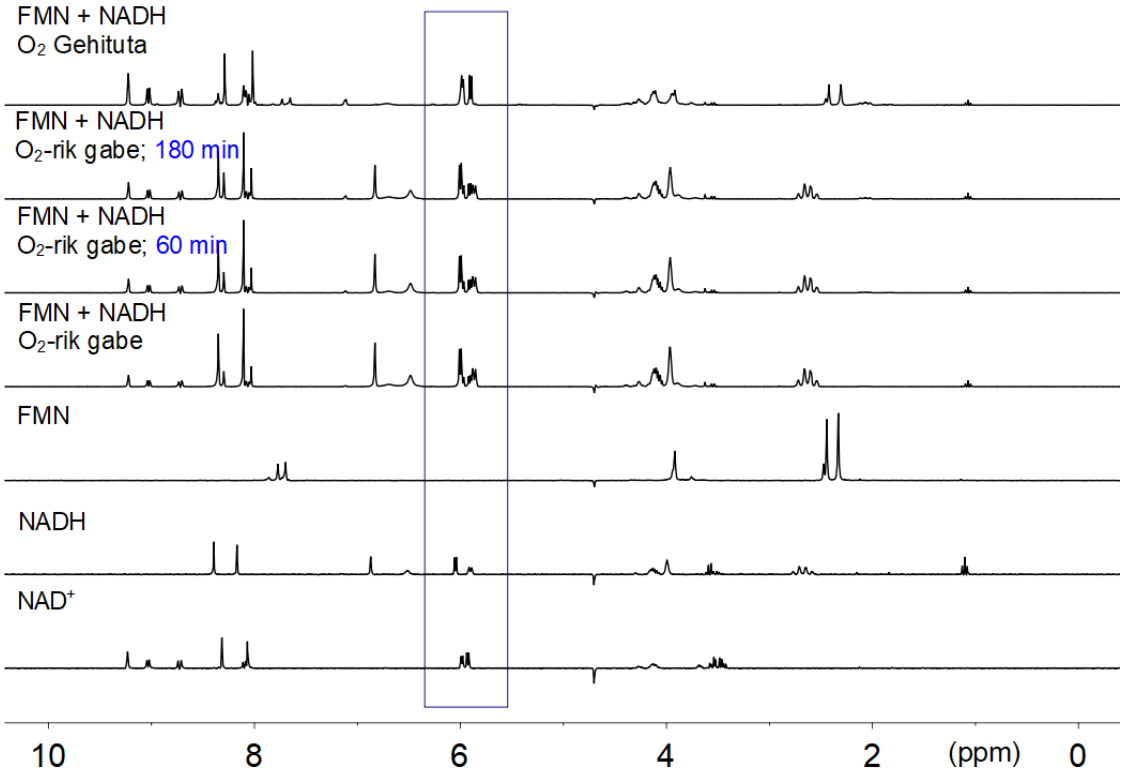

IO 30. Irudia. NADH-ren oxidazio kronologikoa ilunpetan **FMN**-ren presentzian (5:1, 15:3 mM) 18 mM PB (pH 7.0, % 10 D_2O) disoluzioan. NADH-NAD^+ konbertsioaren jarraipena egiteko erabilitako ribosaren H1 eta H1´gailur diagnostikoak, lauki urdinean nabarmendu dira.

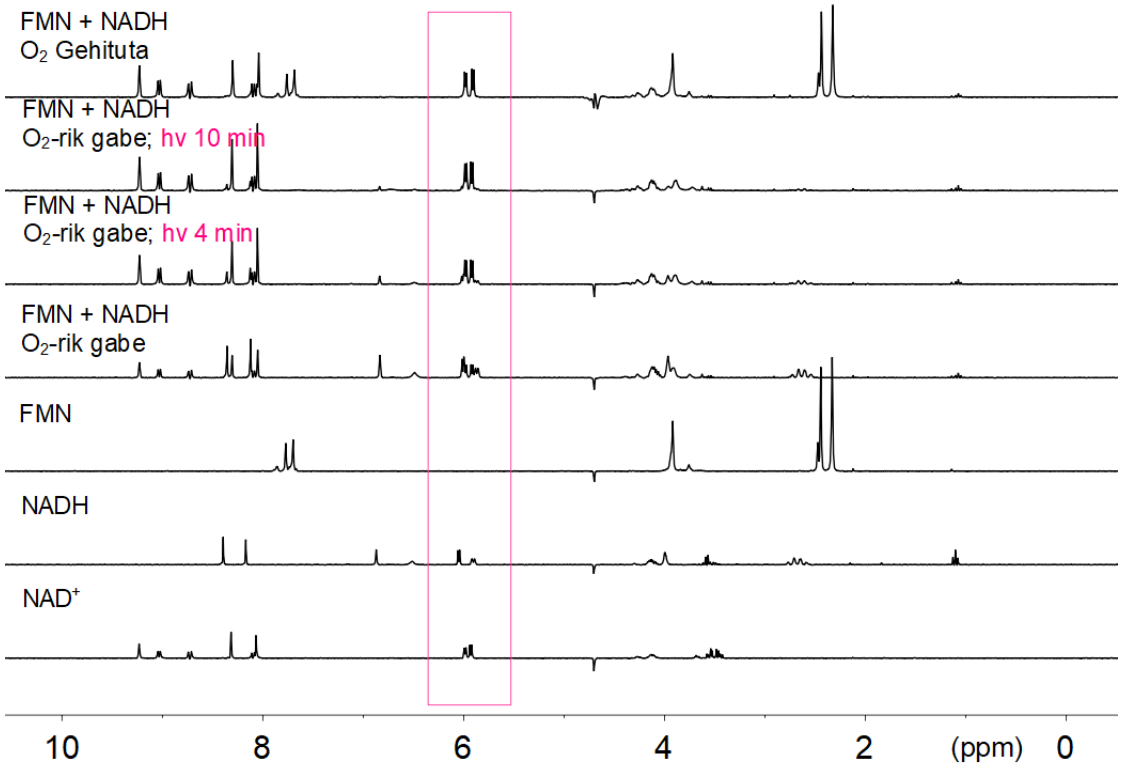

IO 31. Irudia. NADH-ren oxidazio kronologikoa **FMN**-ren presentzian (1:1, 3 mM) 18 mM PB (pH 7.0, % 10 D_2O) disoluzioan, 460 nm-ko argi irradiazioaren menpe (6 $mW \cdot cm^{-2}$). NADH-NAD^+ konbertsioaren jarraipena egiteko erabilitako ribosaren H1 eta H1´gailur diagnostikoak, lauki arrosaz nabarmendu dira.

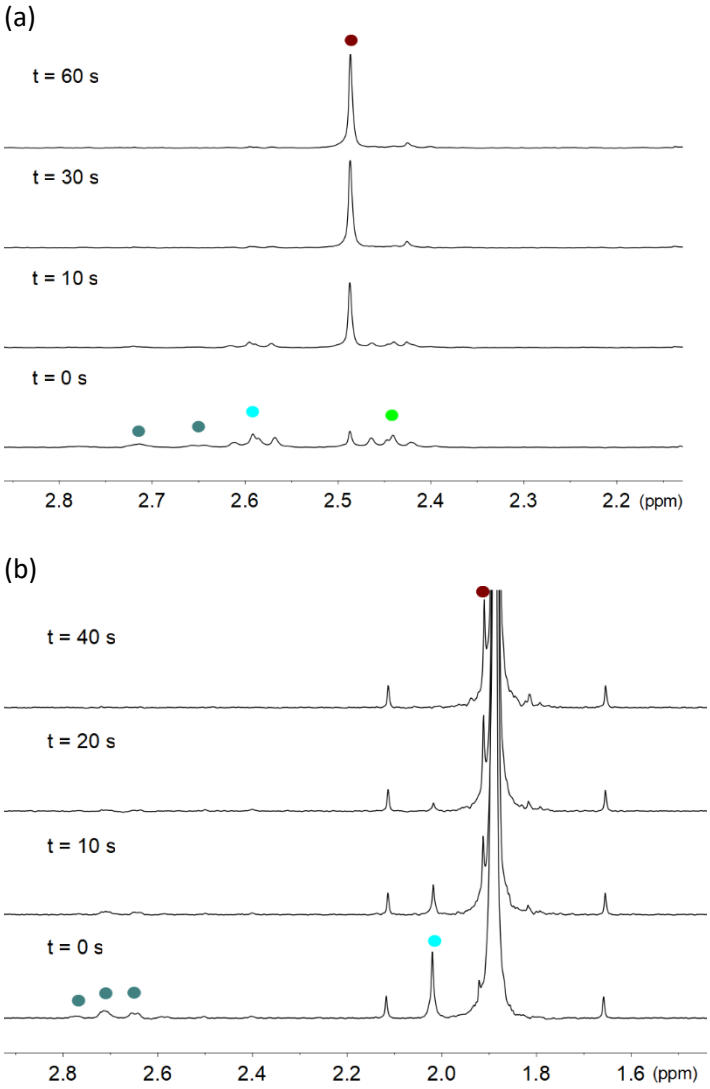

IO 32. Irudia. **1** eta **3** Konplexuen (500 µM) aktibazio fotokatalitikoa 18 mM kakodilato (pH 4.3, % 10 D_2O) disoluzioan, 1mM NADH-ren eta 25 µM **FMN**-ren presentzian, 460 nm-ko argi irradiazioaren menpe (6 $mW{\cdot}cm^{-2}$).
^1H NMR seinaleen etiketak: ● NADH, **1**, (a) ● Pt–OCO**CH_2**$CH_2CO_2^-$, ● Pt–OCOCH_2**CH_2**CO_2^-, ● ^-O_2C**CH_2CH_2**CO_2^- askea; (b) **3**, ● Pt–OCO**CH_3**, ● $^-$OCO**CH_3** askea.

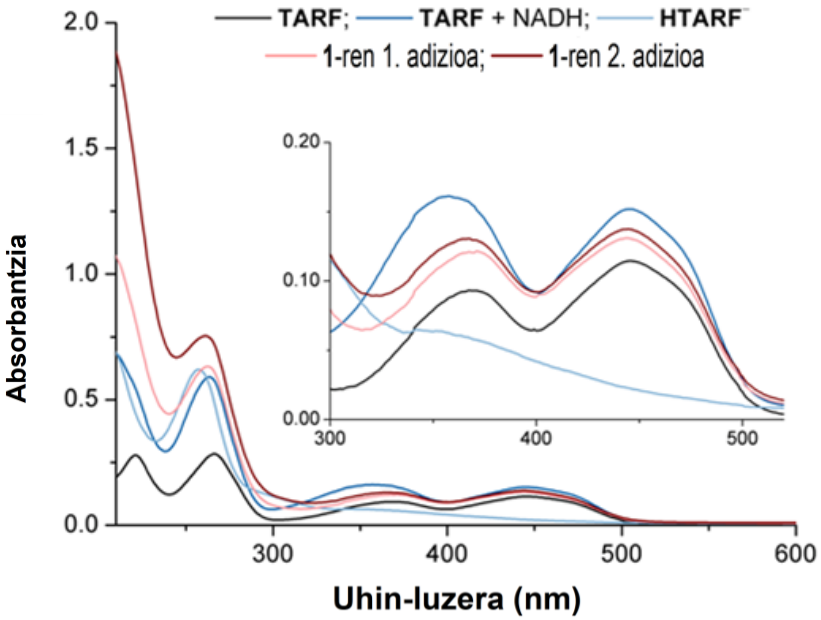

IO 33. Irudia. Oxigenorik gabeko baldintzetan, UMore-Ikus bidez egindako, **HTARF**$^-$ espezieran sorreraren eta **1** substratuak eragindako oxidazioaren (18 mM PB, pH 7.5) jarraipena. **HTARF**$^-$ espeziea, **TARF**-ren (15 µM) eta NADH-ren 1 mol baliokideren presentzian, oxigenorik gabe eta 460 nm-ko argi irradiazioaren menpe (90 s) lortu zen.

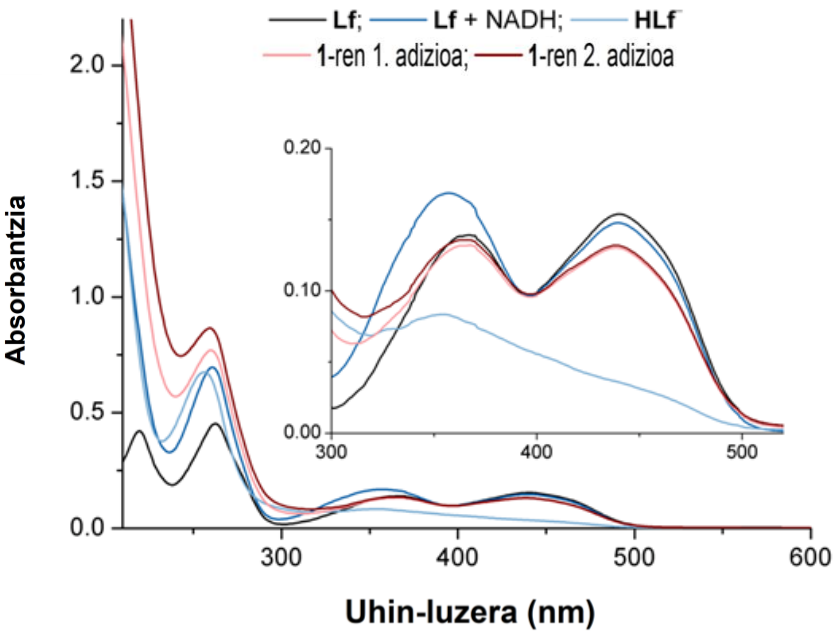

IO 34. Irudia. Oxigenorik gabeko baldintzetan, UMore-Ikus bidez egindako, **HLf**$^-$ espezieran sorreraren eta **1** substratuak eragindako oxidazioaren (18 mM PB, pH 7.5) jarraipena. **HLf**$^-$ espeziea, **Lf**-ren (15 µM) eta NADH-ren 1 mol baliokideren presentzian, oxigenorik gabe eta 460 nm-ko argi irradiazioaren menpe (90 s) lortu zen.

(a)

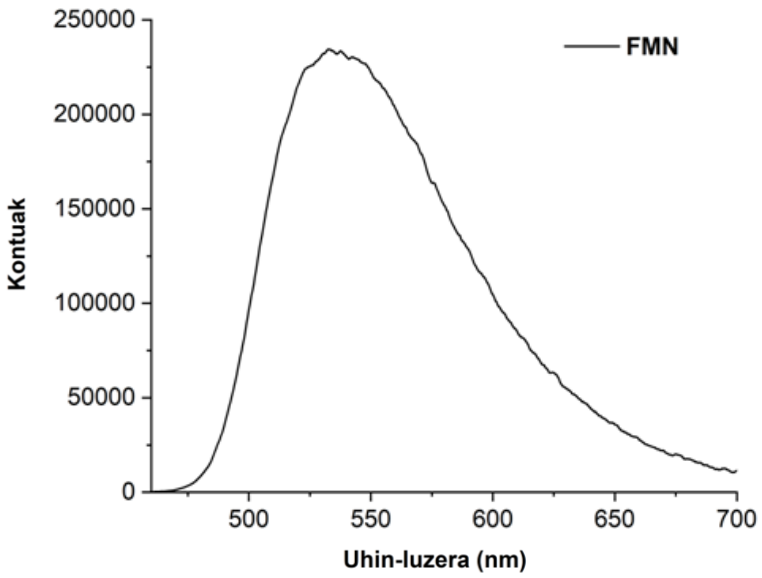

(b)

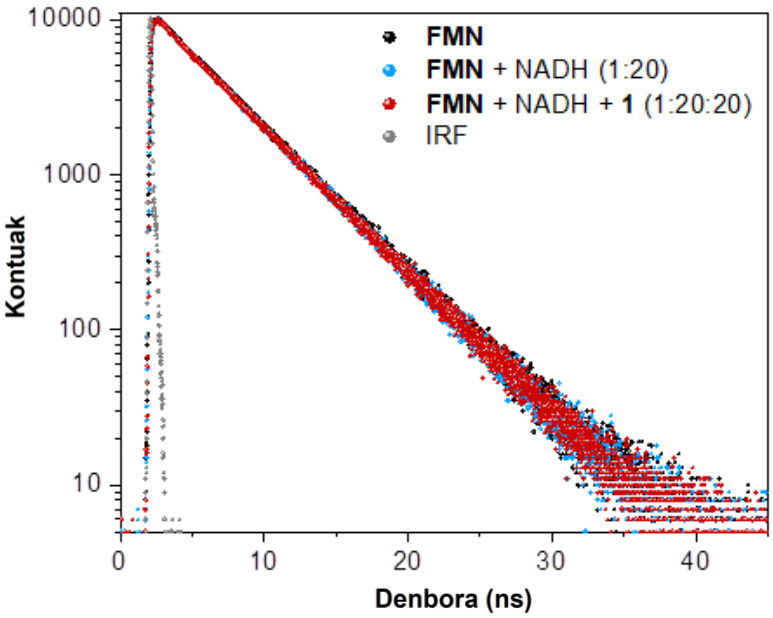

IO 35. Irudia. (a) **FMN**-ren (20 µM) fluoreszentzia emisio espektroa eta (b) **FMN** (20 µM), **FMN** (20 µM) eta NADH (400 µM), eta **FMN** (20 µM), NADH (400 µM) eta **1** (400 µM) disoluzioen beheraldi erradiatiboen kurbak (λ_{kitz} 445 nm, λ_{em} = 540 nm). Beheraldi guztiak monoesponentzialak ziren eta 4.7 ns-ko τ_{Fluo} azaldu zuten.

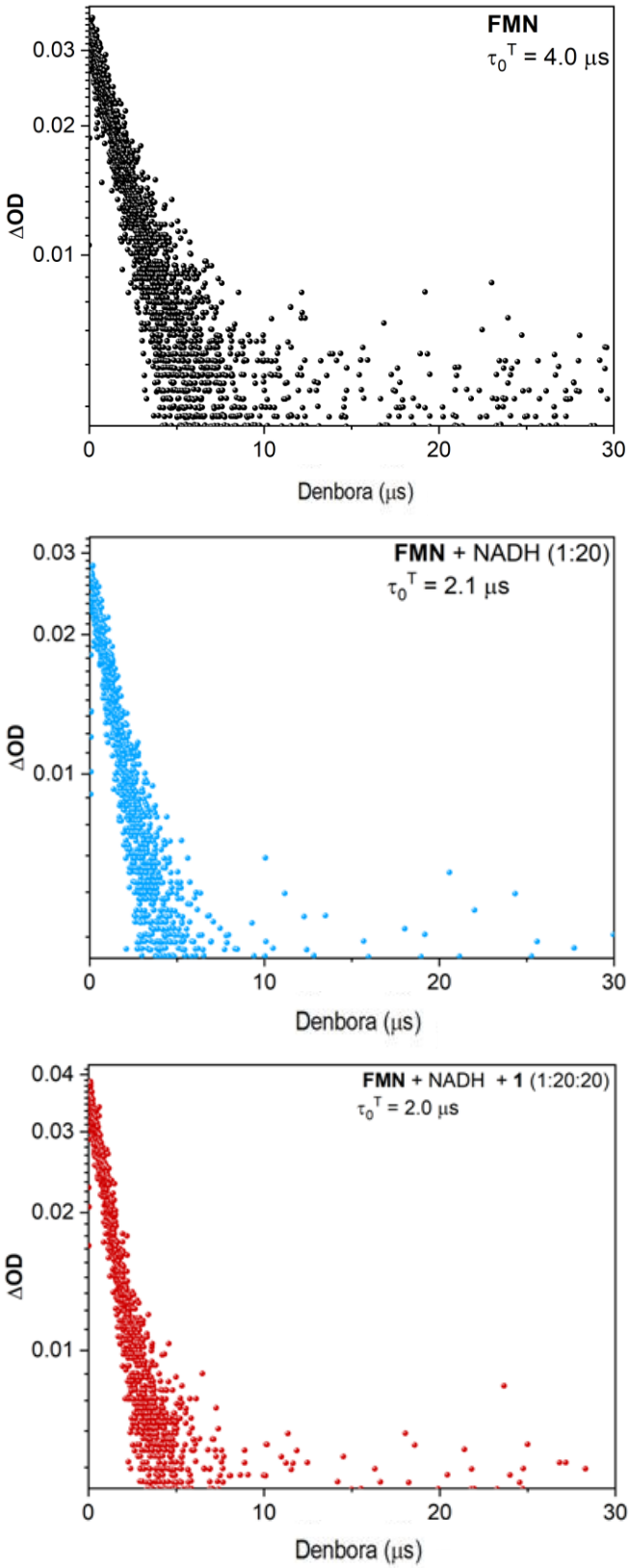

IO 36. Irudia. ^{3}FMN*-ren (λ_{kitz} 445 nm, λ_{abs} = 700 nm) triplete-triplete absortzioaren beheraldia, airez asetutako **FMN** (20 µM), **FMN** (20 µM) eta NADH (400 µM), eta **FMN** (20 µM), NADH (400 µM) eta **1** (400 µM) disoluzioetan.

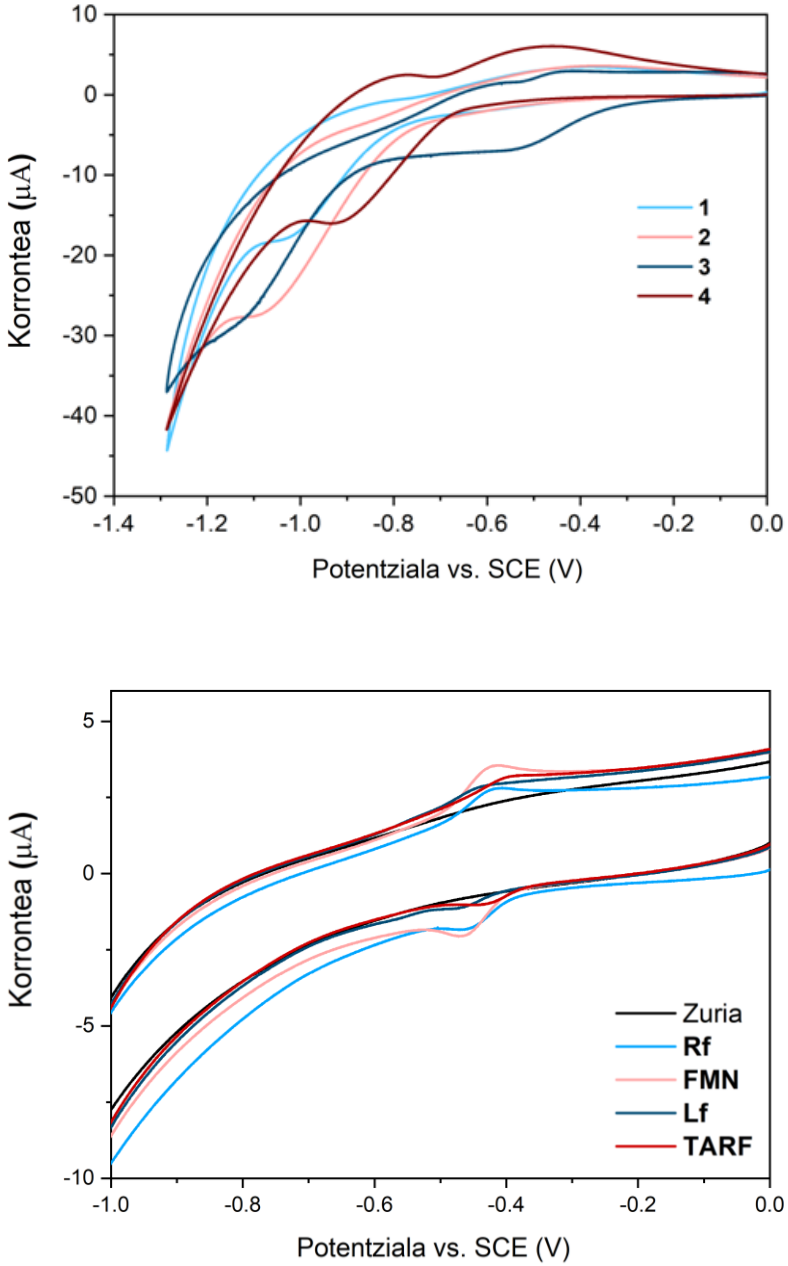

IO 37. Irudia. 1–**4** substratuen eta flabinen voltamograma ziklikoak 0.2 V s^{-1}-tan 0.05 M fosfato (pH 7.4, 0.15 M NaCl) disoluzioan. Metalentzako gailur katodiko potentzialak E_{pc}): **1**, −1.03 V; **2** −1.11 V; **3** −0.56 V; **4**, −0.93 V. Flabinentzako$E_{1/2}$ potentzialak: **Rf**, −0.44 V; **FMN**, −0.44 V; **Lf**, −0.46 V; **TARF**, −0.42 V.

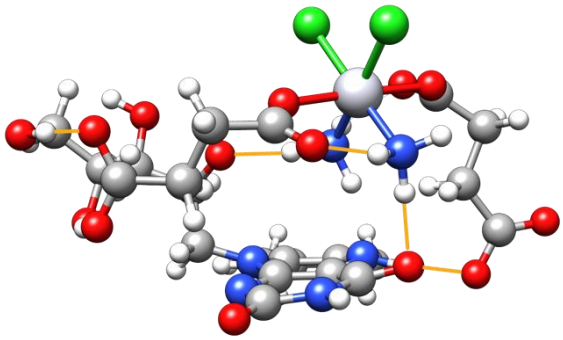

1

ΔE_{wb97xd} = 2.3 kcal/mol
$\Delta E_{cam\text{-}b3lyp}$ = 2.3 kcal/mol

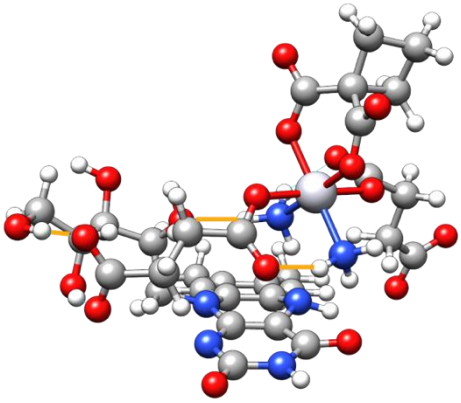

2

ΔE_{wb97xd} = 2.8 kcal/mol
$\Delta E_{cam\text{-}b3lyp}$ = 0.3 kcal/mol

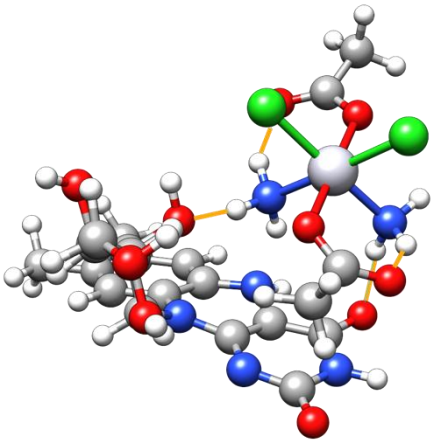

3

ΔE_{wb97xd} = 1.6 kcal/mol
$\Delta E_{cam\text{-}b3lyp}$ = 0.7 kcal/mol

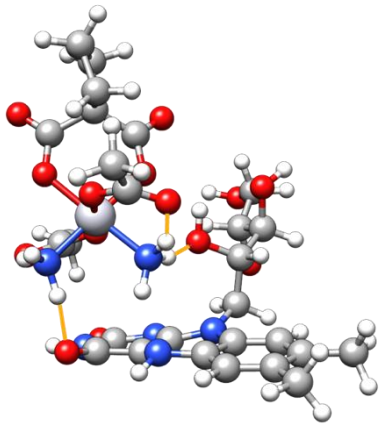

4

ΔE_{wb97xd} =4.5 kcal/mol
$\Delta E_{cam\text{-}b3lyp}$ = -1.1 kcal/mol

IO 38. Irudia. DFT bidez optimizatutako (pbe0/def2-SVP) **1**–**4** substratuen eta **RfH**$^{-}$-ren arteko egonkortasun gutxieneko aduktuen egiturak (H-zubiak marra laranjaz nabarmendu dira). Egitura bakoitzeko, ΔE-ek, eskuizkribi nagusian 4. Irudian agertzen diren aduktu egonkorren eta hemen kalkulatutako aduktuen arteko energía desberdinatuna deskribatzen du ($E_{egonokortasun\ gutxienz} - E_{egonkortasun\ handiena}$). Energiak wb97xd eta cam-b3lyp funtzionalak eta puntu bakarreko kalkuluekin def2-TZVP datu basea erabiliz kalkulatu ziren.

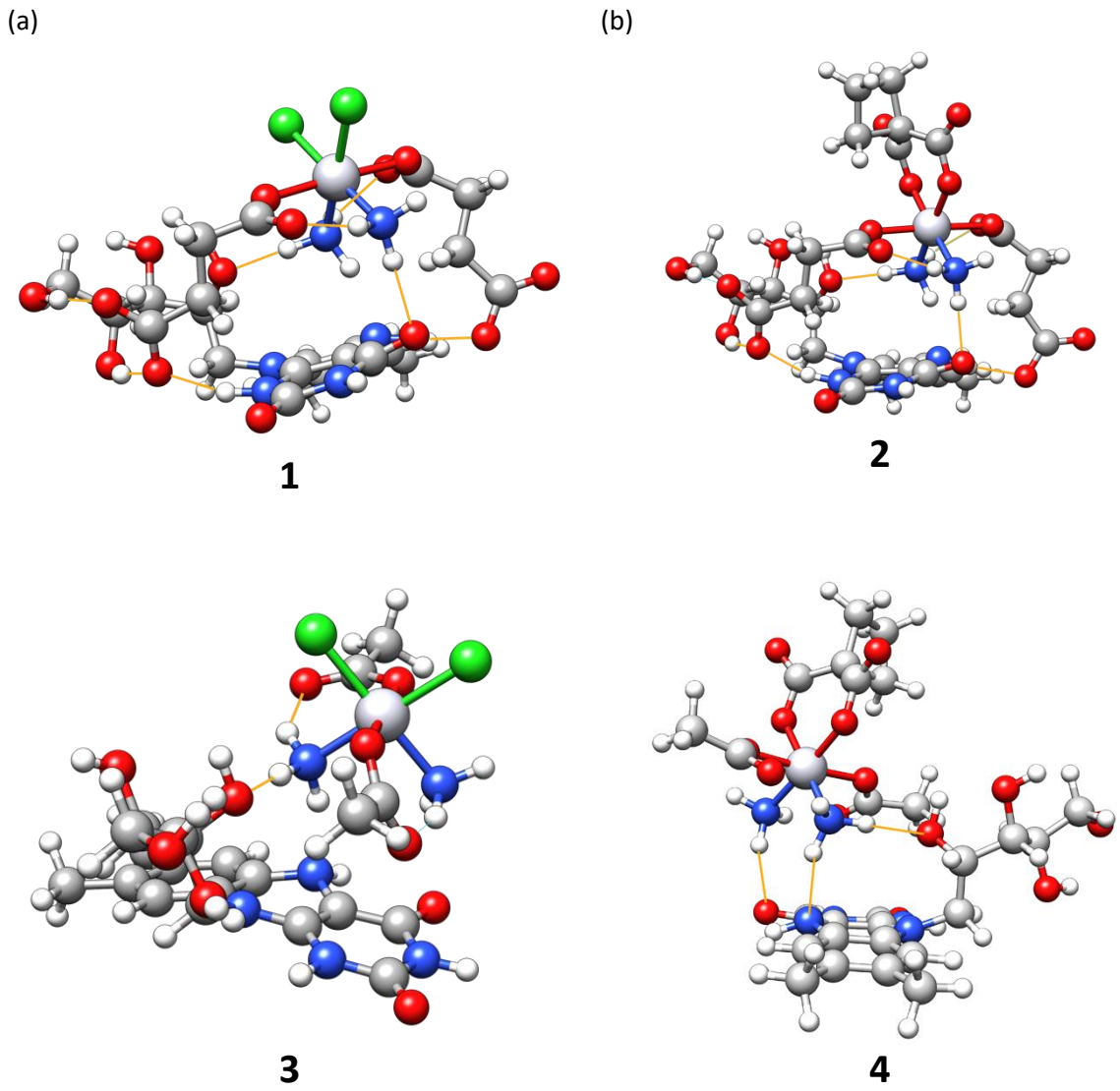

IO 39. Irudia. DFT bidez optimizatutako (pbe0/def2-SVP), **1**–**4** substratuen eta **RfH_2**-ren arteko aduktuen (H-zubiak marra laranjaz nabarmendu dira) egiturak.

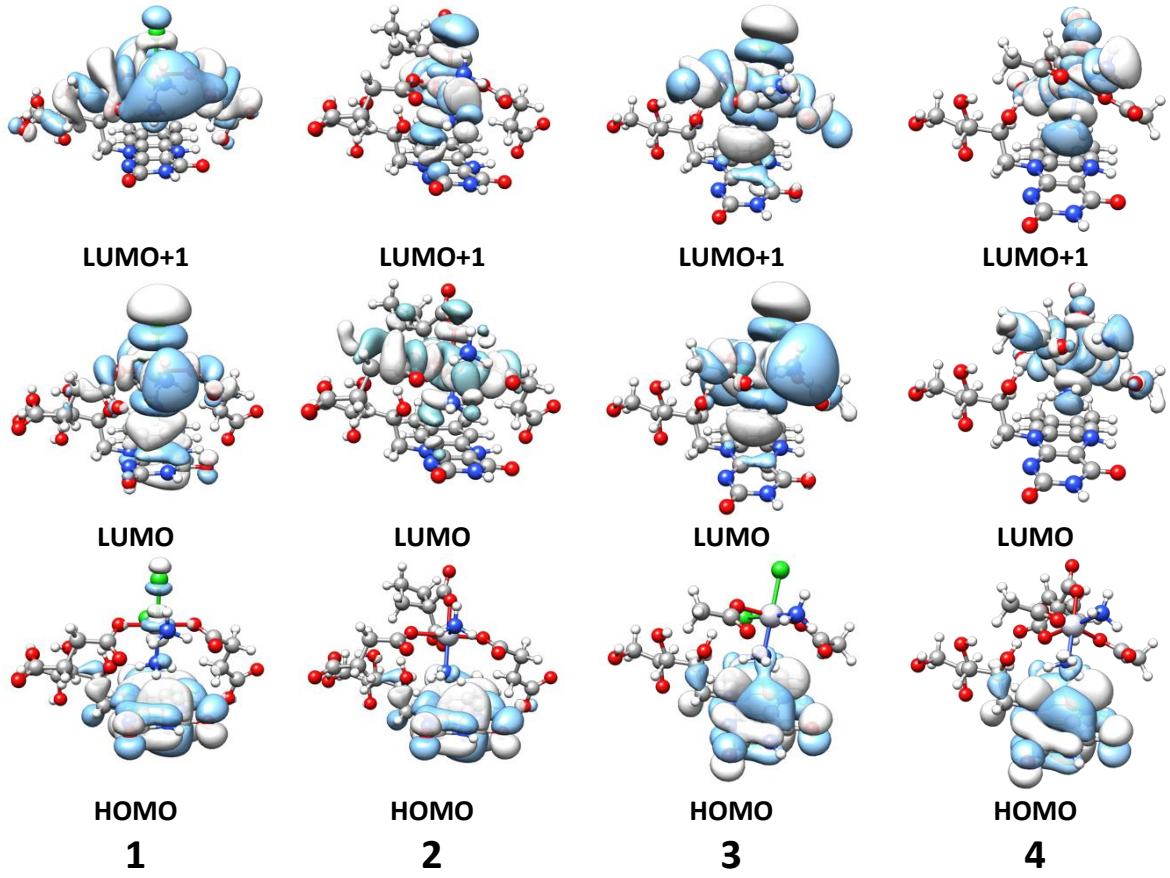

IO 40. Irudia. Egonkortasun handieneko **1**–**4** substratuen eta **RfH**$^{-}$-ren arteko aduktuentzako (pbe0/def2-SVP, grafikatutako isodentsitate azalerak 0.02 $e^{-}\cdot bohr^{-3}$-eko isobalioarekin) aukeratutako DFT muga orbitalak.

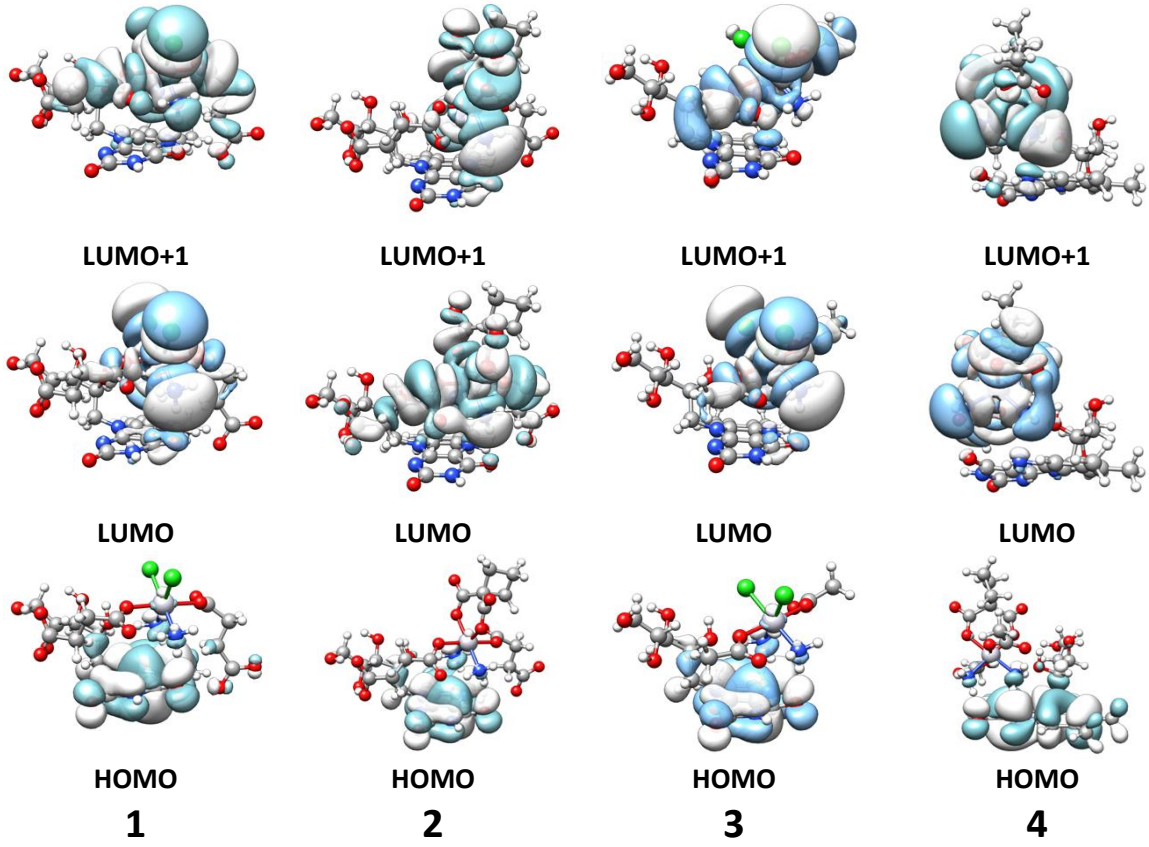

IO 41. Irudia. Egonkortasun txikieneko **1**–**4** substratuen eta $\mathbf{RfH}^{-}$-ren arteko aduktuentzako (pbe0/def2-SVP, grafikatutako isodentsitate azalerak 0.02 $e^{-}\cdot bohr^{-3}$-eko isobalioarekin) aukeratutako DFT muga orbitalak.

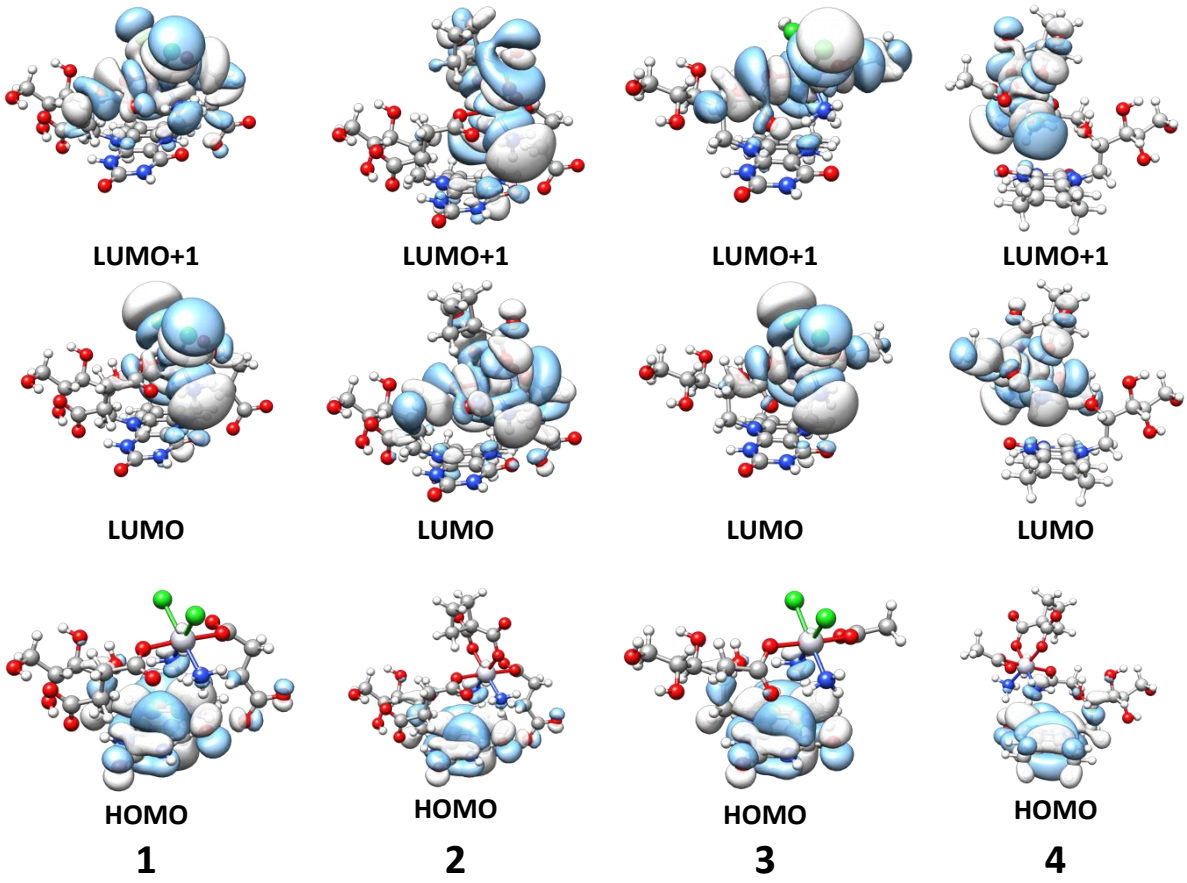

IO 42. Irudia. 1–4 substratuen eta **RfH_2**-ren arteko aduktu egonkorrentzako (pbe0/def2-SVP, grafikatutako isodentsitate azalerak 0.02 $e^{-}\cdot bohr^{-3}$-eko isobalioarekin) aukeratutako DFT muga orbitalak.

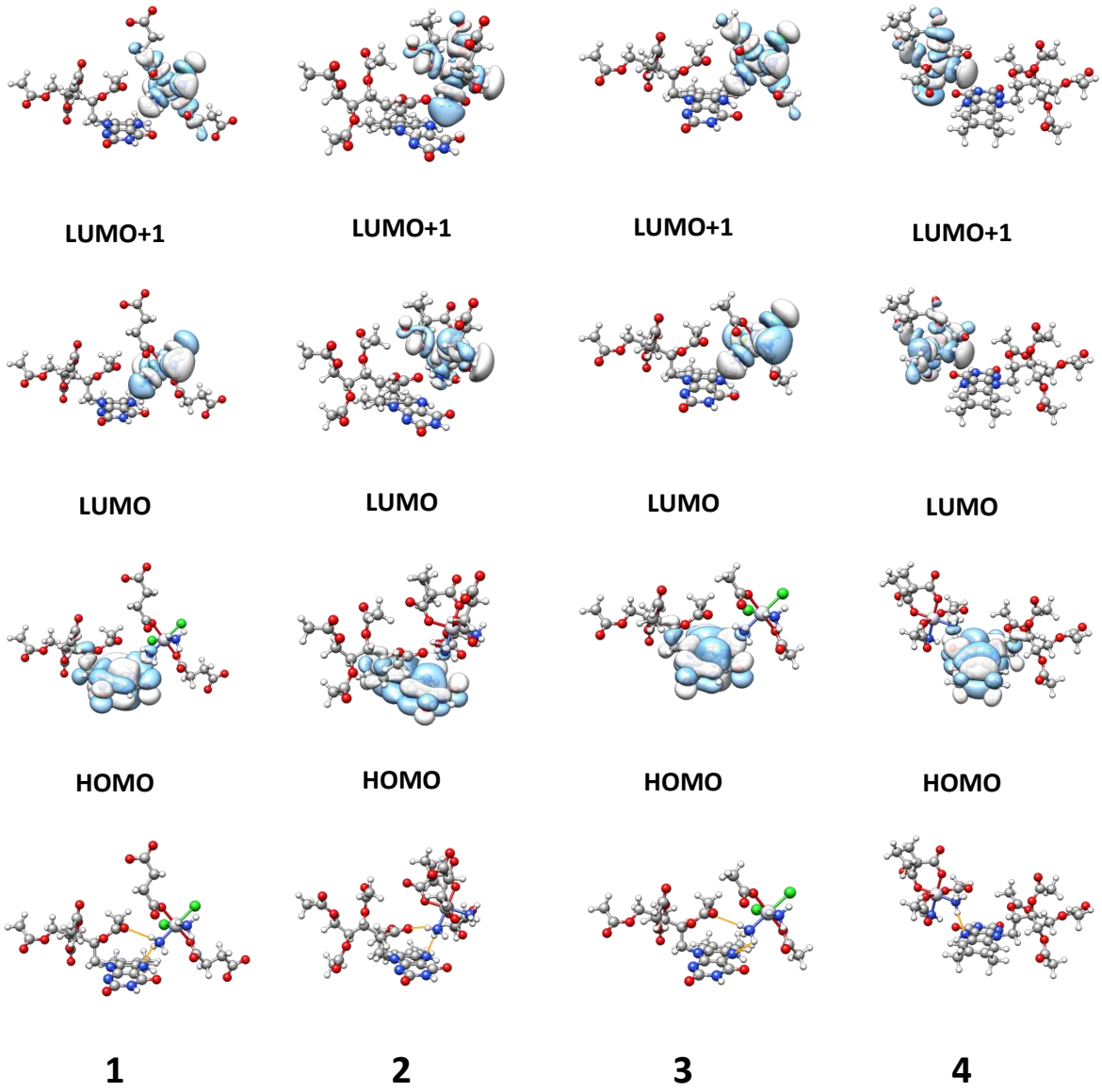

IO 43. Irudia. DFT bidez optimizatutako (pbe0/def2-SVP), **1**–**4** substratuen eta **TARFH**$^{-}$-ren arteko aduktuen (H-zubiak marra laranjaz nabarmendu dira) egiturak eta aukeratutako DFT muga orbitalak grafikatutako isodentsitate azalerak 0.02 $e^{-}\cdot bohr^{-3}$-eko isobalioarekin).

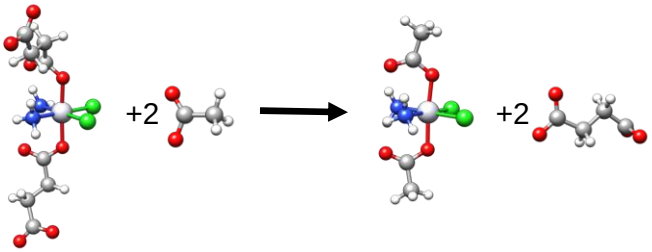

1 → 3

ΔG (kcal/mol)*		
wb97xd	**m062x**	**pbe0**
5.8	4.1	6.1

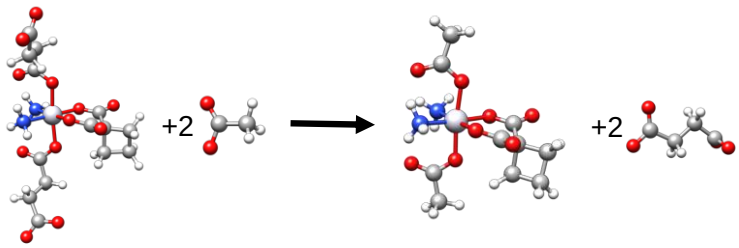

2 → 4

wb97xd	**m062x**	**pbe0**
6.9	5.1	5.5

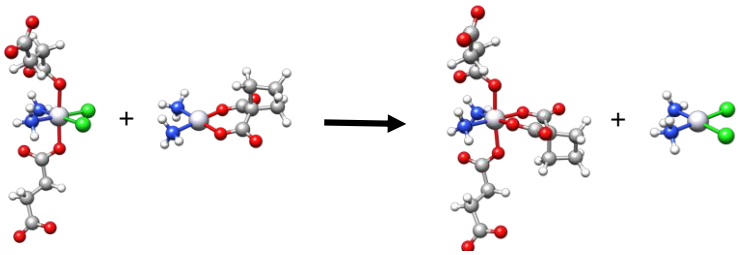

1 → 2

wb97xd	**m062x**	**pbe0**
-7.3	-5.2	-4.2

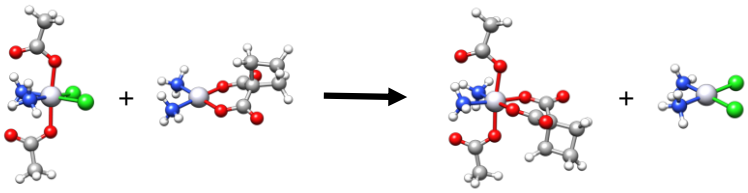

3 → 4

wb97xd	**m062x**	**pbe0**
-6.4	-4.2	-4.8

* **1**–**4** estekatzaile ekuatorialen eta axialen ordezkapen erreakzioen energia askeak (kcal/mol). Kalkulu guztiak, pbe0/def2-SVP optimizatutako geometrietan def2-TZVP datu basea erabiliz egin ziren. Xehetasun gehiagorako ikusi metodo komputazioalak.

IO 44. Irudia. 1–**4** substratuen DFT kalkuluen egonkortasuna def2-TZVP datu basea eta funtzional dezberdinak erabiliz. Egonkortasun erlatiboak: **1** > **3** eta **2** > **4** (ΔG > 0); **1** < **2** eta **3** < **4** (ΔG < 0).

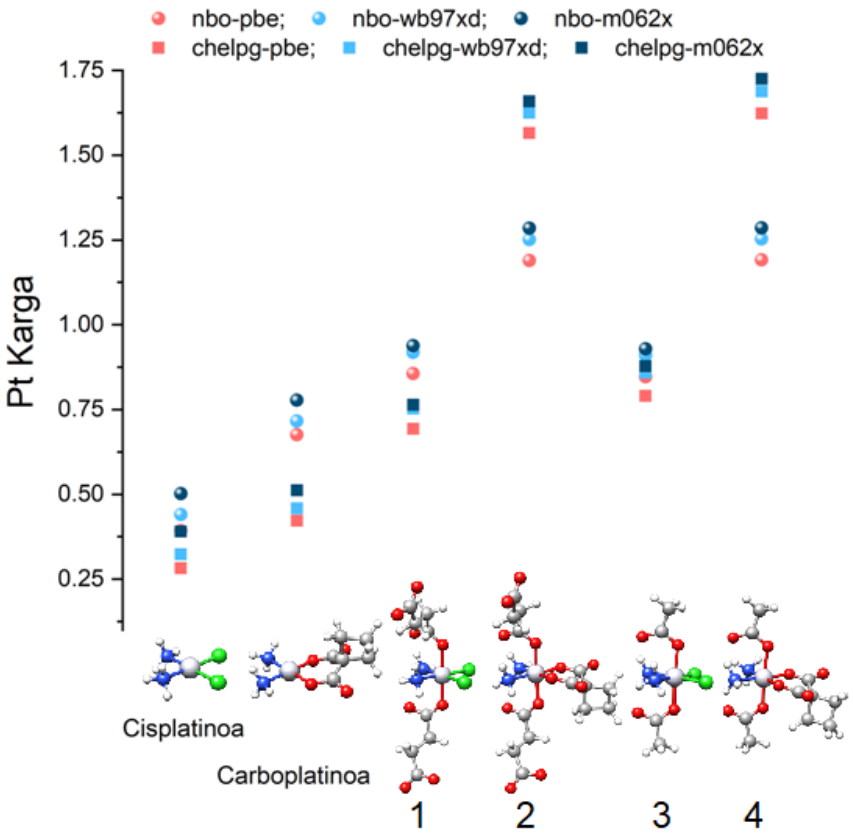

IO 45. Irudia. 1–4, cisplatino eta carboplatino konplexuentzako kalkulatutako Pt karga, DFT mailan nbo eta chelpg metodoak erabiliz (pbe0, wb97xd eta m062x funtzionalak eta def2-TZVP datu basea).

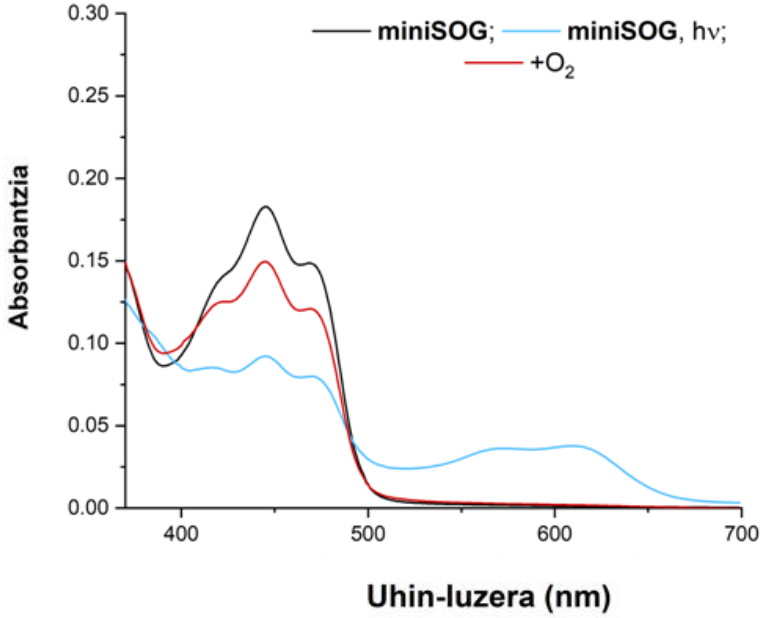

IO 46. Irudia. Argi irradiazioaren menpe, UMore-Ikus bidez egindako **miniSOG**-aren jarraipena oxigenorik eta NADH-rik gabeko baldintzetan eta oxigenoren adizioari erantzuna. **MiniSOG** (15 µM, 18 mM PB, pH 7.4) soluzioak 460 nm-tara (6 $mW \cdot cm^{-2}$, 600 s) irradiatu ziren.

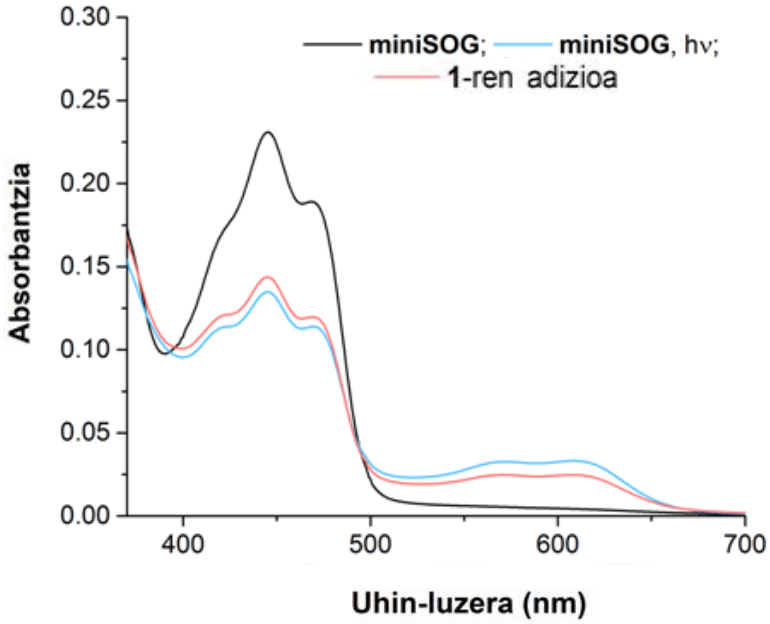

IO 47. Irudia. Argi irradiazioarn menpe, UMore-Ikus bidez egindako **miniSOG**-aren jarraipena oxigenorik eta NADH-rik gabeko baldintzetan eta **1** (80 µM) substratuaren adiziori erantzuna. **MiniSOG** (15 µM, 18 mM PB, pH 7.4) soluzioak 460 nm-tara (6 $mW \cdot cm^{-2}$, 600 s) irradiatu ziren.

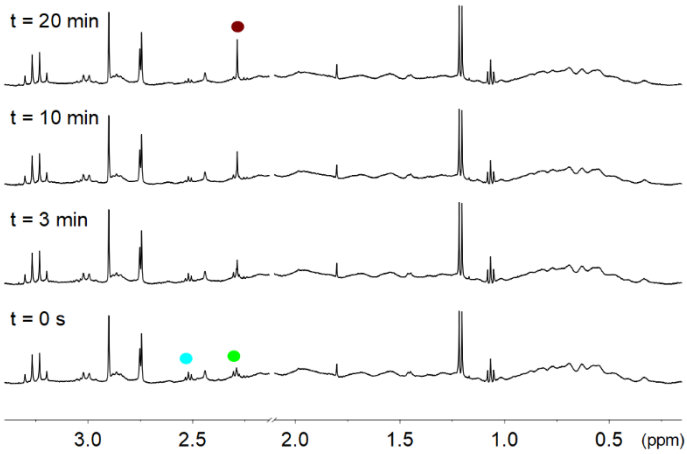

IO 48. Irudia. Oxigenorik gbeko baldintzetan, **1** Konplexuaren (50 µM) aktibazio fotokatalitikoa 18 mM PB (pH 7, % 10 D_2O) disoluzioan, 95 µM **miniSOG**-aren presentzian eta 460 nm-ko argi irradiazioaren menpe (6 $mW \cdot cm^{-2}$). Aipagarria da **miniSOG**, **1** substratua baino gehiago dagoela.

^1H NMR seinaleen etiketak: **1**, ● Pt–OCO**CH_2**$CH_2CO_2^-$, ● Pt–OCOCH_2**CH_2**CO_2^-, ● ^-O_2C**CH_2CH_2**CO_2^- askea.

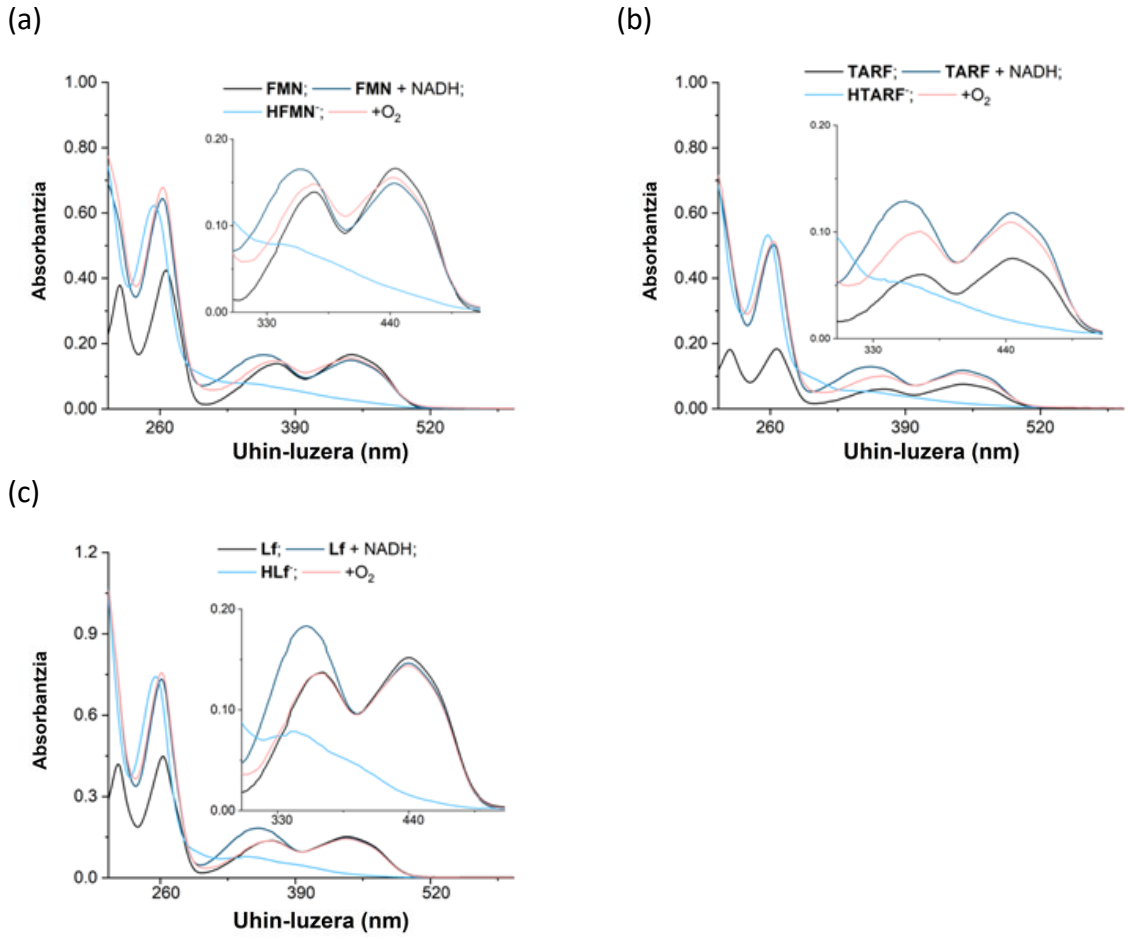

IO 49. Irudia. UMore-Ikus bidez egindako jarraipena, **FMN**-ren (a), **TARF**-ren (b) eta **Lf**-ren erredukzioa (c) argi irradiazioren menpe, NADH-k eraginda eta O_2-k eragindako beroxidazioa. $HFL^{\bullet}$ espezieen sorrera (18 mM PB, pH 7.5) oxigenorik gabeko baldintzetan, flabinak 460 nm-ko irradiazioaren menpe (15 µM, 40–90 s) eta NADH baliokide molen presetzian lortu ziren.

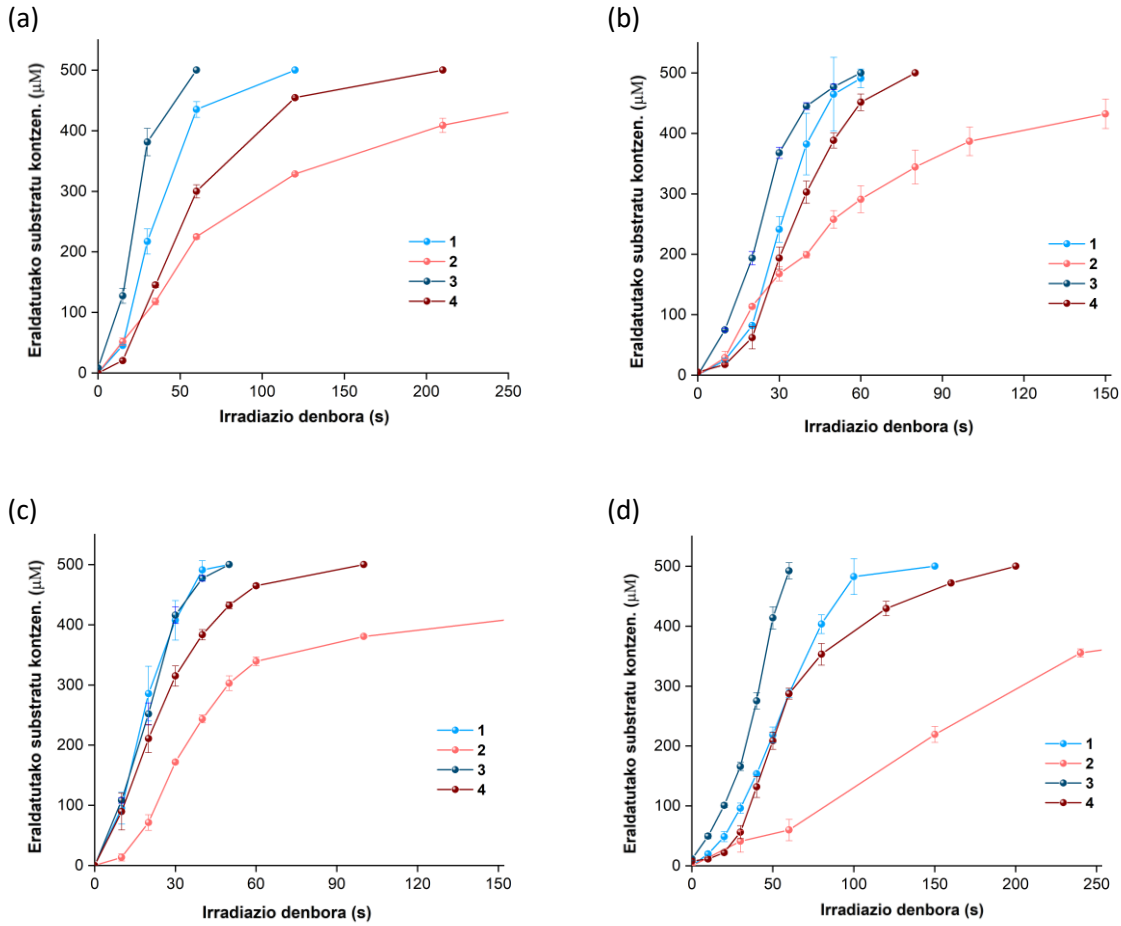

IO 50. Irudia. Rf (a), **FMN** (b), **TARF** (c), **Lf** (d) flabinek eragindako **1**–**4** substratuen konbertsio fotokatalitikoen profil zinetikoak. Erreakzioak, ^{1}H NMR bidez jarraitu ziren, 500 µM **1**–**4**, 1 mM NADH eta 25 µM flabina katalizatzaile erabiliz (18 mM PB, pH 7.0, % 10 D_2O).

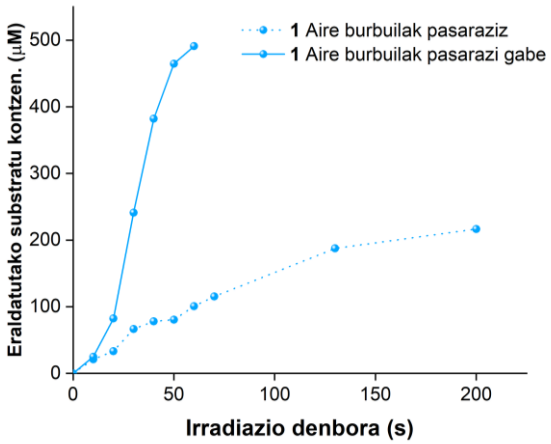

IO 51. Irudia. FMN-k eragindako **1** Substratuaren konbertsio fotokatalitikoaren profil zinetikoa aire burbuilak disoluziotik pasaraziz ala ez. Erreakzioak, ^{1}H NMR bidez jarraitu ziren, 500 µM **1**–**4**, 1 mM NADH eta 25 µM flabina katalizatzaile erabiliz (18 mM PB, pH 7.0, % 10 D_2O).

(a)

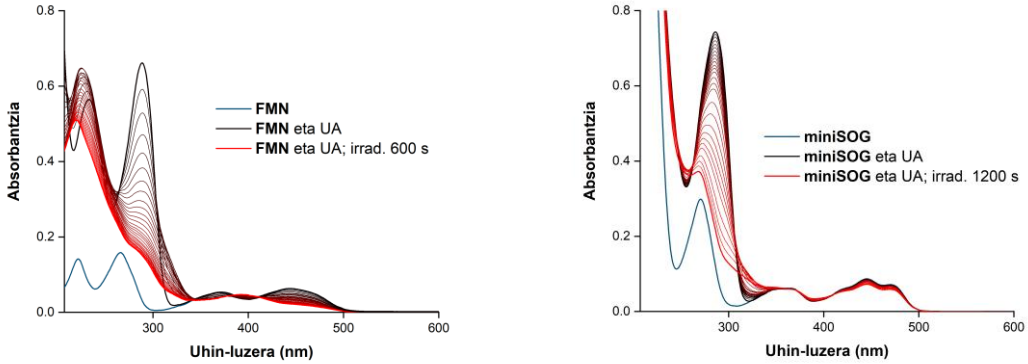

(b)

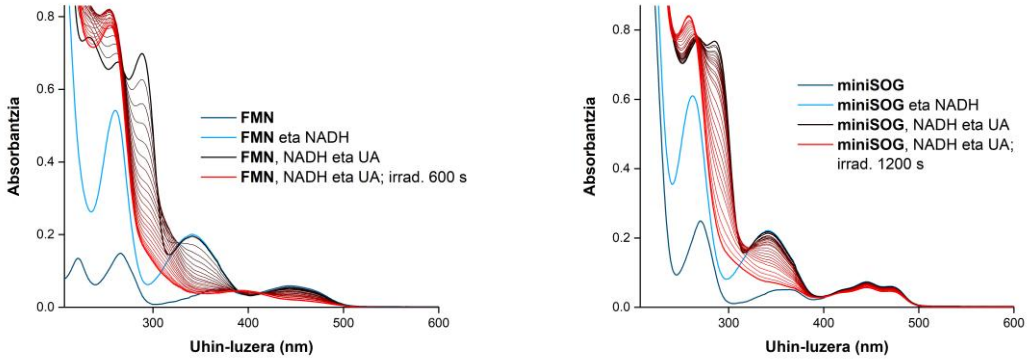

(c)

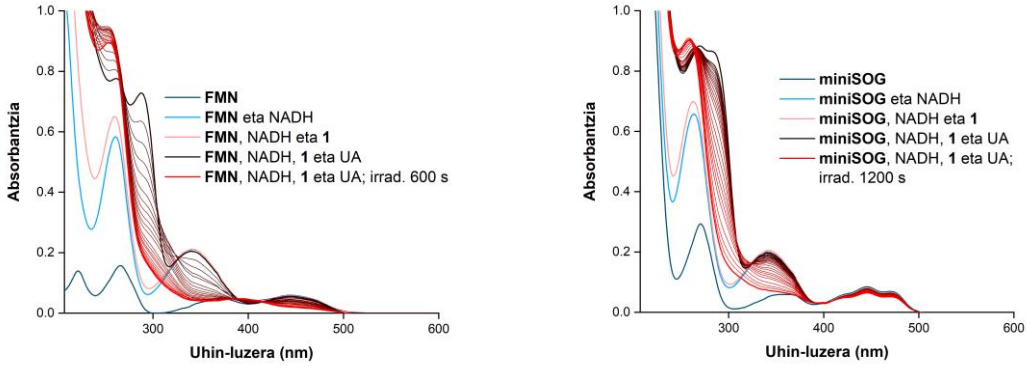

IO 52. Irudia. FMN eta **miniSOG** katalizatzaileen oxigeno singlete sorkuntza, azido urikoa (UA) zunda moduan erabiliz. Opktikoki bat egindako 5 µM **FMN** and **miniSOG** soluzioen aldakuntza espektralak 460 nm-ko irradiazioaren menpe (6 $mW \cdot cm^{-2}$) (a) 50 µM UA-ren, (b) 50 µM UA-ren eta 30 µM NADH-ren, eta (c) 50 µM UA-ren, 30 µM NADH-ren eta 15 µM **1**-ren presentzian.

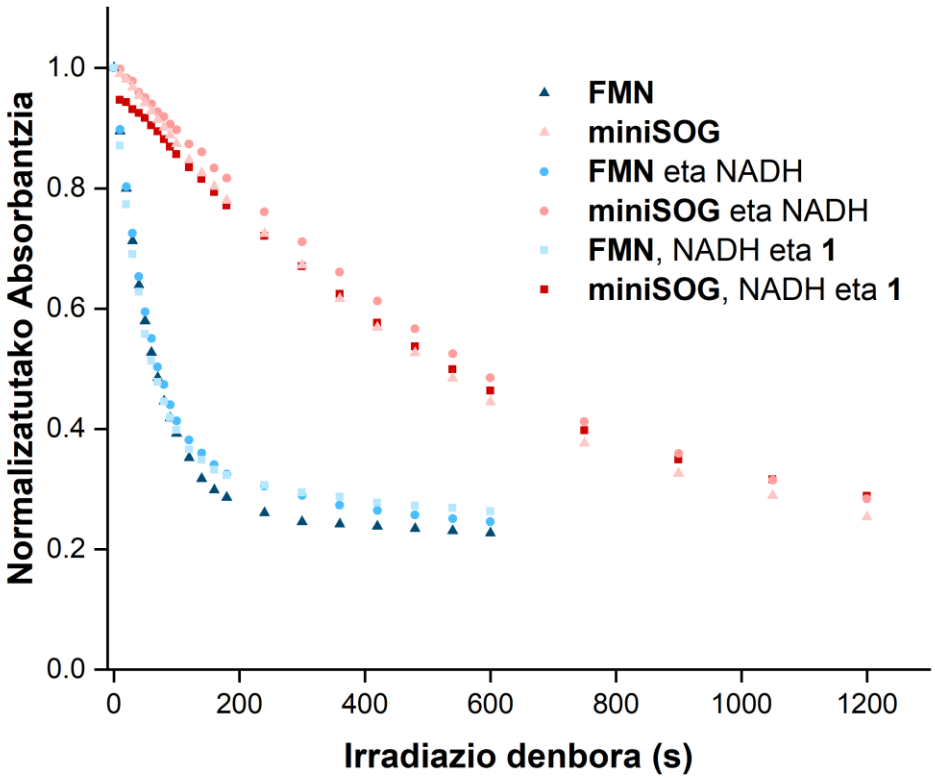

IO 53. Irudia. Azido urikoaren (UA) zuritze abiaduraren alderatzea 292 nm-tan, optikoki bat egindako 5 µM **FMN**-ren (urdina) eta **miniSOG**-ren (gorria) presentzian, baldintza ezberdinetan: (▲) 50 µM UA, (●) 50 µM UA eta 30 µM NADH, eta (■) 50 µM UA, 30 µM NADH eta 15 µM **1**.

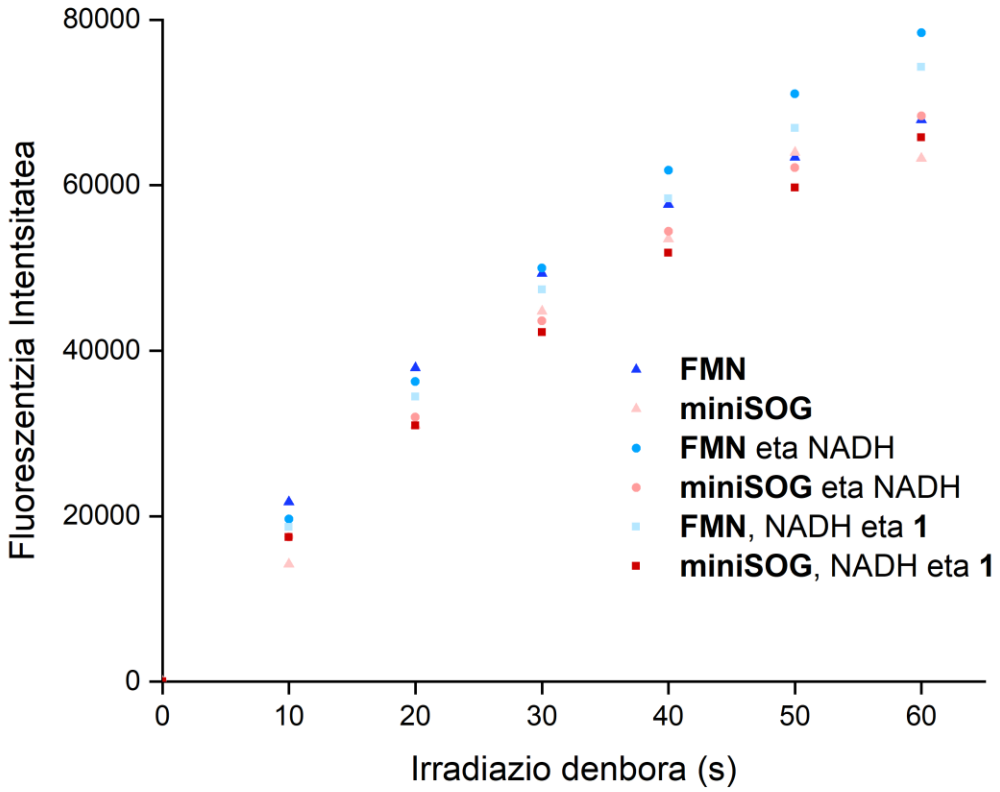

IO 54. Irudia. Argi irradiazioaren menpe, hidroetidiumaren (HE) oxidazioak sortutako produktuaren fluoreszentzia intentsitatea. HE-ren (50 µM) oxidazioa erreaktibo ezberdinen presentzian: (▲) **FMN**/**miniSOG** (5 µM), (●) **FMN**/**miniSOG** (5 µM) eta NADH (30 µM), eta (■) **FMN**/**miniSOG** (5 µM), NADH (30 µM) eta **1** (15 µM).

4. Kapituluaren Eranskina

Pt^{IV} Substratuen konbertsio Fotokatalitikoaren Hobekuntza Ingeniaritza Proteikoaren Bidez

Informazio Osagarria

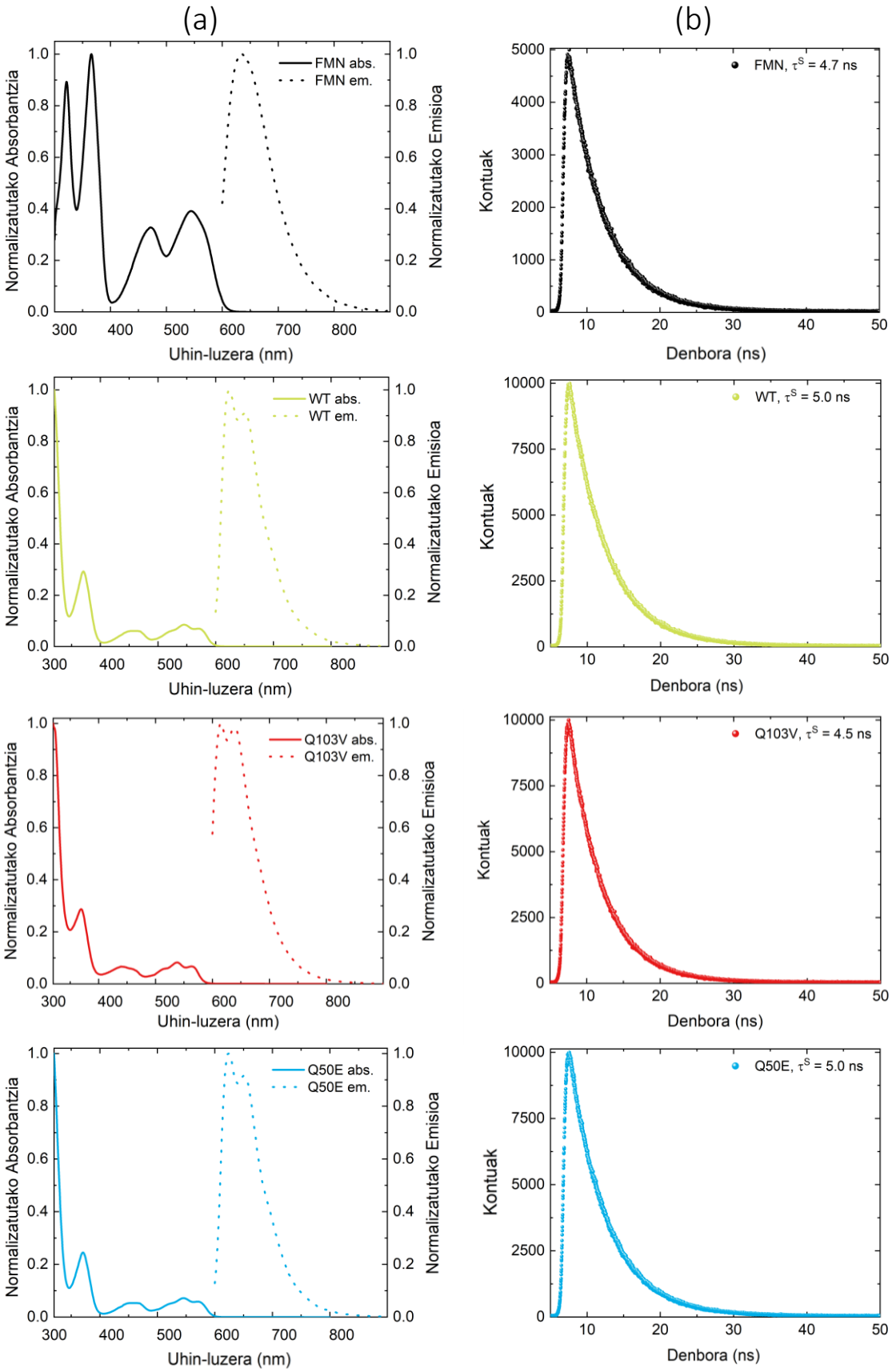
(a)
(b)
FMN abs.
FMN em.
Normalizatutako Absorbantzia
Normalizatutako Emisioa
Uhin-luzera (nm)
FMN, τS = 4.7 ns
Kontuak
Denbora (ns)
WT abs.
WT em.
WT, τS = 5.0 ns
Q103V abs.
Q103V em.
Q103V, τS = 4.5 ns
Q50E abs.
Q50E em.
Q50E, τS = 5.0 ns

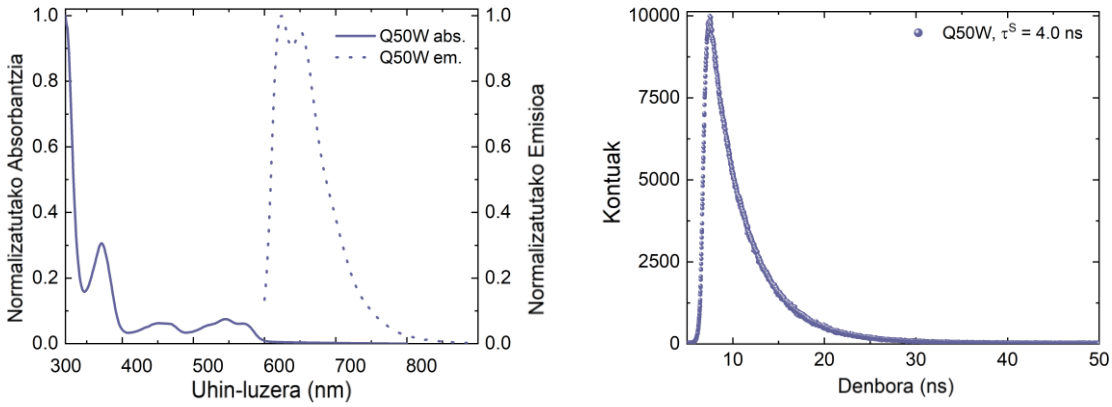

IO 1. Irudia. (a) Absortzio eta Emisio espektroak (λ_{kitz} = 450 nm) eta (b) O_2-ren presentzian, FMN, miniSOG WT, Q103V, Q50E eta Q50W mutanteen fluoreszentzia beheraldi kurbak (τ^S, λ_{kitz} = 485 nm, λ_{em} = 520 nm). Egoera egonkorra eta bizitza-denbora neurketak egiteko 3 and 6 µM miniSOG katalizatzaileen disoluzioak (PB, 20 mM, pH 7) erabili ziren hurrenez hurren. FMN-ren kasuan 15 µM-eko disoluzioa erabili zen.

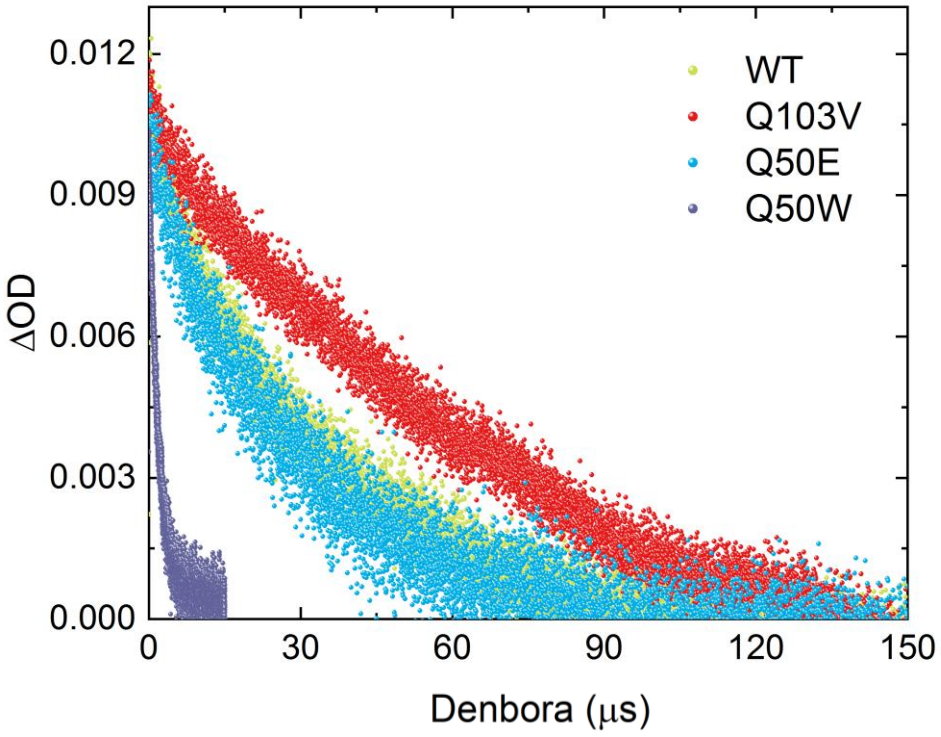

IO 2. Irudia. miniSOG WT eta mutanteen triplete−triplete absrotzioaren beheraldia (τ^T) 720 nm-tan. Neurketa guztiak PB disoluzio indargetzailean (20 mM, pH 7, air-saturated) egin ziren, 20 µM miniSOG proteina erabiliz.

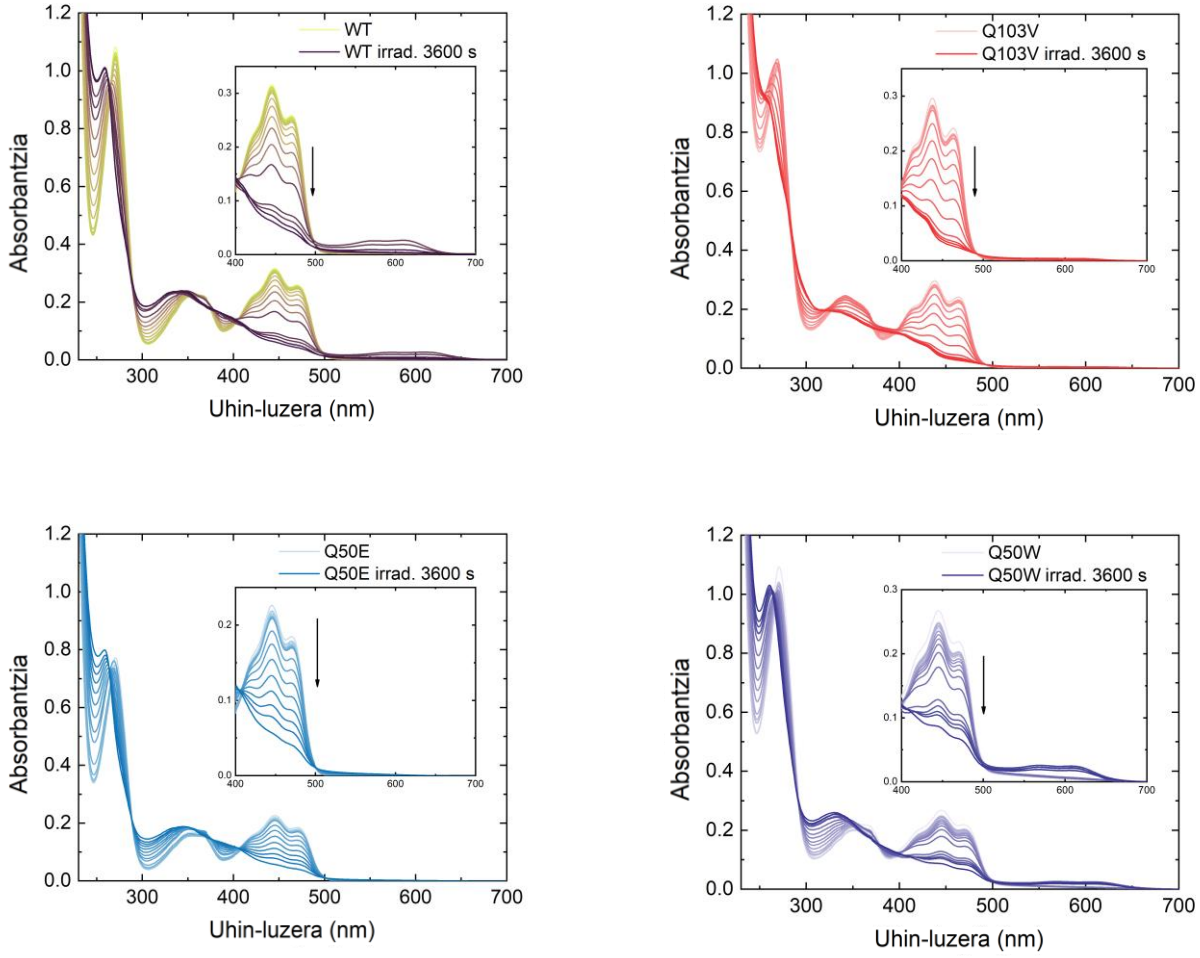

IO 3. Irudia. miniSOG katalizatzaileen fotoegonkortasuna (15 µM) PB disoluzioan (20 mM, pH 7) argi urdinaren irradiazioaren menpe (460 nm, 6 $mW \cdot cm^{-2}$).

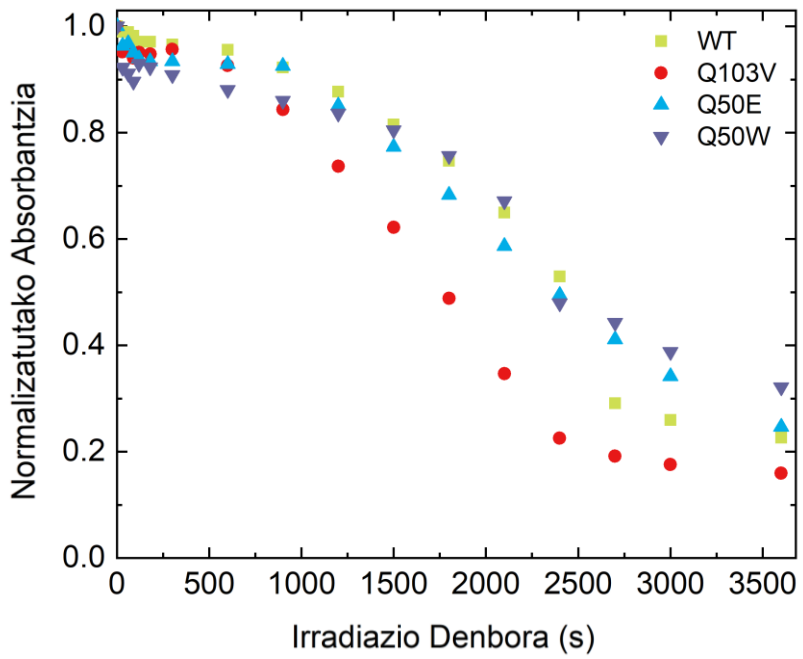

IO 4. Irudia. miniSOG katalizatzaileen (15 µM) fotoegonkortasun profilak (20 mM PB disoluzioan, pH 7) argi urdinaren irradiazioaren menpe (460 nm, 6 mW·cm^{-2}).Datuak, 450 nm-tan absorbantzia jaitsiera jarraituz lortu ziren.

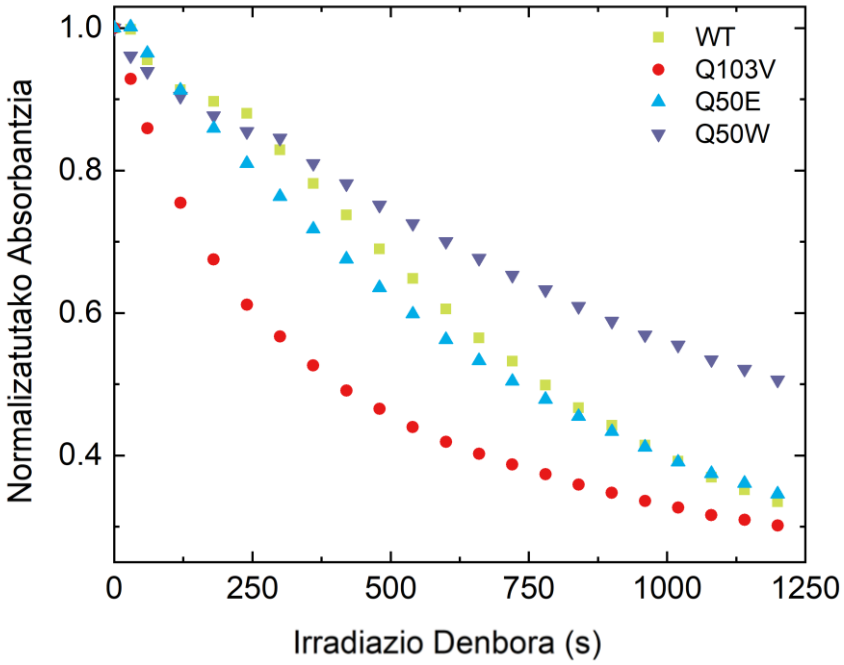

IO 5. Irudia. miniSOG katalizatzaileen (3 µM) oxigeno singlete sorkuntza neurketak, argi urdinaren irradiazioaren menpe (460 nm, 6 mW·cm^{-2}). Azido urikoa (UA, 30 µM) zunda moduan erabili zen zeharkako neurketa hauek egiteko.

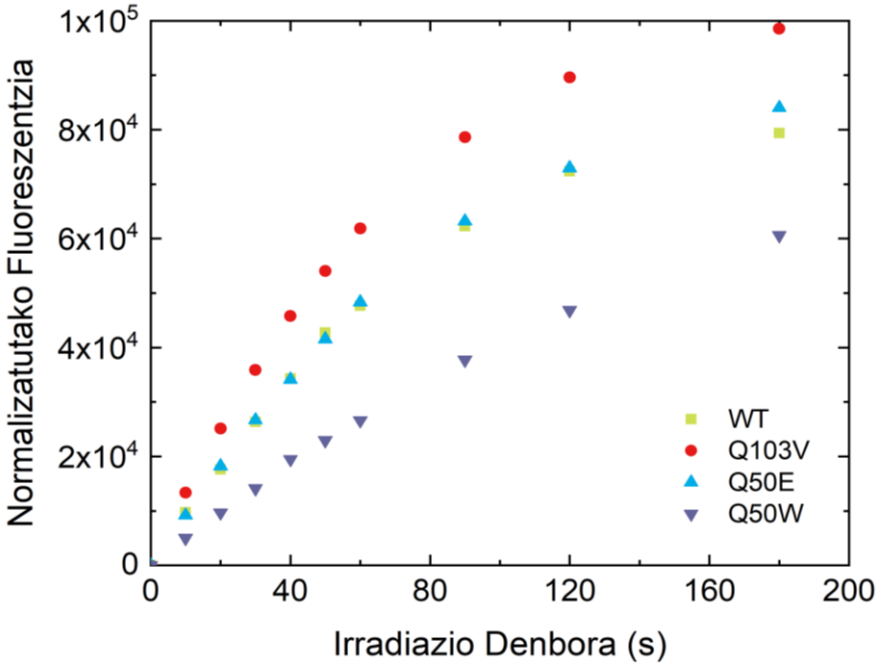

IO 6. Irudia. miniSOG katalizatzaileen (3 µM) ROS produkzioa argi irradiazioaren menpe (460 nm, 6 mW·cm$^{-2.}$) Zeharkako neurketa hau, hidroetidino (HE, 30 µM) oxidazio produktuaren fluoreszentzia (λ_{kitz} 525 nm, λ_{em} 550–800 nm) jarraituz egin zen.

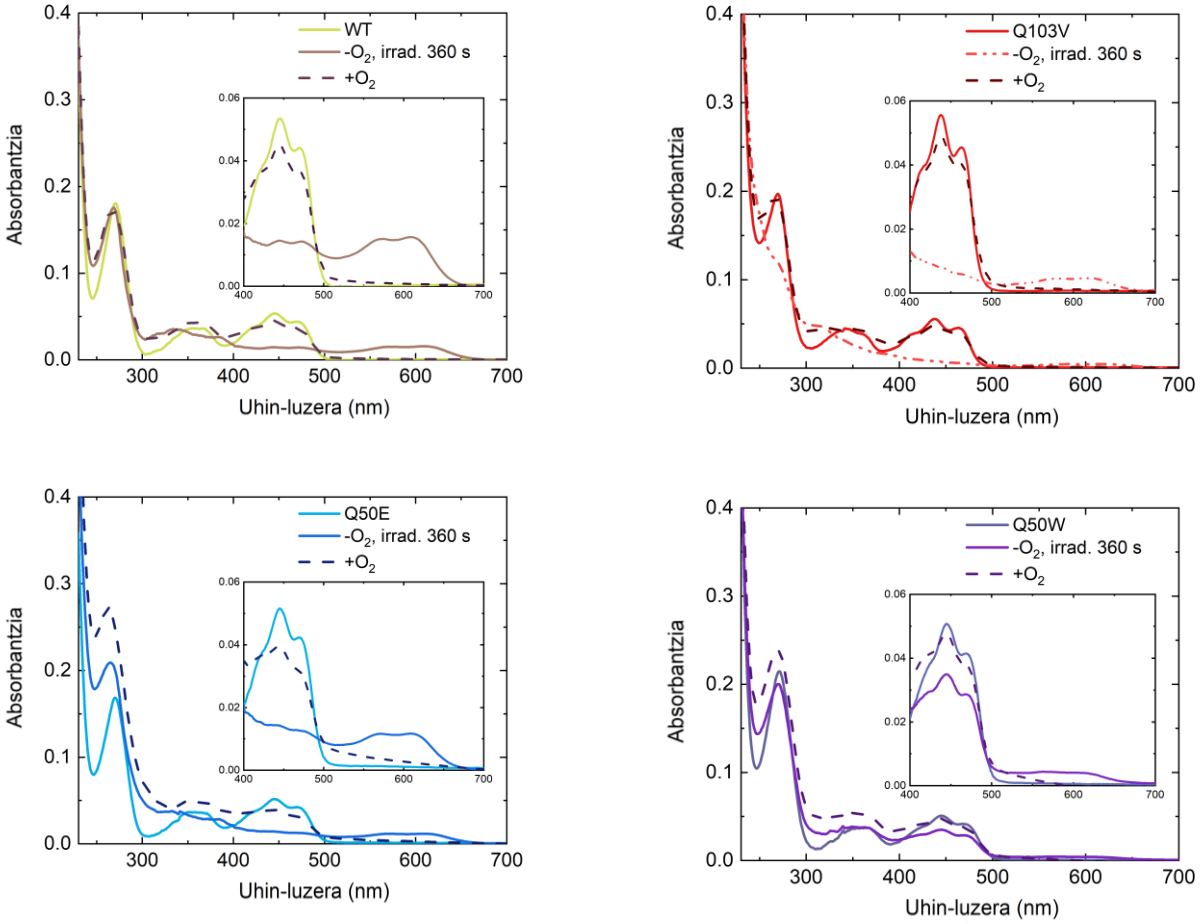

IO 7. Irudia. miniSOG katalizatzaileen fotoegonkortasuna (3 µM) PB disoluzioan (20 mM, pH 7) argi urdinaren irradiazioaren menpe (460 nm, 6 $mW \cdot cm^{-2}$) eta O_2-rik gabe. Argi irradiazioaren ondoren, laginak oxigenoa zuen atmosfera baten menpe jarri ziren semikinona desagerpena jarraitzeko (marra etena).

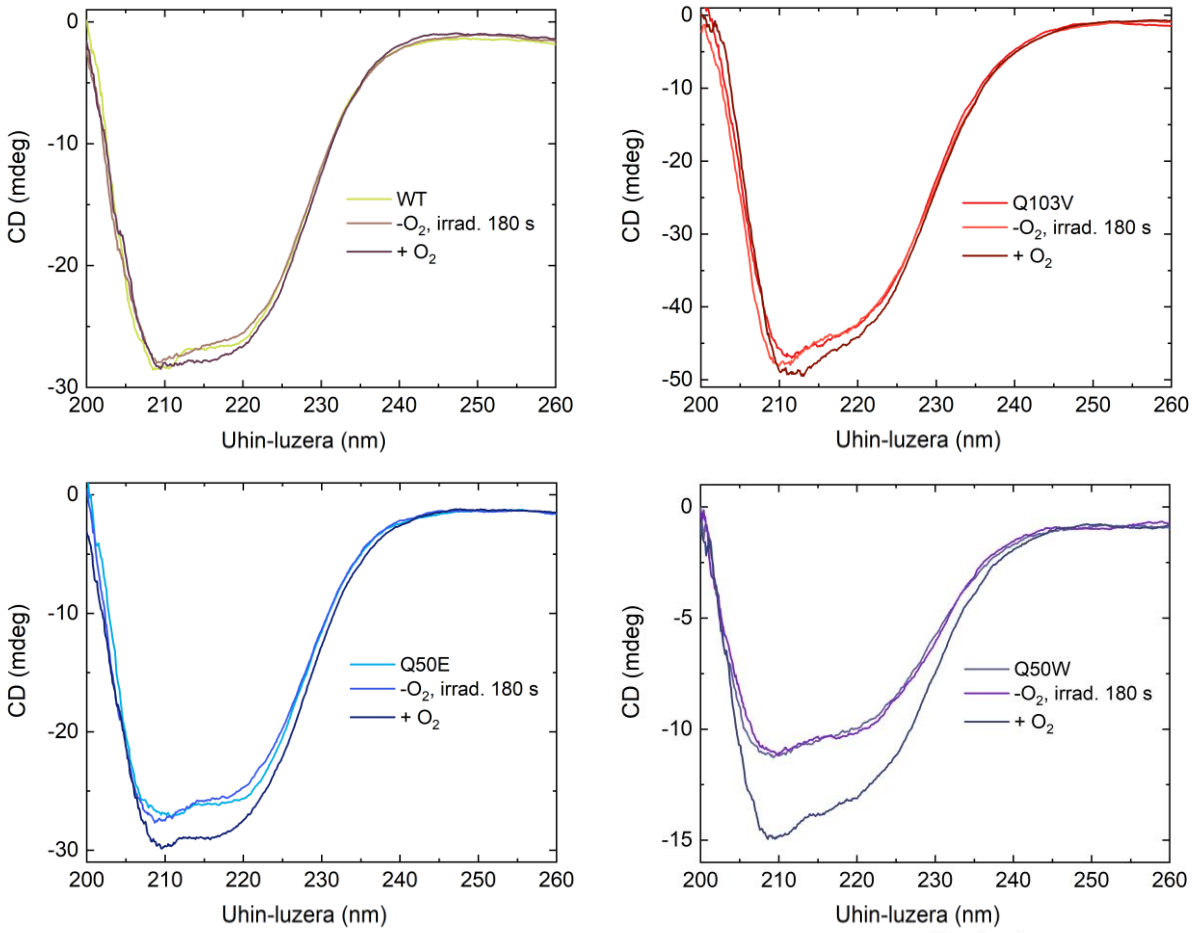

IO 8. Irudia. miniSOG laginen (3 µM) dikroismo zirkularra PB (20 mM, pH 7) disoluzio indargetzailean, O_2-rik gabe 180 segundu irradiatu (460 nm, 6 $mW \cdot cm^{-2}$) ondoren.

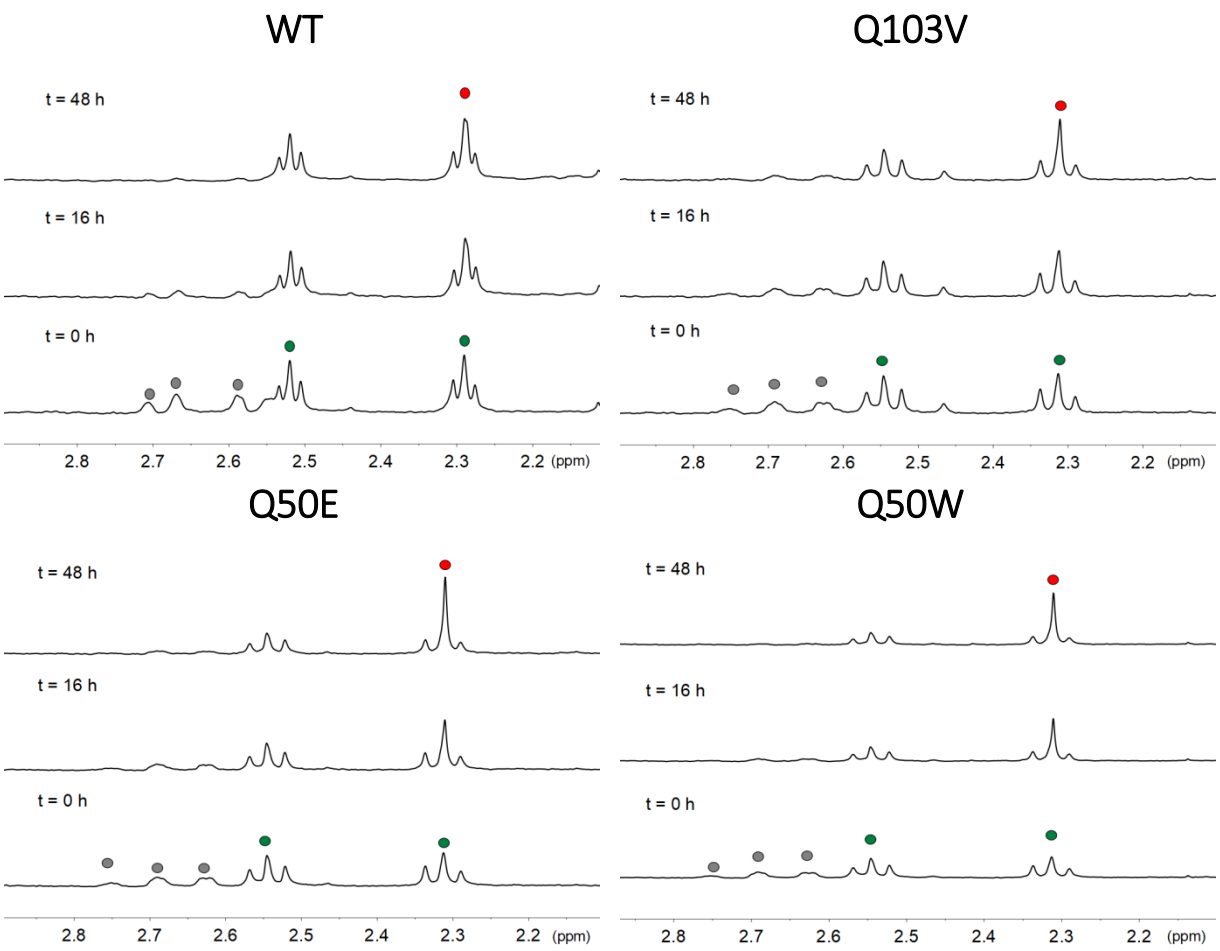

IO 9. Irudia. **1** Konplexuaren (500 µM) egonkortasuna 48 orduz ilunpetan 18 mM PB (pH 7.0, % 10 D_2O) disoluzioan, 1 mM NADH-ren eta 25 µM miniSOG proteina ezberdinen presentzian.
^{1}H NMR seinaleen etiketak: ● NADH; **1**: ● Pt–OCO**CH$_2$**CH$_2$CO$_2^-$, ● Pt–OCOCH$_2$**CH$_2$**CO$_2^-$; ● $^-$O$_2$CCH$_2$CH$_2$CO$_2^-$ askea.
.

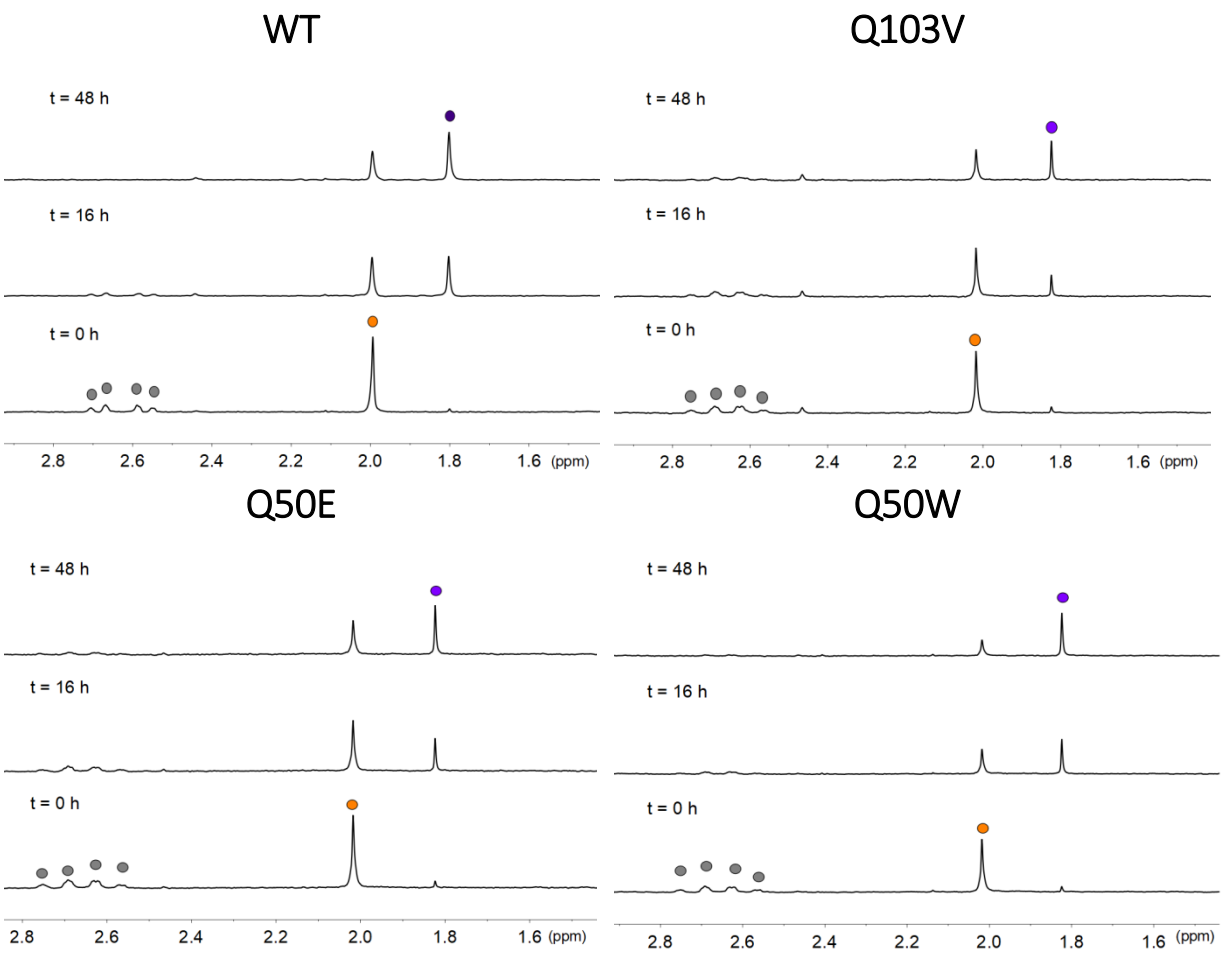

IO 10. Irudia. **2** Konplexuaren (500 µM) egonkortasuna 48 orduz ilunpetan 18 mM PB (pH 7.0, % 10 D_2O) disoluzioan, 1 mM NADH-ren eta 25 µM miniSOG proteina ezberdinen presentzian.
^{1}H NMR seinaleen etiketak: ● NADH; **2**: ● Pt–OCO**CH$_3$**; ● $^-$OCO**CH$_3$** askea.

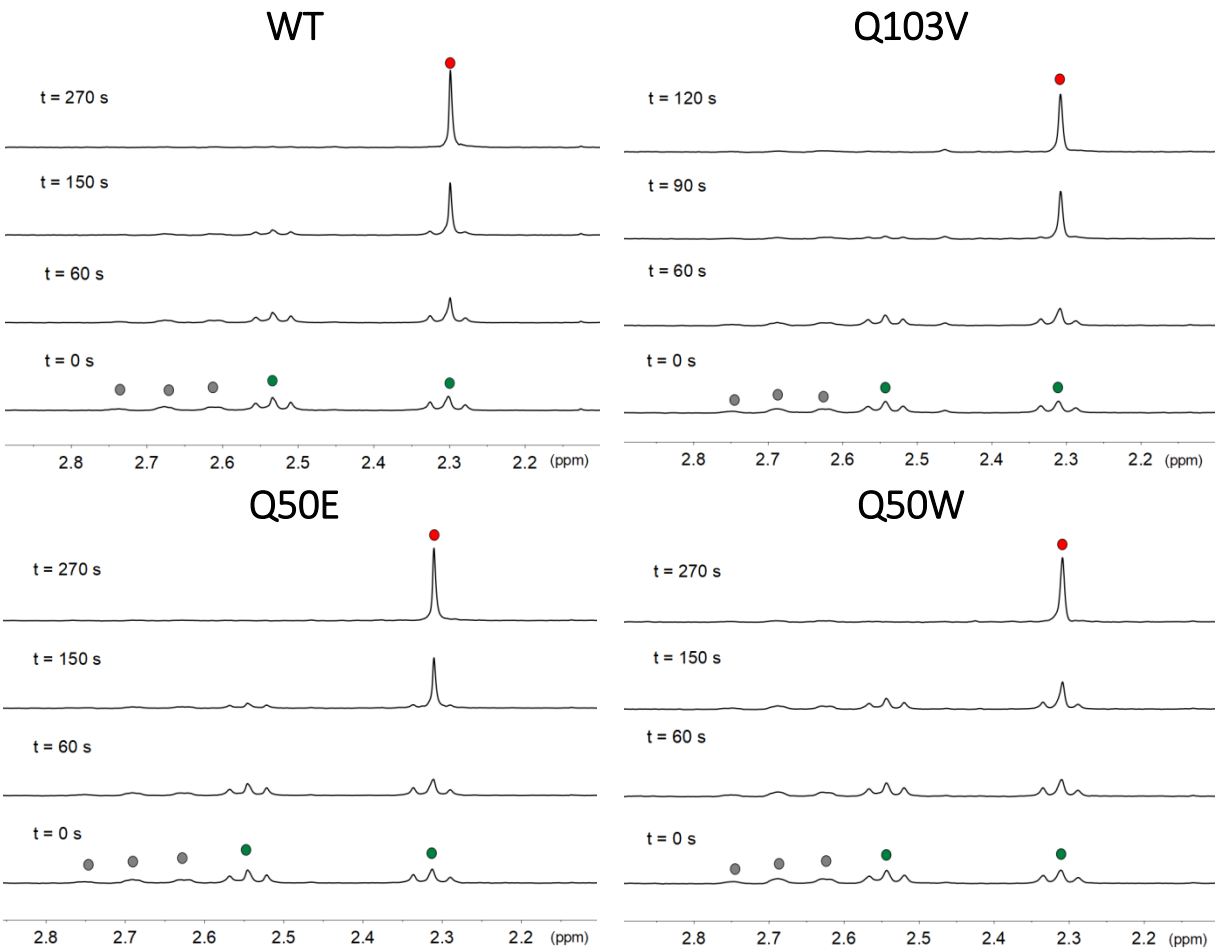

IO 11. Irudia. **1** konplexuaren (500 µM) aktibazio fotokatalitikoa 18 mM PB (pH 7.0, % 10 D_2O) disoluzioan, 1mM NADH-ren eta 25 µM miniSOG proteina ezberdinen presentzian, 460 nm-ko argi irradiazioaren menpe (6 $mW{\cdot}cm^{-2}$). ^1H NMR seinaleen etiketak: ● NADH; **1**: ● Pt–OCO**CH_2**$CH_2CO_2^-$, ● Pt–OCOCH_2**CH_2**CO_2^-; ● $^-O_2CCH_2CH_2CO_2^-$ askea.

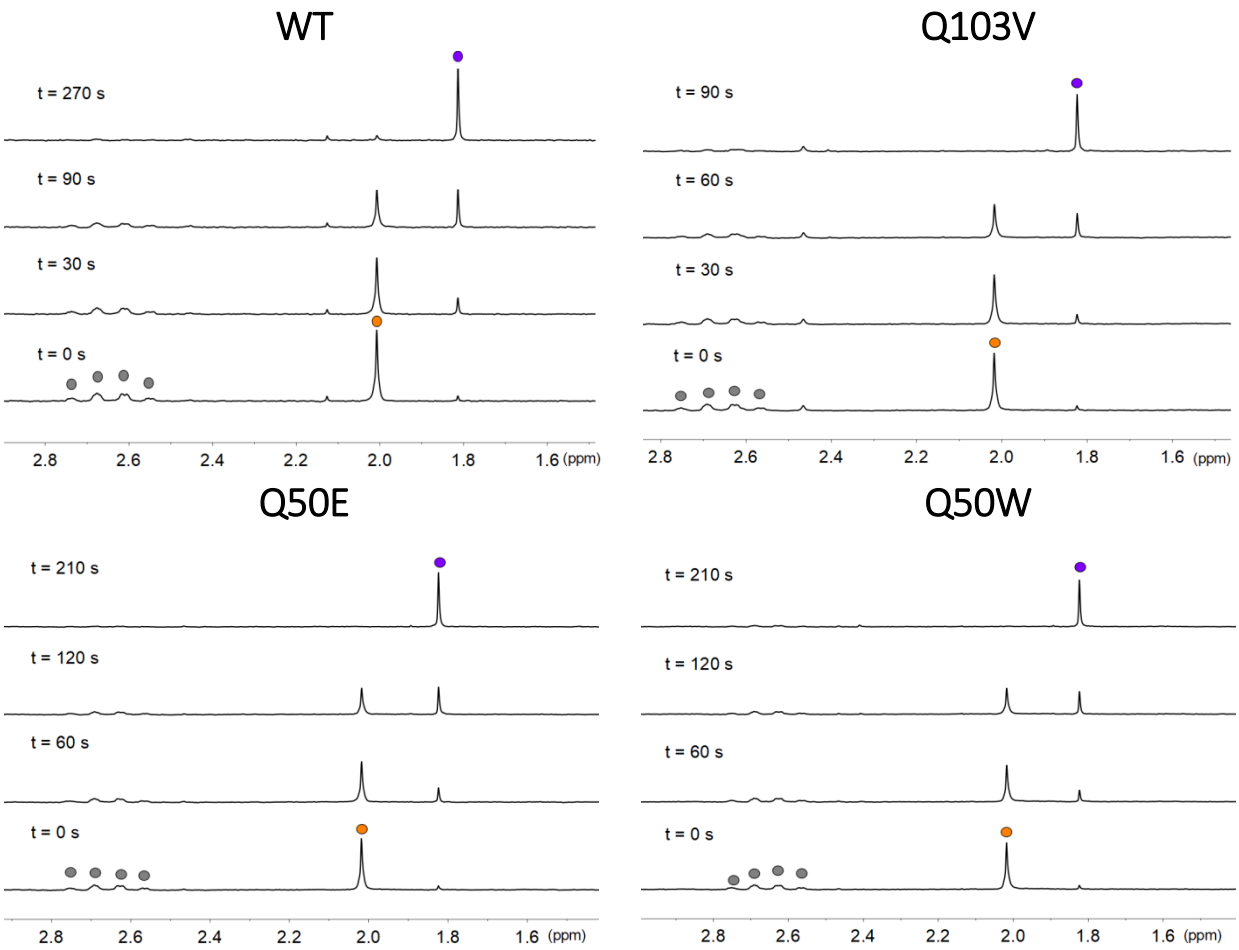

IO 12. Irudia. **2** konplexuaren (500 µM) aktibazio fotokatalitikoa 18 mM PB (pH 7.0, % 10 D_2O) disoluzioan, 1mM NADH-ren eta 25 µM miniSOG proteina ezberdinen presentzian, 460 nm-ko argi irradiazioaren menpe (6 mW·cm^{-2}). ^{1}H NMR seinaleen etiketak: ● NADH; **2**: ● Pt–OCO**CH$_3$**; ● $^-$OCO**CH$_3$** askea.

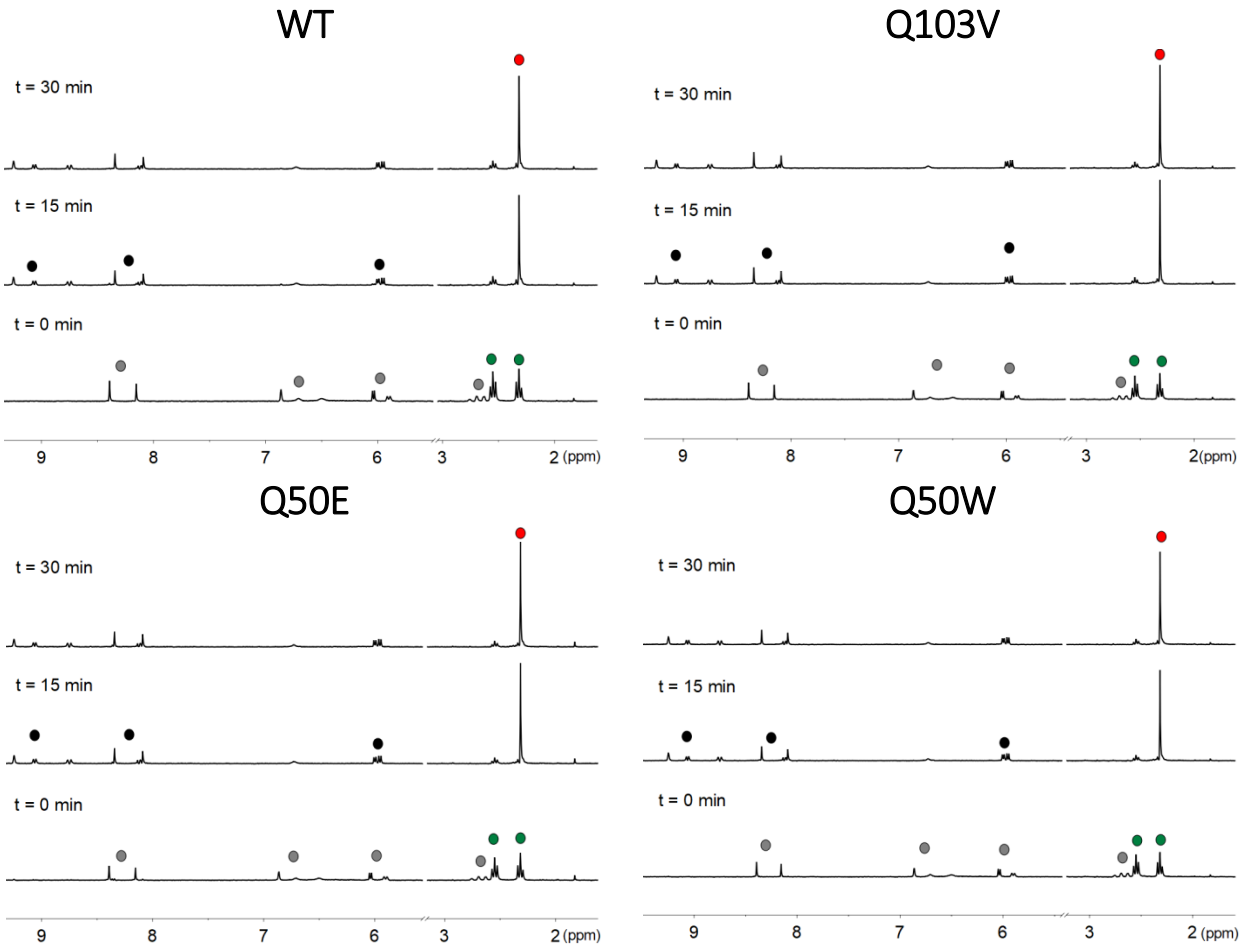

IO 13. Irudia. **1** konplexuaren (500 µM) aktibazio fotokatalitikoa 18 mM PB (pH 7.0, % 10 D_2O) disoluzioan, 1mM NADH-ren eta 1 µM miniSOG proteina ezberdinen presentzian, 460 nm-ko argi irradiazioaren menpe (6 $mW{\cdot}cm^{-2}$). ^1H NMR seinaleen etiketak: ● NADH; ● NAD^+; **1**: ● Pt–OCO**CH_2**$CH_2CO_2^-$, ● Pt–OCOCH_2**CH_2**CO_2^-; ● $^-O_2CCH_2CH_2CO_2^-$ askea.

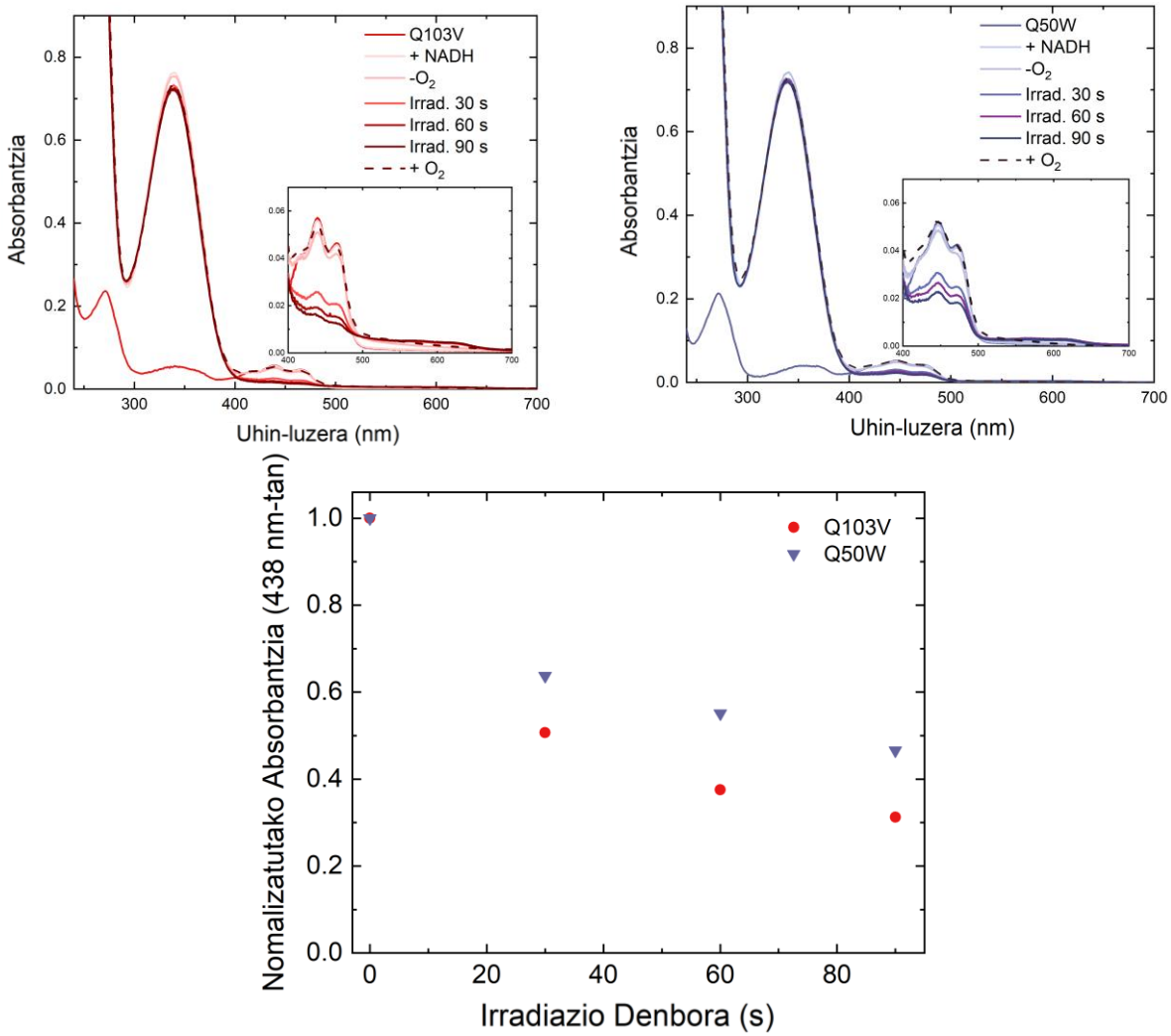

IO 14. Irudia. Q103V eta Q50W mutanteen (3 µM) argiztapena (460 nm, 6 mW·cm^{-2}) PB disoluzio indargetzailean, NADH-ren (120 µM) presentzian eta oxigenorik gabe. Argi irradiazioaren ondoren, laginak oxigenoa zuen atmosfera baten menpe jarri ziren semikinona desagerpena jarraitzeko (marra etena).

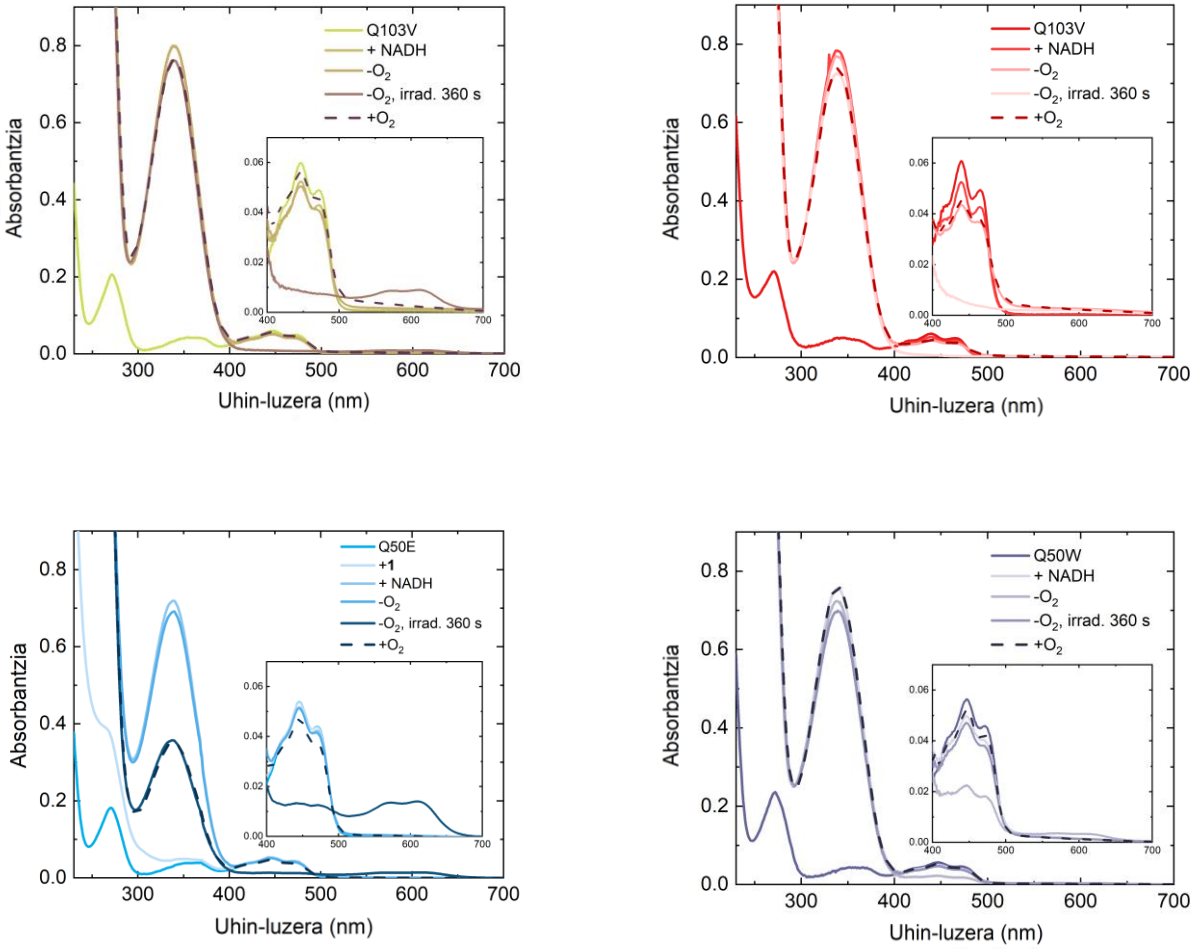

IO 15. Irudia. miniSOG katalizatzaileen fotoegonkortasuna (3 µM) argi urdinaren menpe (460 nm, 6 $mW \cdot cm^{-2}$), PB disoluzio indargetzailean, NADH-ren (120 µM) presentzian eta oxigenorik gabe. Argi irradiazioaren ondoren, laginak oxigenoa zuen atmosfera baten menpe jarri ziren semikinona desagerpena jarraitzeko (marra etena).

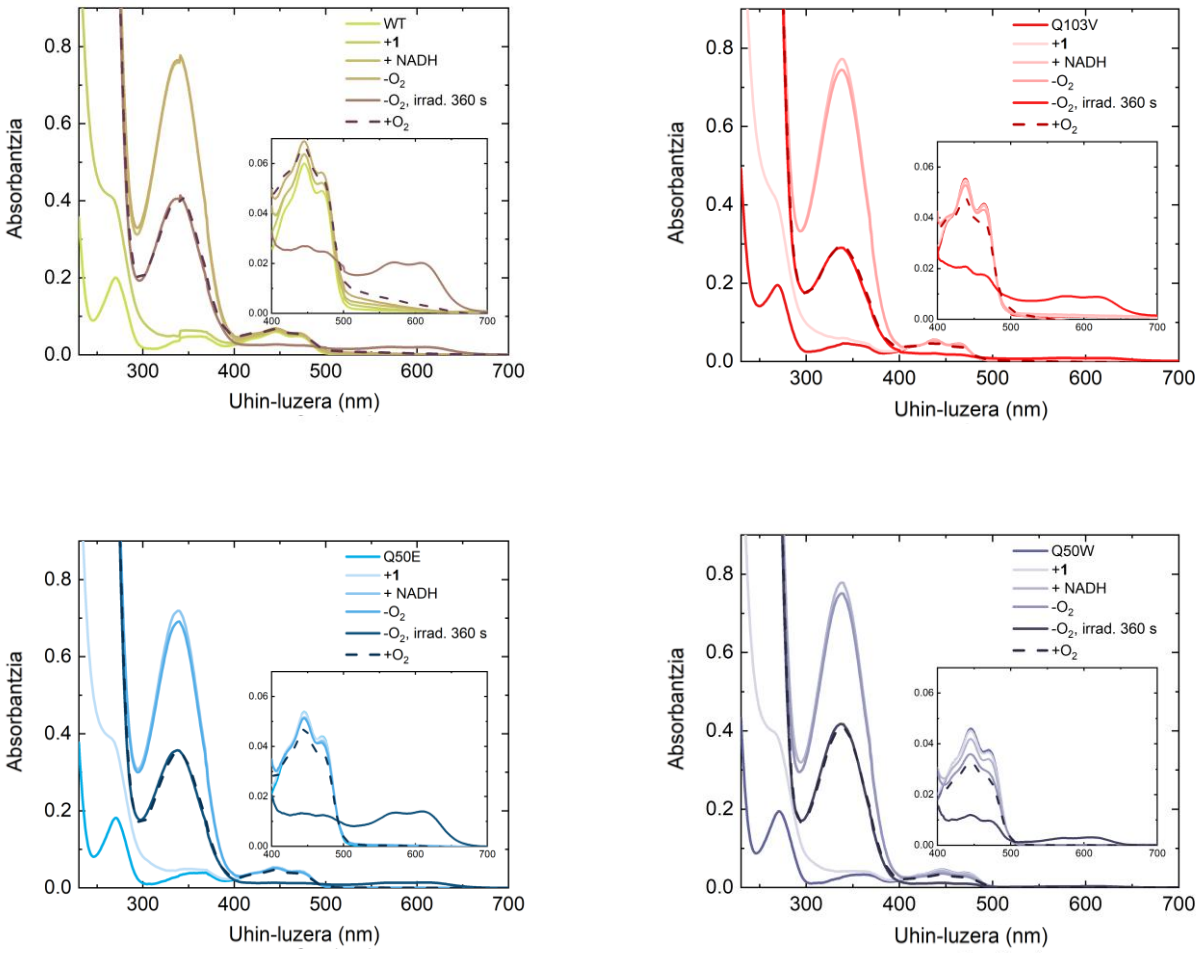

IO 16. Irudia. miniSOG katalizatzaileen fotoegonkortasuna (3 µM) argi urdinaren menpe (460 nm, 6 mW·cm^{-2}), PB disoluzio indargetzailean, NADH-ren (120 µM) eta **1** konplexuaren (60 µM) presentzian eta oxigenorik gabe. Argi irradiazioaren ondoren, laginak oxigenoa zuen atmosfera baten menpe jarri ziren semikinona desagerpena jarraitzeko (marra etena).

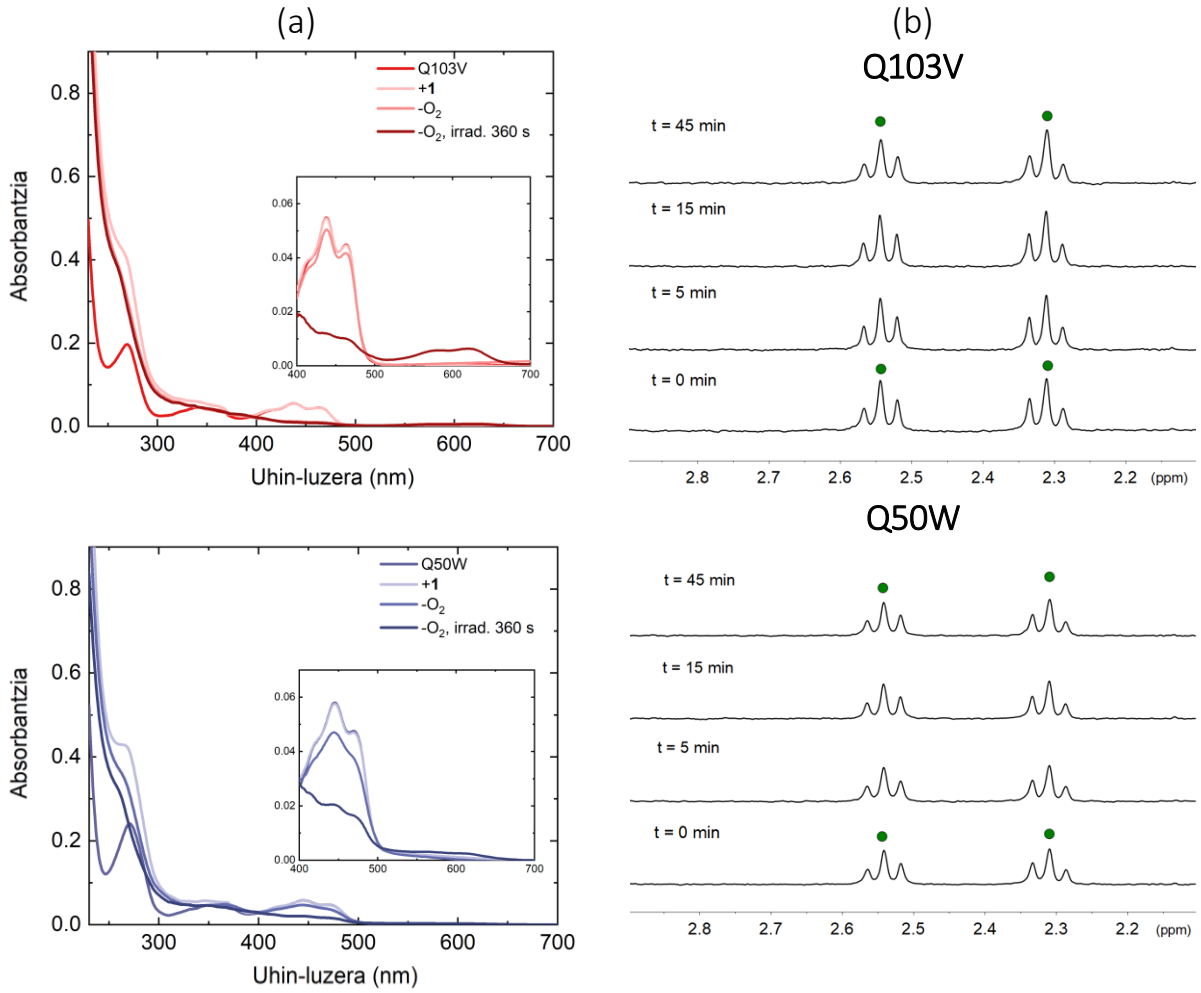

IO 17. Irudia. (a) Q103V eta Q50W muntanteen fotoegonkortasuna (3 µM) argi urdinaren menpe (460 nm, 6 mW·cm^{-2}), PB disoluzio indargetzailean (20 mM, pH 7), **1** konplexuaren (60 µM) presentzian eta oxigenorik gabe. (b) **1** konplexuaren fotoegonkortasuna PB disoluzio indargetzailean 25 µM Q103V eta Q50W mutanteen presentzia denboran zehar. ^{1}H NMR seinaleen etiketak: **1**: ● Pt–OCO**CH$_2$**CH$_2$CO$_2^-$, ● Pt–OCOCH$_2$**CH$_2$**CO$_2^-$.

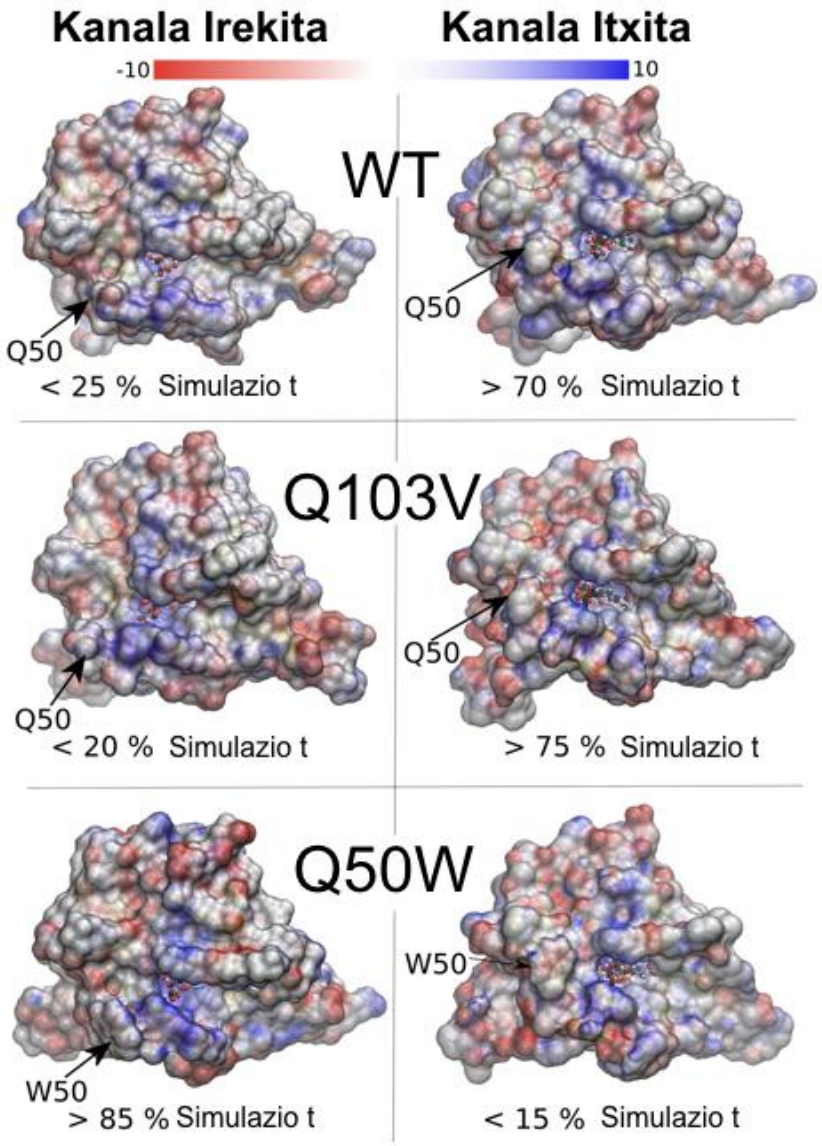

IO 18. Irudia. Itxita eta irekita konformazioetan disolbatzailearentzat eskuragarri dagoen miniSOG mutanteen gainazala, potentzial elektrostatikoaren arabera margotuta ($\pm$ 10 kT/e), eta konformazio bakoitzean egondako denbora %-a.

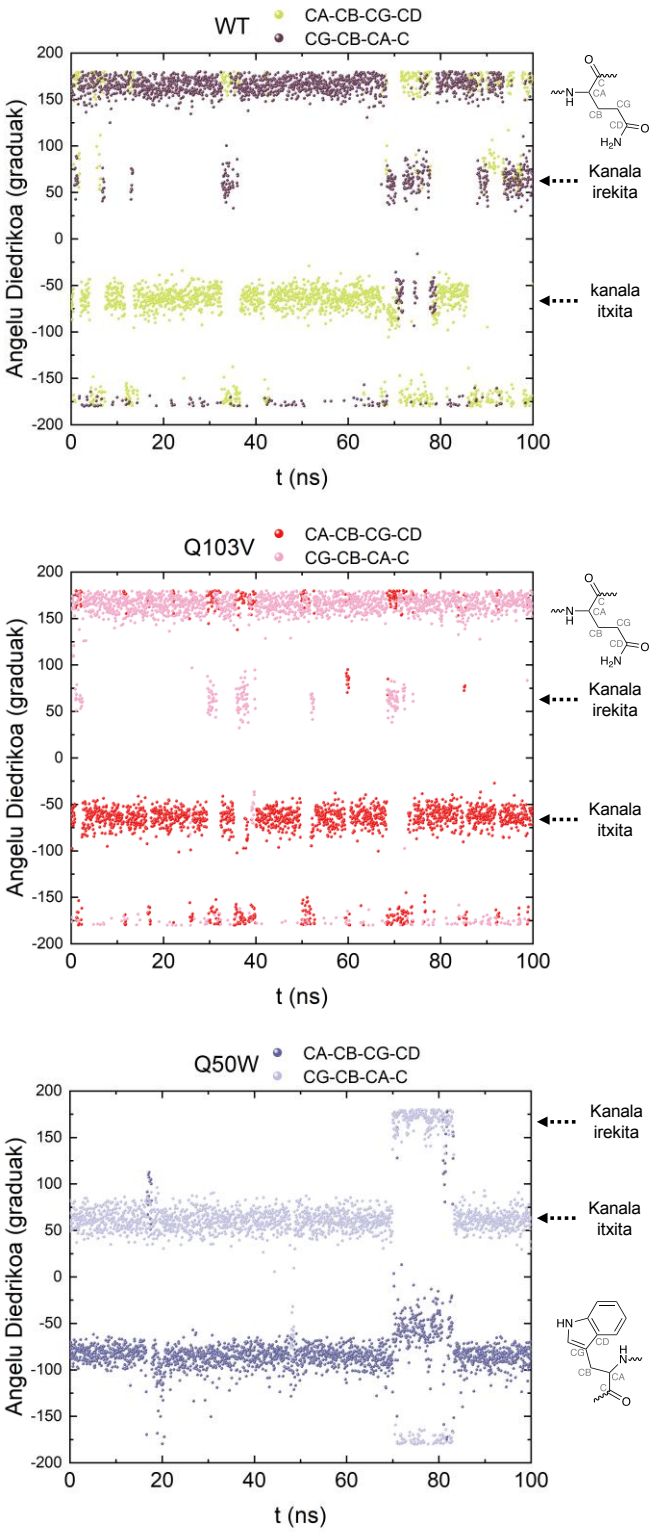

IO 19. Irudia. 50 hondakinaren angelu driedrikoen irudikapena simulazio denboraren arabera. miniSOG proteinaren konformazio kanal irekita eta itxita angelu diedrikoen balioen arabera zehaztu ziren.

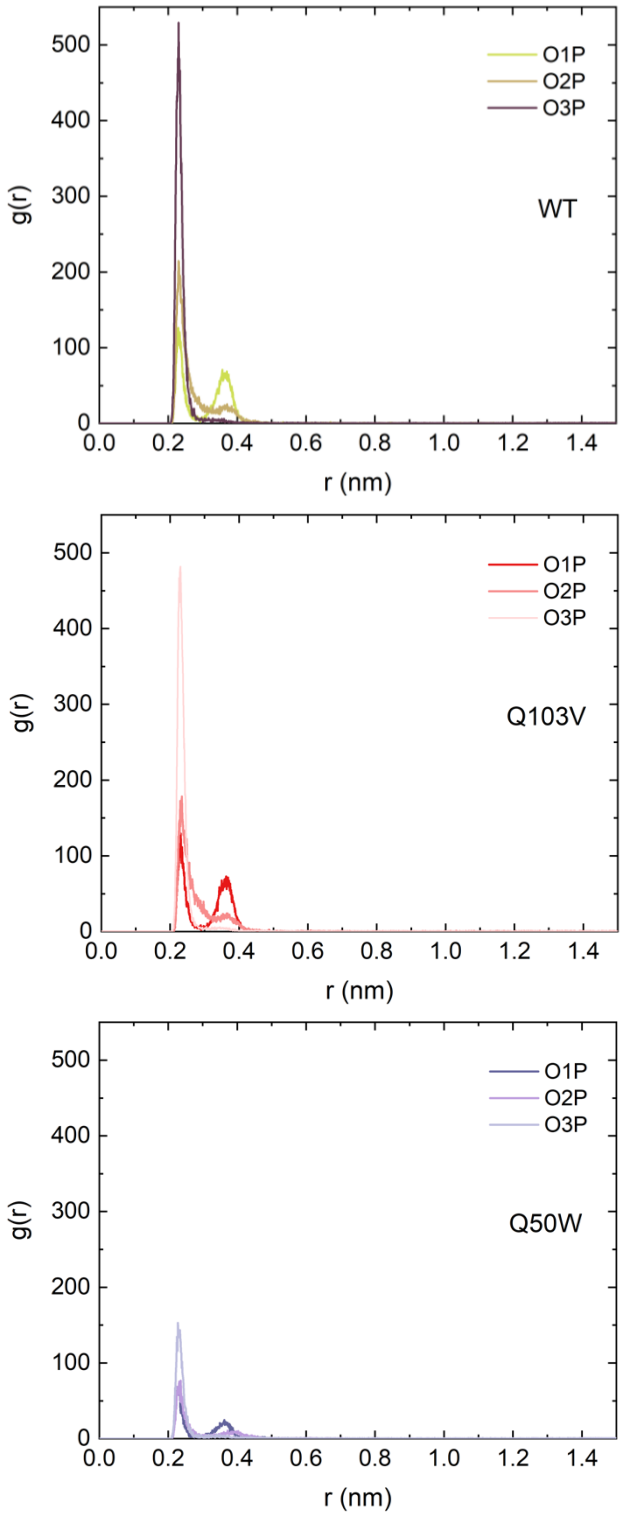

IO 20. Irudia. Fosfato taldearen oxigenoen inguruan Na^+ katioien distribuzio funtzio erradiala (i.e. Na^+ katioiak fosfatoaren oxigenoetatik r distantziara aurkitzeko probabilitate distribuzioa).

DIPC

CIC biomaGUNE

Biomaterialetako Ikerkuntza kooperatiboko Zentroa

Center for Cooperative Research in Biomaterials

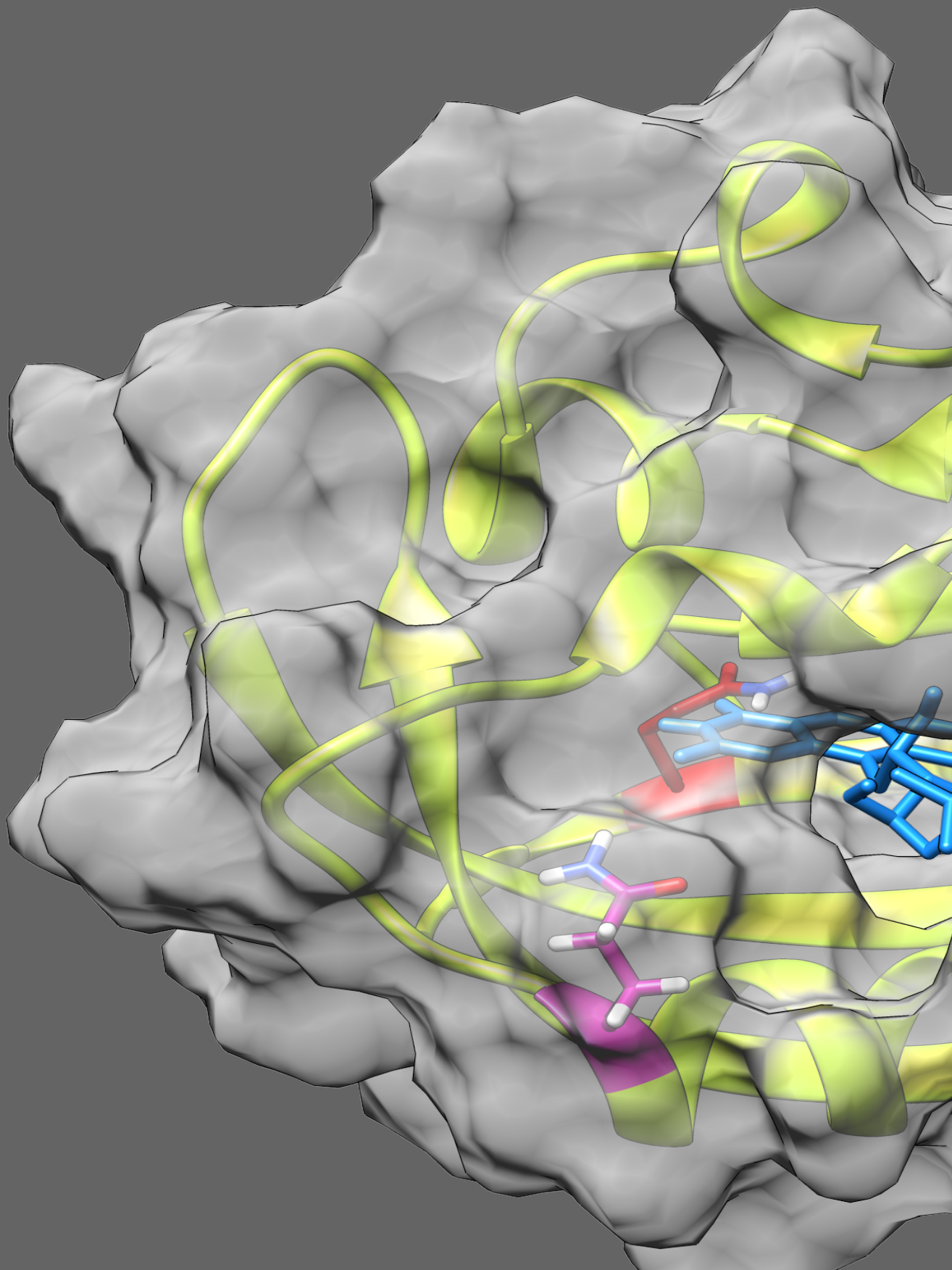

eman ta zabal zazu

UPV EHU